Electrochemistry and catalytic reactions editor's pick
2024

Edited by
Tomas Ramirez Reina and Nosang Vincent Myung

About Frontiers

Frontiers is more than just an open access publisher of scholarly articles: it is a pioneering approach to the world of academia, radically improving the way scholarly research is managed. The grand vision of Frontiers is a world where all people have an equal opportunity to seek, share and generate knowledge. Frontiers provides immediate and permanent online open access to all its publications, but this alone is not enough to realize our grand goals.

Frontiers journal series

The Frontiers journal series is a multi-tier and interdisciplinary set of open-access, online journals, promising a paradigm shift from the current review, selection and dissemination processes in academic publishing. All Frontiers journals are driven by researchers for researchers; therefore, they constitute a service to the scholarly community. At the same time, the *Frontiers journal series* operates on a revolutionary invention, the tiered publishing system, initially addressing specific communities of scholars, and gradually climbing up to broader public understanding, thus serving the interests of the lay society, too.

Dedication to quality

Each Frontiers article is a landmark of the highest quality, thanks to genuinely collaborative interactions between authors and review editors, who include some of the world's best academicians. Research must be certified by peers before entering a stream of knowledge that may eventually reach the public – and shape society; therefore, Frontiers only applies the most rigorous and unbiased reviews. Frontiers revolutionizes research publishing by freely delivering the most outstanding research, evaluated with no bias from both the academic and social point of view. By applying the most advanced information technologies, Frontiers is catapulting scholarly publishing into a new generation.

What are Frontiers Research Topics?

Frontiers Research Topics are very popular trademarks of the *Frontiers journals series*: they are collections of at least ten articles, all centered on a particular subject. With their unique mix of varied contributions from Original Research to Review Articles, Frontiers Research Topics unify the most influential researchers, the latest key findings and historical advances in a hot research area.

Find out more on how to host your own Frontiers Research Topic or contribute to one as an author by contacting the Frontiers editorial office: frontiersin.org/about/contact

Electrochemistry and catalytic reactions editor's pick 2024

Topic editors

Tomas Ramirez Reina — University of Seville, Spain

Nosang Vincent Myung — University of Notre Dame, United States

Table of
contents

Check for updates

Chemical doping of unsubstituted perylene diimide to create radical anions with enhanced stability and tunable photothermal conversion efficiency

Canyan Che[1†], Shaohua Tong[1†], Yanhua Jia[1], Jiaji Yang[1], Xiandong He[1], Shaobo Han[2], Qinglin Jiang[1] and Yuguang Ma[1]*

[1]State Key Laboratory of Luminescent Materials and Devices, Institute of Polymer Optoelectronic Materials and Devices, South China University of Technology, Guangzhou, China, [2]School of Textile Materials and Engineering, Wuyi University, Jiangmen, China

N-doping of perylene diimides (PDIs) to create stable radical anions is significant for harvesting photothermal energy due to their intensive absorption in the near-infrared (NIR) region and non-fluorescence. In this work, a facile and straightforward method has been developed to control the doping of perylene diimide to create radical anions using organic polymer polyethyleneimine (PEI) as a dopant. It was demonstrated that PEI is an effective polymer-reducing agent for the n-doping of PDI toward the controllable generation of radical anions. In addition to the doping process, PEI could suppress the self-assembly aggregation and improve the stability of PDI radical anions. Tunable NIR photothermal conversion efficiency (maximum 47.9%) was also obtained from the radical-anion-rich PDI-PEI composites. This research provides a new strategy to tune the doping level of unsubstituted semiconductor molecules for varying yields of radical anions, suppressing aggregation, improving stability, and obtaining the highest radical anion-based performance.

KEYWORDS

controllable doping, perylene diimide, radical anion, stability, photothermal conversion

1 Introduction

Perylene diimide (PDI) and its derivatives (PDIs) are among the most popular organic dyes and pigments. They are also excellent n-type organic semiconductors with high molecular absorption coefficients, high electronic affinity, high electron mobility, and good photothermal stability (Hu et al., 2021). Radical anions or dianions of PDIs can be easily generated *via* one-electron transfer or two-electron transfer pathways under chemical, electrochemical, or light/thermal-induced reduction. PDI radical anions feature intensive NIR light absorption and photo-energy conversion into heat *via* non-radiative relaxation pathways such as molecular vibrations (Jiao et al., 2015; Yang et al., 2017; Zhang et al., 2018; Yang and Chen, 2019), which makes them promising photothermal materials. Thanks to these features, PDIs' radical anions are widely used as optoelectronic materials in the fields of solar cells (Zhao et al., 2018; Yao et al., 2020; Hu et al., 2021), transistors (Schmidt et al., 2009; Gao and Hu, 2014; Okamoto et al., 2020), electrochromic devices (Ma et al., 2016), thermoelectrics (Russ et al., 2014; Wu et al., 2017), photocatalysis (Ghosh et al., 2014;

Gong et al., 2018; Zhang et al., 2020), and redox flow batteries (Li et al., 2018). Among the large family of PDIs, unsubstituted PDI is the simplest model molecule that is commercially available and inexpensive. However, it is rarely used directly as a photothermal or an organic optoelectronic material due to the instability of its reduced species and strong aggregation of PDI, which result in phase separation during solution processing.

Functionalization is a fundamental strategy used to suppress aggregation, improve solubility, and enhance the stability of reduced molecules (Gao et al., 2014; Zhou et al., 2019; Golshan et al., 2020). The amino-functionalized PDIs have been demonstrated as an especially effective self-n-doping system with enhanced doping capability under mild conditions, according to Powell and Whittaker-Brooks (Powell et al., 2022; Powell and Whittaker-Brooks, 2022). However, molecular functionalization not only requires complex synthesis procedures but also reduces the content of PDI chromophore in the overall molecular weight and elicits a risk of side effects. For example, the resulting functionalized PDIs normally have a larger torsion of the planar backbone and changes in their electronic structure, such as less compact π-π stacking, which is crucial for the intermolecular charge transport along the one-dimensional (1D) π-stacking direction (Chen et al., 2007) and novel properties such as room temperature ferromagnetism (Jiang et al., 2022). Therefore, it is necessary to avoid substituents when exploring the inherent photothermal, magnetic, and optoelectronic properties of the PDI molecule itself (Dong et al., 2020).

However, the inferior solution processability and strong aggregation of neutral and n-doped PDI need to be improved. To track those issues, our group first reported an ionization strategy that employs hydrazine hydrate as a solvent and a strong reducing agent to dissolve and reduce PDI (Jiang et al., 2020; Jiang et al., 2022). As a result, a homogenous mixture of PDI and hydrazine hydrate can be obtained, and the suspension is feasible for film casting. However, only the PDI dianion could be obtained directly after the reduction process because of the strong reducing ability and the excess amount of hydrazine hydrate. PDI radical anions were produced by subsequent spontaneous oxidation of the dry film in the air.

This method has two drawbacks. First, it is a challenge to precisely control the de-doping process of dianions to form anions that can be oxidized to neutral PDI in the following spontaneous oxidation process. Second, it was risky to use the strongly carcinogenic hydrazine hydrate under high temperatures and high pressure during the hydrothermal reaction. Therefore, diluting strong reducing agents or using mild reducing agents to obtain radical anions directly is significant for the controllable generation of PDI radical anions. In another aspect, using a cationic reducing polymer is also conducive to improving the stability of PDI radical anions *via* physical encapsulation and electrostatic interaction. For example, the positively polarized moiety, cucurbit [7]uril (CB [7]), was reported to suppress the quenching of PDI radical anions *via* a supramolecular strategy (Jiao et al., 2015), and tetra cationic cyclophane (ExBox4$^+$) was found to improve the stability of radical anions *via* the surrounding Coulomb attraction and encapsulation (Jiao et al., 2019).

Polyethylenimine (PEI $(C_2H_5N)_n$) with a large number of amine groups is a mild and non-toxic polymer reducing agent that has been used widely in the reduction of noble metal nanoparticles and preparation of corresponding core-shell nanocomposites, such as Au and Ag (Zhang et al., 2013; Mulens-Arias et al., 2019; Demchenko et al., 2020). It has been proved that PEI is an effective doping agent for various organic and inorganic semiconducting materials, such as fullerene derivative (PCBM) (Dong et al., 2016), poly(benzimidazobenzophenanthroline) (BBL) (Yang et al., 2021), naphthalene diimide derivative (P(NDI2OD-T2)) (Long et al., 2017), polythiophene derivatives (PDBTAZ, PPzDPDP-BT, PDBPyBT, and PDQT) (Sun et al., 2015), carbon nanotubes (Rdest and Janas, 2021), graphite oxide (Tadjenant et al., 2020), and MoS$_2$ (Hong et al., 2017). In addition, the cationic polyelectrolyte also helps to improve the stability of reduced products *via* physical encapsulation and strong electrostatic attraction (Remant Bahadur and Uludağ, 2016). However, there is as yet no report on the doping of PEI on unsubstituted PDI or on the effect of PEI in suppressing the aggregation and stabilization of PDI radical anions.

Here, the polymer reducing agent PEI was employed for preparing PDI-PEI composites with varying doping intensity to explore new strategies for controllable doping of PDI and investigate the effect of dopants on aggregation and stability. UV-vis spectroscopy was used to characterize the doping evolution of PDI in the composite with increasing amounts of PEI and to reveal the effect of PEI on suppressing the aggregation of PDI radical anions and monomers together with field emission scanning electron microscopy. Electron paramagnetic resonance was used to demonstrate the formation of radical anions, and dynamic light scattering measurement was carried out to study the particle size of the PDI-PEI composites. The photothermal conversion efficiency of the radical-rich PDI-PEI composites was also investigated based on the amount of radical anions with tunable yield in the composite.

2 Experimental section

2.1 PDI doping

To tune the doping degree of PDI-PEI composites, 0.04 mg/mL PDI (J&K Scientific) was dispersed in N, N-dimethylformamide (DMF, 99.9%, extra dry with molecular sieves, Innochem) with various amounts of PEI (branched, Mw = 600, Energy Chemical) content, then the suspensions were mixed and treated with an ultrasonic homogenizer at the power of 540 W (JY92-IIDN, Scientz), followed by incubation at 140°C for 24 h. The mass ratio of PEI to PDI is 0.5, 1, 2, 5, 10, 20, 50, 80, 100, 200, 300, 400, 500, 800, 1,000, 2000, and 3,000, which corresponds to a PEI repeat unit/PDI molar ratio of 4.5, 9.1, 18.1, 45.3, 72.6, 90.7, 181.3, 453.6, 725.7, 907.1, 1814.3, 4,535.8, 7,257.3, 9,071.6, 18,143.2, and 27,214.7.

2.2 Characterization

UV-vis absorption measurements of the series of reacted PDI-PEI suspensions were carried out with a demountable 2-mm quartz cuvette in a glovebox. UV-vis spectra of hydrazine-hydrate-reduced

PDI and PEI-reduced PDI in DMF in exposure to air were conducted in an ambient atmosphere with quartz of diameter = 10 mm.

Electron paramagnetic resonance (EPR) was recorded on a Bruker E500 EPR spectrometer (300 K, 9.854 GHz, Xband, Karlsruhe, Germany). The microwave power was 6.325 mW, and the amplitude modulation was set to 1 G.

The twinning of PEI on PDI was demonstrated by microscopy and dynamic light scattering measurements. Microscopic images were obtained using a field-emission scanning electron microscope (SEM) (ZEISS, Oberkochen, Germany) at room temperature. The suspensions were deposited onto silicon, followed by drying at 60°C. The dry samples were gold coated for 30 s at 15 mA prior to fixing in the SEM holder for imaging. Dynamic light scattering (DLS, 90Plus PALS, Brookhaven Instruments Corporation) was used to measure the particle size of the PDI suspensions doped with varying PEI content.

The electronic level of PDI aggregates and monomer was estimated from cyclic voltammetry and spectroscopy. Cyclic voltammetry of pristine PDI with and without PEI and monomeric PDI with PEI was carried in a glass cell in a three-electrode system in a glovebox. Glassy carbon was used as the working electrode, Pt mesh was the counter electrode, and Ag/Ag$^+$ was the reference electrode. The reference electrodes were calibrated with Fc/Fc$^+$ before use. Tetrabutylammonium hexafluorophosphate (n-Bu$_4$NPF$_6$, 98%, J&K Scientific) was recrystallized from ethanol and dried at 120°C in an oven for 12 h before being dissolved in DMF and used as an electrolyte.

The LUMO energy level was calculated from the onset reduction potential in the voltammogram according to the following formula:

$$E(LUMO) = -\left(4.8 + E_{red}^{PDI^0} - E_{\frac{1}{2}}^{Fc/Fc^+}\right),$$

where $E_{red}^{PDI^0}$ is the onset reduction potential of the neutral PDI and $E_{1/2}^{Fc/Fc^+}$ is the redox potential of ferrocene/ferrocenium Fc/Fc$^+$ ≈ 0.089 V vs. Ag/Ag$^+$ in a DMF electrolyte with 0.1 M Bu$_4$NPF$_6$.

The HOMO energy level was obtained by

$$E(HOMO) = E(LUMO) - E_{gap},$$

where E_{gap} is the energy gap calculated according to $\Delta E = 1,240$ nm/λ_{onset} and λ_{onset} is the long wavelength edge of the absorption band.

Photothermal conversion data were collected by recording temperature changes of 2 mL of suspension when the laser irradiation was on and off (Blueprint, VCL-808nmM0-2W). The power was set to 1.4 W, and the laser spot radius was 10 mm. The photothermal conversion efficiency, η, was calculated from equation $\eta = \frac{hs\Delta T - Q_{dis}}{I(1-10^{-A_\lambda})}$, where h is the heat transfer coefficient, s is the surface area of the container, ΔT is the temperature change of the PDI-PEI suspension at the maximum steady-state temperature, I is the laser power, A_λ is the absorbance of the composite suspension at 808 nm, and Q_{dis} is the heat associated with the light absorbance of the solvent.

Magnetization was measured using a Quantum Design PPMS-9 with a vibrating sample magnetometer at room temperature. The diamagnetic correction was performed using diamagnetic susceptibility from the sample holder.

3 Results and discussion

The PDI-PEI composite suspension was first prepared by the one-pot synthesis described in the experimental section. As shown in Figure 1, a color change from fuchsia to blue and purple can be recognized by the naked eye from the PDI suspensions with increasing content of PEI, visualizing the varied doping extent of PDI-PEI composite caused by the electron transfer from PEI to PDI. To define the PDI changes, UV-vis spectra of raw PDI and PDI monomer (depolymerized electrochemically) were collected (Supplementary Figure S1). The raw PDI suspension (0.04 mg/mL in DMF, treated with 5 min of high-power sonication) showed a broad UV-vis absorption around 480–550 nm and a new absorption around 590 nm due to aggregation. The neutral monomeric PDI (depolymerized electrochemically) showed a characteristic absorption around 453 nm, 486 nm, and 521 nm, denoted to their (0,2) (0,1), and (0,0) electronic transitions, close to the reported neutral PDI derivatives that featured main absorptions at 458 nm, 490 nm, and 526 nm, respectively (Golshan et al., 2020). The PDI radical was characterized by main absorptions at 707 nm, 797 nm, and 961 nm, and PDI dianions displayed absorptions at 566 nm and 637 nm. The chemically doped PDI is characterized by similar absorptions. With the gradual increase of PEI content (Figures 1B,C), absorption peaks around 698 nm, 791 nm, and 951 nm emerged and increased while the broad absorption around 480–550 nm decreased. This shift was assigned to the process of PDI aggregates being chemically reduced to radical anions ($PDI \xrightarrow{e^-} e^- PDI^{\cdot-}$). When the PEI repeat unit/PDI molar ratio increased to 725.7 (mass ratio of PEI/PDI = 80), the absorption of radical anions saturated, predicting a depletion of neutral PDI and the highest concentration of PDI radical anion (close to 0.04 mg/mL, that is, ~1 electron/molecule on average). The absorption around 565 nm and 637 nm, assigned to the PDI dianion, arose slowly, far before the exhaustion of PDI radical anions, indicating that a small fraction of PDI experiences a chemical disproportionated reaction from a neutral state to dianion directly ($PDI \xrightarrow{2e^-} 2e^- PDI^{2-}$). The intensity of the PDI dianion absorption continued to increase dramatically when more PEI was added, and the concentration of PDI radical anion started to decrease, corresponding to the process of $PDI^{\cdot-} \xrightarrow{e^-} e^- PDI^{2-}$. When the PEI repeat unit/PDI molar ratio increased to 27,214 (or a mass ratio of PEI/PDI = 3,000), the UV-vis absorptions around 698 nm, 791 nm, and 951 nm were comparable to those of the suspensions, which had a PEI repeat unit/PDI molar ratio of 9.1 and 18.1, suggesting a similar fraction of PDI$^-$ but a majority fraction of PDI^{2-} instead of PDI. The largest yield of PDI dianions (~2 electrons/molecule on average) might be obtained if PEI content were increased further. Therefore, the doping level of PDI and the yield of PDI radical anions can be controlled precisely in a wide range with varying content of PEI. The maximum yield of radical anions was a little smaller than 100% due to the disproportional reaction of the neutral to the dianion.

DLS results of PDI-PEI composite in suspension exhibited a positive correlation of hydrodynamic diameter of PDI-PEI particles with PEI content in DMF. As shown in Supplementary Figure S2, the hydrodynamic diameter of the composite increased from 122 nm to 867 nm with an increase in PEI content (the PEI repeat unit/PDI molar ratio increased from 4.5 to 90.7), where
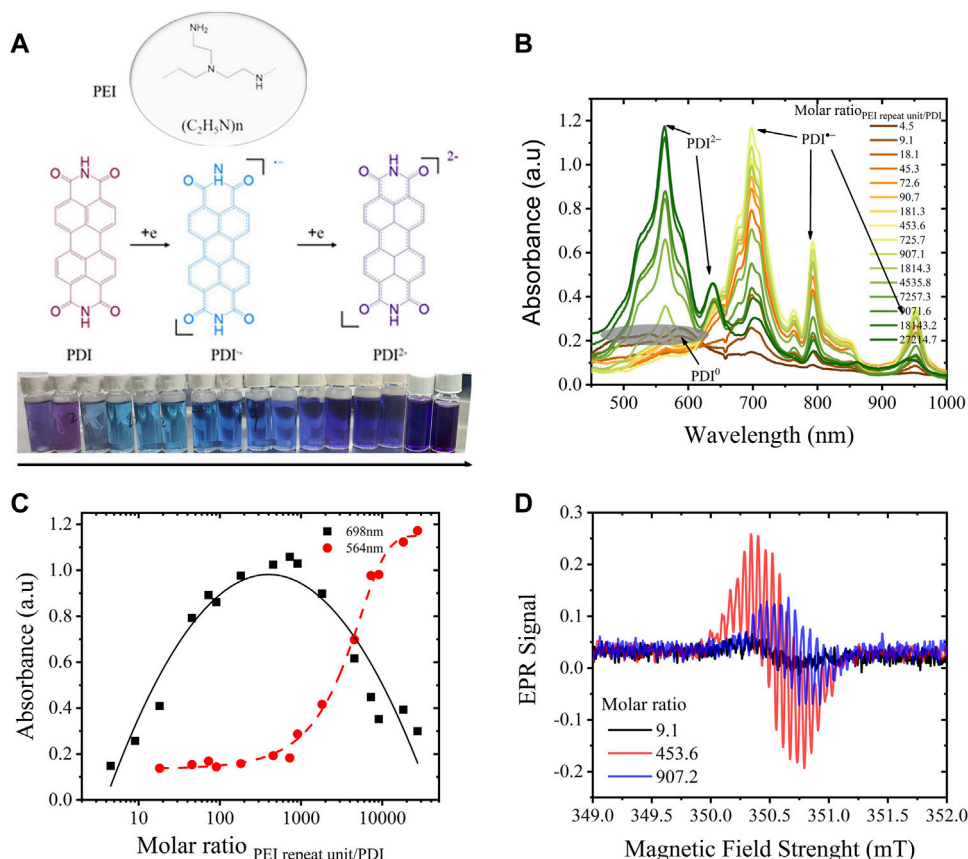
FIGURE 1
(A) Chemical doping of PDI (0.04 mg/mL in DMF) by various amounts of PEI to form radical anions/dianions; **(B)** UV-vis spectra of the reduced PDI-PEI suspensions, the molar ratio of PEI repeat unit/PDI increase from 4.5 to 27215; **(C)** a plot of the intensity of absorption at 698 nm, 564 nm assigned to PDI-and PDI2-, vs molar ratio of PEI repeat unit/PDI; **(D)** Electron paramagnetic resonance spectra of PDI suspension doped with PEI content under a molar ratio of PEI repeat unit to PDI equals to 9.1, 453.6 and 907.2.

neutral PDI was consumed to generate the radical anions. The highest amount of radical anion was created with a PEI repeat unit/PDI molar ratio of 725.7, as illustrated in Figure 1C. The particle size dependence in this range visualized the successful bonding of PEI to the PDI radical anion. The diameter plateau of PDI-PEI particles is around 1 μm. More PDI radical anions were expected to be generated when more PEI was added; the plateau suggests that an electrostatic and steric balance is reached on the PDI radical anion-PEI composite particles before the formation of the PDI dianion-PEI particles. The paramagnetic radical anion caused by electron transfer from PEI to PDI was also demonstrated by electron paramagnetic resonance spectroscopy (Figure 1D), with a well-resolved hyperfine splitting pattern and a g-factor value of 2.00305 (Supplementary Figure S3). Two equivalent N atoms (at imide rings) and two distinct sets of four core-H atoms of PDI$^-$ (H$_a$ and H$_b$) were responsible for the splitting pattern, confirming that electron density is mostly delocalized within the conjugated π-system (Goodson et al., 2013). Even though the intensity of the radicals differs and depends on concentration correlated with the doping state of PDI suspension, a symmetrical pattern was observed in all EPR signals, suggesting a similar delocalization degree of the

electrons. SEM images demonstrated morphological changes of self-assembly PDI in the absence and presence of PEI.

As shown in Figure 2, PDI aggregates can be dispersed into particles around 500 nm after sonication and cast on the silicon substrate. The hydrazine-hydrate-reduced PDI formed nanorods of 50–60 nm width and around 1 μm length by self-assembly of its dianions. A small amount of PEI in the composite (molar ratio of PEI repeat unit/PDI = 9.1) could lead to irregular debris shapes and clusters when the ratio is raised to 907.2. More PEI twinned onto PDI leads to a much more irregular cluster morphology, demonstrating that the presence of PEI in the solution suppressed the self-assembly of reduced PDI to form regular compact rods driven by π-π interactions (Jiang et al., 2022). This suppression of PEI in the self-assembly of the reduced PDI has also been visualized in the decreased ferromagnetism (Supplementary Figure S4).

The effect of PEI in suppressing self-assembly aggregation of neutral PDI was also demonstrated by the UV-vis spectra presented in Figure 3. When the hydrazine-hydrate-reduced PDI was exposed to air, the absorption intensity of typical neutral PDI aggregates at 583 nm increased immediately due to the PDI radical anions being
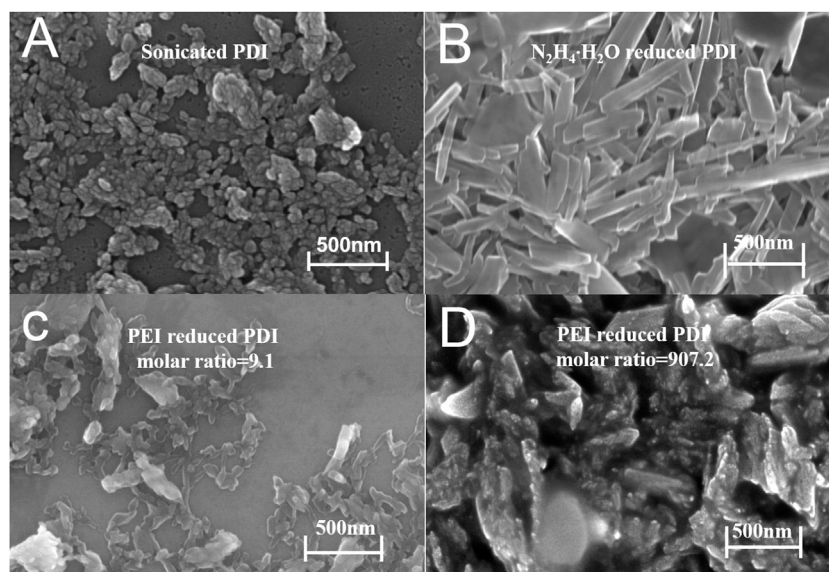
FIGURE 2
SEM images of sonicated PDI **(A)**; hydrazine hydrate reduced PDI **(B)**, and PEI reduced PDI with a molar ratio of PEI repeats unit/PDI equals 9.1 **(C)** and 907.2 **(D)**.
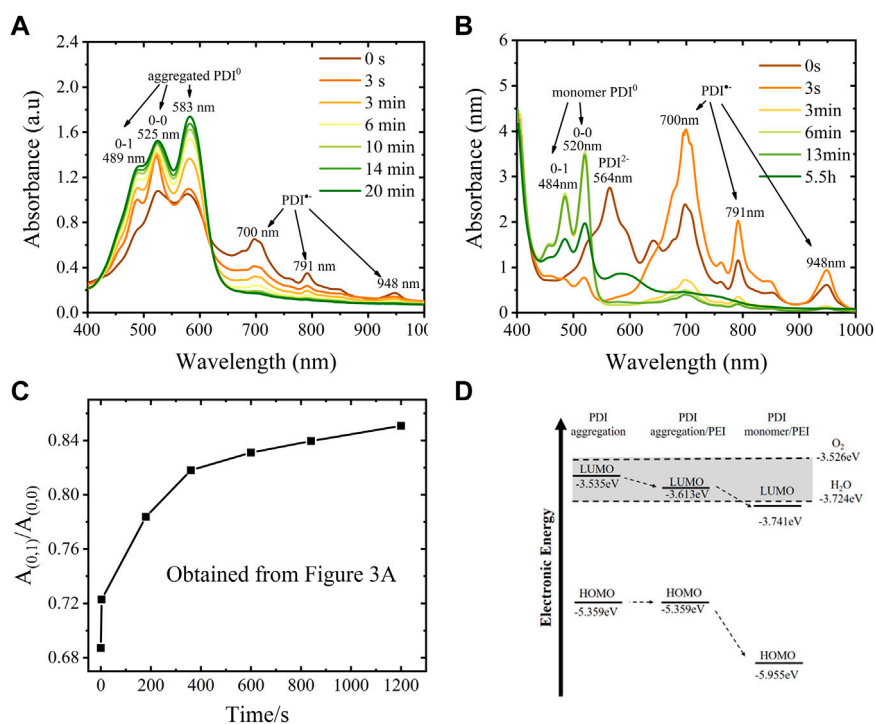
FIGURE 3
Stability of PDI radical anion and dianion using hydrazine hydrate and PEI as a dopant. **(A)** UV-vis spectra of hydrazine hydrate reduced PDI suspension that exposure to air or different time, 50 μL of the reduced suspension(10 mg/mL) was dropped cast on a clean glass substrate and dried at 120°C for 3 hours and then kept at 50°C overnight to remove excess hydrazine hydrate, then the dry film was scraped to dissolve in 5 ml DMF with a dropper in the glovebox before UV-vis spectroscopy, PDI concentration in DMF is ~0.1 mg/mL; **(B)** UV-vis spectra of PEI reduced PDI suspension that exposure to air for a different time; **(C)** A plot of A_{0-1}/A_{0-0} ratio as a function of time exposed to air, the data were obtained from Figure 3A; **(D)** Diagram of the calculated HOMO and LUMO energy of PDI monomer in DMF with or without PEI. The dashed lines are the LUMO energy levels of oxygen and water.

oxidized and becoming neutral aggregates, demonstrating a quick self-assembly-driven aggregation process of neutral PDI without PEI. The aggregation of PDI monomer is observed in hours in the presence of PEI. To be specific, the aggregation was identified to start after 5.5 h, accompanied by the appearance of the new peak around 583 nm, while the amount of neutral PDI monomer (485 nm, 520 nm) continued to increase for at least 13 min due to more PDI radical anions being oxidized into neutral PDI.

The twinning of PEI onto PDI not only limits the aggregating of PDI but also hinders the electron transfer between PDI dianion or radical/PEI composite and the oxidants, which can also improve the stability of PDI radical anions in the air due to physical encapsulation and electrostatic attraction. The UV-vis spectroscopy (Figure 3) illustrates the changes in ambient stability of PDI dianions and radial anions with or without PEI. The absorption peak of the PDI dianion in DMF solvent obtained by dissolving hydrazine-hydrate-reduced-film disappeared from the spectra, demonstrating that the PDI dianion is extremely unstable in DMF with little trace of oxide species as the DMF solvent and containers were deoxygenated overnight in a glovebox where the content of water was below 0.01 ppm, and oxygen was below 5 ppm. When exposed to the air for a longer time, the absorption of radical anions decreased gradually and disappeared in 20 min, while that of aggregated neutral PDI increased continuously. The maximum absorption ratio for the 0–1 vibronic transition (A_{0-1}) and the absorption maxima of the 0–0 vibronic transition A_{0-0}, that is, A_{0-1}/A_{0-0} was observed to increase from 0.69 to 0.85, as shown in Figure 3C, indicating a more proximal packing of neutral PDI at higher monomer concentration according to Xin Wang (Wang et al., 2017) and Benjamin Fimmel et al. (Fimmel et al., 2015). Differently, the PEI-reduced PDI dianion and anion suspension in DMF is relatively stable in the same inert atmosphere and exists for more than a year when stored in a glovebox. However, the PEI-reduced PDI dianion was also very reactive in the air; its main absorption at 565 nm disappeared immediately in 3 s upon exposure to air. The main absorptions of the PDI radical anion at 700 nm, 791 nm, and 959 nm increased dramatically due to the spontaneous oxidation process of $PDI^{2-} \xrightarrow{e^-} e^- PDI^{\cdot-}$ and then decreased gradually due to the following oxidation of $PDI^{\cdot-} \xrightarrow{e^-} e^- PDI$. The radical anion was more stable than the PDI dianion, illustrated by the existing small absorption peaks at 700 nm and 791 nm after 13 min (radical anion monomer) and the small broad absorption at 700–800 nm (radical anion aggregates) after 5.5 h.

The stability of the PDI radical anions in the presence of PEI in DMF solution (up to 13 min for its monomer and up to 5.5 h for its aggregates in contact with air) falls between the imide-position-substituted derivatives and the bay-substituted derivatives reported. For example, Marcon et al. reported self-assembled N, N′-Bis(2phosphonoethyl)-3, 4, 9, 10-perylenediimide radical anions reduced by sodium dithionite persisted for several minutes in the presence of oxygen (Marcon and Brochsztain, 2007). Schmidt et al. synthesized zwitterionic perylene diimide-centered radicals from cationic imidazolium-substituted tetrachloro-substituted perylene-3,4:9,10-tetracarboxylic acid bisimide (Pr_2Im-PDI-Cl_4). The lifetime of its solution in CH_2Cl_2 ($1.35*10^{-5}$ M) was about 1 day, as revealed by UV-vis spectra (Schmidt et al., 2015). He et al. reported the bay-substituted perylene diimide radical anion (N, N-diethylhexyl-1,7-di

(pentafluoro-phenoxyl) perylene diimide, DFPDI) was not only stable to moderate oxidants in ambient air (O_2) and moisture for prolonged times but also was not sensitive to strong oxidants, acid H^+, and strong oxidization metal ions with low limit values (He et al., 2016).

The LUMO-HOMO energy evaluated through voltammetry and UV-vis spectra shows that the electronic state of PDI is affected by PEI, as shown in Figure 3D and Supplementary Figure S5. The LUMO energy level of pristine PDI aggregation is about −3.535 eV, estimated from the onset reduction potential at −1.176 V in a cyclic voltammogram. The presence of PEI (50 mg/mL) in suspension leads to a more positive onset reduction potential of PDI aggregates at −1.098 V, while that of the PDI monomer in the presence of PEI shifted ~0.128 V positively, indicating a lower LUMO energy level for PDI aggregation and PDI monomer in the presence of PEI (−3.613 eV and −3.741 eV, respectively). The corresponding HOMO energies were −5.359 eV, −5.359 eV, and −5.955 eV, respectively, for PDI aggregate without PEI, PDI aggregates in the presence of PEI, and PDI monomer in the presence of PEI when taking their energy gap (1.824 eV, 1.746 eV, and 2.214 eV, respectively) into account. Thus, both the HOMO and LUMO energy levels of PDI monomer in the presence of PEI were found to be lower than those of the PDI aggregation (Figure 3D). Note that the LUMO energy levels of ubiquitous oxidants (oxygen: 3.526 eV, water: 3.724 eV, Supplementary Figure S5C) are close to those of PDI. Lower LUMO and HOMO energy were normally considered to account for the promotion of electron injection and transportation (Gao et al., 2014) and the enhancement of the air stability of the reduction products. Promoted formation of radical anions with extraordinary stability was also reported by Song et al. on naphthalenediimides (NDIs), which had a lower LUMO energy and HOMO energy (Song et al., 2015). Therefore, the decrease of PDI's LUMO energy (0.106 eV for PDI monomer) is important in improving the ambient stability of PDI radical anions.

On the basis of the PDI-PEI composites with varying free radical yields, we anticipated that the highest yield of PDI radicals could attain a more effective NIR photothermal conversion. Hence, photothermal conversion experiments were performed with an 808-nm laser radiation at 1.8 W/cm² at room temperature (29.8°C). The temperature elevations of PDI-PEI suspensions containing varied amounts of PDI radicals were measured and are presented in Figure 4. A blank test demonstrated that the temperature of a pure high concentration of PEI (150 mg/mL) and of pure PDI (0.04 mg/mL) in DMF increased only by 0.9°C and 1.1°C, respectively, within 400 s, while a significant increase in temperature was observed after irradiating DMF suspension with doped PDI-PEI. The consistent dependence of the increased temperature (ΔT) and the photothermal conversion efficiency (η) on the molar ratio of PEI repeat unit/PEI indicates a direct correlation between them and the PDI free radical yield. (The yield of radical anions was estimated from the absorption at 698 nm with the Beer–Lambert law, $A = \varepsilon cL$, where ε is the molar absorptivity, L is the length of the light path, and c is the concentration of the radical anions; the highest yield was normalized to 100% as shown in Figure 4B). The PDI-PEI suspension containing a higher yield of PDI radicals had a greater temperature increase than the suspension containing a lower yield of PDI radicals. An increase of PDI dianions and PEI
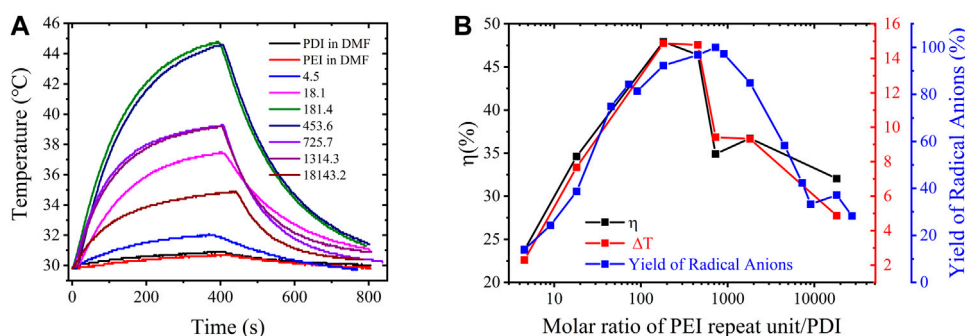
FIGURE 4
Photothermal conversion performance of PEI-PDI suspensions: **(A)** temperature evolution as a function of time (0−400 s) under laser radiation by an 808 nm laser at a power of 1.8 W/cm². PDI (0.04 mg/mL) and PEI (150 mg/mL) in DMF were used as the blank control, PEI-PDI suspensions are of a molar ratio of PEI repeat unit/PDI equals 4.5, 18.1, 181.4, 453.6, 725.7, 1314.3, 18143.2, respectively; **(B)** the evolution of maximum temperature (ΔT), photothermal conversion efficiency (η) and the yield of free radicals in the PEI-PDI suspensions as a function of the molar ratio of PEI repeat unit/PDI. The experiment was conducted in a glovebox.

content does not result in obvious photothermal conversion under irradiation due to no UV-vis absorption in the NIR range. Within 400 s, the temperature of a PDI-PEI suspension with a PDI radical yield of 92.2% (molar ratio of PEI repeat unit/PDI = 181.4) increased by 14.8°C, corresponding to a photothermal conversion efficiency of 47.9% calculated from its cooling curve. Meanwhile, the PDI-PEI suspension with a PDI radical yield of 14.0% (molar ratio of PEI repeat unit/PDI = 4.5) had a temperature increase of 2.3°C and a photothermal conversion efficiency η = 23.7%. The temperature of a PDI-PEI suspension with a PDI radical yield of 37.2% (molar ratio of PEI repeat unit/PDI = 18,143.2) increased by 4.8°C, corresponding to η = 32.0%.

To summarize, the photothermal conversion efficiency was tuned in the range of 23.7% to 47.9% for the PDI-PEI suspensions that have different yields of radical anions generated by varying the amounts of PEI doping. Note that the highest photothermal conversion efficiency of the unsubstituted PDI radical anion (47.9%) is comparable to that of functionalized perylene diimide radical anion salts (54.4%) with tetraphenoxy moieties onto the PDI cores and diisopropylbenzene in the amine position (TPPDI) (10^{-4} M in DMF) (Li et al., 2019). The efficiency is larger than a bola-form amphiphile PDI derivative's radical anions (BPDI radical anion, 16.3%) and the supramolecule composed of BPDI and cucurbit [n]urils (CB [7]) free radical anion (BPDI/(CB [7])$_2$ radical anion, 31.6%) (Jiao et al., 2015). The efficient photothermal conversion exhibited in this benchmark PDI with the simplest molecular structure highlights the necessity to tune the PDI to explore novel properties of this fundamental PDI molecule.

4 Conclusion

In this work, PEI was employed as an effective n-doping agent for feasible and controllable doping of PDI to form radical anions and dianions. DLS and SEM results show that the twinning of PEI on PDI results in an irregular morphology and an increase in PDI diameter. UV spectroscopy reveals the presence of PEI hindered the

aggregation of the neutral PDI monomer. The stability of radical anions was improved compared to imide-position-substituted derivatives, although it falls behind its bay-stable imide-position-substituted derivatives. The radical-rich PDI-PEI suspensions presented tunable NIR photothermal conversion properties (23.7 %–47.9%). This research provides a new strategy to tune the doping level of similar n-type molecules for varying yields of radical anions and also illuminates the control of radical anion-based photothermal conversion efficiency.

Data availability statement

The original contributions presented in the study are included in the article/Supplementary Material; further inquiries can be directed to the corresponding author.

Author contributions

CC and ST performed material preparation, electrochemical analysis, spectroscopy analysis, DLS data analysis, and drafting of the article; YJ and JY performed the SEM test; XH performed the analysis of magnetism; SH participated in the photothermal conversion measurement and analysis; YM and QJ designed the project and revised the manuscript.

Funding

Acknowledgments

The authors would also like to thank Viktor Gueskine and Yuanying Liang for a helpful discussion on the manuscript.

Conflict of interest

The authors declare that the research was conducted in the absence of any commercial or financial relationships that could be construed as a potential conflict of interest.

Publisher's note

All claims expressed in this article are solely those of the authors and do not necessarily represent those of their affiliated organizations, or those of the publisher, the editors, and the reviewers. Any product that may be evaluated in this article, or claim that may be made by its manufacturer, is not guaranteed or endorsed by the publisher.

Supplementary material

The Supplementary Material for this article can be found online at: https://www.frontiersin.org/articles/10.3389/fchem.2023.1187378/full#supplementary-material

SUPPLEMENTARY FIGURE S1
In situ UV-vis spectra of PDI at time = 0 s (black curve) and 500 s (red curve) under constant voltage. Pristine PDI (~$10-4$ M) in DMF with 0.1 M Bu$_4$NPF$_6$ was used as the electrolyte, a constant voltage of -1.8 V (which is enough to reduce PDI to get radical anion and dianion in a relatively short time) was applied at the Pt working electrode, the counter electrode is Pt and the reference electrode is Ag/Ag$^+$.

SUPPLEMENTARY FIGURE S2
Dynamic Light Scattering result of the PDI-PEI suspension.

SUPPLEMENTARY FIGURE S3
g-factor of PDI suspension doped with PEI content under a molar ratio of PEI repeat unit to PDI equals to 9.1, 453.6, and 907.2.

SUPPLEMENTARY FIGURE S4
(A) M-H hysteresis loops measured four times (1st: one day; 2nd: 13 days; 3rd: 22 days; 4th: one month) for the sample molar ratio of PEI repeat unit/PDI = 453.6; **(B)** ferromagnetic contribution extracted from Supplementary Figure S4A.

SUPPLEMENTARY FIGURE S5
LUMO-HOMO energy of PDI with or without PEI: **(A)** Linear sweep voltammograms obtained in the glovebox of PDI aggregation in DMF without PEI (black), with various amounts of PEI (red) and the PDI monomer produced by oxidizing the doped PDI solution with air (blue); **(B)** UV-vis spectra of PDI aggregation in DMF with or without PEI used for the calculation of the energy gap between their HOMO and LUMO. The PDI suspensions in DMF with or without PEI are sonicated before cyclic voltammetry, PDI concentration: 0.05 mg/mL, the numbers in the brackets represent the PEI/PDI mass ratio 0, 1, 10, 50, 100, and 1000. Scan rate: 100 mV/s, working electrode: glassy carbon (Diameter = 3 mm); The LUMO energy for oxygen and water reduction was estimated from onset reduction potential from **(C)** linear sweep voltammograms of DMF electrolyte with saturated O$_2$ or with deoxygenated H$_2$O (glassy carbon as working electrode, scan rate:100 mV/s).

References

Chen, Z., Stepanenko, V., Dehm, V., Prins, P., Siebbeles, L. D. A., Seibt, J., et al. (2007). Photoluminescence and conductivity of self-assembled π–π stacks of perylene bisimide dyes. *Chem. – A Eur. J.* 13, 436–449.

Demchenko, V., Riabov, S., Kobylinskyi, S., Goncharenko, L., Rybalchenko, N., Kruk, A., et al. (2020). Effect of the type of reducing agents of silver ions in interpolyelectrolyte-metal complexes on the structure, morphology and properties of silver-containing nanocomposites. *Sci. Rep.* 10, 7126.

Dong, D., Li, Q., Hou, W., and Zhang, H. (2020). Synthesis, nonlinear optical, magnetic and electrical properties of ultra-stable open-shell pancake bonding linked perylene diimide anion radicals π-oligomer. *J. Mol. Struct.* 1199, 127002. doi:10.1016/j.molstruc.2019.127002

Dong, S., Wan, Y., Wang, Y., Yang, Y., Wang, Y., Zhang, X., et al. (2016). Polyethylenimine as a dual functional additive for electron transporting layer in efficient solution processed planar heterojunction perovskite solar cells. *RSC Adv.* 6, 57793–57798. doi:10.1039/c6ra09976a

Fimmel, B., Son, M., Sung, Y. M., Grüne, M., Engels, B., Kim, D., et al. (2015). Phenylene ethynylene-tethered perylene bisimide folda-dimer and folda-trimer: Investigations on folding features in ground and excited states. *Chem. – A Eur. J.* 21, 615–630. doi:10.1002/chem.201405231

Gao, J., Xiao, C., Jiang, W., and Wang, Z. (2014). Cyano-substituted perylene diimides with linearly correlated LUMO levels. *Org. Lett.* 16, 394–397. doi:10.1021/ol403250r

Gao, X., and Hu, Y. (2014). Development of N-type organic semiconductors for thin film transistors: A viewpoint of molecular Design. *J. Mater. Chem. C* 2, 3099–3117. doi:10.1039/c3tc32046d

Ghosh, I., Ghosh, T., Bardagi Javier, I., and König, B. (2014). Reduction of aryl halides by consecutive visible light-induced electron transfer processes. *Science* 346, 725–728. doi:10.1126/science.1258232

Golshan, M., Rostami-Tapeh-Esmail, E., Salami-Kalajahi, M., and Roghani-Mamaqani, H. (2020). A review on synthesis, photophysical properties, and applications of dendrimers with perylene core. *Eur. Polym. J.* 137, 109933. doi:10.1016/j.eurpolymj.2020.109933

Gong, H.-X., Cao, Z., Li, M.-H., Liao, S.-H., and Lin, M.-J. (2018). Photoexcited perylene diimide radical anions for the reduction of aryl halides:a bay-substituent effect. *Org. Chem. Front.* 5, 2296–2302. doi:10.1039/c8qo00445e

Goodson, F. S., Panda, D. K., Ray, S., Mitra, A., Guha, S., and Saha, S. (2013). Tunable electronic interactions between anions and perylenediimide. *Org. Biomol. Chem.* 11, 4797–4803. doi:10.1039/c3ob40703a

He, E., Wang, J., Liu, H., He, Z., Zhao, H., Bao, W., et al. (2016). Facile synthesis of an isolable and ambient stable bay-substituted perylene diimide radical anion salt and its optical response to base–acid and metal ions. *J. Mater. Sci.* 51, 9229–9238. doi:10.1007/s10853-016-0168-1

Hong, S., Yoo, G., Kim, D. H., Song, W. G., Le, O. K., Hong, Y. K., et al. (2017). The doping mechanism and electrical performance of polyethylenimine-doped MoS2 transistor. *Phys. status solidi C.* 14, 1600262. doi:10.1002/pssc.201600262

Hu, M., Zhang, Y., Liu, X., Zhao, X., Hu, Y., Yang, Z., et al. (2021). Layer-by-Layer solution-processed organic solar cells with perylene diimides as acceptors. *ACS Appl. Mater. Interfaces* 13, 29876–29884. doi:10.1021/acsami.1c06192

Jiang, Q., Sun, H., Zhao, D., Zhang, F., Hu, D., Jiao, F., et al. (2020). High thermoelectric performance in n-type perylene bisimide induced by the soret effect. *Adv. Mater.* 32, 2002752. doi:10.1002/adma.202002752

Jiang, Q., Zhang, J., Mao, Z., Yao, Y., Zhao, D., Jia, Y., et al. (2022). Room-temperature ferromagnetism in perylene diimide organic semiconductor. *Adv. Mater.* 34, e2108103. doi:10.1002/adma.202108103

Jiao, T., Cai, K., Nelson, J. N., Jiao, Y., Qiu, Y., Wu, G., et al. (2019). Stabilizing the naphthalenediimide radical within a tetracationic cyclophane. *J. Am. Chem. Soc.* 141, 16915–16922. doi:10.1021/jacs.9b08926

Jiao, Y., Liu, K., Wang, G., Wang, Y., and Zhang, X. (2015). Supramolecular free radicals: Near-infrared organic materials with enhanced photothermal conversion. *Chem. Sci.* 6, 3975–3980. doi:10.1039/c5sc01167a

Li, L., Gong, H. X., Chen, D. Y., and Lin, M. J. (2018). Stable bifunctional perylene imide radicals for high-performance organic-lithium redox-flow batteries. *Chemistry* 24, 13188–13196. doi:10.1002/chem.201801443

Li, Q., Hou, W., Peng, F., Wang, H., Zhang, S., Dong, D., et al. (2019). Photothermal conversion performance of perylene diimide radical anion salts modified with tunable moieties. *J. Mater. Sci.* 54, 217–227. doi:10.1007/s10853-018-2822-2

Long, D. X., Choi, E.-Y., and Noh, Y.-Y. (2017). High performance and stable naphthalene diimide based n-channel organic field-effect transistors by

polyethylenimine doping. *Dyes Pigments* 142, 323–329. doi:10.1016/j.dyepig.2017.03.053

Ma, W., Qin, L., Gao, Y., Zhang, W., Xie, Z., Yang, B., et al. (2016). A perylene bisimide network for high-performance n-type electrochromism. *Chem. Commun.* 52, 13600–13603. doi:10.1039/c6cc07962h

Marcon, R. O., and Brochsztain, S. (2007). Highly stable 3,4,9,10-perylenediimide radical anions immobilized in robust zirconium phosphonate self-assembled films. *Langmuir* 23, 11972–11976. doi:10.1021/la702642h

Mulens-Arias, V., Nicolás-Boluda, A., Gehanno, A., Balfourier, A., Carn, F., and Gazeau, F. (2019). Polyethyleneimine-assisted one-pot synthesis of quasi-fractal plasmonic gold nanocomposites as a photothermal theranostic agent. *Nanoscale* 11, 3344–3359. doi:10.1039/c8nr09849b

Okamoto, T., Kumagai, S., Fukuzaki, E., Ishii, H., Watanabe, G., Niitsu, N., et al. (2020). Robust, high-performance n-type organic semiconductors. *Sci. Adv.* 6, eaaz0632. doi:10.1126/sciadv.aaz0632

Powell, D., Rhodes, Z., Zhang, X., Miller, E. J., Jonely, M., Hansen, K. R., et al. (2022). Photoactivation properties of self-n-doped perylene diimides: Concentration-dependent radical anion and dianion formation. *ACS Mater. Au* 2, 482–488. doi:10.1021/acsmaterialsau.2c00019

Powell, D., and Whittaker-Brooks, L. (2022). Concepts and principles of self-n-doping in perylene diimide chromophores for applications in biochemistry, energy harvesting, energy storage, and catalysis. *Mater. Horizons* 9, 2026–2052. doi:10.1039/d2mh00279e

Rdest, M., and Janas, D. (2021). Effective doping of single-walled carbon nanotubes with polyethyleneimine. *Materials* 14, 65. doi:10.3390/ma14010065

Remant Bahadur, K. C., and Uludağ, H. (2016). "Chapter 2: PEI and its derivatives for gene therapy," in *Polymers and nanomaterials for gene therapy*. Editor R. Narain (Edmonton, AB: Woodhead Publishing), 29–54.

Russ, B., Robb, M. J., Brunetti, F. G., Miller, P. L., Perry, E. E., Patel, S. N., et al. (2014). Power factor enhancement in solution-processed organic n-type thermoelectrics through molecular Design. *Adv. Mater.* 26, 3473–3477. doi:10.1002/adma.201306116

Schmidt, D., Bialas, D., and Würthner, F. (2015). Ambient stable zwitterionic perylene bisimide-centered radical. *Angew. Chem. Int. Ed.* 54, 3682–3685. doi:10.1002/ange.201408067

Schmidt, R., Oh, J. H., Sun, Y.-S., Deppisch, M., Krause, A.-M., Radacki, K., et al. (2009). High-performance air-stable n-channel organic thin film transistors based on halogenated perylene bisimide semiconductors. *J. Am. Chem. Soc.* 131, 6215–6228. doi:10.1021/ja901077a

Song, Q., Li, F., Wang, Z., and Zhang, X. J. C. S. (2015). A supramolecular strategy for tuning the energy level of naphthalenediimide: Promoted formation of radical anions with extraordinary stability. *Chem. Sci.* 6, 3342–3346. doi:10.1039/c5sc00862j

Sun, B., Hong, W., Thibau, E. S., Aziz, H., Lu, Z.-H., and Li, Y. (2015). Polyethylenimine (PEI) as an effective dopant to conveniently convert ambipolar and p-type polymers into unipolar n-type polymers. *ACS Appl. Mater. Interfaces* 7, 18662–18671. doi:10.1021/acsami.5b05097

Tadjenant, Y., Dokhan, N., Barras, A., Addad, A., Jijie, R., Szunerits, S., et al. (2020). Graphene oxide chemically reduced and functionalized with KOH-PEI for efficient Cr(VI) adsorption and reduction in acidic medium. *Chemosphere* 258, 127316. doi:10.1016/j.chemosphere.2020.127316

Wang, X., Zeng, T., Nourrein, M., Lai, B.-H., Shen, K., Wang, C.-L., et al. (2017). Concentration-dependent self-assembly structures of an amphiphilic perylene diimide with tri(ethylene glycol) substituents at bay positions. *RSC Adv.* 7, 26074–26081. doi:10.1039/c7ra04296e

Wu, G., Zhang, Z. G., Li, Y., Gao, C., Wang, X., and Chen, G. (2017). Exploring high-performance n-type thermoelectric composites using amino-substituted rylene dimides and carbon nanotubes. *ACS Nano* 11, 5746–5752. doi:10.1021/acsnano.7b01279

Yang, C.-Y., Stoeckel, M.-A., Ruoko, T.-P., Wu, H.-Y., Liu, X., Kolhe, N. B., et al. (2021). A high-conductivity n-type polymeric ink for printed electronics. *Nat. Commun.* 12, 2354. doi:10.1038/s41467-021-22528-y

Yang, Y., He, P., Wang, Y., Bai, H., Wang, S., Xu, J.-F., et al. (2017). Supramolecular radical anions triggered by bacteria *in situ* for selective photothermal therapy. *Angew. Chem. Int. Ed.* 56, 16457–16460. doi:10.1002/ange.201708971

Yang, Z., and Chen, X. (2019). Semiconducting perylene diimide nanostructure: Multifunctional phototheranostic nanoplatform. *Accounts Chem. Res.* 52, 1245–1254. doi:10.1021/acs.accounts.9b00064

Yao, J., Qiu, B., Zhang, Z.-G., Xue, L., Wang, R., Zhang, C., et al. (2020). Cathode engineering with perylene-diimide interlayer enabling over 17% efficiency single-junction organic solar cells. *Nat. Commun.* 11, 2726. doi:10.1038/s41467-020-16509-w

Zhang, A.-Q., Cai, L.-J., Sui, L., Qian, D.-J., and Chen, M. (2013). Reducing properties of polymers in the synthesis of noble metal nanoparticles. *Polym. Rev.* 53, 240–276. doi:10.1080/15583724.2013.776587

Zhang, F., Li, W., Jiang, T., Li, X., Shao, Y., Ma, Y., et al. (2020). Real roles of perylene diimides for improving photocatalytic activity. *RSC Adv.* 10, 23024–23037. doi:10.1039/d0ra03421e

Zhang, S., Li, J., Wei, J., and Yin, M. (2018). Perylenediimide chromophore as an efficient photothermal agent for cancer therapy. *Sci. Bull.* 63, 101–107. doi:10.1016/j.scib.2017.12.015

Zhao, Y. Z., Li, K. X., Ding, S. Y., Zhu, M., Ren, H. P., Ma, Q., et al. (2018). The effect of reduction potential on the generation of the perylene diimide radical anions. *Russ. Jounal Phys. Chem.* 92, 1261–1265. doi:10.1134/s003602441807035x

Zhou, Y., Xue, B., Wu, C., Chen, S., Liu, H., Jiu, T., et al. (2019). Sulfur-substituted perylene diimides: Efficient tuning of LUMO levels and visible-light absorption via sulfur redox. *Chem. Commun.* 55, 13570–13573. doi:10.1039/c9cc07040k

Characterization of bipolar plates manufactured with various Pb/C ratios for unitized regenerative fuel cell system

Chanmin Jo[1†], Yoongu Lim[1†], Dae Jun Moon[1†], Seungryul Yoo[2], Dong Chan Seok[2], Seon Yeop Jung[3], Seunghun Jung[4]*, Ho-Young Jung[5]* and Uk Sim[1,6]*

[1]Hydrogen Energy Technology Laboratory, Korea Institute of Energy Technology (KENTECH), Naju, Republic of Korea, [2]Institute of Plasma Technology, Korea Institute of Fusion Energy (KFE), Gunsan, Jeollabuk-do, Republic of Korea, [3]Department of Chemical Engineering, Dankook University, Yongin-si, Gyeonggi-do, Republic of Korea, [4]Department of Mechanical Engineering, Chonnam National University, Gwangju, Republic of Korea, [5]Department of Environment and Energy Engineering, Chonnam National University, Gwangju, Republic of Korea, [6]Center for Energy Storage System, Chonnam National University, Gwangju, Republic of Korea

The weight reduction of the bipolar plate (BP) is essential for commercializing unitized regenerative fuel cells (URFCs). In order to lighten the weight of the bipolar plate, we have used Pb/C composite powder as a cost-effective primary material, which is a mixture of low-density graphite and lead. Further, varied lead-carbon weight ratios (1:8, 1:4, 1:1, 4:1, and 8:1) were investigated for fabricating the bipolar plate by hot-pressing process adding styrene-butadiene rubber (SBR) as a binder. The specific surface area, porosity, and microstructure characteristics corresponding to the varied lead-graphite ratio of the prepared bipolar plates were studied. The relative difference in conductivity upon the compressibility of the plates is also examined. Finally, the wettability and electrochemical properties of the prepared bipolar plates were evaluated through water contact angle and cyclic voltammetry analysis.

KEYWORDS

metal-carbon, composite materials, Pb/C, bipolar plate, unitized regenerative fuel cell (URFC)

1 Introduction

In this contemporary world, energy usage is highly indispensable, but the associated undesirable outcomes in the process of energy production and consumption, such as the greenhouse effect, pollution, carbon dioxide emission, and fuel resource depletion, are steadily increasing. Hence, there is a need for the development and application of environmental-friendly renewable energy (Wang et al., 2015; De Luna et al., 2019; Hussain et al., 2020). Accordingly, effectual research is being conducted worldwide on hydrogen energy that has high energy density and can be continuously produced without carbon dioxide emission (Ozawa et al., 2019; Yue et al., 2021).

In order to utilize such hydrogen energy, water electrolyzer (Gago et al., 2016; An et al., 2019; Klose et al., 2020; Janani et al., 2021) and fuel cell (Du et al., 2016; Ren et al., 2022; Reshetenko et al., 2022) technologies are attracting attention. Hydrogen and oxygen are produced from water through a water electrolysis device using an exchange membrane,

whereas electricity is produced through a chemical reaction between hydrogen and oxygen using a fuel cell. Moreover, research interest in a hybrid system called regenerative fuel cells (RFCs) that can produce hydrogen and electricity by applying water electrolysis and fuel cell technology is increasing (Lim et al., 2020; Rubio-Garcia et al., 2020). However, the RFC is configured to combine both the water electrolyzer and the fuel cell systems. Hence the volume and weight of the RFC as a whole increase due to the volume and weight of each. Thus, an improvised single-device URFC integrating a water electrolyzer and a fuel cell is designed to solve the above issue by switching between both modes (Peng et al., 2020; Zhang et al., 2022). It is a system that has been structurally improved so that the two modes can be used selectively, and research on this is ongoing. Although the volume and weight were reduced by integrating the two devices, there are certain restraints to reducing the weight through this. Hence further research on the weight reduction of the URFC system that requires multiple stacks becomes necessary (Paul and Andrews, 2017). The stacked system used in water electrolyzers and fuel cells consists of a membrane-electrode assembly (MEA) consisting of a bipolar plate, a catalytic electrode, a membrane, and an end plate (Wu et al., 2020). A bipolar plate is inserted between each MEA, and each side of the bipolar plate is in contact with the cathode and anode of the MEA (Gabbasa et al., 2014). Therefore, structurally, the number of bipolar plates also increases according to the number of MEA stacks. A sufficient number of MEA stacks is required for the high power output of the system (Devrim et al., 2015). That is, the weight of the entire system inevitably increases for high power output, and a significant portion of the weight is occupied by the weight of the bipolar plate. Accordingly, since the weight of the entire system increases in proportion to the number, material, size, *etc.*, of the separators, it has limitations in being used in transport systems and in areas requiring many stacks, lightweight or miniaturization (Kolahdooz et al., 2017; Lim et al., 2019; Li et al., 2021).

Among the factors that affect weight, the material constituting the bipolar plate is the most basic element, and to manufacture the bipolar plate efficiently, the economic feasibility of the material, electrical conductivity, weight, corrosion resistance, strength, and required process level are important considerations (Karacan et al., 2020; Wu et al., 2021; Xiong et al., 2021). The main materials used for the bipolar plate are classified into metal, carbon, and composite materials. Among metal materials, stainless steel (SS), Ti, and Al are mainly used for bipolar plates. Chen et al. performed a conductive polymer coating utilizing carbon powder, poly-pyrrole (PPy), and polydopamine (PDA) on the surface of 304 SS. The formed PPy/C-PDA coating layer acted as a physical barrier and showed a protective effect against corrosive substances, improved interfacial contact resistance, and finally improved corrosion resistance (Chen et al., 2020).

Shi et al. showed improved electrical conductivity and corrosion resistance by forming a TiC layer on the surface of a Ti bipolar plate (Shi et al., 2020). Tsai et al. increased surface hydrophobicity and improved corrosion resistance by forming an Au-PTFE coating layer on the surface of an Al bipolar plate (Tsai et al., 2017). Sadhasivam et al. fabricated a lead-based bipolar plate and showed the possibility of applying a cost-effective Pb bipolar plate (Sadhasivam et al., 2020). Pan et al. reported improved corrosion resistance and excellent coating adhesion through CrN coating on Fe-Cr bipolar plates (Pan et al., 2014). Research on bipolar plates of carbon materials

has also been conducted. Yan et al. fabricated a graphite bipolar plate, showing its applicability to 130 stacks level PEMFC (Yan et al., 2006). However, there are certain hinges with the strength of pristine carbon materials, so research is being conducted on composite materials used with polymer materials that act as conductive binders. Yao et al. fabricated a bipolar plate with a mixture of graphite and polymer resin and showed uniform performance in terms of thickness, corrosion resistance, mechanical strength, and electrical and thermal conductivity (Yao et al., 2017). Choi et al. fabricated a thin bipolar plate by mixing carbon fiber and resin and showed electrical conductivity, mechanical strength, and gas permeability compared to carbon BP and metal BP (Choi et al., 2021). Adloo et al. compared bipolar plates made of various carbon materials (graphite, graphene, and highly structured nano-carbon black (HSNCB)) and polypropylene at various ratios. Among them, a bipolar plate made of 23% polypropylene–65% graphite–7% HSNCB–5% polypropylene-maleic anhydride (pp-MAH) exhibited excellent electrical conductivity and flexural strength (Adloo et al., 2016). In order to reduce the weight of bipolar plates, it is essential to use lightweight carbon materials due to their low density. However, carbon alone cannot satisfy all the characteristic requirements of bipolar plates. To solve this problem, metal-carbon composites are being researched to improve the strength, corrosion resistance and conductivity of carbon. Soleimani Alavijeh et al. fabricated a bipolar plate using epoxy, graphite, and nano-copper. Nano-copper was utilized as a filler to increase the strength through proper proportions, and the presence of nano-copper resulted in higher conductivity (Soleimani Alavijeh et al., 2019). Among the various metal candidates, lead is utilized in acid batteries because it is inexpensive and has good conductivity and corrosion resistance, and these properties make it a promising material for bipolar plates for URFCs that need to apply high voltages and operate in the water electrolysis mode, which requires corrosion resistance (Jung et al., 2010; May et al., 2018).

In this study, a bipolar plate using a Pb/C composite material was manufactured by using a carbon material with excellent light weight and conductivity and lead, a metal material with excellent strength and corrosion resistance, to produce a positive plate. The results of the physical and electrochemical properties of the bipolar plates manufactured with various Pb/C ratios suggested the optimal manufacturing conditions of the Pb/C bipolar plates for the URFC system.

2 Experimental methods

2.1 Materials

Graphite (<20 μm) and lead (325 mesh) were purchased from Sigma-Aldrich. Styrene-butadiene rubber (SBR) was purchased from MTI Korea, Republic of Korea. Alumina ball (99.5%, 10 ϕ) was purchased from Labkom, Republic of Korea.

2.2 Fabrication of bipolar plates

Initially, Pb/C powder (weight ratio 8:1, 4:1, 1:1, 1:4, 1:8) in quantities of 60 g, 70 g, 140 g, 210 g, and 360 g were prepared and
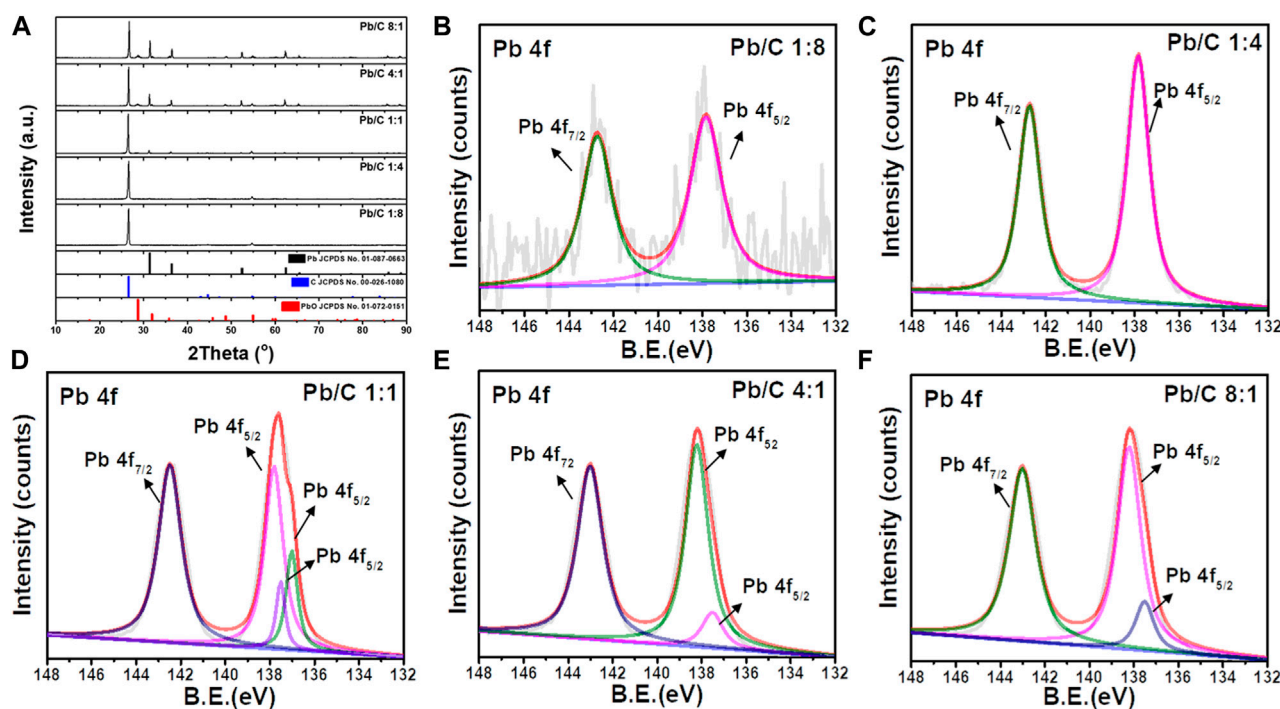
FIGURE 1
(A) X-ray diffraction patterns for different ratio of Pb/C powder, XPS spectra of Pb/C powder **(B)** 1:8, **(C)** 1:4, **(D)** 1:1, **(E)** 4:1 and **(F)** 8:1 ratios.

mixed with 45 g of SBR. The above mixture of Pb/C and binder is transferred to a metal mold of size 75 × 75 mm, which is subjected to a hot press (QM900M, QMESIS, Republic of Korea.). Hot pressing is carried out in three steps. At first, the molds are maintained at 70° for 40 min under 10 MPa, then at 140° for 40 min under 20 MPa, and finally, at 140° for 1 h under 30 MPa. Once the process is done, it is cooled and de-molded to obtain the desired bipolar plates.

2.3 Physicochemical characterizations

The morphology and surface chemistry of the as-obtained Pb/C bipolar plates were studied by scanning electron microscope (SEM, Gemini 500, ZEISS, Germany) and energy dispersive X-ray spectroscopy (EDS, Oxford Instruments, UK), respectively. The powder X-ray diffraction (XRD, Rint 1,000, Rigaku, Japan) patterns of Pb/C bipolar plates were obtained with Cu Kα radiation (λ = 1.5418 Å). X-ray photoelectron spectrum was attained through X-ray photoelectron spectroscopy (XPS, Multilab 2000; UK). The contact angle of Pb/C bipolar plates was determined through a contact angle meter (Phoenix 300, SEO, Republic of Korea). The specific surface area and the total pore volumes of the synthesized bipolar plates were measured with BET, Belsorp mini II (BEL, Japan). Powder resistivity was measured by powder resistivity measurement system (Hantech, Republic of Korea). 2.6 g of each prepared Pb/C powder was placed in a measuring mold and measured using a powder resistivity meter. The pressure range was set from 20 MPa to 200 MPa, and the resistivity, conductivity, and thickness were measured at 20 MPa intervals.

2.4 Electrochemical measurements

Electrochemical characterization of the Pb/C bipolar plate was carried out using potentiostat equipment (Bio-Logic SP150 instrumentation) at room temperature in a three-electrode cell configuration. 0.5 M H_2SO_4 solution was used as an electrolyte. The platinum (Pt) wire and Ag/AgCl reference electrodes were used as counter and reference electrodes. The synthesized plates were cut into 2 × 1 cm² and were used as the working electrodes.

3 Results and discussion

3.1 Characterization of Pb/C bipolar plates

X-ray diffraction (XRD) patterns of Pb/C bipolar plates with a different lead-carbon ratio ranging from 8:1 to 1:8 is shown in Figure 1. The XRD peaks were analyzed with the reference patterns of Pb (JCPDS No. 01-087-0663) and C (JCPDS No. 00-026-1,080) with the addition of PbO (JCPDS No. 01-072-0151) which may result from partial oxidation during the synthesis process. Throughout the different ratios of Pb and C, the high intensity peaks at 26.7° can be indicated as the (002) plane of carbon. Although in 1:4 and 1:8 ratios of Pb and C, the synthesized plates show a low indication of Pb due to the high content of C, the Pb peaks were distinguished at 32.1, 52.4, and 62.3° at the higher ratio from 1:1, 4:1, and 8:1. These peaks correspond to the (111), (220), and (311) planes of Pb, respectively. Furthermore, as the Pb content was increased, the diffraction peaks of PbO were detected at 28.2, 48.8, and 54.8°, which corresponds with (111), (112), and (211)
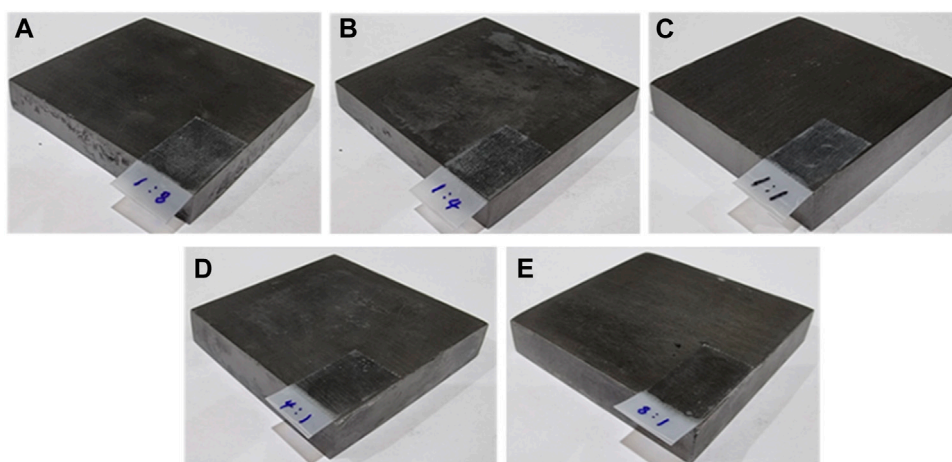
FIGURE 2
Fabricated Pb/C bipolar plates with **(A)** 1:8, **(B)** 1:4, **(C)** 1:1, **(D)** 4:1 and **(E)** 8:1 ratios.
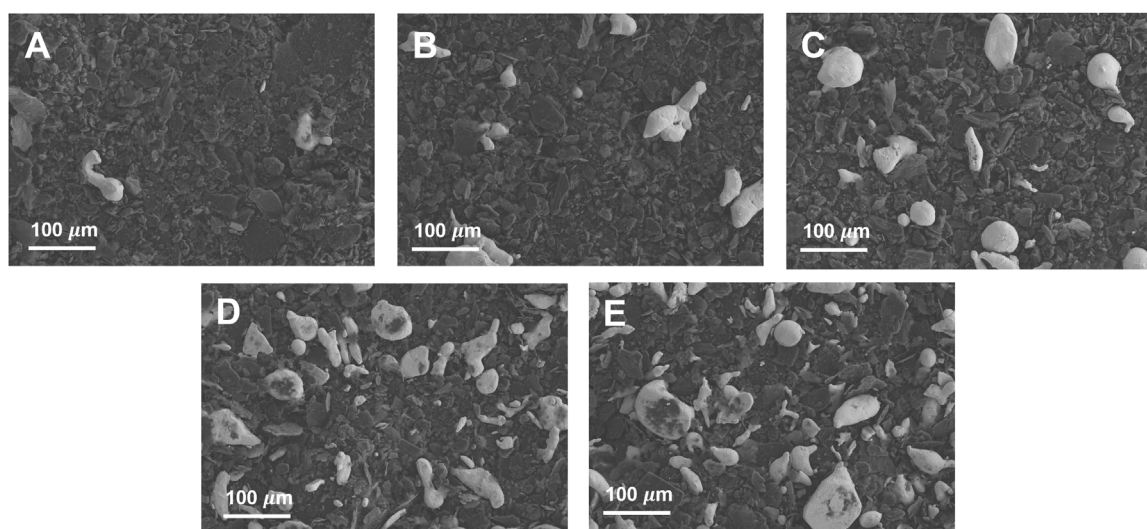
FIGURE 3
SEM surface analysis of Pb/C powders for **(A)** 1:8, **(B)** 1:4, **(C)** 1:1, **(D)** 4:1 and **(E)** 8:1 ratios.

planes of PbO, respectively. The formation of PbO can be due to the high content of Pb, where the excessive Pb was oxidized.

Figures 1B–F shows the XPS analysis results of Pb/C powders with varied lead: carbon ratios. The Pb 4f spectra of Pb/C powders shows the Pb $4f_{5/2}$ and Pb $4f_{7/2}$ peaks of lead oxide at 142.7 eV and 137.8 eV, respectively. The intensity of the Pb peaks increased with the increase of the percentage of Pb. In particular, the Figure 1D of Pb/C 1:1 ratio showed dominant Pb metallic characteristic with a Pb metal peak around 137.0 eV. Based on the XPS peaks and intensities, we found that the higher the percentage of lead mixed in the powder, the more lead oxide was formed. The photographic images of the of fabricated bipolar plates with respect to the Pb:C ratio were displayed in Figures 2A–E. Furthermore, the scanning electron microscopy (SEM) images of prepared bipolar plates with

different Pb and C ratios were analyzed. Although the Pb peaks of 1:4 and 1:8 ratios were barely detectable in XRD patterns, the respective Pb particles were found within the carbon with the size of approximately 50–70 μm, as shown in Figures 3A,B. One could see the presence of Pb as white particles in the SEM images, which becomes more prominent as the Pb content increases. As shown in Figure 3C, the Pb particles grew into more spherical particles in the Pb and C ratio of 1:1. With the high content of Pb in 4:1 and 8:1 (Figures 3D, E), the particles were more embedded in the carbon matrix, and the sizes varied in a wide range from 10 μm to 100 μm.

In Figure 4, the elemental mapping of the SEM images of Pb/C powder according to the mixing ratio was measured. In Figures 4A–E, the Pb particles are sufficiently and evenly dispersed through the ball mill process for Pb/C powder, and the
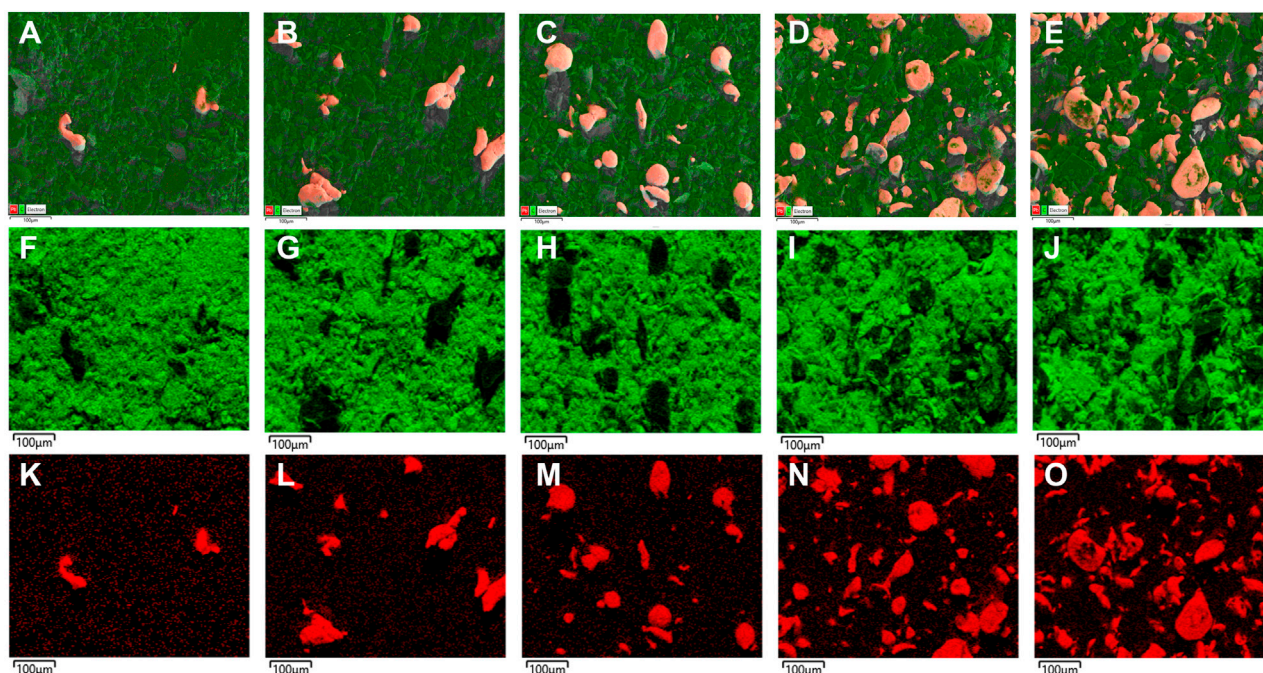
FIGURE 4
Elemental mapping of Pb/C powder in **(A)** 1:8, **(B)** 1:4, **(C)** 1:1, **(D)** 4:1 and **(E)** 8:1 ratios; C element **(F)** 1:8, **(G)** 1:4, **(H)** 1:1, **(I)** 4:1 and **(J)** 8:1 ratios; Pb element **(K)** 1:8, **(L)** 1:4, **(M)** 1:1, **(N)** 4:1 and **(O)** 8:1 ratios.
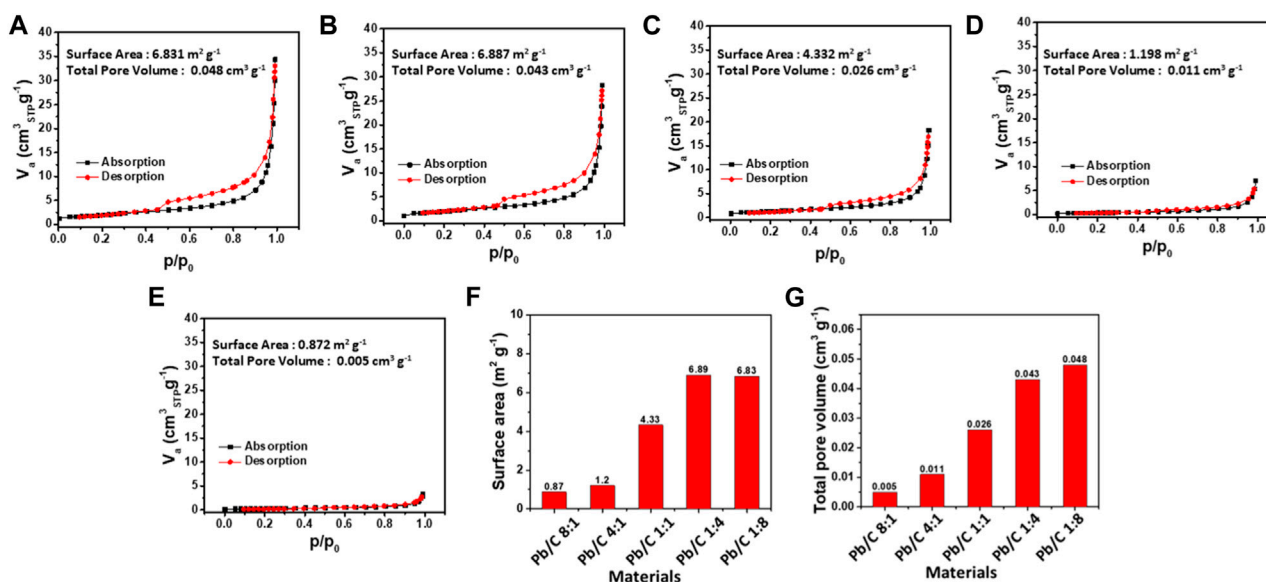
FIGURE 5
N_2 adsorption and desorption of different ratios of Pb/C powder materials; **(A)** 1:8, **(B)** 1:4, **(C)** 1:1, **(D)** 4:1 and **(E)** 8:1 ratios; **(F)** Specific surface area and **(G)** total pore volume comparisons.

number of particles in the image increases with the proportion of Pb with even distribution. In Figures 4F–J; Figures 5K–O, we can see the separate single element mapping images of carbon and lead, respectively.

3.2 Specific surface area and porosity

The Brunauer-Emmett-Teller (BET) analysis was done with N_2 gas adsorption to measure the specific surface area and the pore
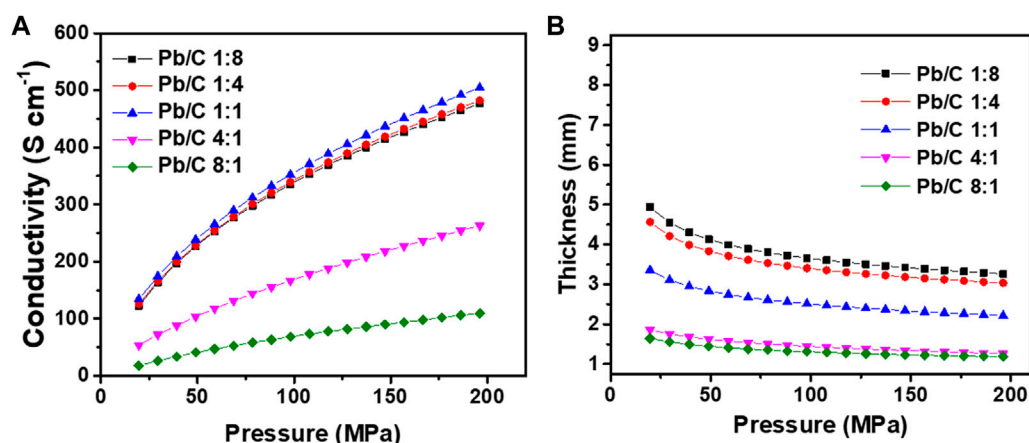
FIGURE 6
Changes in **(A)** electrical conductivity and **(B)** thickness of Pb/C composite powder according to changes in pressure.

volume. The specific surface area of each Pb/C bipolar plate was measured as shown in Figures 5A–G. With the high ratio of C, the specific surface area of 1:8 and 1:4 ratio plates were as large as 6.831 m^2g^{-1} and 6.887 $m^2 g^{-1}$, respectively. A slight decrease was shown in the 1:1 plate with a specific surface area of 4.332 $m^2 g^{-1}$. However, the high Pb ratio, 4:1 and 8:1 plates, showed a great decrease to 1.198 m^2g^{-1} and 0.872 m^2g^{-1}, respectively. The total pore volume of the Pb/C plates shows similar trends to the specific surface area measurement results, where the 1:8 ratio of Pb to C showed the highest pore volume of 0.048 cm^3g^{-1}. Subsequently, the 1:4 ratio plate shows a higher pore volume of 0.043 $cm^3 g^{-1}$ which is due to the less dense carbon property compared to much denser Pb metal. Following the trend, the total pore volumes were measured as 0.026 cm^3g^{-1} (1:1 ratio), 0.011 cm^3g^{-1} (4:1 ratio), and 0.006 $cm^3 g^{-1}$ (8:1 ratio). The BET analysis shows that the higher content of Pb in the 8:1 and 4:1 ratio possesses more metallic alloy-like properties, resulting in much lower pore volumes and a decrease in exposed surface areas. On the other hand, as the C ratio increases from 1:1 to 1:4 and 1:8, the pore volume tends to increase, thereby, the surface area increases. The carbon mixed into the lead lowers the density of the plates for lightweight utilizations.

3.3 Physicochemical analysis

The changes in electrical conductivity and the thickness under pressing pressure were measured as shown in Figure 6. At the low pressure of 20 MPa (Figure 6A), the electrical conductivity of the plate with the lead carbon ratio of 1:1 showed the highest conductivity of 133.94 S cm^{-1} compared to the 1:4 and 1:8 ratio plates with 125.67 S cm^{-1} and 122.48 S cm^{-1}, respectively. On the other hand, where the Pb content increases, an enormous decrease in conductivity was measured as low as 53.76 S cm^{-1} (4:1 ratio) and 18.04 S cm^{-1} (8:1 ratio). These results indicate that carbon has a greater effect on conductivity than lead. As the pressure increases, the conductivity of the plates increases overall. The conductivity of the 1:1 ratio plate was increased by approximately 3.77 folds from

133.94 S cm^{-1}–504.40 S cm^{-1}, which was the highest conductivity among the synthesized bipolar plates at high pressure of 200 MPa.

The conductivity of the 1:4 and 1:8 ratio plates was also greatly increased to 481.99 S cm^{-1} and 476.33 S cm^{-1}, respectively. The plates with higher Pb content have only increased by 91.61 S cm^{-1} for the 4:1 ratio (to 263.03 S cm^{-1} at 200 MPa) and 209.27 S cm^{-1} for the 8:1 ratio (to 109.65 S cm^{-1} at 200 MPa). Figure 6B shows the changes in the thickness of the synthesized bipolar plates under the pressing pressure of 20 MPa–200 MPa. The initial thickness of the plates showed the tendency to decrease as the Pb ratio increased, which may be due to an increase in the total pore volume corresponding with the BET results in Figure 5. The plate with the 1:8 ratio of Pb and C was the thickest with approximately 4.94 mm under 20 MPa of pressing pressure. The plates with other ratios were measured as 4.56 mm (1:4 ratio), 3.56 mm (1:1 ratio), 1.86 mm (4:1 ratio), and 1.65 mm (8:1 ratio). These tendencies correlate with the total pore volumes where the carbon opens the pores within the plates for increased surface area and decreased density. Correspondingly, when the pressure increases to 200 MPa, there is a huge drop in thickness. The thickness of the plates of 1:8, 1:4, and 1:1 ratio gets decreased to 3.26 mm, 3.03 mm, and 1.34 mm, respectively. The high Pb-contented plates showed minor changes in the thickness of 0.60 mm (4:1 ratio) and 0.46 mm (8:1 ratio) due to low pore volumes in the plates.

As shown in Figures 7A–F, the water contact angle measurement was taken to investigate the wettability properties of the synthesized bipolar plates. The wettability indicates the hydrophilicity of the bipolar plates, which can greatly affect the transportation of the electrolyte and the resultant water molecules from the URFC (Ait Djafer et al., 2014). The inner contact angle of the water droplet was measured to identify the hydrophilicity where the 1:1 ratio plate was the highest with an angle of 107.20°. The high angle of inner contact angle indicates that the plate is more hydrophobic, allowing for better transport of the electrolytes and resultant water molecules from URFC. The result also indicates that the 1:1 ratio plate was synthesized much more densely, and the roughness of the surface is distributed evenly. The contact angle of the plate with 1:4 and 4:1 ratio was measured as 95.64° and 81.13, respectively. The
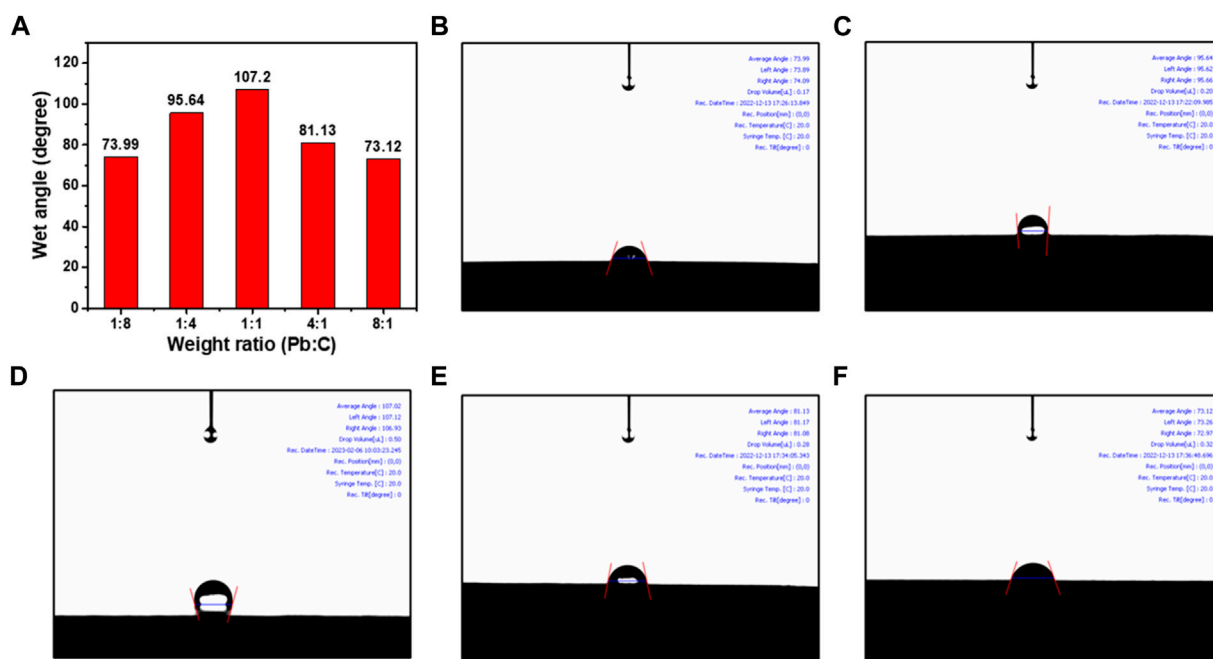
FIGURE 7
Water contact angle measurement results; **(A)** comparison table, Pb/C bipolar plates with ratios of **(B)** 1:8, **(C)** 1:4, **(D)** 1:1, **(E)** 4:1, **(F)** 8:1.
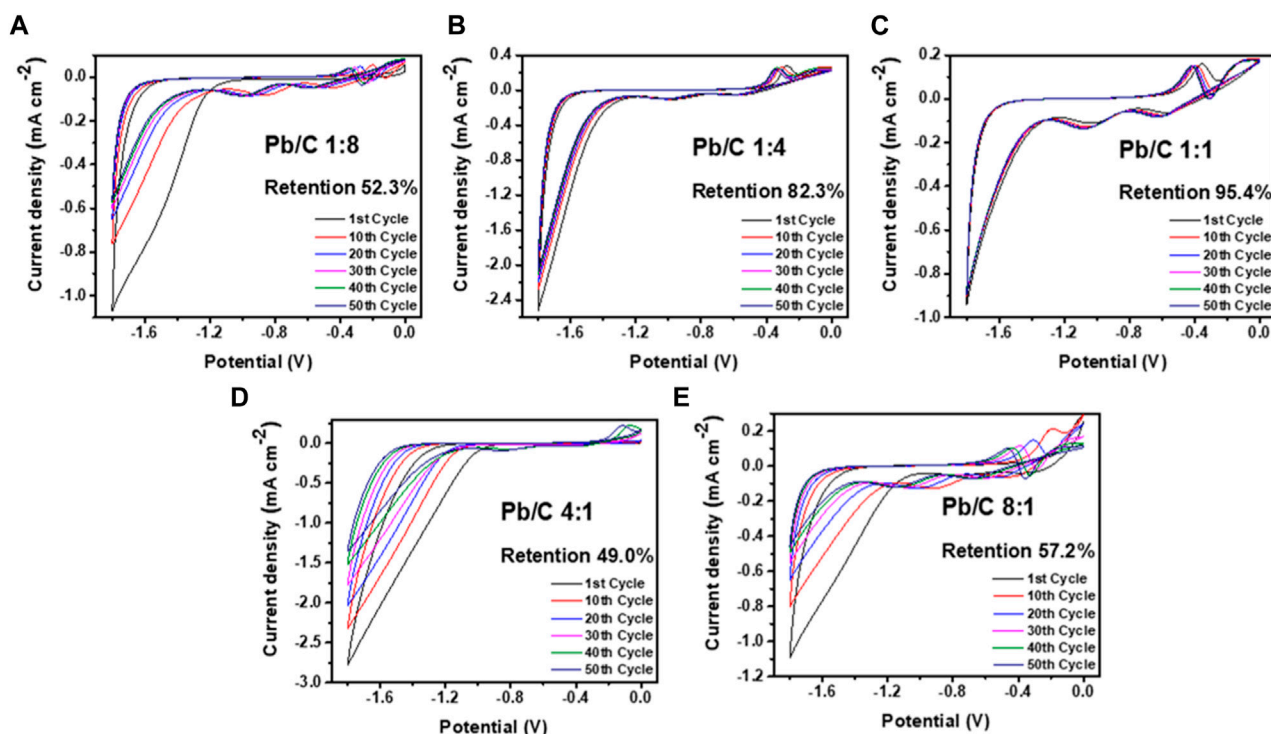
FIGURE 8
CV analysis using negative potentials in acidic medium (0.5 M H_2SO_4) at scan rate of 50 mV/sec; **(A)** 1:8, **(B)** 1:4, **(C)** 1:1, **(D)** 4:1, and **(E)** 8:1 ratios.
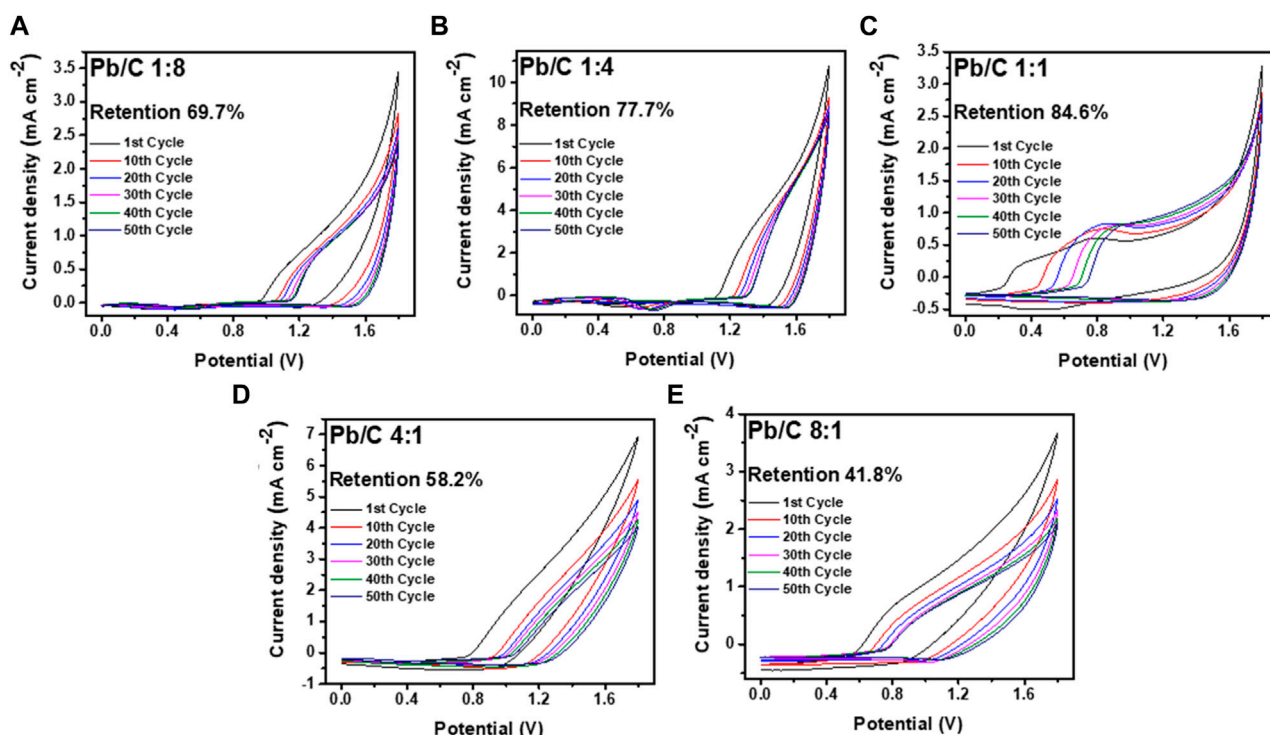
FIGURE 9
CV analysis using positive potentials in acidic medium (0.5 M H_2SO_4) at scan rate of 50 mV/sec; **(A)** 1:8, **(B)** 1:4, **(C)** 1:1, **(D)** 4:1, and **(E)** 8:1 Pb/C ratios.

droplet contact angle decreases when either the Pb or C content in the prepared lead carbon ratios becomes more biased. Both plates with the 1:8 ratio and 8:1 ratio show much lower contact angles of 73.99° and 73.12, respectively, which indicates that the plates are more hydrophilic compared to the 1:1 ratio of Pb and C. Considering the electrical conductivity under the pressing pressure and the wettability properties, the Pb/C bipolar plates, synthesized with a 1:1 ratio, are best suited for utilization in URFC. The plate with a 1:1 ratio of Pb and C also shows moderate effects in thickness under pressing pressure, indicating that the plate can withstand the pressure when stacked in URFC.

3.4 Electrochemical analysis

The electrochemical retention rate was measured to investigate the electrochemical capability through multiple uses for URFCs. Cyclic voltammetry was measured in negative and positive potential ranges, as shown in Figures 8A–E; Figures 9A–E. Each plate was run through 50 cycles in the acidic medium of 0.5 M H_2SO_4 electrolyte in the three-electrode configuration with Pt wire and Ag/AgCl electrode as counter and reference electrodes, respectively. The CV analysis shows the percentage decrease in the current density value at 1.8V compared to the first and 50th cycle results as the retention rate.

Measurement through the negative potential range of - 1.8 V–0.0 V vs. Ag/AgCl, shows that the Pb/C plate with a 1:1 ratio had the highest stability with a 95.4% retention rate over 50 CV cycles. The Pb to C ratio

of the 1:1 plate showed electrochemically most stable performances indicating that it is most suitable for URFC bipolar plate. Subsequently, the 1:4 ratio plate shows better retention, where approximately 82.3% of the first performance was maintained after multiple cycles. The plates with biased Pb or C content showed almost half the retention rate of the 1:1 plate. Both the 1:8 and 8:1 plates showed a retention rate of 52.3% and 57.2%, respectively, whereas the 4:1 plate showed the lowest retention rate of 49.0% after the 50th cycle. The great decrease in retention rate indicates that an even ratio of Pb and C is more electrochemically stable in the negative potentials. The positive potential range of 0 V–1.8 V vs. Ag/AgCl was measured with the same configuration, as shown in Figure 9. Similar to the negative potential, the 1:1 ratio of Pb and C plate showed the highest retention rate over 50 cycles with the rate of 84.6%, followed by 1:4 ratio plate with 77.7% retention. The high Pb ratios of 4:1 and 8:1 also showed a poor retention rate in the positive potentials, with rates of 58.2% and 41.8%, respectively. Comparatively, the 1:8 plate, which showed the lowest retention rate in the negative potentials, had a retention rate of 69.7% which was higher than that of the 4:1 and 8:1 ratios.

Figure 10 shows the potentiodynamic polarization curves of the Pb/C bipolar plate with different compositions of 1:8, 1:4, 1:1, 4:1, and 8:1 ratios in the simulated 0.5 M H_2SO_4 solution. In the range of 0–1.8V (vs. Ag/AgCl), the corrosion potential of Pb/C 1:8, 1:4, 1:1, 4:1, and 8:1 is 0.165 V, 0.167 V, 0.211 V, 0.173 V, and 0.185 V. Thermodynamically, the higher the corrosion potential, the higher the potential must be applied for the reaction to occur. In other words, it has high chemical inertness and corrosion resistance (Zhao
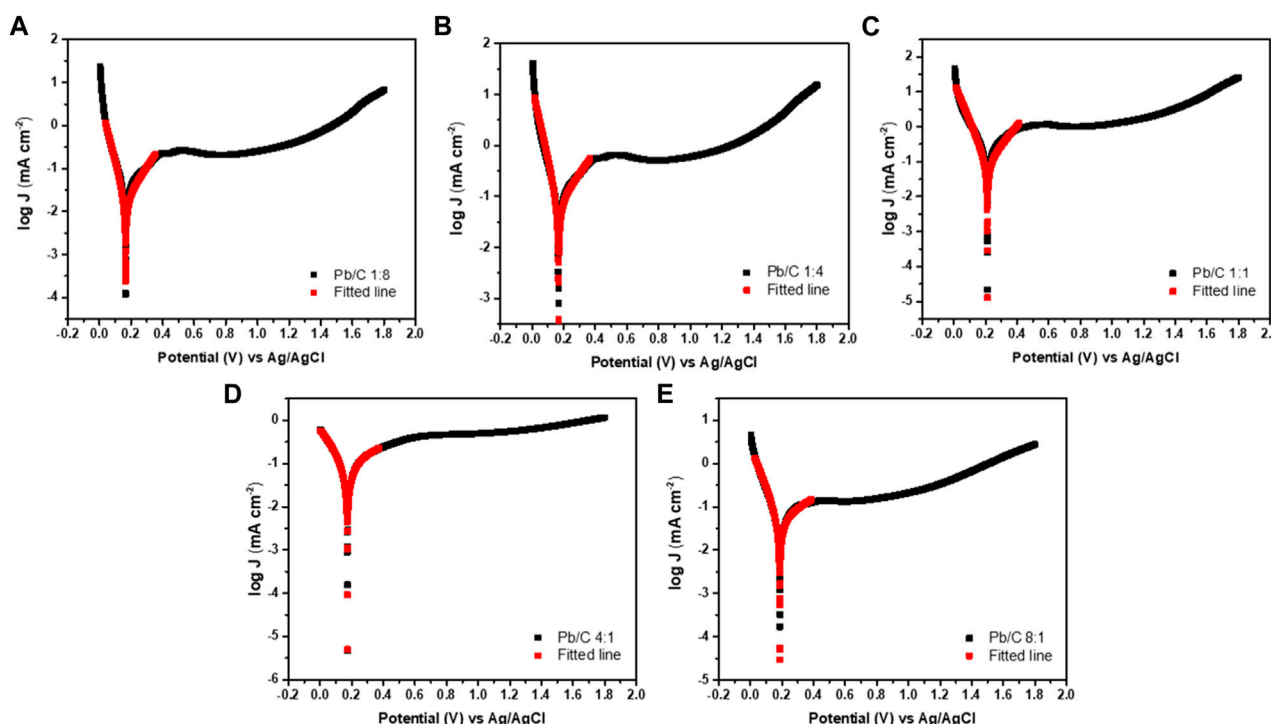
FIGURE 10
Potentiodynamic polarization curves in acidic medium (0.5 M H$_2$SO$_4$); **(A)**1:8, **(B)** 1:4, **(C)**1:1, **(D)**4:1, and **(E)** 8:1 ratios at the scan rate of 50 mV/sec.

et al., 2016). Among the candidates, the corrosion potential of the Pb/C 1:1 ratio was the highest, indicating that the corrosion resistance of the composite separator can be improved if Pb and carbon are combined in an appropriate ratio.

The overall electrochemical analysis indicates that the Pb and C ratio of 1:1 is best suitable for the utilization in URFC as a bipolar plate due to its high durability over multiple cycles. As the ratio of one element increases to the other, the durability tends to degrade in acidic media. The electrical properties under pressing pressure and the electrochemical analysis show that employing the most efficient 1:1 ratio Pb/C bipolar plate will possibly serve the highly efficient electrochemical system, the URFC.

From the analyzed results, it was found that the pressed density, porosity, electrical conductivity, electrochemical durability, and corrosion resistance are different depending on the ratio of carbon and lead and that the properties tend to decrease when the ratio of either carbon or lead increases. This means that bipolar plates made of mixed Pb/C powder and lead below the melting point have bulk properties due to the presence of bulk particles. The distance between particles, porosity between particles, and the degree of grain boundary formation varies depending on the composite powder ratio, which affects electrical conductivity (Khodabakhshi et al., 2020). It also affects the compaction rate and density. Since corrosion resistance increases in proportion to density, increasing the proportion of lead with fewer pores and higher density than carbon improves the corrosion resistance of bipolar plates (Singh et al., 2019). In Figure 1D, XPS spectra of Pb/C powder at a 1:1 ratio show that the Pb metallic characteristic dominates the Pb metallic peak of Pb/C powder at a 1:1 ratio, showing

comprehensive superiority in physical and electrochemical properties over other ratios, which are dominated by lead oxide peaks.

4 Conclusion

In this work, various proportions of lead/carbon composite materials are manufactured by a simple heating-compression process using SBR as a binder, and the electrochemical properties of the prepared bipolar plates are studied for being employed as separators in URFC. The morphological features, surface chemical nature, porosity, specific surface area, conductivity upon compressibility, wettability, and electrochemical performance of the varied proportions of lead carbon composite-based bipolar plates are examined in detail through essential physicochemical and electrochemical characterization techniques. The 1:1 ratio of lead/carbon composites showed better stability and high conductivity among all the prepared variants. The porosity and electrical conductivity of the composite are observed to increase with the increased proportion of carbon. The 1:1 ratio showed high hydrophobicity through a high contact angle, and its highest retention rate during electrochemical analysis ensures the durability of the prepared bipolar plate. Based on these results, we confirmed the possibility of a lead/carbon composite-based to be employed as a separator to URFC and could be a candidate for a new separator for URFC. It will also contribute to the development of separators that can be used not only in URFC but also in various applications.

Data availability statement

Author contributions

Funding

Conflict of interest

The authors declare that the research was conducted in the absence of any commercial or financial relationships that could be construed as a potential conflict of interest.

Publisher's note

All claims expressed in this article are solely those of the authors and do not necessarily represent those of their affiliated organizations, or those of the publisher, the editors and the reviewers. Any product that may be evaluated in this article, or claim that may be made by its manufacturer, is not guaranteed or endorsed by the publisher.

References

Adloo, A., Sadeghi, M., Masoomi, M., and Pazhooh, H. N. (2016). High performance polymeric bipolar plate based on polypropylene/graphite/graphene/nano-carbon black composites for PEM fuel cells. *Renew. Energy* 99, 867–874. doi:10.1016/j.renene.2016.07.062

Ait Djafer, A. Z., Saoula, N., Madaoui, N., and Zerizer, A. (2014). Deposition and characterization of titanium carbide thin films by magnetron sputtering using Ti and TiC targets. *Appl. Surf. Sci.* 312, 57–62. doi:10.1016/j.apsusc.2014.05.084

An, T.-Y., Surendran, S., Kim, H., Choe, W.-S., Kim, J. K., and Sim, U. (2019). A polydopamine-mediated biomimetic facile synthesis of molybdenum carbide-phosphide nanodots encapsulated in carbon shell for electrochemical hydrogen evolution reaction with long-term durability. *Compos. Part B Eng.* 175, 107071. doi:10.1016/j.compositesb.2019.107071

Chen, Z., Zhang, G., Yang, W., Xu, B., Chen, Y., Yin, X., et al. (2020). Superior conducting polypyrrole anti-corrosion coating containing functionalized carbon powders for 304 stainless steel bipolar plates in proton exchange membrane fuel cells. *Chem. Eng. J.* 393, 124675. doi:10.1016/j.cej.2020.124675

Choi, H., Seo, D. J., Choi, W. Y., Choi, S. W., Lee, M. H., Park, Y. J., et al. (2021). An ultralight-weight polymer electrolyte fuel cell based on woven carbon fiber-resin reinforced bipolar plate. *J. Power Sources* 484, 229291. doi:10.1016/j.jpowsour.2020.229291

De Luna, P., Hahn, C., Higgins, D., Jaffer, S. A., Jaramillo, T. F., and Sargent, E. H. (2019). What would it take for renewably powered electrosynthesis to displace petrochemical processes? *Science* 364, eaav3506. doi:10.1126/science.aav3506

Devrim, Y., Devrim, H., and Eroglu, I. (2015). Development of 500 W PEM fuel cell stack for portable power generators. *Int. J. Hydrogen Energy* 40, 7707–7719. doi:10.1016/j.ijhydene.2015.02.005

Du, L., Shao, Y., Sun, J., Yin, G., Liu, J., and Wang, Y. (2016). Advanced catalyst supports for PEM fuel cell cathodes. *Nano Energy* 29, 314–322. doi:10.1016/j.nanoen.2016.03.016

Gabbasa, M., Sopian, K., Fudholi, A., and Asim, N. (2014). A review of unitized regenerative fuel cell stack: Material, design and research achievements. *Int. J. Hydrogen Energy* 39, 17765–17778. doi:10.1016/j.ijhydene.2014.08.121

Gago, A. S., Ansar, S. A., Saruhan, B., Schulz, U., Lettenmeier, P., Cañas, N. A., et al. (2016). Protective coatings on stainless steel bipolar plates for proton exchange membrane (PEM) electrolysers. *J. Power Sources* 307, 815–825. doi:10.1016/j.jpowsour.2015.12.071

Hussain, J., Khan, A., and Zhou, K. (2020). The impact of natural resource depletion on energy use and CO2 emission in belt and road initiative countries: A cross-country analysis. *Energy* 199, 117409. doi:10.1016/j.energy.2020.117409

Janani, G., Surendran, S., Choi, H., An, T.-Y., Han, M.-K., Song, S.-J., et al. (2021). Anchoring of Ni12P5 microbricks in nitrogen-and phosphorus-enriched carbon frameworks: Engineering bifunctional active sites for efficient water-splitting systems. *ACS Sustain. Chem. Eng.* 10, 1182–1194. doi:10.1021/acssuschemeng.1c06514

Jung, H.-Y., Huang, S.-Y., and Popov, B. N. (2010). High-durability titanium bipolar plate modified by electrochemical deposition of platinum for unitized regenerative fuel cell (URFC). *J. Power Sources* 195, 1950–1956. doi:10.1016/j.jpowsour.2009.10.002

Karacan, K., Celik, S., Toros, S., Alkan, M., and Aydin, U. (2020). Investigation of formability of metallic bipolar plates via stamping for light-weight PEM fuel cells. *Int. J. Hydrogen Energy* 45, 35149–35161. doi:10.1016/j.ijhydene.2020.01.251

Khodabakhshi, S., Fulvio, P. F., and Andreoli, E. (2020). Carbon black reborn: Structure and chemistry for renewable energy harnessing. *Carbon* 162, 604–649. doi:10.1016/j.carbon.2020.02.058

Klose, C., Saatkamp, T., Münchinger, A., Bohn, L., Titvinidze, G., Breitwieser, M., et al. (2020). All-hydrocarbon MEA for PEM water electrolysis combining low hydrogen crossover and high efficiency. *Adv. Energy Mater.* 10, 1903995. doi:10.1002/aenm.201903995

Kolahdooz, R., Asghari, S., Rashid-Nadimi, S., and Amirfazli, A. (2017). Integration of finite element analysis and design of experiment for the investigation of critical factors in rubber pad forming of metallic bipolar plates for PEM fuel cells. *Int. J. Hydrogen Energy* 42, 575–589. doi:10.1016/j.ijhydene.2016.11.020

Li, T., Yan, Z., Liu, Z., Yan, Y., and Chen, Y. (2021). Surface microstructure and performance of TiN monolayer film on titanium bipolar plate for PEMFC. *Int. J. Hydrogen Energy* 46, 31382–31390. doi:10.1016/j.ijhydene.2021.07.021

Lim, A., Kim, J., Lee, H. J., Kim, H.-J., Yoo, S. J., Jang, J. H., et al. (2020). Low-loading IrO2 supported on Pt for catalysis of PEM water electrolysis and regenerative fuel cells. *Appl. Catal. B Environ.* 272, 118955. doi:10.1016/j.apcatb.2020.118955

Lim, B. H., Majlan, E. H., Daud, W. R. W., Rosli, M. I., and Husaini, T. (2019). Three-dimensional study of stack on the performance of the proton exchange membrane fuel cell. *Energy* 169, 338–343. doi:10.1016/j.energy.2018.12.021

May, G. J., Davidson, A., and Monahov, B. (2018). Lead batteries for utility energy storage: A review. *J. Energy Storage* 15, 145–157. doi:10.1016/j.est.2017.11.008

Ozawa, A., Kudoh, Y., Kitagawa, N., and Muramatsu, R. (2019). Life cycle CO2 emissions from power generation using hydrogen energy carriers. *Int. J. Hydrogen Energy* 44, 11219–11232. doi:10.1016/j.ijhydene.2019.02.230

Pan, T. J., Zhang, B., Li, J., He, Y. X., and Lin, F. (2014). An investigation on corrosion protection of chromium nitride coated Fe–Cr alloy as a bipolar plate material for proton exchange membrane fuel cells. *J. Power Sources* 269, 81–87. doi:10.1016/j.jpowsour.2014.06.147

Paul, B., and Andrews, J. (2017). PEM unitised reversible/regenerative hydrogen fuel cell systems: State of the art and technical challenges. *Renew. Sustain. Energy Rev.* 79, 585–599. doi:10.1016/j.rser.2017.05.112

Peng, X., Taie, Z., Liu, J., Zhang, Y., Peng, X., Regmi, Y. N., et al. (2020). Hierarchical electrode design of highly efficient and stable unitized regenerative fuel cells (URFCs) for long-term energy storage. *Energy and Environ. Sci.* 13, 4872–4881. doi:10.1039/D0EE03244A

Ren, P., Pei, P., Chen, D., Zhang, L., Li, Y., Song, X., et al. (2022). Corrosion of metallic bipolar plates accelerated by operating conditions in a simulated PEM fuel cell cathode environment. *Renew. Energy* 194, 1277–1287. doi:10.1016/j.renene.2022.05.153

Reshetenko, T., Odgaard, M., Randolf, G., Ohtaki, K. K., Bradley, J. P., Zulevi, B., et al. (2022). Design of PGM-free cathodic catalyst layers for advanced PEM fuel cells. *Appl. Catal. B Environ.* 312, 121424. doi:10.1016/j.apcatb.2022.121424

Rubio-Garcia, J., Kucernak, A., Parra-Puerto, A., Liu, R., and Chakrabarti, B. (2020). Hydrogen/functionalized benzoquinone for a high-performance regenerative fuel cell as a potential large-scale energy storage platform. *J. Mater. Chem. A* 8, 3933–3941. doi:10.1039/C9TA12396B

Sadhasivam, T., Ajeya, K. V., Kim, Y. A., and Jung, H.-Y. (2020). An experimental investigation of the feasibility of Pb based bipolar plate material for unitized regenerative fuel cells system. *Int. J. Hydrogen Energy* 45, 13101–13107. doi:10.1016/j.ijhydene.2020.03.023

Shi, J., Zhang, P., Han, Y., Wang, H., Wang, X., Yu, Y., et al. (2020). Investigation on electrochemical behavior and surface conductivity of titanium carbide modified Ti bipolar plate of PEMFC. *Int. J. Hydrogen Energy* 45, 10050–10058. doi:10.1016/j.ijhydene.2020.01.203

Singh, P., Singh, I. B., and Mondal, D. P. (2019). A comparative study on compressive deformation and corrosion behaviour of heat treated Ti4wt%Al foam of different porosity made of milled and unmilled powders. *Mater. Sci. Eng. C* 98, 918–929. doi:10.1016/j.msec.2019.01.054

Soleimani Alavijeh, M., Kefayati, H., Nozad Golikand, A., and Shariati, S. (2019). Synthesis and characterization of epoxy/graphite/nano-copper nanocomposite for the fabrication of bipolar plate for PEMFCs. *J. Nanostructure Chem.* 9, 11–18. doi:10.1007/s40097-019-0293-x

Tsai, S.-Y., Lin, C.-H., Jian, Y.-J., Hou, K.-H., and Ger, M.-D. (2017). The fabrication and characteristics of electroless nickel and immersion Au-polytetrafluoroethylene composite coating on aluminum alloy 5052 as bipolar plate. *Surf. Coatings Technol.* 313, 151–157. doi:10.1016/j.surfcoat.2017.01.064

Wang, Z. L., Chen, J., and Lin, L. (2015). Progress in triboelectric nanogenerators as a new energy technology and self-powered sensors. *Energy and Environ. Sci.* 8, 2250–2282. doi:10.1039/C5EE01532D

Wu, C. W., Zhang, W., Han, X., Zhang, Y. X., and Ma, G. J. (2020). A systematic review for structure optimization and clamping load design of large proton exchange membrane fuel cell stack. *J. Power Sources* 476, 228724. doi:10.1016/j.jpowsour.2020.228724

Wu, S., Yang, W., Yan, H., Zuo, X., Cao, Z., Li, H., et al. (2021). A review of modified metal bipolar plates for proton exchange membrane fuel cells. *Int. J. Hydrogen Energy* 46, 8672–8701. doi:10.1016/j.ijhydene.2020.12.074

Xiong, K., Wu, W., Wang, S., and Zhang, L. (2021). Modeling, design, materials and fabrication of bipolar plates for proton exchange membrane fuel cell: A review. *Appl. Energy* 301, 117443. doi:10.1016/j.apenergy.2021.117443

Yan, X., Hou, M., Zhang, H., Jing, F., Ming, P., and Yi, B. (2006). Performance of PEMFC with expanded graphite bipolar plates. *J. Power Sources* 160, 252–257. doi:10.1016/j.jpowsour.2006.01.022

Yao, K., Adams, D., Hao, A., Zheng, J. P., Liang, Z., and Nguyen, N. (2017). Highly conductive and strong graphite-phenolic resin composite for bipolar plate applications. *Energy and Fuels* 31, 14320–14331. doi:10.1021/acs.energyfuels.7b02678

Yue, M., Lambert, H., Pahon, E., Roche, R., Jemei, S., and Hissel, D. (2021). Hydrogen energy systems: A critical review of technologies, applications, trends and challenges. *Renew. Sustain. Energy Rev.* 146, 111180. doi:10.1016/j.rser.2021.111180

Zhang, Z., Guo, M., Yu, Z., Yao, S., Wang, J., Qiu, D., et al. (2022). A novel cooperative design with optimized flow field on bipolar plates and hybrid wettability gas diffusion layer for proton exchange membrane unitized regenerative fuel cell. *Energy* 239, 122375. doi:10.1016/j.energy.2021.122375

Zhao, Y., Wei, L., Yi, P., and Peng, L. (2016). Influence of Cr-C film composition on electrical and corrosion properties of 316L stainless steel as bipolar plates for PEMFCs. *Int. J. Hydrogen Energy* 41, 1142–1150. doi:10.1016/j.ijhydene.2015.10.047

Sensitivity enhancement of a Cu (II) metal organic framework-acetylene black-based electrochemical sensor for ultrasensitive detection of imatinib in clinical samples

Xuanming Xu, Shun Li, Xingwei Luan, Chao Xuan, Peng Zhao, Tingting Zhou*, Qingwu Tian* and Deng Pan*

Department of Clinical Laboratory, The Affiliated Hospital of Qingdao University, Qingdao, Shandong, China

Imatinib (IMB), an anticancer drug, is extensively used for chemotherapy to improve the quality of life of cancer patients. The aim of therapeutic drug monitoring (TDM) is to guide and evaluate the medicinal therapy, and then optimize the clinical effect of individual dosing regimens. In this work, a highly sensitive and selective electrochemical sensor based on glassy carbon electrode (GCE) modified with acetylene black (AB) and a Cu (II) metal organic framework (CuMOF) was developed to measure the concentration of IMB. CuMOF with preferable adsorbability and AB with excellent electrical conductivity functioned cooperatively to enhance the analytical determination of IMB. The modified electrodes were characterized using X-rays diffraction (XRD), X-ray photoelectron spectroscopy (XPS), fourier transform infrared (FT-IR), ultraviolet and visible spectrophotometry (UV-vis), electrochemical impedance spectroscopy (EIS), scanning electron microscopy (SEM), energy dispersive X-ray spectroscopy (EDS), brunauer–emmett–teller (BET) and barrett–joyner–halenda (BJH) techniques. Analytical parameters such as the ratio of CuMOF to AB, dropping volumes, pH, scanning rate and accumulation time were investigated through cyclic voltammetry (CV). Under optimal conditions, the sensor exhibited an excellent electrocatalytic response for IMB detection, and two linear detection ranges were obatined of 2.5 nM-1.0 µM and 1.0−6.0 µM with a detection limit (DL) of 1.7 nM (S/N = 3). Finally, the good electroanalytical ability of CuMOF-AB/GCE sensor facilitated the successful determination of IMB in human serum samples. Due to its acceptable selectivity, repeatability and long-term stability, this sensor shows promising application prospects in the detection of IMB in clinical samples.

KEYWORDS

imatinib, metal-organic frameworks, acetylene black, electrochemical sensor, glassy carbon electrode

1 Introduction

Imatinib (IMB, also known by its trade name of Gleevec/Glivec), is a type of chemotherapy medication approved by the Food and Drug Administration (FDA) in 2001 (Diculescu et al., 2009). As a pioneer tyrosine kinase inhibitor (TKI), it is applied to treat certain types of cancers such as chronic myelogenous leukemia (CML) and acute lymphocytic leukemia (ALL), for patients in which the Philadelphia chromosome is positive (Ph+) (Qu et al., 2019). Moreover, imatinib also deregulates the tyrosine kinase activity of *c-Kit* associated with gastrointestinal stromal tumors (GISTs) (Gajski et al., 2019; Li et al., 2022). In addition, this orally administered drug is rapidly absorbed and its absolute bioavailability is generally almost 76% (Peng et al., 2005; Roosendaal et al., 2020). Thus, it can be mainly metabolized by the liver CYP3A4 enzyme into N-desmethyl imatinib, which has a bioactivity similar to that of its parent medicine (Adiwidjaja et al., 2020).

Therapeutic drug monitoring (TDM) refers to the clinical practice of measuring the drug concentrations in biological fluids of patients at specified time intervals and controlling their drug doses in a timely manner to formulate individualized dosing regimens (Mueller-Schoell et al., 2021). Current evidence from clinical trials shows that when the measured steady-state minimum plasma concentrations of IMB were ($C_{min,ss}$) ≥1,000 ng/mL, complete cytogenic response (CcyR) and major molecular response (MMR) resulted in significant improvement in CML patients (Miura, 2015). However, a $C_{min,SS}$ of IMB >3,000 ng/mL was associated with a higher incidence of adverse events (AEs) (Guilhot et al., 2012). Hence the effective therapeutic window of the $C_{min,SS}$ of imatinib should be maintained between 1,000 and 3,000 ng/mL to achieve dose optimization in precise clinical treatment. Remarkably, concentrations of imatinib and its metabolite in plasma have demonstrated significant interindividual variation (Farag et al., 2017).

In the past few decades, various analytical techniques have been developed for IMB determination, such as fluorescence (Yan et al., 2016), liquid chromatography-tandem mass spectrometry (LC–MS/MS) (Kralj et al., 2012), high-performance liquid chromatography (HPLC) (D'Avolio et al., 2012) and capillary electrophoresis (CE) (Rodrı́guez Flores et al., 2003). Among them, liquid chromatography and mass spectrometry have time-consuming pretreatment processes and require professionals with relevant knowledge backgrounds (Chen et al., 2020). Capillary electrophoresis frequently produces unreliable results with limited sensitivity (Sánchez-López et al., 2016), while the drawback of fluorescence is that it is generally vulnerable to interfering substances (Zheng et al., 2019). These shortcomings of the reported approaches have forced researchers to develop rapid and convenient methods. Determination methods based on electrochemical sensors have been extensively applied with a number of advantages, such as timeliness, no complex preprocessing procedures, real-time detection under *in situ* conditions, and highly sensitive and selective analysis of clinical samples (Feng et al., 2021; Wang et al., 2022). Moreover, the presence of electrical activity sites on the IMB surface means that an electrochemical detection method is feasible (Hassan Pour et al., 2021). Accordingly, it is of great significance to establish a simple, fast and low-cost IMB electrochemical detection method.

Metal organic frameworks (MOFs) are a type of porous coordination polymers (PCPs) that have multidimensional network structures, and are synthesized by combining inorganic metal ions or metal clusters with organic ligands (Xu et al., 2010; Zhou et al., 2015; Yola, 2021). By virtue of their expandable pore surfaces, multiple coordination sites and outstanding adsorption capacity, MOFs have recently received significant attention for application in catalysts, supercapacitors, and drug delivery, storage and separation (Zhou et al., 2015; Abbasi et al., 2016; Kumari et al., 2022). Despite these limitations, the application of MOFs in the field of electrochemistry still faces some obstacles, such as poor electrical conductivity and an unstable structure in aqueous environments (Kumari et al., 2022).

As one of the most extensively applied square-hole MOFs, CuMOF ($Cu_3(BTC)_2$ (BTC = 1,3,5-benzenetricarboxylate), also known as HKUST-1) is a potential adsorbent with a changeable large specific surface area, easily adjustable pore size and porous composition (Jahangiri–Dehaghani et al., 2022; Wachholz Junior et al., 2022). Additionally, CuMOFs can be suitable for applications that require the frequent loading and unloading of guests, and the activated empty phase of CuMOF has preferable affinity for IMB through hydrogen bonding (Abbasi et al., 2016). Due to these properties, CuMOF is a good candidate for IMB determination.

Acetylene black (AB), as a special class of porous carbon black, is obtained from acetylene (C_2H_2) which is decomposed exothermically under pressure during oxygen-free conditions (Yang et al., 2014). It is a perfect nonmetallic electrocatalyst due to its superior electrical conductivity, large specific surface area and enhanced electronic transfer efficiency (Xu et al., 2010; Feng et al., 2021).

On the basis of the above analysis, materials with superior electrical conductivity are generally used to improve the electron transfer capability of electrode surfaces modified by MOFs. Until now, combining CuMOF with AB for analytical application has rarely been reported. In this regard, a novel, efficient and lower LOD sensor was fabricated based on properties of AB and CuMOF structures due to excellent sensitivity, high selectivity and outstanding adsorptivity, for the electrochemical analysis of IMB in the present research (as shown in Scheme 1). In addition, the nano-materials were characterized by XRD, XPS, FT-IR, UV-vis, SEM, EDS, BET, and EIS methods. The synthesized materials were used to modify the surface of GCEs and successfully applied for IMB concentration detection in real serum samples.

2 Experimental section

Materials and reagents, equipment, electrode preparation, optimization of procedure parameters and procedures of the real samples are described in the Supplementary Material.

3 Result and discussion

3.1 Characterization of the materials

The surface morphology and structure of AB, CuMOF and CuMOF-AB were evaluated using scanning electron microscopy

SCHEME 1
Modification steps of the proposed CuMOF-AB/GCE sensor. CuMOF-AB was cast on the surface of GCE. An electrochemical workstation consisting of a saturated calomel electrode, platinum (Pt) pillar electrode and modified GCE, was applied for the enhanced detection of IMB in human serum samples.

FIGURE 1
SEM images of AB **(A)**, CuMOF **(B)** and CuMOF-AB **(C)**. SEM mapping images of CuMOF-AB **(D)**.
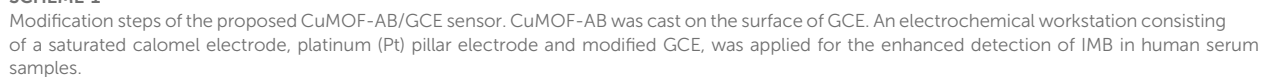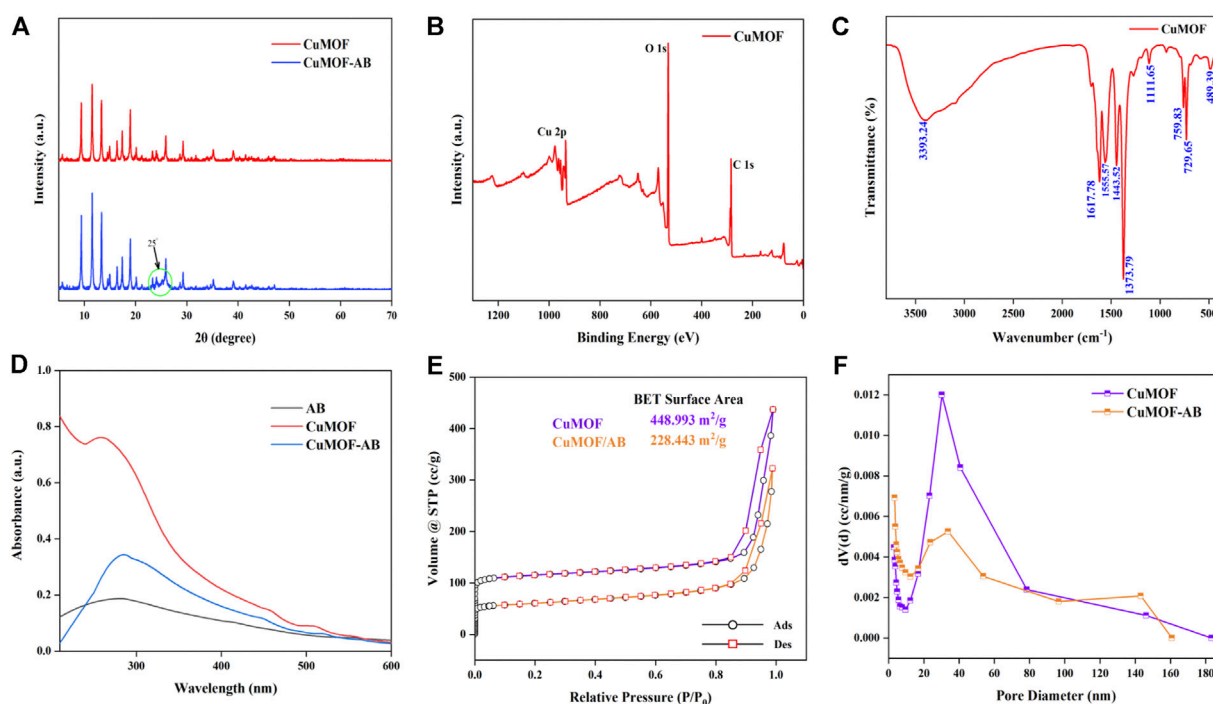
FIGURE 2
XRD **(A)** crystallography of the CuMOF and CuMOF-AB composites. XPS **(B)** and FT-IR **(C)** spectra of CuMOF. UV-visible spectroscopy **(D)** of AB, CuMOF and CuMOF-AB. Nitrogen adsorption–desorption isotherms **(E)** and pore diameter distribution **(F)** of CuMOF and CuMOF-AB.

(SEM) with a 20 kV accelerating voltage. As shown in Figure 1A, the particles of AB were spherical with an average diameter of 50 nm and had homogeneous surfaces with irregular polishing grooves; Figure 1B shows that the CuMOF crystals were octahedral in shape with distinct edges and sharp corners, and the various surface pore sizes enhanced the adsorption capacity. The SEM image shown in Figure 1C displays the morphology of the AB and CuMOF composites, and it was obvious that both materials were interpenetrated. In addition, in the SEM mapping image of CuMOF-AB (Figure 1D), carbon, oxygen and copper were found to be uniformly distributed throughout the nanocomposites. According to the energy dispersive spectroscopy (EDS) spectra of CuMOF (Supplementary Figure S1A), the C, O and Cu contents were 60.55%, 18.11% and 21.34%, respectively. However, from the results of the CuMOF-AB nanocomposite presented in Supplementary Figure S1B, the C content (83.10%) was obviously higher than the Cu and O contents, indicating the existence of AB.

The XRD patterns of CuMOF and CuMOF-AB composites had been provided in Figure 2A. CuMOF showed distinctive diffraction sharp peaks at 2θ of about 9.4°, 11.6°, 13.4°, 14.9°, 16.4°, 17.4° and 19.0° (Li et al., 2018; Rezvani Jalal et al., 2020), and the high peak intensities also could be readily confirmed the high crystalline structure of MOF. According to the previous literature, acetylene black only had a broad peak at 25° due to its amorphous structure (Sun et al., 2015), so the width of the diffraction peaks at 25° increased obviously in the composites.

XPS analysis was used to determine the chemical and electronic states. It could be demonstrated from the spectrum (Figure 2B) that the Cu, C and O elements coexist in CuMOF-AB. The characteristic

peaks of C 1s and O 1s located at the binding energies of about 285 and 532 eV, respectively. In Cu 2p regions, Cu $2p_{3/2}$ peak at 935.1 eV and its shakeup satellites were associated with Cu (II). The peak appearing at 955.1 eV with a satellite at 963.1 eV were assigned to Cu $2p_{1/2}$ (Quan et al., 2021; Zhang et al., 2023).

Confirmation of the synthesis of CuMOF were fairly supported by the outcomes of FT-IR. Figure 2C showed the broad peak around 3393.24 cm^{-1} region were apparent which was assigned to OH bands vibration of intercalated water. The absorption peaks at 1,617, 1,555, and 1,373 cm^{-1} could be assigned to the characteristic vibrations of C=O, and the band at about 1,443 cm^{-1} was ascribed to the C=C stretching in the aromatic structure (Wang et al., 2013). In addition, the absorption bands at 950–600 cm^{-1} were owing to C-H bending of benzene ring (Abbasi et al., 2017).

CuMOF related characteristic absorbance peak was at about 258 nm in the ultraviolet-visible (UV-vis) patterns (Gao et al., 2023). And introduction of AB made the new absorption peak exhibited a positive shift from 258 to 284 nm, indicating that CuMOF-AB nanocomposites had successfully formed (Figure 2D).

The adsorption-desorption isotherms of CuMOF and CuMOF-AB are shown in Figure 2E, which conformed to a *Type I* isotherm according to the IUPAC classification, indicating the existence of mesopores. The dramatic uptake at extremely low P/P_0 was due to the enhanced adsorptive interactions under narrow micropore conditions causing micropore filling (Thommes et al., 2015). Figure 2E shows that the BET specific surface areas of CuMOF and CuMOF-AB were 448.993 and 228.443 m^2/g, and the pore volumes were 0.68 and 0.50 cc/g, respectively. The BJH technique was used to investigate the average pore diameters of CuMOF and
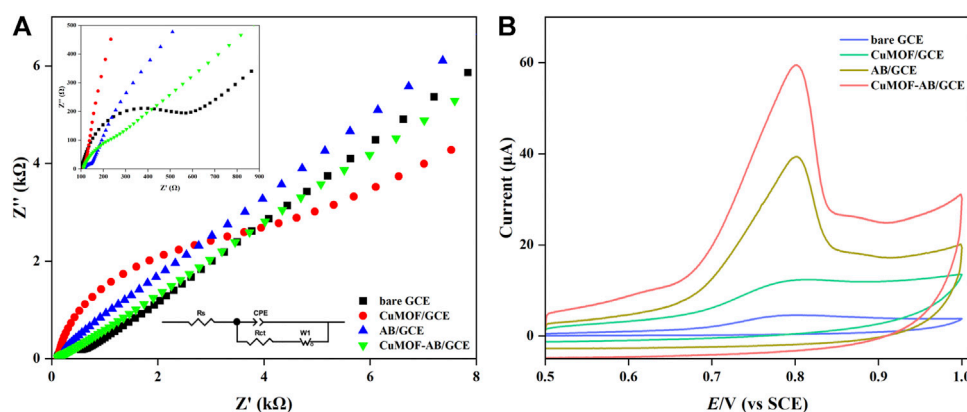
FIGURE 3
(A) Nyquist curves of bare GCE, CuMOF/GCE, AB/GCE and CuMOF-AB/GCE in 0.1 M KCl containing 5 mM $K_3Fe\,[(CN)_6]$ and $K_4Fe\,[(CN)_6]$ solution. The spectra were acquired at 50 mV ac amplitude in the frequency range from 100 kHz to 0.01 Hz **(B)** CVs of the bare GCE, CuMOF/GCE, AB/GCE and CuMOF-AB/GCE in 0.5 μM IMB solution (pH = 7) at a scanning rate of 100 mV/s.

CuMOF-AB, which were found to be 30.257 nm and 3.410 nm, respectively, by the adsorption method (Figure 2F). These results are summarized in Supplementary Table S1. Due to the incorporation of AB, it was clear that compared with CuMOF, the pore size of CuMOF-AB composites changed significantly, indicating that CuMOF-AB nanocomposites were successfully prepared.

3.2 Electrochemical characterization of the modified electrodes

The electroactive surface areas of the bare GCE, AB/GCE and CuMOF-AB/GCE modified electrodes were measured at various scan rates in solution containing 0.25 mM $[Fe(CN)6]^{3-/4-}$ and 0.1 M KCl. Randles-Sevcik equation (Foroughi et al., 2021) was computed to analyze the efficacy of embedded sensor with bare GCE, AB/GCE and CuMOF-AB/GCE at 25°C.

$$I_P = 269000\ n^{3/2}AD^{1/2}Cv^{1/2} \tag{1}$$

Where, I_p is the peak current, n shows the number of electrons consisted in the process (n = 1), D stands for the diffusion coefficient (7.6×10^{-6} cm^2/s), A for the electrode surface area (cm^2), v for the scan rate (V/s) and C for the $[Fe(CN)6]^{3-/4-}$ concentration (mol/cm^3) (Taherizadeh et al., 2023). As shown in Supplementary Figure S2, the slopes from the plot of current against scanning rate square root were used for the calculation of the electroactive surface areas, and A values were 0.08, 0.11, and 0.14 cm^2 for the surfaces of bare GCE, AB/GCE and CuMOF-AB/GCE, respectively. So CuMOF-AB could be reinforced during electroanalysis because an impressive elevation in its electroactive surface area.

EIS, as a powerful characterization technique, is used to measure the impedance of analyzed samples in the appropriate frequency range by applying a sinusoidal voltage or current. Moreover, the actually measured Nyquist spectra are always fitted with equivalent electrical circuits, which are regarded as electrical fingerprints, to evaluate electrochemical properties and behaviors. The high-frequency part of the Nyquist plot indicates charge transfer

resistance (R_{ct}), which is represented by the diameter of the semicircle. In contrast, in the low-frequency region, the straight lines correspond to ion diffusion in redox reactions. In addition, the change in R_{ct} value is determined by the characteristics of the modifiers and modification reaction on the surface (Singh et al., 2023).

The EIS equivalent circuit model of the four different electrodes is shown in Figure 3A (insets), where R_s and W_1 are the electrical resistance of the electrolyte and the Warburg impedance, respectively. To improve accuracy, a constant phase element (CPE) is used to model C_{dl}, which represents the capacitance of a double layer at the electrode and electrolyte (Grossi and Riccò, 2017). In addition, the Nyquist plot (Figure 3A) of the bare GCE showed a relatively large semicircle with an R_{ct} of 600 Ω. After the modification of the GCE with AB, the value of R_{ct} decreased to 66 Ω, which confirmed that the electron-transfer property of AB/GCE improved. For CuMOF/GCE, both the diameter and R_{ct} (6,456 Ω) increased, which demonstrated that the presence of CuMOF hindered electron transfer on the electrode surface, which might have occurred because the CuMOF framework is intrinsically insensitive to electrocatalysis. Compared with the bare GCE and CuMOF/GCE, CuMOF incorporated with AB exhibited additional decreases in R_{ct} (370 Ω). Consequently, it was inferred that AB compensated for the poor conductivity of the CuMOF and notably facilitated fast electron transfer between the $[Fe(CN)_6]^{3-/4-}$ solution and the modified GCE surface.

3.3 Electrochemical behavior of IMB on GCE

To investigate the electrochemical behavior of IMB (3 μM) on different modified electrodes, CV was used to record oxidation currents and potentials in 0.1 M PBS (pH = 7). As shown in Figure 3B, oxidation peaks were observed at approximately +0.82 V in the positive potential scanning, but the corresponding peaks of reduction were not observed in the reverse scanning. This phenomenon proved that the IMB reaction on all the above

modified electrodes was not reversible. The current response of the bare GCE was barely noticeable, revealing that the electron transfer process was extremely slow on the GCE only. In contrast, for the AB-modified electrode and CuMOF-modified electrode, the signals of IMB oxidation were slightly higher than those of the bare electrode. The oxidation peak current of CuMOF-AB/GCE was the largest, indicating that the fabricated CuMOF-AB composite film had better electroanalytical performance. A possible reason for this was the excellent conductivity of AB and the high catalytic and adsorption ability of porous CuMOF, in which the interior pores had Lewis acid coordination copper sites that were readily accessible for catalytic conversions (Schlichte et al., 2004). The adsorption of IMB by CuMOF might be dominated by hydrogen bonding to secondary building units (SBUs) and subsequently to other IMB molecules (Abbasi et al., 2016). These observations elucidated that IMB on CuMOF-AB/GCE exhibited the best electrochemical behavior.

3.4 Optimization of the analytical parameters

To ensure optimal sensing performance, the mass ratio of CuMOF to AB, drop volume of CuMOF-AB on the GCE and accumulation time were studied. While holding other conditions equal, the oxidation peak current gradually increased when increasing the mass ratio from 0:1 to 1.5:1 and then started to decrease as the mass ratio continued to increase (Supplementary Figure S3). A possible explanation for this was that the binding force of hydrogen bonds between the MOFs and IMB was weak due to the lack of CuMOF at low ratios, but at high ratios, the modified electrodes had poor conductivity and impeded electron transfer on the GCE surface, which was attributed to the reduction in the relative content of AB. Therefore, 1.5:1 was selected as the best ratio in this test.

A certain dropping volume of CuMOF-AB was a major and meaningful factor in the test procedures and had to be optimized. The CuMOF-AB volume effect was evaluated ranging from 4 to 8 μL, and the peak current was monitored. As shown in Supplementary Figure S4, the signal of the modified electrode increased up to $V_{CuMOF-AB}$ = 6 μL, and then the current values tended to be constant. These results indicated that the electrode surfaces were not fully covered by the prepared materials when the dropping volume was less than 6 μL, and then they reached a saturation state. Thus, considering material consumption and economic cost, 6 μL was selected as the optimal volume in further analysis. Additionally, the effect of the accumulation time (t_{ac}) of IMB on the sensor response was also investigated. As illustrated in Supplementary Figure S5, the maximum value of the relevant current was procured within 7 min and reached an equilibrium state. IMB adsorption on the GCE achieved saturation after 7 min, so t_{ac} = 7 was chosen for subsequent analysis.

As a quadrivalent base, imatinib is pH-sensitive owing to the presence of an amine and a pyridine group (Qi et al., 2016). Similarly, because most organic compounds are susceptibly influenced by the solution pH value in oxidation reactions, the oxidation behaviors of 3 μM IMB were necessarily evaluated using the fabricated CuMOF-AB/GCE in 0.1 M PBS

with the pH ranging from 3.0 to 9.0. As shown in Supplementary Figures S6 and S4A, the oxidation peak current increased from pH 3.0 to a maximum at pH 7.0 and then markedly decreased with further increases in pH; hence, this pH value was selected as the most appropriate pH. Due to the pK$_a$ of IMB (pK$_{a1}$ = 2.5, pK$_{a2}$ = 4.0 and pK$_{a3}$ = 8.2) (Mioduszewska et al., 2017), this drug was positively charged in solution at pH 7.0 and negatively charged at pH > 8.2. Moreover, because the surfaces of the CuMOF adsorbent were negatively charged when pH > 4 (Azhar et al., 2016), the maximum current was obtained (pH = 7) due to the electrostatic attraction of different charges. It should also be noted that the oxidation peak potentials shifted to more negative potentials as the pH increased, indicating H$^+$ participation in the oxidation process of IMB. Furthermore, Rodríguez (Rodríguez et al., 2018) found that the loss of the two protons from piperazine rings occurred at pK$_a$ values equal to approximately 4.0 and 8.0; hence, the IMB carried two positive charges when pH values were less than 4.0 and had only one positive charge until the pH was up to 8.0. As shown in Supplementary Figure S6, two distinct peaks were observed from pH 3 to 5, and one peak was observed at higher pH values. Moreover, the pH values were linearly correlated with E_P in the range of 3-8, and the linear equation was determined as E_P = −0.024 pH + 0.717 with R^2 = 0.993. The calculated slope was −0.024 (24 mV/pH), which was almost half of the theoretical Nernstian value (59 mV/pH) (Walczak et al., 1997), indicating that two electrons and one proton were involved in the IMB electro-oxidation process. These results were in accordance with those previously reported in the literature (Rodríguez et al., 2018; Rezvani Jalal et al., 2020; Hassan Pour et al., 2021). In addition, the line of E_P vs. pH was broken at approximately pH 8, which was almost coincident with the pK$_{a3}$ value of IMB.

3.5 Electrochemical mechanism of IMB on the CuMOF-AB/GCE

To determine the mechanism of the electrochemical process of CuMOF-AB/GCE, the CV of CuMOF-AB/GCE was collected while varying the scanning rate from 40 to 140 mV/s, as shown in Supplementary Figure S7. Under the optimized conditions, the peak current (I_P) and potential (E_P) progressively moved to positive values as the scanning rate (v) increased. As shown in Figure 4C, the peak current exhibited a great linear relationship with the scanning rates, and the corresponding regression equation was determined to be I (μA) = 0.886v +32.124 (R^2 = 0.996), indicating an adsorption-controlled process of IMB transport on the electrode surface (Rodríguez et al., 2018). Additionally, the linearity (Figure 4D) between E_P and ln v confirmed the intrinsic irreversibility of the IMB electrochemical processes and conformed to Laviron's equation (Laviron, 1979), which is expressed as follows:

$$E_P = E^0 + [RT/(1-\alpha)nF] \ln [RTk_s/(1-\alpha)nF] + [RT/(1-\alpha)nF] \ln v \tag{2}$$

where E^0 is the standard redox potential, R is the molecular gas constant (8.314 J mol^{-1} k^{-1}), T is the Kelvin temperature [T (298.15 K) = 273.15 +
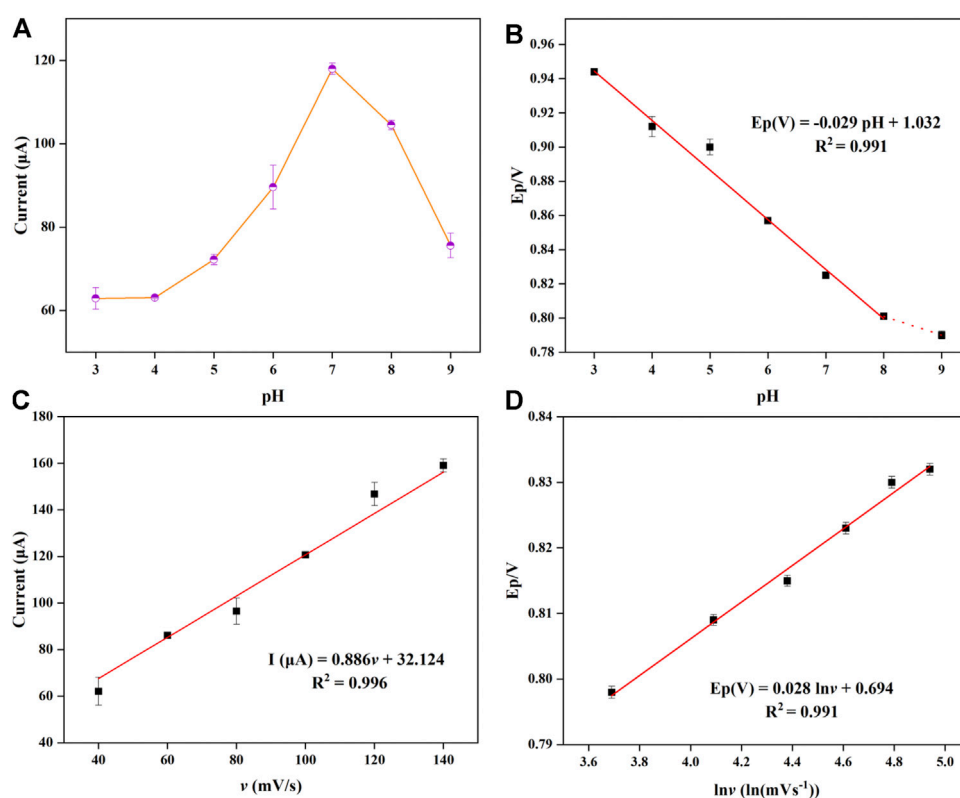
FIGURE 4
(A) Plots of the oxidation peak current vs. pH values from 3.0 to 9.0 at 100 mV/s. **(B)** Potential diagram of different pH values in the presence of 3 µM IMB in PBS solution. **(C)** Corresponding plot of current vs. scanning rate (40–140 mV/s) in the presence of 3 µM IMB in PBS solution. **(D)** Linear relationship between E_P and logarithm of scanning rate.
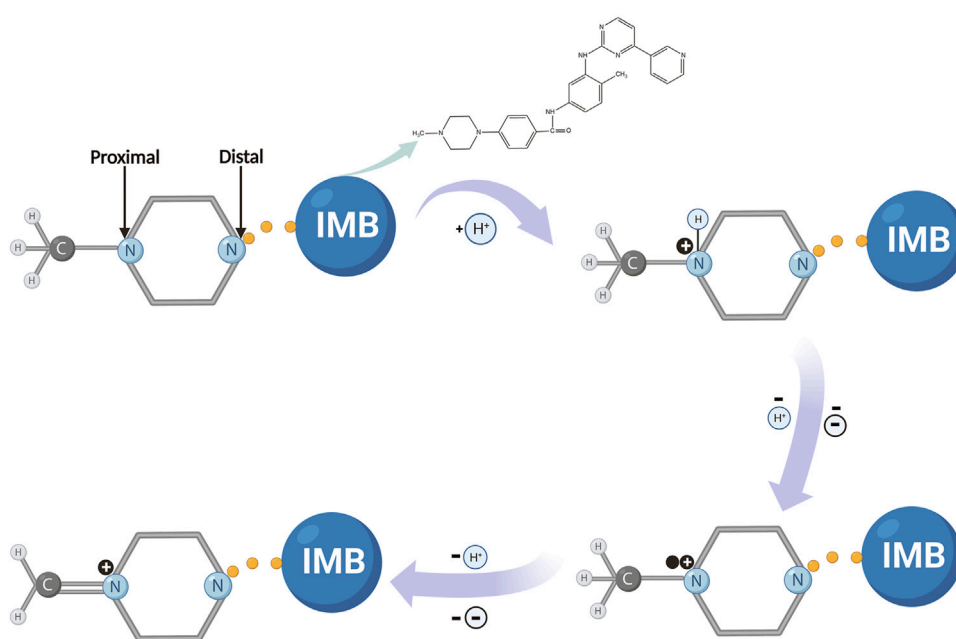
SCHEME 2
Possible reaction mechanism for IMB on the modified electrode.
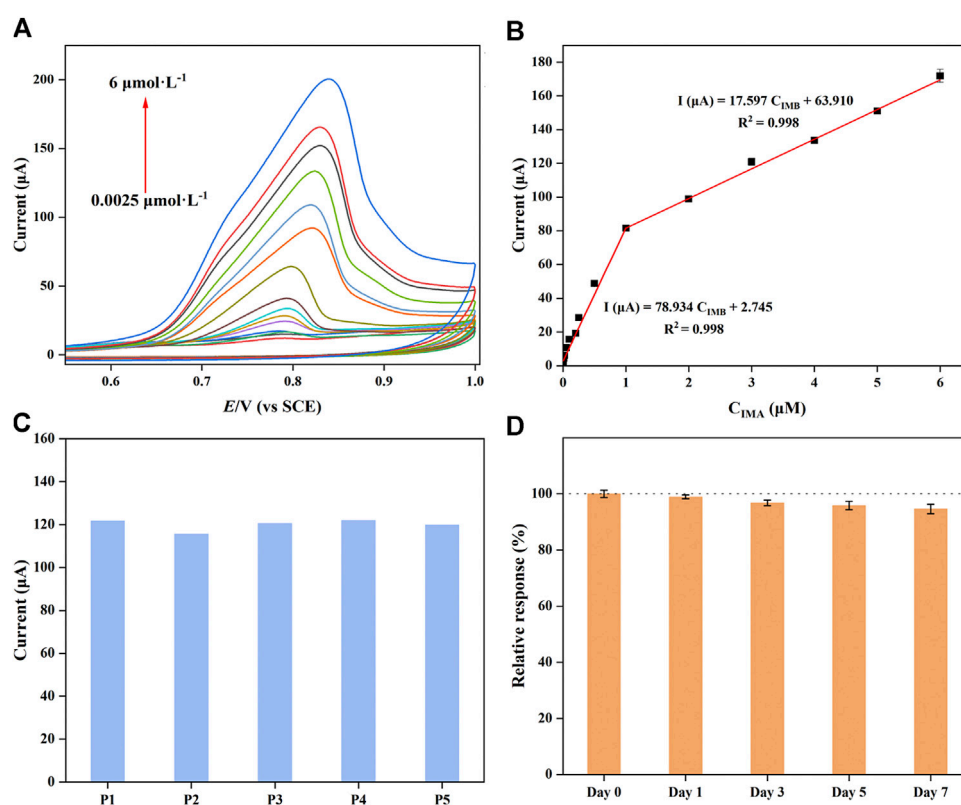
FIGURE 5
(A) Cyclic voltammograms and **(B)** calibration curves of CuMOF-AB/GCE at various concentrations (0.0025−6 µM) during IMB determination in PBS solution (pH = 7). **(C)** CV response of the five parallel electrodes to 3 µM IMB. **(D)** Stability of the fabricated sensors during a 7-day storage period.

TABLE 1 Comparison of various electrochemical sensor performances for IMB determination.

Sensors	Method	Linear range (µM)	LOD (nM)	Ref.
HMDE	SWV	0.019–1.9	5.6	Chen et al. (2014)
BDDE	DPV and CV	0.03–0.25	6.3	Brycht et al. (2016)
MWCNTs/SPCE	SWV and DPV	0.05–0.912	7.0	Rodríguez et al. (2018)
NiO-ZnO/MWCNT/GCE	DPV	0.015–2.0	2.4	Qian et al. (2021)
CuMOF-AB/GCE	CV and EIS	0.0025–6.0	1.7	This work

HMDE: hanging mercury drop electrode; BDDE: boron-doped diamond electrode; MWCNTs: multiwall carbon nanotubes; SPCE: screen-printed electrode; DPV: differential pulse voltammetry; SWV: square-wave voltammetry.

TABLE 2 Investigation of sensor applicability for IMB detection by standard addition method.

Sample	Added (µM)	CV method found (µM)	Recovery (%)	RSD (%) (n = 3)
1	0.5	0.5103	102.04	9.431
	1.0	0.9626	96.26	6.789
	2.0	1.9441	97.20	1.044
2	0.5	0.4654	93.49	4.312
	1.0	1.0601	106.01	2.107
	2.0	2.0169	100.85	2.305

25°C], F is the Faraday constant (96485.333 C mol^{-1}), n is the number of interchanged electrons, k_s is the rate constant of the electrochemical reaction, α is the charge-transfer coefficient, and v is the various scanning rates. According to the slope (0.027) of E_P vs. ln v, the value of $(1-\alpha)$ n was calculated to be equal to 0.94. Moreover, α was usually identified as 0.5 during the irreversible redox reaction; therefore, two electrons were involved in the oxidation of IMB on the surface of CuMOF-AB/GCE. This suggested conclusively that the electron transfer was consistent with that in the above PBS solution (pH = 7), so the possible electro-oxidation mechanism for IMB was proposed as shown in Scheme 2. In this overall mechanism, the nitrogen atom on the piperazine ring of IMB, as a pyridine compound molecule, undergoes electro-oxidation, accompanied by the removal of a proton and two electrons. The process is described as follows. First, the terminal nitrogen on the piperazine ring is protonated. Subsequently, another aliphatic nitrogen (i.e., proximal nitrogen) partially forms a cationic radical after losing a proton and an electron. In the next step, the piperazine moiety loses the same number of protons and electrons to convert into a quaternary Schiff base (Hammerich, 2003; Özkan et al., 2004; Uslu et al., 2005). Notably, this oxidation mechanism for IMB is almost consistent with that of the boron-doped diamond electrode reported by Brycht et al. (Brycht et al., 2016).

3.6 Analytical characteristics of the modified electrode

Under the optimal experimental conditions, the analytical characteristics of the proposed sensor were studied by CV in PBS (0.1 M, pH = 7) during IMB determination. As shown in Figure 5A, as the IMB concentrations gradually increased, the intensity of the response peak current increased simultaneously. Although the catalytic current was positively proportional to concentration variations, the slopes of the calibration curve were different in low- and high-concentration regions. The two corresponding linear regression equations are shown in Figure 5B: I (μA) = 78.934 C_{IMB} + 2.745 (R^2 = 0.998, 2.5 nM–1.0 μM) and I (μA) = 17.597 C_{IMB} + 63.910 (R^2 = 0.998, 1.0–6.0 μM), respectively. These results were attributed to the IMB on the surface of the modified electrode forming monolayer coverage at low concentrations; in contrast, multilayers covered the surface at high concentrations. The limit of detection (LOD) was calculated with the following equation:

$$LOD = \frac{3\sigma_{blank}}{m} \qquad (3)$$

where the signal-to-noise ratio is S/N = 3, σ_{blank} is the standard deviation of the blank and m is the slope value of the calibration curve; hence, the LOD was calculated as 1.7 nM. Compared with other already reported sensors for IMB determination (Table 1), the prepared electrochemical sensor exhibited a wider linear range and a generally lower LOD. And the electrode used for the sensor fabrication was GCE that had various advantages such as cost-effectiveness, admirable modification, facile accessibility and low background current (Jahani et al., 2022) when comparing with other electrodes. However, several reported IMB sensors not only gave higher DLs; but required tedious sample preparation and complicated process. In addition, the satisfactory sensitivity of the modified GCE was attributed to the high specific surface area of CuMOF and the excellent conductivity of AB. Accordingly, as-

fabricated sensor could be potentially able to determine IMB in human serums.

To demonstrate the high selectivity of the proposed sensors, a series of interference tests were performed to evaluate the response of IMB. In this experiment, the tolerance limit resulted in a relative oxidation current error of less than 5% for the determination of 3 μM IMB. Several organic and inorganic interferents, such as anions, cations, vitamins and amino acids, were used to evaluate the capability of anti-interference. According to the results shown in Supplementary Table S2, there was a negligible effect of the mentioned interfering species, indicating these interferences did not influence the responses of IMB determination. Therefore, the electrochemical sensor constructed by CuMOF-AB displayed a good capability of resisting interference and excellent selectivity for IMB determination.

To verify the precision and practicability of the electrochemical electrodes, the repeatability and long-term stability of CuMOF-AB/GCE were investigated. As shown in Figure 5C, five parallel modified electrodes (P1-P5) were constructed in the same batch and used to measure known concentrations of IMB by CV in 1 day. The relative standard deviation (RSD) of the oxidation current was calculated as 2.14%, illustrating that the designed strategy had good reproducibility. Additionally, the stability of the suggested sensors was demonstrated in-sequence by measuring the IMB signals of the current over a period of a week. The results are shown in Figure 5D. The maximal change in current was 5.35%, which proved that the structure of the AB and CuMOF framework had acceptable stability and a long service life.

3.7 Analytical application in real samples

Real sample analysis is essential to evaluate the practicality of the developed electrode in determining the analyte with an acceptable recovery. The applicability and reliability of the fabricated electrodes were investigated by using them for the determination of IMB in human blood serum samples. The samples were prepared by the process described in the **Experimental Section**. According to Table 2, the standard recovery rate of IMB in clinical serums ranged from 93.49% to 106.01% with an RSD between 1.04% and 9.43%. Meanwhile, the accuracy of IMB detection in patient serum samples was compared with LC-MS. The obtained results were summarized in Supplementary Table S3 based on an average of 3 measurements (n = 3), suggesting the acceptable precision of the proposed method. Thus, the fabricated novel sensor can be used as an effective method for measuring IMB anticancer drugs in real biological samples.

4 Conclusion

In the present work, a new electrochemical sensor based on a CuMOF-AB nanocomposite was fabricated for the rapid and sensitive determination of IMB. CuMOF increased the attachment amount of IMB due to its excellent adsorbability, and AB enhanced electron transfer on the electrode surface due to its good conductivity. The effective CuMOF-AB nanocomposite exhibited improved electrocatalysis for IMB oxidation due to its

greater conductivity and active catalytic sites. Under optimal conditions, the prepared sensor exhibited satisfactory selectivity, repeatability, good stability, a lower DL (1.7 nM) and a wider linear range (2.5 nM-1.0 µM and 1.0–6.0 µM, respectively). The CuMOF-AB-based sensor had a wider linear range and lower LOD than those reported for sensors in previous studies. In summary, a novel approach with excellent enforceability was developed for the sensitive and selective monitoring of IMB in biological samples.

Data availability statement

The original contributions presented in the study are included in the article/Supplementary Material, further inquiries can be directed to the corresponding authors.

Ethics statement

The studies involving human participants were reviewed and approved by the Medical Ethics Committee of the Affiliated Hospital of Qingdao University. The patients/participants provided their written informed consent to participate in this study.

Author contributions

XX: investigation, writing-original draft. SL, XL, CX, PZ: investigation, methodology, writing-review and editing. TZ: writing-review and editing. QT: investigation and formal analysis. DP: review, supervision and funding acquisition. All authors listed have made a substantial, direct, and intellectual contribution to the work and approved it for publication.

Funding

Conflict of interest

The authors declare that the research was conducted in the absence of any commercial or financial relationships that could be construed as a potential conflict of interest.

Publisher's note

All claims expressed in this article are solely those of the authors and do not necessarily represent those of their affiliated organizations, or those of the publisher, the editors and the reviewers. Any product that may be evaluated in this article, or claim that may be made by its manufacturer, is not guaranteed or endorsed by the publisher.

Supplementary material

The Supplementary Material for this article can be found online at: https://www.frontiersin.org/articles/10.3389/fchem.2023.1191075/full#supplementary-material

References

Abbasi, A. R., Rizvandi, M., Azadbakht, A., and Rostamnia, S. (2016). Controlled uptake and release of imatinib from ultrasound nanoparticles Cu3(BTC) 2 metal–organic framework in comparison with bulk structure. *J. Colloid Interface Sci.* 471, 112–117. doi:10.1016/j.jcis.2016.03.018

Abbasi, A. R., Karimi, M., and Daasbjerg, K. (2017). Efficient removal of crystal violet and methylene blue from wastewater by ultrasound nanoparticles Cu-MOF in comparison with mechanosynthesis method. *Ultrason. Sonochem* 37, 182–191. doi:10.1016/j.ultsonch.2017.01.007

Adiwidjaja, J., Boddy, A. V., and McLachlan, A. J. (2020). Physiologically-based pharmacokinetic predictions of the effect of curcumin on metabolism of imatinib and bosutinib: *In vitro* and *in vivo* disconnect. *Pharm. Res.* 37 (7), 128. doi:10.1007/s11095-020-02834-8

Azhar, M. R., Abid, H. R., Sun, H., Periasamy, V., Tadé, M. O., and Wang, S. (2016). Excellent performance of copper based metal organic framework in adsorptive removal of toxic sulfonamide antibiotics from wastewater. *J. Colloid Interface Sci.* 478, 344–352. doi:10.1016/j.jcis.2016.06.032

Brycht, M., Kaczmarska, K., Uslu, B., Ozkan, S. A., and Skrzypek, S. (2016). Sensitive determination of anticancer drug imatinib in spiked human urine samples by differential pulse voltammetry on anodically pretreated boron-doped diamond electrode. *Diam. Relat. Mater* 68, 13–22. doi:10.1016/j.diamond.2016.05.007

Chen, H., Wang, X., Chopra, S., Adams, E., and Van Schepdael, A. (2014). Development and validation of an indirect pulsed electrochemical detection method for monitoring the inhibition of Abl1 tyrosine kinase. *J. Pharm. Biomed. Anal.* 90, 52–57. doi:10.1016/j.jpba.2013.11.022

Chen, S., Wang, C., Zhang, M., Zhang, W., Qi, J., Sun, X., et al. (2020). N-doped Cu-MOFs for efficient electrochemical determination of dopamine and sulfanilamide. *J. Hazard Mater* 390, 122157. doi:10.1016/j.jhazmat.2020.122157

D'Avolio, A., Simiele, M., De Francia, S., Ariaudo, A., Baietto, L., Cusato, J., et al. (2012). HPLC–MS method for the simultaneous quantification of the antileukemia drugs imatinib, dasatinib and nilotinib in human peripheral blood mononuclear cell (PBMC). *J. Pharm. Biomed. Anal.* 59, 109–116. doi:10.1016/j.jpba.2011.10.003

Diculescu, V. C., Chiorcea-Paquim, A.-M., Tugulea, L., Vivan, M., and Oliveira-Brett, A.-M. (2009). Interaction of imatinib with liposomes: Voltammetric and AFM characterization. *Bioelectrochemistry* 74 (2), 278–288. doi:10.1016/j.bioelechem.2008.10.003

Farag, S., Verheijen, R. B., Martijn Kerst, J., Cats, A., Huitema, A. D. R., and Steeghs, N. (2017). Imatinib pharmacokinetics in a large observational cohort of gastrointestinal stromal tumour patients. *Clin. Pharmacokinet.* 56 (3), 287–292. doi:10.1007/s40262-016-0439-7

Feng, J., Deng, P., Xiao, J., Li, J., Tian, Y., Wu, Y., et al. (2021). New voltammetric method for determination of tyrosine in foodstuffs using an oxygen-functionalized multi-walled carbon nanotubes modified acetylene black paste electrode. *J. Food Compos Anal.* 96, 103708. doi:10.1016/j.jfca.2020.103708

Foroughi, M. M., Jahani, S., Aramesh-Boroujeni, Z., Vakili Fathabadi, M., Hashemipour Rafsanjani, H., and Rostaminasab Dolatabad, M. (2021). Template-free synthesis of ZnO/Fe3O4/Carbon magnetic nanocomposite: Nanotubes with hexagonal cross sections and their electrocatalytic property for simultaneous determination of oxymorphone and heroin. *Microchem J.* 170, 106679. doi:10.1016/j.microc.2021.106679

Gajski, G., Gerić, M., Domijan, A. M., Golubović, I., and Garaj-Vrhovac, V. (2019). Evaluation of oxidative stress responses in human circulating blood cells after imatinib mesylate treatment - implications its mechanism of action. *Saudi Pharm. J.* 27 (8), 1216–1221. doi:10.1016/j.jsps.2019.10.005

Gao, Y., Zhou, D., Xu, Q., Li, J., Luo, W., Yang, J., et al. (2023). Metal–organic framework-mediated bioorthogonal reaction to immobilize bacteria for ultrasensitive fluorescence counting immunoassays. *ACS Appl. Mater Interfaces* 15 (4), 5010–5018. doi:10.1021/acsami.2c21350

Grossi, M., and Riccò, B. (2017). Electrical impedance spectroscopy (EIS) for biological analysis and food characterization: A review. *J. Sens. Sens. Syst.* 6 (2), 303–325. doi:10.5194/jsss-6-303-2017

Guilhot, F., Hughes, T. P., Cortes, J., Druker, B. J., Baccarani, M., Gathmann, I., et al. (2012). Plasma exposure of imatinib and its correlation with clinical response in the tyrosine kinase inhibitor optimization and selectivity trial. *Haematologica* 97 (5), 731–738. doi:10.3324/haematol.2011.045666

Hammerich, O. (2003). Electrochemical reactions and mechanisms in organic Chemistry, by james grimshaw. *Electrochim Acta* 48 (11), 1623–1624. doi:10.1016/S0013-4686(03)00086-0

Hassan Pour, B., Haghnazari, N., Keshavarzi, F., Ahmadi, E., and Rahimian Zarif, B. (2021). High sensitive electrochemical sensor for imatinib based on metal-organic frameworks and multiwall carbon nanotubes nanocomposite. *Microchem J.* 165, 106147. doi:10.1016/j.microc.2021.106147

Jahangiri–Dehaghani, F., Zare, H. R., Shekari, Z., and Benvidi, A. (2022). Development of an electrochemical aptasensor based on Au nanoparticles decorated on metal–organic framework nanosheets and p-biphenol electroactive label for the measurement of aflatoxin B1 in a rice flour sample. *Anal. Bioanal. Chem.* 414 (5), 1973–1985. doi:10.1007/s00216-021-03833-3

Jahani, S., Sedighi, A., Toolabi, A., and Foroughi, M. M. (2022). Development and characterization of La2O3 nanoparticles@snowflake-like Cu2S nanostructure composite modified electrode and application for simultaneous detection of catechol, hydroquinone and resorcinol as an electrochemical sensor. *Electrochim Acta* 416, 140261. doi:10.1016/j.electacta.2022.140261

Kralj, E., Trontelj, J., Pajič, T., and Kristl, A. (2012). Simultaneous measurement of imatinib, nilotinib and dasatinib in dried blood spot by ultra high performance liquid chromatography tandem mass spectrometry. *J. Chromatogr. B* 903, 150–156. doi:10.1016/j.jchromb.2012.07.011

Kumari, V., Pal Singh, P., and Kaushal, S. (2022). Synthesis and applications of metal-organic frameworks and graphene-based composites: A review. *Polyhedron* 214, 115645. doi:10.1016/j.poly.2021.115645

Laviron, E. (1979). General expression of the linear potential sweep voltammogram in the case of diffusionless electrochemical systems. *J. Electroanal. Chem. Interfacial Electrochem* 101 (1), 19–28. doi:10.1016/S0022-0728(79)80075-3

Li, J., Xia, J., Zhang, F., Wang, Z., and Liu, Q. (2018). An electrochemical sensor based on copper-based metal-organic frameworks-graphene composites for determination of dihydroxybenzene isomers in water. *Talanta* 181, 80–86. doi:10.1016/j.talanta.2018.01.002

Li, G. Z., Fairweather, M., Raut, C. P., and Wang, J. (2022). Use of neoadjuvant imatinib to facilitate minimally invasive resection of gastric gastrointestinal stromal tumors. *Ann. Surg. Oncol.* 29 (11), 7104–7113. doi:10.1245/s10434-022-11891-9

Mioduszewska, K., Dołżonek, J., Wyrzykowski, D., Kubik, Ł., Wiczling, P., Sikorska, C., et al. (2017). Overview of experimental and computational methods for the determination of the pKa values of 5-fluorouracil, cyclophosphamide, ifosfamide, imatinib and methotrexate. *Trac. Trends Anal. Chem.* 97, 283–296. doi:10.1016/j.trac.2017.09.009

Miura, M. (2015). Therapeutic drug monitoring of imatinib, nilotinib, and dasatinib for patients with chronic myeloid leukemia. *Biol. Pharm. Bull.* 38 (5), 645–654. doi:10.1248/bpb.b15-00103

Mueller-Schoell, A., Groenland, S. L., Scherf-Clavel, O., van Dyk, M., Huisinga, W., Michelet, R., et al. (2021). Therapeutic drug monitoring of oral targeted antineoplastic drugs. *Eur. J. Clin. Pharmacol.* 77 (4), 441–464. doi:10.1007/s00228-020-03014-8

Özkan, S. A., Uslu, B., and Zuman, P. (2004). Electrochemical oxidation of sildenafil citrate (Viagra) on carbon electrodes. *Anal. Chim. Acta* 501 (2), 227–233. doi:10.1016/j.aca.2003.09.033

Peng, B., Lloyd, P., and Schran, H. (2005). Clinical pharmacokinetics of imatinib. *Clin. Pharmacokinet.* 44 (9), 879–894. doi:10.2165/00003088-200544090-00001

Qi, C., Cai, Q., Zhao, P., Jia, X., Lu, N., He, L., et al. (2016). The metal-organic framework MIL-101(Cr) as efficient adsorbent in a vortex-assisted dispersive solid-phase extraction of imatinib mesylate in rat plasma coupled with ultra-performance liquid chromatography/mass spectrometry: Application to a pharmacokinetic study. *J. Chromatogr. A* 1449, 30–38. doi:10.1016/j.chroma.2016.04.055

Qian, L., Durairaj, S., Prins, S., and Chen, A. (2021). Nanomaterial-based electrochemical sensors and biosensors for the detection of pharmaceutical compounds. *Biosens. Bioelectron.* 175, 112836. doi:10.1016/j.bios.2020.112836

Qu, P., Han, J., Qiu, Y., Yu, H., Hao, J., Jin, R., et al. (2019). Huaier extract enhances the treatment efficacy of imatinib in Ik6+ Ph+ acute lymphoblastic leukemia. *Biomed. Pharmacother.* 117, 109071. doi:10.1016/j.biopha.2019.109071

Quan, J., Wang, G., and Jin, Z. (2021). Tactfully assembled CuMOF/CdS S-Scheme heterojunction for high-performance photocatalytic H2 evolution under visible light. *ACS Appl. Energy Mater* 4 (8), 8550–8562. doi:10.1021/acsaem.1c01755

Rezvani Jalal, N., Madrakian, T., Afkhami, A., and Ghoorchian, A. (2020). *In situ* growth of metal–organic framework HKUST-1 on graphene oxide nanoribbons with high electrochemical sensing performance in imatinib determination. *ACS Appl. Mater Interfaces* 12 (4), 4859–4869. doi:10.1021/acsami.9b18097

Rodríguez, J., Castañeda, G., and Lizcano, I. (2018). Electrochemical sensor for leukemia drug imatinib determination in urine by adsorptive striping square wave voltammetry using modified screen-printed electrodes. *Electrochim Acta* 269, 668–675. doi:10.1016/j.electacta.2018.03.051

Rodrı́guez Flores, J., Berzas, J. J., Castañeda, G., and Rodrı́guez, N. (2003). Direct and fast capillary zone electrophoretic method for the determination of Gleevec and its main metabolite in human urine. *J. Chromatogr. B* 794 (2), 381–388. doi:10.1016/S1570-0232(03)00518-X

Roosendaal, J., Groenland, S. L., Rosing, H., Lucas, L., Venekamp, N., Nuijen, B., et al. (2020). Determination of the absolute bioavailability of oral imatinib using a stable isotopically labeled intravenous imatinib-d8 microdose. *Eur. J. Clin. Pharmacol.* 76 (8), 1075–1082. doi:10.1007/s00228-020-02888-y

Sánchez-López, E., Marina, M. L., and Crego, A. L. (2016). Improving the sensitivity in chiral capillary electrophoresis. *Electrophoresis* 37 (1), 19–34. doi:10.1002/elps.201500315

Schlichte, K., Kratzke, T., and Kaskel, S. (2004). Improved synthesis, thermal stability and catalytic properties of the metal-organic framework compound Cu3(BTC)2. *Microporous Mesoporous Mater* 73 (1), 81–88. doi:10.1016/j.micromeso.2003.12.027

Singh, A. K., Jaiswal, N., Tiwari, I., Ahmad, M., and Silva, S. R. P. (2023). Electrochemical biosensors based on *in situ* grown carbon nanotubes on gold microelectrode array fabricated on glass substrate for glucose determination. *Microchim. Acta* 190 (2), 55. doi:10.1007/s00604-022-05626-6

Sun, Y., Wang, S., Cheng, H., Dai, Y., Yu, J., and Wu, J. (2015). Synthesis of a ternary polyaniline@acetylene black-sulfur material by continuous two-step liquid phase for lithium sulfur batteries. *Electrochim Acta* 158, 143–151. doi:10.1016/j.electacta.2015.01.150

Taherizadeh, M., Jahani, S., Moradalizadeh, M., and Foroughi, M. M. (2023). Synthesis of a dual-functional terbium doped copper oxide nanoflowers for high-efficiently electrochemical sensing of ofloxacin, pefloxacin and gatifloxacin. *Talanta* 255, 124216. doi:10.1016/j.talanta.2022.124216

Thommes, M., Kaneko, K., Neimark, A. V., Olivier, J. P., Rodriguez-Reinoso, F., Rouquerol, J., et al. (2015). Physisorption of gases, with special reference to the evaluation of surface area and pore size distribution (IUPAC Technical Report). *Pure Appl. Chem.* 87 (9-10), 1051–1069. doi:10.1515/pac-2014-1117

Uslu, B., Dogan, B., Özkan, S. A., and Aboul-Enein, H. Y. (2005). Electrochemical behavior of vardenafil on glassy carbon electrode: Determination in tablets and human serum. *Anal. Chim. Acta* 552 (1), 127–134. doi:10.1016/j.aca.2005.07.040

Wachholz Junior, D., Deroco, P. B., and Kubota, L. T. (2022). A copper-based metal-organic framework/reduced graphene oxide-modified electrode for electrochemical detection of paraquat. *Microchim. Acta* 189 (8), 278. doi:10.1007/s00604-022-05358-7

Walczak, M. M., Dryer, D. A., Jacobson, D. D., Foss, M. G., and Flynn, N. T. (1997). pH dependent redox couple: An illustration of the Nernst equation. *J. Chem. Educ.* 74 (10), 1195. doi:10.1021/ed074p1195

Wang, F., Guo, H., Chai, Y., Li, Y., and Liu, C. (2013). The controlled regulation of morphology and size of HKUST-1 by "coordination modulation method". *Microporous Mesoporous Mater* 173, 181–188. doi:10.1016/j.micromeso.2013.02.023

Wang, H., Jiang, S., Pan, J., Lin, J., Wang, J., Li, M., et al. (2022). Nanomaterials-based electrochemical sensors for the detection of natural antioxidants in food and biological samples: Research progress. *Microchim. Acta* 189 (9), 318. doi:10.1007/s00604-022-05403-5

Xu, N., Ding, Y., Ai, H., and Fei, J. (2010). Acetylene black-ionic liquids composite electrode: A novel platform for electrochemical sensing. *Microchim. Acta* 170 (1), 165–170. doi:10.1007/s00604-010-0384-3

Yan, Z., Zhang, Z., and Chen, J. (2016). Biomass-based carbon dots: Synthesis and application in imatinib determination. *Sens. Actuators B* 225, 469–473. doi:10.1016/j.snb.2015.10.107

Yang, X.-B., Zhu, W., Qin, K., and Wang, H.-Y. (2014). Preparation of lamellar carbon matrix for sulfur as cathode material of lithium-sulfur batteries. *Electrochim Acta* 143, 374–382. doi:10.1016/j.electacta.2014.07.080

Yola, M. L. (2021). Sensitive sandwich-type voltammetric immunosensor for breast cancer biomarker HER2 detection based on gold nanoparticles decorated Cu-MOF and Cu2ZnSnS4 NPs/Pt/g-C3N4 composite. *Microchim. Acta* 188 (3), 78. doi:10.1007/s00604-021-04735-y

Zhang, Y., He, K., Han, N., Wang, L., Huang, J., She, H., et al. (2023). Integration between CuMOF and g-C3N4 for effective suppressing charge recombination in photocatalytic peroxymonosulfate activation. *J. Alloys Compd.* 952, 170008. doi:10.1016/j.jallcom.2023.170008

Zheng, H., Ying, X., Wang, W., Chen, Z., Shao, C., Zhou, H., et al. (2019). Study of sensitivity evaluation on ridgetail white prawn (Exopalaemon carinicauda) quality examination methods. *Int. J. Food Prop.* 22 (1), 942–951. doi:10.1080/10942912.2019.1617304

Zhou, J., Li, X., Yang, L., Yan, S., Wang, M., Cheng, D., et al. (2015). The Cu-MOF-199/single-walled carbon nanotubes modified electrode for simultaneous determination of hydroquinone and catechol with extended linear ranges and lower detection limits. *Anal. Chim. Acta* 899, 57–65. doi:10.1016/j.aca.2015.09.054

Time-resolved *in situ* vibrational spectroscopy for electrocatalysis: challenge and opportunity

Danya Lyu[1,2], Jinchang Xu[1,2] and Zhenyou Wang[1,2]*

[1]GBA Branch of Aerospace Information Research Institute, Chinese Academy of Science, Guangzhou, China, [2]Guangdong Provincial Key Laboratory of Terahertz Quantum Electromagnetics, Guangzhou, China

Understanding the structure-activity relationship of catalysts and the reaction pathway is crucial for designing efficient, selective, and stable electrocatalytic systems. *In situ* vibrational spectroscopy provides a unique tool for decoding molecular-level factors involved in electrocatalytic reactions. Typically, spectra are recorded when the system reaches steady states under set potentials, known as steady-state measurements, providing static pictures of electrode properties at specific potentials. However, transient information that is crucial for understanding the dynamic of electrocatalytic reactions remains elusive. Thus, time-resolved *in situ* vibrational spectroscopies are developed. This mini review summarizes time-resolved *in situ* infrared and Raman techniques and discusses their application in electrocatalytic research. With different time resolutions, these time-resolved techniques can capture unique dynamic processes of electrocatalytic reactions, short-lived intermediates, and the surface structure revolution that would be missed in steady-state measurements alone. Therefore, they are essential for understanding complex reaction mechanisms and can help unravel important molecular-level information hidden in steady states. Additionally, improving spectral time resolution, exploring low/ultralow frequency detection, and developing operando time-resolved devices are proposed as areas for advancing time-resolved techniques and their further applications in electrocatalytic research.

KEYWORDS

time-resolved spectroscopy, *in situ*, infrared, Raman, ATR-SEIRAS, SERS

1 Introduction

Electron-transfer reactions at the electrode surface can be categorized as inner- or outer-sphere reactions. For an outer-sphere reaction, the electrons transfer tunnelling through a solvent layer, thus, no direct chemical interaction between the electrode and active species occurs. Therefore, the electron-transfer rate is exponentially increased with the applied overpotential. In contrast, electrocatalysis involves typical inner-sphere reactions where the electron-transfer rate is highly rated to the surface structure of the catalyst and reaction pathway, in addition to the applied overpotential making it far more complicated than an outer-sphere reaction.

The rational design of highly efficient electrocatalytic systems requires a profound awareness of the structure-activity relationship of the catalysts and the reaction pathway. Theoretical simulations such as density functional theory (DFT) can provide some cues of the critical adsorption sites and interface structures. Morphology and structure detection techniques such as scanning electron microscopy, transmission electron microscopy, atomic

force microscopy, X-ray absorption, X-ray diffraction, X-ray photoelectron spectroscopy, electron paramagnetic resonance, Mössbauer spectroscopy, etc., have been applied both *in situ* and *ex situ* to monitor the structure evolution, coordination environment, valence state, electronic property, etc., (Zhang et al., 2019; Chen et al., 2023). However, direct spectral evidence of molecular-level factors is still challenging to obtain. Therefore, *in situ* vibrational spectroscopy including Raman, Infrared (IR), and sum frequency generation (SFG) spectroscopy able to capture the molecular fingerprint information are necessary (Xu et al., 2021; Liu et al., 2022). SFG, a non-linear spectroscopy, benefits from the specific interfacial selection rules and is easy for pump-probe time-resolved studies. Recently, phase-sensitive second-harmonic generation, a specific sum frequency nonlinear effect, was developed to measure the electrochemical potential of zero charge at the Pt-water interface (Xu et al., 2023). But these techniques highly rely on well-trained specialists and sophisticated devices thus, hasn't been widely applied yet (Li et al., 2022). This mini review focuses on the mostly used time-resolved *in situ* strategies of IR and Raman spectroscopies and discusses their applications in electrocatalytic research.

Herein, "*in situ*" refers to the measurements performed during the reaction under relevant reaction conditions. In comparison, "operando" measurements are taken under reaction conditions similar to those of realistic reactors. (Bañares, 2005; Yang et al., 2021). As a powerful tool, the *in situ* vibrational spectra are typically obtained under a series of preset potentials with stable currents as a steady-state method. Highly reproducible spectra and rich information such as the structure of the catalysts, adsorbed intermediates, structure of the interfacial solvents, et al. are obtained (Zhu et al., 2020; He et al., 2023). However, valuable transient information such as the dynamic kinetic, relaxation of the interfacial structure, and ultrashort lived intermediate is inevitably missed by using the steady-state measurement alone. Hence, various time-resolved IR and Raman spectroscopic techniques with different time resolutions are developed.

2 Time-resolved *in situ* fourier-transformed infrared (FTIR) study

Infrared spectroscopy exploits the specific absorption of infrared radiation at characteristic frequencies of molecular vibrations. It has been widely used to monitor functional groups, molecular symmetry, and interactions between catalysts and molecules during electrochemical reactions (Chalmers and Griffiths, 2002). External reflection and internal reflection also known as attenuated total reflection (ATR) are two main types of detection modes used in *in situ* measurements. As surface-enhanced infrared absorption has been proved on many important transient metals such as Cu and Pt, that surface-enhanced infrared reflection absorption spectroscopy (SEIRAS) coupled with ATR detection mode is widely used in spectroelectrochemistry (Liu et al., 2021; Cuesta, 2022).

Linear scan mode is provided by commercial FTIRs. As it is easy to implement without any additional accessory, it is widely used to monitor electrochemical reactions under a second-time regime. As an example, Zhu et al. studied the CO_2RR on the Cu thin film combining real-time ATR-SEIRAS with isotopic labeling (Zhu et al.,

2017). Surface $^{12}CO_2$ and surface adsorbed ^{12}CO were observed in the $KH^{12}CO_3$ electrolyte saturated with $^{12}CO_2$ (Figure 1A). Interestingly, new peaks assigned to surface $^{13}CO_2$ and adsorbed ^{13}CO were observed in the $KH^{13}CO_3$ electrolyte saturated with $^{12}CO_2$ (Figure 1B) indicating the existence of an equilibrium between CO_2 and bicarbonate anions in the electrolyte. This result provided that the CO_2 source of CO_2RR is from the surface equilibrium rather than the free CO_2 (Figure 1C). The drawback of linear scan is that it is unable to catch up with fast electrochemical reactions as each spectrum takes hundreds of ms to collect (Pérez-Martínez et al., 2021). Combing *in situ* ATR-FTIR with on-line mass spectrometry can capture the reaction kinetics of surface species and volatile products simultaneously, helping to evaluate the contribution of partial reactions (Heinen et al., 2007a; Heinen et al., 2007b). Besides, polarization modulation is applied in time-resolved infrared reflection absorption measurement to character the coordination and symmetry of surface species such as cyanide (Hosseini et al., 2018).

High temporal-resolution detection methods with ms and μs resolution based on the FT-IR had been developed. One is rapid-scan time-resolved FT-IR which employs moving mirrors to reduce the scan time to the ms scale and is useful for monitoring processes with a half-life time 100 ms (Li et al., 2012). An example of this technique's application is the oxidation of methanol on a Pt microelectrode in a thin-layer cell combined with external reflection detection mode (Zhou et al., 2004). To overcome the low mass transport rate, a Pt microelectrode and a flow cell were specially designed to reduce the electrode time constant down to 100 μs. Cyclic voltammograms and IR spectra can be recorded simultaneously at a high potential scan rate up to 200 mV/s (Figure 1D). The study observed linearly bonded CO (CO_L) and bridge-bonded CO (CO_B) under −0.17 V and −0.54 V vs. SCE respectively. Furthermore, the difference in potential between CO_L and CO_B indicates that the activation energy of methanol oxidation via CO_B is lower than CO_L, revealing a dual reaction mechanism.

Another approach is the step-scan method where the moving mirror is moved in a series of fixed steps. At each step, a full interferogram is collected and Fourier transformed into a single spectrum point. The time delay between successive interferograms is controlled by the rate of movement of the moving mirror. The resulting two-dimensional data arrays consisting of time-delayed interferograms at each wavenumber can be used to generate kinetic information. (Ataka et al., 1999). Osawa et al. first reported the *in situ* step-scan time-resolved FTIR with a sub-millisecond resolution to monitor a one-electron reduction of heptylviologen (Osawa et al., 1994). Zhou et al. reported the monitoring of CO oxidation on Pt microelectrode, an irreversible reaction by using a thin layer cell at a time resolution of 250 μs (Zhou et al., 2005).

Instead of using the moving mirror in the step-scan method, as an alternative, dual frequency comb IR laser spectroscopy achieved microsecond time resolution by using a heterodyned detector to record the interference signal generated by two IR laser combs (Lins et al., 2020). Eliminating the need for successive mirror movements greatly reduces the sampling time by two orders of magnitude. In a recent study, transient evolution of 4-dimethylaminopyridine on the electrode surface was investigated through ATR-SEIRAS mode. Time-resolved integrated peak area of 1,628 cm^{-1} was recorded
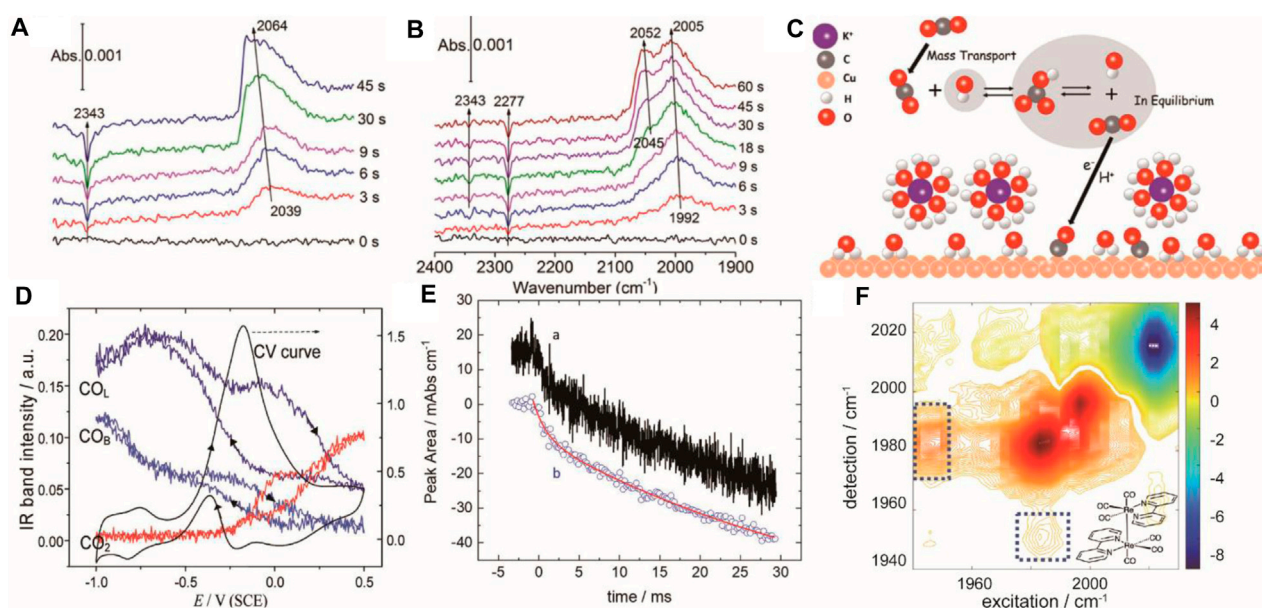
FIGURE 1
Real-time ATR-SEIRAS spectra recorded after stepping the Cu thin film electrode to −0.6 V in a CO_2 saturated 0.1 M $KH^{12}CO_3$ **(A)** and $KH^{13}CO_3$ **(B)** solution. Adapted with permission from (Zhu et al., 2017). Copyright 2017 American Chemical Society; **(C)** schematic diagram of equilibrium between CO_2 and bicarbonate anions in the electrolyte during the CO_2RR. Adapted with permission from (Zhu et al., 2017). Copyright 2017 American Chemical Society. **(D)** IR intensity of CO_L, CO_B, and CO_2 with the CV. Adapted with permission from (Li et al., 2012). Copyright 2012 American Chemical Society **(E)** Dual comb IR spectra of integrated peak area of 4-dimethylaminopyridine at 1,628 cm^{-1} with 20 μs **(A)** and 200 μs **(B)** time binning. Adapted with permission from (Lins et al., 2020). Copyright 2020 American Chemical Society; **(F)** Difference 2D-IR spectra of Re (bpy) (CO)$_3$Cl at −1.6 V. Adapted with permission from (Kiefer et al., 2021). Copyright 2021 American Chemical Society.

and fitted by a double exponential function of time to calculate the surface diffusion coefficient (Figure 1E). This method achieved the time resolution of 10 μs and a detection limit of 5% of a monolayer. Additionally, another ultrafast technique, time-resolved 2D-IR, can display both frequency and time domain information. It involves the excitation of a sample with two laser pulses separated by a time delay, followed by detection of the emitted IR radiation at different frequencies and time delays. It has been used for *in situ* monitoring of CO_2RR using Re (bpy) (CO)$_3$Cl as the catalyst based on the transmission mode. The reaction intermediate, Re-Re dimer, was directly observed from the difference spectrum (Figure 1F).

3 Time-resolved *in situ* Raman study

As a complementary of IR, Raman spectroscopy is also used to identify functional groups in a molecule involving changes in polarizability (Chalmers and Griffiths, 2002). The weak Raman signal of water makes Raman spectroscopy a powerful tool to monitor aqueous reactions. Surface-enhanced Raman spectroscopy (SERS), a near-field effect, meriting from the electromagnetic field and chemical enhancement, is suitable to detect surface information such as interfacial composition and adsorbents. Usually, the signal of normal Raman is weak so SERS or resonance Raman is frequently used in time-resolved studies (McCreery and Packard, 1989).

An early approach to achieve microsecond time resolution in electrochemical measurements was reported by using a potential

averaging method equipped with a charge-coupled device (CCD) (Tian et al., 1991; Tian et al., 1996). In this method, a square-wave potential modulation was applied to the electrode, and the obtained spectrum contains all the average information at two potentials. The signal of each potential was separated through deconvolution. This technique offers improved time resolution compared to the response time of CCD as the time resolution solely depends on the electrochemical response. Important surface structures such as the potential related adsorption orientation and SERS active sites can be obtained.

An alternative method for obtaining time-resolved spectra in electrochemical measurements is to perform simultaneous sampling of Raman and electric signals during a transient electrochemical test. Gao et al. first utilized this approach to demonstrate time-resolved SERS in conjunction with a cyclic voltammetry test using a spectrograph-multichannel detector. The potential sweep rate was 5 mV/s and spectral integration time was 5 s due to the limited sensitivity of the detector at the 1980 s (Gao et al., 1988). Ruiter et al. adopted this approach to investigate the CO_2 reduction reaction on Cu (oxide) electrode during the cyclic voltammetry. They used a potential sweep rate of 10 mV/s and spectral sampling time of 1 s to obtain vibration modes of copper oxides, carbonate/bicarbonate, and CO. (Figures 2A, B) (de Ruiter et al., 2022). Furthermore, they observed evidence of low-overpotential CO_2-to-CO activation. Despite applying a low potential scan rate, the Raman signal remained a potential-average result as the spectra sampling rate was longer than the potential scan. With the rapid development of photoelectric detector, millisecond-resolved SERS was illustrated by Zong et al., equipped with a high-speed readout EMCCD that was

FIGURE 2
(A) Time-resolved SERS data of electrodeposited copper during the cyclic voltammetry at 10 mV/s. Adapted with permission from (de Ruiter et al., 2022). **(B)** Raman spectra of typical moments corresponding to the dashed lines in **(A)**. Adapted with permission from (de Ruiter et al., 2022). **(C)** Scheme of transient electrochemical SERS and the synchronization sequence of the trigger. (Zong et al., 2015). Copyright 2015 American Chemical Society. **(D)** Scheme of the pump-probe mode setup with the modulation of Raman intensity and potential vs. time. Adapted with permission from (D'Amario et al., 2022).

trigged synchronically by the potentiostat without repetitive cycled acquisitions (Figure 2C) (Zong et al., 2015). In this manner, the Raman signal and current were precisely correlated. Most recently, stimulated Raman spectroscopy, a three-order nonlinear effect, was deployed to monitor species near the electrode's surface during a redox model reaction with a millisecond-to-second resolution, helping to overcome the limitation that only a few electrode materials are SERS active (Xu and Suntivich, 2023).

Pump-probe method, a general technique applied in ultrafast time-resolved spectroscopy, is also applied in electrochemical research. However, instead of using pump light, electrochemical tests like chronoamperometry and potential sweep typically serve as the trigger for reactions. Due to the limited sampling time of a typical CCD (~100 ms), gated detectors are generally employed for high time-resolved experiments. (Shi et al., 1990, 1997). Previous studies have reported sub-millisecond resolution systems equipped with a nanosecond pulse laser and an ICCD camera, wherein the formation of monocation radical of heptylviologn was monitored (Misono et al., 1993). More recently, D'Amario et al. provided a simple modification of a commercial confocal Raman system with a time resolution of sub-microsecond (0.6 ms) by a CCD camera. A high-frequency square wave step was used to trigger the reaction, while a modulated continuous laser served as the detection light. (Figure 2D) (D'Amario et al., 2022). By isolating relevant difference bands of transient species from those throughout whole pumping frequencies, they could obtain a detailed understanding of the reaction mechanism. Nevertheless, the pump-probe method's drawback is that the system must at least partially revert to its initial state.

4 Outlook

In this mini review, we provide a summary of the current instrumental methods of time-resolved vibrational spectroscopies and their applications in electrocatalysis research. With the rapid development of photoelectric detectors, there are immense opportunities to improve our understanding of electrocatalytic energy conversion. Herein, three main opportunities and challenges are addressed.

(1) Improve spectral time resolution.

To investigate short-lived intermediates in electrocatalytic reactions, it is necessary to employ time-resolved techniques with a temporal resolution of milliseconds to microseconds. Distinguishing between active and poisoned intermediates is important for understanding the pathway of electrocatalytic reaction. Time-resolved techniques can monitor intermediate generation, decay, and conversion processes, enabling determination of reaction kinetics and intermediate lifetimes, thus, revealing reaction kinetics. Microsecond time-resolved vibrational spectroscopy techniques still remain challenging. At this time scale, electrochemical process of the system needs to be carefully cheeked. For example, the charging process of the electric double layer controls the RC time constant that determines the test time zone. The mass transport process affects the thickness of the diffusion layer and kinetic behaviour according to Fick's law. Thus, flow cells and ultramicroelectrodes are particularly designed and used to reduce the RC time constant. Besides, charge transfer is

another important process in electrocatalytic reactions. To probe such ultrafast processes under the ns-fs scale, ultrafast techniques are required such as the pump-probe, and pump-push-probe strategies that pulse laser acts as the trigger instead of the potential. The limitation lies in the potentiostat, as the response time of commercial potentiostat is much longer than the laser that customized potentiostat is needed (Zwaschka et al., 2021).

(2) Explore low/ultralow frequency detection.

The low and ultralow frequency range is crucial to understanding the structural and interactional information of catalysis, such as adsorption bonds, surface lattice species, and local strain, but has been seldom explored. Low frequency detection is quite difficult for ATR-SEIRAS due to the strong optical absorption of the conventional Si prism used in the electrolytic cell. Recently, a micromachined Si wafer window was developed that extends the detection window of ATR-SEIRAS down to 650 cm^{-1} which was applied to probe the surface structure and additives (Ma et al., 2020; Mao et al., 2022). However, the detection below 650 cm^{-1} is even quite challenging due to the lack of appropriate IR sources. Recently, synchrotron radiation and free electron laser with tenable wavelength and ps resolution has been launched which makes a great opportunity for low frequency detection and time-resolved research (Ye et al., 2016). Both synchrotron radiation source and free electron laser are served as national projects, not easy to access for a common lab. On the contrary, the ultralow frequency (5 ~ 200 cm^{-1}) detection of Raman is much easier to implement as there are commercial BragGate notch filters to choose from. Taking advantage of the ultralow-frequency Raman, direct observation of structural changes (photon mode) of the metal clusters became possible (Kato et al., 2020). It can also be used to observe the extra molecular vibration mode of surface adsorption species revealing the specific structural and environmental information of electrode-electrolyte interface (Inagaki et al., 2017; Kondo et al., 2022).

(3) Develop new methods and devices under operando conditions.

During the *in situ* experiment, the mostly used spectral electrolytic cell and electrode such as a thin layer electrolytic cell and metal electrode, are typically designed for lab-scale research, which is far from industrial usage. Operando experiment is required to bridge the gap between lab research and realistic scenarios. One approach is to design special electrolytic cells that meet the optical detection requirements and also provide similar working conditions as realistic devices. For example, systematic operando studies of membrane electrodes are still lacking to correlate liquid-gas-solid multiphase information (Li et al., 2022). Another approach is to design operando optical sensors (Huang et al., 2022), such as a hollow-core optical fiber-based Raman probe can be embedded into a Li-ion pouch cell for the operando detection of liquid electrolyte species (Miele et al., 2022) and chalcogenide glass fiber-based IR probes can directly traverse through commercial Na (Li)-ion batteries for the real-time monitoring of electrolyte evolution (Gervillié-Mouravieff et al., 2022). These pioneer works provide inspired insights and opportunities for the development of vibrational spectroscopy tools for online simultaneous investigation under real-operational conditions.

Author contributions

DL prepared the manuscript. JX and ZW revised the manuscript. All authors contributed to the article and approved the submitted version.

Funding

Conflict of interest

The authors declare that the research was conducted in the absence of any commercial or financial relationships that could be construed as a potential conflict of interest.

Publisher's note

All claims expressed in this article are solely those of the authors and do not necessarily represent those of their affiliated organizations, or those of the publisher, the editors and the reviewers. Any product that may be evaluated in this article, or claim that may be made by its manufacturer, is not guaranteed or endorsed by the publisher.

References

Ataka, K., Hara, Y., and Osawa, M. (1999). A new approach to electrode kinetics and dynamics by potential modulated Fourier transform infrared spectroscopy. *J. Electroanal. Chem.* 473 (1), 34–42. doi:10.1016/S0022-0728(99)00119-9

Bañares, M. A. (2005). Operando methodology: Combination of *in situ* spectroscopy and simultaneous activity measurements under catalytic reaction conditions. *Catal. Today* 100 (1), 71–77. doi:10.1016/j.cattod.2004.12.017

Chalmers, J. M., and Griffiths, P. R. (2002). *Handbook of vibrational spectroscopy*. Wiley.

Chen, M., Liu, D., Qiao, L., Zhou, P., Feng, J., Ng, K. W., et al. (2023). *In-situ*/operando Raman techniques for in-depth understanding on electrocatalysis. *Chem. Eng. J.* 461, 141939. doi:10.1016/j.cej.2023.141939

Cuesta, A. (2022). ATR-SEIRAS for time-resolved studies of electrode–electrolyte interfaces. *Curr. Opin. Electrochem.* 35, 101041. doi:10.1016/j.coelec.2022.101041

D'Amario, L., Stella, M. B., Edvinsson, T., Persico, M., Messinger, J., and Dau, H. (2022). Towards time resolved characterization of electrochemical reactions: Electrochemically-induced Raman spectroscopy. *Chem. Sci.* 13 (36), 10734–10742. doi:10.1039/D2SC01967A

de Ruiter, J., An, H., Wu, L., Gijsberg, Z., Yang, S., Hartman, T., et al. (2022). Probing the dynamics of low-overpotential CO2-to-CO activation on copper electrodes with time-resolved Raman spectroscopy. *J. Am. Chem. Soc.* 144 (33), 15047–15058. doi:10.1021/jacs.2c03172

Gao, P., Gosztola, D., and Weaver, M. J. (1988). Surface-enhanced Raman spectroscopy as a probe of electroorganic reaction pathways. 1. Processes involving adsorbed nitrobenzene, azobenzene, and related species. *J. Phys. Chem.* 92 (25), 7122–7130. doi:10.1021/j100336a018

Gervillié-Mouravieff, C., Boussard-Plédel, C., Huang, J., Leau, C., Blanquer, L. A., Yahia, M. B., et al. (2022). Unlocking cell chemistry evolution with operando fibre optic infrared spectroscopy in commercial Na(Li)-ion batteries. *Nat. Energy* 7 (12), 1157–1169. doi:10.1038/s41560-022-01141-3

He, Q.-F., Zhang, Y.-J., Yang, Z.-L., Dong, J.-C., Lin, X.-M., and Li, J.-F. (2023). Surface-enhanced Raman spectroscopy: Principles, methods, and applications in energy systems. *Chin. J. Chem.* 41 (3), 355–369. doi:10.1002/cjoc.202200535

Heinen, M., Chen, Y.-X., Jusys, Z., and Behm, R. J. (2007a). Room temperature COad desorption/exchange kinetics on Pt electrodes—a combined *in situ* IR and mass spectrometry study. *ChemPhysChem* 8 (17), 2484–2489. doi:10.1002/cphc.200700425

Heinen, M., Chen, Y. X., Jusys, Z., and Behm, R. J. (2007b). CO adsorption kinetics and adlayer build-up studied by combined ATR-FTIR spectroscopy and on-line DEMS under continuous flow conditions. *Electrochim. Acta* 53 (3), 1279–1289. doi:10.1016/j.electacta.2007.05.020

Hosseini, P., Wittstock, G., and Brand, I. (2018). Infrared spectroelectrochemical analysis of potential dependent changes in cobalt hexacyanoferrate and copper hexacyanoferrate films on gold electrodes. *J. Electroanal. Chem.* 812, 199–206. doi:10.1016/j.jelechem.2017.12.029

Huang, J., Boles, S. T., and Tarascon, J.-M. (2022). Sensing as the key to battery lifetime and sustainability. *Nat. Sustain.* 5 (3), 194–204. doi:10.1038/s41893-022-00859-y

Inagaki, M., Motobayashi, K., and Ikeda, K. (2017). Electrochemical THz-SERS observation of thiol monolayers on Au(111) and (100) using nanoparticle-assisted gap-mode plasmon excitation. *J. Phys. Chem. Lett.* 8 (17), 4236–4240. doi:10.1021/acs.jpclett.7b01901

Kato, M., Shichibu, Y., Ogura, K., Iwasaki, M., Sugiuchi, M., Konishi, K., et al. (2020). Terahertz Raman spectroscopy of ligand-protected Au8 clusters. *J. Phys. Chem. Lett.* 11 (19), 7996–8001. doi:10.1021/acs.jpclett.0c02227

Kiefer, L. M., Michocki, L. B., and Kubarych, K. J. (2021). Transmission mode 2D-IR spectroelectrochemistry of *in situ* electrocatalytic intermediates. *J. Phys. Chem. Lett.* 12 (15), 3712–3717. doi:10.1021/acs.jpclett.1c00504

Kondo, T., Inagaki, M., Motobayashi, K., and Ikeda, K. (2022). *In situ* mass analysis of surface reactions using surface-enhanced Raman spectroscopy covering a wide range of frequencies. *Catal. Sci. Technol.* 12 (8), 2670–2676. doi:10.1039/D2CY00229A

Li, H., Jiang, K., Zou, S.-Z., and Cai, W.-B. (2022). Fundamental aspects in CO2 electroreduction reaction and solutions from *in situ* vibrational spectroscopies. *Chin. J. Catal.* 43 (11), 2772–2791. doi:10.1016/S1872-2067(22)64095-6

Li, J.-T., Zhou, Z.-Y., Broadwell, I., and Sun, S.-G. (2012). *In-situ* infrared spectroscopic studies of electrochemical energy conversion and storage. *Acc. Chem. Res.* 45 (4), 485–494. doi:10.1021/ar200215t

Lins, E., Read, S., Unni, B., Rosendahl, S. M., and Burgess, I. J. (2020). Microsecond resolved infrared spectroelectrochemistry using dual frequency comb IR lasers. *Anal. Chem.* 92 (9), 6241–6244. doi:10.1021/acs.analchem.0c00260

Liu, H., Qi, Z., and Song, L. (2021). *In situ* electrocatalytic infrared spectroscopy for dynamic reactions. *J. Phys. Chem. C* 125 (44), 24289–24300. doi:10.1021/acs.jpcc.1c07689

Liu, S., D'Amario, L., Jiang, S., and Dau, H. (2022). Selected applications of operando Raman spectroscopy in electrocatalysis research. *Curr. Opin. Electrochem.* 35, 101042. doi:10.1016/j.coelec.2022.101042

Ma, X.-Y., Ding, C., Li, H., Jiang, K., Duan, S., and Cai, W.-B. (2020). Revisiting the acetaldehyde oxidation reaction on a Pt electrode by high-sensitivity and wide-frequency infrared spectroscopy. *J. Phys. Chem. Lett.* 11 (20), 8727–8734. doi:10.1021/acs.jpclett.0c02558

Mao, Z., Wu, Y., Ma, X.-Y., Zheng, L., Zhang, X.-G., and Cai, W.-B. (2022). *In situ* wide-frequency surface-enhanced infrared absorption spectroscopy enables one to decipher the interfacial structure of a Cu plating additive. *J. Phys. Chem. Lett.* 13 (39), 9079–9084. doi:10.1021/acs.jpclett.2c02541

McCreery, R. L., and Packard, R. T. (1989). Raman monitoring of dynamic electrochemical events. *Anal. Chem.* 61 (13), 775A–789A. doi:10.1021/ac00188a001

Miele, E., Dose, W. M., Manyakin, I., Frosz, M. H., Ruff, Z., De Volder, M. F. L., et al. (2022). Hollow-core optical fibre sensors for operando Raman spectroscopy

investigation of Li-ion battery liquid electrolytes. *Nat. Commun.* 13 (1), 1651. doi:10.1038/s41467-022-29330-4

Misono, Y., Shibasaki, K., Yamasawa, N., Mineo, Y., and Itoh, K. (1993). Time-resolved resonance Raman and surface-enhanced resonance Raman scattering study on monocation radical formation processes of heptylviologen at silver electrode surfaces. *J. Phys. Chem.* 97 (22), 6054–6059. doi:10.1021/j100124a044

Osawa, M., Yoshii, K., Ataka, K.-i., and Yotsuyanagi, T. (1994). Real-time monitoring of electrochemical dynamics by submillisecond time-resolved surface-enhanced infrared attenuated-total-reflection spectroscopy. *Langmuir* 10 (3), 640–642. doi:10.1021/la00015a009

Pérez-Martínez, L., Machado de los Toyos, L. M., Shibuya, J. J. T., and Cuesta, A. (2021). Methanol dehydrogenation on Pt electrodes: Active sites and role of adsorbed spectators revealed through time-resolved ATR-SEIRAS. *ACS Catal.* 11 (21), 13483–13495. doi:10.1021/acscatal.1c03870

Shi, C., Zhang, W., Birke, R. L., and Lombardi, J. R. (1990). Detection of short-lived intermediates in electrochemical reactions using time-resolved surface-enhanced Raman spectroscopy. *J. Phys. Chem.* 94 (12), 4766–4769. doi:10.1021/j100375a004

Shi, C., Zhang, W., Birke, R. L., and Lombardi, J. R. (1997). SERS investigation of the adsorption and electroreduction of 4-cyanopyridine on a silver electrode. *J. Electroanal. Chem.* 423 (1), 67–81. doi:10.1016/S0022-0728(96)04810-3

Tian, Z. Q., Li, W. H., Mao, B. W., Zou, S. Z., and Gao, J. S. (1996). Potential-Averaged surface-enhanced Raman spectroscopy. *Appl. Spectrosc.* 50 (12), 1569–1577. doi:10.1366/0003702963904575

Tian, Z. Q., Lin, W. F., and Mao, B. W. (1991). Potential averaged surface-enhanced Raman spectroscopic SCN– adsorbed at Ag electrodes. *J. Electroanal. Chem.* 319 (1), 403–408. doi:10.1016/0022-0728(91)87098-O

Xu, P., and Suntivich, J. (2023). Time-resolved monitoring of electrochemical reactions using *in situ* stimulated Raman spectroscopy. *ACS Sustain. Chem. Eng.* 11 (1), 13–17. doi:10.1021/acssuschemeng.2c04873

Xu, P., von Rueden, A. D., Schimmenti, R., Mavrikakis, M., and Suntivich, J. (2023). Optical method for quantifying the potential of zero charge at the platinum–water electrochemical interface. *Nat. Mat.* 22 (4), 503–510. doi:10.1038/s41563-023-01474-8

Xu, Z., Liang, Z., Guo, W., and Zou, R. (2021). *In situ*/operando vibrational spectroscopy for the investigation of advanced nanostructured electrocatalysts. *Coord. Chem. Rev.* 436, 213824. doi:10.1016/j.ccr.2021.213824

Yang, Y., Xiong, Y., Zeng, R., Lu, X., Krumov, M., Huang, X., et al. (2021). Operando methods in electrocatalysis. *ACS Catal.* 11 (3), 1136–1178. doi:10.1021/acscatal.0c04789

Ye, J.-Y., Jiang, Y.-X., Sheng, T., and Sun, S.-G. (2016). *In-situ* FTIR spectroscopic studies of electrocatalytic reactions and processes. *Nano Energy* 29, 414–427. doi:10.1016/j.nanoen.2016.06.023

Zhang, L., Qian, T., Zhu, X., Hu, Z., Wang, M., Zhang, L., et al. (2019). *In situ* optical spectroscopy characterization for optimal design of lithium–sulfur batteries. *Chem. Soc. Rev.* 48 (22), 5432–5453. doi:10.1039/C9CS00381A

Zhou, Z.-Y., Lin, S.-C., Chen, S.-P., and Sun, S.-G. (2005). *In situ* step-scan time-resolved microscope FTIR spectroscopy working with a thin-layer cell. *Electrochem. Commun.* 7 (5), 490–495. doi:10.1016/j.elecom.2005.03.001

Zhou, Z.-Y., Tian, N., Chen, Y.-J., Chen, S.-P., and Sun, S.-G. (2004). *In situ* rapid-scan time-resolved microscope FTIR spectroelectrochemistry: Study of the dynamic processes of methanol oxidation on a nanostructured Pt electrode. *J. Electroanal. Chem.* 573 (1), 111–119. doi:10.1016/j.jelechem.2004.07.003

Zhu, S., Jiang, B., Cai, W.-B., and Shao, M. (2017). Direct observation on reaction intermediates and the role of bicarbonate anions in CO2 electrochemical reduction reaction on Cu surfaces. *J. Am. Chem. Soc.* 139 (44), 15664–15667. doi:10.1021/jacs.7b10462

Zhu, Y., Wang, J., Chu, H., Chu, Y.-C., and Chen, H. M. (2020). *In situ*/operando studies for designing next-generation electrocatalysts. *ACS Energy Lett.* 5 (4), 1281–1291. doi:10.1021/acsenergylett.0c00305

Zong, C., Chen, C.-J., Zhang, M., Wu, D.-Y., and Ren, B. (2015). Transient electrochemical surface-enhanced Raman spectroscopy: A millisecond time-resolved study of an electrochemical redox process. *J. Am. Chem. Soc.* 137 (36), 11768–11774. doi:10.1021/jacs.5b07197

Zwaschka, G., Lapointe, F., Campen, R. K., and Tong, Y. (2021). Characterization of ultrafast processes at metal/solution interfaces: Towards femtoelectrochemistry. *Curr. Opin. Electrochem.* 29, 100813. doi:10.1016/j.coelec.2021.100813

Frontiers | Frontiers in Chemistry

Research progress of organic liquid electrolyte for sodium ion battery

Jia Zhang[1,2,3], Jianwei Li[1,2], Huaiyou Wang[1,2]* and Min Wang[1,2]*

[1]Key Laboratory of Comprehensive and Highly Efficient Utilization of Salt Lake Resources, Qinghai Institute of Salt Lakes, Chinese Academy of Sciences, Xining, China, [2]Key Laboratory of Salt Lake Resources Chemistry of Qinghai Province, Xining, China, [3]School of Chemical Sciences, University of Chinese Academy of Sciences, Beijing, China

Electrochemical energy storage technology has attracted widespread attention due to its low cost and high energy efficiency in recent years. Among the electrochemical energy storage technologies, sodium ion batteries have been widely focused due to the advantages of abundant sodium resources, low price and similar properties to lithium. In the basic structure of sodium ion battery, the electrolyte determines the electrochemical window and electrochemical performance of the battery, controls the properties of the electrode/electrolyte interface, and affects the safety of sodium ion batteries. Organic liquid electrolytes are widely used because of their low viscosity, high dielectric constant, and compatibility with common cathodes and anodes. However, there are problems such as low oxidation potential, high flammability and safety hazards. Therefore, the development of novel, low-cost, high-performance organic liquid electrolytes is essential for the commercial application of sodium ion batteries. In this paper, the basic requirements and main classifications of organic liquid electrolytes for sodium ion batteries have been introduced. The current research status of organic liquid electrolytes for sodium ion batteries has been highlighted, including compatibility with various types of electrodes and electrochemical properties such as multiplicative performance and cycling performance of electrode materials in electrolytes. The composition, formation mechanism and regulation strategies of interfacial films have been explained. Finally, the development trends of sodium ion battery electrolytes in terms of compatibility with materials, safety and stable interfacial film formation are pointed out in the future.

1 Introduction

Fossil fuels are the most widely used energy source in the world, however, its non-renewable and unsustainable nature makes it increasingly depleted, and the burning of fossil fuels causes a series of problems such as global warming and atmospheric pollution (Gao et al., 2020). Therefore, the development of renewable energy is becoming more and more important. However, the conversion of renewable energy into electrical energy is variable, intermittent and unpredictable (Cao et al., 2013), so it is necessary to develop energy storage technology to realize the scale of grid-connected storage of electrical energy and guarantee the continuous and stable electricity supply to users (Dunn et al., 2011). Electrochemical

energy storage technologies have received much attention due to their high energy efficiency and high power density (Dunn et al., 2011; Yang et al., 2011). However, few, if any, electrochemical grid-scale energy storage technologies, when implemented at system-level, are currently "low cost" and "long lifetime", especially when compared to standard natural gas peaker plants. Electrochemical energy storage technologies certainly have the potential to become "low cost" and "long lifetime" in future. More research is needed to achieve this goal and make it economically attractive compared to fossil fuels (Larcher and Tarascon, 2015).

As a mainstream electrochemical energy storage technology, lithium-ion batteries are widely used in our life by virtue of their high energy density and long cycle life. Additionally, the manufacturing scale of lithium-ion batteries continues to expand, which will inevitably cause huge consumption of lithium resources and soaring prices (Li et al., 2017). The element lithium is not abundant and unevenly distributed in the earth's crust (Pan et al., 2013), and in China, it is 70% of the lithium used depends on imports (RONG et al., 2020). In order to avoid the problem of "neck" due to the shortage of resources, it is necessary to develop an energy storage technology that is comparable to lithium-ion batteries. In the periodic table, sodium and lithium are metal elements in the same group and posess similar physical and chemical properties. The earth is rich in sodium, with an elemental content of about 23,000 ppm (lithium content is only about 17 ppm), making it sixth place in terms of abundance. Sodium is distributed all over the world, completely free from resource and geographical constraints. Therefore, sodium-ion batteries have a greater promise than lithium-ion batteries. The research of sodium ion battery can mitigate resource problem of new energy battery development caused by the shortage of lithium resources. Sodium ion batteries (SIBs) include sodium-sulfur batteries, sodium-salt batteries (ZEBRA batteries), sodium-air batteries, organic-based sodium-ion batteries and aqueous-based sodium-ion batteries. Among them, sodium-sulfur batteries are based on the electrochemical reaction of sodium and sulfur to generate sodium polysulfide, and are characterized by high power and energy density, temperature stability, and low cost because of the abundant cost of its raw materials, and have already achieved large-scale production (Wen et al., 2008). ZEBRA batteries use common salt and nickel as the raw materials for the electrodes, and are combined with ceramic electrolyte and molten salt. This combination provides battery systems with high specific energy and power. ZEBRA battery technology has been industrialized for all types of electric cars and hybrid electric buses (Dustmann, 2004). Sodium-air batteries, organic sodium-ion batteries and aqueous sodium-ion batteries are still in the research phase. Sodium ion battery also has the advantages of low cost, excellent fast charging and low temperature performance, good safety performance, etc. The manufacturing of sodium ion battery can follow the production process and equipment of existing lithium ion battery, which is considered as one of the transformative technologies in the field of large-scale energy storage, and its industrialization prospect is quite optimistic and has important economic and strategic significance (Fang et al., 2018; Lu et al., 2018; ZHOU et al., 2020). Therefore, sodium ion batteries are called the "rising star" of the energy storage field.

Sodium ion battery is mainly composed of three parts: cathode, anode and electrolyte. The working principle is similar to that of lithium-ion battery. During the charging process, the cathode material loses electrons in the oxidation reaction and electrons move from the external circuit to the anode, while sodium ions (Na^+) are removed from the cathode and enter the electrolyte, then migrate through the electrolyte to the vicinity of the anode and finally embedded in the anode material; during the discharge process, the anode electrode material loses electrons in the oxidation reaction and electrons move through the external circuit to the cathode, while Na^+ is removed from the anode material and embedded in the anode material. In the process of discharge, the anode material loses electrons through oxidation and electrons move to the cathode through the external circuit (Pan et al., 2013). As one of the main components of sodium ion battery, electrolyte has an important role in conducting ions and participating in the redox reaction of cathode and anode (ZHU et al., 2016). Electrolyte is the "bridge" connecting cathode and anode. The performance of the electrolyte directly affects the performance of sodium ion batteries. During the charging and discharging process, the electrolyte itself decomposes or reacts with the electrode material to form an interface. The interfacial film on the anode is called the solid electrolyte interphase (SEI), and the interfacial film on the cathode is called the cathodic electrolyte interphase (CEI). CEI and SEI largely determine the electrochemical performance of the battery system (Lin et al., 2019). At present, sodium ion battery electrolyte system mainly includes aqueous electrolyte and non-aqueous electrolyte. Non-aqueous electrolyte contains organic liquid electrolyte and solid electrolyte. The recyclability of aqueous electrolyte is excellent but its electrochemical window is narrow and the overall energy density is low (LIU et al., 2018b). Solid electrolytes generally have higher impedance and polarization, leading to a decrease in battery capacity. Moreover, the solid electrolyte itself has a narrow electrochemical window, and the mismatch with high-voltage electrodes will cause side reactions, leading to the deterioration of battery cycling performance (Hu et al., 2020; Gao et al., 2021). In a comprehensive comparison, organic liquid electrolytes have good properties, such as electrochemical stability within a certain electrochemical window, sufficiently high ionic conductivity, and good compatibility with various electrode materials. Therefore, organic liquid electrolytes are the most promising electrolytes for sodium ion batteries in practical applications.

This paper summarizes the research progress of organic liquid electrolytes for sodium ion batteries by discussing the basic requirements and composition of organic electrolytes for sodium ion batteries, the current research status of organic liquid electrolytes, the composition and requirements of the interface between electrolytes and electrodes and the regulation strategies. Finally, the performance of organic electrolyte and the nature of interfacial film are synthesized, and some suggestions on the future development trend of organic electrolyte for sodium ion batteries are proposed, in order to provide some help to the research of sodium ion battery electrolyte and sodium ion battery energy storage science and technology.

FIGURE 1
Main components of sodium ion battery electrolyte (Hu et al., 2020).
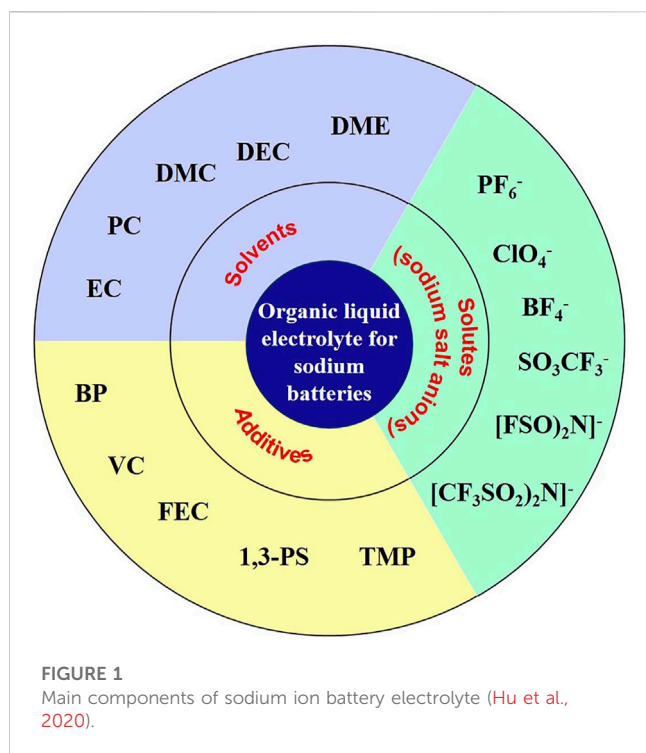
2 Components and basic requirements of organic liquid electrolytes

As a bridge connecting cathode and anode, the electrolyte assumes the role of transporting ions between cathode and anode and is an important part of the battery, whichplays a vital role in performance of the battery in terms of multiplicity, cycle life, safety and self-discharge. Organic liquid electrolyte is also customarily called organic electrolyte. Electrolyte is mainly composed of solvent, solute and additives (Figure 1), which together determine the properties of electrolyte.

2.1 Solvent

Solvent is one of the important components of organic liquid electrolytes. Electrolyte solvents need to satisfy the most basic conditions such as stability, non-toxicity and cheapness. Besides, the electrolyte solvent should have a wide electrochemical stability window, sufficient sodium salt solubility, high dielectric constant, low viscosity and wide liquid range (i.e., low melting point and high boiling point). The solvent should also maintain electrochemical stability or promote the formation of a high-quality passivation layer during cell operation. However, these different and sometimes conflicting requirements for the same solvent are difficult to be met by a single solvent, and therefore multiple solvents are often used in combination. The main solvents currently used in sodium ion batteries are ester solvents and ether solvents. These two types of organic solvents have provided excellent performance in battery applications (Fenton, 1973; Armand et al., 2009; Monti et al., 2014; Hong et al., 2015; Ponrouch et al., 2015; Niu et al., 2019; Wang et al., 2020).

Ester solvents are a more commonly used class of solvents, especially cyclic [propylene carbonate (PC) and ethylene carbonate

(EC)] and chain [dimethyl carbonate (DMC), diethyl carbonate (DEC) and methyl ethyl carbonate (EMC)] carbonates are most commonly used, and electrolytes of carbonate solvents tend to have the advantages of high ionic conductivity and good oxidation resistance (Ponrouch et al., 2012). The relevant physical and chemical properties of carbonate solvents are shown in Table 1. The dielectric constant of ether solvents is much lower than that of cyclic carbonates, but higher than that of chain carbonates. The resistance to oxidation is relatively poor, and they tend to decompose at high voltages. However, ether solvents generate thinner SEI on anode with higher initial Coulomb efficiency, and ether solvents are more compatible with anode such as metallic sodium and can co-embed graphite with sodium ions and show good reversibility, making graphite that cannot be embedded with sodium in ester solvents can be used as anode in this solvent system (Dubois et al., 1997). In the actual application process, the use of two or even a variety of solvent mix is a more common method (Komaba et al., 2011b), the ratio of different solvents is controlled, and the advantages of multiple solvents are integrated to maximize the performance of electrolytes.

2.2 Sodium salt

Sodium salts are another important component of organic liquid electrolytes and play a vital role in the performance of electrolytes (Che et al., 2017). For the selection of sodium salt. Firstly, the sodium salt should have sufficient solubility and dissociation ability in the solvent, and the dissociated cations should be free to move without obstacles to provide sufficient charge carriers. Secondly, the sodium salt should remain electrochemically stable within a certain electrochemical window without oxidation or reduction. The sodium salt and the solvent together determine the redox potential of the electrolyte, and the salt anion and the solvent are coupled by electrostatic interaction, which affects the oxidative stability of the electrolyte. In addition, the sodium salt should have good chemical stability as well as safety, remaining chemically inert to the diaphragm, solvent, electrode and collector fluid. If the sodium salt can effectively promote the formation of SEI film at the interface between electrode and electrolyte, it can better enhance the electrochemical performance of electrolyte, such as cycling stability (Strauss, 1993; Borodin and Jow, 2010; Ponrouch et al., 2015; Eshetu et al., 2019; Fadel et al., 2019). The commonly used sodium salts are sodium perchlorate ($NaClO_4$), sodium tetrafluoroborate ($NaBF_4$), sodium hexafluoroborate ($NaPF_6$), sodium trifluoromethanesulfonate ($NaCF_3SO_3$, abbreviated as NaOTf), sodium bis(fluorosulfonyl) imide [$Na(FSO_2)_2N$, abbreviated as NaFSI] and sodium bis(trifluoromethanesulfonyl)imide [$Na(CF_3SO_2)_2N$, abbreviated as NaTFSI] (Hu et al., 2020). The advantages and disadvantages of these sodium salts are shown in Table 2.

Based on the fact that each of the commonly used sodium salts has its own advantages and disadvantages, which are difficult to overcome. Hybrid systems combining two or more sodium salts have also been investigated, and the aim of avoiding disadvantages is expected to be realized, but the results are not significant. Therefore, it is necessary to develop new sodium salts (Hu et al., 2020). Some new salts that have been synthesized and

TABLE 1 Physical and chemical properties of some commonly used organic solvents (Xu, 2004; Kamath et al., 2014; Vignarooban et al., 2016; Chen et al., 2019; Wang M. et al., 2022).

Solvents	Density/ g·cm⁻³	Boiling point/°C	Melting point/°C	Viscosity/ 10⁻³ Pa s 25°C	Dielectric constant/ F m⁻¹ 25°C	HOMO/ eV	LUMO/ eV
DMC	1.063	91	4.6	0.59	3.107	−0.2488	−0.0091
DEC	0.969	126	−74.3	0.75	2.805	−0.2426	−0.0036
EC	1.321	248	36.4	2.1	89.78	−0.2585	−0.0177
PC	1.200	242	−48.8	2.53	64.92	−0.2547	−0.0149
EMC	1.006	110	−53.0	0.65	2.95	−0.2557	−0.0062

TABLE 2 Physical and chemical properties, advantages and disadvantages of commonly used sodium salts (Devlin and Herley, 1987; Ponrouch et al., 2012; Bhide et al., 2014; Evans et al., 2014; Ponrouch et al., 2015; Eshetu et al., 2016; Eshetu et al., 2019; Forsyth et al., 2019; Goktas et al., 2019; Minh Phuong et al., 2019; Hu et al., 2020; Wang et al., 2020).

Name of sodium salt	Anion structure	Molecular weight/·mol⁻¹	Melting point/°C	Advantages	Disadvantages
NaClO₄		122.4	468	Strong oxidation resistance, suitable for high voltage systems	Explosive in the dry state and difficult to remove the moisture contained
NaBF₄		109.8	384	High thermal stability, good safety, easy to make aluminum foil passivation	Harder to dissociate in solvents, low electrical conductivity
NaPF₆		167.9	300	High solubility and high conductivity in different kinds of solvents, easily passivates aluminum foil	Poor chemical stability, easily decomposes to NaF and PF₅
NaSO₃CF₃ (NaOTf)		172.1	248	high oxidation resistance and thermal stability	Easy formation of ion pairs in organic solvents, low conductivity of electrolyte
Na[(FSO₂)₂N](NaFSI)		203.3	118	High electrical conductivity, good thermal stability	Narrow electrochemical window, aluminum foil corrosion occurring around 3.8 V
Na[(CF₃SO₂)2N] (NaTFSI)		303.1	257	High electrical conductivity, good thermal and water stability, and oxidation resistance	Severe aluminum-collector corrosion

reported are sodium difluorooxalate borate (NaODFB), sodium 4,5-dicyano-2-(trifluoromethyl)imidazolate (NaTDI), sodium 4,5-dicyano-2-(pentafluoroethyl)imidazolate (NaPDI), sodium bisoxalate borate (NaBOB), sodium bis [salicylato (2-)]-borate (NaBSB), sodium salicylic benzylic acid borate (NaBDSB), sodium tetraphenyl borate (NaBPh₄), *etc.*

2.3 Additives

Additives are the third main component of organic liquid electrolytes. Additives are components that are present in small amounts (less than 5%) in the electrolyte and are characterized by high specificity and small dosage. By adding a small amount of additives, it is possible to make up for the deficiencies of the original electrolyte and significantly optimize the specific performance of the battery without increasing the production cost or changing the production process (Xu, 2014; Wang et al., 2020). According to

the function of additives, they are divided into film-forming additives, flame retardant additives, overcharge protection additives and other types of additives (Zhang, 2006).

The most studied are film-forming additives, which are usually easily consumed. During the initial activation cycle they participate and contribute to the formation of the interface between the electrode and the electrolyte, leaving a chemical signal only at the interface and not in the electrolyte itself. The ideal film-forming additives should have higher Fermi energy (E_g) located in the highest occupied molecular orbital-lowest unoccupied molecular orbital gap than solvents, electrolyte salts, *etc.*, so that they preferentially undergo oxidation or reduction, which in turn improves the film-forming quality and efficiency of the SEI film and effectively enhances the electrochemical performance of the cell (Goodenough and Kim, 2010; Zhu et al., 2017; Niu et al., 2019). The mechanism of action of various additives is shown in Table 3. Other types of additives including acidity enhancers, impurity scavengers, viscosity reducers, free radical scavengers, *etc.*, Also have potential applications in sodium ion batteries (Ponrouch et al., 2015).

TABLE 3 Mechanism of action of different types of additives.

Additive type	Name	Mechanism of action	References
Film-forming additives	Vinylidene carbonate (VC)	VC contains unsaturated double bonds that can be broken above the PC and EC decomposition potentials, resulting in macromolecular network polymers that participate in the formation of SEI films	Hwang et al. (2017b)
	Fluoroethylene carbonate (FEC)	The central atom of the FEC has a strong electron-acquisition ability because of the strong electron-absorption effect of the halogen atoms. At high potentials on the anode surface, the electrons of the central atom can be reduced, resulting in a stable SEI film	Komaba et al. (2011a); Darwiche et al. (2012); Qian et al. (2012); Qian et al. (2013); Wang et al. (2014); Yabuuchi et al. (2014); Jang et al. (2015); Sadan et al. (2018)
	Propylene-1,3-sulfolactone (PST) Vinyl sulfate (DTD)	In PST and DTD, the central S atoms are more electronegative than C atoms, resulting in the preferential formation of stable SEI films containing S compounds on the anode surface. These additives improve the high and low temperature performance of the cells and reduce the continuous increase of the interfacial impedance	Che et al. (2018)
	Sodium difluoroxalate borate (NaODFB)	NaODFB can form NaF with small particle size on the electrode surface, which has good film-forming effect	Yan et al. (2019)
Flame retardant additives	Phosphorus containing flame retardant additives including trimethyl phosphate (TMP), triethyl phosphate (TEP), triphenyl phosphate (TPP), tributyl phosphate (TBP), dimethyl methyl phosphate (DMMP), three (2,2,2-trifluoroethyl) phosphite (TFEP) and ethoxy (pentafluoro) cyclotriphosphonitrile (EFPN)*etc.*	When these flame retardant additives are heated, P-containing radicals with flame retardant properties are released, and the phosphorus-containing radicals then capture the hydrogen in the organic radical chain combustion reaction, terminating the chain reaction and making the combustion of organic electrolytes difficult	Hu et al. (2020)
	Fluorinated flame retardant additives including methyl nonafluorobutyl ether (MFE), perfluorinated (2-methyl-3-pentanone) (PFMP) and 1,1,2,2-tetrafluoroethyl-2,2,3,3-tetrafluoropropyl ether (HFE)*etc.*	When encountering an open flame, it is preferred to evaporate and absorb a large amount of heat from the surrounding area, thus extinguishing the flame, and has excellent flame retardancy	Feng et al. (2015b); Zheng et al. (2020)
Overcharge protection additive	Biphenyl (BP)	Prevent overcharging events by accepting additional charge through the redox shuttle	Feng et al. (2015a)
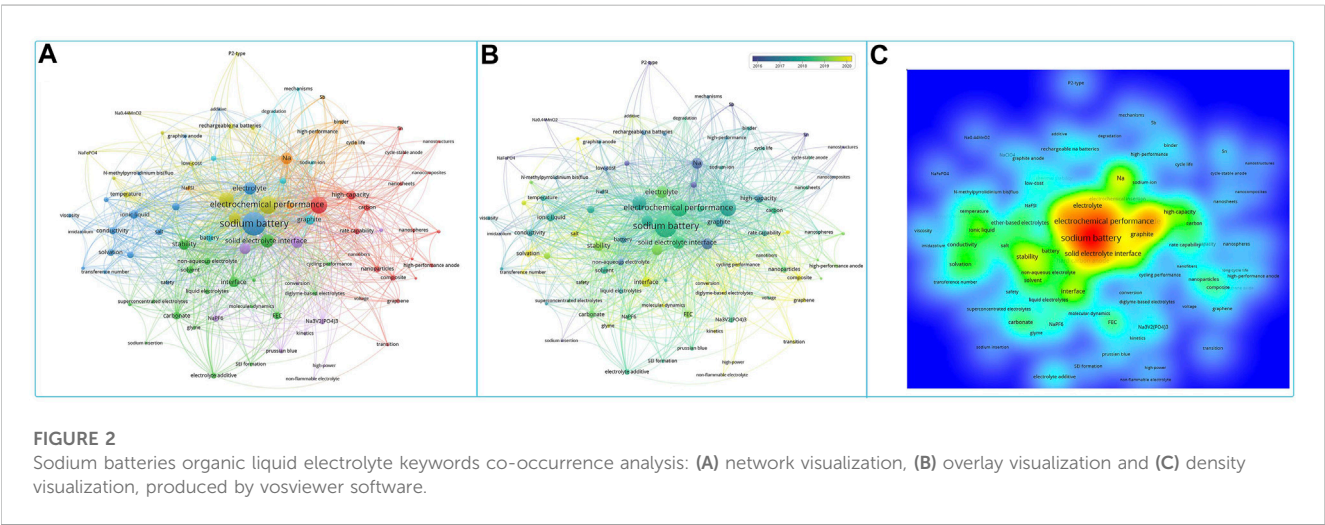
FIGURE 2
Sodium batteries organic liquid electrolyte keywords co-occurrence analysis: **(A)** network visualization, **(B)** overlay visualization and **(C)** density visualization, produced by vosviewer software.
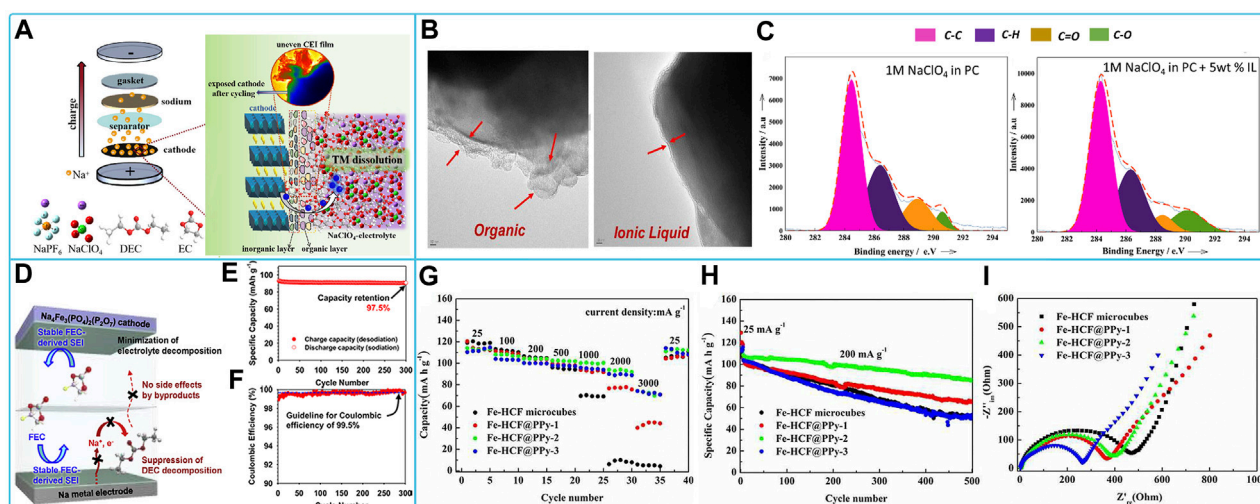
FIGURE 3
Compatibility of sodium $NaClO_4$-based electrolytes with different cathode materials: **(A)** Schematic evolution of CEI film of $Na_{0.67}Ni_{0.15}Fe_{0.2}Mn_{0.65}O_2$ (N-NFM) cathode in $NaClO_4$-based electrolytes (Wang S. et al., 2021). **(B)** HR-TEM images of NVP/C electrodes after 50 cycles with organic electrolyte and organic + IL electrolyte respectively and **(C)** XPS C1s Peaks for NVP/C cathodes after 50cycles with Organic and Organic + IL electrolytes (Manohar et al., 2018a). **(D)** Diagram of the interaction, **(E)** cycling performance and **(F)** Coulombic efficiency of $Na_4Fe_3(PO_4)_2(P_2O_7)$ electrode in $NaClO_4$-based electrolyte with FEC (Lee et al., 2016). **(G)** Discharge capacities, **(H)** long-term cycling stability and **(I)** EIS spectra of Fe-HCF and Fe-HCF@PPy electrodes in NaClO4-EC/PC electrolyte (Tang et al., 2016).

3 Current status of research on organic liquid electrolytes

Sodium ion battery organic liquid electrolytes are classified according to sodium salts and are mainly divided into sodium perchlorate ($NaClO_4$)-based organic liquid electrolytes, sodium hexafluorophosphate ($NaPF_6$)-based organic liquid electrolytes, sodium bis(fluorosulfonyl)imide (NaFSI)-based organic liquid electrolytes, sodium bis(trifluoromethylsulfonyl)imide (NaTFSI)-based organic liquid electrolytes, and sodium difluoroxalate borate (NaODFB)-based organic liquid electrolytes. Figure 2 shows the keyword clustering analysis of the literature related to organic liquid electrolytes for sodium ion batteries over the years. The overview of research in this field was presented, including electrodes, electrolytes, solid electrolyte interfacial films, and electrochemical properties. In addition to the traditional electrochemical testing of different electrode materials with matching electrolytes, the study of solid electrolyte interfacial membranes and the development of new organic liquid electrolytes are gradually attracting the attention of researchers in recent years. The following section will focus on the compatibility of different types of sodium ion battery electrolytes with each electrode.

3.1 Sodium perchlorate ($NaClO_4$)-based organic liquid electrolytes

$NaClO_4$-based organic liquid electrolyte is a widely used electrolyte for sodium ion batteries with good compatibility with common cathode materials (layered oxides, polyanionic compounds, and Prussian blue-like compounds). The battery system consisting of layered oxide and sodium perchlorate-based

organic liquid electrolytes exhibited suitable reversible capacity, rate capability, and cycle life. The binary layered oxides P2-$Na_xCo_{0.7}Mn_{0.3}O_2$ ($x \approx 1$) perform well in the electrolyte of $NaClO_4$ dissolved in PC with FEC, which is easier to coordinate with the ClO_4^- on the cathode surface than the PC solvent and contributes to the formation of the NaF protective layer on the cathode surface (Cheng et al., 2019). Ternary layered oxides $Na_{0.67}Ni_{0.15}Fe_{0.2}Mn_{0.65}O_2$ (N-NFM) CEI membranes formed in $NaClO_4$ based electrolytes in EC/DEC contain more organic compounds but less inorganic compounds, leading to increased impedance. In addition, CEI membranes are sensitive to perchlorate, which has strong oxidizing properties. A small fraction of the CEI film peels off from the cathode surface, accelerating the dissolution of transition metal (TM) ions and leading to reactivation of electrolyte decomposition (Wang S. et al., 2021). The mechanism of action and subsequent solubilization of TM ions by CEI films is shown in Figure 3A. Therefore, further optimization of electrolyte replenishment is required. Polyanionic compounds have a very solid framework matched to $NaClO_4$ electrolytes, allowing for higher cyclability and safety, and have been extensively studied by researchers. For example, $Na_3V_2(PO_4)_3$(NVP) showed high discharge capacity and coulomb efficiency with good cycling and rate capability, cycle life in 0.9 M $NaClO_4$ dissolved in triethyl phosphate (TEP) electrolyte solution (Liu et al., 2019), and 1 M $NaClO_4$ in PC added with 5 wt% [C_3mpyr] [NTf2] IL (Manohar et al., 2018a). TEP electrolyte has non-flammable and high safety features. The IL additive makes the passivation layer organic and IL-containing and with sulfur in the surface film, and the surface film is more stable (Figures 3B,C). $Na_2VM(PO_4)_3$ (M = Ga or Al) behaves differently in an electrolyte of 1 M $NaClO_4$ with EC/PC = 1:1 v/v, FEC of 5 vol%, which is attributed to the fact that $Na_3VAl(PO_4)_3$ possesses a larger diffusion bottleneck to transfer more electrons

FIGURE 4
Compatibility of sodium NaClO$_4$-based electrolytes with different anode materials: **(A)** Schematic illustration of the behavior of the HC electrode in the different ratios NaClO$_4$/TMP electrolytes (Liu X. et al., 2018). **(B)** Schematic evolution of SEI film of Na$_2$Ti$_3$O$_7$@C with different electrolytes (Wen et al., 2023). **(C)** Capacity retention of hollow NP-based γ-Fe$_2$O$_3$ electrodes at different rates (Koo et al., 2013).

than Na$_3$VGa(PO$_4$)$_3$ and exhibits a higher redox reaction potential (Wang Q. et al., 2021). Therefore, the V^{5+}/V^{4+} redox reaction can be induced by the substitution of smaller-sized low-valent (≤+3) cations, which improves the utilization efficiency of the V^{5+}/V^{4+} redox reaction. The Na$_4$Fe$_3$(PO$_4$)$_2$(P$_2$O$_7$) cathode formed a protective surface film in the EC/PC/DEC (5/3/2, v/v/v) electrolyte with 0.5 M NaClO$_4$ added with FEC and prevented undesirable decomposition of the linear carbonate, leading to excellent cycling performance of the cathode (Figures 3D–F) (Lee et al., 2016). The discharge capacity, impedance, multiplicity performance, cycling stability, and capacity retention of Prussian blue-like cathode materials sodium hexacyanoferric (Fe-HCF) composites coated with polypyrrole (PPy) were greatly improved in the EC/PC electrolyte of NaClO$_4$ (Figures 3G–I) (Tang et al., 2016). The insertion of Na$^+$ in a series of Prussian blue compounds in organic carbonate electrolytes of NaClO$_4$ was investigated. KFe [Fe(CN)$_6$] provides the highest reversible capacity at ~3.6 V for both the high-spin and low-spin Fe^{3+}/Fe^{2+} couples (Lu et al., 2012; Wang Q. et al., 2022).

There have also been a number of studies on the compatibility of sodium perchlorate-based organic liquid electrolytes with anode. The most commonly used anode materials are intercalation type materials (e.g., hard carbon). Hard carbon as the anode of sodium ion batteries showed good compatibility with NaClO$_4$ electrolytes with solvent of EC, PC, DMC and DEC exhibiting high specific capacity and good capacity retention. The electrochemical properties of hard carbon in electrolyte are further enhanced by the action of some additives (e.g., 1-ethyl-3-methylimidazolium bis(fluoromethanesulfonyl)imide (EMImFSI) (Benchakar et al., 2020), N,N-diethyl-N-methoxyethylammonium bis(trifluoromethanesulfonyl)imide (DEMETFSI) (Egashira et al., 2012), FEC (Liu X. et al., 2018; Pan et al., 2018; Rangom et al., 2019)). For example, The reversibility of sodium insertion became evident at a volume content of 70% of DEMETFSI (Egashira et al., 2012). FEC promotes the formation of the initial sodiuming process SEI and improves the cycle life. By using added FEC and high salt-to-solvent molar ratio TMP electrolytes, it is possible to achieve both low R$_{SEI}$ and very small R$_{ct}$ on HC electrodes, thereby simultaneously inhibiting TMP decomposition and building thin and dense SEI membranes (Figure 4A). The electrolyte with a 5 vol% FEC ratio of 1:3 NaClO$_4$/trimethyl phosphate (TMP) exhibited considerable reversible capacity

(238 mAh g^{-1} at 20 mA g^{-1}), long-term cycle life up to 1,500 cycles, 84% capacity retention at 200 mA g^{-1}, and high rate capability (Liu X. et al., 2018). Graphite-based intercalated anode perform well in electrolytes with solvent combinations of EC/DEC (Luo et al., 2015), EC/DMC (Wang S.-W. et al., 2017), and PC (Wang et al., 2013). In addition to carbon materials, other inserted anodes have been investigated, such as TiO$_2$, Na$_2$Ti$_3$O$_7$. TiO$_2$ in 1M NaClO$_4$ in EC/PC electrolyte exhibits the best high-magnification performance of all titanium-based sodium ion anode materials reported so far (Wu et al., 2014). The SEI film generated in Na$_2$Ti$_3$O$_7$@C anode material with sodium perchlorate (NaClO$_4$)-based EC/DEC electrolyte contains more Na$_2$CO$_3$ and NaF, which is caused by the continuous decomposition of NaClO$_4$ salt in carbonate solvent. This makes the SEI film thicker and the interfacial impedance greater, leading to a decrease in cell cycling performance, this is in contrast to the NaOTf electrolyte (Figure 4B) (Wen et al., 2023). Metal oxides/sulfides/phosphides are typical conversion electrodes in SIBs, which typically suffer from poor conversion reaction reversibility and shuttle effects. Similar to other electrode materials, stable cycling of conversion electrodes relies on dense SEIs to provide stability and suppress losses of high mechanical strength actives. Hollow γ-Fe$_2$O$_3$ nanoparticles in PC electrolytes of NaClO$_4$ showed superior performance in terms of capacity retention, Coulomb efficiency, multiplicative performance, and cycle life (Figure 4C) (Koo et al., 2013).

In general, NaClO$_4$-based organic liquid electrolyte has been widely used as a relatively mature electrolyte for sodium ion batteries. NaClO$_4$ electrolyte has contributed to the improvement of energy density of sodium ion batteries with its own stability and oxidation resistance along with some high-voltage cathode materials. However, the compatibility with some positive and negative electrodes is not very good, and it will promote the dissolution of transition metal ions as well as the generation of thick SEI films, which may require a combination of additives and different solvent combinations to optimize the electrolyte in the future.

3.2 Sodium hexafluorophosphate (NaPF$_6$)-based organic liquid electrolytes

NaPF$_6$-based organic liquid electrolyte is also one of the commonly used electrolytes for sodium ion batteries. Studies on
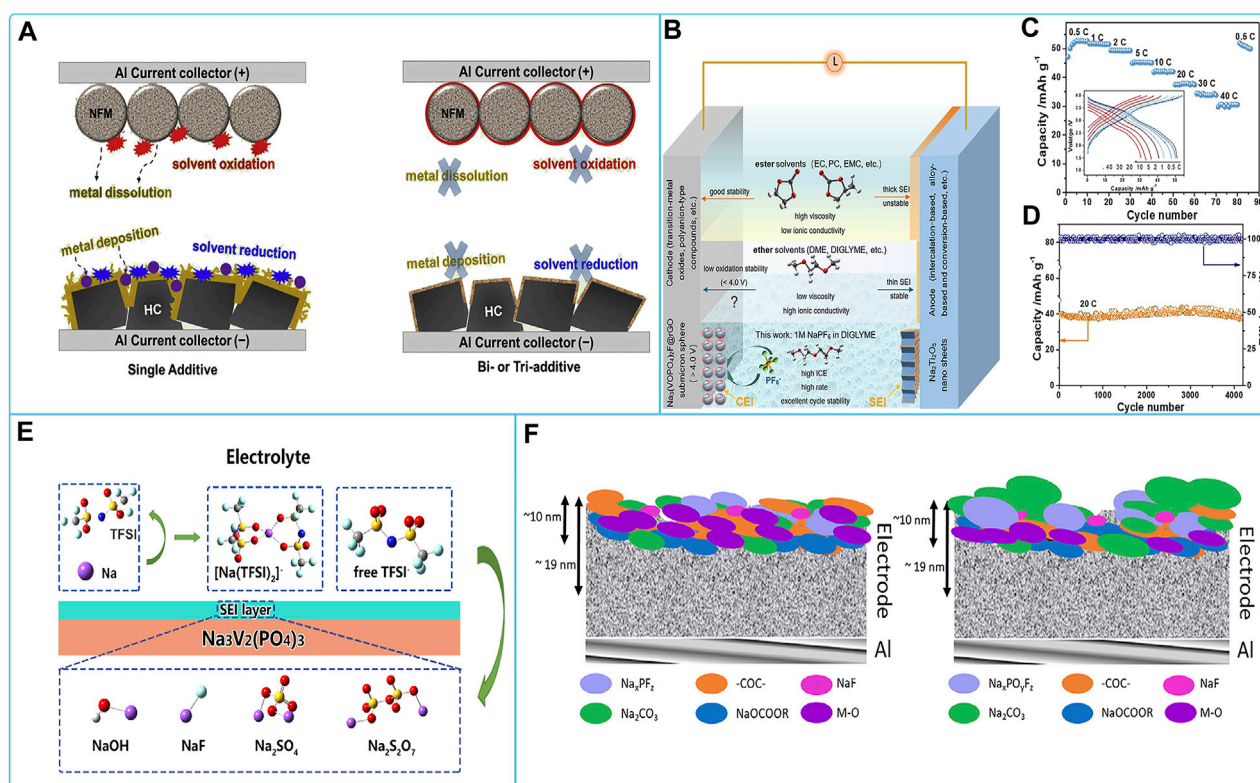
FIGURE 5
Compatibility of sodium NaPF₆-based electrolytes with different cathode materials: **(A)** Schematic summary on the role of PST and DTD additives in NFM/HC full cell (Che et al., 2018). **(B)** Illustration of effects of electrolyte system, **(C)** rate performance and **(D)** cycling performance on NVOPF@rGO//Na₂Ti₂O₅ full cell (Ba et al., 2022). **(E)** The diagram of SEI layer formation mechanism on the Na₃V₂(PO₄)₃ cathode in NaPF₆/BMITFSI IL electrolyte (Wu et al., 2018). **(F)** Schematic of the CEI on the Na₄Co₃(PO₄)₂P₂O₇ electrode after 1 st Na⁺ extraction and insertion (Zarrabeitia et al., 2021).

related cathode materials are often paired with NaPF₆-based organic liquid electrolytes for a series of electrochemical tests. First is the layered oxide cathode material. The layered oxide exhibits excellent retention and outstanding multiplicative performance, specific capacity, capacity retention and long-term cycling stability in NaPF₆-based electrolytes. Among them, The CEI film formed by Na$_{0.67}$Ni$_{0.15}$Fe$_{0.2}$Mn$_{0.65}$O₂ (N-NFM) in NaPF6-based electrolyte is dense and homogeneous, which effectively inhibits the dissolution of transition metal ions and provides a low-energy barrier for Na⁺ transport (Wang S. et al., 2021). The NaNi$_{1/3}$Fe$_{1/3}$Mn$_{1/3}$O₂ cathode material, paired with a hard carbon anode, maintains up to 92.2% capacity after 1,000 cycles at 1C between 2.0 V and 3.8 V using an optimized electrolyte of 1 M NaPF₆ dissolved in 1:1 (v/v) PC-EMC +2 wt% FEC, 1 wt% PST, and 1 wt% DTD. The PST and DTD additives promote the formation of a robust SEI on the anode and prevent the dissolution of transition metal ions by inducing the formation of a dense and dense electrolyte (Figure 5A) (Che et al., 2018). The second type of cathode material that is often adapted to NaPF₆ electrolytes is the polyanionic compound cathode material. Polyanionic compounds matching NaPF₆ ester and ether electrolytes have been reported. Na₃(VOPO₄)₂F (NVOPF)/rGO 3D sub-microspheres and Na₂Ti₂O₅ nanosheet anode electrode and NaPF₆ diglyme electrolyte, the full cell was further designed with high initial Coulombic efficiency (90%), excellent multiplicative performance (40°C) and ultra-stable cycling performance

(>4,000 cycles without degradation) (Figures 5C,D). The electrolyte defines a robust fluorine-rich inorganic-organic interface, which effectively improves the interface and promotes ultra-fast charge transfer (Figure 5B) (Ba et al., 2022). The SEI layer between Na₃V₂(PO₄)₃ and NaPF₆/1-butyl-3-methylimidazolium bis (trifluoromethanesulfonyl) imide (BMITFSI) ionic liquid electrolyte consists of NaOH, Na₂SO₄, Na₂S₂O₇ and NaF (Figure 5E). This is the reason for its good electrochemical properties (Wu et al., 2018). Half-cell tests of Na₄Co₃(PO₄)₂P₂O₇ in an electrolyte solution of EC/DEC with 1 M NaPF₆ showed the formation of a double layer in the fully Na⁺ extracted state of charge, with semi-organic-rich material found in the subsurface region near the electrode and more organic material in the outermost surface region near the electrode. At the same time, an additional outermost inorganic cover layer consisting of sodium carbonate and sodium fluorophosphate was formed after complete Na⁺ insertion (Figure 5F). Therefore, the Na₄Co₃(PO₄)₂P₂O₇ cathode provided excellent cycling performance (Zarrabeitia et al., 2021). The third cathode material used to match the NaPF₆-based electrolyte is a Prussian blue-like compound. The Prussian blue cathode electrode exhibits enhanced capacity retention in a volume ratio of 7: 3 of di-(2,2,2 trifluoroethyl) carbonate (TFEC)/fluoroethylene carbonate (FEC) consisting of 0.9 mol L⁻¹ NaPF₆. The electrolyte has excellent flame retardancy and good compatibility with sodium electrodes. The polycarbonate formed on the cathode surface plays an important role in the studied

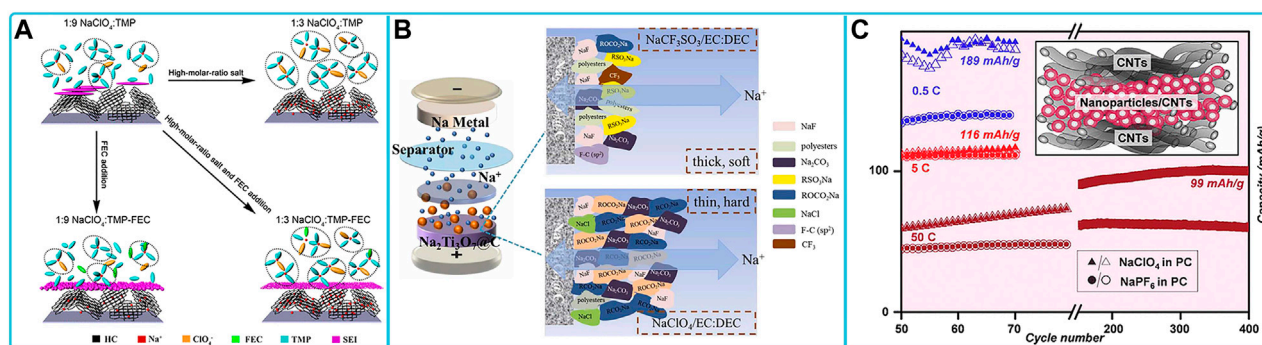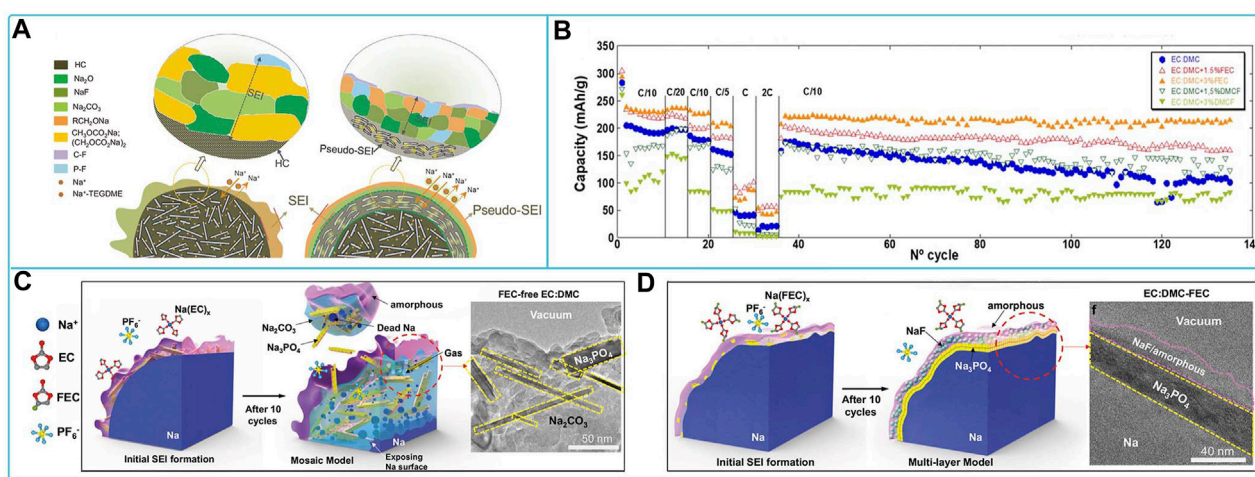**FIGURE 6**
Compatibility of sodium NaPF6-based electrolytes with different anode materials: **(A)** Schematic illustration of SEI and pseudo-SEI structures and chemistry for Na$^+$ storage in HC anodes in $NaPF_6$ based ester and ether electrolytes (Ma et al., 2021). **(B)** Cycle capacity for HC electrodes using 1 M NaPF6 in EC:DMC with addition of 1.5% and 3% of FEC or DMCF (Fondard et al., 2020). **(C, D)** Representation of free FEC and FEC electrolyte additives in tuning the microstructure of SEI on Na metals during cycling, respectively (Han et al., 2021).

electrolyte system by enhancing the ionic conductivity and reducing the impedance of the solid electrolyte interphase (SEI) layer (Zeng et al., 2020).

Researchers often choose $NaPF_6$-based organic liquid electrolytes for the study of anode materials (intercalation-type, conversion-type materials, and non-metallic materials). Hard carbon HC performs well in $NaPF_6$ electrolytes with ester and ether solvents. Among them, The TEGDME-based $NaPF_6$ electrolyte can exhibit excellent rate capability, capacity retention and cyclic Coulombic efficiency at the HC anode. This is because the stable layer-by-layer SEI in the TEGDME-based electrolyte combined with the solvent layer "pseudo-SEI" on the HC facilitates high-performance Na$^+$ ion storage in the HC and extends the cycle life of the HC anode material (Figure 6A) (Ma et al., 2021). In the EC/DMC electrolyte, the use of 3% FEC significantly increased the total capacity and capacity retention, while the use of DMCF additive had a negative impact on capacity but provided better cycling performance than the additive-free electrolyte (Figure 6B) (Fondard et al., 2020). The good performance can be attributed to the SEI composition consisting mainly of sodium ethylene dicarbonate NaO_2CO-C_2H_4-OCO_2Na (NEDC) and NaF. FEC as an additive promotes the production of NaF, which enhances the NEDC-rich SEI and results in a significant increase in capacity retention during cycling. Graphite-based materials have good reversible capacity and good cycling performance in $NaPF_6$/diethylene glycol dimethyl ether (DEGDME) electrolytes (Han et al., 2015; Cabello et al., 2017; Nacimiento et al., 2019; Li Z. et al., 2021; Zheng et al., 2022). Transformation-based electrode materials (e.g., copper phosphorothioate (Cu_3PS_4) (Brehm et al., 2020), dandelion-shaped manganese sulfide (DS-MnS) (Duong Tung et al., 2018), tin phosphide (Sn_4P_3/C) electrodes (Luis Gomez-Camer et al., 2019), TiS_2 (Tao et al., 2018), *etc.*) are also often studied matching $NaPF_6$-based organic liquid electrolytes. The choice of solvent is often ether-based solvents (diethylene glycol dimethyl

ether, DME), and to a lesser extent, esters. In these electrolytes the converted electrode materials exhibit high capacity, cycling performance, multiplicative performance, first turn Coulomb efficiency, *etc.* It indicates that the conversion-type electrodes have high compatibility with ether-based $NaPF_6$ electrolytes. Non-metallic elemental anode materials [Micron Pb particles (Darwiche et al., 2016), and Bi electrodes (Wang C. et al., 2017; Li Y. et al., 2021)] exhibit good electrochemical performance in $NaPF_6$-based diethylene glycol dimethyl ether electrolytes and good compatibility with NVP and NVPF cathode materials, and the full-cell test solution exhibited good performance. For the study of sodium metal electrodes in $NaPF_6$-based electrolytes, EC/DMC is often chosen as the solvent. When FEC is added, the Na metal electrode forms a multilayer SEI structure, including an external NaF-rich amorphous phase and an internal Na_3PO_4 phase. This layered structure stabilizes the SEI and prevents further reactions between the electrolyte and the Na metal. Without FEC, the carbonate-based electrolyte containing $NaPF_6$ reacts with the metal electrode to produce an unstable SEI, rich in Na_2CO_3 and Na_3PO_4, which continuously depletes the cell's sodium reserves during cycling (Figures 6C,D) (Han et al., 2021). The Na metal deposition/dissolution efficiency increased with increasing NaDFP concentration when sodium difluorophosphate NaDFP additive was added. NaDFP suppressed the overpotential and interfacial resistance. A high multiplicative capacity and long cycle life of 76.3% capacity retention after 500 cycles were achieved with 1 wt % NaDFP. The NaDFP-containing electrolyte formed a more stable SEI layer than the pure electrolyte, thus mitigating further degradation of the electrolyte (Yang et al., 2021). In specific glyme (chain ether) electrolytes, the sodium-metal interface produces a thin, homogeneous inorganic SEI composed primarily of Na_2O and NaF that may not support extensive or extreme cycling conditions, but the addition of FEC provides a more robust SEI to facilitate a large number of consistent sodium plating and stripping cycles (Seh et al., 2015; Sarkar et al., 2023).
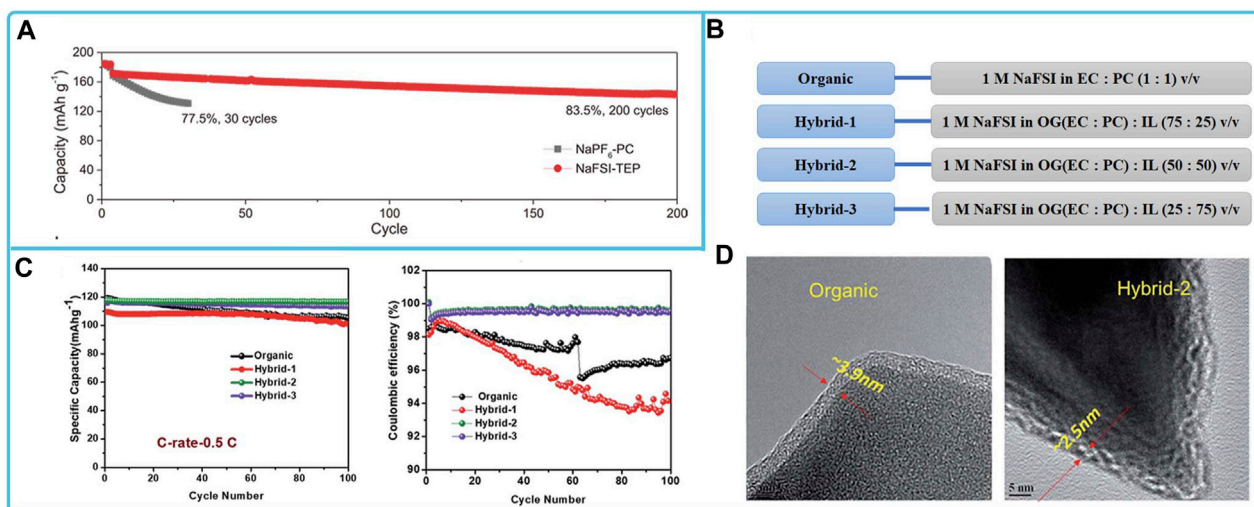
FIGURE 7
Compatibility of sodium NaFSI-based electrolytes with different cathode materials: **(A)** Long-cycling performance of hard-carbon||NaNMC full cells in two electrolytes (Jin et al., 2022). **(B)** Organic and hybrid electrolyte compositions, **(C)** cycling performance and Coulombic efficiency of NVP@C with organic and hybrid electrolytes at 0.5C and **(D)** HR-TEM images of NVP@C electrodes after cycling with the organic and hybrid-2 electrolyte, respectively (Manohar et al., 2018b).

In general, NaPF$_6$-based organic electrolytes, as a commercially available electrolyte, have good compatibility with common cathode and anode materials. NaPF$_6$ shows superior performance in ether solvents compared to other sodium salts. However, the study of NaPF$_6$-based electrolyte body solutions (e.g., solvation structure, sodium ion transport kinetics) is still at the beginning stage and will be further enhanced to reveal the reasons for their superior electrochemical performance in the future.

3.3 Sodium bis(fluorosulfonyl)imide (NaFSI) based organic liquid electrolyte

The cathode materials matched to NaFSI electrolytes mainly include layered oxides, polyanionic compounds, and organics. For the compatibility study of layered oxide cathode materials with NaFSI-based organic liquid electrolytes, the solvents used with NaFSI are esters, ethers, ionic liquids. Among them, NaNi$_{0.68}$Mn$_{0.22}$Co$_{0.10}$O$_2$ (NaNMC) exhibited good long-cycle performance and capacity retention in the phosphate electrolyte NaFSI-TEP (Figure 7A). The stable cycling can be attributed to the formation of a stable CEI layer on the NaNMC cathode, which suppresses the surface reconstruction of the cathode, the dissolution of transition metals at the cathode, and the persistent side reactions at the electrolyte/electrode interface (Jin et al., 2022). NaFe$_{0.4}$Ni$_{0.3}$Ti$_{0.3}$O$_2$ matches well in electrolytes using IL solvents (e.g., C$_3$C$_1$pyrrFSI). This ionic liquid electrolyte enhances the formation of passivation layer on the surface of Al current collectors, stabilizes the surface to 5 V, and prevents Al corrosion even at 55°C (Otaegui et al., 2015). For the compatibility study of polyanionic compounds with NaFSI electrolytes, NVP in NaFSI electrolytes with ester solvents and ionic liquids has high Coulombic efficiency, fast charging capability, stable cycling, high reversible capacity and capacity retention (Jian et al., 2013; Manohar et al.,

2018b; Zheng et al., 2018; Li et al., 2022). Among them, the ionic liquid can promote the formation of a stable and thin SEI layer on the surface, which improves the discharge capacity and cycling performance of NVP@C cathode materials (Figures 7C,D) (Manohar et al., 2018b).

The anode materials matched to NaFSI electrolyte mainly include intercalation type materials, alloy type materials, conversion type materials and Na metal electrodes. The NaFSI electrolytes suitable for the study of intercalation-type materials include ester electrolytes, ether electrolytes, and ionic liquid electrolytes. Among them, in 3 mol dm^{-3} NaFSI/PC + EC electrolyte, an organic-inorganic equilibrium SEI (mainly composed of (CH$_2$)$_n$ and NaF) was formed on the surface of the hard carbon electrode. This SEI not only enables easy charge transfer and fast Na$^+$ transport, but also exhibits strong passivation ability and excellent durability (Patra et al., 2019). CMK half-cells exhibit extraordinary cycling stability and high reversible capacity in a 3.8 M NaFSI IL electrolyte in C$_3$mpyrFSI (Figure 8A). This is due to the contribution of anionic decomposition species in ILs leading to inorganic SEI on mesoporous carbon CMK electrodes with high ionic conductivity, which promotes Na$^+$ desolvation and diffusion kinetics. This rapid Na + migration facilitates improved reaction rates and cycling stability (Sun et al., 2021). Graphite materials do not perform well in the ether electrolyte of NaFSI, where side reactions occur between the electrolyte and the graphite electrode, and the formation of SEI films, which consist mainly of salt decomposition products and hydrocarbons, as shown in Figure 8B, leading to a low Coulomb efficiency of the studied cell system (Maibach et al., 2017; Goktas et al., 2019). For the study of Na metal electrodes in NaFSI-based organic electrolytes, electrolytes that have been reported are high concentration electrolytes with NaFSI and ester and ether electrolytes with additives. Among them, The Na|| Na$_3$V$_2$(PO$_4$)$_3$ cell is stable for nearly 1,400 cycles at 2 C in a highly concentrated electrolyte of DME with the addition of a small
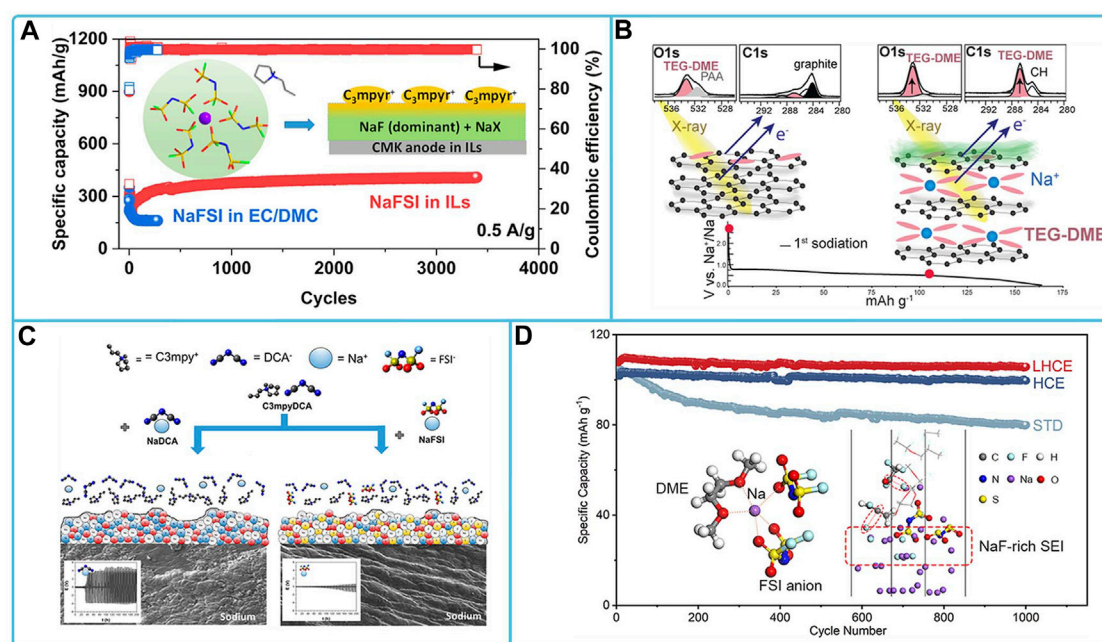
FIGURE 8
Compatibility of sodium NaFSI-based electrolytes with different anode materials: **(A)** cycling stability tests of Na/CMK cells in carbonate and ionic liquid electrolytes (Sun et al., 2021). **(B)** Schematic representation of the surface processes occurring at this particular graphite/TEG-DME electrolyte interface (Maibach et al., 2017). **(C)** Schematic representation of the sodium-solvated and interfacial structures of NaFSI and NaDCA on sodium-metal surfaces in the [C₃mpyr]DCA IL systems (Forsyth et al., 2019). **(D)** Cycling performance Na/NVP in NaFSI/DME electrolyte with TTE using STD, HCE, and LHCE, and schematic of Na⁺ solventization and formation of SEI on sodium metal surface (Wang Y. et al., 2021).

amount of SbF_3 at 4 mol L^{-1} NaFSI and also exhibits excellent multiplicative performance of 80 mAh g^{-1} at 40°C. This is because the SbF_3 additive forms a hard Na-Sb alloy layer, while the high concentration contributes to the formation of a dense NaF-rich SEI layer on the Na metal surface. This bilayer structure of the SEI layer effectively prevents dendrite growth and provides fast interfacial ion transport (Fang et al., 2020). The addition of NaFSI to methyl propylpyrrole dicyandiamide ([C₃mpyr]DCA) ionic liquid produces a more stable SEI layer (Figure 8C) (Forsyth et al., 2019). The addition of 1,1,2,2-tetrafluoroethyl-2,2,3,3-tetrafluoropropylether (TTE) to 3.8 M NaFSI/DME electrolyte forms a localized high concentration electrolyte (LHCE), which helps to construct a stable SEI for SMBs. TTE also decomposes on Na metal anodes, synergistically forming dense SEI with low surface resistance and good mechanical properties, rich in NaF, which facilitates the transport of Na⁺ ions and inhibits the growth of Na dendrites (Figure 8D) (Wang Y. et al., 2021). Transformation-based anode materials (e.g., $Cu_{1.8}S/C$ (Li H. et al., 2021), SnP nanocrystals (NCs) (Liu J. et al., 2018), tin phosphide (Sn_4P_3) (Mogensen et al., 2017; Mogensen et al., 2018)) in FSI-based organic electrolytes exhibited stable cycling ability and high capacity. Both NaFSI and FEC additives contribute to the formation of a stable NaF-rich SEI on the anode surface.

In general, NaFSI electrolytes dissolved in carbonate ester and ionic liquids exhibit better electrochemical performance and have better compatibility for hard carbon electrodes and sodium metal electrodes compared to other sodium salt electrolytes. In the future, combining different types of cathode and anode electrodes to assemble a complete battery for electrochemical testing, as well as

contributing to the design and implementation of flame-retardant batteries, may be the trend for this electrolyte.

3.4 Sodium bis(trifluoromethylsulfonyl) imide (NaTFSI)-based organic liquid electrolyte

The cathode materials adapted to NaTFSI-based organic liquid electrolytes for electrochemical testing mainly include layered oxides and polyanionic compounds. Layered oxides (P2-type $Na_{2/3}Ni_{1/3}Mn_{2/3}O_2$ (Risthaus et al., 2018), $Na_{0.45}Ni_{0.22}Co_{0.11}Mn_{0.66}O_2$ (Chagas et al., 2014), and $Na_{0.44}MnO_2$ (Stigliano et al., 2022)) exhibited high discharge capacity and capacity retention in the ionic liquid electrolyte with NaTFSI. For the polyanionic compound, $NaFePO_4$/Na half-cells in sodium bis(trifluoromethanesulfonyl)imide (NaTFSI)-bonded butylmethylpyrrolidine (BMP)-TFSI ionic liquid (IL) electrolyte operate at 3 V. This IL electrolyte shows high thermal stability and non-flammability. $NaFePO_4$ has the best capacity at 50 °C in 0.5 M NaTFSI mixed IL electrolyte (Wongittharom et al., 2014).

The most commonly used anode material for NaTFSI organic electrolyte is hard carbon. NaTFSI organic electrolytes used for hard carbon electrodes include ester electrolytes and ionic liquid electrolytes. Among them, hard carbon electrodes in 2 M NaTFSI/EC:DMC electrolyte provided the best initial reversible capacity, high electrochemical stability, and good cycling stability. In addition, a sharp capacity decay was observed after cycling in an ultra-high concentration electrolyte (5 M NaTFSI/EC: DMC) (Figures 9A,B) (Chen et al., 2020). In NaTFSI/EC: DMC
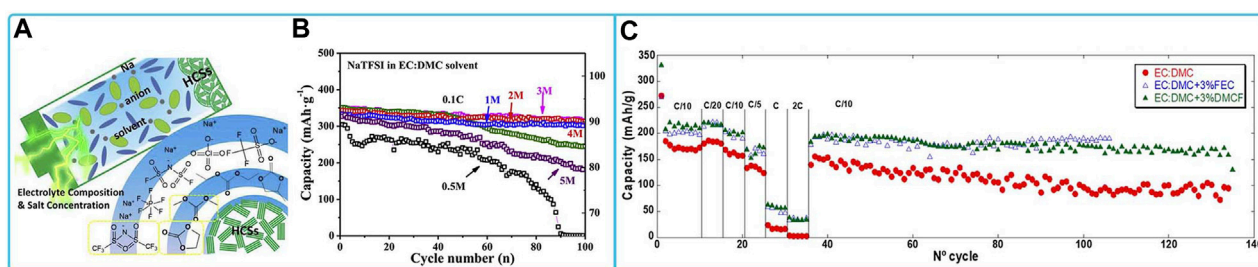
FIGURE 9
Compatibility of sodium NaFSI-based electrolytes with HCSs materials: **(A)** Schematic diagram of the interaction mechanism of HCSs electrodes in ultra-high concentration electrolytes and **(B)** cycling performance at 0.1C of HCSs in electrolytes with different salt concentrations (Chen et al., 2020). **(C)** Cycling capacity for HC electrodes using 1 M NaPF$_6$ in EC:DMC with addition of 1.5% and 3% of FEC or DMCF(Fondard et al., 2020).

electrolyte, the addition of FEC or DMCF was found to be beneficial for overall capacity and capacity retention during cycling (Figure 9C) (Fondard et al., 2020).

In addition, some applications of NaTFSI-based electrolytes in full batteries have been reported. For example, the full cell consisting of Na$_3$V$_2$(PO$_4$)$_2$F$_3$ cathode and (Na$_{2+x}$Ti$_4$O$_9$/C) anode exhibited high capacity retention in a nonflammable low eutectic solvent (DES) including sodium bis(trifluoromethane) sulfonate (NaTFSI) dissolved in N-methylacetamide (NMA). The improved electrochemical stability was associated with a stronger surface film formed at the electrode/electrolyte interface (De Sloovere et al., 2022). P2-Na$_{0.6}$Ni$_{0.22}$Fe$_{0.11}$Mn$_{0.66}$O$_2$ cathode and Nanostructured Sb-C composite anode cells in a 0.2M NaTFSIPyr$_{14}$TFSI ionic liquid-based electrolyte exhibited high specific capacity for the full cell. The electrolyte has a high ionic conductivity and high thermal stability. The anodic stability of this electrolyte was up to 4.7 V vs. Na$^+$/Na (Hasa et al., 2016).

In general, NaTFSI ionic liquid electrolytes show good electrochemical performance. However, there are some problems, such as corrosion of the aluminum foil, capacity decay and some disadvantages of the ionic liquid electrolyte itself (e.g., high viscosity, poor wettability to the electrode, *etc.*). Efforts are still needed to improve these shortcomings in the future.

3.5 Sodium difluoroxalate borate (NaODFB)-based organic liquid electrolyte

Sodium difluoro (oxalato)borate (NaODFB) is a new chelated sodium salt discovered by researchers in recent years. Only a few articles have been published to study this electrolyte. Chen et al. (Chen et al., 2015) found that Na/Na$_{0.44}$MnO$_2$ half-cells combined with NaDFOB-based electrolytes exhibited greatly enhanced multiplicative capacity and cycling performance. Sun et al. (Sun et al., 2020) developed a high-capacity nanoconstrained FeF$_3$ SIB-based cathode and found that the best cycling performance was achieved using NaDFOB salts in a ternary electrolyte (EC:DEC: DMC), with much higher cycling performance compared to the conventionally used NaClO$_4$, which was associated with the formation of a thin and conformal CEI protective film on the cathode. They further predicted that the DFOB anion reduction-mediated radical oligomer/polymer pathway may be an important

part of the formation of CEI films. As shown in Figure 10A. Wang et al. (2023) investigated the compatibility of NaODFB electrolyte with NVP cathode.1 M NaODFB-DME electrolyte contributed to the formation of thinner CEI film on the surface of NVP material with low content of B$_2$O$_3$, which resulted in high specific capacity and capacity retention of the cell. Zhao et al. (2022) investigated the compatibility of NaODFB ether electrolyte with HC anode at high temperature. The Na/HC half-cell with 1 M NaODFB in DME has a high reversible capacity of 249.9 mAh/g at 100 mA/g and 55°C, exhibiting excellent cycling stability attributed to the SEI membrane groups B-F and B-O containing inorganic substances. Gao et al. (2022) found that there was a dense and smooth SEI film on the surface of sodium sheets after cycling in NaODFB-based carbonate electrolyte, and the SEI film could effectively inhibit the growth of sodium dendrites. They provide insight into the underlying mechanism of the protective effect provided by SEI derived from sodium difluoro (oxalate)borate (NaDFOB) (Figure 10B). The pre-reduction of the DFOB$^-$ contributes to the formation of SEI and inhibits the decomposition of the carbonate solvent, and the DFOB$^-$ is gradually transformed into a borate- and fluoride-rich SEI with cycling. The protective effect of SEI is optimized at 50 cycles, resulting in a threefold increase in the lifetime of the sodium metal batteries.

In summary, NaDFOB has high compatibility with various common solvents used for NIBs, which means that NaDFOB may be very effective for various electrode materials for other NIBs. However, the preliminary work mainly focused on its application as an additive. We should optimize the electrolyte of NaODFB as the main salt and apply it to the full battery. Further studies on the complex interactions of NaDFOB electrolytes with different solvents with various electrode materials are also necessary. The goal of exploring its full potential as a emerging and high-performance electrolyte for sodium ion batteries will be realized in the future.

4 Composition, formation mechanism and regulation strategy of the interface between electrolyte and electrode

The study of the solid-liquid interface formed between electrolyte and electrode material is a hot research topic in the field of batteries. The solid-liquid interface film is formed between
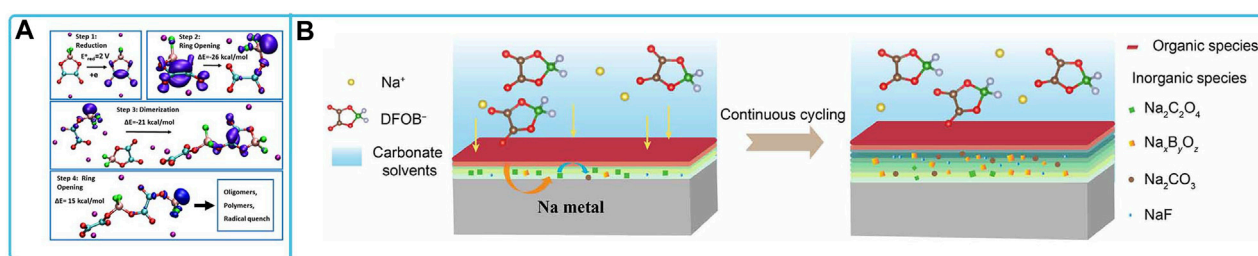
FIGURE 10
Compatibility of sodium NaODFB-based electrolytes with different electrode materials: **(A)** Pathway of CEI film formation by FeF_3 in NaODFB-based electrolyte (Chen et al., 2015). **(B)** Schematic illustrations of the NaDFOB-derived SEI structure on the surface of sodium metal (Gao et al., 2022).

the electrolyte and electrode material during the first cycle of charging and discharging, and the presence of the interface film prevents the electrolyte from continuously contacting the electrode material and decomposing, thus allowing the electrochemical window of the electrolyte to be extended. Factors such as the denseness, thickness and components of the solid-liquid interfacial film have a great influence on the cycling performance of the battery, and obtaining a stable interfacial film with protective effect and stable Na^+ transport has been the goal pursued by researchers.

4.1 Composition

In 1979, Peled (1979) found that alkali and alkaline earth metals in non-aqueous batteries form a surface film in contact with the electrolyte, which is an intermediate phase between the metal and the electrolyte and has the characteristics of an electrolyte, and hence the concept of "solid electrolyte interphase (SEI)" was introduced. At this time he considers the SEI model to be a simple two-dimensional passivation film structure. In 1997, Peled et al. (1997) suggested the mosaic model by arguing that insolubles generated from all types of reduction reactions of the electrolyte occurring simultaneously are deposited randomly mixed on the anode and stacked on each other to form a mosaic-like structure. In this model, grain boundaries and interfaces in SEI may act as electron conduction paths to promote the growth of dendrites and electron leakage. In 1999, Aurbach et al. (1999) proposed a multilayer structure of SEI films in lithium-ion battery systems using various means such as infrared spectroscopy, Raman spectroscopy, X-ray photoelectron spectroscopy, and electrochemical impedance spectroscopy, arguing that the passivation film formed at the beginning of the metallic Li surface is unstable and changes during the electrochemical process, with various types of substances forming one by one, and that traces of water in the electrolyte, solute Anion decomposition products also continue to influence the generated SEI film to form a multilayer film structure. This dynamic concept has also been applied to sodium ion batteries to derive bilayer and even multilayer structure models.

It is generally believed that the electrode-electrolyte interfacial film consists of the inorganic layer located on the inside connected to the electrode material and the organic layer located on the outside extending into the electrolyte. The inorganic layer is mostly

inorganic with some sodium, and the organic layer is mostly organic with sodium formed by the reaction of solvent molecules with sodium. The formation of such a bilayer structure can be divided into two stages, namely, the formation of a bilayer on the surface when electrons flow into the anode and the participation of electrons in the reaction process. When the anode is filled with electrons, Na^+ will be enriched on the electrode surface to form a bilayer. At the beginning the passivation film is thin and electron transfer is easy, so the double electron reaction occurs preferentially. The solvent molecules of the solubilized coordinated Na^+ get electrons to be reduced and are more likely to produce inorganic products such as Na_2CO_3 and Na_2O, which are precipitated on the electrode surface, while at the same time, sodium salt anions or additives may also participate in the reaction to produce NaF, NaCl, NaS, and Na_2SO_4, etc (Hu et al., 2020). The positive effect of NaF on dense SEI formation and unstable interphase growth control. Content increases appropriately to suppress the solubility of organic sodium carbonate ($NaO_2CO-C_2H_4-OCO_2Na$) and promote the conductivity of Na^+ through the SEI layer, thus improving the electrochemical properties, whereas an increase in Na_2CO_3 content does not (Fondard et al., 2020). F-S or S=O species were also detected in the case of FSI^- or bis(trifluoromethane) sulfonylimine ($TFSI^-$) anions (Ding et al., 2019). However, as the thickness of the membrane increases, electron transfer is blocked and single-electron reactions begin to dominate, with organic species such as $ROCO_2Na$ (R is an organic group) organically accumulating on the inorganic layer to form an organic layer. The specific species of the organic and inorganic components depend on the reaction between the electrode surface and the electrolyte. Different electrode materials have different SEI components in different electrolyte systems. The thickness of the SEI film is usually between a few nanometers and tens of nanometers, which is mainly related to the electron tunneling distance, and if there is no surface damage or decomposition, after reaching the longest distance of electron tunneling, the solvent will not be able to continue to get electrons to be reduced and thus stop decomposing, and the thickness change of the SEI film will decrease and become an electron insulator and ion conductor, and stabilized (Hu et al., 2020). Recently, Cui et al. (Zhang et al., 2022) revealed the original structure and redefined the composition of SEI by using advanced cryo-electron microscopy to characterize the swelling state of SEI in various electrolytes, and showed that the swelling behavior depends on the electrolyte type

FIGURE 11
Schematic diagram of **(A)** the energy of the electrode and electrolyte (Gebresilassie Eshetu et al., 2018), **(B)** specific adsorption (Zhang and Zhao, 2009), **(C)** ion solventization (Li et al., 2020), **(D)** interface film formation, and **(E)** interfacial film growth and evolution.
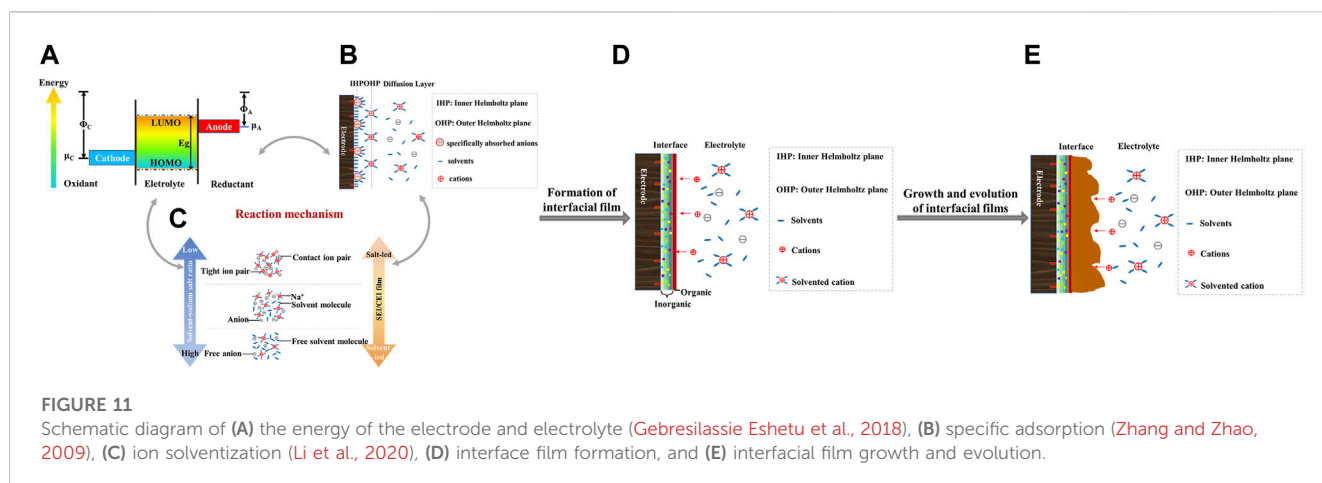
and profoundly affects the ion transport in SEI. In the inorganic-rich SEI, the swelling rate is lower, resulting in a more stable electrochemical cycle of the cell.

The ideal SEI film should have the following characteristics: (i) good electronic insulator, preventing the electrolyte from being oxidized or reduced by charge transfer on the surface; (ii) good sodium ion conductivity, selectively allowing the passage of Na$^+$ and preventing the solvent from entering the electrode material or directly contacting the electrode; (iii) good chemical and electrochemical stability, with no side reactions in the cell system; (iv) good thermal stability, stably adhering to the surface of the electrode material even at high temperatures; (v) homogeneous, dense and thin, possessing good mechanical properties and not easily flaking and dissolving (Hu et al., 2020).

4.2 Formation mechanism

The formation of the interfacial film is mainly the result of a combination of three factors: the energy polarization difference between the electrode and the electrolyte, the specific adsorption behavior and the ion solvation behavior, and the formation is accompanied by the interfacial growth and evolution. The specific formation mechanism is shown in Figure 11. The details of each part are developed below.

The interfacial film arises from the difference in energy states between the two main parts of the electrode and the electrolyte (Gauthier et al., 2015). If the electrochemical potential μ$_A$ of the anode is higher than the lowest unoccupied molecular orbital LUMO of the electrolyte, electrons are spontaneously transferred from the anode to the electrolyte, which leads to the reduction of the electrolyte and the formation of the interfacial film. Similarly, when the electrochemical potential μ$_C$ of the cathode is lower than the highest occupied molecular orbital level HOMO of the electrolyte, electrons are transferred from the electrolyte to the anode and the solvent molecules of the electrolyte lose electrons leading to oxidation of the solvent, while the anode gains electrons and the transition metal cations (such as Mn^{4+}, Ni^{4+}, Co^{4+}, *etc.*) in the material are reduced (Wang et al., 2020). The interfacial film on the surface of the anode, called SEI, is distinguished from the anode, and the products of electrolyte oxidation decomposition remain on

the surface of the cathode, defined as the CEI passivation layer. To ensure a higher energy density, one chooses to initiate the redox reaction of the electrode at a voltage that exceeds the stability of the electrolyte. It is well known that non-aqueous electrolytes typically used in Li-ion batteries are oxidized if the operating voltage is higher than about 4.5 V with respect to Li$^+$/Li. Given that the equilibrium potential of Na$^+$/Na is 0.3 V higher than that of Li$^+$/Li, some commonly used carbonate electrolytes will become thermodynamically unstable if the voltage in SIBs is higher than about 4.2 V (vs. Na$^+$/Na) (You and Manthiram, 2018).

Specific adsorption behavior and ion solvation behavior are also the main factors affecting the formation of interfacial layers. The occurrence of specific adsorption behavior precedes the ion solvation behavior, i.e., the strong interaction of some substances with the electrode surface promotes the formation of interfacial films. The interfacial film model includes the inner Helmholtz plane (IHP) and the outer Helmholtz plane (OHP). In general, the specific absorption behavior of unsolvated molecules is mainly present in IHP, while ionic solvated structures are mainly present in OHP (Zhang and Zhao, 2009). The enrichment of specific substances initially adsorbed on the electrode surface determines the initial interfacial composition and structure, while the ion solvation structure subsequently acts to promote the growth of the interfacial layer (Yan et al., 2020). For ionic solventization behavior, the solventized structure is mainly related to the coordination of alkali metal cations (e.g., Na$^+$) to electronegative atoms of the solvent molecule (e.g., carbonyl/ether oxygen) or anions (e.g., fluorine in NaPF$_6$ salts). Their binding energy depends strongly on the type of cation, anion and solvent. Differences in the solvation structure and diffusion kinetics in different electrolytes subsequently lead to differences in the electrochemical properties of their organic and inorganic interfacial products. In addition, differences in ion solvation structures can lead to different degrees of changes in the electrolyte LUMO energy levels. The solventized Na$^+$ structure at the molecular level in the electrolyte can change the preferential decomposition order of the solvent and the anion. As the salt concentration increases, the anions become more involved in the solventized shell layer, driving the transfer of LUMO from the solvent to the anion and forming an inorganic-rich interface (Xing et al., 2018). Thus, changes in the solventization

FIGURE 12
Modulation strategies for interfacial films.
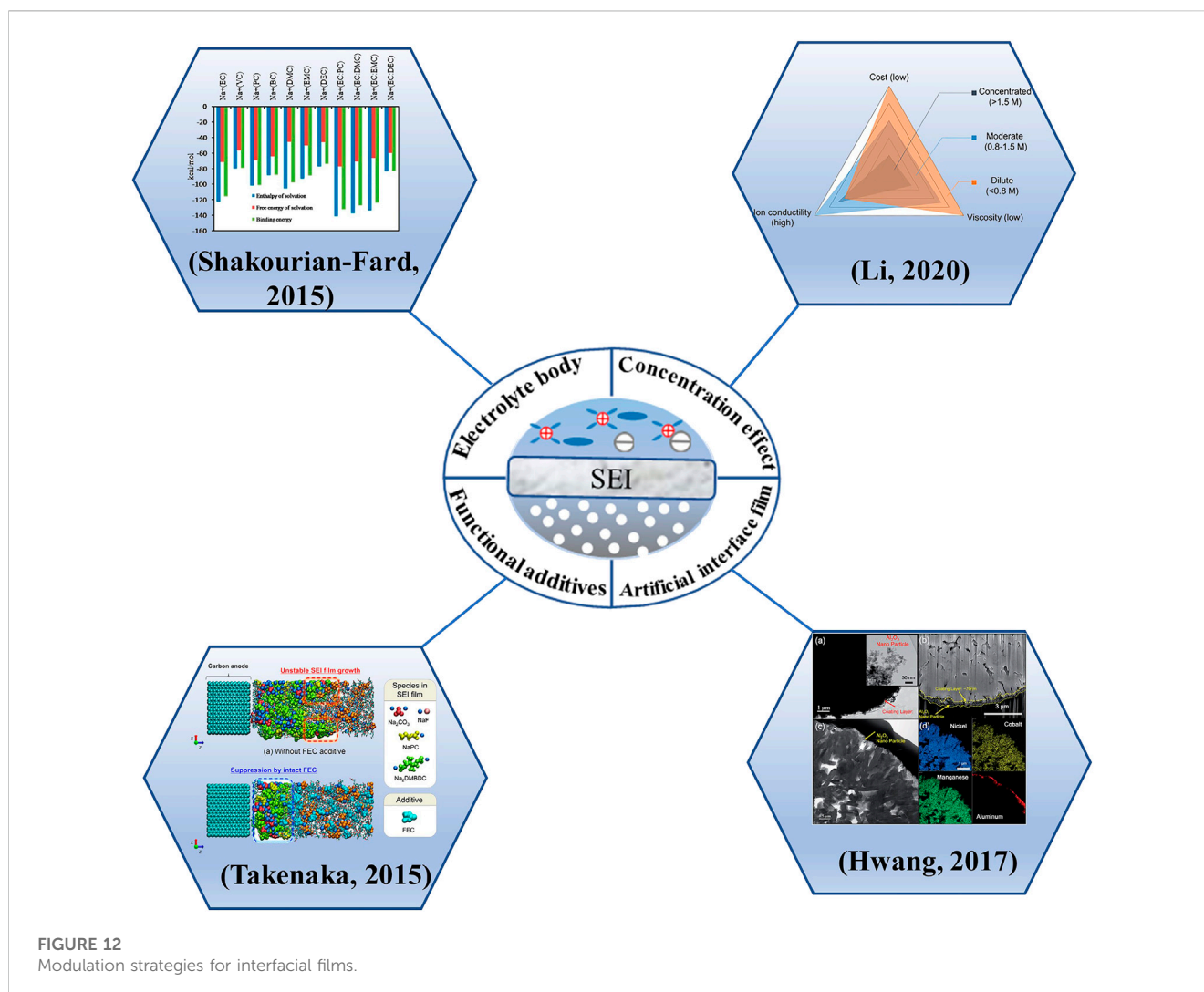
environment will alter the previous order of solvent molecule or anion consumption, determining the initial composition formation of the internal interfacial layer, further affecting the organic/inorganic composition arrangement, structural evolution and overall ion transport capacity. The ionic solventization behavior is the main induction of surface interfacial phase formation and depends on the reduction/oxidation order of solvent molecules or anions (Li et al., 2020). The solvent-induced interfacial layer is dominated by the predominant organic matter in dilute electrolytes. However, the anion-induced interfacial layer in highly concentrated electrolytes consists of more inorganic species, such as NaF, NaCl and Na_2CO_3 (Zeng et al., 2018; Zheng et al., 2018; Yamada et al., 2019).

In addition to the regulation of specific adsorbed species during electrochemistry, the subsequent interfacial evolution is extremely important. The successive interfacial reactions are mainly driven by electron transfer based on a radical reaction mechanism. Usually, the outer organic layer is vulnerable to attack due to the preferential propagation of free radicals at the interface between the outer interfacial phase layer and the electrolyte, leading to organic polymerization (Soto et al., 2015). The evolutionary origin of the interfacial layer is therefore largely dependent on the electrochemical stability of the outer organic components. It determines which component is polymerized first and to what extent the dissolution and growth of the interfacial layer can occur. In particular, for some carbon anode materials with special microstructures (e.g., mesopores or nanopores), inward growth may occur inside the material (Bommier et al., 2016). The interfacial phase growth is related to the electrochemical reactivity of the components in the matrix electrolyte in addition to the interfacial phase components. In addition, the transport of sodium ions in the interfacial layer is a key factor affecting the evolution of the interfacial layer growth. The migration of Na^+ ions in the interfacial layer is related to the desolvation process associated with the solventization behavior, the migration of Na^+ ions through the interfacial reaction products, and the crystallinity and composition distribution of the interfacial layer. Among them, the desolvation behavior of Na^+ at the electrode/electrolyte interface is a key step in determining the reaction rate. The ion desolvation energy potential depends on a combination of factors such as the strength of ion-solvent or ion-ion interactions, the choice of electrode, the presence of interfacial membrane, and the composition or structural condition of the interfacial membrane (Yamada and Yamada, 2015; Yan et al., 2020).

4.3 Regulation strategy

At present, the regulation strategy for interfacial film mainly includes four parts: electrolyte body regulation, concentration regulation, addition of functional additives and construction of artificial interfacial film (Figure 12). They are described as follows.

4.3.1 Electrolyte body

The actual state of the SEI actually depends on the choice of electrolyte composition, which determines to what extent the arrangement of inorganic and organic substances favors the final interfacial function. The current interfacial manipulation through the electrolyte ontology is mostly focused on the solventized structure of Na$^+$, where the electrolyte solvent, salt anion, is involved (Hou et al., 2019), and a smaller percentage of external organic compounds by changing the solvent and sodium salt combination.

Solvents, as one of the participants in the solventized structure, mainly include esters, ethers and ionic liquids. For ester-based electrolytes, linear solvents can reduce the electrolyte viscosity and enhance the wettability, but usually linear solvents (DMC, DEC) are weakly coordinated with Na$^+$ in the solventized structure, and therefore have high reactivity with the outer interfacial layer, which makes the interfacial layer unstable and may also increase the solubility of the interfacial layer (Xia et al., 2011; Ponrouch et al., 2013; Eshetu et al., 2016). The solventization of Na$^+$ with cyclic EC and EC:PC is more favorable than that of linear solvents. Although the structural differences between EC and PC are small, the methyl group in PC may hinder the aggregation of reaction products from the perspective of long-term cell operation, resulting in insufficient formation of interphase layers (Takenaka and Nagaoka, 2019). In addition, since the LUMO level of Na$^+$-solvent complexes decreases by 2–3 ev in varying degrees compared to a single solvent, the Na$^+$-solvent complexes are more easily reduced on the anode surface and the increase in the HOMOLUMO energy band gap also leads to a longer operating window of the electrolyte. The addition of EC solvents to PC, DMC, EMC or DEC solvents results in the formation of a co-solvent, which reduces the band gap (Shakourian-Fard et al., 2015). Therefore, mixing different ratios of cyclic molecules (e.g., EC and PC) and chain molecules (DMC and DEC)) may lead to unexpected advantages. For ether solvents, such solvents can not only co-insert Na$^+$ into graphite (Jache and Adelhelm, 2014; Kim et al., 2015; Cohn et al., 2016; Seidl et al., 2017), but also modulate the SEI passivation layer of the anode electrode material so that the interfacial phase composition has a better sodium ion transport rate and the generated passivation layer is thin and uniform (Soto et al., 2015; Wang C. et al., 2017; Zhang et al., 2017; He et al., 2018; Huang et al., 2019; Li et al., 2019). Among them, the special structure of amorphous Na$_2$CO$_3$ and NaF particles dispersed in polyether species improves the electrical conductivity of Na$^+$ (Huang et al., 2019). However, the ether-derived interfacial phase is slightly lower than the ester-derived interfacial phase in terms of long-cycle performance. One optimizes the formation of the interfacial layer for high rate and long cycle performance by combining ester and ether, where the thick and loose ester-SEI is initially formed on the inside and the thin and dense ether-SEI is on the outside (Bai et al., 2018). ILs are actually salts in liquid state at room temperature compared to conventional molecular solvents (such as carbonates and ethers), which exhibit relatively low ionic conductivity due to strong interactions between their anions and cations, but they have the advantage of high electrochemical and thermal stability due to their low vapor pressure and low flammability. Therefore, hybrid electrolytes obtained by mixing ionic liquids with conventional molecular solvents such as organic carbonates can be used, thus combining all advantages to obtain interfacial layers with better performance (Monti et al., 2016; Manohar et al., 2018b).

Anionic salts, another major player in the solventized structure, play a crucial role in the oxidative decomposition of electrolytes along with the solvent. Some anions, such as BF$_4^-$ and PF$_6^-$, have been found to reduce the oxidative stability of common carbonate solvents, such as EC, PC and DMC, through fluorine or proton transfer reactions (Borodin and Jow, 2010). In addition, oxidation between the salt anion and the solvent through electrostatic interactions may occur accompanied by charge transfer phenomena to reach the final coupled state. This determines the oxidative stability of the solventized salt (Fadel et al., 2019). When Na$^+$ is transported through the interfacial layer, anions with lower donor numbers (e.g., PF$_6^-$ and ClO$_4^-$) are more easily desolvated (Browning et al., 2017). Therefore, different anion-solvent complexes can have different effects on electrolyte oxidation stability during electrolyte decomposition on the cathode surface (Borodin and Jow, 2010; Xing et al., 2011; Cresce et al., 2015; Fadel et al., 2019). Different salts (e.g., NaClO$_4$, NaFSI, NaTFSI) undergo different pathways when decomposed on the cathode surface, resulting in components with different properties that affect the performance of the interfacial layer. Therefore, mixed anions may provide additional benefits in regulating the interfacial chemistry.

4.3.2 Concentration effect

The concentration effect is an important interfacial modulation strategy, and adjusting the optimized concentration can accordingly modulate the interfacial passivation chemistry to achieve an organic-inorganic equilibrium SEI layer. Traditionally, most electrolytes with optimized salt concentrations around 1 M exhibit the highest ionic conductivity (Yamada et al., 2019). Although the increase in salt concentration decreases the ionic conductivity, it exhibits special advantages in terms of enhanced interfacial properties and electrochemical behavior that conventional electrolytes do not possess. The decomposition order between solvent and salt differs with salt concentration. At conventional dilution concentrations the solvent decomposes preferentially, while at high concentrations, where there are almost no free solvent molecules left due to the urgent need to satisfy the dissolution of a large number of cations, the anion is forced to be decomposed first (Yamada and Yamada, 2015; 2017; Yamada et al., 2019; Yan et al., 2020). Li et al. (2020) found that, by reducing the sodium salt concentration (0.3 mol NaPF$_6$/EC + PC (1:1 by volume)), the solvent molecules can fully occupy the Na$^+$ solventized sheath layer, and the CEI and SEI films with high organic content (high C + O ratio) can be obtained on the cathode and anode sides. As the concentration of PF$_6^-$ is reduced, the decomposition by-products such as F, which has a corrosive effect on the electrode materials, are reduced, and the obtained SEI and CEI films are more stable. On the contrary, when applying high salt concentration electrolyte, the Na$^+$ solvated sheath

layer (or ligand layer) is almost occupied by anions. This will bring some special advantages. For example, the interfacial mass transfer process is changed and fast reactions can be performed on the electrode, the electrolyte volatility is weakened, the thermodynamic stability is enhanced and the safety is improved, the good SEI film can be formed on the electrode, and the Al collector is protected from anion corrosion. Increasing sodium salt concentration has an effect on the properties of the Na^+ solubilization environment (Wahlers et al., 2016; Chen et al., 2018; Kankanamge et al., 2018; Li et al., 2018), charge transport mechanism (Forsyth et al., 2016; Kankanamge et al., 2018), and Na^+ conductivity (Forsyth et al., 2016; Kankanamge et al., 2018). In addition, the overall ionic conductivity of the ether solvent-based electrolytes showed a tendency to increase with increasing sodium salt concentration. Electrolytes based on ionic liquid solvents promote ionic movement with the continuous addition of salts (Chen et al., 2018). Therefore, there are concepts of hyperconcentration and localized high concentration electrolytes have been proposed in recent years. Superconcentration because it promotes preferential passivation of LUMO-level reducing anions, which in turn creates a more powerful inorganic SEI that can better mitigate the more severe solubility problems of organic components. Moreover, a lower percentage of free solvent molecules will mitigate the tendency of soluble components to dissolve into the electrolyte (Takada et al., 2017). Localized high electrolyte concentrations not only do not alter the local dissolution environment of the concentrated electrolyte, but also provide the advantage of interface enhancement or suppression of undesirable interface problems (Zheng et al., 2018; Yamada et al., 2019).

4.3.3 Functional additives

Additivity refers to the introduction of small doses of foreign molecules into the parent electrolyte. As one of the most economical interfacial modulation strategies, the addition of additives not only does not interfere with the overall properties of the electrolyte, but also significantly tunes the interfacial layer properties to better form films for interphase passivation for electrode protection and thus improve the overall electrochemical performance. Currently, FEC is the most widely reported and effective additive. Its energy gap, E_g is located between the HOMO-LUMO gap of salt and solvent, thus FEC can stabilize the interfacial layer by sacrificing decomposition in advance thus avoiding destructive decomposition of electrolyte (Wang et al., 2020). For example, the reason for the good performance in EC-based electrolytes containing FEC is that FEC has lower decomposition energy compared to EC solvents, and the presence of FEC also enhances the decomposition energy of EC molecules, so that its early decomposition in EC-based electrolytes promotes the generation of interfacial films (Kumar et al., 2016). In PC-based electrolytes, FEC also shows good film formation due to its still early decomposition compared to PC (Takenaka et al., 2015). It should be noted here that due to the strong electronegativity of F atoms, FEC attracts the positive charge of organic products, and excess FEC prevents the formation of dimers between organic monomer products, a phenomenon that causes undesired interfacial layer growth and adversely affects the stability of interfacial films (Takenaka et al., 2015; Simone et al., 2017; Bouibes et al., 2018). In addition to FEC, other additives as described above also contribute to the formation

of stable interfacial films and need to be used in combination with different electrolyte and electrode systems for screening. In addition, the combined use of different additives may also be beneficial to achieve the desired stable interfacial film.

4.3.4 Artificial interface film

Usually, the electrode itself is attacked by the highly reactive electrolyte, which may undergo structural changes or cause surface defects, *etc*. This will lead to further decomposition of the electrolyte, resulting in lower first-loop Coulomb efficiency and thicker interfacial films. Therefore, surface coating of the electrode can effectively improve its surface properties and improve the compatibility with the electrolyte. In fact, some of the cladding work done at the cathode is also equivalent to artificially creating CEI films. By using atomic layer deposition (ALD) to coat metal oxides (AlO_3, TiO_2 and MgO), metal fluorides and even solid electrolytes on the surface of the cathode material, these coatings maintain the stability of the reversible phase change of the cathode material during charging and discharging, or prevent the erosion of the cathode material by by-products such as HF, or provide better channels for Na^+ transport provides a better channel and acts as a CEI film. For example, Sun et al. (Hwang et al., 2017a) changed the interfacial properties of the cathode by coating a layer of nano-Al_2O_3 on the surface of $Na[Ni_{0.6}Co_{0.2}Mn_{0.2}]O_2$ cathode. On the one hand, nano-Al_2O_3 can react with F present in the electrolyte to reduce the content of HF and prevent the continuous accumulation of NaF as a by-product to hinder Na^+ conduction; on the other hand, AlF_3, the product of nano-Al_2O_3 and HF, can enhance the protection of the cathode material by CEI film as a good component of CEI film. With the synergistic effect of the two, the change of interfacial impedance of the coated cathode material during the cycling process was significantly smaller than that before the coating, and the presence of the coating layer also helped to reduce the leaching of transition metals from the active material. Ye et al. (2022) reported an *in situ* artificial CEI construction strategy based on a spontaneous redox reaction between a pre-sodiumed organic solvent and a polyvinylidene fluoride (PVDF) binder. Applying this strategy to PB cathodes, the chemically pretreated PB cathodes were successfully coated with a NaF-rich interfacial phase on the electrode surface to keep them away from electrolyte attack and maintain cycling stability. This artificial CEI based on the interaction between PVDF and organic solvents is not much affected by the surface properties of the cathode material and is expected to be applied to other cathode materials. Therefore, the construction of artificial interfacial film is also an effective means to improve the compatibility of electrode with electrolyte and avoid some side reactions.

In summary, there are four common effective strategies for the regulation of solid electrolyte interfacial film. In practice, it is necessary to consider the characteristics of the electrolyte and electrode materials to choose the appropriate regulation. If the electrolyte body has a great influence on the interfacial membrane, it can try to use different salt and solvent mixing to regulate the interfacial membrane. If the electrolyte interfacial film is regulated on the basis of not changing the electrolyte body, the concentration of electrolyte or functional additives can be changed to achieve the purpose of regulating the appropriate interfacial film. If the interfacial film formed inside the battery system is unstable and cannot be improved by adjusting the electrolyte body, concentration, or additives, a suitable artificial interfacial film can be constructed from the electrodes to realize excellent electrochemical performance.

5 Conclusion and outlook

With the advantages of abundant sodium resources and low cost, sodium ion batteries are a promising energy storage battery system. At present, researchers at home and abroad have developed a variety of feasible cathode and anode materials for sodium ion batteries. The electrolyte of sodium ion battery, as a medium for the cathode and anode materials to participate in the redox reaction, has an important influence on the thermodynamic and kinetic properties of the sodium ion battery system, such as the structural stability of the electrode materials, the composition and structure of the SEI, the multiplicative performance, cycling stability and thermal stability of the battery. Therefore, electrolyte is also the key to determine the battery performance. This paper introduces the research progress of organic liquid electrolytes for sodium ion batteries from the basic requirements and composition of organic liquid electrolytes, the current research status of organic liquid electrolytes, and the composition, requirements and regulation strategies of the interface between electrolytes and electrodes. First, an overview of organic liquid electrolytes is introduced, followed by the classification of organic liquid electrolytes from the perspective of sodium salts, and the compatibility and electrochemical properties of each sodium salt electrolyte with cathode and anode are introduced. Finally, the strategy for electrolyte regulation of interfacial film is explained. At present, organic liquid electrolytes for sodium ion batteries still have problems such as narrow electrochemical windows and poor stability of SEI films. The development of new, low-cost and high-performance sodium ion battery electrolytes is crucial for the commercialization of sodium ion batteries. Future research on organic liquid electrolytes for sodium ion batteries can be carried out from the following aspects.

(1) Optimization of each individual component of the organic liquid electrolyte, including its own physical and chemical properties such as viscosity, conductivity, stability, *etc.* The compatibility of the electrolyte with the electrode material is also crucial. For example, the commonly used ester electrolyte cannot be applied to graphite anode materials, but the ether electrolyte allows sodium ions to enter the interlayer energy storage in a solventized form. The selection of additives also needs to consider the compatibility with electrolyte and electrode materials as well. In addition, in the future, we should try to explore the internal energy balance of solvent molecules from the perspective of molecular dynamics simulation and analyze the sodium storage mechanism of sodium ion battery in combination with the special structure of electrode materials, which is more conducive to enhance the matching of electrolyte and electrode materials to achieve high capacity requirements. In conclusion, we should focus on the matching of electrode electrolyte and the development of new sodium salts and additives to achieve high performance of sodium ion batteries.

(2) Battery safety is the most important key indicator of market and customer concern. Commonly used organic electrolytes cannot operate properly in high temperature environments, so the use of stable Na salts and non-flammable solvents including ionic liquids and phosphate esters to replace traditional flammable solvents, as well as the addition of flame retardant additives and overcharge additives are within consideration to achieve sodium ion battery safety. In general, the use of stable Na salts increases the thermal stability of the electrolyte, and high concentrations of the electrolyte exhibit reduced flammability. The use of non-flammable solvents instead of traditional flammable solvents is attractive because they can make the electrolyte completely non-flammable. Electrolyte reformulation consisting of flame retardant additives and overcharge additives is economical and effective. However, the high cost required for nonflammable electrolytes is a significant limitation to their commercialization.

(3) The electrolyte of sodium ion battery, as a medium for the cathode and anode materials to participate in the redox reaction, its redox window, the migration and diffusion of sodium ions, the solventized structure of sodium ions, and the coupling correlation effect between sodium ions and anions or solvents are the key factors that determine the interfacial properties of electrode materials. In addition, the sensitive nature of the interfacial phase increases the difficulty of characterization and limits our understanding of the interfacial phase. Regulation of electrolyte proprieties, concentration effects, electrolyte additives, and artificial interfacial films are effective methods to manipulate interphase formation. To meet the requirements of applications, the enhancement of interfacial composition, structure, and stability requires more fundamental work, theoretical computational studies, and advanced testing and analysis methods.

In conclusion, in the context of the imminent commercialization of sodium-ion batteries, substantial progress has been made in the research on positive and negative electrode materials. For example, the anode materials currently used in commercialized sodium-ion batteries are all hard carbon. There are already examples of commercialized production of the three main types of cathode materials. However, the organic electrolyte system used is still the solvents (EC:PC, EC:DEC or PC as a single solvent) and the sodium salts (NaClO$_4$ and NaPF$_6$). There is still a long way to go for the commercialization of organic liquid electrolytes corresponding to specific scenarios (high voltage, wide temperature, non-flammable). In the future, for the development of organic liquid electrolytes, great efforts are still needed to design safer electrolytes and more stable interfaces for SIBs. The optimization of electrolyte and solid electrolyte interface films will further bring sodium ion batteries closer to practical applications, allowing them to be widely used in the direction of large-scale energy storage and promoting commercial applications.

Author contributions

JZ: Writing–original draft, Writing–review and editing. JL: Writing–review and editing. HW: Writing–review and editing. MW: Conceptualization, Supervision, Writing–review and editing.

Conflict of interest

The authors declare that the research was conducted in the absence of any commercial or financial relationships that could be construed as a potential conflict of interest.

Publisher's note

All claims expressed in this article are solely those of the authors and do not necessarily represent those of their affiliated organizations, or those of the publisher, the editors and the reviewers. Any product that may be evaluated in this article, or claim that may be made by its manufacturer, is not guaranteed or endorsed by the publisher.

References

Armand, M., Endres, F., Macfarlane, D. R., Ohno, H., and Scrosati, B. (2009). Ionic-liquid materials for the electrochemical challenges of the future. *Nat. Mater.* 8, 621–629. doi:10.1038/nmat2448

Aurbach, D., Markovsky, B., Levi, M. D., Levi, E., Schechter, A., Moshkovich, M., et al. (1999). New insights into the interactions between electrode materials and electrolyte solutions for advanced nonaqueous batteries. *J. Power Sources* 81, 95–111. doi:10.1016/s0378-7753(99)00187-1

Ba, D., Gui, Q., Liu, W., Wang, Z., Li, Y., and Liu, J. (2022). Robust cathode-ether electrolyte interphase on interfacial redox assembled fluorophosphate enabling high-rate and ultrastable sodium ion full cells. *Nano Energy* 94, 106918. doi:10.1016/j.nanoen.2022.106918

Bai, P., He, Y., Xiong, P., Zhao, X., Xu, K., and Xu, Y. (2018). Long cycle life and high rate sodium-ion chemistry for hard carbon anodes. *Energy Storage Mater.* 13, 274–282. doi:10.1016/j.ensm.2018.02.002

Benchakar, M., Naejus, R., Damas, C., and Santos-Pena, J. (2020). Exploring the use of EMImFSI ionic liquid as additive or co-solvent for room temperature sodium ion battery electrolytes. *Electrochimica Acta* 330, 135193. doi:10.1016/j.electacta.2019.135193

Bhide, A., Hofmann, J., Dürr, A. K., Janek, J., and Adelhelm, P. (2014). Electrochemical stability of non-aqueous electrolytes for sodium-ion batteries and their compatibility with Na 0.7 CoO 2. *Phys. Chem. Chem. Phys.* 16, 1987–1998. doi:10.1039/c3cp53077a

Bommier, C., Leonard, D., Jian, Z., Stickle, W. F., Greaney, P. A., and Ji, X. (2016). New paradigms on the nature of solid electrolyte interphase formation and capacity fading of hard carbon anodes in Na-ion batteries. *Adv. Mater. Interfaces* 3, 1600449. doi:10.1002/admi.201600449

Borodin, O., and Jow, T. R. (2010). Quantum chemistry studies of the oxidative stability of carbonate, sulfone and sulfonate-based electrolytes doped with BF4-PF6-anions. *ECS Transcations* 33, 77–84. doi:10.1149/1.3563092

Bouibes, A., Takenaka, N., Fujie, T., Kubota, K., Komaba, S., and Nagaoka, M. (2018). Concentration effect of fluoroethylene carbonate on the formation of solid electrolyte interphase layer in sodium-ion batteries. *Acs Appl. Mater. Interfaces* 10, 28525–28532. doi:10.1021/acsami.8b07530

Brehm, W., Santhosha, A. L., Zhang, Z., Neumann, C., Turchanin, A., Martin, A., et al. (2020). Copper thiophosphate (Cu3PS4) as electrode for sodium-ion batteries with ether electrolyte. *Adv. Funct. Mater.* 30, 1910583. doi:10.1002/adfm.201910583

Browning, K. L., Sacci, R. L., and Veith, G. M. (2017). Energetics of Na+ transport through the electrode/cathode interface in single solvent electrolytes. *J. Electrochem. Soc.* 164, A580–A586. doi:10.1149/2.0311704jes

Cabello, M., Chyrka, T., Klee, R., Aragon, M. J., Bai, X., Lavela, P., et al. (2017). Treasure Na-ion anode from trash coke by adept electrolyte selection. *J. Power Sources* 347, 127–135. doi:10.1016/j.jpowsour.2017.02.065

Cao, J., Wan, Y., Tu, G., Zhang, S., Xia, A., Liu, X., et al. (2013). Information system architecture for smart grids. *Chin. J. Comput.* 36, 143–167. doi:10.3724/SP.J.1016.2013.00143

Chagas, L. G., Buchholz, D., Wu, L., Vortmann, B., and Passerini, S. (2014). Unexpected performance of layered sodium-ion cathode material in ionic liquid-based electrolyte. *J. Power Sources* 247, 377–383. doi:10.1016/j.jpowsour.2013.08.118

Che, H., Chen, S., Xie, Y., Wang, H., Amine, K., Liao, X.-Z., et al. (2017). Electrolyte design strategies and research progress for room-temperature sodium-ion batteries. *Energy & Environ. Sci.* 10, 1075–1101. doi:10.1039/c7ee00524e

Che, H., Yang, X., Wang, H., Liao, X.-Z., Zhang, S. S., Wang, C., et al. (2018). Long cycle life of sodium-ion pouch cell achieved by using multiple electrolyte additives. *J. Power Sources* 407, 173–179. doi:10.1016/j.jpowsour.2018.08.025

Chen, C., Wu, M., Liu, J., Xu, Z., Zaghib, K., and Wang, Y. (2020). Effects of ester-based electrolyte composition and salt concentration on the Na-storage stability of hard carbon anodes. *J. Power Sources* 471, 228455. doi:10.1016/j.jpowsour.2020.228455

Chen, F., Howlett, P., and Forsyth, M. (2018). Na-ion solvation and high transference number in superconcentrated ionic liquid electrolytes: A theoretical approach. *J. Phys. Chem. C* 122, 105–114. doi:10.1021/acs.jpcc.7b09322

Chen, J., Huang, Z., Wang, C., Porter, S., Wang, B., Lie, W., et al. (2015). Sodium-difluoro(oxalato)borate (NaDFOB): A new electrolyte salt for Na-ion batteries. *Chem. Commun.* 51, 9809–9812. doi:10.1039/c5cc02901e

Chen, M., Pan, Z., Jin, X., Chen, Z., Zhong, Y., Wang, X., et al. (2019). A highly integrated All-manganese battery with oxide nanoparticles supported on the cathode

and anode by super-aligned carbon nanotubes. *J. Mater. Chem. A* 7, 4494–4504. doi:10.1039/c8ta11415c

Cheng, Z., Mao, Y., Dong, Q., Jin, F., Shen, Y., and Chen, L. (2019). Fluoroethylene carbonate as an additive for sodium-ion batteries: Effect on the sodium cathode. *Acta Physico-Chimica Sin.* 35, 868–875. doi:10.3866/pku.whxb201811033

Cohn, A. P., Share, K., Carter, R., Oakes, L., and Pint, C. L. (2016). Ultrafast solvent-assisted sodium ion intercalation into highly crystalline few-layered graphene. *Nano Lett.* 16, 543–548. doi:10.1021/acs.nanolett.5b04187

Cresce, A. V. W., Gobet, M., Borodin, O., Peng, J., Russell, S. M., Wikner, E., et al. (2015). Anion solvation in carbonate-based electrolytes. *J. Phys. Chem. C* 119, 27255–27264. doi:10.1021/acs.jpcc.5b08895

Darwiche, A., Dugas, R., Fraisse, B., and Monconduit, L. (2016). Reinstating lead for high-loaded efficient negative electrode for rechargeable sodium-ion battery. *J. Power Sources* 304, 1–8. doi:10.1016/j.jpowsour.2015.10.087

Darwiche, A., Marino, C., Sougrati, M. T., Fraisse, B., Stievano, L., and Monconduit, L. (2012). Better cycling performances of bulk Sb in Na-ion batteries compared to Li-ion systems: An unexpected electrochemical mechanism. *J. Am. Chem. Soc.* 134, 20805–20811. doi:10.1021/ja310347x

De Sloovere, D., Vanpoucke, D. E. P., Paulus, A., Joos, B., Calvi, L., Vranken, T., et al. (2022). Deep eutectic solvents as nonflammable electrolytes for durable sodium-ion batteries. *Adv. Energy Sustain. Res.* 3, 2100159. doi:10.1002/aesr.202100159

Devlin, D. J., and Herley, P. J. (1987). Thermal decomposition and dehydration of sodium perchlorate monohydrate. *React. solids* 3, 75–84. doi:10.1016/0168-7336(87)80019-0

Ding, Y., Guo, X., Qian, Y., Zhang, L., Xue, L., Goodenough, J. B., et al. (2019). A liquid-metal-enabled versatile organic alkali-ion battery. *Adv. Mater.* 31, 1806956. doi:10.1002/adma.201806956

Dubois, M., Ghanbaja, J., and Billaud, D. (1997). Electrochemical intercalation of sodium ions into poly(para-phenylene) in carbonate-based electrolytes. *Synth. Met.* 90, 127–134. doi:10.1016/s0379-6779(97)81261-1

Dunn, B., Kamath, H., and Tarascon, J.-M. (2011). Electrical energy storage for the grid: A battery of choices. *Science* 334, 928–935. doi:10.1126/science.1212741

Duong Tung, P., Sambandam, B., Kim, S., Jo, J., Kim, S., Park, S., et al. (2018). Dandelion-shaped manganese sulfide in ether-based electrolyte for enhanced performance sodium-ion batteries. *Commun. Chem.* 1, 83. doi:10.1038/s42004-018-0084-1

Dustmann, C.-H. (2004). Advances in ZEBRA batteries. *J. power sources* 127, 85–92. doi:10.1016/j.jpowsour.2003.09.039

Egashira, M., Tanaka, T., Yoshimoto, N., and Morita, M. (2012). Influence of ionic liquid species in non-aqueous electrolyte on sodium insertion into hard carbon. *Electrochemistry* 80, 755–758. doi:10.5796/electrochemistry.80.755

Eshetu, G. G., Diemant, T., Hekmatfar, M., Grugeon, S., Behm, R. J., Laruelle, S., et al. (2019). Impact of the electrolyte salt anion on the solid electrolyte interphase formation in sodium ion batteries. *Nano Energy* 55, 327–340. doi:10.1016/j.nanoen.2018.10.040

Eshetu, G. G., Grugeon, S., Kim, H., Jeong, S., Wu, L., Gachot, G., et al. (2016). Comprehensive insights into the reactivity of electrolytes based on sodium ions. *Chemsuschem* 9, 462–471. doi:10.1002/cssc.201501605

Evans, T., Olson, J., Bhat, V., and Lee, S.-H. (2014). Corrosion of stainless steel battery components by bis(fluorosulfonyl)imide based ionic liquid electrolytes. *J. Power Sources* 269, 616–620. doi:10.1016/j.jpowsour.2014.07.047

Fadel, E. R., Faglioni, F., Samsonidze, G., Molinari, N., Merinov, B. V., Goddard, W. A., Iii, et al. (2019). Role of solvent-anion charge transfer in oxidative degradation of battery electrolytes. *Nat. Commun.* 10, 3360. doi:10.1038/s41467-019-11317-3

Fang, W., Jiang, H., Zheng, Y., Zheng, H., Liang, X., Sun, Y., et al. (2020). A bilayer interface formed in high concentration electrolyte with SbF3 additive for long-cycle and high-rate sodium metal battery. *J. Power Sources* 455, 227956. doi:10.1016/j.jpowsour.2020.227956

Fang, Y., Xiao, L., Chen, Z., Ai, X., Cao, Y., and Yang, H. (2018). Recent advances in sodium-ion battery materials. *Electrochem. Energy Rev.* 1, 294–323. doi:10.1007/s41918-018-0008-x

Feng, J., Ci, L., and Xiong, S. (2015a). Biphenyl as overcharge protection additive for nonaqueous sodium batteries. *Rsc Adv.* 5, 96649–96652. doi:10.1039/c5ra19988c

Feng, J., Zhang, Z., Li, L., Yang, J., Xiong, S., and Qian, Y. (2015b). Ether-based nonflammable electrolyte for room temperature sodium battery. *J. Power Sources* 284, 222–226. doi:10.1016/j.jpowsour.2015.03.038

Fenton, D., Parker, J., and Wright, P. (1973). Complexes of alkali metal ions with poly (ethylene oxide). *polymer* 14, 589. doi:10.1016/0032-3861(73)90146-8

Fondard, J., Irisarri, E., Courreges, C., Palacin, M. R., Ponrouch, A., and Dedryvere, R. (2020). SEI composition on hard carbon in Na-ion batteries after long cycling: Influence of salts (NaPF6, NaTFSI) and additives (FEC, DMCF). *J. Electrochem. Soc.* 167, 070526. doi:10.1149/1945-7111/ab75fd

Forsyth, M., Hilder, M., Zhang, Y., Chen, F., Carre, L., Rakov, D. A., et al. (2019). Tuning sodium interfacial chemistry with mixed-anion ionic liquid electrolytes. *Acs Appl. Mater. Interfaces* 11, 43093–43106. doi:10.1021/acsami.9b12913

Forsyth, M., Yoon, H., Chen, F., Zhu, H., Macfarlane, D. R., Armand, M., et al. (2016). Novel Na+ ion diffusion mechanism in mixed organic-inorganic ionic liquid electrolyte leading to high Na+ transference number and stable, high rate electrochemical cycling of sodium cells. *J. Phys. Chem. C* 120, 4276–4286. doi:10.1021/acs.jpcc.5b11746

Gao, H., Grundish, N. S., Zhao, Y., Zhou, A., and Goodenough, J. B. (2021). Formation of stable interphase of polymer-in-salt electrolyte in all-solid-state lithium batteries. *Energy Mater. Adv.* 2020, 1–10. doi:10.34133/2020/1932952

Gao, L., Chen, J., Chen, Q., and Kong, X. (2022). The chemical evolution of solid electrolyte interface in sodium metal batteries. *Sci. Adv.* 8, eabm4606. doi:10.1126/sciadv.abm4606

Gao, Y., Chen, G., Wang, X., Bai, Y., and Wu, C. (2020). Safety of electrolytes for sodium-ion batteries:Strategies and progress. *Energy Storage Sci. Technol.* 9, 1309–1317. doi:10.19799/j.cnki.2095-4239.2020.0230

Gauthier, M., Carney, T. J., Grimaud, A., Giordano, L., Pour, N., Chang, H.-H., et al. (2015). Electrode-electrolyte interface in Li-ion batteries: Current understanding and new insights. *J. Phys. Chem. Lett.* 6, 4653–4672. doi:10.1021/acs.jpclett.5b01727

Gebresilassie Eshetu, G., Martinez-Ibanez, M., Sanchez-Diez, E., Gracia, I., Li, C., Rodriguez-Martinez, L. M., et al. (2018). Electrolyte additives for room-temperature, sodium-based, rechargeable batteries. *Chemistry-an Asian J.* 13, 2770–2780. doi:10.1002/asia.201800839

Goktas, M., Bolli, C., Buchheim, J., Berg, E. J., Novak, P., Bonilla, F., et al. (2019). Stable and unstable diglyme-based electrolytes for batteries with sodium or graphite as electrode. *Acs Appl. Mater. Interfaces* 11, 32844–32855. doi:10.1021/acsami.9b06760

Goodenough, J. B., and Kim, Y. (2010). Challenges for rechargeable Li batteries. *Chem. Mater.* 22, 587–603. doi:10.1021/cm901452z

Han, B., Zou, Y., Zhang, Z., Yang, X., Shi, X., Meng, H., et al. (2021). Probing the Na metal solid electrolyte interphase via cryo-transmission electron microscopy. *Nat. Commun.* 12, 3066. doi:10.1038/s41467-021-23368-6

Han, P., Han, X., Yao, J., Liu, Z., Cao, X., and Cui, G. (2015). Flexible graphite film with laser drilling pores as novel integrated anode free of metal current collector for sodium ion battery. *Electrochem. Commun.* 61, 84–88. doi:10.1016/j.elecom.2015.10.009

Hasa, I., Passerini, S., and Hassoun, J. (2016). Characteristics of an ionic liquid electrolyte for sodium-ion batteries. *J. Power Sources* 303, 203–207. doi:10.1016/j.jpowsour.2015.10.100

He, Y., Bai, P., Gao, S., and Xu, Y. (2018). Marriage of an ether-based electrolyte with hard carbon anodes creates superior sodium-ion batteries with high mass loading. *Acs Appl. Mater. Interfaces* 10, 41380–41388. doi:10.1021/acsami.8b15274

Hong, S., Kim, Y., Park, Y., Choi, A., Choi, N., and Lee, K. (2015). Charge carriers in rechargeable batteries: Na ions vs. Li ions. *Energy Environ. Sci.* 6, 2067. doi:10.1039/c3ee40811f

Hou, T., Yang, G., Rajput, N. N., Self, J., Park, S.-W., Nanda, J., et al. (2019). The influence of FEC on the solvation structure and reduction reaction of LiPF6/EC electrolytes and its implication for solid electrolyte interphase formation. *Nano Energy* 64, 103881. doi:10.1016/j.nanoen.2019.103881

Hu, Y., Lu, Y., and Liquan, C. (2020). *Na-ion batteries*. Beijing: Science and Technology.

Huang, J., Guo, X., Du, X., Lin, X., Huang, J.-Q., Tan, H., et al. (2019). Nanostructures of solid electrolyte interphases and their consequences for microsized Sn anodes in sodium ion batteries. *Energy & Environ. Sci.* 12, 1550–1557. doi:10.1039/c8ee03632b

Hwang, J.-Y., Myung, S.-T., Choi, J. U., Yoon, C. S., Yashiro, H., and Sun, Y.-K. (2017a). Resolving the degradation pathways of the O3-type layered oxide cathode surface through the nano-scale aluminum oxide coating for high-energy density sodium-ion batteries. *J. Mater. Chem. A* 5, 23671–23680. doi:10.1039/c7ta08443a

Hwang, J.-Y., Myung, S.-T., and Sun, Y.-K. (2017b). Sodium-ion batteries: Present and future. *Chem. Soc. Rev.* 46, 3529–3614. doi:10.1039/c6cs00776g

Jache, B., and Adelhelm, P. (2014). Use of graphite as a highly reversible electrode with superior cycle life for sodium-ion batteries by making use of Co-intercalation phenomena. *Angew. Chemie-International Ed.* 53, 10333–10337. doi:10.1002/ange.201403734

Jang, J. Y., Lee, Y., Kim, Y., Lee, J., Lee, S.-M., Lee, K. T., et al. (2015). Interfacial architectures based on a binary additive combination for high-performance Sn4P3 anodes in sodium-ion batteries. *J. Mater. Chem. A* 3, 8332–8338. doi:10.1039/c5ta00724k

Jian, Z., Han, W., Lu, X., Yang, H., Hu, Y.-S., Zhou, J., et al. (2013). Superior electrochemical performance and storage mechanism of Na3V2(PO4)3 cathode for room-temperature sodium-ion batteries. *Adv. Energy Mater.* 3, 156–160. doi:10.1002/aenm.201200558

Jin, Y., Xu, Y., Xiao, B., Engelhard, M. H., Yi, R., Vo, T. D., et al. (2022). Stabilizing interfacial reactions for stable cycling of high-voltage sodium batteries. *Adv. Funct. Mater.* 32. doi:10.1002/adfm.202204995

Kamath, G., Cutler, R. W., Deshmukh, S. A., Shakourian-Fard, M., Parrish, R., Huether, J., et al. (2014). *In silico* based rank-order determination and experiments on nonaqueous electrolytes for sodium ion battery applications. *J. Phys. Chem. C* 118, 13406–13416. doi:10.1021/jp502319p

Kankanamge, S. R. G., Li, K., Fulfer, K. D., Du, P., Jorn, R., Kumar, R., et al. (2018). Mechanism behind the unusually high conductivities of high concentrated sodium ion glyme-based electrolytes. *J. Phys. Chem. C* 122, 25237–25246. doi:10.1021/acs.jpcc.8b06991

Kim, H., Hong, J., Yoon, G., Kim, H., Park, K.-Y., Park, M.-S., et al. (2015). Sodium intercalation chemistry in graphite. *Energy & Environ. Sci.* 8, 2963–2969. doi:10.1039/c5ee02051d

Komaba, S., Ishikawa, T., Yabuuchi, N., Murata, W., Ito, A., and Ohsawa, Y. (2011a). Fluorinated ethylene carbonate as electrolyte additive for rechargeable Na batteries. *Acs Appl. Mater. Interfaces* 3, 4165–4168. doi:10.1021/am200973k

Komaba, S., Murata, W., Ishikawa, T., Yabuuchi, N., Ozeki, T., Nakayama, T., et al. (2011b). Electrochemical Na insertion and solid electrolyte interphase for hard-carbon electrodes and application to Na-ion batteries. *Adv. Funct. Mater.* 21, 3859–3867. doi:10.1002/adfm.201100854

Koo, B., Chattopadhyay, S., Shibata, T., Prakapenka, V. B., Johnson, C. S., Rajh, T., et al. (2013). Intercalation of sodium ions into hollow iron oxide nanoparticles. *Chem. Mater.* 25, 245–252. doi:10.1021/cm303611z

Kumar, H., Detsi, E., Abraham, D. P., and Shenoy, V. B. (2016). Fundamental mechanisms of solvent decomposition involved in solid-electrolyte interphase formation in sodium ion batteries. *Chem. Mater.* 28, 8930–8941. doi:10.1021/acs.chemmater.6b03403

Larcher, D., and Tarascon, J. M. (2015). Towards greener and more sustainable batteries for electrical energy storage. *Nat. Chem.* 7, 19–29. doi:10.1038/nchem.2085

Lee, Y., Lee, J., Kim, H., Kang, K., and Choi, N.-S. (2016). Highly stable linear carbonate-containing electrolytes with fluoroethylene carbonate for high-performance cathodes in sodium-ion batteries. *J. Power Sources* 320, 49–58. doi:10.1016/j.jpowsour.2016.04.070

Li, H., Chen, H., Shen, X., Liu, X., Fang, Y., Zhong, F., et al. (2022). High-voltage and intrinsically safe sodium metal batteries enabled by nonflammable fluorinated phosphate electrolytes. *Acs Appl. Mater. Interfaces* 14, 43387–43396. doi:10.1021/acsami.2c13295

Li, H., Zhang, H., Diemant, T., Behm, R. J., Geiger, D., Kaiser, U., et al. (2021a). Reversible copper sulfide conversion in nonflammable trimethyl phosphate electrolytes for safe sodium-ion batteries. *Small Struct.* 2, 2100035. doi:10.1002/sstr.202100035

Li, K., Kankanamge, S. R. G., Weldeghiorghis, T. K., Jorn, R., Kuroda, D. G., and Kumar, R. (2018). Predicting ion association in sodium electrolytes: A transferrable model for investigating glymes. *J. Phys. Chem. C* 122, 4747–4756. doi:10.1021/acs.jpcc.7b09995

Li, K., Zhang, J., Lin, D., Wang, D.-W., Li, B., Lv, W., et al. (2019). Evolution of the electrochemical interface in sodium ion batteries with ether electrolytes. *Nat. Commun.* 10, 725. doi:10.1038/s41467-019-08506-5

Li, Y., Lu, Y., Zhao, C., Hu, Y.-S., Titirici, M.-M., Li, H., et al. (2017). Recent advances of electrode materials for low-cost sodium-ion batteries towards practical application for grid energy storage. *Energy Storage Mater.* 7, 130–151. doi:10.1016/j.ensm.2017.01.002

Li, Y., Yang, Y., Lu, Y., Zhou, Q., Qi, X., Meng, Q., et al. (2020). Ultralow-concentration electrolyte for Na-ion batteries. *Acs Energy Lett.* 5, 1156–1158. doi:10.1021/acsenergylett.0c00337

Li, Y., Zhong, X., Wu, X., Li, M., Zhang, W., and Wang, D. (2021b). Bi/C nanosheet microspheres with an open pore structure as anodes for sodium ion batteries with high capacity, excellent rate performance and long cycle life. *J. Mater. Chem. A* 9, 22364–22372. doi:10.1039/d1ta06948a

Li, Z., Tian, Z., Zhang, C., Wang, F., Ye, C., Han, F., et al. (2021c). An AlCl3 coordinating interlayer spacing in microcrystalline graphite facilitates ultra-stable and high-performance sodium storage. *Nanoscale* 13, 10468–10477. doi:10.1039/d1nr01660a

Lin, Z., Xia, Q., Wang, W., Li, W., and Chou, S. (2019). Recent research progresses in ether- and ester-based electrolytes for sodium-ion batteries. *Infomat* 1, 376–389. doi:10.1002/inf2.12023

Liu, J., Wang, S., Kravchyk, K., Ibanez, M., Krumeich, F., Widmer, R., et al. (2018a). SnP nanocrystals as anode materials for Na-ion batteries. *J. Mater. Chem. A* 6, 10958–10966. doi:10.1039/c8ta01492b

Liu, S., Shao, L., Zhang, X., Tao, Z., and Chen, J. (2018b). Knockdown of long noncoding RNA (lncRNA) metastasis-associated lung adenocarcinoma transcript 1 (MALAT1) inhibits proliferation, migration, and invasion and promotes apoptosis by targeting miR-124 in retinoblastoma. *Acta Physico-Chimica Sin.* 34, 581–591. doi:10.3727/096504017X14953948675403

Liu, X., Jiang, X., Zeng, Z., Ai, X., Yang, H., Zhong, F., et al. (2018c). High capacity and cycle-stable hard carbon anode for nonflammable sodium-ion batteries. *Acs Appl. Mater. Interfaces* 10, 38141–38150. doi:10.1021/acsami.8b16129

Liu, X., Jiang, X., Zhong, F., Feng, X., Chen, W., Ai, X., et al. (2019). High-safety symmetric sodium-ion batteries based on nonflammable phosphate electrolyte and double Na3V2(PO4)(3) electrodes. *Acs Appl. Mater. Interfaces* 11, 27833–27838. doi:10.1021/acsami.9b07614

Lu, Y.-X., Zhao, C.-L., Rong, X.-H., Chen, L.-Q., and Hu, Y.-S. (2018). Research progress of materials and devices for room-temperature Na-ion batteries. *Acta Phys. Sin.* 67, 120601. doi:10.7498/aps.67.20180847

Lu, Y., Wang, L., Cheng, J., and Goodenough, J. B. (2012). Prussian blue: A new framework of electrode materials for sodium batteries. *Chem. Commun.* 48, 6544–6546. doi:10.1039/c2cc31777j

Luis Gomez-Camer, J., Acebedo, B., Ortiz-Vitoriano, N., Monterrubio, I., Galceran, M., and Rojo, T. (2019). Unravelling the impact of electrolyte nature on Sn4P3/C negative electrodes for Na-ion batteries. *J. Mater. Chem. A* 7, 18434–18441. doi:10.1039/c9ta04288a

Luo, X.-F., Yang, C.-H., and Chang, J.-K. (2015). Correlations between electrochemical Na+ storage properties and physiochemical characteristics of holey graphene nanosheets. *J. Mater. Chem. A* 3, 17282–17289. doi:10.1039/c5ta03687a

Ma, M., Cai, H., Xu, C., Huang, R., Wang, S., Pan, H., et al. (2021). Engineering solid electrolyte interface at nano-scale for high-performance hard carbon in sodium-ion batteries. *Adv. Funct. Mater.* 31, 2100278. doi:10.1002/adfm.202100278

Maibach, J., Jeschull, F., Brandell, D., Edstrom, K., and Valvo, M. (2017). Surface layer evolution on graphite during electrochemical sodium-tetraglyme Co-intercalation. *Acs Appl. Mater. Interfaces* 9, 12373–12381. doi:10.1021/acsami.6b16536

Manohar, C. V., Forsyth, M., Macfarlane, D. R., and Mitra, S. (2018a). Role of N-propyl-N-methyl pyrrolidinium bis(trifluoromethanesulfonyl)imide as an electrolyte additive in sodium battery electrochemistry. *Energy Technol.* 6, 2232–2237. doi:10.1002/ente.201800123

Manohar, C. V., Raj, A. K., Kar, M., Forsyth, M., Macfarlane, D. R., and Mitra, S. (2018b). Stability enhancing ionic liquid hybrid electrolyte for NVP@C based sodium batteries. *Sustain. Energy & Fuels* 2, 566–576. doi:10.1039/c7se00537g

Minh Phuong, D., Bucher, N., Nagasubramanian, A., Markovits, I., Tian, B., Fischer, P. J., et al. (2019). Effect of conducting salts in ionic liquid electrolytes for enhanced cyclability of sodium-ion batteries. *Acs Appl. Mater. Interfaces* 11, 23972–23981. doi:10.1021/acsami.9b03279

Mogensen, R., Maibach, J., Brant, W. R., Brandell, D., and Younesi, R. (2017). Evolution of the solid electrolyte interphase on tin phosphide anodes in sodium ion batteries probed by hard x-ray photoelectron spectroscopy. *Electrochimica Acta* 245, 696–704. doi:10.1016/j.electacta.2017.05.173

Mogensen, R., Maibach, J., Naylor, A. J., and Younesi, R. (2018). Capacity fading mechanism of tin phosphide anodes in sodium-ion batteries. *Dalton Trans.* 47, 10752–10758. doi:10.1039/c8dt01068d

Monti, D., Jónsson, E., Palacín, M. R., and Johansson, P. (2014). Ionic liquid based electrolytes for sodium-ion batteries: Na+ solvation and ionic conductivity. *J. Power Sources* 245, 630–636. doi:10.1016/j.jpowsour.2013.06.153

Monti, D., Ponrouch, A., Rosa Palacin, M., and Johansson, P. (2016). Towards safer sodium-ion batteries via organic solvent/ionic liquid based hybrid electrolytes. *J. Power Sources* 324, 712–721. doi:10.1016/j.jpowsour.2016.06.003

Nacimiento, F., Cabello, M., Ortiz, G. F., Alcantara, R., Lavela, P., and Tirado, J. L. (2019). Morphological adaptability of graphitic carbon nanofibers to enhance sodium insertion in a diglyme-based electrolyte. *Dalton Trans.* 48, 5417–5424. doi:10.1039/c9dt00563c

Niu, Y. B., Yin, Y. X., and Guo, Y. G. (2019). Nonaqueous sodium-ion full cells: Status, strategies, and prospects. *Small* 15, e1900233. doi:10.1002/smll.201900233

Otaegui, L., Goikolea, E., Aguesse, F., Armand, M., Rojo, T., and Singh, G. (2015). Effect of the electrolytic solvent and temperature on aluminium current collector stability: A case of sodium-ion battery cathode. *J. Power Sources* 297, 168–173. doi:10.1016/j.jpowsour.2015.07.084

Pan, H., Hu, Y.-S., and Chen, L. (2013). Room-temperature stationary sodium-ion batteries for large-scale electric energy storage. *Energy & Environ. Sci.* 6, 2338–2360. doi:10.1039/c3ee40847g

Pan, K., Lu, H., Zhong, F., Ai, X., Yang, H., and Cao, Y. (2018). Understanding the electrochemical compatibility and reaction mechanism on Na metal and hard carbon anodes of PC-based electrolytes for sodium-ion batteries. *Acs Appl. Mater. Interfaces* 10, 39651–39660. doi:10.1021/acsami.8b13236

Patra, J., Huang, H.-T., Xue, W., Wang, C., Helal, A. S., Li, J., et al. (2019). Moderately concentrated electrolyte improves solid-electrolyte interphase and sodium storage performance of hard carbon. *Energy Storage Mater.* 16, 146–154. doi:10.1016/j.ensm.2018.04.022

Peled, E. (1979). The electrochemical-behavior of alkali and alkaline-earth metals in non-aqueous battery systems - the solid electrolyte interphase model. *J. Electrochem. Soc.* 126, 2047–2051. doi:10.1149/1.2128859

Peled, E., Golodnitsky, D., and Ardel, G. (1997). Advanced model for solid electrolyte interphase electrodes in liquid and polymer electrolytes. *J. Electrochem. Soc.* 144, L208–L210. doi:10.1149/1.1837858

Ponrouch, A., Dedryvere, R., Monti, D., Demet, A. E., Mba, J. M. A., Croguennec, L., et al. (2013). Towards high energy density sodium ion batteries through electrolyte optimization. *Energy & Environ. Sci.* 6, 2361–2369. doi:10.1039/c3ee41379a

Ponrouch, A., Marchante, E., Courty, M., Tarascon, J.-M., and Palacin, M. R. (2012). In search of an optimized electrolyte for Na-ion batteries. *Energy & Environ. Sci.* 5, 8572–8583. doi:10.1039/c2ee22258b

Ponrouch, A., Monti, D., Boschin, A., Steen, B., Johansson, P., and Palacin, M. R. (2015). Non-aqueous electrolytes for sodium-ion batteries. *J. Mater. Chem. A* 3, 22–42. doi:10.1039/c4ta04428b

Qian, J., Chen, Y., Wu, L., Cao, Y., Ai, X., and Yang, H. (2012). High capacity Na-storage and superior cyclability of nanocomposite Sb/C anode for Na-ion batteries. *Chem. Commun.* 48, 7070–7072. doi:10.1039/c2cc32730a

Qian, J., Wu, X., Cao, Y., Ai, X., and Yang, H. (2013). High capacity and rate capability of amorphous phosphorus for sodium ion batteries. *Angew. Chem.* 125, 4731–4734. doi:10.1002/ange.201209689

Rangom, Y., Gaddam, R. R., Duignan, T. T., and Zhao, X. S. (2019). Improvement of hard carbon electrode performance by manipulating SEI formation at high charging rates. *Acs Appl. Mater. Interfaces* 11, 34796–34804. doi:10.1021/acsami.9b07449

Risthaus, T., Zhou, D., Cao, X., He, X., Qiu, B., Wang, J., et al. (2018). A high-capacity P2 Na2/3Ni1/3Mn2/3O2 cathode material for sodium ion batteries with oxygen activity. *J. Power Sources* 395, 16–24. doi:10.1016/j.jpowsour.2018.05.026

Rong, X., Lu, Y., Qi, X., Zhou, Q., Kong, W., Tang, K., et al. (2020). Na-ion batteries: From fundamental research to engineering exploration. *Energy Storage Sci. Technol.* 9, 515–522. doi:10.19799/j.cnki.2095-4239.2020.0054

Sadan, M. K., Choi, S.-H., Kim, H. H., Kim, C., Cho, G.-B., Kim, K.-W., et al. (2018). Effect of sodium salts on the cycling performance of tin anode in sodium ion batteries. *Ionics* 24, 753–761. doi:10.1007/s11581-017-2243-2

Sarkar, S., Lefler, M. J., Vishnugopi, B. S., Nuwayhid, R. B., Love, C. T., Carter, R., et al. (2023). Fluorinated ethylene carbonate as additive to glyme electrolytes for robust sodium solid electrolyte interface. *Cell Rep. Phys. Sci.* 4, 101356. doi:10.1016/j.xcrp.2023.101356

Seh, Z. W., Sun, J., Sun, Y., and Cui, Y. (2015). A highly reversible room-temperature sodium metal anode. *Acs Central Sci.* 1, 449–455. doi:10.1021/acscentsci.5b00328

Seidl, L., Bucher, N., Chu, E., Hartung, S., Martens, S., Schneider, O., et al. (2017). Intercalation of solvated Na-ions into graphite. *Energy & Environ. Sci.* 10, 1631–1642. doi:10.1039/c7ee00546f

Shakourian-Fard, M., Kamath, G., Smith, K., Xiong, H., and Sankaranarayanan, S. K. R. S. (2015). Trends in Na-ion solvation with alkyl-carbonate electrolytes for sodium-ion batteries: Insights from first-principles calculations. *J. Phys. Chem. C* 119, 22747–22759. doi:10.1021/acs.jpcc.5b04706

Simone, V., Lecarme, L., Simonin, L., and Martinet, S. (2017). Identification and quantification of the main electrolyte decomposition by-product in Na-ion batteries through FEC: Towards an improvement of safety and lifetime. *J. Electrochem. Soc.* 164, A145–A150. doi:10.1149/2.0671702jes

Soto, F. A., Ma, Y., De La Hoz, J. M. M., Seminario, J. M., and Balbuena, P. B. (2015). Formation and growth mechanisms of solid-electrolyte interphase layers in rechargeable batteries. *Chem. Mater.* 27, 7990–8000. doi:10.1021/acs.chemmater.5b03358

Stigliano, P., Ferrara, C., Pianta, N., Gentile, A., Mezzomo, L., Lorenzi, R., et al. (2022). Physicochemical properties of Pyr(13)TFSI-NaTFSI electrolyte for sodium batteries. *Electrochimica Acta* 412, 140123. doi:10.1016/j.electacta.2022.140123

Strauss, S. H. (1993). The search for larger and more weakly coordinating anions. *Chem. Rev.* 93, 927–942. doi:10.1021/cr00019a005

Sun, J., O'dell, L. A., Armand, M., Howlett, P. C., and Forsyth, M. (2021). Anion-derived solid-electrolyte interphase enables long life Na-ion batteries using superconcentrated ionic liquid electrolytes. *Acs Energy Lett.* 6, 2481–2490. doi:10.1021/acsenergylett.1c00816

Sun, Z., Fu, W., Liu, M. Z., Lu, P., Zhao, E., Magasinski, A., et al. (2020). A nanoconfined iron(iii) fluoride cathode in a NaDFOB electrolyte: Towards high-performance sodium-ion batteries. *J. Mater. Chem. A* 8, 4091–4098. doi:10.1039/c9ta12853k

Takada, K., Yamada, Y., Watanabe, E., Wang, J., Sodeyama, K., Tateyama, Y., et al. (2017). Unusual passivation ability of superconcentrated electrolytes toward hard carbon negative electrodes in sodium-ion batteries. *Acs Appl. Mater. Interfaces* 9, 33802–33809. doi:10.1021/acsami.7b08414

Takenaka, N., and Nagaoka, M. (2019). Microscopic elucidation of solid-electrolyte interphase (SEI) film formation via atomistic reaction simulations: Importance of functional groups of electrolyte and intact additive molecules. *Chem. Rec.* 19, 799–810. doi:10.1002/tcr.201800137

Takenaka, N., Sakai, H., Suzuki, Y., Uppula, P., and Nagaoka, M. (2015). A computational chemical insight into microscopic additive effect on solid electrolyte interphase film formation in sodium-ion batteries: Suppression of unstable film growth by intact fluoroethylene carbonate. *J. Phys. Chem. C* 119, 18046–18055. doi:10.1021/acs.jpcc.5b04206

Tang, Y., Zhang, W., Xue, L., Ding, X., Wang, T., Liu, X., et al. (2016). Polypyrrole-promoted superior cyclability and rate capability of NaxFe Fe(CN)(6) cathodes for sodium-ion batteries. *J. Mater. Chem. A* 4, 6036–6041. doi:10.1039/c6ta00876c

Tao, H., Zhou, M., Wang, R., Wang, K., Cheng, S., and Jiang, K. (2018). TiS2 as an advanced conversion electrode for sodium-ion batteries with ultra-high capacity and long-cycle life. *Adv. Sci.* 5, 1801021. doi:10.1002/advs.201801021

Vignarooban, K., Kushagra, R., Elango, A., Badami, P., Mellander, B. E., Xu, X., et al. (2016). Current trends and future challenges of electrolytes for sodium-ion batteries. *Int. J. Hydrogen Energy* 41, 2829–2846. doi:10.1016/j.ijhydene.2015.12.090

Wen, Z., Cao, J., Gu, Z., Xu, X., Zhang, F., and Lin, Z. (2008). Research on sodium sulfur battery for energy storage. *Solid State Ionics* 179, 1697–1701. doi:10.1016/j.ssi.2008.01.070

Wahlers, J., Fulfer, K. D., Harding, D. P., Kuroda, D. G., Kumar, R., and Jorn, R. (2016). Solvation structure and concentration in glyme-based sodium electrolytes: A combined spectroscopic and computational study. *J. Phys. Chem. C* 120, 17949–17959. doi:10.1021/acs.jpcc.6b06160

Wang, C., Wang, L., Li, F., Cheng, F., and Chen, J. (2017a). Bulk bismuth as a high-capacity and ultralong cycle-life anode for sodium-ion batteries by coupling with glyme-based electrolytes. *Adv. Mater.* 29, 1702212. doi:10.1002/adma.201702212

Wang, E., Niu, Y., Yin, Y.-X., and Guo, Y.-G. (2020). Manipulating electrode/electrolyte interphases of sodium-ion batteries: Strategies and perspectives. *ACS Mater. Lett.* 3, 18–41. doi:10.1021/acsmaterialslett.0c00356

Wang, J., Lu, H., Zhang, J., and Li, S. (2023). Improved interfacial property of Na3V2(PO4)(3)@C cathode: Application of NaODFB-based ether electrolyte in sodium-ion batteries. *J. Electrochem. Energy Convers. Storage* 20. doi:10.1115/1.4054389

Wang, M., Wang, Q., Ding, X., Wang, Y., Xin, Y., Singh, P., et al. (2022a). The prospect and challenges of sodium-ion batteries for low-temperature conditions. *Interdiscip. Mater.* 1, 373–395. doi:10.1002/idm2.12040

Wang, Q., Gao, H., Li, J., Liu, G.-B., and Jin, H. (2021a). Importance of crystallographic sites on sodium-ion extraction from NASICON-structured cathodes for sodium-ion batteries. *Acs Appl. Mater. Interfaces* 13, 14312–14320. doi:10.1021/acsami.1c01663

Wang, Q., Li, J., Jin, H., Xin, S., and Gao, H. (2022b). Prussian-blue materials: Revealing new opportunities for rechargeable batteries. *Infomat* 4. doi:10.1002/inf2.12311

Wang, S.-W., Hu, H.-F., Wang, D.-Y., and Shen, C. (2017b). AFM investigation of solid electrolyte interphase on Hopg anode in sodium ion battery. *J. Inorg. Mater.* 32, 596–602. doi:10.15541/jim20160472

Wang, S., Li, C., Fan, X., Wen, S., Lu, H., Dong, H., et al. (2021b). Selection of sodium salt electrolyte compatible with Na0.67Ni0.15Fe0.2Mn0.65O2 cathode for sodium-ion batteries. *Energy Technol.* 9, 2100190. doi:10.1002/ente.202100190

Wang, Y.-X., Chou, S.-L., Liu, H.-K., and Dou, S.-X. (2013). Reduced graphene oxide with superior cycling stability and rate capability for sodium storage. *Carbon* 57, 202–208. doi:10.1016/j.carbon.2013.01.064

Wang, Y.-X., Lim, Y.-G., Park, M.-S., Chou, S.-L., Kim, J. H., Liu, H.-K., et al. (2014). Ultrafine SnO 2 nanoparticle loading onto reduced graphene oxide as anodes for sodium-ion batteries with superior rate and cycling performances. *J. Mater. Chem. A* 2, 529–534. doi:10.1039/c3ta13592f

Wang, Y., Jiang, R., Liu, Y., Zheng, H., Fang, W., Liang, X., et al. (2021c). Enhanced sodium metal/electrolyte interface by a localized high-concentration electrolyte for sodium metal batteries: First-principles calculations and experimental studies. *Acs Appl. Energy Mater.* 4, 7376–7384. doi:10.1021/acsaem.1c01573

Wen, S., Li, X., Zhang, J., Wang, J., Ding, H., Zhang, N., et al. (2023). Effects of sodium salts on compatibility between Na2Ti3O7@C anode and electrolyte for sodium-ion batteries. *J. Alloys Compd.* 930, 167380. doi:10.1016/j.jallcom.2022.167380

Wongittharom, N., Lee, T.-C., Wang, C.-H., Wang, Y.-C., and Chang, J.-K. (2014). Electrochemical performance of Na/NaFePO4 sodium-ion batteries with ionic liquid electrolytes. *J. Mater. Chem. A* 2, 5655–5661. doi:10.1039/c3ta15273a

Wu, F., Zhu, N., Bai, Y., Li, Y., Wang, Z., Ni, Q., et al. (2018). Unveil the mechanism of solid electrolyte interphase formed by a novel NaPF6/BMITFSI ionic liquid electrolyte. *Nano Energy* 51, 524–532. doi:10.1016/j.nanoen.2018.07.003

Wu, L., Buchholz, D., Bresser, D., Chagas, L. G., and Passerini, S. (2014). Anatase TiO2 nanoparticles for high power sodium-ion anodes. *J. Power Sources* 251, 379–385. doi:10.1016/j.jpowsour.2013.11.083

Xia, X., Obrovac, M. N., and Dahn, J. R. (2011). Comparison of the reactivity of NaxC6 and LixC6 with non-aqueous solvents and electrolytes. *Electrochem. Solid State Lett.* 14, A130–A133. doi:10.1149/1.3606364

Xing, L., Borodin, O., Smith, G. D., and Li, W. (2011). Density functional theory study of the role of anions on the oxidative decomposition reaction of propylene carbonate. *J. Phys. Chem. A* 115, 13896–13905. doi:10.1021/jp206153n

Xing, L., Zheng, X., Schroeder, M., Alvarado, J., Cresce, A. V. W., Xu, K., et al. (2018). Deciphering the ethylene carbonate-propylene carbonate mystery in Li-ion batteries. *Accounts Chem. Res.* 51, 282–289. doi:10.1021/acs.accounts.7b00474

Xu, K. (2014). Electrolytes and interphases in Li-ion batteries and beyond. *Chem. Rev.* 114, 11503–11618. doi:10.1021/cr500003w

Xu, K. (2004). Nonaqueous liquid electrolytes for lithium-based rechargeable batteries. *Chem. Rev.* 104, 4303–4417. doi:10.1021/cr030203g

Yabuuchi, N., Kubota, K., Dahbi, M., and Komaba, S. (2014). Research development on sodium-ion batteries. *Chem. Rev.* 114, 11636–11682. doi:10.1021/cr500192f

Yamada, Y., Wang, J., Ko, S., Watanabe, E., and Yamada, A. (2019). Advances and issues in developing salt-concentrated battery electrolytes. *Nat. Energy* 4, 269–280. doi:10.1038/s41560-019-0336-z

Yamada, Y., and Yamada, A. (2015). Review-superconcentrated electrolytes for lithium batteries. *J. Electrochem. Soc.* 162, A2406–A2423. doi:10.1149/2.0041514jes

Yamada, Y., and Yamada, A. (2017). Superconcentrated electrolytes to create new interfacial chemistry in non-aqueous and aqueous rechargeable batteries. *Chem. Lett.* 46, 1056–1064. doi:10.1246/cl.170284

Yan, C., Xu, R., Xiao, Y., Ding, J.-F., Xu, L., Li, B.-Q., et al. (2020). Toward critical electrode/electrolyte interfaces in rechargeable batteries. *Adv. Funct. Mater.* 30, 1909887. doi:10.1002/adfm.201909887

Yan, G., Reeves, K., Foix, D., Li, Z., Cometto, C., Mariyappan, S., et al. (2019). A new electrolyte formulation for securing high temperature cycling and storage performances of Na-ion batteries. *Adv. Energy Mater.* 9, 1901431. doi:10.1002/aenm.201901431

Yang, H., Hwang, J., Tonouchi, Y., Matsumoto, K., and Hagiwara, R. (2021). Sodium difluorophosphate: Facile synthesis, structure, and electrochemical behavior as an additive for sodium-ion batteries. *J. Mater. Chem. A* 9, 3637–3647. doi:10.1039/d0ta11689k

Yang, Z., Zhang, J., Kintner-Meyer, M. C. W., Lu, X., Choi, D., Lemmon, J. P., et al. (2011). Electrochemical energy storage for green grid. *Chem. Rev.* 111, 3577–3613. doi:10.1021/cr100290v

Ye, M., You, S., Xiong, J., Yang, Y., Zhang, Y., and Li, C. C. (2022). *In-situ* construction of a NaF-rich cathode-electrolyte interface on Prussian blue toward a 3000-cycle-life sodium-ion battery. *Mater. Today Energy* 23, 100898. doi:10.1016/j.mtener.2021.100898

You, Y., and Manthiram, A. (2018). Progress in high-voltage cathode materials for rechargeable sodium-ion batteries. *Adv. Energy Mater.* 8, 1701785. doi:10.1002/aenm.201701785

Zarrabeitia, M., Casas-Cabanas, M., and Munoz-Marquez, M. A. (2021). Understanding the electrode - electrolyte interphase of high voltage positive electrode Na4Co3(PO4)(2)P2O7 for rechargeable sodium-ion batteries. *Electrochimica Acta* 372, 137846. doi:10.1016/j.electacta.2021.137846

Zeng, G., Liu, Y., Gu, C., Zhang, K., An, Y., Wei, C., et al. (2020). A nonflammable fluorinated carbonate electrolyte for sodium-ion batteries. *Acta Physico-Chimica Sin.* 36. doi:10.3866/PKU.WHXB201905006

Zeng, Z., Murugesan, V., Han, K. S., Jiang, X., Cao, Y., Xiao, L., et al. (2018). Non-flammable electrolytes with high salt-to-solvent ratios for Li-ion and Li-metal batteries. *Nat. Energy* 3, 674–681. doi:10.1038/s41560-018-0196-y

Zhang, J., Wang, D.-W., Lv, W., Zhang, S., Liang, Q., Zheng, D., et al. (2017). Achieving superb sodium storage performance on carbon anodes through an ether-derived solid electrolyte interphase. *Energy & Environ. Sci.* 10, 370–376. doi:10.1039/c6ee03367a

Zhang, L. L., and Zhao, X. S. (2009). Carbon-based materials as supercapacitor electrodes. *Chem. Soc. Rev.* 38, 2520–2531. doi:10.1039/b813846j

Zhang, S. S. (2006). A review on electrolyte additives for lithium-ion batteries. *J. Power Sources* 162, 1379–1394. doi:10.1016/j.jpowsour.2006.07.074

Zhang, Z., Li, Y., Xu, R., Zhou, W., Li, Y., Oyakhire, S. T., et al. (2022). Capturing the swelling of solid-electrolyte interphase in lithium metal batteries. *Science* 375, 66–70. doi:10.1126/science.abi8703

Zhao, D., Lu, H., Li, S., Wang, P., and Fan, X. (2022). Boosting the cycling stability of hard carbon with NaODFB-based electrolyte at high temperature. *Mater. Today Chem.* 24, 100866. doi:10.1016/j.mtchem.2022.100866

Zheng, C., Chen, Y., Xu, X., Lin, Q., Wang, H., Xue, Q., et al. (2022). Diglyme-based electrolytes boosting high-rate and stable sodium-ion storage for three-dimensional VS4/Reduced graphene oxide hybrid anodes. *J. Power Sources* 526, 231098. doi:10.1016/j.jpowsour.2022.231098

Zheng, J., Chen, S., Zhao, W., Song, J., Engelhard, M. H., and Zhang, J.-G. (2018). Extremely stable sodium metal batteries enabled by localized high-concentration electrolytes. *Acs Energy Lett.* 3, 315–321. doi:10.1021/acsenergylett.7b01213

Zheng, X., Gu, Z., Liu, X., Wang, Z., Wen, J., Wu, X., et al. (2020). Bridging the immiscibility of an all-fluoride fire extinguishant with highly-fluorinated electrolytes toward safe sodium metal batteries. *Energy & Environ. Sci.* 13, 1788–1798. doi:10.1039/d0ee00694g

Zhou, Q., Xingguo, Q., Lu, Y., Rong, X., Tang, F., Kong, W., et al. (2020). The necessity of establishing Na-ion battery standards. *Energy Storage Sci. Technol.* 9, 1225–1233. doi:10.19799/j.cnki.2095-4239.2020.0085

Zhu, N., Wu, F., Wu, C., Bai, Y., and Li, Y. (2016). *Recent Adv. electrolytes sodium-ion Batter.* Energy Storage Sci. Technol. 5, 285–291. doi:10.3969/j.issn.2095-4239.2016.03.004

Zhu, Y., Luo, X., Zhi, H., Yang, X., Xing, L., Liao, Y., et al. (2017). Structural exfoliation of layered cathode under high voltage and its suppression by interface film derived from electrolyte additive. *Acs Appl. Mater. Interfaces* 9, 12021–12034. doi:10.1021/acsami.7b00032

DFT-assisted low-dimensional carbon-based electrocatalysts design and mechanism study: a review

Yun Han[1,2], Hongzhe Xu[1,2], Qin Li[1,2], Aijun Du[3] and Xuecheng Yan[1]*

[1]Queensland Micro- and Nanotechnology Centre, Griffith University, Nathan Campus, Brisbane, QLD, Australia, [2]School of Engineering and Built Environment, Griffith University, Nathan Campus, Brisbane, QLD, Australia, [3]School of Chemistry and Physics and Centre for Materials Science, Queensland University of Technology, Gardens Point Campus, Brisbane, QLD, Australia

Low-dimensional carbon-based (LDC) materials have attracted extensive research attention in electrocatalysis because of their unique advantages such as structural diversity, low cost, and chemical tolerance. They have been widely used in a broad range of electrochemical reactions to relieve environmental pollution and energy crisis. Typical examples include hydrogen evolution reaction (HER), oxygen evolution reaction (OER), oxygen reduction reaction (ORR), carbon dioxide reduction reaction (CO_2RR), and nitrogen reduction reaction (NRR). Traditional "trial and error" strategies greatly slowed down the rational design of electrocatalysts for these important applications. Recent studies show that the combination of density functional theory (DFT) calculations and experimental research is capable of accurately predicting the structures of electrocatalysts, thus revealing the catalytic mechanisms. Herein, current well-recognized collaboration methods of theory and practice are reviewed. The commonly used calculation methods and the basic functionals are briefly summarized. Special attention is paid to descriptors that are widely accepted as a bridge linking the structure and activity and the breakthroughs for high-volume accurate prediction of electrocatalysts. Importantly, correlated multiple descriptors are used to systematically describe the complicated interfacial electrocatalytic processes of LDC catalysts. Furthermore, machine learning and high-throughput simulations are crucial in assisting the discovery of new multiple descriptors and reaction mechanisms. This review will guide the further development of LDC electrocatalysts for extended applications from the aspect of DFT computations.

1 Introduction

Environmental pollution and energy crisis are the two main critical issues of modern society caused by the excessive use of fossil fuels. Acid rain, haze, and greenhouse effects have disastrously affected the normal life of human beings (Turner John, 2004; Hubert and Nenad, 2009; Dai et al., 2015). On the one hand, great efforts have been devoted to the investigation and utilization of renewable clean energy and the efficient conversion between
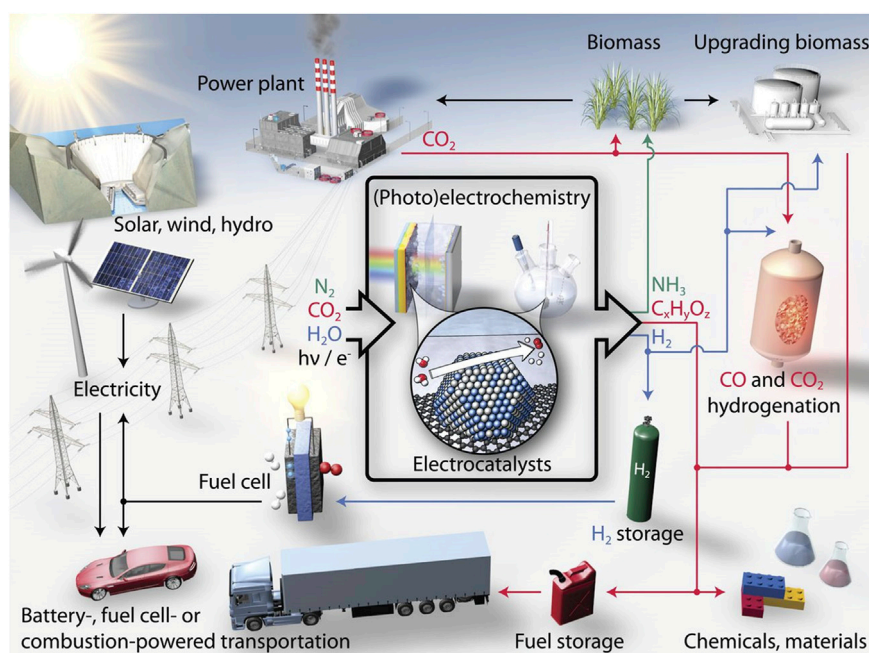
FIGURE 1
Schematic of a sustainable energy landscape based on electrocatalysis. Reproduced with permission (Seh et al., 2017). Copyright 2017, American Association for the Advancement of Science.

electrical and chemical energy, i.e., electrocatalytic hydrolysis and fuel cells (Chu and Majumdar, 2012; Abas et al., 2015). Greenhouse gas recycling, on the other hand, is also regarded as one of the most promising techniques to reduce air pollution, for example, the reduction of CO_2. Therefore, effective electrochemical reactions, such as hydrogen evolution reaction (HER) and oxygen evolution reaction (OER) for water splitting, oxygen reduction reaction (ORR) for fuel cell, and carbon-dioxide reduction reaction (CO_2RR) are highly expected to solve the above issues (Figure 1). (Karunadasa et al., 2010; Seh et al., 2017) However, the performance of these electrochemical reactions is severely hampered by their sluggish kinetics, which can be significantly improved with the introduction of efficient electrode catalysts (Liang et al., 2013; Zou and Zhang, 2015).

Noble metal-based materials such as platinum (Pt) and ruthenium (Ru) are widely used as benchmark catalysts. However, the scarcity and high cost impede their industrial mass production. Therefore, non-noble metals and even metal-free electrocatalysts have been intensively studied and remarkable progress has been reached (Yan X et al., 2016; Sui et al., 2017; Zhang L et al., 2018; Liu et al., 2019; Han et al., 2023a; He et al., 2023). Up to now, low-dimensional carbon materials, such as 2D graphene nanosheets (G), 1D carbon nanotubes (CNT), and 0D fullerenes, have been widely used for fabricating a series of non-noble metals and even metal-free catalysts for energy conversion. This is because of their unique properties such as tunable molecular structures, spatial confinement and surface effect, abundance and excellent oxidation, and corrosion resistance. Various defects and heteroatoms are embedded into carbon substrates, such as transition metals, nitrogen, and boron, which can greatly improve their catalytic efficiency (Kroto et al., 1985; Chen et al., 2002; Novoselov et al., 2004; Hsieh et al., 2009; Chen et al., 2013; Zhuo

et al., 2013; Jia et al., 2016; Yan Y et al., 2016; He et al., 2017; Guo et al., 2018; Mao et al., 2019a).

It is difficult to reveal the catalytic mechanism and actual active sites of electrocatalysts only via experimental study. For instance, previous studies show that pyridinic nitrogen is responsible for the ORR in N-doped carbon-based metal-free catalysts (Wu et al., 2015; Liu and Dai, 2016), while other studies suggest that the active sites are graphitic nitrogen (Liu et al., 2010; Lin et al., 2013). Therefore, the current quest is to develop appropriate methodologies to provide a comprehensive understanding of the catalyst structures at electronic levels, which will promote the comprehension of the reaction mechanisms and guide future experimental studies (Bora et al., 2019). Nowadays, based on the first principles, the modern density functional theory (DFT) calculation has become an irreplaceable modeling toolkit for scientists in a variety of research areas. Two main strategies of DFT calculation-assisted design of electrocatalysts have been established by theoretical and experimental chemists. The first one is dominated by theoretical calculations, dedicated to achieving a rational design of high-performance catalysts. It is crucial to identify the most important parameters to reveal the relationships between structures and performance, which are the so-called descriptors and can considerably boost the traditional trial-and-error approach. Machine-learning and high-throughput calculations have also been developed to efficiently screen active sites and descriptors for the targeted catalysts. The second one is dominated by experimental testing and characterizations, assisted by calculating the change during the catalysis process such as step-energy, molecular and electronic structure, and electron transition that can reveal the reaction mechanism accurately. In this review, we will mainly summarize the history and concepts of modern DFT, the

heterogeneous electrocatalytic surface-related descriptors, the combination of experiment and calculation, and recent achievements of low-dimensional carbon-based electrocatalysts for energy storage and conversion applications.

2 Overview of DFT

Quantum chemistry is mainly based on quantum mechanics principles, and the main goal of all first-principle calculations is to obtain the electronic wave function ψ that characterizes the state of the system, for which the Schrödinger equation must be solved. Theoretical computing has received increasing attention from the chemistry community as computer technology has progressed. However, the traditional Wave Function Theory (WFT) method has two fatal shortcomings. First, the wave function ψ of a system with N electrons will contain 3N coordinate variables. Therefore, a 3N-dimensional wave function image, which is difficult to describe visually, will be a stumbling block in solving the Schrödinger equation. Second, the Schrödinger equation for a multi-electron system is too computationally intensive to be calculated accurately. Modern DFT has become a viable option to solve these drawbacks.

2.1 History of modern DFT

The homogeneous electron-gas model, commonly known as the Thomas–Fermi model, was proposed by Thomas and Fermi in 1927, and it has established a firm foundation for DFT. The ground state energy of the electron system is directly represented in terms of electron density instead of the wave function, which drastically reduces the freedom degree of the system (Thomas, 1927). In 1964, Hohenberg and Kohn proposed an inhomogeneous electron-gas model based on the Thomas–Fermi model and proved that two theorems served as the fundamentals of modern DFT (Hohenberg and Kohn, 1964). The first theorem stated that the nuclear potential energy $V(r)$ of all electrons in a system that has n interacting electrons is a unique function of the electronic density $\rho(r)$. This could be presented as the Hohenberg-Kohn (HK) equation as shown in Eq. (2.1).

$$E_V[\rho] = \rho(r)V(r)dr + F_{HK}[\rho] \qquad (2.1)$$

Here, $F_{HK}[\rho] = T[\rho] + E_{ee}[\rho]$, where $T[\rho]$ is the sum of electronic kinetic energy and $E_{ee}[\rho]$ is electron–electron repulsion. Clearly, $F_{HK}[\rho]$ is independent of the external potential field. However, the HK equation cannot be directly employed for the calculation of the total energy of the system due to the unknown specific form of $F_{HK}[\rho]$. The second theory proposed a density minimum principle, stating that the ground state energy of any trial electron density $\rho(r)$ cannot be lower than the true ground system. Hence, it can be inferred that as the $\rho(r)$ approaches the true electron density, the calculated system energy becomes closer to the ground-state energy of the system. Then the Euler-Lagrange equation can be obtained as shown in Eq. (2.2).

$$\mu = \frac{\delta E_V[\rho]}{\delta \rho(r)} = V_{cxt}(r) + \frac{\delta F_{HK}[\rho]}{\delta \rho(r)} \qquad (2.2)$$

Where, $V_{cxt}(r)$ represents an external potential. Therefore, if $F_{HK}[\rho]$ is confirmed, $\rho(r)$ and $E_V[\rho]$ can be solved by Eq. (2.2).
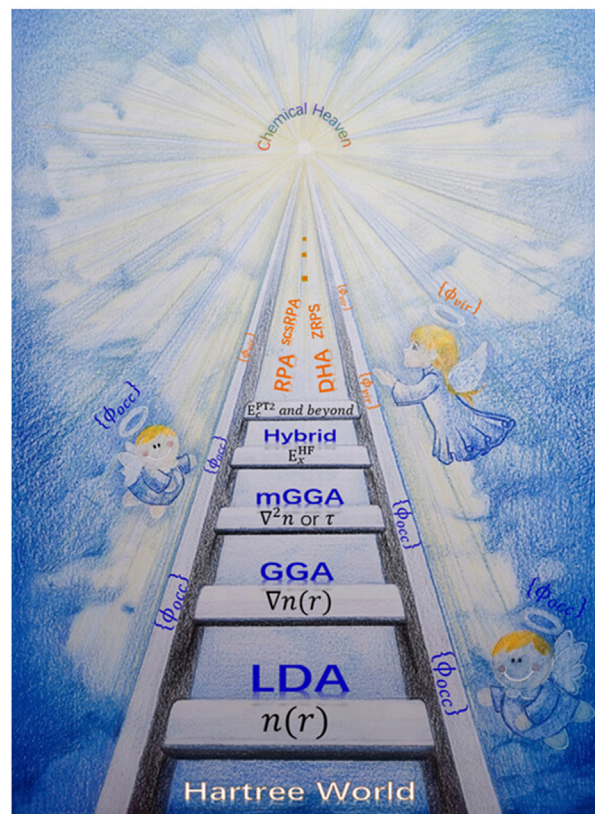
FIGURE 2
Illustration of Jacob's Ladder of DFT. Reproduced with permission. (Zhang et al., 2020). Copyright 2020, John Wiley and Sons.

However, the exact expression for $F_{HK}[\rho]$ remains an unsolved challenge until now. In 1965, building upon the Thomas–Fermi model's shortcomings and drawing inspiration from the Hartree-Fock method, Kohn and Sham revealed a brand-new approach to derive the $F_{HK}[\rho]$ approximately. $F_{HK}[\rho]$ can be divided into three parts and can be presented: (Kohn and Sham, 1965).

$$F_{HK}[\rho] = T_s[\rho] + J[\rho] + E_{xc}[\rho] \qquad (2.3)$$

Where, $T_s[\rho]$ and $J[\rho]$ are the kinetic energy and coulombic correlation energy of independent electrons, respectively. $E_{xc}[\rho]$ is a functional with a small magnitude called exchange–correlation (XC) energy that can be approximated, and it can be presented as:

$$E_{xc}[\rho] = T[\rho] - T_s[\rho] + V_{ee}[\rho] - J[\rho] \qquad (2.4)$$

Due to $T_s[\rho]$ and $J[\rho]$ comprising the primary components of Fock exchange energy $F_{HK}[\rho]$, the remaining $E_{xc}[\rho]$ is a functional with relatively small values. Even when subjected to approximate treatment, the errors associated with this part are not particularly large. By variation, we can get the famous Kohn–Sham (KS) equation:

$$\hat{H}_{KS}\varnothing_i \equiv \left[-\frac{1}{2}\nabla^2 + V(r) + \int \rho(r')\big/\big|r - r'\big| dr' + V_{xc}(r) \right]\varnothing_i(r)$$
$$= \varepsilon_i \varnothing_i(r) \qquad (2.5)$$

And XC potential can be defined by:

$$V_{xc}(r) = \delta E_{xc}[\rho]/\delta \rho(r) \qquad (2.6)$$

Overall, there is no approximation and the Kohn–Sham equation is accurate. However, the $E_{xc}[\rho]$ component of the Kohn–Sham equation still lacks a rigorous expression form, making it impossible to use in practical calculations. Instead, several types of approximate XC generalized functionals must be built to gradually approximate the real system. In simple terms, when solving the KS equations, we need to start with an initial guess for the electron density, use it to solve the KS orbitals, and then calculate the electron density distribution function with the obtained KS orbitals. This distribution function is then used in the KS equations for further iterations, repeating this process until the electron density distribution converges. This iterative approach, which progressively refines the solution through approximations, is the main source of errors in DFT calculations.

2.2 Exchange−correlation (XC) functional

Typical approximations such as local density approximation (LDA), generalized gradient approximation (GGA), meta-GGA, and hybrid functional are shown in the well-known Jacob's ladder from Hartree world to Chemical accuracy heaven (Figure 2). (Mattsson, 2002; Tao et al., 2003; Zhang and Xu, 2020)

The approximation for LDA is that the charge density changes slowly with position and behaves similarly to the local heterogeneous electron cloud, so the XC energy can be presented as:

$$E_{XC}^{LDA}[n] = \int dr n(r) \varepsilon_{XC}(n) \qquad (2.7)$$

The LDA method only considers local charge density, which is accurate for a uniform electron gas model but is clearly not applicable to real systems where the electron density is not perfectly uniform. Therefore, this method provides a rough approximation when computing the real systems and tends to overestimate binding energies.

To improve the accuracy of the LDA method, the GGA method describes electron density with the assistance of density gradient and can be presented as:

$$E_{XC}^{GGA} \propto \int dr f(n, \nabla n) \qquad (2.8)$$

BLYP (Becke, 1988; Lee et al., 1988), PW91 (Perdew et al., 1992; White and Bird, 1994), and PBE (Perdew et al., 1996) are the commonly used approximated density functionals of the GGA method. The Becke exchange functional is a gradient-corrected exchange functional that considers the gradient of the electron density. The Lee-Yang-Parr (LYP) correlation functional incorporates the correlation energy of electrons. By combining these two components, BLYP aims to provide a more accurate description of electron-electron interactions and correlation effects in molecular systems. PW91 combines the Perdew-Wang exchange functional with the Perdew-Wang correlation functional. The exchange functional accounts for the exchange energy of electrons, while the correlation functional deals with electron-electron correlation effects. The PBE functional captures both the exchange and correlation effects in the electron-electron interaction.

It has been found to perform well for a wide range of systems, including molecules, solids, and surfaces, making it a popular option in DFT calculations.

Based on the GGA method, meta-GGAs, such as TPSS, TPSSh, and M06-L (Zhao et al., 2006; Zhao and Truhlar, 2006; Zhao and Truhlar, 2008), introduced kinetic energy density variables but with better accuracy accompanied by a significant increase in computational cost.

By partially combining accurate XC functional in the DFT, the hybrid functional could improve the calculation accuracy. The most popular one is the B3LYP functional (Stephens et al., 1994), which can be described as:

$$E_{XC}^{B3LYP} = A \cdot E_X^{LDA} + (1-A)E_X^{HF} + B \cdot \Delta E_X^{Beck} + C \cdot E_C^{LYP}$$
$$+ (1-C)E_C^{VWN} \qquad (2.9)$$

Where A = 0.8, B = 0.72, and C = 0.81. E_X^{LDA} is the LDA exchange functional, E_X^{HF} is the Hartree–Fock exact exchange functional, ΔE_X^{Beck} is the Becke exchange functional, E_C^{LYP} is the LYP correlation functional, and E_C^{VWN} is the VWN local spin density approximation to the correlation functional.

Calculations involving periodic systems frequently employ the HSE functional (Heyd and Scuseria, 2004), which is represented by the following equation:

$$E_{XC}^{HSE} = A \cdot E_X^{HF,SR}(\omega) + (1-A)E_X^{PBE,SR}(\omega) + E_X^{PBE,LR}(\omega) + E_C^{PBE}$$
$$(2.10)$$

Where A is the mixing parameter, and ω is an adjustable parameter controlling the short range of the interaction. The standard values of $A = 0.25$ and $\omega = 0.2$ of HSE06 (Heyd et al., 2003) have been shown to give good results for most systems. $E_X^{HF,SR}(\omega)$ is the short-range Hartree-Fock exact exchange functional, $E_X^{PBE,SR}(\omega)$ and $E_X^{PBE,LR}(\omega)$ are the short- and long-range components of the PBE exchange functional, and E_C^{PBE} is the PBE correlation functional.

2.3 Periodic system

To deal with periodic systems, supercell models (primitive cells in three dimensions (X, Y, and Z) with periodic repetition) are frequently used. Vacuum space greater than 10 Å is added in the Z-direction to eliminate the interaction. In condensed matter physics, Bloch's theorem states that solutions to the Schrödinger equation in a periodic potential take the form of a plane wave modulated by a periodic function and can be written as:

$$\Psi(r) = u_k(r)e^{ikr} \qquad (2.11)$$

Where r is the position, Ψ is the wave function, and k is the wave vector. Based on the Bloch theorem, the electronic band structure is involved in investigating surface science, and electronic states at numerous k points should be calculated. In practical calculations, however, a finite number of k points is used; the higher the density of the k points, the lower the inaccuracy will be. In general, the number of k points for metal systems is higher than that of the oxide systems.

For periodic systems, the electron wave function can be expanded with numerous plane wave functions. However, only

plane-wave basis sets with kinetic energy lower than the cut-off energy are considered in practical calculations, which would result in a systematic error (Kresse and Furthmüller, 1996a; Kresse and Furthmüller, 1996b). Therefore, a pseudopotential that can replace the true atomic potential of the nucleus and inner electrons is introduced to reduce systematic error. Currently, the most widely used plane-wave methods are the ultra-soft pseudopotential (US-PP) plane wave method and the projector augmented wave (PAW) method (Kresse and Joubert, 1999).

2.4 DFT + U scheme

DFT calculations cannot adequately describe systems with physical properties that are controlled by many body electronic interactions (correlated systems) because it is typically challenging to model the dependence of the XC functional on electronic charge density. The over-delocalize valence electrons and over-stabilize metallic ground states are considered to be the main problems of DFT to describe correlated systems. Therefore, the DFT + U approach has been developed to enhance the description of the ground state of correlated systems (Dudarev et al., 1998). The key advantage of the DFT + U method is that it is within the realm of DFT, making it easy to implement in the existing DFT codes. Besides, its computational cost is only slightly higher than that of normal DFT computations. The local and semi-local density functionals that allow LDA + U and GGA + U computational operations can be enhanced with this 'U' correction. The primary function of the 'U' correction is to add an additional Hubbard-like term to the strong on-site Coulomb interaction of localized electrons. The on-site Coulomb term U and the site exchange term J are the two parameters that represent the strength of the on-site interactions for the purpose of practical DFT + U implementation in computational chemistry. Parameters 'U and J' are typically derived semi-empirically although *ab initio* computations can yield them (Tolba et al., 2018).

$$E(DFT + U) = E(DFT) + \frac{U_{eff}}{2}\sum_\sigma Tr[\rho^\sigma - \rho^\sigma \rho^\sigma] \quad (2.12)$$

It has become a standard to use the parameter: $U_{eff} = U - J$ in place of the interaction U in the simplified LDA + U form. U_{eff} is frequently utilized because the 'J' has been shown to be essential for describing the electronic structure of specific classes of materials, typically those subject to high spin-orbit coupling.

2.5 Molecular dynamics simulation

Molecular dynamics (MD) simulation, which is based on Newton's laws of motion, can simulate the trajectory of each atom in a system at a certain temperature, thus the system's dynamic properties can be calculated. However, the standard DFT can only be used to calculate a system's static properties at 0 K. Briefly, for a given configuration and initial velocity of each atom, the MD simulation can be divided into three steps. Firstly, the forces acting on each atom in the system are calculated to determine the system's acceleration. Secondly, the configuration of the system after Δt time can be obtained according to Newton's three laws.

Thirdly, the calculation of the forces in the first step is continued based on this configuration, and the results of the system evolving with time can be finally obtained by repeated recurrence. MD simulation can be further classified into two types: Classic MD simulation and *ab initio* MD (AIMD) simulation, depending on how the forces are calculated in the first step. Classic MD simulation builds the potential energy function from the empirical force field and calculates the force at each step using the gradient of the potential energy function. AIMD simulation, on the other hand, can be used to accurately calculate the force at each step by the *ab initio* quantum chemical method (Nosé, 1984; Hoover, 1985; Kresse and Hafner, 1993).

Unfortunately, AIMD is constrained by its suitability for small simulation systems and limited simulation durations. The utilization of force fields, however, can expedite the computation process. Nevertheless, for an extended period, there existed a gap between computationally demanding electronic structure-based DFT calculations and the more efficient yet less precise empirical potentials or force fields founded on physical approximations and intuition (Kocer et al., 2022). This situation witnessed substantial improvement with the emergence of machine learning potentials (MLPs) in 1995 (Blank et al., 1995). Modern MLPs have the capacity to discern the shape of multidimensional potential energy surfaces from high-level DFT calculations and subsequently incorporate the derived analytical atomic interactions (force fields) into large-scale simulations, such as MD, with negligible accuracy compromise (Handley and Popelier, 2010; Friederich et al., 2021; Unke et al., 2021). Over the last two decades, numerous types of MLPs have been introduced, including neural network potentials (NNPs) (Lorenz et al., 2004; Behler and Parrinello, 2007), Gaussian approximation potentials (GAPs) (Bartók et al., 2010), and gradient domain machine learning (GDML) (Chmiela et al., 2019). Among them, NNPs exhibit a formidable combination of neural network expressive capabilities and the availability of extensive datasets like the QM9 dataset (Ruddigkeit et al., 2012), Material Project (Jain et al., 2013), and Open Catalyst 2020 (Chanussot et al., 2021), rendering them exceptionally well-suited for expediting high-accuracy MD calculations (Takamoto et al., 2022). Additionally, beyond reliance on existing databases, on-the-fly machine learning enables the construction of precise force fields from newly sampled data with minimal training overhead (Jinnouchi et al., 2019; Jinnouchi et al., 2020). In this adaptive process, during each step, a decision is made whether to perform an *ab initio* calculation and potentially incorporate the data into the force field or to employ the existing force field and skip the learning phase for that specific step.

Furthermore, Metadynamics is an atomistic simulation technique based on MD that operates within the same system to expedite the exploration of rare events and calculate the free energies of intricate molecular systems (Laio and Parrinello, 2002; Iannuzzi et al., 2003). This technique functions by iteratively 'filling' the system's potential energy surface using a series of Gaussian functions centered along its trajectory, all guided by a carefully selected set of collective variables (CVs). This process compels the system to transition from one energy minimum to another (Bussi and Laio, 2020). Metadynamics provides several advantages in free energy calculations. Firstly, it accelerates the sampling of high-energy events within the studied system by progressively moving it from low-energy regions to high-energy areas via the inclusion of a

sequence of repulsive potentials. Secondly, it facilitates the establishment of high-dimensional reaction pathways, enabling the computation of multidimensional free energy data, including two-dimensional free energy potential surfaces. Thirdly, because it gradually elevates the studied system's energy from low to high regions, this approach excels in discovering optimal reaction pathways. Lastly, this method does not require a prior prediction of the reaction pathway within the studied system (Barducci et al., 2011). One limitation of Metadynamics lies in the difficulty of determining the optimal point for terminating the simulation. Without proper termination, the bias potential keeps increasing, possibly leading the system intoreaction regions that hold no interest in our study. The application of Well-Tempered Metadynamics effectively mitigates this limitation (Barducci et al., 2008).

2.6 Transition state theory

The transition state (TS), also known as the saddle point, is the highest energy point on the potential energy surface (PES) where the reactants (initial state, IS) generate products (final state, FS) along the minimum energy path. Within the transition state theory (TST), we assume that IS and TS are in quasi-equilibrium, and the main task is to find out the free energy barrier for the transition, which is the energy difference between IS and FS. Based on TST, the transition rate can also be calculated. The Dimer method (Henkelman and Jónsson, 1999) and the climbing image nudged elastic band (CINEB) approach (Henkelman et al., 2000) are the two most popular calculating techniques.

The dimer method can be used to find out the saddle points by two images of the system, which is the so-called 'dimer'. Driven by the saddle point search algorithm, the dimer is moved uphill on the potential energy surface, away from the vicinity of the potential energy minimum of the IS and toward a saddle point. The dimer is rotated along the way to identify the potential energy mode with the lowest curvature at the dimer's location. Since the Dimer technique only uses the first derivatives of the energy, the major benefit is not requiring the time-consuming computation of the minimal eigenvalue of the Hessian matrix. The Dimer technique also has the advantage of having less stringent initial configuration requirements.

The nudged elastic band (NEB) method is an efficient method for identifying the minimum energy path (MEP) between a given initial and the final state of a transition, which has also been widely used to estimate transition rates. A set of images between the IS and FS of the system are created, often on the order of 4–20. Then the adjacent images are contacted by a collection of spring interactions, which can form an elastic band and ensure the continuity of the path. The band is brought to the MEP by an optimization process that minimizes the force acting on the images. The drawback of the NEB method is that it requires the intermediates to be evenly spaced throughout the optimization process, and the predicted TS may be slightly deviated from the actual TS. The CINEB method was developed to address this issue. The force on the highest image is the full force resulting from the potential with the component along the elastic band inverted, showing that it will not be influenced by spring forces. As a result, the intermediates will gradually move to the higher energy direction and reach the actual TS.

2.7 Advanced simulation tools and methods

Currently, the computational hydrogen electrode (CHE) model is the most commonly employed and straightforward model for assessing catalytic activity (Peterson et al., 2010). This model uses half of the chemical potential of H_2 in the gas phase at 0 V to represent the chemical potential of a proton-electron pair $(G(\frac{1}{2}H_2) = G(H^+ + e^-))$. When a potential U is applied to the catalytic system, the chemical potential can be adjusted as (Peterson et al., 2010):

$$G\left(\frac{1}{2}H_2\right) - eU = G(H^+ + e^-) \qquad (2.13)$$

Where e is the positive charge. Consequently, it becomes feasible to calculate the reaction-free energy (ΔG) of proton-coupled electron transfer (PCET) reactions, enabling a qualitative assessment of catalytic activity. Nonetheless, the CHE model falls short of representing the exact catalytic environment due to the neglect of sensitive parameters affecting catalytic performance, such as solvent, pH, and applied potential. To achieve a more precise simulation of electrochemical reactions, multiple approaches and tools have been developed and applied to consider the impact of the reaction environment.

2.7.1 Solvent effect

Two primary approaches can be used to address the solvent effects: implicit and explicit solvation models. The implicit solvation model employs a polarizable medium, typically characterized by the dielectric constant (ε), to represent the solvent, while an electric field is constructed to depict the solvent's charge distribution (Xu and Carter, 2019). Currently, two representative implicit solvation models are the solvation model based on solute electron density (SMD) (Marenich et al., 2009) and the conductor-like solution model (COSMO) (Klamt and Schüürmann, 1993). While the implicit solvation model permits a qualitative description of solvent effects at minimal computational cost, it falls short in describing specific interactions, such as hydrogen bonds (Ling et al., 2022).

On the other hand, the explicit solvation model precisely incorporates solvent molecules, atoms, and cations into the calculation systems, enabling direct observation of electrode/electrolyte and adsorbates/electrolyte interactions. When considering the most common water/electrode interfaces in electrocatalysis, two explicit solvation models are generally employed: icelike water bilayers and the electric double layer (Gross and Sakong, 2022). In the meantime, AIMD is typically employed to obtain reliable atomic configurations of the electrode/electrolyte interfaces, incurring significantly higher computational costs. Therefore, to strike a balance between computational accuracy and cost-effectiveness, the Quantum Mechanics/Molecular Mechanics (QMMM) method has been developed. With this approach, quantum mechanical (QM) computations are employed to simulate critical reaction components, such as adsorbates and electrode/electrolyte interfaces, while classical force fields or implicit solvation models are employed to handle the surrounding solvent environment. The primary challenge in the QMMM method is effectively partitioning the QM and MM fields to ensure an accurate representation of critical effects (Li et al., 2020).

2.7.2 Applied electrode potential (U)

In experimental macroscopic systems, both reaction temperatures and the chemical potential of the electrolyte and electrode remain constant throughout the reaction. However, in most common DFT calculations, a limited number of atoms is typically treated within the canonical (NVT) or NPT ensemble and the total number of electrons in the simulated cells remains constant. Consequently, this leads to significant variations in the electrochemical potential (Fermi level) during a reaction. To address this problem and achieve a setup closer to the fluctuating particle numbers found in experimental conditions, the combination of the grand-canonical (GC) ensemble (VTμ) with DFT emerges as a natural choice for atomistic simulations (Melander et al., 2018). GC-DFT provides a method to investigate electrochemical microscopic systems in thermodynamic equilibrium, offering insights into phenomena characterized by long-time and length scales (Groß, 2021). During the fixed-potential grand canonical calculations, varying the total charge of the system can result in the fixed electrode potential (Fermi level) (Gao and Wang, 2021). Furthermore, by the fixed-potential method, we can easily calculate the potential-dependent reaction barriers and avoid the inaccurate assumption about the charge transfer coefficients in the constant-charge calculations. Currently, great developments have been reached in the field of methodology and models, such as continuum charging methods (Gauthier et al., 2019) and constant-potential hybrid-solvation dynamical model (CP-HS-DM) (Zhao and Liu, 2021), making complicated NEB and AIMD simulations stable and possible.

3 Theoretical guidance in catalyst design and mechanism study

Nowadays, a series of well-known carbon-based electrocatalysts have been fabricated through the combinations of various modification methods and substrate materials, such as heteroatom-doped graphene, defective graphene, Mxenes, heteroatom-doped carbon nanotubes/ribbons, and modified carbon dots (Yan et al., 2020; Zhou et al., 2020; Li et al., 2021; Ding et al., 2022; Song et al., 2022; Sun et al., 2022; Tang et al., 2022; Wu Q. et al., 2022; Wu Y. et al., 2022). However, the design of state-of-the-art electrocatalysts still relies on inefficient trial-and-error approaches, and the catalytic mechanism is still controversial and difficult to reveal only through experimental research. DFT calculations are thus utilized to address two issues: 1) predicting catalytic performance and guiding the synthesis of electrocatalysts and 2) investigating and corroborating the mechanism of electrocatalysis in conjunction with experimental study.

3.1 Application of theoretical guidance in designing electrocatalysts: descriptors

To predict the performance of electrocatalysts, computational scientists mainly focus on the most important microscopic properties of the catalysts that determine the macroscopic catalytic performance. Since the early 20th century, catalysts with high activity, according to the traditional Sabatier principle, should bind atoms and molecules with an ideal bond strength: not too weak to activate the reactants and not too strong to desorb the products. Therefore, a volcano-shape relationship between bond strength and catalytic activity has been proposed to represent the predictivity of many descriptors (Che, 2013). Due to the lack of quantitativeness and inability to undergo experimental validation, this principle is not very predictive. The "bond strength" between the relevant intermediates and the catalysts has been described during the past decades by the extraction of electronic and structural properties such as the descriptors.

3.1.1 d-band center theory

The well-known d-band center theory proposed by Nørskov et al. has laid the foundation for a series of descriptors (Nørskov, 1991; Hammer and Norskov, 1995; Nilsson et al., 2005). It explains the interactions between atoms or molecules and the surface based on adsorbate orbitals and d-orbitals of atoms on the surface. The energy of the d states (the center of the d states) relative to the Fermi level is a good indicator of the bond strength. The higher the d states are in energy relative to the Fermi level, the higher in energy the antibonding states and the stronger the bond will be (Figure 3). Stamenkovic et al., for example, investigated the ORR activity of various Pt$_3$M (M = Ti, V, Fe, Co, and Ni) alloys with Pt-skin and Pt-skeleton surface structures, employing both experimental and computational methods (Stamenkovic et al., 2007). They constructed a volcano plot using experimentally measured activity and theoretically calculated d-band center values. This analysis revealed that Pt$_3$Co, Pt$_3$Fe, and Pt$_3$Ni exhibited significantly enhanced ORR activity compared to pure Pt.

The d-band center theory can also be applied to low-dimensional electrocatalysts (Wu et al., 2016; Gao G. et al., 2018; Tao et al., 2019; Ye et al., 2020; Jiao et al., 2022). For instance, Ling et al. established correlations between the d-band center and the adsorption strengths of *OH, *O, and *OOH, along with the potential of elementary reactions for OER on β_{12} boron monolayer (β_{12}-BM)-supported single-atom catalysts (SACs) (Ling et al., 2017). Ni SACs supported on β_{12}-BM exhibited a moderate energy level of the d-band center, resulting in a lower overpotential for OER compared to the other systems under study. Additionally, they proposed an optimal d-band center at −2.82 eV, at which β_{12}-BM-supported SACs would theoretically have the lowest overpotential for OER. Deng et al. designed a series of N-doped graphene-supported transition metal atom-pair catalysts (TM APCs) models for efficient NRR (Deng et al., 2020). Twenty kinds of transition metal atoms were systematically studied and were proven by COHP and orbital interaction analysis; the d-band center can be used as a descriptor to describe the NRR performance of the TM APCs. For defective graphene-supported Fe and Al nanoparticles, Lim and co-workers found that the d-band center of the Fe and Al nanoparticles shifts closer to the Fermi level, indicating a potential increase in the catalytic reactivity associated with the graphene surface. Zhou et al. systematically explored the HER activity of transition metals, transition metal oxides, and carbide substrates covered by nitrogen-doped graphitic sheets and found that the HER activity is correlated to the C p_z-band center, which is similar to the d-band center theory and determined in turn by the degree of electronic coupling between the graphitic

FIGURE 3
Illustration of the use of the *d*-band model. **(A)** The main origin of a shift in the *d*-band center ε_d is a change in the interatomic distances within an overlayer. **(B)** Electrochemically measured changes in the hydrogen adsorption energy (E_{SCE}) for Pd overlayers on a number of metals are shown to scale well with the calculated shift of the *d*-band center ($\delta\varepsilon_d$). Reproduced with permission (Kibler et al., 2005). Copyright 2005, John Wiley and Sons.

sheet and the metal substrate, enabling the rational design of high-performance hybrid graphitic carbon/transition metal electrocatalysts (Zhou et al., 2018).

3.1.2 Fermi softness

When oxygen atoms are adsorbed on Pt$_3$Y (111) surface, even though the surface *d*-band center of Y is higher than that of Pt, the binding strength of Pt-O is stronger than Y-O, defying the *d*-band center theory. However, it can be reasonably explained by the "Fermi softness" (S_F), which was developed by Huang and co-workers to describe the electronic structures of a solid surface (Huang et al., 2016). All the bands' occupied and unoccupied states contribute to the bonding, but those closer to the Fermi level (E_F) are more significant (Figure 4A). A reactivity weight function $w(E)$ with a Fermi level peak is created to determine a weighted summation of the density of states of a solid surface ($\int g(E)w(E)dE$) (Figure 4B). The resultant property is the finite-temperature chemical softness, known as S_F, which is an accurate descriptor of the surface reactivity. This property is obtained when such a weight function is defined as the derivative of the Fermi-Dirac distribution function at a certain non-zero temperature. For example, the S_F is identical to the density of states at the Fermi level ($g(E_F)$) without spreading (i.e., $kT = 0$ eV), which does not closely resemble the surface reactivity (Figure 4C). Then, the S_F displays a substantial association with the surface reactivity when the nominal electronic temperature is changed to 0.4 eV (Figure 4D).

Fermi softness can also be an efficient descriptor to predict the catalytic performance of carbon-based catalysts (Gao R. et al., 2018; Gao Z. et al., 2018; Yang et al., 2018; Xiong et al., 2020; Wang and Zhang, 2022). Gao and co-workers designed a series of catalysts named Fe/GS, which are composed of Fe atom that serves as the active site and different graphene such as single and double vacancy graphene that serve as the substrate (Gao Z. Y. et al., 2018). They further found that the Fermi softness of Fe/GS and the O$_2$ adsorption energy exhibit a strong positive linear correlation ($R^2 = 0.81$) at $kT = 1.15$ eV. The Fermi softness is also used to describe the adsorption activity of Mn-modified graphene catalyst by Wu's group (Xie et al., 2022). They discovered a substantial

negative correlation ($R^2 = 0.93$) between Fermi softness and adsorption energy at $kT = 2.8$ eV. The Fermi softness is increased with the increase of the adsorption energy.

3.1.3 Energy-based descriptors

Adsorption-free energies (ΔG) of key intermediates are utilized as activity descriptors for recognized reactions, including ΔG_H for HER (Han et al., 2023b), ΔG_O for ORR (Han et al., 2023a), ΔG_{CO} for CO$_2$RR (Chen et al., 2022a), and ΔG_N for NRR (Fang et al., 2023). For instance, DFT calculations were conducted on the MoS$_2$ edge, yielding a ΔG_H of 0.08 eV, which closely approaches the optimal value of 0 eV (Hinnemann et al., 2005). Subsequently, experimental confirmation established that MoS$_2$ edges serve as the catalytically active sites for HER (Jaramillo et al., 2007). Through the calculation of free energies of N$_2$ adsorption and the formation energy of the key intermediate *NCON, Kou et al. found that V$_2$N$_6$ sites efficiently catalyze the cleavage of N-N bonds and the coupling of C-N bonds, facilitating effective urea production (Liu J. et al., 2023). Through calculating ORR energy profiles on various active sites within defective graphene, including pyridinic N sites, adjacent carbon atoms, and edge-located pentagon defects, Yao and colleagues determined that pentagon defects serve as the primary active sites for acidic ORR. Subsequent experimental studies have also validated these findings (Jia et al., 2019).

In multi-step catalytic processes, the adsorption and desorption of the intermediates occur during the concerted proton–electron transfer steps, and the adsorption energies of the intermediates follow a linear scaling relationship (Man et al., 2011; J. K. Nørskov et al., 2005; Nørskov et al., 2004). For example, the relationship between the adsorption energies of the intermediates of OER and ORR, such as *O, *OH, and *OOH, can be presented by:

$$\Delta G_2^{(i)} = A_{1,2}^{(i)} \cdot \Delta G_1^{(i)} + B_{1,2}^{(i)} \tag{3.1}$$

Where $\Delta G_1^{(i)}$ and $\Delta G_2^{(i)}$ represent the chemisorption energies of oxygen intermediates and $A_{1,2}^{(i)}$ and $B_{1,2}^{(i)}$ represent the slope and intercept, respectively, derived from the fitting of adsorption energy
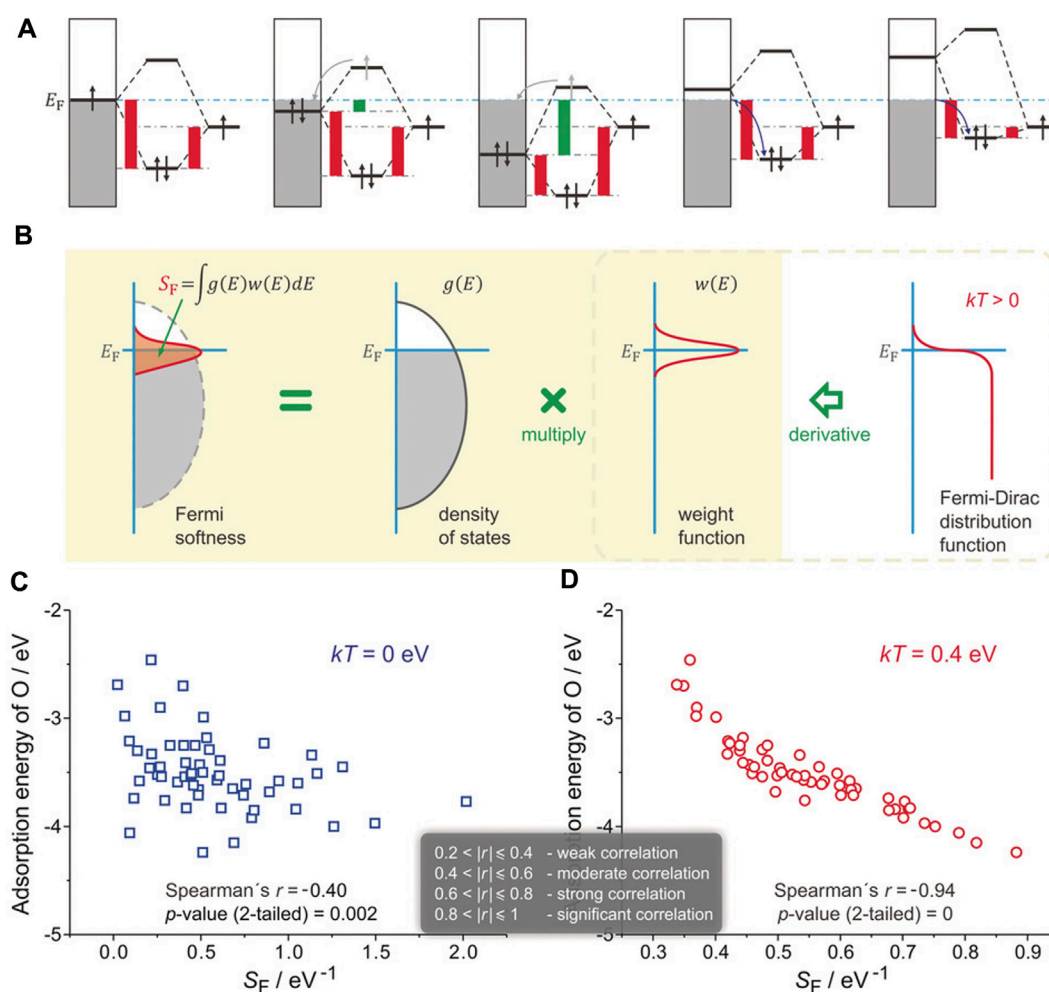
FIGURE 4
Definition of Fermi softness (S_F) and its correlation with surface reactivity. **(A)** Energy analysis of surface bonding. **(B)** S_F is defined as a weighted sum of the density of states. **(C)** S_F that without and **(D)** with spreading. Reproduced with permission (Huang et al., 2016). Copyright 2016, John Wiley and Sons.

data (Abild-Pedersen et al., 2007; Calle-Vallejo et al., 2015a). Fundamentally, the quantity of valence electrons of the atoms attached to the surface has a significant impact on the slope of Eq. (3.1) on closed-packed and low-index surfaces. Since the oxygen atom in OH* only requires one electron to comply with the octet rule, whereas O* requires two, the slope between the adsorption energies of *OH and *O is roughly 1/2. Scaling relationships offer a possible solution to use a few descriptors to fully present the numerous factors influencing a catalytic reaction. Combined with the Sabatier principle, volcano curves can be derived from this linear relationship to reveal the connection between structures and performance. In many cases, ΔG_{OH} and $\Delta G_O - \Delta G_{OH}$ are considered as the descriptors for ORR and OER, respectively (Zheng et al., 2015; Seh et al., 2017; Mao et al., 2018). According to the statistical findings, the free energy difference for monodentate adsorbates can be concluded as $\Delta G_{OOH} = \Delta G_{OH} + 3.2 \pm (0.2)$ eV (Man et al., 2011).

3.1.4 Multiple descriptors

The excellent descriptors include e_g-filling (Matsumoto et al., 1977a; Matsumoto et al., 1977b), average O-$2p$-state energy ($\bar{\varepsilon}_{2p}$),

(Lee et al., 2011; Grimaud et al., 2013) surface distortion (Chattot et al., 2018), and generalized coordination numbers ($\overline{CN}$). (Calle-Vallejo et al., 2014; Calle-Vallejo et al., 2015b) Normally, a single descriptor cannot completely predict the performance and synergistic effect of complicated mixed-phase catalysts. Some interface parameters that can demonstrate or influence electron distribution reconfiguration, for instance, adsorption energy (Tran and Ulissi, 2018; Guo C. et al., 2019; Wan et al., 2021), charge transfer (Guan et al., 2019; Mao et al., 2021), surface properties (defects/microstructure/facet) (Back et al., 2019; Parker et al., 2020), and bond length (Wexler et al., 2018; Zhu et al., 2019; Zheng et al., 2020), may serve as the descriptors to predict the best catalysts. Furthermore, a variety of descriptors have been used for describing the reactions with the assistance of machine learning and high-throughput calculations.

Different reaction mechanisms can be used to explain the complex NRR, including distal, alternating, and enzymatic (Figure 5A). To identify the viable routes and theoretical onset potentials by the classical approach, all chemical intermediates will be systematically investigated, which will be inefficient for large-
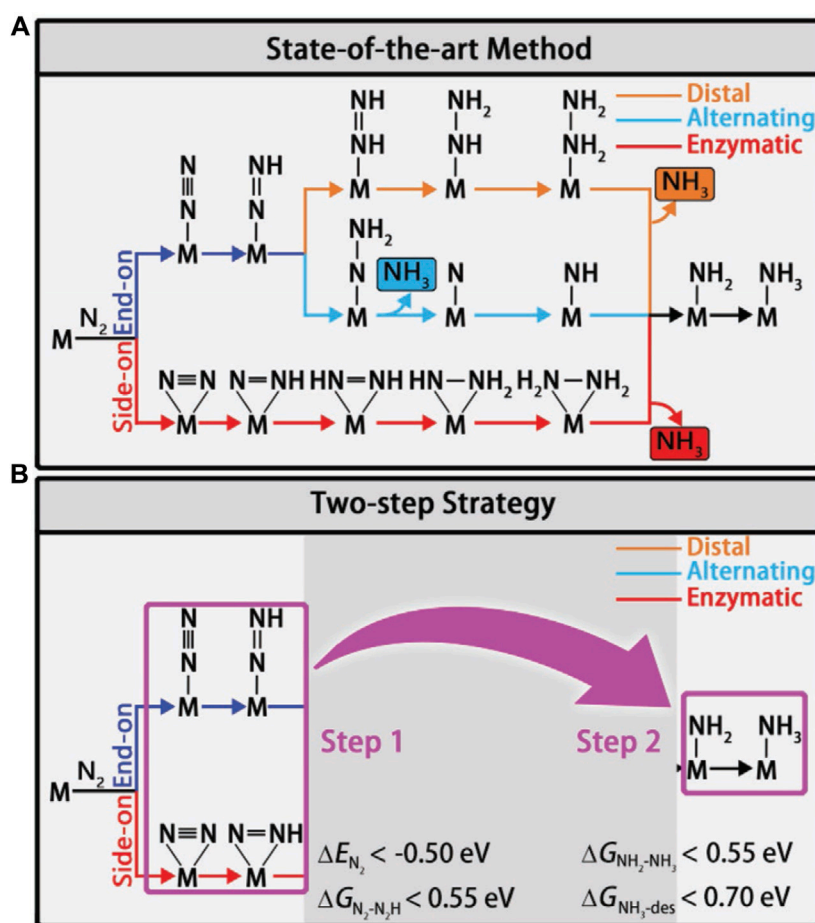
FIGURE 5
(A) Schematic depiction of different mechanisms for N_2 reduction. **(B)** Flowchart of the two-step screening procedure for NRR catalysts. Reproduced with permission (Ling et al., 2018a). Copyright 2018, John Wiley and Sons.

scale catalyst screening. Ling *et al.* focused on two "stable to instable" transitions in the NRR process (Eq. 3.2 and 3.3). They set up a two-step method (Figure 5B) to efficiently and accurately screen the nitride-doped-graphene-supported single-atom catalysts (N-G-supported SACs) (Ling et al., 2018a).

$$^{*}N_2 + H^+ + e^- = {}^{*}N_2H \qquad (3.2)$$

$$^{*}NH_2 + H^+ + e^- = {}^{*}NH_3 \qquad (3.3)$$
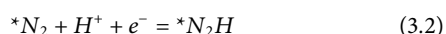
In the first step, the systems with low activity are disregarded by using the descriptors ΔE_{N_2} (adsorption energy of N_2) and $\Delta G_{N_2-N_2H}$ (free energy change of Eq. (3.2)). In the second step, among the systems that meet the requirements of the first step, high-performance catalysts are sought after using the descriptors ΔG_{NH_3-des} (free energy for NH_3 desorption) and $\Delta G_{NH_2-NH_3}$ (free energy change of Eq. (3.3)). Out of 540 N-G-supported SAC systems, 10 interesting candidates with high NRR catalytic activity were selected using the two-step high-throughput screen approach. For example, W_1C_3 demonstrates the best performance with a low onset potential of 0.25 V. Zhou and co-workers also used multiple descriptors to predict the NRR performance of transition metal atoms filled with boron nitride nanotubes (BNNTs) (Zhou et al.,

2020). The diameter of BNNTs, work function, and electron transfer from metal to BNNTs, which have negative correlations with the adsorption energy of N_2, can serve as efficient descriptors to select highly active catalysts.

3.2 Application of theoretical calculations in revealing the reaction mechanism

With the development of modern characterization techniques, an increasing number of *in situ* characterization tools are used to observe the catalytic reaction processes, aiming to accurately uncover the catalytic mechanism. However, it is still difficult to identify the actual active site and reaction intermediates of complex catalytic reactions by pure experimental study. In terms of CO_2RR, through different reaction routes, the products of CO_2RR can be carbon monoxide, formic acid, ethylene, or ethanol. Depending on whether the adsorption sites change or not during the catalytic processes, the actual reaction paths and intermediates and the competition between the carbon-carbon coupling reaction and HER are all unknown and difficult to elucidate experimentally (Zhang et al., 2021). For instance, Dual-atom catalysts (DACs)

have been considered promising candidates for C_2 product generation due to their ability to offer two metal sites that enhance *CO coverage on the surface. However, experimental results indicate that most DACs exhibit high Faradic efficiency for CO, while the formation of multi-carbon products is seldom observed (Gong et al., 2022; Hao et al., 2022; Zhao et al., 2022). Li and colleagues conducted DFT calculations and discovered a deviation from the conventional hypothesis, suggesting that C−C coupling typically does not occur at the metal-top sites (Yang et al., 2023). Surface Pourbaix analyses indicate that CO preferably occupies the bridge sites between two metals, potentially impeding subsequent C−C coupling reactions. Furthermore, based on energy variations, it is not feasible for C−C coupling to occur on the surface of a DAC, both in terms of thermodynamics and kinetics. In experimental settings, oxide-derived copper (OD-Cu) has demonstrated exceptional performance, displaying remarkable selectivity toward C_{2+} products even at low potentials (Cheng et al., 2021; Chen et al., 2022b). Nevertheless, the understanding of the atomic structures of active sites in OD-Cu remains limited due to its inherent complexity. Cheng et al. conducted multiscale computations based on first principles to simulate the synthesis, characterization, and performance assessment of Cu nanoparticles deposited on carbon nanotubes (CNTs) (Cheng et al., 2017). Their investigation identified two active sites that show an undercoordinated surface square structure adjacent to a subsurface stacking fault and exhibit lower formation energies for *COCOH compared to the Cu (100) surface sites.

Meanwhile, theoretical calculation is a key method to compensate for experimental shortcomings because it can investigate the electronic-scale change during the catalytic reaction. In the past decades, the use of theoretical simulations in defective electrocatalysis has greatly aided the catalytic mechanism analysis of novel catalysts (Hu et al., 2021; Khan et al., 2021; Lan et al., 2021; Liu A et al., 2021).

With the assistance of DFT calculations, Zhang *et al.* systematically investigated the origins of the high-performance atomic Co-Pt embedded into nitrogen-doped graphene (A-CoPt-NC) (Zhang B-W et al., 2018). A stable adsorption state of the intermediate in the HER is proved by the electron distribution calculations. The disappearance of charge depletion on the surface of the outer layer can improve the adsorption of protons to the catalyst. Li and co-workers synthesized a new HER electrocatalyst (Li M. et al., 2018). Carbon quantum dots were used to support ruthenium nanoparticles (Ru@CQDs). It shows superior catalytic activity and durability in alkaline conditions. DFT calculations provide compelling evidence of the excellent HER catalytic activity of Ru supported in the N-doped CQDs layer. The calculation results show the synergistic effect of doped N atoms and Ru clusters, and both are beneficial in reducing the dissociation energy of H_2O. The electron transfer from Ru and H_2O to C atoms, which is proved by the difference charge density analysis, can polarize Ru clusters, thus contributing to the dissociation of H_2O. Meanwhile, the dissociated H atoms are held together by Ru and H interactions to form the H_2 molecule (Figure 6).

As can be seen from the above discussions, theoretical calculation is an indispensable method to investigate the relationship between structures and performance. A reaction

model will be built to thoroughly study the basic reaction path of the reaction, identify the crucial steps that determine the reaction rate, and then optimize the chemical reaction conditions. It is obvious that theoretical calculations are beneficial in identifying the basic process and reaction paths of electrocatalysis at the atomic level. Furthermore, the design of catalysts and the controllable synthesis of the desired structures can be aided by the DFT simulations, which can be utilized as a prediction tool. Theoretical modelings can also be used in catalyst structure optimization and validation of the design outcomes, as well as to support experimental study.

4 Recent advances in computational studies on low-dimensional carbon-based electrocatalysts

4.1 Hydrogen evolution reaction (HER)

Hydrogen is one of the most promising clean energy sources to replace fossil fuels, and it also has the highest energy density among existing fuels. Water splitting is a sustainable way of producing hydrogen compared to industrial reduction of natural gas (CH_4). Hydrogen evolution reaction (HER) is the cathodic half-cell reaction of water electrolysis (Karunadasa et al., 2010). The large overpotential restricts its practical application and high-performance electrocatalysts are needed to boost the HER. Noble metal-based catalysts such as Pt/C and RuO_2 are commonly considered to be the most efficient HER electrocatalysts; however, scarcity and low durability limit their mass industrial production (Andreadis and Tsiakaras, 2006; Hao et al., 2016). To date, many high-performance low-dimensional carbon-based non-noble metals and even metal-free electrocatalysts have been designed and fabricated to be the alternatives of noble metal materials. In this part, the fundamental concepts and recent developments in HER electrocatalysts will be summarized.

HER is a two proton-electron transfer step (PETS) process. The first step is the Volmer reaction, i.e., the adsorption of hydrogen, which is presented in Eq. (4.1a) (acidic condition) and 4.1b (alkaline condition).

$$H^+ + e^- + {}^* \rightarrow H^* \tag{4.1a}$$
$$H_2O + e^- + {}^* \rightarrow H^* + OH^- \tag{4.1b}$$
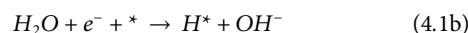
The second step can be the Heyrovsky reaction or the Tafel reaction. Equation (4.2a) (acidic condition) and 4.2b (alkaline condition) show the Heyrovsky reaction and Eq. (4.3) shows the Tafel reaction.

$$H^* + H^+ + e^- \rightarrow H_2 + {}^* \tag{4.2a}$$
$$H^* + H_2O + e^- \rightarrow H_2 + OH^- + {}^* \tag{4.2b}$$
$$2H^* \rightarrow H_2 + {}^* \tag{4.3}$$
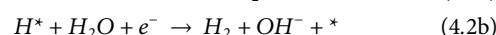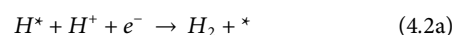
In which, * represents the active site on the catalyst surface.

For the design of low-cost and efficient electrocatalysts, it is crucial to reduce the amount of precious metals being used, which can be achieved in two ways. Firstly, the specific activity per metal atom usually increases with the downsize of metal particles (Figure 7). (Yang et al., 2013) Therefore, single-atom catalysts (SAC) that contain isolated metal atoms singly dispersed on
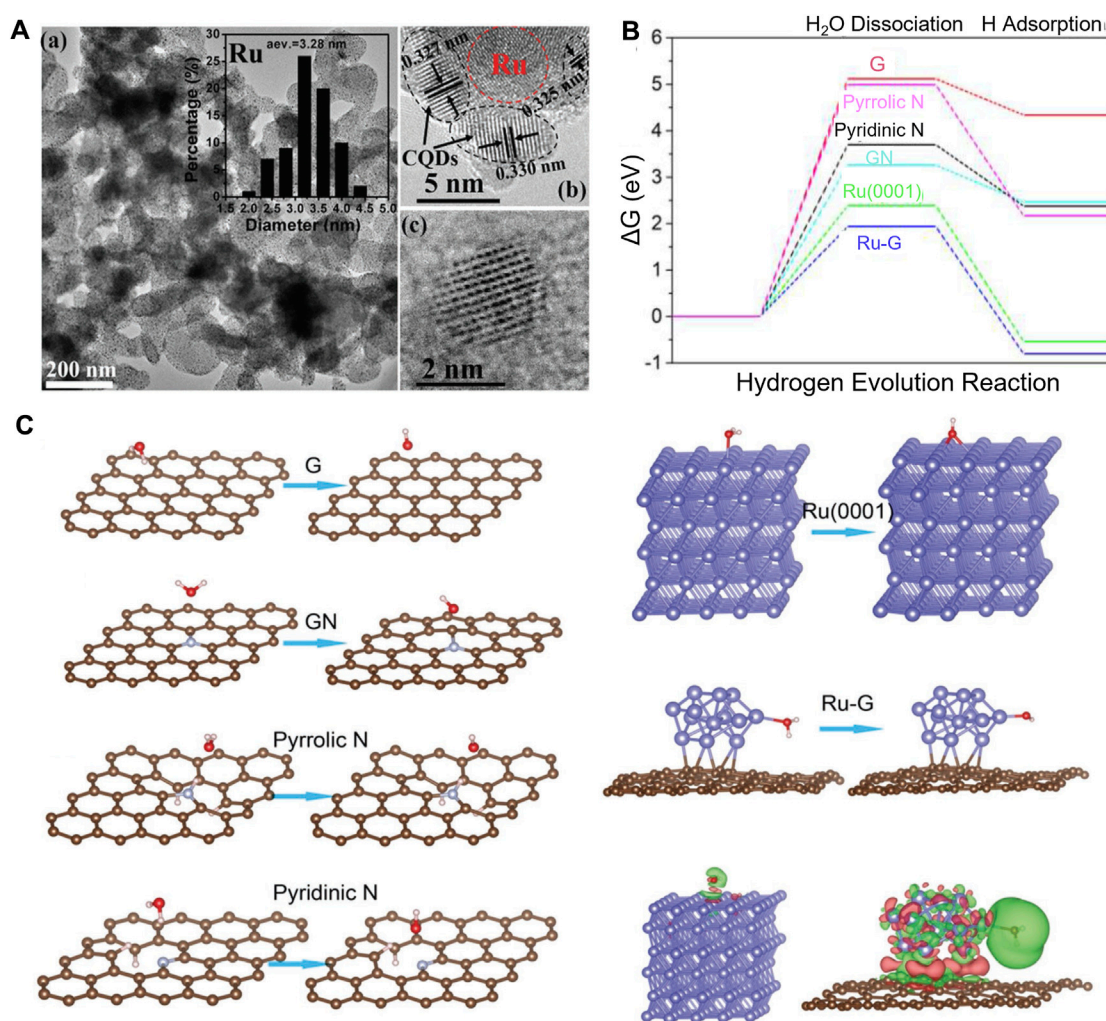
FIGURE 6
(A) TEM and HRTEM images of Ru@CQDs. **(B)** Calculated HER relative energy diagram. **(C)** Adsorption and dissociation of the H_2O molecule on different surfaces. Reproduced with permission (Li M. et al., 2018). Copyright 2018, John Wiley and Sons.

supports have attracted extensive research attention. Alternatively, non-noble metal atoms or functional groups can also be anchored on the substrate to tune the electronic structures of noble-metal active sites (Sun et al., 2013; Gao G. et al., 2018; Li W. et al., 2018; Ren et al., 2020; Yang et al., 2022). Ye and co-workers designed a novel Pt SAC using aniline-stacked graphene as the support (Pt SASs/AG). It shows excellent HER performance with η = 12 mV at 10 mA cm^{-2} and a mass current density of 22,400 Ag_{Pt}^{-1} at η = 50 mV, which is 46 times higher than that of the commercial 20 wt% Pt/C (Ye et al., 2019). Moreover, the Pt SASs/AG catalyst presents outstanding stability. With the assistance of DFT calculations, they found that the interaction between the atomical Pt and the nitrogen of aniline makes the d-band center of Pt downshift to −2.465 eV, which is close to that of Pt (111) (−2.687 eV). Additionally, the density of states (DOS) near the Fermi level of Pt in Pt SASs/AG catalyst is as large as that of Pt in Pt (111), eventually promoting the HER activity.

Secondly, non-noble metals such as transition metals are used as efficient HER catalysts, and even metal-free catalysts with excellent performance were designed and synthesized experimentally (Fan

et al., 2016; He et al., 2017; Zhang L et al., 2018; He et al., 2019; Ahsan et al., 2021; Yasin et al., 2022; Han et al., 2023b; Yin and Du, 2023). For example, using the first principle DFT calculations, 3D, 4D, and 5D transition metal SACs in N-doped 2D graphene and nanographene of various sizes are screened for HER by Fung et al. (Fung et al., 2020) For most SACs, a d-band center downshift will occur when moving from graphene to nanographene, indicating that the hydrogen adsorption on metal SACs can be tuned by adjusting the size and dimension of the substrate. V, Rh, and Ir embedded in N-doped nanographene show much better HER activity than those on the extended 2D graphene. The machine learning models (kernel ridge regression, decision trees (random forest), and neural networks) and the SISSO (Sure Independence Screening and Sparsifying Operator) method are employed to accurately predict the ΔG_H using various proposed descriptors; the results are shown in Figures 8A–D. Topological defect-based and complex defect-based carbon materials are also promising electrocatalysts. Yao and co-workers synthesized a series of defective carbons via a facile nitrogen removal procedure from

FIGURE 7
Schematic illustration of the changes of surface-free energy and specific activity per metal atom with metal particle size and the support effects on stabilizing single atoms. Reproduced with permission (Yang et al., 2013). Copyright 2013, American Chemical Society.
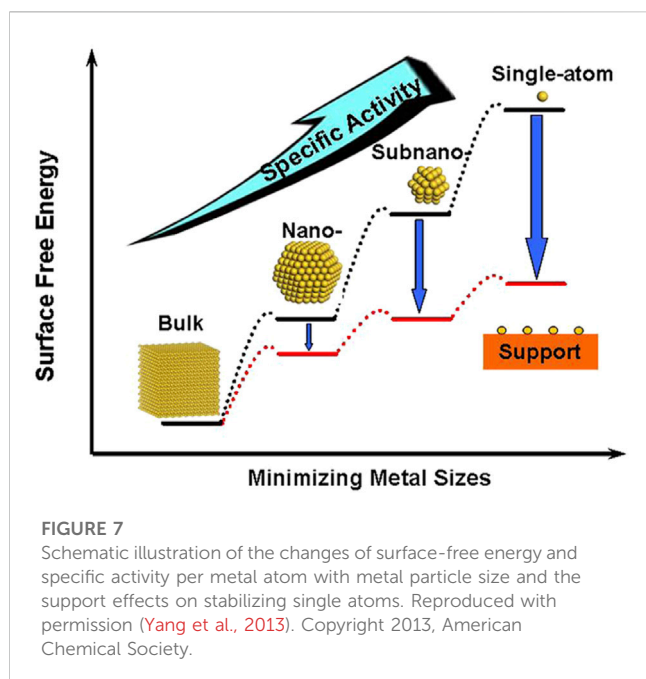
N-doped graphene, and the edge-defect model called 7557-4 shows outstanding HER performance with the lowest calculated free energy of 0.187 eV (Figures 8E,F). (Jia et al., 2016) DFT calculations were also performed to better understand the underlying catalytic mechanisms. The analysis of the frontier molecular orbitals shows that the catalytic activity of edge atoms is laid on their most contribution to the highest occupied molecular orbital (HOMO) and lowest unoccupied molecular orbital (LUMO), which are highly correlated with the catalytic reactions (Figures 8G,H).

4.2 Oxygen evolution reaction (OER) and oxygen reduction reaction (ORR)

Oxygen evolution reaction (OER, $2H_2O\ (l) \rightarrow O_2\ (g) + 4e^- + 4H^+$) is the anode half-cell reaction of water splitting containing four electron transitions, as shown in Eq. 4.4. Oxygen reduction reaction (ORR, $O_2\ (g) + 4e^- + 4H^+ \rightarrow 2H_2O\ (l)$, Eq. 4.5) is the revise reaction of the OER, which is the cathodic reaction of fuel cells and zinc-air batteries (Gasteiger et al., 2005).

$$H_2O\ (l) + ^* \rightarrow OH^* + e^- + H^+ \tag{4.4a}$$

$$OH^* \rightarrow O^* + e^- + H^+ \tag{4.4b}$$

$$O^* + H_2O\ (l) \rightarrow OOH^* + e^- + H^+ \tag{4.4c}$$

$$OOH^* \rightarrow O_2 + e^- + H^+ \tag{4.4d}$$

$$O_2 + e^- + H^+ \rightarrow OOH^* \tag{4.5a}$$

$$OOH^* + e^- + H^+ \rightarrow O^* + H_2O\ (l) \tag{4.5b}$$

$$O^* + e^- + H^+ \rightarrow OH^* \tag{4.5c}$$

$$OH^* + e^- + H^+ \rightarrow H_2O\ (l) + ^* \tag{4.5d}$$
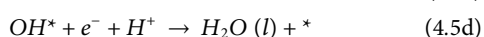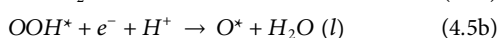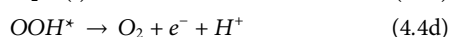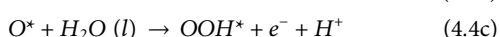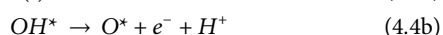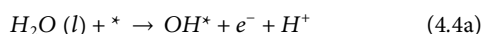
Both the OER and ORR are restricted by the sluggish kinetic and high reaction energy barriers, thus electrocatalysts are needed to accelerate their reaction rates. However, the high cost and low abundance of current commercial noble metal-based catalysts, i.e., Pt/C for ORR, RuO_2 and IrO_2 for OER severely hinder their widespread applications. Similarly, the strategies of lowering the cost and improving the performance of the HER catalysts are also applicable to the OER and ORR electrocatalysts, and great achievements have been accomplished (Zhu et al., 2018; He et al., 2020a; Wang et al., 2020a; Yan et al., 2020; Yang et al., 2020; Yan et al., 2021; Xu et al., 2023). Zhang *et al.* anchored atomical distributed Ni atoms onto an N-doped hollow carbon matrix (HCM@Ni-N) (Zhang et al., 2019). In alkaline conditions, the HCM@Ni-N only requires an OER overpotential of 304 mV to reach the current density of 10 mA cm^{-2}, which is much lower than that of the RuO_2 (393 mV), suggesting excellent OER activity of the prepared catalyst. Through the calculated distributions of charge density, they found that the electronic distribution of N-doped HCM was changed obviously after the Ni decoration (Figure 9A). In addition, the *3d* orbital of Ni in HCM@Ni-N shows a leftward shift, and the *d*-band center of the Ni was downshifted from −0.94 eV to −2.04 eV as a result of the Ni-N interaction (Figure 9B). According to the *d*-band center theory, this change could facilitate the desorption of adsorbates and reduce the energy barrier. The free energy pathways of the OER can also be calculated by DFT simulations and they are in good agreement with the experimental results (Figures 9C,D). By encapsulating Co and β-Mo$_2$C into N-doped carbon nanotubes (Co/β-Mo$_2$C@N-CNT), Ouyang and co-workers successfully fabricated a bifunctional electrocatalyst for the HER and OER in an alkaline electrolyte (Ouyang et al., 2019). Based on the heterointerface between Co and β-Mo$_2$C, the OER activity of β-Mo$_2$C is enhanced significantly. With the assistance of DFT calculations, they proved that the joint effect of N-CNTs, Co, and β-Mo$_2$C resulted in the low energy barriers of the intermediates, thus greatly improving the HER and OER kinetics.

Under the guidance of DFT calculations, Wang *et al.* successfully synthesized a series of topological carbon defects through a facile N-removing strategy, among which adjacent pentagons (A-C5) show the best catalytic performance for the ORR and the edge divacancy defects (C585-2) are favorable for the HER (Wang et al., 2020b). DFT calculations were applied to investigate the relationship between the original carbon structure, the type of N configuration obtained, and the corresponding defect structures, for example, perfect carbon network *versus* graphitic-N *versus* C585 (Figure 10A), edge-rich hexagonal structure *versus* pyridinic-N *versus* S-C5 (Figure 10B), and edge-rich pentagon *versus* pyrrolic-N *versus* A-C5 (Figure 10C). By a spontaneous gas-foaming method, Jiang and co-workers fabricated a range of promising trifunctional electrocatalysts named defect-rich N-doped ultrathin carbon nanosheets for HER, OER, and ORR (Jiang et al., 2019). In rechargeable Zn-air batteries, NCN-1000-5 exhibits a high energy density (806 Wh/kg), a low charge/recharge voltage gap (0.77 V), and an extremely long cycle life (over 300 h). DFT calculations were used to identify the intrinsic active sites for the electrochemical reactions. The catalytic performance of various active sites for the ORR and OER was investigated, and the results are shown in the volcano plot (Figure 10D). The armchair edge carbon atoms, which are adjacent to the graphitic-N, possess the lowest overpotential, thus they should be the optimal catalytic active center for the specific electrocatalysis (Figures 10E–G).
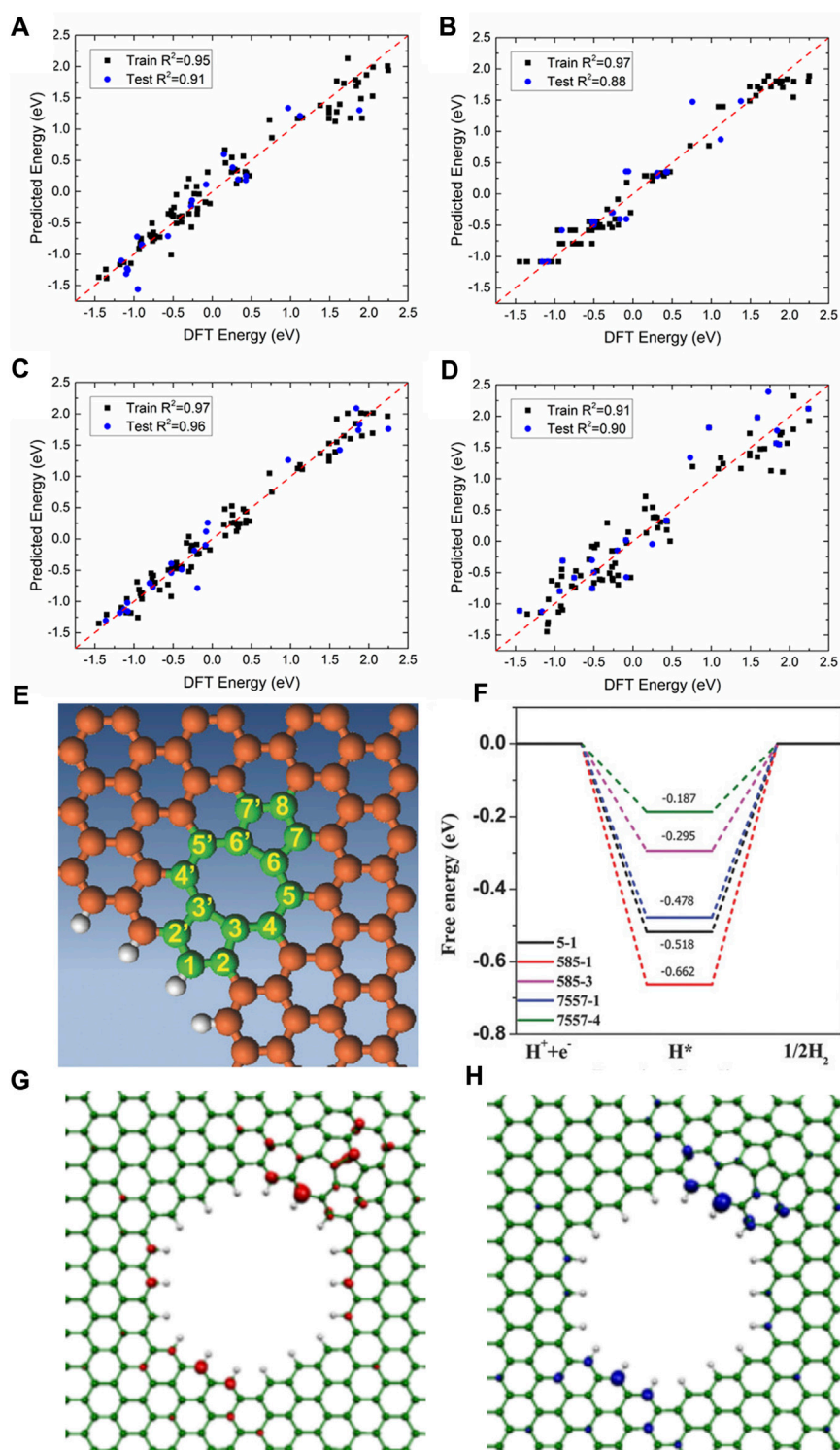
FIGURE 8
Comparison of DFT-calculated *versus* machine learning-predicted ΔG_H using **(A)** kernel ridge regression, **(B)** random forest regression, **(C)** neural network regression, and **(D)** SISSO regression. Reproduced with permission (Fung et al., 2020). Copyright 2020, American Chemical Society. **(E)** Mechanism study model of 7557defect. **(F)** Schematic energy profiles for the HER pathway. **(G)** HOMO and **(H)** LUMO orbitals for 7557 defect. Reproduced with permission (Jia et al., 2016). Copyright 2016, John Wiley and Sons.

FIGURE 9
(A) Calculated distribution of charge density for HCM@Ni-N. **(B)** Schematic band diagrams of HCM@Ni and HCM@Ni-N. **(C)** Proposed mechanism of O_2 evolution over HCM@Ni-N. **(D)** Free energy diagram at 0 V for OER over HCM, HCM@N, HCM@Ni, and HCM@Ni-N. The bold lines indicate the rate-determining step. Reproduced with permission (Zhang et al., 2019). Copyright 2019, John Wiley and Sons.
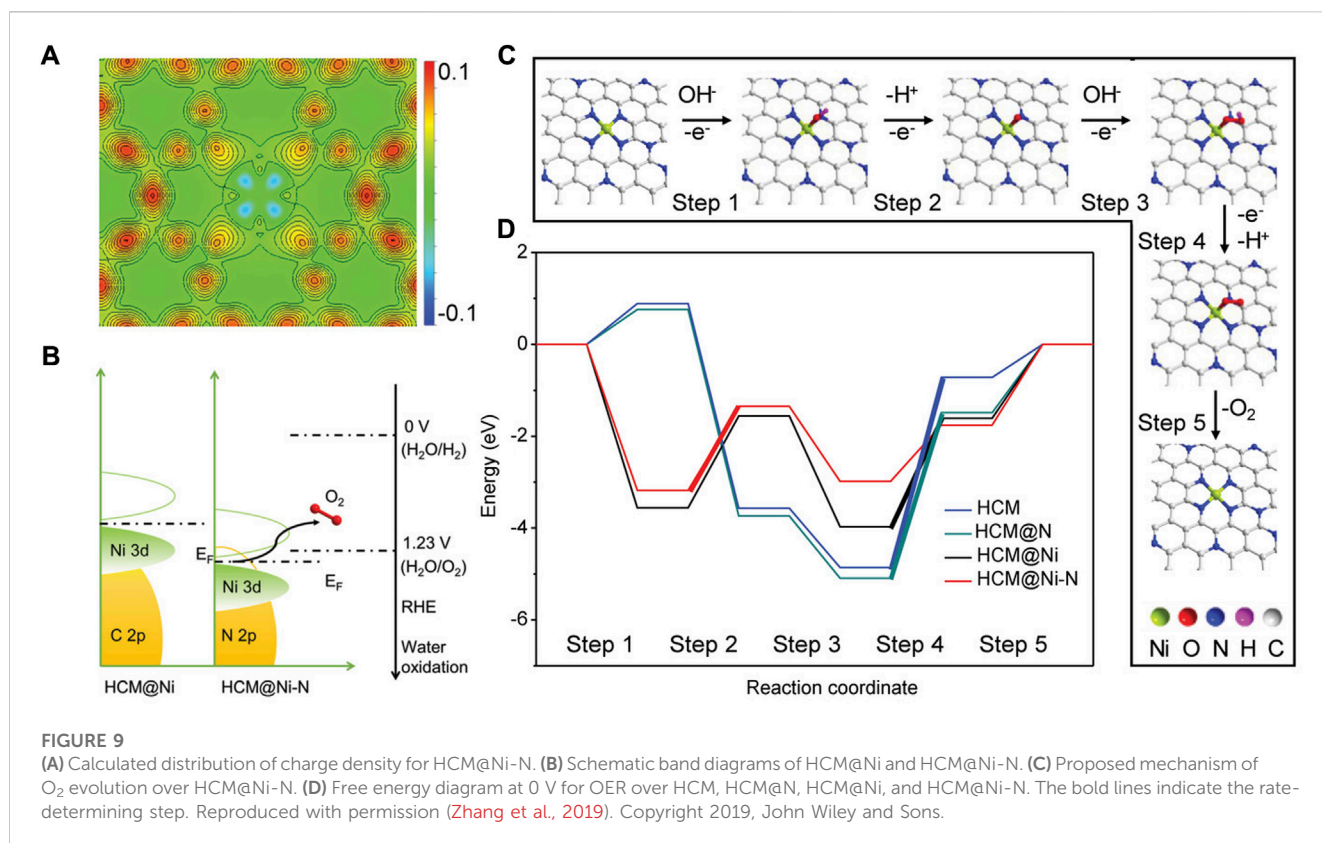
4.3 Carbon dioxide reduction reaction (CO$_2$RR)

Carbon dioxide reduction reaction (CO$_2$RR) could convert CO$_2$ to many value-added chemicals, such as CO, CH$_4$, CH$_3$OH, and C$_2$H$_5$OH (Eq. 4.6) (Whipple and Kenis, 2010; Chen J. et al., 2021; Chen S. et al., 2021), which can be directly used as fuels to replace fossil fuels like gasoline and natural gas. Therefore, the CO$_2$RR could significantly relieve the greenhouse gas effect. However, the hydrogen atoms necessary for the reduction of CO$_2$ molecules are transported from the aqueous solution, so the HER must be considered as the competitive reaction. The high cost of the currently used noble metal-based catalysts and the low selectivity of CO$_2$RR are still the biggest obstacles to its industrialization. Therefore, developing highly efficient and selective non-noble metal CO$_2$RR catalysts based on earth-abundant elements has attracted the most attention in this promising research field (Back et al., 2017; Mao et al., 2020a; He et al., 2020b; Er et al., 2021; Zha et al., 2021; Powar et al., 2022).

$$CO_2 + e^- \rightarrow CO_2^- \quad E^\ominus = -1.90\,V \quad (4.6a)$$

$$CO_2 + 2H^+ + 2e^- \rightarrow CO + H_2O \quad E^\ominus = -0.52\,V \quad (4.6b)$$

$$CO_2 + 2H^+ + 2e^- \rightarrow HCOOH \quad E^\ominus = -0.61\,V \quad (4.6c)$$

$$CO_2 + 4H^+ + 4e^- \rightarrow HCOH + H_2O \quad E^\ominus = -0.51\,V \quad (4.6d)$$

$$CO_2 + 6H^+ + 6e^- \rightarrow CH_3OH + H_2O \quad E^\ominus = -0.38\,V \quad (4.6e)$$

$$CO_2 + 8H^+ + 8e^- \rightarrow CH_4 + 2H_2O \quad E^\ominus = -0.24\,V \quad (4.6f)$$

$$CO_2 + 12H^+ + 12e^- \rightarrow C_2H_4 + 4H_2O \quad E^\ominus = -0.34\,V \quad (4.6g)$$
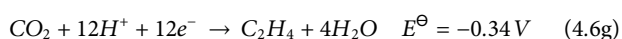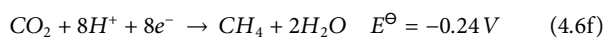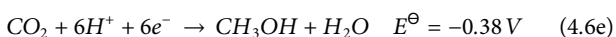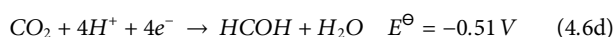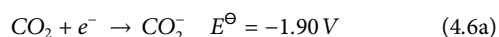
The initial stage of CO$_2$ reduction is CO$_2$ adsorption, which is a crucial step of the CO$_2$RR. Zhu *et al.* systematically investigated the adsorption of CO$_2$ on the g-C$_3$N$_4$ surface by DFT calculations (Zhu et al., 2017). Through analyzing the electronic properties such as the band gap, density of states, work function, HOMO, and LUMO, they found that the two-coordinated N atoms, which contributed to both valance band and conduction band edge, have the most negative adsorption energy (−0.4181) for CO$_2$ molecule. CO$_2$ can be effectively captured and activated on Si due to the "acceptance and back-donation" of electrons between the Si dopant and CO$_2$ molecule. Accordingly, Mao and co-workers designed an experimentally synthesizable electrocatalyst called silicon-doped graphene edges (Si chain@G) (Mao et al., 2019b). The catalytic performance of the Si@ZZG (Si atoms doped into the zigzag edge of graphene) and Si@ACG (Si atoms doped into the armchair edge of graphene) was exhaustively studied through DFT calculations (Figure 11A). CO$_2$ can be well captured and efficiently activated on Si@G. The binding energy at the zigzag and armchair edges is −0.65 eV and −0.83 eV, respectively. Remarkably, CO$_2$ can be converted to CH$_3$OH effectively when the Si@ACG is served as the active site. Moreover, Si chain@G with multiple Si active sites which are beneficial to product multiple-carbon productions was also investigated. They found that the Si chain@ZZG has a high selectivity to transform CO$_2$ to C$_2$H$_5$OH with an extreme low limiting potential of −0.6 V under the optimal theoretical reaction pathway (Figures 11B,C).

Transition metal atoms can also be excellent CO$_2$RR active centers. Guo *et al.* established calculation models with Fe, Co, and Ni single atoms embedded onto graphitic carbon nitride (Fe/Co/Ni-C$_3$N$_4$) and systematically investigated the structures of the
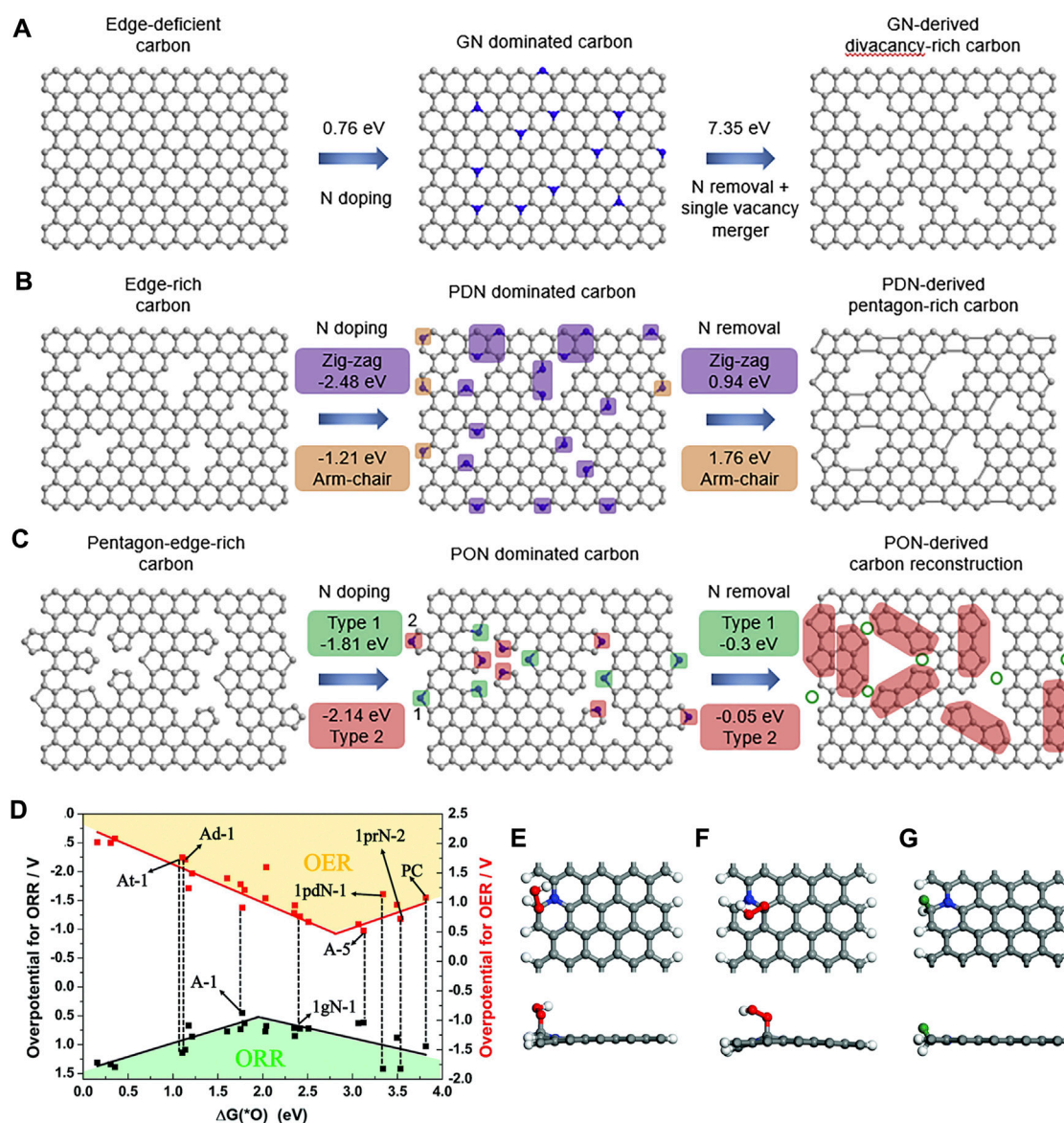
FIGURE 10
Computational simulation of specific N-doping and removing process in different carbon models: **(A)** Schematic and formation energy calculation of transformation from edge-deficient carbon to GN-dominated carbon and then to divacancy-rich carbon. **(B)** Schematic and formation energy calculations of transformation from edge-rich carbon to PDN-dominated carbon and then to pentagon-rich carbon. **(C)** Schematic and formation energy calculations of transformation from pentagon-edge-rich carbon to PON-dominated carbon and then to special carbon reconstruction. Reproduced with permission (Wang et al., 2020b). Copyright 2020, Elsevier. **(D)** The volcano plot for the ORR and OER by plotting the overpotential as a function of $\Delta G(*O)$ at various possible active sites. The top and side views of the active site **(E)** A-1 for the ORR, **(F)** A-3 for the OER with OOH adsorbed, and **(G)** A-1 for the HER; the green ball represents the adsorbed H ($\theta = 2.27\%$). Reproduced with permission (Jiang et al., 2019). Copyright 2008, Royal Society of Chemistry.

electrocatalysts, CO_2 adsorption configurations, and the reduction mechanisms (Guo X. et al., 2019). g-C_3N_4 with six-fold cavities was selected as the substrate, and the introduced Ni, Co, and Fe atoms are located from the corner to the center of the cavity. The PDOS of the metal d orbital and adsorbed CO_2 indicated that CO_2 could be chemically adsorbed on Co-C_3N_4 and Fe-C_3N_4 but physically adsorbed on Ni-C_3N_4 (Figures 12A,B). Guo *et al.* also probed the reaction pathway and mechanism of different C1 products and thoroughly calculated

the limiting potentials for the production of CO, HCOOH, CH_3OH, and CH_4. They found that Co-C_3N_4 has superior CO_2RR activity and selectivity for CH_3OH (Figure 12C). Currently, copper (Cu) is found to be one of the best catalysts for achieving the high activity reduction of CO_2 to hydrocarbons since *CO_2 and *COOH can be effectively collected from Cu-based catalysts (Raciti and Wang, 2018). Due to the hydration of non-adsorbing CO_2 molecules, Pb, Hg, Cd, and Bi also demonstrate good catalytic performance for producing
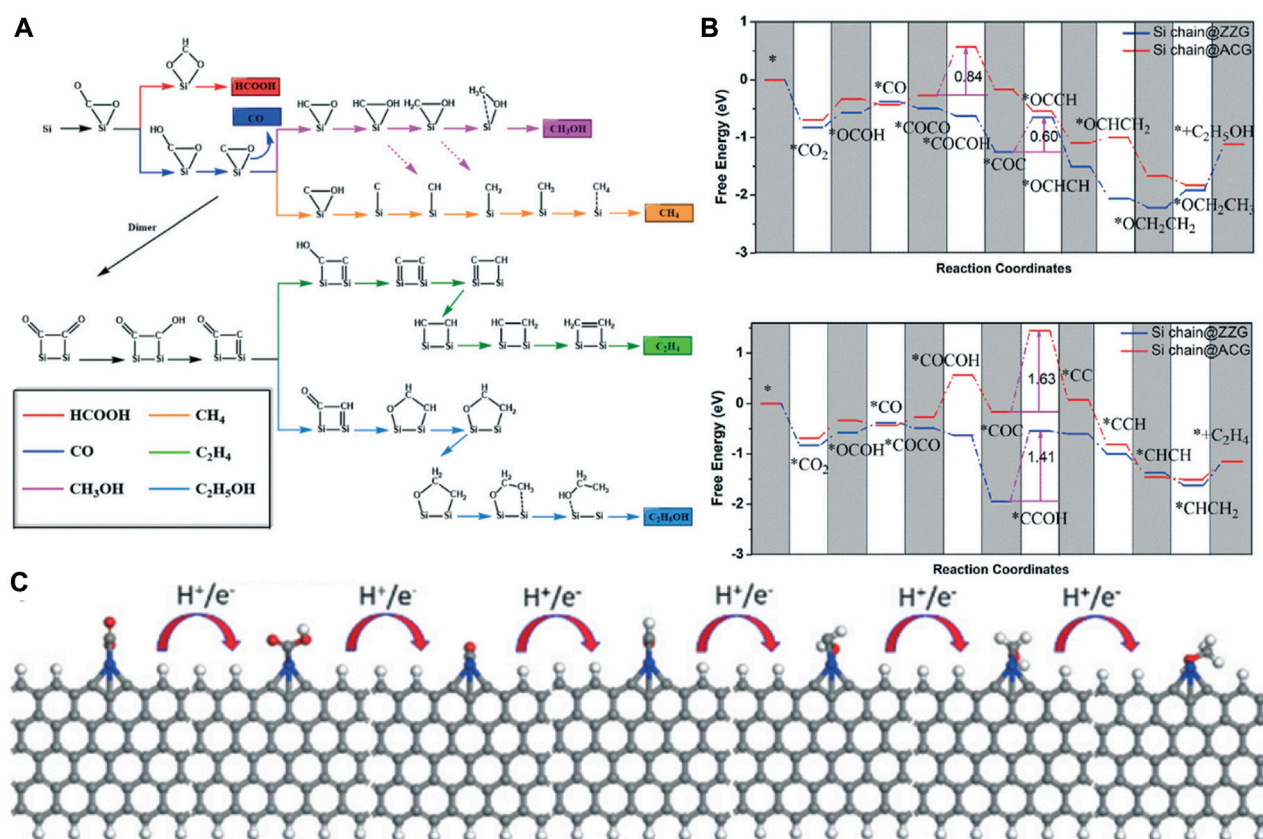
FIGURE 11
(A) Possible reaction pathways for the electrocatalytic reduction of CO_2 to six different products. **(B)** Gibbs free energy diagrams of CO_2 reduction reactions to CH_3OH and C_2H_4 on Si chain@ZZG and Si chain@ACG. **(C)** The optimized structures for CO_2 reduction to CH_3OH on the zigzag edge. Reproduced with permission (Mao et al., 2019b). Copyright 2011, Royal Society of Chemistry.
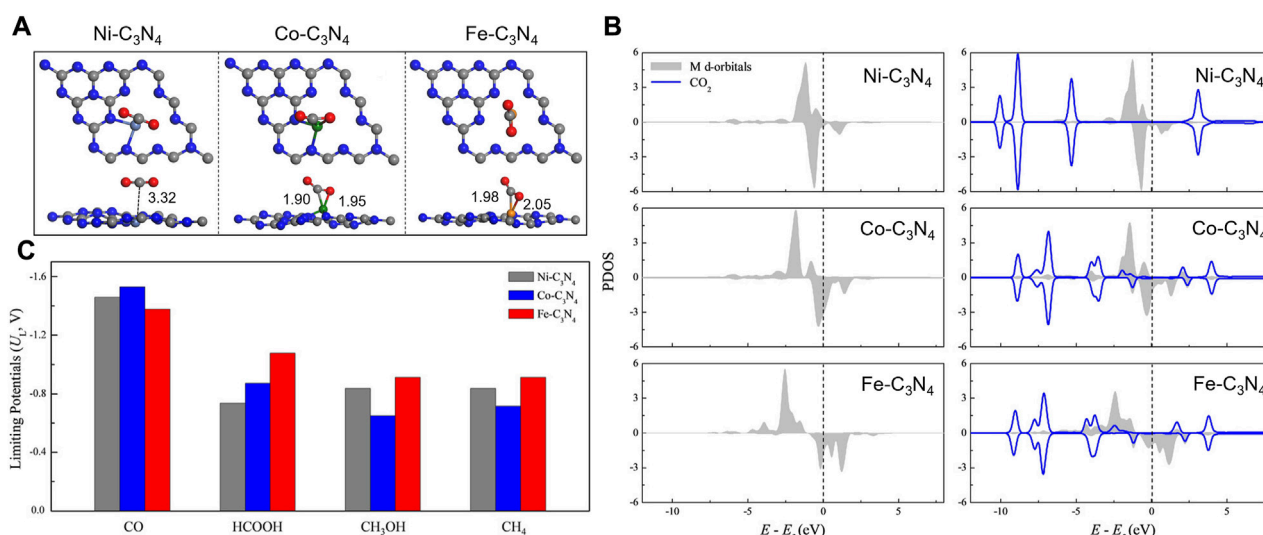
FIGURE 12
(A) The most stable CO_2 adsorption configurations. **(B)** PDOS of the metal d orbital before and after adsorption (including the adsorbent CO_2 total DOS). **(C)** Summary of the limiting potentials for the productions of CO, HCOOH, CH_3OH, and CH_4. Reproduced with permission (Guo X et al., 2019). Copyright 2019, John Wiley and Sons.
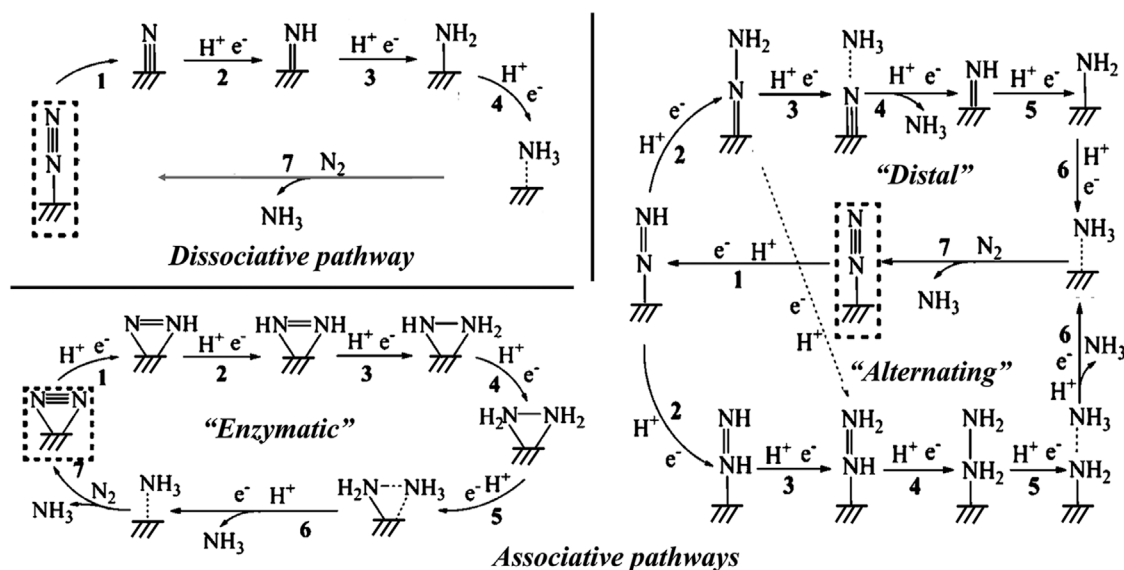
FIGURE 13
Schematic depiction of the dissociative pathways and the associative pathways (including distal, alternating, and enzymatic pathways) for catalytic conversion of N_2 to NH_3. Reproduced with permission (Li et al., 2016). Copyright 2016, American Chemical Society.

formate (Mao et al., 2020b). Other transition metals such as Ni, Fe, Pd, and Ti exhibit low CO_2RR selectivity because the HER is much more favorable due to the strong H-bonding (Back et al., 2017).

4.4 Nitrogen reduction reaction (NRR)

Nitrogen is the most abundant element on the earth, and it is essential for all organisms including animals and plants. Ammonia (NH_3) is one of the most important industrial compounds due to its wide use in different fields. However, the ultra-stable N≡N triple bond greatly impedes the nitrogen fixation reaction. The industrial Haber-Bosch process uses N_2 and H_2 as the raw materials, consuming excessive energy because of the high reaction temperature (350°C–550°C) and pressure (150–350 atm) (van der Ham et al., 2014; Chen Jingguang et al., 2018). Therefore, the conversion of N_2 to NH_3 under ambient conditions is a promising research area. Recently, electrocatalytic nitrogen reduction reaction (NRR) has attracted increasing research attention because of its obvious advantages such as low energy consumption, reduced reaction temperature, and enhanced productivity (Li et al., 2016; Cui et al., 2018; He et al., 2020c; Liu Y et al., 2021; Ruiyi et al., 2021; Samal et al., 2021; Wang and Mao, 2021; Zhou et al., 2022; Fang et al., 2023; Liu H. et al., 2023). Figure 13 shows the possible reaction pathways of the catalytic conversion of N_2 to NH_3.

The first and most important step of the NRR is the adsorption of N_2 to the active sites, which requires the atoms containing not fully occupied orbitals to accept the lone-pair electrons from the σ orbital of N_2. Therefore, transition metals

would be ideal electron acceptors due to their half-occupied d orbitals, and they have the potential to be promising NRR electrocatalysts (Lan et al., 2013; Le et al., 2014; Han et al., 2019). Ling and co-workers established a computational model that anchored Mo atoms onto N-doped carbon (Mo_1-N_1C_2) and studied its NRR catalytic performance using the first principle calculations (Ling et al., 2018b). Firstly, the bonding energy of N_2 adsorbed on M_1-N_1C_2 (M = Cu, Pd, Pt, and Mo) is investigated; only Mo_1-N_1C_2 shows strong adsorption of N_2 with the adsorption energy of −1.19 and −1.18 eV for side-on and end-on adsorption, respectively. In addition, the N≡N bond length has increased from 1.12 Å (isolated N_2 molecule) to 1.18 Å (side-on) and 1.14 Å (end-on) (Figures 14A–C). Accordingly, Mo is selected as the potential electrocatalyst, and the possible reaction pathways are calculated. As shown in Figure 14 D, Mo_1-N_1C_2 has a low overpotential of 0.24 V and it can catalyze the NRR through an enzymatic pathway. It is worth noting that the generated NH_3 can be removed quickly from the Mo_1-N_1C_2 catalyst with a free-energy uphill of only 0.47 eV, which is much lower than that of the previously reported catalysts.

In recent years, metal-free catalysts have also emerged as an important category of electrocatalysts for ammonia formation. Boron (B) has the potential to be used in NRR processes because of its Lewis acid-like characteristics and electron-deficient nature, which is different from other main group elements. The outer orbital of B undergoes hybridization to produce sp^2 orbitals, which can accept electrons from the N_2 σ-bond and donate electrons from the filled $2p$ orbitals to the antibonding π*-orbitals of N_2. This finding has been supported by a number of recent investigations (Ling et al., 2018c; Yu et al., 2018; Mao et al., 2019c). For instance, Yu's group reported that B-doped graphene could effectively catalyze the NRR with a high Faradic efficiency
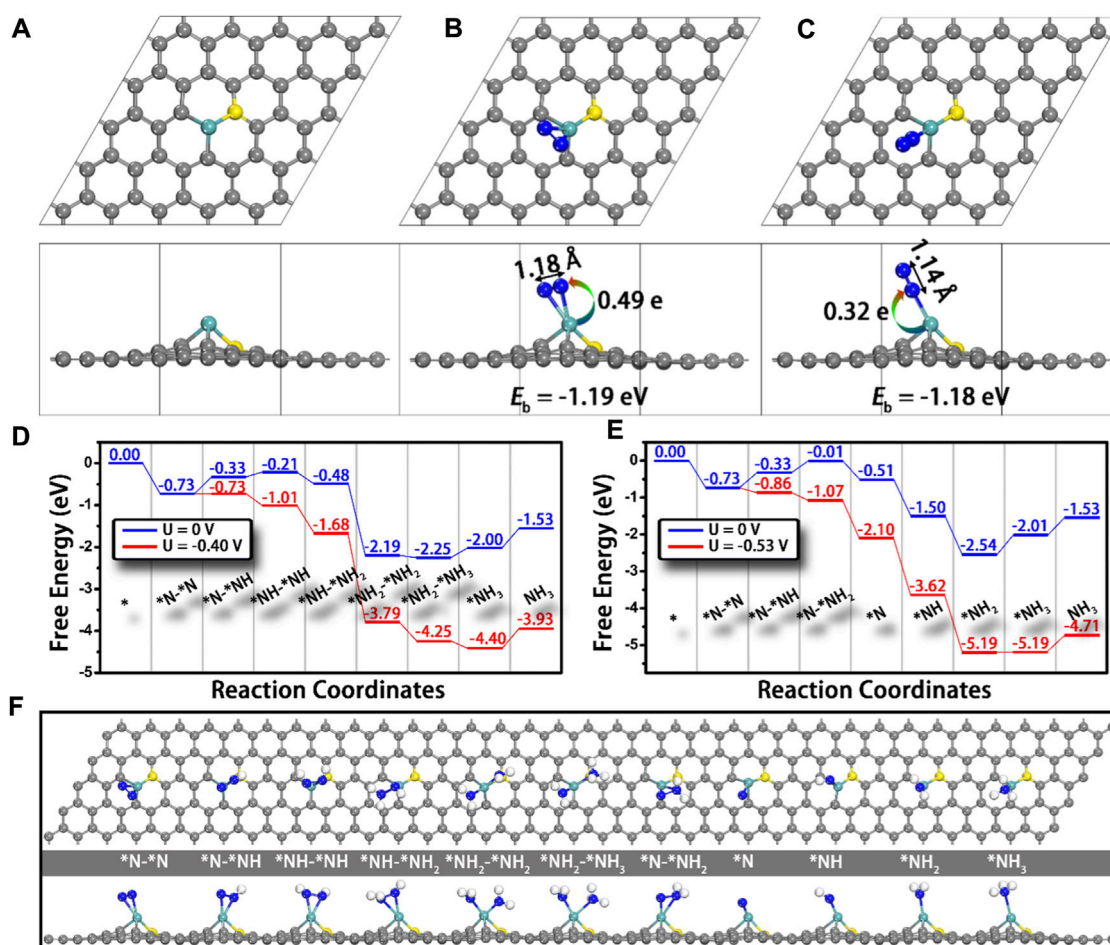
FIGURE 14
Top and side views of the structures of **(A)** Mo_1-N_1C_2, and Mo_1-N_1C_2 with N_2 adsorption through **(B)** side-on and **(C)** end-on patterns. N–N bond lengths and charge transfer from Mo_1-N_1C_2 to N_2 are also presented. Free-energy diagrams for N_2 reduction through **(D)** enzymatic and **(E)** consecutive mechanisms at different applied potentials as well as **(F)** the corresponding structures of the reaction intermediates. Gray, cyan, yellow, and blue balls represent the C, Mo, doped N, and adsorbed N atoms, respectively. Reproduced with permission (Ling et al., 2018b). Copyright 2018, American Chemical Society.

of 10.8% for NH_3 production in aqueous solutions under ambient conditions at −0.5 V (*versus* RHE), with the electron redistribution at the active site constituting the reduction process (Yu et al., 2018). However, the theoretically calculated overpotential remains very high, so there is still a great need for more suitable substrates to sustain B atoms. In addition, the detailed reaction mechanism of the N_2 activation and reduction for non-metallic catalysts is yet to be uncovered, suggesting that new methods of nitrogen capture and activation should be exploited to increase the efficiency of nitrogen fixation.

5 Conclusions and outlook

In summary, the development of modern DFT was briefly introduced, and the applications of theoretical calculations such as descriptors suited to material screening and mechanism studies in carbon-based heterogeneous catalysts were reviewed. Afterward,

recent achievements of carbon-based electrocatalysts were presented. As shown in Figure 15, the development of supercomputer technology could improve the accuracy of the theoretical calculations. With the assistance of machine learning and high-throughput computing, the prediction and screening ability of computational simulation has gradually enhanced and become more closely integrated with experimental work. Besides, DFT calculations can simulate a more realistic reaction environment and material structures, which could improve the efficiency and accuracy of the mechanism explanation. Particularly, low-dimensional carbon-based materials have demonstrated tremendous potential in electrocatalysis due to their distinctive features, including 1) diverse and controllable structures as well as excellent environmental tolerance; 2) inherent substrate materials can be easily doped by heteroatoms; 3) various defects can serve as the active sites. However, similar to other kinds of excellent electrocatalysts, carbon-based electrocatalysts also face severe limitations in the rational design and practical application. More
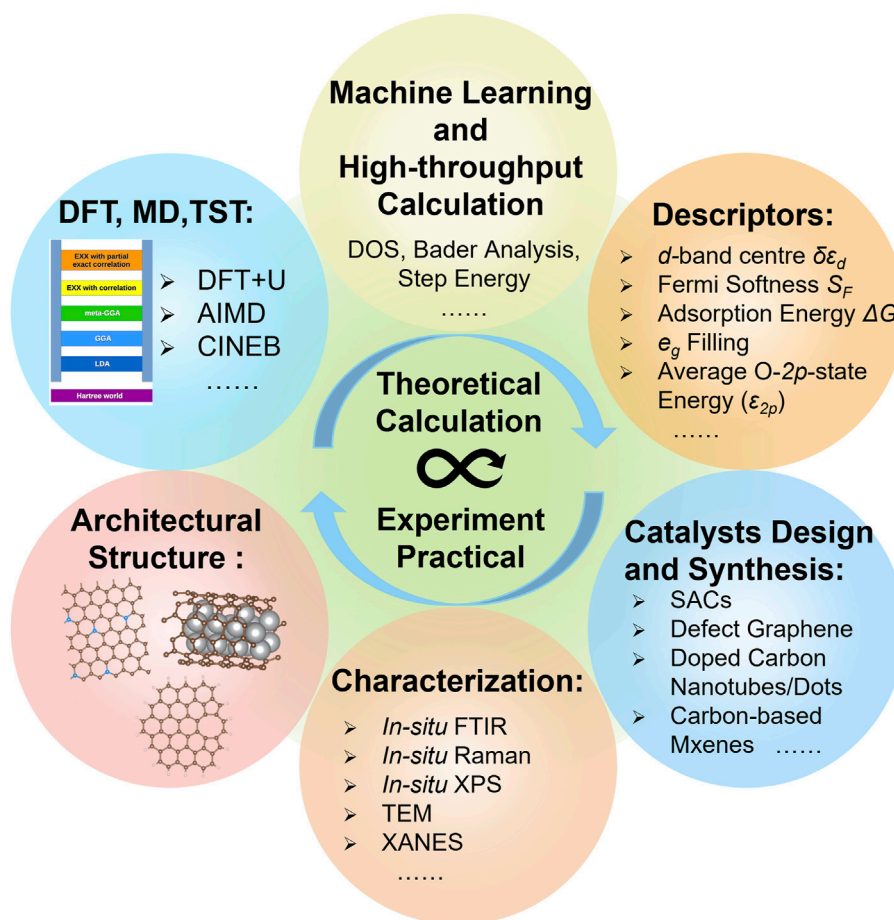
FIGURE 15
Schematic illustration showing the combination of theoretical calculations and experimental studies.

universal, accurate, and measurable descriptors should be developed, and additional research attention should be focused on the synthesis of catalysts. The following important issues and challenges deserve further investigation.

(1) Microkinetic modeling is a bridge that can connect quantum-chemical data with macroscopic behaviors in surface reactions. However, the existing theoretical approaches and functionals describing interface charge cannot meet the requirement of evaluating kinetics and reaction barriers of elementary steps under realistic reaction environments. For example, the widely used CHE model can only obtain the reaction-free energies, without the consideration of the non-electrochemical processes, proton-electron transfer, and the recombination of electrons and holes. More advancements in kinetic modeling are needed to fully uncover the relationship between coverage, potential dependency of activation energies, adsorbate-adsorbate interactions, and pH effects. For interfacial catalytic processes, multiscale modeling can facilitate the understanding of the transport effects. Alternatively, assisted by advanced sampling methods, such as slow-growth (SG), metadynamics, and umbrella sampling, AIMD can compensate for the shortcomings of the CHE models.

Meanwhile, grand-canonic fixed-potential DFT calculations offer a feasible way to evaluate the catalytic performance at equilibrium states, which is the same as the experimental setup.

(2) The combination of multiple descriptors to effectively describe the relationship between structures and performance is indispensable. This is because it may be impossible to accurately predict the activity trends of complicated multi-phase catalysts only using one descriptor. Meanwhile, the simulation results of completed calculations, such as explicit SG-AIMD simulation, are highly dependent on the selection of collective variables. Importantly, machine learning, high-throughput calculations, and force-field approaches should be applied to uncover more general descriptors and advanced models, leading to higher efficient reaction mechanisms investigation and catalytic performance prediction.

(3) In addition to kinetics and reaction barriers, the stability of the catalysts plays a pivotal role in practical applications. Several commonly employed simulation methods are used to assess the stability of designed catalysts. For instance, retaining a stable structure during AIMD simulations is often interpreted as a sign of catalyst stability; nevertheless, the limited simulation duration reduces the reliability of the results. Another commonly used method, Pourbaix diagrams, cannot fully

overcome the limitation of thermodynamic formation energy, even considering factors such as pH and applied potential. Hence, there is a pressing need to develop a dependable approach for evaluating the stability of electrocatalysts, which deserves more attention in research.

(4) Selectivity is also a critical parameter in assessing the catalytic performance of electrocatalysts. In simulations, the selectivity of electrocatalysts is often evaluated by comparing formation energies, adsorption energies of reactants, or energy barriers of potential determining steps (PDS). However, these evaluations are typically based on the CHE model and do not consider the real reaction environment, which substantially impacts the selectivity of catalysts. Consequently, it is still unclear how to effectively assess the selectivity, while microkinetic models that consider various environmental factors may prove to be a successful solution.

(5) Synthesis of electrocatalysts with abundant active sites is also crucial, for instance, the formation process of specific defect structures and the synthesis of SACs with specific density are yet to be improved. Theoretical scientists have been focusing on improving the activity of electrocatalysts. However, rational design and synthesis strategies for large-scale production of carbon-based electrocatalysts are also one of the stumbling blocks for practical applications. More attention should be focused on the synthesis of electrocatalysts with the targeted active site for a specific reaction.

(6) The scaling relationship between oxygen adsorbates in OER, ORR, and CO_2RR has the possibility to develop efficient descriptors. However, it also restricts the lowest overpotential of electrocatalytic reactions, for example, the predicted lowest overpotential is $(3.2–2.46)$ eV/2e ≈ 0.4 V for both ORR and OER. Therefore, how to break the scaling relationship is also a prospective research topic in the near future. One possible solution is stabilizing the key intermediates, and the other method is exploring new reaction mechanisms to avoid the formation of key intermediates.

Author contributions

YH: Conceptualization, Writing–original draft. HX: Writing–review and editing. QL: Supervision, Writing–review and editing. AD: Conceptualization, Funding acquisition, Project administration, Supervision, Writing–review and editing. XY: Conceptualization, Funding acquisition, Project administration, Supervision, Writing–review and editing.

Funding

Conflict of interest

The authors declare that the research was conducted in the absence of any commercial or financial relationships that could be construed as a potential conflict of interest.

The author(s) declared that they were an editorial board member of Frontiers, at the time of submission. This had no impact on the peer review process and the final decision

Publisher's note

All claims expressed in this article are solely those of the authors and do not necessarily represent those of their affiliated organizations, or those of the publisher, the editors and the reviewers. Any product that may be evaluated in this article, or claim that may be made by its manufacturer, is not guaranteed or endorsed by the publisher.

References

Abas, N., Kalair, A., and Khan, N. (2015). Review of fossil fuels and future energy technologies. *Futures* 69, 31–49. doi:10.1016/j.futures.2015.03.003

Abild-Pedersen, F., Greeley, J., Studt, F., Rossmeisl, J., Munter, T. R., Moses, P. G., et al. (2007). Scaling properties of adsorption energies for hydrogen-containing molecules on transition-metal surfaces. *Phys. Rev. Lett.* 99, 016105. doi:10.1103/PhysRevLett.99.016105

Ahsan, M. A., He, T., Eid, K., Abdullah, A. M., Curry, M. L., Du, A., et al. (2021). Tuning the intermolecular electron transfer of low-dimensional and metal-free BCN/C_{60} electrocatalysts via interfacial defects for efficient hydrogen and oxygen electrochemistry. *J. Am. Chem. Soc.* 143, 1203–1215. doi:10.1021/jacs.0c12386

Andreadis, G., and Tsiakaras, P. (2006). Ethanol crossover and direct ethanol PEM fuel cell performance modeling and experimental validation. *Chem. Eng. Sci.* 61, 7497–7508. doi:10.1016/j.ces.2006.08.028

Back, S., Lim, J., Kim, N. Y., Kim, Y. H., and Jung, Y. (2017). Single-atom catalysts for CO_2 electroreduction with significant activity and selectivity improvements. *Chem. Sci.* 8, 1090–1096. doi:10.1039/c6sc03911a

Back, S., Tran, K., and Ulissi, Z. W. (2019). Toward a design of active oxygen evolution catalysts: insights from automated density functional theory calculations and machine learning. *ACS Catal.* 9, 7651–7659. doi:10.1021/acscatal.9b02416

Barducci, A., Bonomi, M., and Parrinello, M. (2011). Metadynamics. *WIREs Comput. Mol. Sci.* 1, 826–843. doi:10.1002/wcms.31

Barducci, A., Bussi, G., and Parrinello, M. (2008). Well-tempered metadynamics: a smoothly converging and tunable free-energy method. *Phys. Rev. Lett.* 100, 020603. doi:10.1103/PhysRevLett.100.020603

Bartók, A. P., Payne, M. C., Kondor, R., and Csányi, G. (2010). Gaussian approximation potentials: the accuracy of quantum mechanics, without the electrons. *Phys. Rev. Lett.* 104, 136403. doi:10.1103/PhysRevLett.104.136403

Becke, A. D. (1988). Density-functional exchange-energy approximation with correct asymptotic behavior. *Phys. Rev. A* 38, 3098–3100. doi:10.1103/PhysRevA.38.3098

Behler, J., and Parrinello, M. (2007). Generalized neural-network representation of high-dimensional potential-energy surfaces. *Phys. Rev. Lett.* 98, 146401. doi:10.1103/PhysRevLett.98.146401

Blank, T. B., Brown, S. D., Calhoun, A. W., and Doren, D. J. (1995). Neural network models of potential energy surfaces. *J. Chem. Phys.* 103, 4129–4137. doi:10.1063/1.469597

Bora, T., Dousse, A., Sharma, K., Sarma, K., Baev, A., Hornyak, G. L., et al. (2019). Modeling nanomaterial physical properties: theory and simulation. *Int. J. Smart Nano Mater.* 10, 116–143. doi:10.1080/19475411.2018.1541935

Bussi, G., and Laio, A. (2020). Using metadynamics to explore complex free-energy landscapes. *Nat. Rev. Phys.* 2, 200–212. doi:10.1038/s42254-020-0153-0

Calle-Vallejo, F., Loffreda, D., Koper, M. T., and Sautet, P. (2015a). Introducing structural sensitivity into adsorption-energy scaling relations by means of coordination numbers. *Nat. Chem.* 7, 403–410. doi:10.1038/nchem.2226

Calle-Vallejo, F., Martínez, J. I., García-Lastra, J. M., Sautet, P., and Loffreda, D. (2014). Fast prediction of adsorption properties for platinum nanocatalysts with generalized coordination numbers. *Angew. Chem. Int. Ed.* 53, 8316–8319. doi:10.1002/anie.201402958

Calle-Vallejo, F., Tymoczko, J., Colic, V., Vu Quang, H., Marcus, D. P., Morgenstern, K., et al. (2015b). Finding optimal surface sites on heterogeneous catalysts by counting nearest neighbors. *Science* 350, 185–189. doi:10.1126/science.aab3501

Chanussot, L., Das, A., Goyal, S., Lavril, T., Shuaibi, M., Riviere, M., et al. (2021). Open catalyst 2020 (OC20) dataset and community challenges. *ACS Catal.* 11, 6059–6072. doi:10.1021/acscatal.0c04525

Chattot, R., Le Bacq, O., Beermann, V., Kühl, S., Herranz, J., Henning, S., et al. (2018). Surface distortion as a unifying concept and descriptor in oxygen reduction reaction electrocatalysis. *Nat. Mater* 17, 827–833. doi:10.1038/s41563-018-0133-2

Che, M. (2013). Nobel prize in chemistry 1912 to sabatier: organic chemistry or catalysis? *Catal. Today* 218-219, 162–171. doi:10.1016/j.cattod.2013.07.006

Chen, B., Parker, G., Han, J., Meyyappan, M., and Cassell, A. M. (2002). Heterogeneous single-walled carbon nanotube catalyst discovery and optimization. *Chem. Mater* 14, 1891–1896. doi:10.1021/cm0116828

Chen, J., Wang, T., Li, Z., Yang, B., Zhang, Q., Lei, L., et al. (2021). Recent progress and perspective of electrochemical CO_2 reduction towards C_2–C_5 products over non-precious metal heterogeneous electrocatalysts. *Nano Res.* 14, 3188–3207. doi:10.1007/s12274-021-3335-x

Chen Jingguang, G., Richard, M. C., Seefeldt Lance, C., L Bren Kara, R. M. B., Marcetta, Y. D., et al. (2018). Beyond fossil fuel–driven nitrogen transformations. *Science* 360, eaar6611. doi:10.1126/science.aar6611

Chen, S., Li, W.-H., Jiang, W., Yang, J., Zhu, J., Wang, L., et al. (2022a). MOF encapsulating N-heterocyclic carbene-ligated copper single-atom site catalyst towards efficient methane electrosynthesis. *Angew. Chem. Int. Ed.* 61, e202114450. doi:10.1002/anie.202114450

Chen, S., Wang, B., Zhu, J., Wang, L., Ou, H., Zhang, Z., et al. (2021). Lewis acid site-promoted single-atomic Cu catalyzes electrochemical CO_2 methanation. *Nano Lett.* 21, 7325–7331. doi:10.1021/acs.nanolett.1c02502

Chen, S., Zhang, Z., Jiang, W., Zhang, S., Zhu, J., Wang, L., et al. (2022b). Engineering water molecules activation center on multisite electrocatalysts for enhanced CO_2 methanation. *J. Am. Chem. Soc.* 144, 12807–12815. doi:10.1021/jacs.2c03875

Chen, Y., Wang, J., Meng, X., Zhong, Y., Li, R., Sun, X., et al. (2013). Pt–SnO_2/nitrogen-doped CNT hybrid catalysts for proton-exchange membrane fuel cells (PEMFC): effects of crystalline and amorphous SnO_2 by atomic layer deposition. *J. Power Sources* 238, 144–149. doi:10.1016/j.jpowsour.2013.03.093

Cheng, D., Zhao, Z.-J., Zhang, G., Yang, P., Li, L., Gao, H., et al. (2021). The nature of active sites for carbon dioxide electroreduction over oxide-derived copper catalysts. *Nat. Commun.* 12, 395. doi:10.1038/s41467-020-20615-0

Cheng, T., Xiao, H., and Goddard, W. A. (2017). Nature of the active sites for CO reduction on copper nanoparticles; suggestions for optimizing performance. *J. Am. Chem. Soc.* 139, 11642–11645. doi:10.1021/jacs.7b03300

Chmiela, S., Sauceda, H. E., Poltavsky, I., Müller, K.-R., and Tkatchenko, A. (2019). sGDML: constructing accurate and data efficient molecular force fields using machine learning. *Comput. Phys. Commun.* 240, 38–45. doi:10.1016/j.cpc.2019.02.007

Chu, S., and Majumdar, A. (2012). Opportunities and challenges for a sustainable energy future. *Nature* 488, 294–303. doi:10.1038/nature11475

Cui, X., Tang, C., and Zhang, Q. (2018). A review of electrocatalytic reduction of dinitrogen to ammonia under ambient conditions. *Adv. Energy Mater* 8. doi:10.1002/aenm.201800369

Dai, L., Xue, Y., Qu, L., Choi, H.-J., and Baek, J.-B. (2015). Metal-free catalysts for oxygen reduction reaction. *Chem. Rev.* 115, 4823–4892. doi:10.1021/cr5003563

Deng, T., Cen, C., Shen, H., Wang, S., Guo, J., Cai, S., et al. (2020). Atom-pair catalysts supported by N-doped graphene for the nitrogen reduction reaction: d-band center-based descriptor. *J. Phys. Chem. Lett.* 11, 6320–6329. doi:10.1021/acs.jpclett.0c01450

Ding, P., Song, H., Chang, J., and Lu, S. (2022). N-doped carbon dots coupled NiFe-LDH hybrids for robust electrocatalytic alkaline water and seawater oxidation. *Nano Res.* 15, 7063–7070. doi:10.1007/s12274-022-4377-4

Dudarev, S. L., Botton, G. A., Savrasov, S. Y., Humphreys, C. J., and Sutton, A. P. (1998). Electron-energy-loss spectra and the structural stability of nickel oxide: an LSDA+U study. *Phys. Rev. B* 57, 1505–1509. doi:10.1103/PhysRevB.57.1505

Er, C.-C., Tang, J.-Y., Fung, C.-M., Tan, L.-L., Medhekar, N. V., and Chai, S.-P. (2021). Atomistic insights into the reformation of CH_4 with CO_2 on metal-free gC_3N_4: unraveling the reaction mechanisms using first-principles DFT calculations. *J. Phys. Chem. C* 125, 23021–23028. doi:10.1021/acs.jpcc.1c06981

Fan, L., Liu, P. F., Yan, X., Gu, L., Yang, Z. Z., Yang, H. G., et al. (2016). Atomically isolated nickel species anchored on graphitized carbon for efficient hydrogen evolution electrocatalysis. *Nat. Commun.* 7, 10667. doi:10.1038/ncomms10667

Fang, Q., Yin, H., Mao, X., Han, Y., Yan, C., O'Mullane, A. P., et al. (2023). Theoretical evaluation of highly efficient nitrate reduction to ammonia on InBi. *J. Phys. Chem. Lett.* 14, 2410–2415. doi:10.1021/acs.jpclett.2c03900

Friederich, P., Häse, F., Proppe, J., and Aspuru-Guzik, A. (2021). Machine-learned potentials for next-generation matter simulations. *Nat. Mater* 20, 750–761. doi:10.1038/s41563-020-0777-6

Fung, V., Hu, G., Wu, Z., and Jiang, D.-E. (2020). Descriptors for hydrogen evolution on single atom catalysts in nitrogen-doped graphene. *J. Phys. Chem. C* 124, 19571–19578. doi:10.1021/acs.jpcc.0c04432

Gao, G., and Wang, L.-W. (2021). A potential and pH inclusive microkinetic model for hydrogen reactions on Pt surface. *Chem. Catal.* 1, 1331–1345. doi:10.1016/j.checat.2021.10.006

Gao, G., Bottle, S., and Du, A. (2018). Understanding the activity and selectivity of single atom catalysts for hydrogen and oxygen evolution via ab initial study. *Catal. Sci. Technol.* 8, 996–1001. doi:10.1039/C7CY02463K

Gao, R., Pan, L., Wang, H., Zhang, X., Wang, L., and Zou, J.-J. (2018). Ultradispersed nickel phosphide on phosphorus-doped carbon with tailored d-band center for efficient and chemoselective hydrogenation of nitroarenes. *ACS Catal.* 8, 8420–8429. doi:10.1021/acscatal.8b02091

Gao, Z., Sun, Y., Li, M., Yang, W., and Ding, X. (2018). Adsorption sensitivity of Fe decorated different graphene supports toward toxic gas molecules (CO and NO). *Appl. Surf. Sci.* 456, 351–359. doi:10.1016/j.apsusc.2018.06.112

Gao, Z. Y., Yang, W. J., Ding, X. L., Lv, G., and Yan, W. P. (2018). Support effects on adsorption and catalytic activation of O_2 in single atom iron catalysts with graphene-based substrates. *Phys. Chem. Chem. Phys.* 20, 7333–7341. doi:10.1039/c7cp08301g

Gasteiger, H. A., Kocha, S. S., Sompalli, B., and Wagner, F. T. (2005). Activity benchmarks and requirements for Pt, Pt-alloy, and non-Pt oxygen reduction catalysts for PEMFCs. *Appl. Catal. B Environ.* 56, 9–35. doi:10.1016/j.apcatb.2004.06.021

Gauthier, J. A., Dickens, C. F., Heenen, H. H., Vijay, S., Ringe, S., and Chan, K. (2019). Unified approach to implicit and explicit solvent simulations of electrochemical reaction energetics. *J. Chem. Theory Comput.* 15, 6895–6906. doi:10.1021/acs.jctc.9b00717

Gong, Y.-N., Cao, C.-Y., Shi, W.-J., Zhang, J.-H., Deng, J.-H., Lu, T.-B., et al. (2022). Modulating the electronic structures of dual-atom catalysts via coordination environment engineering for boosting CO_2 electroreduction. *Angew. Chem. Int. Ed.* 61, e202215187. doi:10.1002/anie.202215187

Grimaud, A., May, K. J., Carlton, C. E., Lee, Y.-L., Risch, M., Hong, W. T., et al. (2013). Double perovskites as a family of highly active catalysts for oxygen evolution in alkaline solution. *Nat. Commun.* 4, 2439. doi:10.1038/ncomms3439

Gross, A., and Sakong, S. (2022). *Ab initio* simulations of water/metal interfaces. *Chem. Rev.* 122, 10746–10776. doi:10.1021/acs.chemrev.1c00679

Groß, A. (2021). Grand-canonical approaches to understand structures and processes at electrochemical interfaces from an atomistic perspective. *Curr. Opin. Electrochem.* 27, 100684. doi:10.1016/j.coelec.2020.100684

Guan, D., Zhou, J., Hu, Z., Zhou, W., Xu, X., Zhong, Y., et al. (2019). Searching general sufficient-and-necessary conditions for ultrafast hydrogen-evolving electrocatalysis. *Adv. Funct. Mater* 29, 1900704. doi:10.1002/adfm.201900704

Guo, C., Zhang, T., Deng, X., Liang, X., Guo, W., Lu, X., et al. (2019). Electrochemical CO_2 reduction to C_1 products on single nickel/cobalt/iron-doped graphitic carbon nitride: a DFT study. *ChemSusChem* 12, 5126–5132. doi:10.1002/cssc.201902483

Guo, X., Lin, S., Gu, J., Zhang, S., Chen, Z., and Huang, S. (2019). Simultaneously achieving high activity and selectivity toward two-electron O_2 electroreduction: the power of single-atom catalysts. *ACS Catal.* 9, 11042–11054. doi:10.1021/acscatal.9b02778

Guo, Y., Yuan, P., Zhang, J., Xia, H., Cheng, F., Zhou, M., et al. (2018). Co_2P–CoN double active centers confined in N-doped carbon nanotube: heterostructural engineering for trifunctional catalysis toward HER, ORR, OER, and Zn–air batteries driven water splitting. *Adv. Funct. Mater* 28, 1805641. doi:10.1002/adfm.201805641

Hammer, B., and Norskov, J. K. (1995). Why gold is the noblest of all the metals. *Nature* 376, 238–240. doi:10.1038/376238a0

Han, L., Liu, X., Chen, J., Lin, R., Liu, H., Lü, F., et al. (2019). Atomically dispersed molybdenum catalysts for efficient ambient nitrogen fixation. *Angew. Chem. Int. Ed.* 58, 2321–2325. doi:10.1002/anie.201811728

Han, Y., Yan, X., Wu, Q., Xu, H., Li, Q., Du, A., et al. (2023a). Defect-derived catalysis mechanism of electrochemical reactions in two-dimensional carbon materials. *Small Struct.*, 2300036. doi:10.1002/sstr.202300036

Han, Y., Mao, X., Yan, X., Wu, Q., Xu, H., Fang, Q., et al. (2023b). Carbon nanotubes encapsulated transition metals for efficient hydrogen evolution reaction: coupling effect of 3d orbital and π-bond. *Mater. Today Chem.* 30, 101573. doi:10.1016/j.mtchem.2023.101573

Handley, C. M., and Popelier, P. L. A. (2010). Potential energy surfaces fitted by artificial neural networks. *J. Phys. Chem. A* 114, 3371–3383. doi:10.1021/jp9105585

Hao, Q., Zhong, H.-X., Wang, J.-Z., Liu, K.-H., Yan, J.-M., Ren, Z.-H., et al. (2022). Nickel dual-atom sites for electrochemical carbon dioxide reduction. *Nat. Synth.* 1, 719–728. doi:10.1038/s44160-022-00138-w

Hao, Y., Wang, X., Shen, J., Yuan, J., Wang, A.-J., Niu, L., et al. (2016). One-pot synthesis of single-crystal Pt nanoplates uniformly deposited on reduced graphene oxide, and their high activity and stability on the electrocalalytic oxidation of methanol. *Nanotechnology* 27, 145602. doi:10.1088/0957-4484/27/14/145602

He, T., Gao, G., Kou, L., Will, G., and Du, A. (2017). Endohedral metallofullerenes (M@C60) as efficient catalysts for highly active hydrogen evolution reaction. *J. Catal.* 354, 231–235. doi:10.1016/j.jcat.2017.08.025

He, T., Kong, Y., Zhou, T., Zhang, J., Santiago, A. R. P., Du, A., et al. (2023). Rational modulation of single atom coordination microenvironments in a BCN monolayer for multifunctional electrocatalysis. *Small*, 2302429. doi:10.1002/smll.202302429

He, T., Santiago, A. R. P., and Du, A. (2020c). Atomically embedded asymmetrical dual-metal dimers on N-doped graphene for ultra-efficient nitrogen reduction reaction. *J. Catal.* 388, 77–83. doi:10.1016/j.jcat.2020.05.009

He, T., Zhang, C., and Du, A. (2019). Single-atom supported on graphene grain boundary as an efficient electrocatalyst for hydrogen evolution reaction. *Chem. Eng. Sci.* 194, 58–63. doi:10.1016/j.ces.2018.03.028

He, T., Zhang, C., Will, G., and Du, A. (2020b). Cobalt porphyrin supported on graphene/Ni (111) surface: enhanced oxygen evolution/reduction reaction and the role of electron coupling. *Catal. Today* 351, 113–118. doi:10.1016/j.cattod.2018.10.056

He, T., Zhang, L., Kour, G., and Du, A. (2020a). Electrochemical reduction of carbon dioxide on precise number of Fe atoms anchored graphdiyne. *J. CO2 Util.* 37, 272–277. doi:10.1016/j.jcou.2019.12.025

Henkelman, G., and Jónsson, H. (1999). A dimer method for finding saddle points on high dimensional potential surfaces using only first derivatives. *J. Chem. Phys.* 111, 7010–7022. doi:10.1063/1.480097

Henkelman, G., Uberuaga, B. P., and Jónsson, H. (2000). A climbing image nudged elastic band method for finding saddle points and minimum energy paths. *J. Chem. Phys.* 113, 9901–9904. doi:10.1063/1.1329672

Heyd, J., and Scuseria, G. E. (2004). Efficient hybrid density functional calculations in solids: assessment of the Heyd–Scuseria–Ernzerhof screened Coulomb hybrid functional. *J. Chem. Phys.* 121, 1187–1192. doi:10.1063/1.1760074

Heyd, J., Scuseria, G. E., and Ernzerhof, M. (2003). Hybrid functionals based on a screened Coulomb potential. *J. Chem. Phys.* 118, 8207–8215. doi:10.1063/1.1564060

Hinnemann, B., Moses, P. G., Bonde, J., Jørgensen, K. P., Nielsen, J. H., Horch, S., et al. (2005). Biomimetic hydrogen evolution: MoS2 nanoparticles as catalyst for hydrogen evolution. *J. Am. Chem. Soc.* 127, 5308–5309. doi:10.1021/ja0504690

Hohenberg, P., and Kohn, W. (1964). Inhomogeneous electron gas. *Phys. Rev.* 136, B864–B871. doi:10.1103/PhysRev.136.B864

Hoover, W. G. (1985). Canonical dynamics: equilibrium phase-space distributions. *Phys. Rev. A* 31, 1695–1697. doi:10.1103/PhysRevA.31.1695

Hsieh, C.-T., Lin, J.-Y., and Wei, J.-L. (2009). Deposition and electrochemical activity of Pt-based bimetallic nanocatalysts on carbon nanotube electrodes. *Int. J. Hydrogen Energy* 34, 685–693. doi:10.1016/j.ijhydene.2008.11.008

Hu, C., Hu, Y., Fan, C., Yang, L., Zhang, Y., Li, H., et al. (2021). Surface-enhanced Raman spectroscopic evidence of key intermediate species and role of NiFe dual-catalytic center in water oxidation. *Angewandte Chemie Int. ed Engl.* 60, 19774–19778. doi:10.1002/anie.202103888

Huang, B., Xiao, L., Lu, J., and Zhuang, L. (2016). Spatially resolved quantification of the surface reactivity of solid catalysts. *Angew. Chem. Int. Ed.* 55, 6239–6243. doi:10.1002/anie.201601824

Hubert, A. G., and Nenad, M. M. (2009). Just a dream—or future reality? *Science* 324, 48–49. doi:10.1126/science.1172083

Iannuzzi, M., Laio, A., and Parrinello, M. (2003). Efficient exploration of reactive potential energy surfaces using car-parrinello molecular dynamics. *Phys. Rev. Lett.* 90, 238302. doi:10.1103/PhysRevLett.90.238302

Jain, A., Ong, S. P., Hautier, G., Chen, W., Richards, W. D., Dacek, S., et al. (2013). Commentary: the Materials Project: a materials genome approach to accelerating materials innovation. *Apl. Mater.* 1, 011002. doi:10.1063/1.4812323

Jaramillo, T. F., Jørgensen, K. P., Bonde, J., Nielsen, J. H., Horch, S., and Chorkendorff, I. (2007). Identification of active edge sites for electrochemical H₂ evolution from MoS₂ nanocatalysts. *Science* 317, 100–102. doi:10.1126/science.1141483

Jia, Y., Zhang, L., Du, A., Gao, G., Chen, J., Yan, X., et al. (2016). Defect graphene as a trifunctional catalyst for electrochemical reactions. *Adv. Mater* 28, 9532–9538. doi:10.1002/adma.201602912

Jia, Y., Zhang, L., Zhuang, L., Liu, H., Yan, X., Wang, X., et al. (2019). Identification of active sites for acidic oxygen reduction on carbon catalysts with and without nitrogen doping. *Nat. Catal.* 2, 688–695. doi:10.1038/s41929-019-0297-4

Jiang, H., Gu, J., Zheng, X., Liu, M., Qiu, X., Wang, L., et al. (2019). Defect-rich and ultrathin N doped carbon nanosheets as advanced trifunctional metal-free electrocatalysts for the ORR, OER and HER. *Energy Environ. Sci.* 12, 322–333. doi:10.1039/c8ee03276a

Jiao, S., Fu, X., and Huang, H. (2022). Descriptors for the evaluation of electrocatalytic reactions: d-band theory and beyond. *Adv. Funct. Mater* 32, 2107651. doi:10.1002/adfm.202107651

Jinnouchi, R., Karsai, F., Verdi, C., Asahi, R., and Kresse, G. (2020). Descriptors representing two- and three-body atomic distributions and their effects on the accuracy of machine-learned inter-atomic potentials. *J. Chem. Phys.* 152, 234102. doi:10.1063/5.0009491

Jinnouchi, R., Lahnsteiner, J., Karsai, F., Kresse, G., and Bokdam, M. (2019). Phase transitions of hybrid perovskites simulated by machine-learning force fields trained on the fly with bayesian inference. *Phys. Rev. Lett.* 122, 225701. doi:10.1103/PhysRevLett.122.225701

Karunadasa, H. I., Chang, C. J., and Long, J. R. (2010). A molecular molybdenum-oxo catalyst for generating hydrogen from water. *Nature* 464, 1329–1333. doi:10.1038/nature08969

Khan, K., Liu, T., Arif, M., Yan, X., Hossain, M. D., Rehman, F., et al. (2021). Laser-irradiated holey graphene-supported single-atom catalyst towards hydrogen evolution and oxygen reduction. *Adv. Energy Mater* 11, 2101619. doi:10.1002/aenm.202101619

Kibler, L. A., El-Aziz, A. M., Hoyer, R., and Kolb, D. M. (2005). Tuning reaction rates by lateral strain in a palladium monolayer. *Angew. Chem. Int. Ed.* 44, 2080–2084. doi:10.1002/anie.200462127

Klamt, A., and Schüürmann, G. (1993). COSMO: a new approach to dielectric screening in solvents with explicit expressions for the screening energy and its gradient. *J. Chem. Soc. Perkin Trans.* 2, 799–805. doi:10.1039/P29930000799

Kocer, E., Ko, T. W., and Behler, J. (2022). Neural network potentials: a concise overview of methods. *Annu. Rev. Phys. Chem.* 73, 163–186. doi:10.1146/annurev-physchem-082720-034254

Kohn, W., and Sham, L. J. (1965). Self-consistent equations including exchange and correlation effects. *Phys. Rev.* 140, A1133–A1138. doi:10.1103/PhysRev.140.A1133

Kresse, G., and Furthmüller, J. (1996a). Efficiency of ab-initio total energy calculations for metals and semiconductors using a plane-wave basis set. *Comput. Mater Sci.* 6, 15–50. doi:10.1016/0927-0256(96)00008-0

Kresse, G., and Furthmüller, J. (1996b). Efficient iterative schemes for *ab initio* total-energy calculations using a plane-wave basis set. *Phys. Rev. B* 54, 11169–11186. doi:10.1103/PhysRevB.54.11169

Kresse, G., and Hafner, J. (1993). *Ab initio* molecular dynamics for liquid metals. *Phys. Rev. B* 47, 558–561. doi:10.1103/PhysRevB.47.558

Kresse, G., and Joubert, D. (1999). From ultrasoft pseudopotentials to the projector augmented-wave method. *Phys. Rev. B* 59, 1758–1775. doi:10.1103/PhysRevB.59.1758

Kroto, H. W., Heath, J. R., O'Brien, S. C., Curl, R. F., and Smalley, R. E. (1985). C₆₀: buckminsterfullerene. *Nature* 318, 162–163. doi:10.1038/318162a0

Laio, A., and Parrinello, M. (2002). Escaping free-energy minima. *Proc. Natl. Acad. Sci.* 99, 12562–12566. doi:10.1073/pnas.202427399

Lan, J., Luo, M., Han, J., Peng, M., Duan, H., and Tan, Y. (2021). Nanoporous B₁₃C₂ towards highly efficient electrochemical nitrogen fixation. *Small* 17, 2102814. doi:10.1002/smll.202102814

Lan, R., Irvine, J. T. S., and Tao, S. (2013). Synthesis of ammonia directly from air and water at ambient temperature and pressure. *Sci. Rep.* 3, 1145. doi:10.1038/srep01145

Le, Y. Q., Gu, J., and Tian, W. Q. (2014). Nitrogen-fixation catalyst based on graphene: every part counts. *Chem. Commun. (Camb)* 50, 13319–13322. doi:10.1039/c4cc01950d

Lee, C., Yang, W., and Parr, R. G. (1988). Development of the Colle-Salvetti correlation-energy formula into a functional of the electron density. *Phys. Rev. B* 37, 785–789. doi:10.1103/PhysRevB.37.785

Lee, Y.-L., Kleis, J., Rossmeisl, J., Shao-Horn, Y., and Morgan, D. (2011). Prediction of solid oxide fuel cell cathode activity with first-principles descriptors. *Energy Environ. Sci.* 4. doi:10.1039/c1ee02032c

Li, D., Wang, B., Long, X., Xu, W., Xia, Y., Yang, D., et al. (2021). Controlled asymmetric charge distribution of active centers in conjugated polymers for oxygen reduction. *Angew. Chem. Int. Ed.* 60, 26483–26488. doi:10.1002/anie.202109057

Li, M., Zhu, Y., Song, N., Wang, C., and Lu, X. (2018). Fabrication of Pt nanoparticles on nitrogen-doped carbon/Ni nanofibers for improved hydrogen evolution activity. *J. Colloid Interface Sci.* 514, 199–207. doi:10.1016/j.jcis.2017.12.028

Li, P., Ouyang, Y., Lu, S., Bai, X., Zhang, Y., Shi, L., et al. (2020). Perspective on theoretical methods and modeling relating to electro-catalysis processes. *Chem. Commun.* 56, 9937–9949. doi:10.1039/D0CC02998J

Li, W., Liu, Y., Wu, M., Feng, X., Redfern, S. A. T., Shang, Y., et al. (2018). Carbon-quantum-dots-loaded ruthenium nanoparticles as an efficient electrocatalyst for hydrogen production in alkaline media. *Adv. Mater* 30, e1800676. doi:10.1002/adma.201800676

Li, X.-F., Li, Q.-K., Cheng, J., Liu, L., Yan, Q., Wu, Y., et al. (2016). Conversion of dinitrogen to ammonia by FeN3-embedded graphene. *J. Am. Chem. Soc.* 138, 8706–8709. doi:10.1021/jacs.6b04778

Liang, Y., Li, Y., Wang, H., and Dai, H. (2013). Strongly coupled inorganic/nanocarbon hybrid materials for advanced electrocatalysis. *J. Am. Chem. Soc.* 135, 2013–2036. doi:10.1021/ja3089923

Lin, Z., Waller, G. H., Liu, Y., Liu, M., and Wong, C.-P. (2013). 3D Nitrogen-doped graphene prepared by pyrolysis of graphene oxide with polypyrrole for electrocatalysis of oxygen reduction reaction. *Nano Energy* 2, 241–248. doi:10.1016/j.nanoen.2012.09.002

Ling, C., Bai, X., Ouyang, Y., Du, A., and Wang, J. (2018a). Single molybdenum atom anchored on N-doped carbon as a promising electrocatalyst for nitrogen reduction into ammonia at ambient conditions. *J. Phys. Chem. C* 122, 16842–16847. doi:10.1021/acs.jpcc.8b05257

Ling, C., Cui, Y., Lu, S., Bai, X., and Wang, J. (2022). How computations accelerate electrocatalyst discovery. *Chem* 8, 1575–1610. doi:10.1016/j.chempr.2022.03.015

Ling, C., Niu, X., Li, Q., Du, A., and Wang, J. (2018b). Metal-free single atom catalyst for N₂ fixation driven by visible light. *J. Am. Chem. Soc.* 140, 14161–14168. doi:10.1021/jacs.8b07472

Ling, C., Ouyang, Y., Li, Q., Bai, X., Mao, X., Du, A., et al. (2018c). A general two-step strategy–based high-throughput screening of single atom catalysts for nitrogen fixation. *Small Methods* 3. doi:10.1002/smtd.201800376

Ling, C., Shi, L., Ouyang, Y., Zeng, X. C., and Wang, J. (2017). Nanosheet supported single-metal atom bifunctional catalyst for overall water splitting. *Nano Lett.* 17, 5133–5139. doi:10.1021/acs.nanolett.7b02518

Liu, Smith, S. C., Gu, Y., and Kou, L. (2023). C—N coupling enabled by N—N bond breaking for electrochemical urea production. *Adv. Funct. Mater* 2305894. doi:10.1002/adfm.202305894

Liu, H., Qu, M., Du, A., and Sun, Q. (2023). N_2 reduction in uranium-doped C_2N/C_3N_4 monolayers: a DFT computational study. *New J. Chem.* 47, 13880–13887. doi:10.1039/D3NJ01668D

Liu, M., Zhao, Z., Duan, X., and Huang, Y. (2019). Nanoscale structure design for high-performance Pt-based ORR catalysts. *Adv. Mater* 31, 1802234. doi:10.1002/adma.201802234

Liu, R., Wu, D., Feng, X., and Müllen, K. (2010). Nitrogen-doped ordered mesoporous graphitic arrays with high electrocatalytic activity for oxygen reduction. *Angew. Chem. Int. Ed.* 49, 2565–2569. doi:10.1002/anie.200907289

Liu, X., and Dai, L. (2016). Carbon-based metal-free catalysts. *Nat. Rev. Mater* 1, 16064. doi:10.1038/natrevmats.2016.64

Liu, Y., Xue, Y., Hui, L., Yu, H., Fang, Y., He, F., et al. (2021). Porous graphdiyne loading CoO_x quantum dots for fixation nitrogen reaction. *Nano Energy* 89, 106333. doi:10.1016/j.nanoen.2021.106333

Liu, A, Yang, Y., Kong, D., Ren, X., Gao, M., Liang, X., et al. (2021). DFT study of the defective carbon materials with vacancy and heteroatom as catalyst for NRR. *Appl. Surf. Sci.* 536, 147851. doi:10.1016/j.apsusc.2020.147851

Lorenz, S., Groß, A., and Scheffler, M. (2004). Representing high-dimensional potential-energy surfaces for reactions at surfaces by neural networks. *Chem. Phys. Lett.* 395, 210–215. doi:10.1016/j.cplett.2004.07.076

Man, I. C., Su, H.-Y., Calle-Vallejo, F., Hansen, H. A., Martínez, J. I., Inoglu, N. G., et al. (2011). Universality in oxygen evolution electrocatalysis on oxide surfaces. *ChemCatChem* 3, 1159–1165. doi:10.1002/cctc.201000397

Mao, X., Kour, G., Zhang, L., He, T., Wang, S., Yan, C., et al. (2019a). Silicon-doped graphene edges: an efficient metal-free catalyst for the reduction of CO_2 into methanol and ethanol. *Catal. Sci. Technol.* 9, 6800–6807. doi:10.1039/c9cy01709g

Mao, X., Ling, C., Tang, C., Yan, C., Zhu, Z., and Du, A. (2018). Predicting a new class of metal-organic frameworks as efficient catalyst for bi-functional oxygen evolution/reduction reactions. *J. Catal.* 367, 206–211. doi:10.1016/j.jcat.2018.09.012

Mao, X., Tang, C., He, T., Wijethunge, D., Yan, C., Zhu, Z., et al. (2020b). Computational screening of MN_4 (M = Ti-Cu) based metal organic frameworks for CO_2 reduction using the d-band centre as a descriptor. *Nanoscale* 12, 6188–6194. doi:10.1039/c9nr09529b

Mao, X., Wang, L., Xu, Y., Wang, P., Li, Y., and Zhao, J. (2021). Computational high-throughput screening of alloy nanoclusters for electrocatalytic hydrogen evolution. *npj Comput. Mater.* 7, 46. doi:10.1038/s41524-021-00514-8

Mao, X., Wijethunge, D., Zhang, L., Wang, S., Yan, C., Zhu, Z., et al. (2020a). Metal-free graphene/boron nitride heterointerface for CO_2 reduction: surface curvature controls catalytic activity and selectivity. *EcoMat* 2, e12013. doi:10.1002/eom2.12013

Mao, X., Zhang, L., Kour, G., Zhou, S., Wang, S., Yan, C., et al. (2019c). Defective graphene on the transition-metal surface: formation of efficient bifunctional catalysts for oxygen evolution/reduction reactions in alkaline media. *ACS Appl. Mater Interfaces* 11, 17410–17415. doi:10.1021/acsami.9b02588

Mao, X., Zhou, S., Yan, C., Zhu, Z., and Du, A. (2019b). A single boron atom doped boron nitride edge as a metal-free catalyst for N2 fixation. *Phys. Chem. Chem. Phys.* 21, 1110–1116. doi:10.1039/c8cp07064d

Marenich, A. V., Cramer, C. J., and Truhlar, D. G. (2009). Universal solvation model based on solute electron density and on a continuum model of the solvent defined by the bulk dielectric constant and atomic surface tensions. *J. Phys. Chem. B* 113, 6378–6396. doi:10.1021/jp810292n

Matsumoto, H. Y., and Tamura, H. (1977b). Catalytic activity for electrochemical reduction of oxygen of lanthanum nickel oxide and related oxides. *J. Electroanal. Chem. Interfacial Electrochem.* 79, 319–326. doi:10.1016/S0022-0728(77)80453-1

Matsumoto, H. Y., and Tamura, H. (1977a). Influence of the nature of the conduction band of transition metal oxides on catalytic activity for oxygen reduction. *J. Electroanal. Chem. Interfacial Electrochem.* 83, 237–243. doi:10.1016/S0022-0728(77)80169-1

Mattsson, A. E. (2002). In pursuit of the "divine" functional. *Science* 298, 759–760. doi:10.1126/science.1077710

Melander, M. M., Kuisma, M. J., Christensen, T. E. K., and Honkala, K. (2018). Grand-canonical approach to density functional theory of electrocatalytic systems: thermodynamics of solid-liquid interfaces at constant ion and electrode potentials. *J. Chem. Phys.* 150, 041706. doi:10.1063/1.5047829

Nilsson, A., Pettersson, L. G. M., Hammer, B., Bligaard, T., Christensen, C. H., and Nørskov, J. K. (2005). The electronic structure effect in heterogeneous catalysis. *Catal. Lett.* 100, 111–114. doi:10.1007/s10562-004-3434-9

Nørskov, J. K. (1991). Electronic factors in catalysis. *Prog. Surf. Sci.* 38, 103–144. doi:10.1016/0079-6816(91)90007-Q

Nørskov, J. K., Rossmeisl, J., Logadottir, A., Lindqvist, L., Kitchin, J. R., Bligaard, T., et al. (2004). Origin of the overpotential for oxygen reduction at a fuel-cell cathode. *J. Phys. Chem. B* 108, 17886–17892. doi:10.1021/jp047349j

Nørskov, J. K., Bligaard, T., Logadottir, A., Kitchin, J. R., Chen, J. G., Pandelov, S., et al. (2005). Trends in the exchange current for hydrogen evolution. *J. Electrochem Soc.* 152. doi:10.1149/1.1856988

Nosé, S. (1984). A unified formulation of the constant temperature molecular dynamics methods. *J. Chem. Phys.* 81, 511–519. doi:10.1063/1.447334

Novoselov, K. S., Geim, A. K., Morozov, S. V., Jiang, D., Zhang, Y., Dubonos, S. V., et al. (2004). Electric field effect in atomically thin carbon films. *Science* 306, 666–669. doi:10.1126/science.1102896

Ouyang, T., Ye, Y. Q., Wu, C. Y., Xiao, K., and Liu, Z. Q. (2019). Heterostructures composed of N-doped carbon nanotubes encapsulating cobalt and beta-Mo_2C nanoparticles as bifunctional electrodes for water splitting. *Angew. Chem. Int. Ed.* 58, 4923–4928. doi:10.1002/anie.201814262

Parker, A. J., Opletal, G., and Barnard, A. S. (2020). Classification of platinum nanoparticle catalysts using machine learning. *J. Appl. Phys.* 128, 014301. doi:10.1063/5.0009129

Perdew, J. P., Burke, K., and Ernzerhof, M. (1996). Generalized gradient approximation made simple. *Phys. Rev. Lett.* 77, 3865–3868. doi:10.1103/PhysRevLett.77.3865

Perdew, J. P., Chevary, J. A., Vosko, S. H., Jackson, K. A., Pederson, M. R., Singh, D. J., et al. (1992). Atoms, molecules, solids, and surfaces: applications of the generalized gradient approximation for exchange and correlation. *Phys. Rev. B* 46, 6671–6687. doi:10.1103/PhysRevB.46.6671

Peterson, A. A., Abild-Pedersen, F., Studt, F., Rossmeisl, J., and Nørskov, J. K. (2010). How copper catalyzes the electroreduction of carbon dioxide into hydrocarbon fuels. *Energy Environ. Sci.* 3, 1311–1315. doi:10.1039/C0EE00071J

Powar, N. S., Hiragond, C. B., Bae, D., and In, S.-I. (2022). Two-dimensional metal carbides for electro- and photocatalytic CO_2 reduction: review. *J. CO2 Util.* 55, 101814. doi:10.1016/j.jcou.2021.101814 (

Raciti, D., and Wang, C. (2018). Recent advances in CO_2 reduction electrocatalysis on copper. *ACS Energy Lett.* 3, 1545–1556. doi:10.1021/acsenergylett.8b00553

Ren, X., Lv, Q., Liu, L., Liu, B., Wang, Y., Liu, A., et al. (2020). Current progress of Pt and Pt-based electrocatalysts used for fuel cells. *Sustain. Energy Fuels* 4, 15–30. doi:10.1039/c9se00460b

Ruddigkeit, L., van Deursen, R., Blum, L. C., and Reymond, J.-L. (2012). Enumeration of 166 billion organic small molecules in the chemical universe database GDB-17. *J. Chem. Inf. Model* 52, 2864–2875. doi:10.1021/ci300415d

Ruiyi, L., Keyang, H., Pengwu, X., Wendong, W., Nana, L., Haiyan, Z., et al. (2021). Synthesis of a ruthenium–graphene quantum dot–graphene hybrid as a promising single-atom catalyst for electrochemical nitrogen reduction with ultrahigh yield rate and selectivity. *J. Mater Chem. A* 9, 24582–24589. doi:10.1039/d1ta07158k

Samal, P. P., Poonam, and Krishnamurty, S. (2021). Substrate augmented catalytic activity towards NRR: a case study of Li doped Al clusters on defective graphene. *Appl. Surf. Sci.* 566, 150586. doi:10.1016/j.apsusc.2021.150586

Seh, Z. W., Kibsgaard, J., Dickens, C. F., Chorkendorff, I., Nørskov, J. K., and Jaramillo, T. F. (2017). Combining theory and experiment in electrocatalysis: insights into materials design. *Science* 355, eaad4998. doi:10.1126/science.aad4998

Song, H., Yu, J., Tang, Z., Yang, B., and Lu, S. (2022). Halogen-doped carbon dots on amorphous cobalt phosphide as robust electrocatalysts for overall water splitting. *Adv. Energy Mater* 12, 2102573. doi:10.1002/aenm.202102573

Stamenkovic, V. R., Mun, B. S., Arenz, M., Mayrhofer, K. J. J., Lucas, C. A., Wang, G., et al. (2007). Trends in electrocatalysis on extended and nanoscale Pt-bimetallic alloy surfaces. *Nat. Mater* 6, 241–247. doi:10.1038/nmat1840

Stephens, P. J., Devlin, F. J., Chabalowski, C. F., and Frisch, M. J. (1994). *Ab initio* calculation of vibrational absorption and circular dichroism spectra using density functional force fields. *J. Phys. Chem.* 98, 5. doi:10.1021/j100096a001

Sui, S., Wang, X., Zhou, X., Su, Y., Riffat, S., and Liu, C.-J. (2017). A comprehensive review of Pt electrocatalysts for the oxygen reduction reaction: nanostructure, activity, mechanism and carbon support in PEM fuel cells. *J. Mater Chem. A* 5, 1808–1825. doi:10.1039/C6TA08580F

Sun, S., Zhang, G., Gauquelin, N., Chen, N., Zhou, J., Yang, S., et al. (2013). Single-atom catalysis using Pt/graphene achieved through atomic layer deposition. *Sci. Rep.* 3, 1775. doi:10.1038/srep01775

Sun, Y., Cai, P., Yang, D., and Yao, X. (2022). Single-site catalysis in heterogeneous electro-Fenton reaction for wastewater remediation. *Chem. Catal.* 2, 679–692. doi:10.1016/j.checat.2022.02.002

Takamoto, S., Shinagawa, C., Motoki, D., Nakago, K., Li, W., Kurata, I., et al. (2022). Towards universal neural network potential for material discovery applicable to arbitrary combination of 45 elements. *Nat. Commun.* 13, 2991. doi:10.1038/s41467-022-30687-9

Tang, Y., Yang, C., Xu, X., Kang, Y., Henzie, J., Que, W., et al. (2022). MXene nanoarchitectonics: defect-engineered 2D MXenes towards enhanced electrochemical water splitting. *Adv. Energy Mater* 12, 2103867. doi:10.1002/aenm.202103867

Tao, J., Perdew, J. P., Staroverov, V. N., and Scuseria, G. E. (2003). Climbing the density functional ladder: nonempirical meta--generalized gradient approximation designed for molecules and solids. *Phys. Rev. Lett.* 91, 146401. doi:10.1103/PhysRevLett.91.146401

Tao, L., Qiao, M., Jin, R., Li, Y., Xiao, Z., Wang, Y., et al. (2019). Bridging the surface charge and catalytic activity of a defective carbon electrocatalyst. *Angew. Chem. Int. Ed.* 58, 1019–1024. doi:10.1002/anie.201810207

Thomas, L. H. (1927). The calculation of atomic fields. *Math. Proc. Camb. Philosophical Soc.* 23, 542–548. doi:10.1017/S0305004100011683

Tolba, S. A., Gameel, K. M., Ali, B. A., Almossalami, H. A., and Allam, N. K. (2018). The DFT+ U: approaches, accuracy, and applications. *Density Funct. Calculations-Recent Progresses Theory Appl.* 1, 5772.

Tran, K., and Ulissi, Z. W. (2018). Active learning across intermetallics to guide discovery of electrocatalysts for CO_2 reduction and H_2 evolution. *Nat. Catal.* 1, 696–703. doi:10.1038/s41929-018-0142-1

Turner John, A. (2004). Sustainable hydrogen production. *Science* 305, 972–974. doi:10.1126/science.1103197

Unke, O. T., Chmiela, S., Sauceda, H. E., Gastegger, M., Poltavsky, I., Schütt, K. T., et al. (2021). Machine learning force fields. *Chem. Rev.* 121, 10142–10186. doi:10.1021/acs.chemrev.0c01111

van der Ham, C. J., Koper, M. T., and Hetterscheid, D. G. (2014). Challenges in reduction of dinitrogen by proton and electron transfer. *Chem. Soc. Rev.* 43, 5183–5191. doi:10.1039/c4cs00085d

Wan, X., Zhang, Z., Niu, H., Yin, Y., Kuai, C., Wang, J., et al. (2021). Machine-learning-accelerated catalytic activity predictions of transition metal phthalocyanine dual-metal-site catalysts for CO_2 reduction. *J. Phys. Chem. Lett.* 12, 6111–6118. doi:10.1021/acs.jpclett.1c01526

Wang, B., and Zhang, F. (2022). Main descriptors to correlate structures with the performances of electrocatalysts. *Angew. Chem. Int. Ed.* 61, e202111026. doi:10.1002/anie.202111026

Wang, F., and Mao, J. (2021). Effect of N-doping on graphene: NRR activity and N-source. *Diam. Relat. Mater* 118, 108494. doi:10.1016/j.diamond.2021.108494

Wang, X., Jia, Y., Mao, X., Liu, D., He, W., Li, J., et al. (2020a). Edge-rich $Fe-N_4$ active sites in defective carbon for oxygen reduction catalysis. *Adv. Mater* 32, 2000966. doi:10.1002/adma.202000966

Wang, X., Jia, Y., Mao, X., Zhang, L., Liu, D., Song, L., et al. (2020b). A directional synthesis for topological defect in carbon. *Chem* 6, 2009–2023. doi:10.1016/j.chempr.2020.05.010

Wexler, R. B., Martirez, J. M. P., and Rappe, A. M. (2018). Chemical pressure-driven enhancement of the hydrogen evolving activity of Ni_2P from nonmetal surface doping interpreted via machine learning. *J. Am. Chem. Soc.* 140, 4678–4683. doi:10.1021/jacs.8b00947

Whipple, D. T., and Kenis, P. J. A. (2010). Prospects of CO_2 utilization via direct heterogeneous electrochemical reduction. *J. Phys. Chem. Lett.* 1, 3451–3458. doi:10.1021/jz1012627

White, J. A., and Bird, D. M. (1994). Implementation of gradient-corrected exchange-correlation potentials in Car-Parrinello total-energy calculations. *Phys. Rev. B* 50, 4954–4957. doi:10.1103/PhysRevB.50.4954

Wu, J., Ma, L., Yadav, R. M., Yang, Y., Zhang, X., Vajtai, R., et al. (2015). Nitrogen-doped graphene with pyridinic dominance as a highly active and stable electrocatalyst for oxygen reduction. *ACS Appl. Mater Interfaces* 7, 14763–14769. doi:10.1021/acsami.5b02902

Wu, J., Ma, S., Sun, J., Gold, J. I., Tiwary, C., Kim, B., et al. (2016). A metal-free electrocatalyst for carbon dioxide reduction to multi-carbon hydrocarbons and oxygenates. *Nat. Commun.* 7, 13869. doi:10.1038/ncomms13869

Wu, Q., Jia, Y., Liu, Q., Mao, X., Guo, Q., Yan, X., et al. (2022). Ultra-dense carbon defects as highly active sites for oxygen reduction catalysis. *Chem*. doi:10.1016/j.chempr.2022.06.013

Wu, Y., Wei, W., Yu, R., Xia, L., Hong, X., Zhu, J., et al. (2022). Anchoring sub-nanometer Pt clusters on crumpled paper-like MXene enables high hydrogen evolution mass activity. *Adv. Funct. Mater* 32, 2110910. doi:10.1002/adfm.202110910,

Xie, T., Wang, P., Tian, C., Zhao, G., Jia, J., He, C., et al. (2022). Adsorption characteristics of gas molecules adsorbed on graphene doped with Mn: a first principle study. *Molecules* 27. doi:10.3390/molecules27072315

Xiong, Y., Dong, J., Huang, Z.-Q., Xin, P., Chen, W., Wang, Y., et al. (2020). Single-atom Rh/N-doped carbon electrocatalyst for formic acid oxidation. *Nat. Nanotechnol.* 15, 390–397. doi:10.1038/s41565-020-0665-x

Xu, H., Han, Y., Wu, Q., Jia, Y., Li, Q., Yan, X., et al. (2023). Iridium-based electrocatalysts for the acidic oxygen evolution reaction: engineering strategies to enhance the activity and stability. *Mater Chem. Front.* 7, 1248–1267. doi:10.1039/D2QM01220K

Xu, S., and Carter, E. A. (2019). Theoretical insights into heterogeneous (Photo) electrochemical CO_2 reduction. *Chem. Rev.* 119, 6631–6669. doi:10.1021/acs.chemrev.8b00481

Yan, X., Jia, Y., Chen, J., Zhu, Z., and Yao, X. (2016). Defective-activated-carbon-supported Mn-Co nanoparticles as a highly efficient electrocatalyst for oxygen reduction. *Adv. Mater* 28, 8771–8778. doi:10.1002/adma.201601651

Yan, X., Jia, Y., Wang, K., Jin, Z., Dong, C.-L., Huang, Y.-C., et al. (2020). Controllable synthesis of $Fe-N_4$ species for acidic oxygen reduction. *Carbon Energy* 2, 452–460. doi:10.1002/cey2.47

Yan, X., Zhuang, L., Zhu, Z., and Yao, X. (2021). Defect engineering and characterization of active sites for efficient electrocatalysis. *Nanoscale* 13, 3327–3345. doi:10.1039/d0nr08976a

Yan, Y., Xia, B. Y., Zhao, B., and Wang, X. (2016). A review on noble-metal-free bifunctional heterogeneous catalysts for overall electrochemical water splitting. *J. Mater Chem. A* 4, 17587–17603. doi:10.1039/c6ta08075h

Yang, Q., Jia, Y., Wei, F., Zhuang, L., Yang, D., Liu, J., et al. (2020). Understanding the activity of $Co-N_4-xC_x$ in atomic metal catalysts for oxygen reduction catalysis. *Angew. Chem. Int. Ed.* 59, 6122–6127. doi:10.1002/anie.202000324

Yang, Q., Liu, H., Yuan, P., Jia, Y., Zhuang, L., Zhang, H., et al. (2022). Single carbon vacancy traps atomic platinum for hydrogen evolution catalysis. *J. Am. Chem. Soc.* 144, 2171–2178. doi:10.1021/jacs.1c10814

Yang, W., Gao, Z., Ding, X., Lv, G., and Yan, W. (2018). The adsorption characteristics of mercury species on single atom iron catalysts with different graphene-based substrates. *Appl. Surf. Sci.* 455, 940–951. doi:10.1016/j.apsusc.2018.06.031

Yang, W., Jia, Z., Zhou, B., Chen, L., Ding, X., Jiao, L., et al. (2023). Why is C–C coupling in CO_2 reduction still difficult on dual-atom electrocatalysts? *ACS Catal.*, 9695–9705. doi:10.1021/acscatal.3c01768

Yang, X.-F., Wang, A., Qiao, B., Li, J., Liu, J., and Zhang, T. (2013). Single-atom catalysts: a new frontier in heterogeneous catalysis. *Acc. Chem. Res.* 46, 1740–1748. doi:10.1021/ar300361m

Yasin, G., Ibraheem, S., Ali, S., Arif, M., Ibrahim, S., Iqbal, R., et al. (2022). Defects-engineered tailoring of tri-doped interlinked metal-free bifunctional catalyst with lower gibbs free energy of OER/HER intermediates for overall water splitting. *Mater. Today Chem.* 23, 100634. doi:10.1016/j.mtchem.2021.100634

Ye, L., Ying, Y., Sun, D., Zhang, Z., Fei, L., Wen, Z., et al. (2020). Highly efficient porous carbon electrocatalyst with controllable N-species content for selective CO_2 reduction. *Angew. Chem. Int. Ed.* 59, 3244–3251. doi:10.1002/anie.201912751

Ye, S., Luo, F., Zhang, Q., Zhang, P., Xu, T., Wang, Q., et al. (2019). Highly stable single Pt atomic sites anchored on aniline-stacked graphene for hydrogen evolution reaction. *Energy Environ. Sci.* 12, 1000–1007. doi:10.1039/c8ee02888e

Yin, H., and Du, A. (2023). Activating the hydrogen evolution reaction in low-dimensional carbon by partial hydrogenation: role of the hybrid sp^2-sp^3 orbital interface. *ChemPhysMater.* doi:10.1016/j.chphma.2022.12.001

Yu, X., Han, P., Wei, Z., Huang, L., Gu, Z., Peng, S., et al. (2018). Boron-doped graphene for electrocatalytic N_2 reduction. *Joule* 2, 1610–1622. doi:10.1016/j.joule.2018.06.007

Zha, W., Liu, D., Ma, Z., Wang, Y., Wei, Y., Ma, X., et al. (2021). Efficient electrochemical CO_2 reduction on C_2N monolayer supported transition metals trimer catalysts: a DFT study. *Appl. Surf. Sci.* 564, 150331. doi:10.1016/j.apsusc.2021.150331

Zhang, B.-W., Yang, H.-L., Wang, Y.-X., Dou, S.-X., and Liu, H.-K. (2018). A comprehensive review on controlling surface composition of Pt-based bimetallic electrocatalysts. *Adv. Energy Mater* 8, 1703597. doi:10.1002/aenm.201703597

Zhang, H., Liu, Y., Chen, T., Zhang, J., Zhang, J., and D Lou, X. W. (2019). Unveiling the activity origin of electrocatalytic oxygen evolution over isolated Ni atoms supported on a N-doped carbon matrix. *Adv. Mater* 31, e1904548. doi:10.1002/adma.201904548

Zhang, I. Y., and Xu, X. (2020). On the top rung of Jacob's ladder of density functional theory: toward resolving the dilemma of SIE and NCE. *WIREs Comput. Mol. Sci.* 11. doi:10.1002/wcms.1490

Zhang, L., Fischer, J. M. T. A., Jia, Y., Yan, X., Xu, W., Wang, X., et al. (2018). Coordination of atomic Co–Pt coupling species at carbon defects as active sites for oxygen reduction reaction. *J. Am. Chem. Soc.* 140, 10757–10763. doi:10.1021/jacs.8b04647

Zhang, L., Jia, Y., Yan, X., and Yao, X. (2018). Activity origins in nanocarbons for the electrocatalytic hydrogen evolution reaction. *Small* 14, 1800235. doi:10.1002/smll.201800235

Zhang, N., Yang, B., Liu, K., Li, H., Chen, G., Qiu, X., et al. (2021). Machine learning in screening high performance electrocatalysts for CO_2 reduction. *Small Methods* 5, 2100987. doi:10.1002/smtd.202100987

Zhao, X., and Liu, Y. (2021). Origin of selective production of hydrogen peroxide by electrochemical oxygen reduction. *J. Am. Chem. Soc.* 143, 9423–9428. doi:10.1021/jacs.1c02186

Zhao, X., Zhao, K., Liu, Y., Su, Y., Chen, S., Yu, H., et al. (2022). Highly efficient electrochemical CO2 reduction on a precise homonuclear diatomic Fe–Fe catalyst. *ACS Catal.* 12, 11412–11420. doi:10.1021/acscatal.2c03149

Zhao, Y., Schultz, N. E., and Truhlar, D. G. (2006). Design of density functionals by combining the method of constraint satisfaction with parametrization for thermochemistry, thermochemical kinetics, and noncovalent interactions. *J. Chem. Theory Comput.* 2, 364–382. doi:10.1021/ct0502763

Zhao, Y., and Truhlar, D. G. (2006). A new local density functional for main-group thermochemistry, transition metal bonding, thermochemical kinetics, and noncovalent interactions. *J. Chem. Phys.* 125, 194101. doi:10.1063/1.2370993

Zhao, Y., and Truhlar, D. G. (2008). Density functionals with broad applicability in chemistry. *Acc. Chem. Res.* 41, 157–167. doi:10.1021/ar700111a

Zheng, J., Sun, X., Qiu, C., Yan, Y., Yao, Z., Deng, S., et al. (2020). High-throughput screening of hydrogen evolution reaction catalysts in MXene materials. *J. Phys. Chem. C* 124, 13695–13705. doi:10.1021/acs.jpcc.0c02265

Zheng, Y., Jiao, Y., and Qiao, S. Z. (2015). Engineering of carbon-based electrocatalysts for emerging energy conversion: from fundamentality to functionality. *Adv. Mater* 27, 5372–5378. doi:10.1002/adma.201500821

Zhou, S., Yang, X., Pei, W., Liu, N., and Zhao, J. (2018). Heterostructures of MXenes and N-doped graphene as highly active bifunctional electrocatalysts. *Nanoscale* 10, 10876–10883. doi:10.1039/c8nr01090k

Zhou, S., Yang, X., Xu, X., Dou, S. X., Du, Y., and Zhao, J. (2020). Boron nitride nanotubes for ammonia synthesis: activation by filling transition metals. *J. Am. Chem. Soc.* 142, 308–317. doi:10.1021/jacs.9b10588

Zhou, Y., Wei, B., Cao, H., An, Z., Li, M., Huo, Y., et al. (2022). Electroreduction of nitrogen to ammonia by single-atom catalysis with synergistic boron-carbon nitrogen nanotubes. *J. Environ. Chem. Eng.* 10, 107752. doi:10.1016/j.jece.2022.107752

Zhu, B., Zhang, L., Xu, D., Cheng, B., and Yu, J. (2017). Adsorption investigation of CO_2 on g-C_3N_4 surface by DFT calculation. *J. CO2 Util.* 21, 327–335. doi:10.1016/j.jcou.2017.07.021

Zhu, M., Zhou, Y., Sun, Y., Zhu, C., Hu, L., Gao, J., et al. (2018). Cobalt phosphide/carbon dots composite as an efficient electrocatalyst for oxygen evolution reaction. *Dalton Trans.* 47, 5459–5464. doi:10.1039/c7dt04291d

Zhu, X., Yan, J., Gu, M., Liu, T., Dai, Y., Gu, Y., et al. (2019). Activity origin and design principles for oxygen reduction on dual-metal-site catalysts: a combined density functional theory and machine learning study. *J. Phys. Chem. Lett.* 10, 7760–7766. doi:10.1021/acs.jpclett.9b03392

Zhuo, J., Wang, T., Zhang, G., Liu, L., Gan, L., and Li, M. (2013). Salts of $C_{60}(OH)_8$ electrodeposited onto a glassy carbon electrode: surprising catalytic performance in the hydrogen evolution reaction. *Angew. Chem. Int. Ed.* 52, 10867–10870. doi:10.1002/anie.201305328

Zou, X., and Zhang, Y. (2015). Noble metal-free hydrogen evolution catalysts for water splitting. *Chem. Soc. Rev.* 44, 5148–5180. doi:10.1039/c4cs00448e

One-dimensional modeling of heterogeneous catalytic chemical looping steam methane reforming in an adiabatic packed bed reactor

Haris Qayyum[1], Izzat Iqbal Cheema[1], Mohsin Abdullah[2], Muhammad Amin[3], Imtiaz Afzal Khan[4], Eui-Jong Lee[5] and Kang Hoon Lee[6]*

[1]Department of Chemical Engineering, University of Engineering and Technology, Lahore, Lahore, Punjab, Pakistan, [2]Department of Energy Systems Engineering, NFC Institute of Engineering and Technology, Multan, Pakistan, [3]Interdisciplinary Research Center for Hydrogen and Energy Storage (Tire II)-Research and Innovation, King Fahd University of Petroleum and Minerals (KFUPM), Dhahran, Saudi Arabia, [4]Department of Civil and Environmental Engineering, Hanyang University, Seoul, Republic of Korea, [5]Department of Environmental Engineering, Daegu University, Gyeongsan, Republic of Korea, [6]Department of Energy and Environmental Engineering, The Catholic University of Korea, Bucheon-si, Republic of Korea

Hydrogen production via chemical looping steam methane reforming (CL-SMR) is among the most promising current technologies. This work presents the development in gPROMS Model Builder 4.1.0® of a 1D model of an adiabatic packed bed reactor used for chemical looping reforming (CLR). The catalyst used for this process was 18 wt. % NiO with the support of Al_2O_3. A brief thermodynamic analysis using Chemical Equilibrium Application (CEA) was carried out to identify the optimum operating conditions. The model was simulated for 10 complete CL-SMR cycles. The effects of variations in temperature, pressure, gas mass velocity, nickel oxide concentration, reactor length, and particle diameter were studied to investigate the performance of the CL-SMR process under these variations. A parametric analysis was carried out for different ranges of conditions: temperatures from 600 to 1,000 K, pressure from 1 to 5 bar, gas mass velocity between 0.5 and 0.9 $kg \cdot m^{-2} s^{-1}$, nickel oxide concentration values between 0.1 and 1 $mol \cdot m^{-3}$, particle diameters between 0.7 and 1 mm, and fuel reactor (FR) lengths between 0.5 and 1.5 m. At the optimum temperature (950 K), pressure (1 bar), and steam-to-carbon molar ratio (3/1), with an increase in particle diameter from 0.7 to 1 mm, an 18% decrease in methane conversion and a 9.5% increase in hydrogen yield were observed. Similarly, with an increase in FR length from 0.5 m to 1.5 m, a delay in the temperature drop was observed.

KEYWORDS

hydrogen, chemical looping, reforming, energy, gPROMS, methane reforming

1 Introduction

During the last couple of decades, global warming has emerged as one of the major problems confronting the Earth's climate. According to an Intergovernmental Panel for Climate Change (IPCC) report, the temperature of the Earth has been rising drastically since 1850, with the last 4 decades (1980–2020) being considered the warmest (Intergovernmental panel of climate change IPCC, 2021). The main reason behind the rise in the temperature of the Earth is excessive emission of greenhouse gases (GHGs), such as N_2O, H_2O, CH_4, CO_2,

SF_6, and chlorofluorocarbons (CFCs), into the atmosphere. CO_2 gas makes the highest contribution to GHGs, at 78% (Abbas et al., 2017). The emission of CO_2 poses a high level of risk to the atmosphere due to its high efficiency in absorbing energy and its emission on a large scale (Rasheed et al., 2019). In 2021, 79% of total world energy was produced from fossil fuels, which emitted a total of 36.64 Gt of CO_2, representing a 10.2% increase over CO_2 emissions observed in 2018 (International Energy Agency IEA, 2022). Furthermore, it is expected that global energy demands will increase by up to 40% by 2040. In 2021, the total energy produced by Pakistan was 75.50 Mtoe, with CO_2 emissions of 219.8 MT, which represents a 251.4% increase in CO_2 emissions as compared to 1990. In comparison to 2021, it is estimated that by 2040 the consumption of natural gas for energy production will increase by up to 35% (Pakistan Energy demand forecast, 2021). With the rising energy demands, limited fossil fuel reserves, and environmental concerns, sustainable alternatives and environmentally friendly sources of energy are attracting attention and demanding greater research focus for the development of improved technology (International Energy Agency, 2017).

Hydrogen is recognized as one of the most suitable energy sources for clean energy production, as combustion of H_2 is free of harmful pollutant emissions; due to this quality, researchers currently consider it to be the fuel of the future (Ma et al., 2016). Water vapor is the only byproduct produced along with energy production during combustion of H_2. No harmful pollutants, such as CO_x, SO_x, particulate matters, or soot, are produced during combustion of H_2 (Sharma and Ghoshal, 2015). H_2 can be used as an energy carrier for both industrial and domestic usage. Due to its high conversion efficiency, low pollution, and recyclability, H_2 is considered to be a perfect energy source (Liu et al., 2020). The combustion of H_2 produces more energy per unit mass than any other fuel, including gasoline, coal, and methane (Dutta, 2014).

The processes used for production of H_2 are gasification, pyrolysis, reforming, and electrolysis (Luo et al., 2018). At present, nearly 96% of the world's H_2 production is fossil fuel-based, for example, from coal, crude oil, and natural gas. Among these, natural gas is the most prominent source used for H_2 production (Omoniyi and Dupont, 2018; Stoppacher et al., 2022). There are numerous methods used for the manufacture of H_2 from natural gas, e.g., partial oxidation (PO_x), steam methane reforming (SMR), and autothermal reforming (ATR). At present, approximately 75% of total H_2 production across the world is SMR-based (Dutta, 2014). The SMR process occurs in two steps (see Appendix B) under mild pressure conditions of 20–35 atm and at an elevated temperature (between 800°C and 1,000°C). In the initial step (Appendix B, equation B1), CH_4 is converted into H_2; in the second step (equation B2), the water–gas shift (WGS) reaction takes place (Jin et al., 2023). The overall chemical reaction of the SMR process (Appendix B) is extremely endothermic and therefore requires an external heat source (Luo et al., 2018).

The main problem in the SMR process is the choice of oxygen transfer material (OTM), which can be tackled by maintaining appropriate specifications, such as high selectivity, high stability, and high reactivity with CH_4, along with high resistance to carbon deposition (Pashchenko, 2018). In order from highest to lowest, the reactivity of OTMs with CH_4 is as follows: NiO, CuO, Mn_2O_3, Fe_2O_3
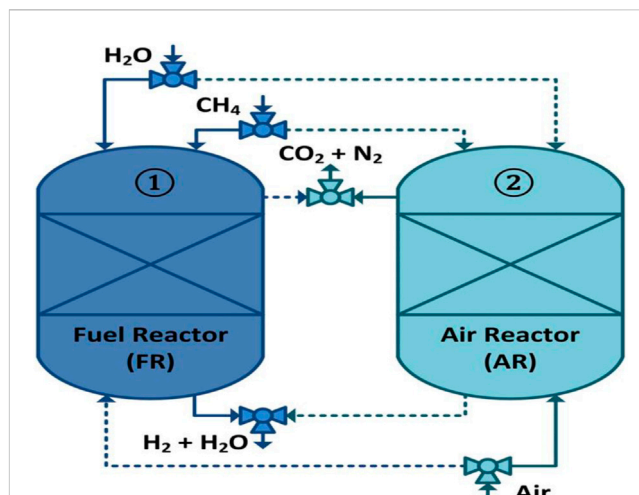
FIGURE 1
Schematic illustration of the CL-SMR process. Solid lines represent active streams, and dotted lines represent streams that are not active.

(Luo et al., 2018). Metallic nickel (Ni) is most often used as a catalyst in the SMR process, and the most widely preferred OTM is also Ni-based oxide (LeValley et al., 2014). The SMR process is quite expensive, as losses in effectiveness occur with the passage of time, along with catalyst degradation (May et al., 1996).

In 2000, the chemical looping reforming (CLR) technique was introduced by Lyon and Cole (Lyon and Cole, 2000). The term *chemical looping* (CL) was given to this approach due to the transportation of oxygen as part of the process. The metal reduced during SMR reactions is subsequently oxidized for the beginning of the new CL cycle; see Figure 1.

The chemical reaction equations for chemical looping–steam methane reforming (CL-SMR) are shown in Appendix B (B1 to B7 and B8 occur in a fuel reactor and an air reactor, respectively) (Luo et al., 2018). The main benefits of CL-SMR over SMR are as follows: 1) no external combustion is required; 2) steam and the catalyst are required in smaller quantities; 3) emission of sulfur pollutants is very low; and 4) there is zero formation of thermal NO_x (Garcia-Labiano et al., 2009; Pröll et al., 2010; Liu et al., 2020). Therefore, chemical looping technology has recently attracted increasing attention, and a great deal of research has been carried out in the development of this technology.

2 Literature review

In the 1950s, Lewis et al. (1951) presented the basic idea of chemical looping to produce CO_2 and syngas by using iron- and copper-based OTMs from carbonaceous fuel. Lewis and Gilliland (Lewis et al., 1954) also introduced the idea of using two interconnected fluidized bed reactors (FBRs) for the circulation of solid particles. The concept was the same as the chemical looping combustion (CLC) process. Later, Richter et al. (1983) recommended the principle of CLC, in which they considered the metal oxides CuO and NiO as OTMs in a formation of connected FBRs to increase the efficiency of a power plant. In

1987, Ishida et al. (1987) introduced the term CLC for the first time. They reduced the exergy losses that occurred during the conversion of fuel-based energy to thermal-based energy in conventional power plants by using natural gas.

The concept of chemical looping reforming (CLR) was originally proposed in 2001 by Mattisson and Lyngfelt (2001). CLR works on the same basic principles as chemical looping combustion (CLC), but instead of thermal-based energy, the end product is H_2. Mattisson et al. (2004) recommended that the oxygen fraction in steam should not be more than 0.3 of the total oxygen in order to maintain a high temperature and promote conversion of CH_4.

2.1 Progress in oxygen carriers

Zafar et al. (2006) tested NiO, CuO, Fe_2O_3, and Mn_2O_3 on two supports, SiO_2 and $MgAl_2O_4$, in a laboratory-scale fluidized bed reactor (FBR). They discovered that $MgAl_2O_4$ showed higher reactivity levels than SiO_2 during redox reactions. For H_2 production from CH_4, Rydén et al. (2008a); Rydén (2008) worked with atmospheric and pressurized CLR processes. Based on their findings, they concluded that the pressurized process achieved 5% higher efficiency due to a reduction in the energy requirements of H_2 compression. Additionally, they tested Fe_2O_3/$MgAl_2O_4$ as an OTM with addition of an NiO layer. They discovered that, with a 1% addition of NiO on the OTM surface, the reactivity increased, and thus the selectivity of CH_4 toward H_2 and CO. Johansson et al. (2008) studied NiO as an OTM on two different supports, $MgAl_2O_4$ and $NiAl_2O_4$. They concluded that NiO/$MgAl_2O_4$ had a lower tendency toward carbon formation and a higher tendency toward CH_4 conversion. Diego et al. (Lu et al., 2018) studied the behavior of NiO as an OTM on several supports, such as γ-Al_2O_3, θ-Al_2O_3, and α-Al_2O_3. They determined that the OTM impregnated on α-Al_2O_3 showed the highest reactivity during the reduction reaction, whereas it showed the lowest reactivity on γ-Al_2O_3. They also observed that, with an increase in the H_2O-to-CH_4 ratio and a decrease in temperature, the deposition of carbon during the reduction reaction occurred. de Diego et al. (2009) also studied the CLR working process with an Ni-based OTM on α-Al_2O_3 and γ-Al_2O_3 supports in a 900 W continuous reactor. They used different operating variables, such as different solid circulation rates, H_2O-to-CH_4 molar ratios from 0 to 0.5, and fuel reactor (FR) temperatures between 800°C and 900°C, to analyze the effects of these variables on CH_4 conversion and product distribution. Rydén et al. (2006); Rydén et al. (2008b); Rydén et al. (2009) tested an Ni-based OTM on different supports, such as α-Al_2O_3, γ-Al_2O_3, $MgAl_2O_4$, and ZrO_2-MgO, in 500 W CLR continuous reactors. They achieved the complete conversion of CH_4 and high selectivity toward H_2 and CO in all units. Pröll et al. (2010) tested an Ni-based OTM on $NiAl_2O_4$-MgO for the CLR process in a 140 kW pilot plant. They analyzed the results in a temperature range between 750°C and 900°C. All the aforementioned studies were conducted at atmospheric pressure. Ortiz et al. (2010) studied the performance of a pressurized CLR process (up to 10 bar) in 900 W units and found results similar to those obtained with OTMs at atmospheric pressure by de Diego et al. (2009). Zainab et al. (Ibrahim et al., 2018) studied the CL reforming of shale gas using NiO on Al_2O_3 and CaO/Al_2O_3 in a packed bed reactor (PBR) at 1 bar, 750°C, and with a

steam-to-carbon molar ratio of 3. They observed that significant deactivation of catalyst (NiO on CaO/Al_2O_3) occurred after consecutive nine redox cycles. Before catalyst deterioration, fuel conversion was above 80%, which shows that steam reforming processes are highly favored by a high temperature.

2.2 Progress in CLR modeling

For the purposes of scale-up, design, and optimization of the CLR process, modeling and simulation of air and fuel-based reactors would appear to be beneficial. Halabi et al. (2008) developed a 1D model of an FBR for investigation of performance in terms of conversion of CH_4, H_2 yield, H_2 purity, and reforming efficiency of autothermal reforming (ATR). They assumed that the process was adiabatic in nature. Monnerat et al. (2003) developed a model for AR to determine the effect of the quantity of O_2 on the temperature of the reactor. They also developed a model of oxidation of an Ni catalyst for unsteady-state conditions. Hoang and Chan (2004) developed a 2D model of the reformer in order to simulate the conversion behavior of the reactant. Zhou et al. (2013) developed a 1D model of a PFR for the reduction and CLC processes, using NiO as a catalyst. They assumed isothermal and isobaric conditions. Adams and Barton (2009) developed a 2D heterogeneous model of PBR for the WGS reaction. The model established could be applied to both low- and high-temperature shift reactions and was also suitable for simulation of a catalyst-based process with known kinetic data. Grigorios et al. (Pantoleontos et al., 2012) developed a model to examine the dynamic behavior of an industrial heterogeneous catalytic packed bed reactor (PBR) for the SMR process. The model described the physicochemical processes that take place in both the gas and solid phases, accounting for diffusional limitations within the catalyst particles.

Ghouse and Adams (2013) developed a 2D heterogeneous model of SMR. They assumed perfect mixing of the species without any carbon deposition. In their work, the equations of energy and mass transfer in the solid and gas phases were considered. Zhou et al. (2015) developed a three-phase hydrodynamic model of CL reduction with NiO as the catalyst and CH_4 as the fuel for the analysis of experimental data. They incorporated pressure change, energy balances, mass balances, and the effect of entrainment of oxygen carriers in the freeboard region, which improves overall fuel combustion efficiency and solid conversion. They also studied the effects of mass transfer, oxygen carrier entrainment, and bubble size on the performance of the CL reducer. They found that smaller bubbles are more desirable to increase fuel combustion efficiency. Morgado et al. (2017) developed an FBR model for comparison of CH_4 conversion, H_2 production, the drop in temperature, and length of reactor for CLR and GSR. This model employed perfect phenomenological closures for the turbulent and fast fluidization regimes and for the bubbling phenomenon. Simulations were carried out to examine the degree of OTM consumption, which is considered to be an important process variable. According to the authors, GSR is more suitable for pure H_2 production with integrated CO_2 capture and CLR for power generation. Diglio et al. (2016) presented work on the numerical analysis of an ATR in a PBR with NiO as the catalyst and CH_4 as fuel. They theoretically

quantified the challenges, such as the choice of the duration of the oxidation and reduction phases, the startup temperature, and the cycle design, through numerical simulation. They concluded that suitable choices of duration for the reduction and oxidation phases and of initial temperature are essential requirements for the performance of the CLR process. Singhal et al. (2017) proposed a multiscale model of a packed bed CLR. They presented a comparison of two reactive flows at two different scales: 1) a particle-resolved direct numerical simulation, and 2) a 1D packed bed model. According to their findings, in order to utilize the model to improve an industrial-scale model, the volume of gas generated by the SMR reaction, reactant diffusion within the particles, and clear reaction order in equilibrium conditions are required.

Chenlong et al. (2019) investigated the CLR process of acetic acid by using Fe-doped $LaNiO_3$ perovskites with different Ni-to-Fe ratios. They found that Ni/Fe perovskites were more stable than $LaNiO_3$ perovskites, although $LaNiO_3$ showed more activity in gas production. Minbeom et al. (Lee et al., 2020) studied the effect of transition metals at B-sites (B = Fe, Ni, Mn) of $LaCoO_3$ on CL-SMR. According to their findings, Fe showed more selective oxidation of methane to syngas, the highest H_2 purity, and the greatest extent of steam regeneration. Dragomir et al. (Bukur et al., 2019) investigated the redox properties of two Ni-based oxygen carriers, namely, Al and Zr. During the CLR process for successive cycles, with the help of a thermogravimetric analyzer and an *in situ* magnetometer, they found that a high degree of redox activity was seen during cyclic study of CL-SMR using the Zr-supported oxygen carrier than using the Al-supported oxygen carrier, and that the degree of redox activity increased gradually with the number of cycles. On the other hand, they observed moderate crystalline growth during Al use, while there was a decrease in crystalline size during the use of Zr.

Mathematical modeling of various sub-models, such as AR (oxidation of catalyst), FR (SMR with reduction of catalyst), and the WGS reaction of the CL-SMR process, has been reported on in the literature. However, to the best of the authors' knowledge, model-based study of CL-SMR with NiO as a catalyst in a PBR at low pressure and with different OTM particle diameters has not yet been considered. Therefore, in this work, we considered a 1D mathematical model of the CL-SMR process in a PBR with NiO as a catalyst at low pressure (1 bar). For the implementation of the model and to determine the effects of various operating conditions, parameters such as temperature, pressure, gas mass flow velocity, void fraction, and particle diameter were considered.

3 Methodology

In this section, a one-dimensional heterogenous model is considered in order to understand the behavior of the physicochemical processes involved in CL-SMR; the material balance and energy balance in the gaseous and solid phases are implemented along with the model assumptions. Subsequently, a thermodynamic analysis is considered in order to determine the optimum operational conditions. Finally, the implementation of model in gPROMS, along with boundary and initial conditions, is discussed.

In the implementation of the model, the following assumptions have been adopted, in consideration of work by Abbas et al. (2017):

a) The reactor is operating under adiabatic conditions, with no heat entering or leaving the system. The main purpose of assuming the system to be adiabatic is to study the behavior of the temperature within the reactor under different conditions.
b) This model is applicable for ideal behavior, because the gases used in the system are considered to be ideal gases and equation used for these gases is the ideal gas equation.
c) Temperature change in the catalyst is not considered, as the changes within the catalyst are negligible and to consider these would makes the model very complex and sensitive. Due to this sensitivity, it would be very difficult to study the model under different operating conditions.
d) In the reactor, the plug flow pattern of gases and the temperature and concentration gradients along the length of the reactor are considered. In comparison to the axial direction, negligible changes in temperature and concentration are observed in the radial direction.

The model equations consist of equations representing material and energy balance for the gaseous phase (Eqs. 1, 2) and the solid phase (Eqs. 3, 4), and the pressure drop (Eq. 5).

$$\varepsilon_b\left(\frac{\partial C_i}{\partial t}\right) + \left(\frac{\partial u C_i}{\partial z}\right) + k_{g,i}\, a_v\, \left(C_i - C_{i,s}\right) = \varepsilon_b\, D_z\left(\frac{\partial^2 C_i}{\partial z^2}\right) \quad (1)$$

$$\varepsilon_b\, \rho g\left(\frac{\partial T}{\partial t}\right) + u\rho\, C_{pg}\left(\frac{\partial T}{\partial z}\right) = h_f a_v\, (Ts - T) + \lambda z^f\left(\frac{\partial^2 T}{\partial z^2}\right) \quad (2)$$

$$k_{g,i}\, a_v\, \left(C_i - C_{i,s}\right) = (1 - \varepsilon_b)\, \rho_{cat}\, r_{i+} v\rho_{cat}\, r_i \quad (3)$$

$$\rho_{bed}\, C_{p,bed}\left(\frac{\partial T_s}{\partial t}\right) + h_f\, a_v\, (T_s - T) = v(1 - \varepsilon_b)\, \rho_{cat}\Sigma - H_{rxn,j}\eta_j R_j \quad (4)$$

$$\frac{\Delta P g_c}{L} = \left(\frac{150}{d_p{}^2}\right)\left(\frac{(1 - \varepsilon_b)^2}{\varepsilon_b{}^3}\right)u\, \mu + \left(\frac{1.75}{d_p}\right)\left(\frac{(1 - \varepsilon_b)^2}{\varepsilon_b{}^3}\right)\rho_g\, u^2 \quad (5)$$

The supporting equations required for the calculation of the physical property terms used in mathematical model Eqs. 1–3 and Eq. 4 to Eq. 5 are provided in Supplementary Table SA; these include the dispersion coefficient (Supplementary Equation SA1), thermal conductivities (Supplementary Equations SA1, SA3), the mass transfer coefficient along with its supportive dimensionless numbers (Supplementary Equations SA1–SA7), and the heat transfer coefficient along with its supportive dimensionless number (Supplementary Equations SA8–SA11).

Additionally, the material balance for the chemical reactions (Supplementary Equations SB1–SB4) involves oxygen transfer material, as expressed by Eqs. 6, 7. It is important to mention that, in order to reduce the complexity of the model, only major chemical reactions are considered; minor or side reactions, such as methane decomposition, carbon gasification with steam, and dry methane reforming, have been neglected. With this assumption, the overall model-based results still represent the real process with error below 1% (Rasheed et al., 2019).

$$\frac{dC_{Ni}}{dt} = (2R_1 + R_2 + R_3 + R_4)M_{Ni} \quad (6)$$

$$\frac{dC_{Nio}}{dt} = -(2R_1 + R_2 + R_3 + R_4)M_{NiO} \quad (7)$$

In Eqs. 6, 7, R_1 to R_4 represent the reaction rate of the chemical reaction Supplementary Equations SB1–SB4, respectively. The

TABLE 1 Initial and boundary conditions required for modeling of Chemical Looping Steam methane reforming (CL-SMR).

Initial conditions	
$C_{i,o}$/mol m^{-3} where $i\epsilon$ {CH$_4$, CO, H$_2$, H$_2$O, CO$_2$ and N$_2$}	[2.53, 0, 0.11, 7.6, 0, 2.53]
$C_{NiO,o}$/mol m^{-3}	0.1
T_o/K	950
P_o/bar	1
$T_{s,o}$/K	950
X/%	0
Boundary conditions	
Inlet of reactor ($z = 0$)	Outlet of reactor ($z = L$)
$C_i = C_{i,o}$; $T = T_o$; $P = P_o$; $T_s = T_{s,o}$	$(\frac{\partial C_i}{\partial t})= 0$; $(\frac{\partial T}{\partial z})= 0$; $(\frac{\partial T_s}{\partial z})= 0$

TABLE 2 Parameters used in the implementation of CL-SMR model (Abbas et al., 2017).

Parameters	Values
Void fraction, ε_b/μm	0.50
Reactor length, L/m	1.50
Specific surface area per unit volume, a_v/m^2 m^{-3}	300
Density of catalyst, ρ_{cat}/kg m^{-3}	550
Density of catalyst bed, ρ_{bed}/kg m^{-3}	1,625
Heat capacity of bed, Cp$_{bed}$/J kg K^{-1}	980
Viscosity of gases, μ_g/kg m^{-1} s^{-1}	0.0181E-3
Particle diameter, d_p/m	0.0010
Avg. molecular diffusivity, D_m/m^2 s^{-1}	1.6E-5
Gas mass velocity, G_s/kg m^{-2} s^{-1}	0.50
Thermal conductivity of gases, λ_g/W m^{-1} K^{-1}	3E-2
Thermal conductivity of solids, λ_s/W m^{-1} K^{-1}	13.80
Avg. molecular weight, M_{av}/g mol^{-1}	20.02
Molecular weight of Ni, M_{Ni}/g mol^{-1}	58.69
Molecular weight of NiO, M_{NiO}/g mol^{-1}	74.69
Initial specific surface area of OTM, a_o/m^2 kg$_{carrier}$	102

required reaction rate equations for R_1 (Supplementary Equation SB1), R_2 (Supplementary Equation SB2), R_3 (Supplementary Equation SB3), and R_4 (Supplementary Equation SB4) are provided in Supplementary Appendix SB.

3.1 Implementation of the model

For prediction of the behavior of the reactors (fuel and air) shown in Figure 1, the differential and algebraic equations, along with boundary and initial conditions, were implemented in gPROMS Model Builder 4.1.0®. The initial and boundary

conditions used in solving model equations 12 to 18 are provided in Table 1. The first-order BFDM was used to solve Eqs. 12–18, A.1 to A.11 (Supplementary Appendix SA), and B.1 to B.14 (Supplementary Appendix SB).

From Supplementary Appendix SB, it can be seen that initially (at t = 0), there is no trace of gaseous stream present in the reactor, but a small amount of H$_2$ has been considered, because with a zero value the rate of reaction of the reforming reactions (equations B.5 to B.7) becomes infinite due to the denominator term in the rate equation; therefore, a minute quantity of H$_2$ has been fed into the reactor along with the reactant concentration in order to simulate the reactor model thoroughly, as listed in Table 2. Additionally, the parameters required to simulate the model in gPROMS are provided in Table 2.

4 Thermodynamic analysis of CL-SMR

To determine the optimum operational conditions of the CL-SMR process, thermodynamic analysis needs to be carried out under equilibrium conditions. In this section, the Chemical Equilibrium Application (CEA) software is used to generate the results for the equilibrium conditions.

Minimization of Gibbs free energy is the basis of the CEA software (Rydén et al., 2009). The gases species H$_2$, H$_2$O, CO, CO$_2$, CH$_4$, O$_2$, N$_2$, Ni, and NiO were considered in implementation of the thermodynamic analysis in CEA. The stoichiometric molar balance of N$_2$ was used for calculation of the equilibrium output of each component, which further assisted in the determination of the total product moles at equilibrium. The effects of pressure and temperature on X_{CH_4}, H$_2$ purity, and H$_2$ yield were examined under equilibrium conditions with the help of CEA and the built model (Eqs. 1–7; Supplementary Appendix SA, Supplementary Equations S1–S11; Supplementary Appendix SB, Supplementary Equations B1–B14). Eqs. 8–10 were used for calculation of the fraction of X_{CH_4}, H$_2$ purity, and H$_2$ yield, respectively.

$$X_{CH_4} = \frac{\dot{n}_{CH_4,in} - \dot{n}_{CH_4,out}}{\dot{n}_{CH_4,in}} \quad (8)$$

$$H_2 \text{ purity} = \frac{\dot{n}_{H_2,out}}{\dot{n}_{CH_4,out} + \dot{n}_{H_2,out} + \dot{n}_{CO,out} + \dot{n}_{CO_2,out}} \quad (9)$$

$$H_2 \text{ yield} = \frac{M_{H_2} \times \dot{n}_{H_2,out}}{M_{CH_4} \times \dot{n}_{CH_4,in}} \quad (10)$$

The performance of CL-SMR for a steam-to-carbon (S/C) molar ratio of 3 and an NiO/C ratio of 1/1 was examined to determine the effect of temperature between 600 and 1,000 K and the effect of pressure between 1 and 5 bar under equilibrium conditions with the help of CEA.

4.1 Outputs of chemical equilibrium of CL-SMR

The effects of temperature and pressure on X_{CH_4}, H$_2$ purity, and H$_2$ yield are shown in Figures 2, 3, respectively. In addition, comparisons are also made between the CEA-based and model-based results. It is important to mention that Figures 2, 3 show only the results for optimum pressure and temperature, respectively.
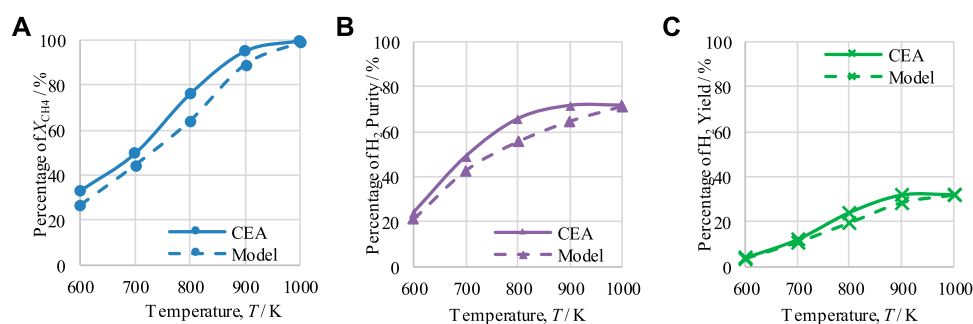
FIGURE 2
Thermodynamic analysis of the CL-SMR process at 1 bar, S/C M ratio of 3, and NiO-to-C molar ratio of 1/1, indicating the effect of temperature on **(A)** X_{CH4}, **(B)** H_2 purity, and **(C)** H_2 yield.
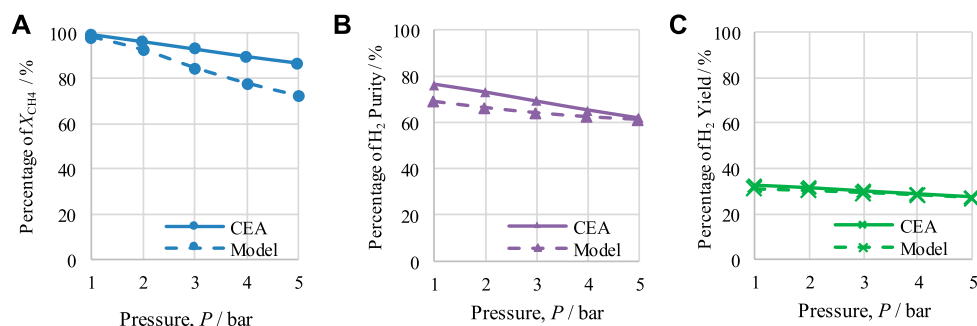
FIGURE 3
Thermodynamic analysis of the CL-SMR process at 950 K, S/C M ratio of 3, and NiO-to-C molar ratio of 1/1, indicating the effect of pressure on **(A)** X_{CH4}, **(B)** H_2-purity, and **(C)** H_2-yield.

CEA plots of CH_4 conversion, H_2 purity, and H_2 yield at 600–1000 K for pressure ranging from 1 to 5 bar are presented in Supplementary Appendix SC (see Supplementary Figures C1–C3).

The results for X_{CH_4}, H_2 purity, and H_2 yield at 1 bar are shown in Figure 2. It can be seen that, at 1 bar, increasing the temperature from 600 to 950 K also induces an increase in CH_4 conversion, H_2 purity, and H_2 yield from 33% to 99.2%, 24.3%–71.5%, and 4%–32.1%, respectively. From 950 K onward, a minor change in the CH_4 conversion value is observed, and a decline in observed for H_2 purity and H_2 yield. Therefore, 950 K is considered to be the optimal operating temperature for CL-SMR for attainment of maximum H_2 purity and yield. The average difference between the CEA and model-based results was calculated by dividing the sum of the difference between CEA and model-based results by the total number of points; this resulted in differences of 5.97% for X_{CH_4}, 5.53% for H_2 purity, and 1.91% for H_2 yield.

Figure 3 shows the effects of varying pressure between 1 and 5 bar. The operating conditions for the equilibrium study of CL-SMR of 950 K, an S/C M ratio of 3, and an NiO-to-C of 1/1 are maintained. It can be seen that with the rise in the operating pressure from 1 to 5 bar the values for CH_4 conversion, H_2 purity, and H_2 yield decrease from 99.2% to 86.6%, 76.5% to 61.3%, and 32.6% to 27.5%, respectively. Therefore, it can be concluded that, under the conditions implemented, the most suitable operating pressure for

the CL-SMR process is 1 bar. The average difference calculated were 7.7% for X_{CH4}, 4.52% for H_2 purity, and 0.85% for H_2 yield.

As the CEA values are based on equilibrium conditions, the model values should not be higher than those generated using CEA. Comparing the results of both studies, CEA and model-based, it can be observed from Figures 2, 3 that the model-based study values did not exceed the equilibrium values of the CEA results, falling below them in all cases; this is acceptable and proves the correctness of the model.

5 Results and discussion

In this section, the developed models of the FR and AR are first validated with experimental results given in the literature. Subsequently, a cyclic study of the CL-SMR process is conducted and the behavior of the gases and OTM is observed for 10 cycles. Finally, sensitivity analyses are performed for the variables C_{NiO}, G_s, and d_p.

5.1 Validation of the model

This section describes the validation of the model of the CL-SMR process. Validation is performed in two steps: first, the FR model results are discussed and validated in connection with
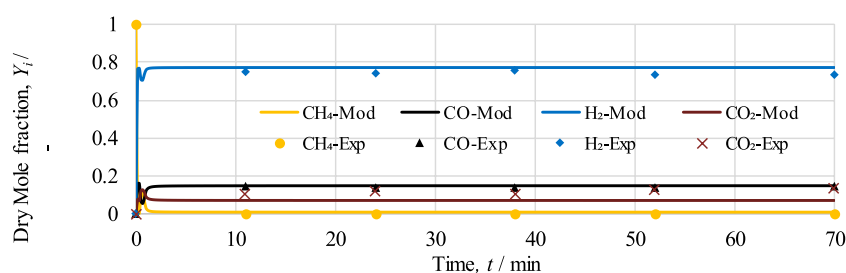
FIGURE 4
Dry mole fraction of outlet gases, $y_i \in \{CH_4, H_2, CO, CO_2\}$, at 973 K, 1 bar, and S/C of 2. Solid lines represent the modeling data (MOD), while markers represent the values in the experimental data (EXP).

experimental results found in the literature. Subsequently, validation of the AR model is performed separately.

5.1.1 Fuel reactor

To authenticate the developed model of the fuel reactor (FR) considered in CL-SMR, the work of Pooya *et al.* (Azadi et al., 2011) is used. Pooya *et al.* considered 10% NiO as the OTM in an adiabatic packed bed reactor of length 60 cm and 10 cm internal diameter. The operational conditions of 973 K and 1 bar along, with 5% CH_4 and 10% H_2O in N_2 feed gas, are considered for model validation. The mole fractions of gases in dry conditions obtained from experimental and model-based works are given in Figure 4. It is important to mention that during the experimental study (Azadi et al., 2011), a delay of 30 min was observed by Pooya *et al.* at beginning of the experiment. Essentially, this time delay was due to the induction period of gases in the reformer. However, for model validation, this experimental time delay has been neglected, as induction period was not considered, and values are adjusted accordingly.

In Figure 4, it can be seen that initially variation can be observed at the start of the model-based results, which is essentially due to the occurrence of reduction and SMR reactions. Once the reactions proceed, within less than 2 min, methane conversion approaches 100%, and the mole fraction of H_2 increases from 0% to 77% and subsequently remains constant throughout the process. The average differences between model and experimental values for CH_4, CO, H_2, and CO_2 are 0.9%, 0.7%, 2.7%, and 4.8%, respectively. Based on the trends, it can be determined that model-based results are in good accordance with the experimental values for the stable range of 11 min onward. However, due to the unavailability of experimental data for the time interval between 0 and 11 min, the dynamic response occurring in the experimental work cannot be compared.

5.1.2 Air reactor

The experimental work by Monnerat et al. (2003) used for the validation of the model in terms of OTM in the air reactor. An adiabatic packed bed reactor of length 230 mm and internal diameter 9 mm was used for oxidation of the catalyst. First, the temperature profiles from the model-based and experimental work are compared for operational pressure 1.5 bar and 10% O_2 in feed gas; see Figure 5A. Subsequently, 10% O_2 feed intake under temperature and pressure conditions of 773 K and 1.5 bar is considered; see Figure 5B.

As shown in Figure 5A, a rapid initial increase in temperature is observed due to the exothermic nature of the oxidation process; specifically, at the beginning of the process, all the Ni is available for oxidation. After 45 s, a decrease in temperature is observed due to the decrease in the Ni concentration. From the initial temperature of 773 K, a maximum temperature rise of 51 K is observed in the model-based work, whereas in the experimental study, a 51 K rise is observed. After 180 s of operation, the temperature reaches 776 K or 781 K in the model-based and experimental studies, respectively. The average temperature difference between the model and experimental results is 5.6 K. As shown in Figures 5A, B sudden initial rise in the amount of O_2 at exit of the AR occurs until 70 s. After that, the slope in the curve representing the amount of O_2 at exit of the AR decreases, becoming a horizontal straight line until 200 s. After 75 s of operation, the dry mole fraction of O_2 at exit of the AR reaches 0.085 or 0.071 in the model-based and experimental results, respectively. The average difference in the O_2 mole fraction between the model and experimental results is 0.012. Overall, based on the figure, it can be seen that the model results are in good agreement with the experimental work.

5.2 Cyclic study of the CL-SMR process

The optimum operating conditions have already been determined by the thermodynamic analysis using CEA for the cyclic study of the CL-SMR process, as shown in Figure 1. In the FR in CL-SMR, a feed consisting of CH_4 gas, steam, and N_2 is introduced at 950 K, at 1 bar, and with a steam-to-carbon (S/C) molar ratio of 3/1. As shown in Figure 6, it can be observed that with entrance of the feed into the fuel reactor (FR), an immediate decrease in temperature is observed, specifically, a drop of approximately 11 K within 10 s. This decrease in temperature is due to the dominance of the endothermic nature of the reduction reaction. Subsequently, between 10 and 50 s, a further drop in temperature of 5 K is observed; in this phase, the chemical reactions, which are exothermic in nature, show their dominance along with the reduction reactions. Within less than a minute (50 s), almost 95% of the NiO is converted into Ni, catalyzing the SMR reaction. Within another minute (specifically, between 50 and 110 s), the temperature further drops; specifically, it falls by more than 10 times (from 933 to 775 K). This drop is due to the dominance of the SMR reaction, which is highly endothermic in
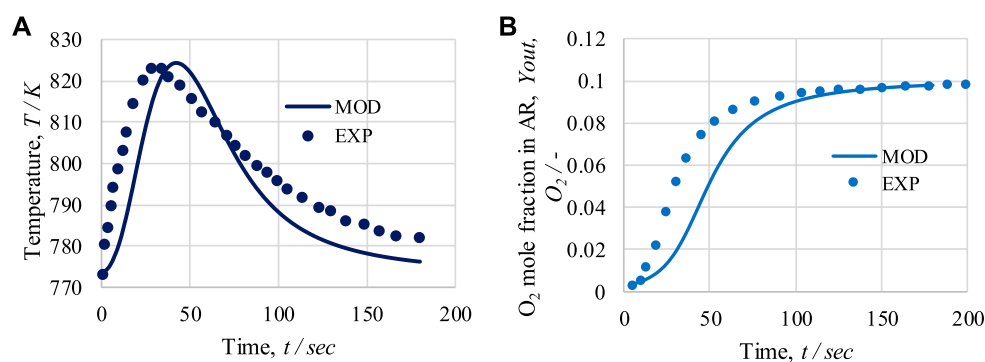
FIGURE 5
For the air reactor: **(A)** temperature profile at 1.5 bar and 10 mol% of O_2 in feed; **(B)** O_2 mole fraction at the outlet for 773 K, 1.5 bar, and 10 mol% of O_2 in feed. Solid lines represent modeling (MOD) results; markers represent experimental (EXP) results.
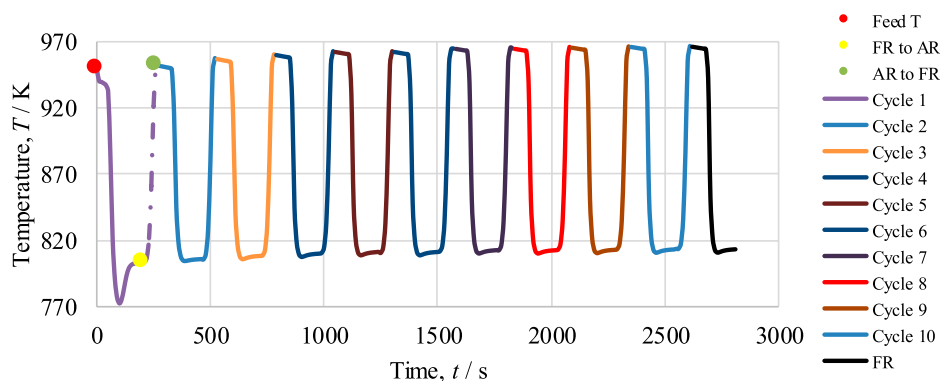
FIGURE 6
Cyclic study of the CL–SMR process for 10 cycles. The red dot indicates the start of the fuel reactor (FR) cycle; the yellow dot indicates the end of the FR cycle and start of the in reactor (AR) cycle; and the green dot indicates the end of the AR cycle.

nature. Subsequently, a rise in the temperature of the process from 775 to 803 K is observed; this rise is due to the exothermic nature of the WGS reaction. After 190 s, an overall drop in NiO % conversion and temperature can be observed; these fall by approximately 99.5% and 146 K, respectively. The yellow dot in Figure 6 indicates the end of the fuel reactor cycle, and from here onward, the air reactor cycle begins.

In the second part of CL-SMR, the reduced Ni is transferred into the air reactor (AR) for oxidation by injection of air (21% O_2 and 79% N_2) at 1 bar and 804 K. As soon as the feed has passed through the reactor, the temperature of the reactor increases from 804 to 952 K within 70 s. Subsequently, the temperature of the air reactor (AR) starts decreasing due to the decrease in the concentration of available Ni for oxidation. For reduction reaction and SMR reaction, a higher temperature is needed in the fuel reactor (FR), so the oxidation process stops when the temperature reaches 952 K. Subsequently, the feed is turned off for the AR and turned on for the FR. The green dot indicates the completion of the AR cycle, as well as the combined completion of the AR and FR cycles; see Figure 6. The FR and AR cycles together form a complete CL-SMR cycle. The CL-SMR process was studied for ten cycles. The behavior and concentrations of

gases (CH_4, CO, CO_2, H_2, H_2O, and NiO) during these ten cycles are shown in Figure 7. Each cycle of CL-SMR took 280 s to complete (see Figure 6). In the initial two cycles of the CL-SMR process, these is some variation in the outlet concentrations of gases and OTM. After this point, the variation in the concentrations of gases disappears as the number of cycles increases and the process moves toward the steady state. Values for X_{CH4}, H_2 purity, and H_2 yield for this ten-cycle study are presented in Figure 8. In every cycle, 97.5% CH_4 conversion, 69% H_2 purity, and an overall H_2 yield of 27.5% were achieved.

5.2.1 Comparison of outlet concentrations and reaction rates during cycles 1 and 2

The outlet concentrations of gases during cycles 1 and 2 are shown in Figure 9. In the pre-breakthrough period, both the cycles show the same kind of variation in the outlet concentrations of gases. However, during the breakthrough period (i.e., from 70 s to 110 s), both the figures show differences in the variation in the outlet concentrations of gases, mainly for H_2 and H_2O. After 100 s, the concentrations of H_2 and H_2O during cycle 1 are 4.77 mol·m^{-3} and 5.49 mol·m^{-3}, respectively, while during cycle 2, the concentrations
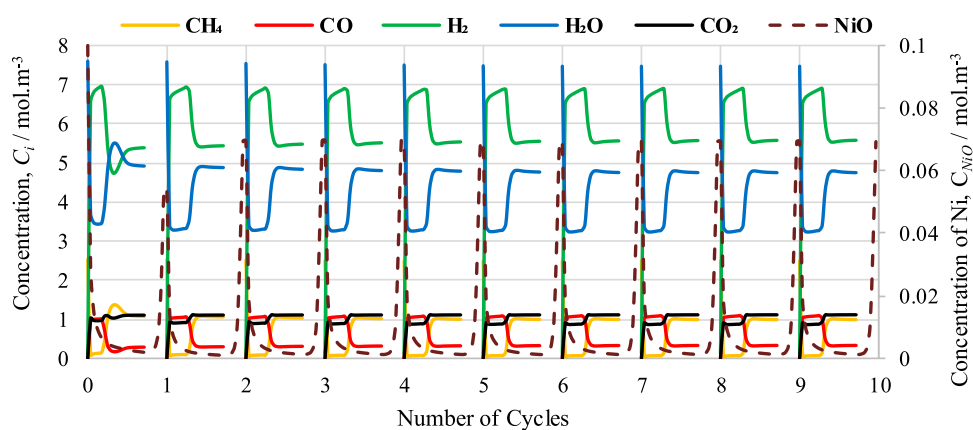
FIGURE 7
Cyclic study of outlet concentration of gases: CH_4, CO, CO_2, H_2, H_2O, and NiO.
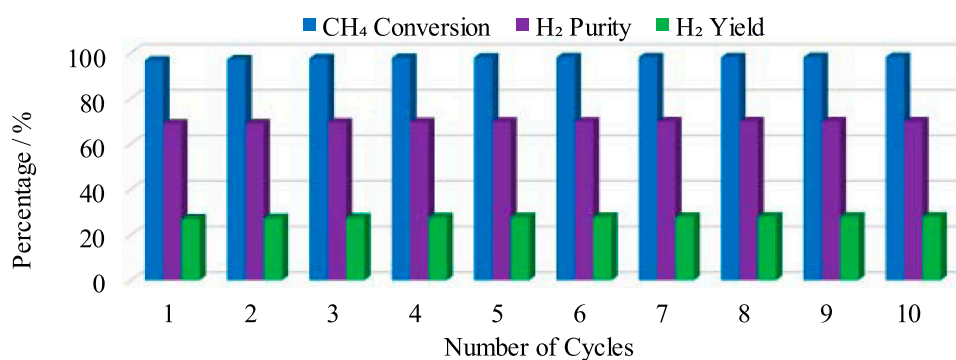
FIGURE 8
X_{CH4}, H_2 purity, and H_2 yield during a cyclic study of the CL-SMR process for 10 cycles.
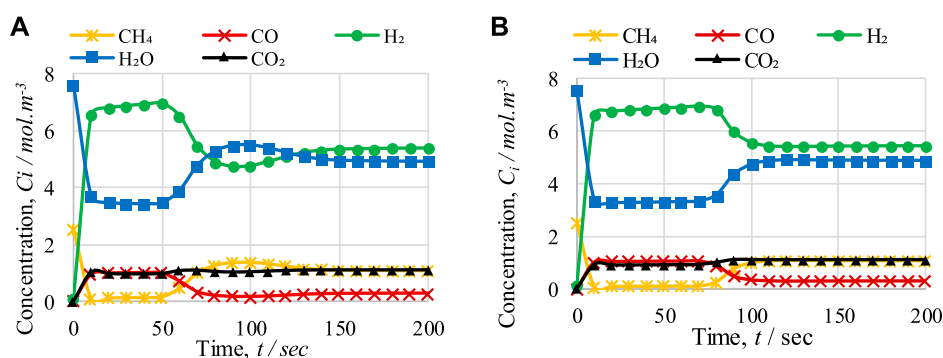
FIGURE 9
Comparison of FR outlet concentrations of gases with respect to time during **(A)** cycle 1 and **(B)** cycle 2 of CL-SMR.

of H_2 and H_2O are 5.56 mol·m^{-3} and 4.73 mol·m^{-3}, respectively; this inconsistency is due to the difference in temperature drop between the cycles. In Figure 6, it can be seen that after 100 s of operation, the temperature drops to 772 K in cycle 1 and 804 K in cycle 2. This

difference of 32 K is the main reason for the difference in the variation in the outlet concentration of gases, because the optimum temperature range for the SMR reaction is 900–1,100 K. As shown in Figures 9A, B, it can be observed that
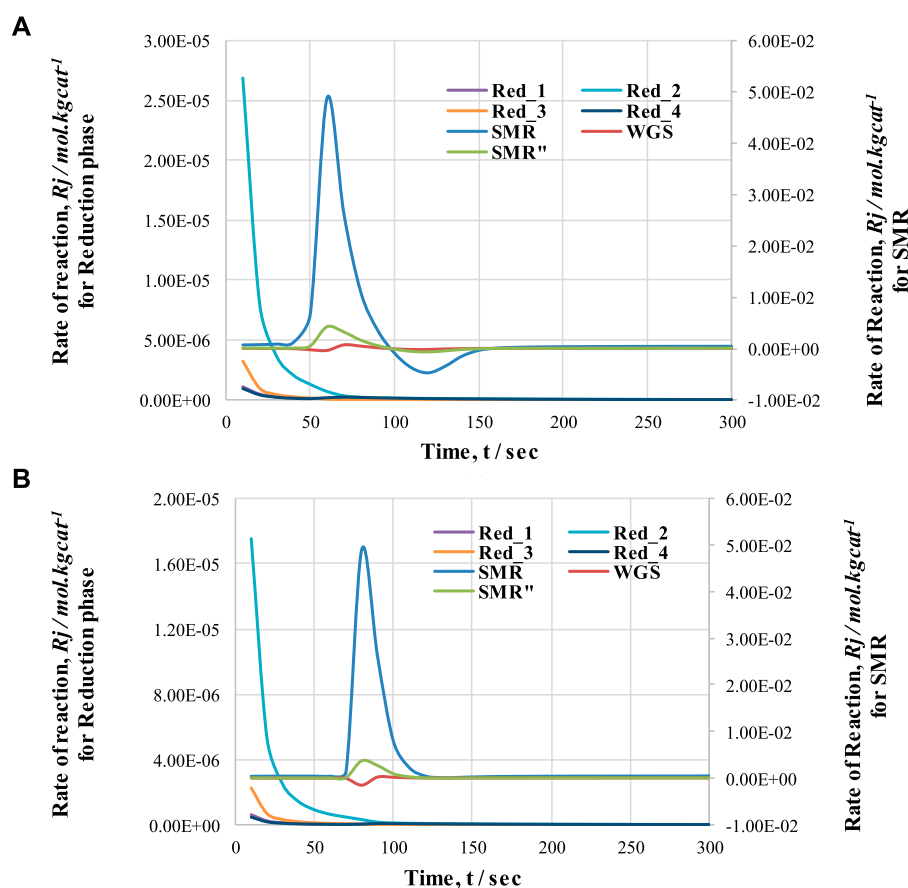
FIGURE 10
Comparison of rate of reactions (SMR and reduction) with respect to time during **(A)** cycle 1 and **(B)** cycle 2 of CL-SMR.

in the pre-breakthrough period, a drop of 2.44 mol·m^{-3} and 3.9 mol·m^{-3} (cycle 1) and 2.442 mol·m^{-3} and 4.3 mol·m^{-3} (cycle 2) occurs in the concentration of CH_4 and H_2O, respectively. In contrast, a rise of 6.59, 0.97, and 0.98 mol·m^{-3} (cycle 1) and 6.61, 1.03, and 0.92 mol·m^{-3} (cycle 2) can be observed in the concentration of H_2, CO, and CO_2, respectively.

Figure 10 shows the rate of reactions for cycle 1 and cycle 2. This graph indicates that the reduction reactions are so fast that they show variation in the reaction rate within the first 20 s of the process, and convert all the NiO into Ni. The drop and rise in the concentrations of gases during first the 20 s is due to the activation of reduction reactions; in these reactions, NiO reacts with CH_4 to form H_2, CO, and CO_2. A decrease in CH_4 concentration and increases in H_2, CO, and CO_2 concentration can be observed. Subsequently, until 60 s, the change in gas concentrations remains constant; at this point, the pre-breakthrough period ends and the breakthrough period begins. Unlike the pre-breakthrough period, during the breakthrough period the concentrations of CH_4 and H_2O increase, whereas the concentration of H_2 decreases. This large change in concentration is due to the activation of the SMR reaction, which is highly endothermic. The SMR reaction is more dominant than the other two reactions (WGS and overall SMR) here. This change in reaction rate also indicates the reason for the change in concentrations of outlet gases from the FR.

5.3 Sensitivity analysis

In this section, a sensitivity analysis is carried out by observing the impact of concentration of NiO (C_{NiO}) and gas mass velocity (G_s) on the temperature profile of the CL-SMR process, as well as the impact of particle diameter (d_P) and reactor length L on CH_4 conversion, H_2 purity, and H_2 yield.

5.3.1 Effect of C_{NiO} and G_s

The effects of NiO concentration (C_{NiO}) and G_s on the temperature of the fuel reactor (FR) were studied; the results are presented in Figures 11A, B, respectively. In Figure 11A, it can be seen that with a rise in the NiO concentration, the duration of the pre-breakthrough period increases because of the greater amount of NiO available for reduction reactions, but the drop in temperature decreases, e.g., from 155 to 24 K for a change in NiO concentration in the FR from 0.1 to 1 mol·m^{-3}. The reduction in the temperature drop is due to the smaller amount of CH_4 available for the SMR reaction, which is highly endothermic in nature, as more CH_4 is consumed during the reduction reactions because of the larger amount of NiO. In contrast, in Figure 11B, it can be seen that with an increase in the value of G_s from 0.5 to 0.9 kg m^{-2} s^{-1}, the duration of the pre-breakthrough period decreases, as the reactants remain lower in the reactor at the higher value of G_s. With an increase in G_s, the drop in temperature increases from 150 to 190 K.
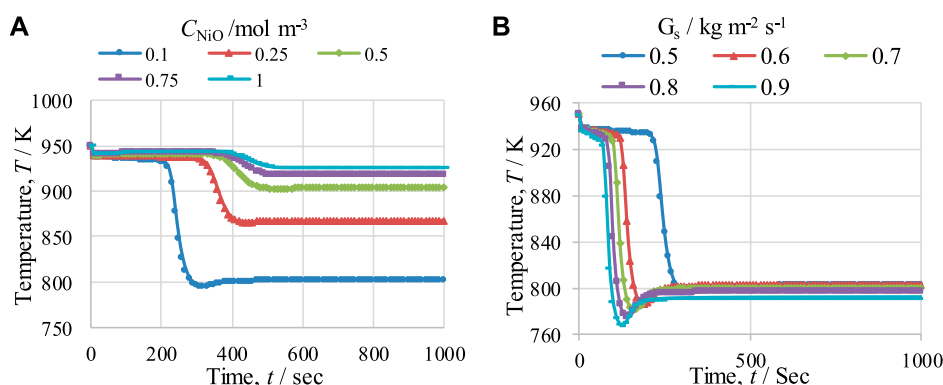
FIGURE 11
Temperature profiles for the fuel reactor (FR) at 950 K, at 1 bar, and with a steam-to-carbon molar ratio of 3, showing the effects of **(A)** NiO concentration (C_{NiO}) and **(B)** gas mass flow velocity (G_s).
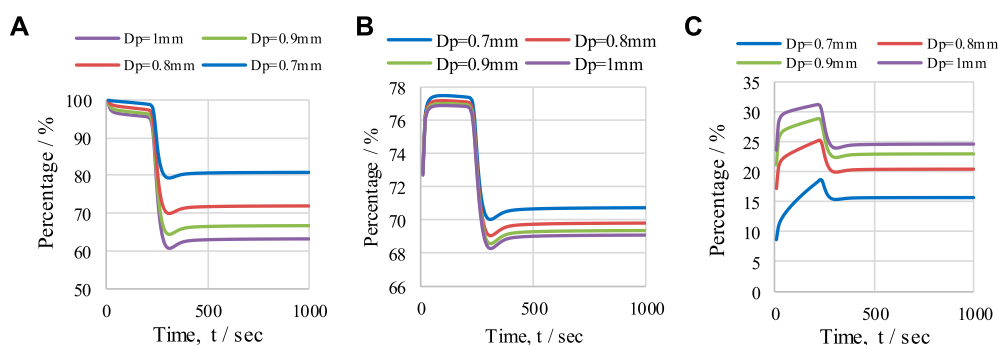
FIGURE 12
The effect of OTM particle diameter (0.7–1 mm) under operating conditions of 950 K, with S/C M ratio of 3, on **(A)** X_{CH4}, **(B)** H_2 purity, and **(C)** H_2 yield. Effect of reactor length (L) on temperature (T) profile.

This is because the availability of gas for the SMR reaction per unit area and time is enhanced with the increase in G_s, and so the temperature drop also increases. Similarly, at lower values of Gs, more CH_4 is consumed before the breakthrough period in the reduction reaction and less CH_4 is available for the SMR reaction, which reduces the temperature drop during the breakthrough period.

5.3.2 Effect of particle diameter

The effect of OTM particle diameter was studied to observe the overall performance of the CL-SMR process. The operating conditions of 950 K, 1 bar, and an S/C M ratio of 3 were maintained. The values of X_{CH4}, H_2 purity, and H_2-yield, for particle diameters ranging from 0.7 to 1 mm, are presented in Figure 12. A decrease in X_{CH4} from 81% to 63% is observed as the diameter of the particles increases from 0.7 to 1 mm; see Figure 12A. Similarly, a minor decrease in H_2 purity (see Figure 12B) from 71% to 69% is also observed with this increase in the OTM particle diameter. This is because, with an increase in the size of OTM particles, less surface area is available to the gases for reaction, and therefore reductions in CH_4 conversion and H_2 purity is detected. The size of the OTM particle is inversely proportional to

CH_4 conversion and H_2 purity. On the other hand, H_2 yield in the CL-SMR process increases from 15.5% to 25% (see Figure 12C) with the increase in particle diameter from 0.7 to 1 mm. This increase in H_2 yield is due to more formation of H_2 per unit mole of CH_4 entering the reactor. However, in the reactor, the variation in X_{CH4}, H_2 purity, and H_2-yield over time directly relates to the temperature variation.

5.3.3 Effect of Reactor Length (L) on Temperature (T) profile

The effect of FR length on temperature variation in the reactor at pressure of 1 bar, a temperature of 950K, and with an S/C ratio of 3 over a given period of time is presented in Figure 13. The behavior of the temperature profile in the reactor was examined for three different lengths of reactor (namely, 0.5 m, 1 m, and 1.5 m). From the graph, it can be seen that with an increase in the length of the FR, a delay in the temperature drop is observed, while the temperature profiles were almost identical for all lengths of reactor. This delay in temperature drop is because of the time taken to consume the oxygen carrier during the reduction reaction in the reactor: as the length of the reactor increases, the length of the bed of OTM also increases. The maximum temperature drops for 0.5 m, 1 m, and
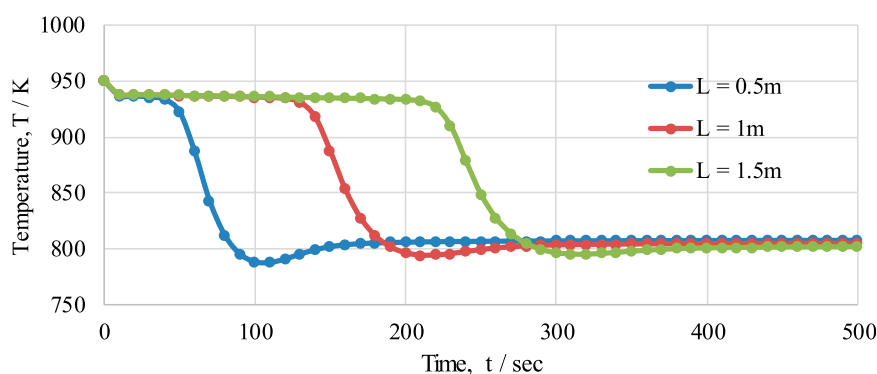
FIGURE 13
The effect of different fuel reactor lengths (0.5 m, 1 m, and 1.5 m) on the temperature profile of the fuel reactor in the CL-SMR process.

1.5 m length are 163 K, 157 K, and 152 K, respectively; similarly, the amounts of time taken to reach the steady state are 200 s, 300 s, and 400 s, respectively, as shown in the figure.

6 Conclusion and outlook

A one-dimensional simulation of a heterogenous catalytic CL-SMR process in an adiabatic PBR, at low pressure, was conducted in gPROMS Model Builder®. First, a thermodynamic analysis of the process was carried out, using CEA, to identify the optimum temperature (950 K) and pressure (1 bar) conditions for the CL-SMR process at an S/C M ratio of 3. Next, the effects of temperature and pressure on X_{CH4}, H_2 yield, and H_2 purity in the CL-SMR process were studied at equilibrium conditions; the findings were compared with the results of the validated model. The effects of increasing temperature (from 600 to 1000 K) and pressure (from 1 to 5 bar) on X_{CH4}, H_2 yield, and H_2 purity in the CL-SMR process were positive and negative, respectively. This adiabatic model of the CL-SMR process was run for 10 cycles. It was observed that during each cycle the changes in the values of X_{CH4}, H_2 purity, and H_2 yield were negligible.

The effect of reaction rate, along with a comparison of the first two cycles of CL-SMR, were also presented. The behavior of temperature in the FR was examined for different values of Gs (0.5–0.9 kg m^{-2} s^{-1}) and C_{NiO} (0.1–1 mol m^{-3}). It was concluded that, with an increase in the value of G_s, the delay in the temperature drop or the duration of pre-breakthrough period was decreased. An increase in the concentration of NiO was found to reduce the temperature drop in the FR. The effect of OTM particle diameter on CL-SMR performance was also studied. It was concluded that, with decrease in particle size from 1 to 0.7 mm, there was an increase in X_{CH4} and H_2 purity, but a decrease in H_2 yield. Finally, the effect of reactor length on the temperature variation profile within the fuel reactor was also studied, with three different lengths examined (0.5 m, 1 m, and 1.5 m). With an increase in the length of the FR, a delay in the temperature drop and activation of the SMR was observed, while the behavior of the temperature profile remained the same for each length. From this study, it can be concluded that the model developed here is effective and that the process runs at optimum temperature and pressure values for 10 cycles without any change in OTM concentration or products.

Data availability statement

The original contributions presented in the study are included in the article/Supplementary Material, further inquiries can be directed to the corresponding author.

Author contributions

HQ: Conceptualization, Investigation, Methodology, Writing–original draft. IC: Data curation, Formal Analysis, Investigation, Visualization, Writing–review and editing. MoA: Data curation, Software, Validation, Visualization, Writing–review and editing. MuA: Data curation, Methodology, Validation, Visualization, Writing–review and editing. IK: Data curation, Formal Analysis, Validation, Visualization, Writing–review and editing. E-JL: Project administration, Resources, Supervision, Writing–review and editing. KL: Funding acquisition, Project administration, Supervision, Writing–review and editing.

Funding

Acknowledgments

Conflict of interest

The authors declare that the research was conducted in the absence of any commercial or financial relationships that could be construed as a potential conflict of interest.

Publisher's note

All claims expressed in this article are solely those of the authors and do not necessarily represent those of their affiliated organizations, or those of the publisher, the editors and the reviewers. Any product that may be evaluated in this article, or claim that may be made by its manufacturer, is not guaranteed or endorsed by the publisher.

Supplementary material

The Supplementary Material for this article can be found online at: https://www.frontiersin.org/articles/10.3389/fchem.2023.1295455/full#supplementary-material

References

Abbas, S. Z., Dupont, V., and Mahmud, T. (2017). Modelling of high purity H2 production via sorption enhanced chemical looping steam reforming of methane in a packed bed reactor. Fuel 202, 271–286. doi:10.1016/j.fuel.2017.03.072

Adams, T. A., and Barton, P. I. (2009). A dynamic two-dimensional heterogeneous model for water gas shift reactors. Int. J. Hydrogen Energy 34, 8877–8891. doi:10.1016/j.ijhydene.2009.08.045

Azadi, P., Otomo, J., Hatano, H., Oshima, Y., and Farnood, R. (2011). Interactions of supported nickel and nickel oxide catalysts with methane and steam at high temperatures. Chem. Eng. Sci. 66, 4196–4202. doi:10.1016/j.ces.2011.06.002

Bukur, D. B., Silvester, L., Fischer, N., Claeys, M., and Lemonidou, A. A. (2019). On the use of an in situ magnetometer to study redox and sintering properties of NiO based oxygen carrier materials for chemical looping steam methane reforming. Int. J. Hydrogen Energy 44, 18093–18102. doi:10.1016/j.ijhydene.2019.05.045

Chenlong, L., Sha, L., chen, D., Xiao, Y., Tianle, L., and Wang, W. (2019). Hydrogen-rich syngas production by chemical looping steam reforming of acetic acid as bio-oil model compound over Fe-doped LaNiO3 oxygen carriers, 17732–17741.Hydrogen energy

de Diego, L. F., Ortiz, M., García-Labiano, F., Adánez, J., Abad, A., and Gayán, P. (2009). Hydrogen production by chemical-looping reforming in a circulating fluidized bed reactor using Ni-based oxygen Carriers. J. Power Sources 192, 27–34. doi:10.1016/j.jpowsour.2008.11.038

Diglio, G., Bareschino, P., Mancusi, E., and Pepe, F. (2016). Simulation of hydrogen production through chemical looping reforming process in a packed-bed reactor. Chem. Eng. Res. Des. 105, 137–151. doi:10.1016/j.cherd.2015.11.013

Dueso, C., Ortiz, M., Abad, A., García-Labiano, F., Luis, F., Gayán, P., et al. (2012). Reduction and oxidation kinetics of nickel-based oxygen-carriers for chemical-looping combustion and chemical-looping reforming. Chem. Eng. J. 188, 142–154. doi:10.1016/j.cej.2012.01.124

Dutta, S. (2014). A review on production, storage of hydrogen and its utilization as an energy resource. J. Industrial Eng. Chem. 20, 1148–1156. doi:10.1016/j.jiec.2013.07.037

Edwards, M., and Richardson, J. (1968). Gas dispersion in packed beds. Chem. Eng. Sci. 23, 109–123. doi:10.1016/0009-2509(68)87056-3

Fan, J., Zhu, J., Jiang, L., Li, P., and Liu, H. (2016). Comparative exergy analysis of chemical looping combustion thermally coupled and conventional steam methane reforming for hydrogen production. J. Clean. Prod. 131, 247–258. doi:10.1016/j.jclepro.2016.05.040

Garcia-Labiano, F., de Diego, L. F., Gayan, P., Adanez, J., Abad, A., and Dueso, C. (2009). Effect of fuel gas composition in chemical-looping combustion with Ni-based oxygen carriers. 1. Fate of sulfur. Ind. Eng. Chem. Res. 48, 2499–2508. doi:10.1021/ie801332z

Geankoplis, C. J. (1993). Transport processes and unit operations.

Ghouse, J. H., and Adams, T. A. (2013). A multi-scale dynamic two-dimensional heterogeneous model for catalytic steam methane reforming reactors. Int. J. Hydrogen Energy 38, 9984–9999. doi:10.1016/j.ijhydene.2013.05.170

Halabi, M., De Croon, M., Van der Schaaf, J., Cobden, P., and Schouten, J. (2008). Modeling and analysis of auto thermal reforming of methane to hydrogen in a fixed bed reformer. Chem. Eng. J. 137, 568–578. doi:10.1016/j.cej.2007.05.019

Handley, D., and Heggs, P. J. (1969). The effect of thermal conductivity of the packing material on transient heat transfer in a fixed bed. Int. J. Heat. Mass Transf. 12, 549–570. doi:10.1016/0017-9310(69)90038-6

Hoang, D. L., and Chan, S. H. (2004). Modeling of a catalytic autothermal methane reformer for fuel cell applications. Appl. Catal. A General 268, 207–216. doi:10.1016/j.apcata.2004.03.056

Ibrahim, Z., Dupont, V., and Mahmud, T. (2018). Steam reforming of shale gas in a packed bed reactor with and without chemical looping using nickel-based oxygen carrier. Int. J. hydrogen energy 43, 6904–6917. doi:10.1016/j.ijhydene.2018.02.083

Iliuta, I., Tahoces, R., Patience, G. S., Rifflart, S., and Luck, F. (2010). Chemical-looping combustion process: kinetics and mathematical modeling. AIChE J. 56, 1063–1079. doi:10.1002/aic.11967

Intergovernmental panel of climate change (IPCC) (2021). The physical science basis. Available at: https://www.ipcc.ch/report/ar6/wg1/downloads/report/IPCC_AR6_WGI_SPM.pdf.

International Energy Agency (2017). International energy outlook. Available at: https://www.eia.gov/outlooks/ieo/pdf/0484(2017).pdf.

International Energy Agency (IEA) (2022). World energy outlook. Available at: https://iea.blob.core.windows.net/assets/830fe099-5530-48f2-a7c1-11f35d510983/WorldEnergyOutlook2022.pdf.

Ishida, M., Zheng, D., and Akehata, T. (1987). Evaluation of a chemical-looping-combustion power-generation system by graphic exergy analysis. Energy 12, 147–154. doi:10.1016/0360-5442(87)90119-8

Jin, G., Li, K., Zhang, L., Luo, Y., Chen, D., and dong He, D. (2023). In situ observation of the promoting effect of H2S on the formation of efficient MoS2 catalyst for CH4/CO2 reforming. Sep. Purif. Technol. 308 (2023), 122883. doi:10.1016/j.seppur.2022.122883

Jin, H., and Ishida, M. (2002). Reactivity study on natural-gas-fueled chemical-looping combustion by a fixed-bed reactor. Industrial Eng. Chem. Res. 41, 4004–4007. doi:10.1021/ie020184l

Johansson, M., Mattisson, T., Lyngfelt, A., and Abad, A. (2008). Using continuous and pulse experiments to compare two promising nickel-based oxygen carriers for use in chemical-looping technologies. Fuel 87, 988–1001. doi:10.1016/j.fuel.2007.08.010

Lee, M., Lim, H. S., Kim, Y., and Lee, J. W. (2020). Enhancement of highly-concentrated hydrogen productivity in chemical looping steam methane reforming using Fe-substituted LaCoO3. Energy Convers. Manag. 207, 112507–118904. doi:10.1016/j.enconman.2020.112507

LeValley, T. L., Richard, A. R., and Fan, M. (2014). The progress in water gas shift and steam reforming hydrogen production technologies–a review. Int. J. hydrogen energy 39, 16983–17000. doi:10.1016/j.ijhydene.2014.08.041

Lewis, W. K., and Gilliland, E. R. (1954). Production of pure carbon dioxide. patent, 665–972.

Lewis, W. K., Gilliland, E. R., and Sweeney, W. P. (1951). Gasification of carbon metal oxides in a fluidized power bed. Chem. Eng. Prog. 89, 251–256.

Liu, L., Hong, D., Wang, N., and Guo, X. (2020). High purity H2 production from sorption enhanced bio-ethanol reforming via sol-gel-derived Ni–CaO–Al2O3 bi-functional materials. Int. J. Hydrogen Energy 45, 34449–34460. doi:10.1016/j.ijhydene.2020.02.158

Lu, C., Li, K., Zeng, C., Zhu, X., Wei, Y., Zheng, M., et al. (2018). Chemical looping reforming of methane using magnetite as oxygen carrier: structure evolution and reduction kinetics. Appl. Energy 211, 1–14. doi:10.1016/j.apenergy.2017.11.049

Luo, M., Yi, Y., Wang, S., Wang, Z., Du, M., Pan, J., et al. (2018). Review of hydrogen production using chemical-looping technology. Renew. Sustain. Energy Rev. 81, 3186–3214. doi:10.1016/j.rser.2017.07.007

Lyon, R. K., and Cole, J. A. (2000). Unmixed combustion: an alternative to fire. Combust. Flame 121, 249–261. doi:10.1016/s0010-2180(99)00136-4

Ma, H., Zeng, L., Tian, H., Li, D., Wang, X., Li, X., et al. (2016). Efficient hydrogen production from ethanol steam reforming over La-modified ordered mesoporous Ni-based catalysts. Appl. Catal. B Environ. 181, 321–331. doi:10.1016/j.apcatb.2015.08.019

Mattisson, T., Johansson, M., and Lyngfelt, A. (2006). The use of NiO as an oxygen carrier in chemical-looping combustion. Fuel 85, 736–747. doi:10.1016/j.fuel.2005.07.021

Mattisson, T., and Lyngfelt, A. (2001). Applications of chemical-looping combustion with capture of CO. Second nordic mini symposium on carbon dioxide capture and storage.

Mattisson, T., Zafar, Q., Lyngfelt, A., and Gevert, B. (2004). "Integrated hydrogen and power production from natural gas with CO2 capture", In Proc 15th World Hydrogen Energy Conf (WHEC), Yokohama: Japan, 3485–3496.

May, L., Da Silveira, I. T., and Vianna, C. (1996). Criteria for the evaluation of damage and remaining life in reformer furnace tubes. *Int. J. Press. vessels Pip.* 66, 233–241. doi:10.1016/0308-0161(95)00098-4

Monnerat, B., Kiwi-Minsker, L., and Renken, A. (2003). Mathematical modelling of the unsteady-state oxidation of nickel gauze catalysts. *Chem. Eng. Sci.* 58, 4911–4919. doi:10.1016/j.ces.2002.11.006

Morgado, J. F., Cloete, S., Morud, J., Gurker, T., and Amini, S. (2017). Modelling study of two chemical looping reforming reactor configurations: looping vs. switching. *Powder Technol.* 316, 599–613. doi:10.1016/j.powtec.2016.11.059

Omoniyi, O. A., and Dupont, V. (2018). Chemical looping steam reforming of acetic acid in a packed bed reactor. *Appl. Catal. B Environ.* 226, 258–268. doi:10.1016/j.apcatb.2017.12.027

Ortiz, M., de Diego, L. F., Abad, A., García-Labiano, F., Gayán, P., and Adánez, J. (2010). Hydrogen production by auto-thermal chemical-looping reforming in a pressurized fluidized bed reactor using Ni-based oxygen carriers. *Int. J. Hydrogen Energy* 35, 151–160. doi:10.1016/j.ijhydene.2009.10.068

Pakistan Energy demand forecast (2021). Pakistan Energy demand forecast. IEP report – 1, 2021 https://www.pc.gov.pk/uploads/report/IEP_Report_FINAL.pdf.

Pantoleontos, G., Kikkinides, E. S., and Georgiadis, M. C. (2012). A heterogeneous dynamic model for the simulation and optimisation of the steam methane reforming reactor. *Int. J. hydrogen energy* 37, 16346–16358. doi:10.1016/j.ijhydene.2012.02.125

Pashchenko, D. (2018). Effect of the geometric dimensionality of computational domain on the results of CFD modelling of steam methane reforming. *Int. J. hydrogen energy*, 1–12.

Pröll, T., Nordenkampf, J. B., Kolbitsch, P., and Hermann, H. (2010). Syngas and a separate nitrogen/argon stream via chemical looping reforming–A 140 kW pilot plant study. *Fuel* 89, 1249–1256. doi:10.1016/j.fuel.2009.09.033

Rasheed, A. A., Jalil, A. A., Gambo, Y., Ibrahim, M., Hambali, H. U., and Shahul Hamid, M. Y. (2019). A review on catalyst development for dry reforming of methane to syngas: recent advances. *Renew. Sustain. Energy Rev.* 108, 175–193. doi:10.1016/j.rser.2019.03.054

Richter, H. J., and Knoche, K. F. (1983). "Reversibility of combustion process," in *Efficiency and costing, second law analysis of process. ACS symposium series.* Editor R. A. Gaggioli (Washington DC: American Chemical Society), 235, 71–85.

Rydén, M. (2008). *"Hydrogen production with fossil fuels with carbon dioxide capture, using chemical-looping technologies." PhD Thesis. Göteborg.* Sweden: Chalmers University of Technology.

Rydén, M., Lyngfelt, A., and Mattisson, T. (2006). Synthesis gas generation by chemical looping reforming in a continuously operating laboratory reactor. *Fuel* 85, 1631–1641. doi:10.1016/j.fuel.2006.02.004

Rydén, M., Lyngfelt, A., and Mattisson, T. (2008b). Chemical-looping combustion and chemical-looping reforming in a circulating fluidized-bed reactor using Ni based oxygen carriers. *Energ Fuel* 28, 2585–2597. doi:10.1021/ef800065m

Rydén, M., Lyngfelt, A., Mattisson, T., Chen, D., Holmen, A., and Bjørgum, E. (2008a). Novel oxygen-carrier materials for chemical-looping combustion and chemical-looping reforming; LaxSr1−xFeyCo1−yO3−δ perovskites and mixed-metal oxides of NiO, Fe2O3 and Mn3O4. *Int. J. Greenh. Gas. Control* 2, 21–36. doi:10.1016/s1750-5836(07)00107-7

Rydén, M., Lyngfelt, M. J. A., and Mattisson, T. (2009). NiO supported on Mg–ZrO2 as oxygen carrier for chemical-looping combustion and chemical-looping reforming. *Energ Environ. Sci.* 2, 970–981. doi:10.1039/b904370e

Sharma, S., and Ghoshal, S. K. (2015). Hydrogen the future transportation fuel: from production to applications. *Renew. Sustain. energy Rev.* 43, 1151–1158. doi:10.1016/j.rser.2014.11.093

Singhal, A., Cloete, S., and Amini, S. (2017). Multiscale modelling of packed bed chemical looping reforming. *Energy Procedia* 136, 349–355. doi:10.1016/j.egypro.2017.10.287

Stoppacher, B., Bock, S., Malli, K., Lammer, M., and Hacker, V. (2022). The influence of hydrogen sulfide contaminations on hydrogen production in chemical looping processes. *Fuel* 307 (2021), 121677. doi:10.1016/j.fuel.2021.121677

Xu, J., and Froment, G. F. (1989). Methane steam reforming, methanation and water-gas shift: I. Intrinsic kinetics. *AIChE J.* 35, 88–96. doi:10.1002/aic.690350109

Yagi, S., Kunii, D., and Wakao, N. (1960). Studies on axial effective thermal conductivities in packed beds. *AIChE J.* 6, 543–546. doi:10.1002/aic.690060407

Zafar, Q., Mattisson, T., and Gevert, B. (2006). Redox investigation of some oxides of transition-state metals Ni, Cu, Fe, and Mn supported on SiO2 and MgAl2O4. *Fuel* 20, 34–44. doi:10.1021/ef0501389

Zhang, Y., Zu, Y., dong He, D., Liang, J., Zhu, L., Mei, Y., et al. (2022). The tailored role of "defect" sites on γ-alumina: a key to yield an efficient methane dry reforming catalyst with superior nickel utilization". *Appl. Catal. B Environ.* 315 (2022), 121539. doi:10.1016/j.apcatb.2022.121539

Zhou, Z., Han, L., and Bollas, G. M. (2013). Model-based analysis of bench-scale fixed bed units for chemical-looping combustion. *Chem. Eng. J.* 233, 331–348. doi:10.1016/j.cej.2013.08.025

Zhou, Z., Han, L., and Bollas, G. M. (2015). Model-assisted analysis of fluidized bed chemical-looping reactors. *Chem. Eng. Sci.* 134, 619–631. doi:10.1016/j.ces.2015.05.037

Nomenclature

a	Specific surface area/m^2 kg$_{carrier}^{-1}$
C	Concentration/mol m^{-3}
C_p	Heat capacity/J kg^{-1} K^{-1}
D	Dispersion coefficient/m^2 s^{-1}
d	Diameter/mm
D_m	Molecular Diffusivity/m^2 s^{-1}
E	Activation energy/J mol^{-1}
G	Gibbs free energy/J
Gs	Gas mass velocity/Kg m^{-2} s^{-1}
H	Heat of reaction/J mol^{-1}
ΔH	Heat of adsorption/J mol^{-1}
hf	Gas to solid heat transfer coefficient/W m^{-2} s^{-1}
jD	Chilton–Colburn factor of heat transfer
jH	Chilton–Colburn factor of mass transfer
K	Adsorption constant
k	Kinetic rate constant
K_g	Gas to solid mass transfer coefficient/m^3 m^{-2} s^{-1}
Kj	Thermodynamic equilibrium constant
k_o	References temperature dependent kinetic rate constant
P	Total gas pressure/bar
Pr	Prandtl number
R	Rate of reaction/mol kg$_{cat}^{-1}$ s^{-1}
r	Rate of formation or consumption/mol kg$_{cat}^{-1}$ s^{-1}
Re	Reynolds number
R_g	Ideal gas constant/J mol^{-1} K^{-1}
S_{ci}	Schmitt number
T	Temperature/K
u	Velocity of gases/m s^{-1}
X	Conversion/- Molecular diffusivity/m^2 s^{-1}

Greek letters

η	Effectiveness factor
ρ	Density/kg m^{-3}
ε	Porosity
Ω	Unitless term in reaction kinetics
μ	Gas viscosity/kg m^{-1} s^{-1}
λ	Thermal conductivity/W m^{-1} k^{-1}

Subscripts

b	Bed
cat	Catalyst
g	Gas phase
i	Gas species
j	No. of reaction
o	Initial value
p	particle
rxn	Reaction
s	Solid phase
z	Axial direction

Frontiers in Chemistry

Economy of scale for green hydrogen-derived fuel production in Nepal

Biraj Singh Thapa*[†], Bishnu Pandey[†] and Rahul Ghimire

Green Hydrogen Laboratory, School of Engineering, Department of Mechanical Engineering, Kathmandu University, Dhulikhel, Nepal

Opportunity for future green hydrogen development in Nepal comes with end-use infrastructural challenges. The heavy reliance of industries on fossil fuels (63.4%) despite the abundance of hydroelectricity poses an additional challenge to the green transition of Nepal. The presented work aims to study the possibility of storing and utilizing spilled hydroelectricity due to runoff rivers as a compatible alternative to imported petroleum fuels. This is achieved by converting green hydrogen from water electrolysis and carbon dioxide from carbon capture of hard-to-abate industries into synthetic methane for heating applications via the Sabatier process. An economy-of-scale study was conducted to identify the optimal scale for the reference case (Industries in Makwanpur District Nepal) for establishing the Synthetic Natural Gas (SNG) production industry. The techno-economic assessment was carried out for pilot scale and reference scale production unit individually. Uncertainty and sensitivity analyses were performed to study the project profitability and the sensitivity of the parameters influencing the feasibility of the production plant. The reference scale for the production of Synthetic Natural Gas was determined to be 40 Tons Per Day (TPD), with a total capital investment of around 72.15 Million USD. Electricity was identified as the most sensitive parameter affecting the levelized cost of production (LCOP). The 40 TPD plant was found to be price competitive to LPG when electricity price is subsidized below 3.55 NPR/unit (2.7 c/unit) from 12 NPR/unit (9.2 c/unit). In the case of the 2 TPD plant, for it to be profitable, the price of electricity must be subsidized to well below 2 NPR/kWh. The study concludes that the possibility of SNG production in Nepal is profitable and price-competitive at large scales and at the same time limited by the low round efficiency due to conversion losses. Additionally, it was observed that highly favorable conditions driven by government policies would be required for the pilot-scale SNG project to be feasible.

1 Introduction

Despite the positive advancements in renewable energy, such as increased solar PV installations and electric car sales, a new record for global carbon dioxide (CO_2) emissions was set, with 37 billion metric tons (Gt) in 2022. The amount was 1% higher than previously anticipated (Grubler et al., 2018; Hussain et al., 2021; International Energy Agency, 2023). According to a study, there is an emphasis on the necessity for global CO_2 emissions to be restricted by approximately 45% from 2010 levels by 2030, with the goal of reaching net zero

FIGURE 1
Energy mix of Nepalese Industrial and Residential Sector (Water and Energy Commission Secretariat, 2022).
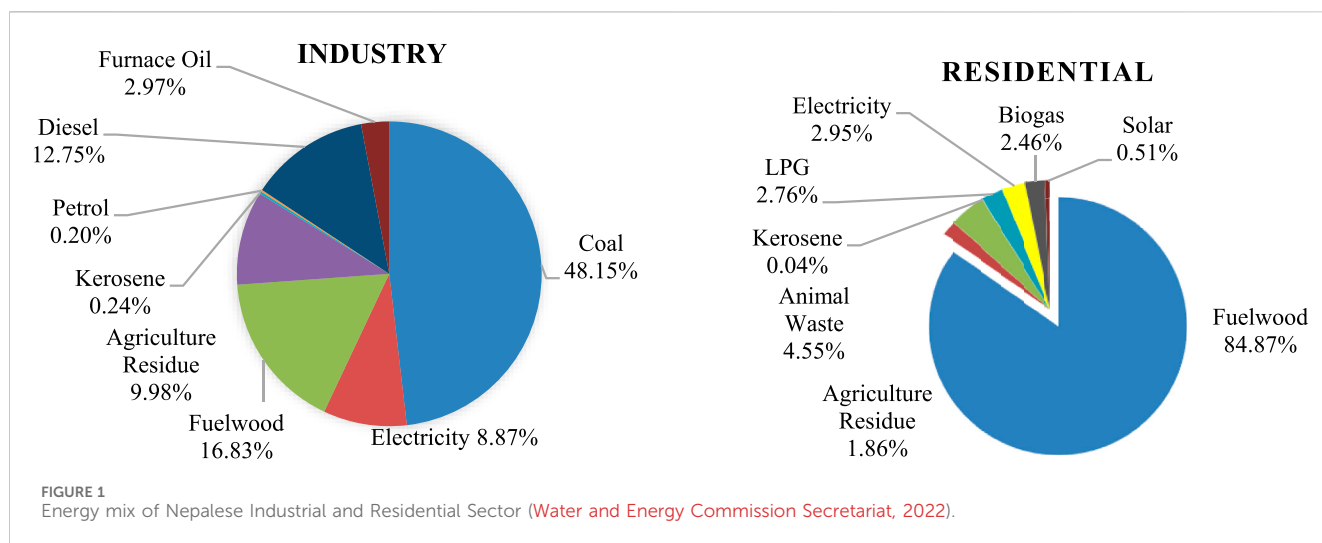
by 2050 (Leahy et al., 2020; Intergovernmental Panel on Climate Change, 2022). To attain this, an urgent need exists for energy sources that are both sustainable, scalable, and adaptable, offering high energy density as viable alternatives to ensure a secure energy supply while mitigating the environmental impact associated with current non-renewable energy sources (Li et al., 2017). As a promising, low or zero-carbon energy source, hydrogen is acknowledged with significant potential as an energy carrier in the future. Projections suggest that green hydrogen will have a pivotal role in the global energy transformation (International Energy Agency, 2015)., given its adaptability and high heat value (120–140 MJ/kg) compared to gasoline (44 MJ/kg) and coal (20 MJ/kg) (Hosseini and Wahid, 2016; Francesco, 2018). Additionally, its use in CO_2 recycling via the Sabatier Process offers energy-efficient solutions for addressing global energy demand and combating global warming (Dutta, 2014; Shastri et al., 2022).

Nepal's low greenhouse gas emissions, coupled with its vulnerability due to melting Himalayas, drive the search for carbon-neutral solutions. However, the country's annual investment of nearly 10% of its GDP, approximately 200 million USD, in fossil fuel imports is expected to rise due to population growth, inefficient operation, and increased economic production (Bhandari and Pandit, 2018; Nepal Oil Corporation, 2023). In Nepal, the primary energy source for 84.87% of households is fuel wood, while Liquefied Petroleum Gas (LPG) has experienced a 2.76% increase in usage over the last decade with over 33.1% of households employing it, particularly in urban areas, where it constitutes the second most common cooking fuel at 54.1% (Figure 1) (Water and Energy Commission Secretariat, 2022). Similarly, fossil fuels are heavily relied upon by Nepalese industries with a total energy consumption of 114.5PJ (Water and Energy Commission Secretariat, 2022) which is predominantly coal (48%) worth NRS 27.19 billion, imported in the fiscal year 2020–21, according to Nepal Rastra Bank.

On the other hand, Nepal has abundant renewable energy in the form of hydropower and solar resources with a current generation capacity of 2684 MW of hydroelectricity in 2023. (Nepal Electricity Authority, 2023). Nepal has 7231.3 MW hydropower projects under construction, with 20,000 MW in development stages. By 2030, the 16,820 GWh of surplus energy is projected. Exporting excess hydroelectricity faces geopolitical and pricing hurdles. Developing high-energy industries and grid management is a rapid government and developer task (Thapa et al., 2021). Moreover, over 90% of Nepal's existing hydropower plants are runoff river type (Bhatt 2017) poses problems related to seasonal peaking, and in the absence of a lack of energy storage facilities Green Hydrogen and Hydrogen synthetic fuels provide better energy management opportunities.

Surplus hydropower can make 67,277 to 336,400 tons of green hydrogen with the use of 20% and 100% surplus energy in 2030, convertible to Synthetic Natural Gas using CO_2 from cement, addressing compatible energy needs (Warsi et al., 2020; Thapa et al., 2021). Given the inadequacy of current hydrogen infrastructure and imbalance in electricity supply during dry seasons, the conversion to Synthetic Natural Gas (SNG) is deemed necessary. Annually, 3.6 million MT of CO_2 is emitted by 72 cement plants in Nepal, with the potential for 1.3 million MT of SNG production as a substitute for heating fuel. (Zimmermann et al., 2020; Szima and Cormos, 2021). According to the Power-to-Gas concept, SNG can be produced by hydrogenating CO_2 as following chemical equation:

$$CO_2 + 4H_2 \xrightarrow{\text{Ru/}\gamma-\text{Al}_2\text{O}_3/365\,°C} CH_4$$
$$+2H_2O \; \Delta H_R \,(298\,K) = -165\, KJ/mol \tag{1}$$
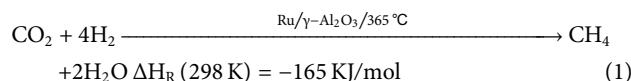
Methanation, a commonly employed technique for carbon monoxide and carbon dioxide elimination in chemical processes like ammonia production and natural gas purification, typically involves the conversion of small amounts of carbon dioxide. Bulk conversion can be hindered by the potential for numerous side reactions. Despite this, 128 Power-to-Gas (PtG) projects are recognized in Europe, with 27 already completed and 38 scheduled for future commissioning (Wulf et al., 2018). The CO_2 methanation plants are primarily of small scale, while the 6 MW Audi e-gas plant is an exception. Electrolysis gained prominence when, in 2014, it was coupled with a methanation reactor and a coal-powered plant by Buchholz et al., 2014, achieving 53% efficiency, later theoretically claimed to be improved up to 80%

for solid oxide electrolysis cell by Giglio et al., 2015, which has not reached technological maturity yet. The cost of hydrogen is a significant factor in SNG production, as identified by Szima and Cormos, 2021. A techno-economic assessment for SNG production was carried out by Becker et al., 2019, including the Organic Rankine Cycle for heat recovery, reporting SNG production costs as low as ~2 USD/kg.

In Nepal, the concept of hydrogen and Synthetic Natural Gas is relatively new, and no work has been done to find the feasibility of the SNG plant. The study focuses on the process design, economy of scale, and a techno-economic assessment for the reference and pilot scale SNG plants focusing on the Hetauda industrial area in Makwanpur District.

2 Methodology

The present investigation consists of the development of a simulation model for SNG production utilizing ASPEN Plus Software to find out the required sizing of the equipment. The manufacturer's data and economic analysis tools were used to analyze the economics of SNG production for the sized equipment of different scales. The risk analysis was done using Monte Carlo simulations. The following section details the requisite input, distinct process simulation models, and the resulting output.

2.1 Resources

In Nepalese industries, despite the bad reliability the older technologies for thermal purposes were gradually being replaced by electricity, coal and fuelwood continued to dominate. During COVID-19 restrictions, a 5.8% decrease in energy consumption was experienced in the sector in 2020, but an impressive 29% growth was witnessed in 2021, demonstrating the sector's adaptability and recovery capabilities (Water and Energy Commission Secretariat, 2022).

The Hetauda Industrial District is one of Nepal's largest industrial hubs located in Makwanpur District, encompassing 103 industries across various sectors, including plastic, cement, and mining industries. In this district, the industrial sector accounts for 813,800 GJ of energy consumption which is mostly carbon-emitting fuel (72%) (Makwanpur District District Development Committee Makwanpur Government of Nepal Ministry of Environment Alternative Energy Promotion Centre, 2011). The study is conducted to address the unreliable nature of hydroelectricity in Nepal, particularly stemming from runoff river projects. It aims to explore the conversion to e-fuel, which can be adapted and utilized directly for a range of heating applications. A centralized distribution system is assumed for the synthetic methane gas produced from co-located SNG plants, with the reference case designed to ensure that the industrial clean energy requirements (585,936 GJ) in Makwanpur District are entirely replaced by the generated SNG. The method chosen for hydrogen production involves water electrolysis using PEM electrolyzers. CO_2 is assumed to be sourced from a nearby Cement Industry named Hetauda Cement, which has an estimated daily cement-making capacity of 750 tonnes when operated at full capacity, resulting the

possible CO_2 emissions of 489.75 tonnes Eq. (2). For this study, it is assumed that the clinker is also produced in the factory to avoid confusion related to the emission factor. The cost of the equipment used in establishing the plant is obtained from supplier quotations and literature (Becker et al., 2019). Parameters such as the stages in the reaction, temperature, pressure, the type of catalyst (Chein and Wang, 2020), and reaction kinetics have been extensively studied and are known to exert a significant influence on the efficiency of the SNG production plant.

$$\text{Emission } E_{CO2} = \text{Cemen Production (I)} * \text{Emission Factor} (\epsilon) \quad (2)$$

(Lei et al., 2011)

$$\epsilon = 0.653$$

(Lei et al., 2011).

2.2 Models

The process simulation model employed in this study was developed in Aspen Plus software, a process modeling tool designed to replicate real-world chemical processes. The following section depicts the process model developed through the Aspen Plus software as in Figure 2 and the details are tabulated in Table 1.

2.2.1 Electrolysis

In the present work, the electrolytic production of hydrogen is envisioned to be geographically co-located with hydropower-generated electricity to meet the demand for green hydrogen in SNG production. The process of water electrolysis involves the breakdown of the water into hydrogen and oxygen by a direct supply of current as shown in the following equation: (Shiva Kumar and Himabindu, 2019):

Anode: $OH^- \rightarrow \frac{1}{2}O_2 + H_2O + 2e^-$
Cathode: $H_2O + 2e^- \rightarrow H_2 + 2OH^-$
Overall: $H_2O + energy \rightarrow 2H_2 + O_2$
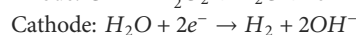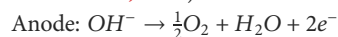
The Aspen Plus Software was used to examine a Proton Exchange Membrane (PEM) electrolyzer with a 70% efficiency (Wirkert et al., 2020). Subsequently, the hydrogen generated from the electrolyzer was simulated to be fed into the reactor at 25 bars from a high-pressure buffer tank compressed using a pneumatic reciprocating compressor. The simulations revealed that a 2 TPD SNG plant would require approximately 42 kg/h of hydrogen gas, along with 378 kg of deionized water and 2,520 kW of electrical power. An integrated ~140 kW air compression unit delivers air at a pressure of 5 bars to operate a pneumatic hydrogen compressor to deliver hydrogen at 25 bars maintaining a 42 kg/h flow rate. Additionally, a valuable by-product of 336 kg/h of oxygen would be concurrently generated. However, it should be noted that the cost of selling oxygen was not considered in this analysis. Figure 2 display the detailed of the major components. The specifications for the electrolyzer were verified through a quotation from the manufacturer "Light Bridge," based in South Korea.

2.2.2 Amine based carbon dioxide (CO_2) capture for CO_2 capture from cement industry

Numerous advanced methods exist for capturing carbon dioxide, including adsorption, physical absorption, chemical absorption, cryogenic separation, and membrane-based

FIGURE 2
Schematic of the process diagram of the SNG production system.
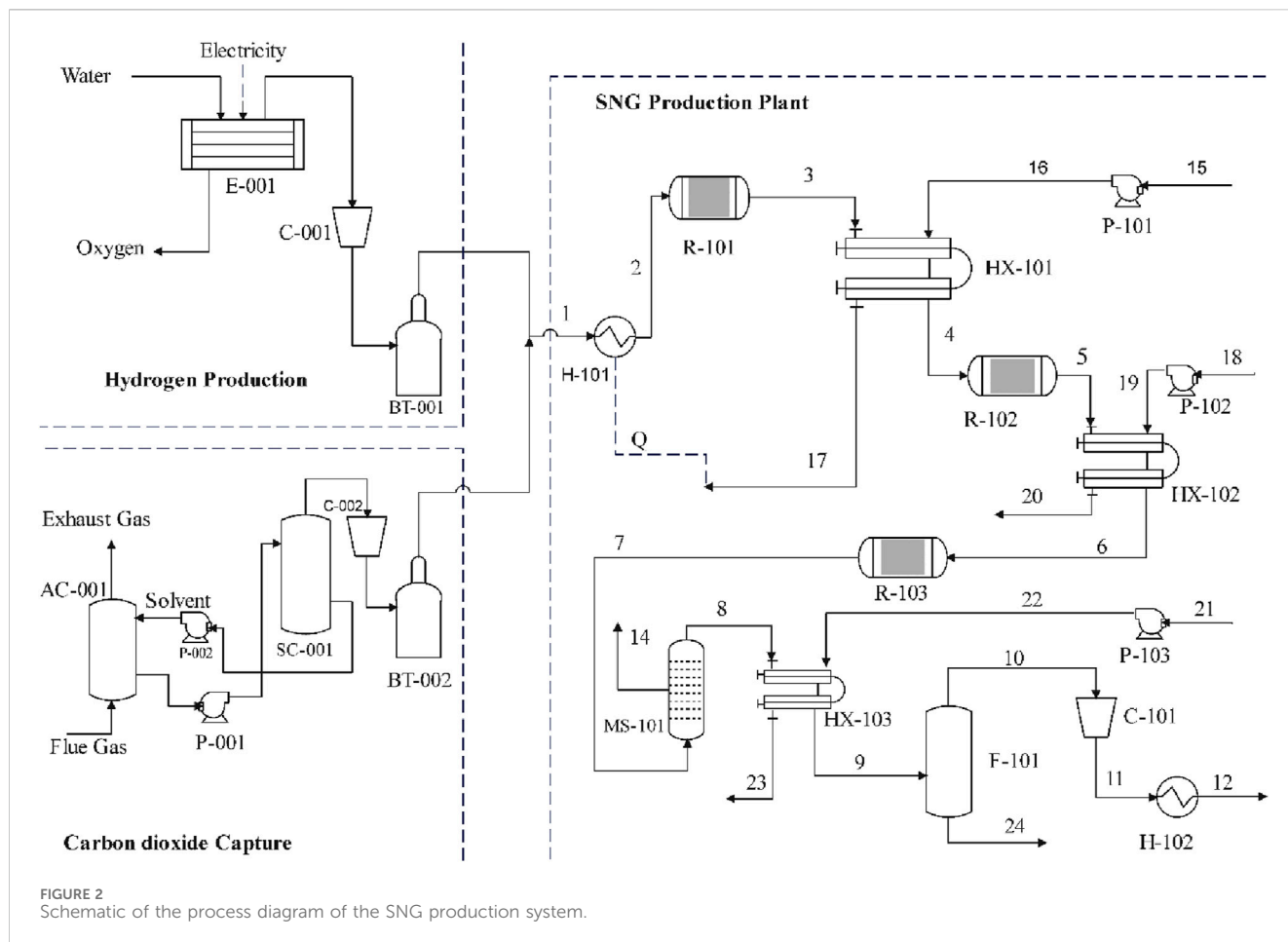
TABLE 1 Equipment code with corresponding equipment name.

Code	Equipment name	Code	Equipment name
E-001	Electrolyzer	H-101	Pre-heater
C-001	Compressor for H_2	R-101	Packed bed reactor 1
BT-001	Tank for H_2	HX-101	Heat Exchanger 1
AC-001	Absorption Column for CO_2	R-102	Packed bed reactor 2
SC-001	Stripping Column for CO_2	HX-102	Heat Exchanger 2
P-001	Pump for solvent	R-103	Packed bed reactor 3
P-002	Pump for solvent	MS-101	Membrane Separator 1
C-002	Compressor for CO_2	HX-103	Heat Exchanger 3
BT-002	Tank for CO_2	F-101	Flash Separator
P-101	Pump for coolant 1	C-101	Compressor for SNG
P-102	Pump for coolant 2	H-102	Cooler
P-103	Pump for coolant 3		

absorption. Among these alternatives, amine-based separation technology stands out as a well-established and commercially viable technique. It can be integrated into an existing cement plant in Nepal for extraction of CO_2 from the flue gas (Bosoaga et al., 2009; Plaza et al., 2020; Devkota et al., 2021). The simplified

technical analysis of the CO_2 capture plant was done in Aspen taking reference from Plaza et al., 2020; Devkota et al., 2021 as in Figure 2, and the optimum size of the equipment and the utilities required for the capture process were obtained. Results from the simulations show that a CO_2 flow rate of 236.3 kg/h will be required for the daily production of 2 tons of CH_4 (stored in BT-002 at 25°C) with an electrical power requirement of 330 kW including the compressor (CO_2 gas compressor (120 kW), Liquefaction Compressor (90 kW)) and all the Pumps (Cooling water pump (15 kW), Lean MEA pump (15 kW), Rich MEA pump (15 kW), Cooler pump (15 kW), Caustic pump (30 kW) etc. Aqueous monoethanolamine (MEA) was selected as an absorbent for capturing CO_2 from the flue gas of conventional CO_2-emitting plants. The Carbon Capture plant efficiency was assumed to be 90%. Detailed major components are presented in Figure 2 and Table 2.

2.2.3 Thermo-catalytic Sabatier process to produce Synthetic Natural Gas (CH_4)

Synthetic Methane (Synthetic Natural Gas) is produced through the Sabatier process, which involves the utilization of CO_2 captured from industrial flue gas and H_2 generated via water electrolysis in the presence of a catalyst Eq. (1), Here, the Ruthenium, i.e., 0.5 wt% Ru/γ-Al_2O_3 was used for simulations due to its 96% yield to methane gas with no CO production at 300°C (Falbo et al., 2018) whereas Nickel has high selectivity and low cost but is more prone to catalyst deactivation it only gives 80% yield to methane gas along with CO

TABLE 2 Details of the sized equipment for synthetic natural gas plant.

Specialized unit	Sizing (kW)	Input	Output	Power Consumption (kW)
Electrolyzer Unit	2,750	• 378 l/h deionized Water	42 kg/h H2 at 25 bar and 336 kg/h O2	2,659
		• 35,000 l/h Cooling water		
CO_2 Capture Unit (amine-based)	330	• 12.4% CO_2 in flue gas at 1.013 bar and 40 ℃	99.9% CO2 at 25 bar and 25 ℃	330
SNG Production Unit	96	• 21.48 kg/h H_2 at 25 bar and 20.5 bar and 25 ℃	83.33 kg/h of CH_4 at100 bar and 25 ℃	96
Total		• 236.25 kg/h CO_2 at 20 bar and 25 ℃		3085

production at 400°C on 20% Ni/γ-Al_2O_3 (Chein and Wang, 2020). The SNG production plant was modeled in Aspen Plus software. The reactor used is a packed bed reactor (RPLUG).

The Plant feed of CO_2 is chosen to be consistent with the 4:1 H_2:CO_2 molar ratio from the stoichiometry of the reaction. The CO_2 is distributed such that the ratio of H_2:CO_2 is always greater than 4:1 as suggested by Arita and Iizuka, 2015. The three reactor stages with 80%, 70%, and, 60% CO_2 conversion efficiency for the first, second, and third stages respectively were selected as stated by Becker et al. (2019) for the following reasons: i) to enable water purging, driving the reverse WGS reaction, ii) to avoid the necessity of bulk recycling with two or fewer reactors, and iii) to enhance reactor efficiency while managing capital costs. The supply of hydrogen and carbon dioxide was set at 42 kg/h at 25 bar pressure and 249.96 kg/h at 25 bar pressure respectively. The electrical power required for the preheaters for the initial heating of the input gases (later the heat from the exothermic reaction is used for preheating using heat exchangers), pumps, and compressor is 96 kW. The kinetics of the CO_2 methanation on a Ru-based catalyst was used as given by Falbo et al., 2018.

2.3 Cost estimation model

In this analysis, the estimation of equipment cost (C) involves a comprehensive consideration of various elements as in Eq. (3). These elements incorporate the cost in the reference year (C_R), the recommended plant size for the equipment determined using the Aspen Plus model (S), the size in the reference year (S_R), the chemical engineering plant cost index for the year 2022 (CI_{22}), the cost index for chemical engineering plants in the reference year (CI_R), and a scale factor (sf) that can vary within the range of 0.6–0.8, as depicted in the provided Table 3. (Turton, 2012a; Devkota et al., 2021).

$$C = C_R \times \frac{S}{S_R} \times \frac{CI_{22}}{CI_R} \times sf \qquad (3)$$

Subsequently, the equipment cost derived from the equation above is combined with the expenses for installation, piping, buildings, electrical, and instrumentation costs to compute the total capital investment for each piece of equipment. The annual repair and maintenance cost are accounted for as 2.5% (Ali Khan et al., 2021) of the total capital expenditure, with labor costs being determined using the formula

found in R. Turton's book. The costs for electricity, de-ionized water, and cooling water are taken from the standards set by the Nepal Electricity Authority and various water distribution bodies in Nepal.

The sizing factor for the Electrolyzer and the carbon capture unit was directly taken from literature but the SNG plant uses heat exchangers and cooling towers to reuse the heat and there were lack of similar concept was found in the literature hence the major equipment's were sized based on the plant schematic in Becker et al., 2019 and sizing factors in Turton, 2012a book.

3 Economic assessment

After conducting a technical assessment and equipment sizing for the 2 TPD SNG plant, the cost estimation model was used to calculate the cost of the required equipments. To enhance the accuracy of the cost estimation, the costs were cross-referenced with those provided by suppliers. Selections of NEL-Hydrogen's "M Series" MC 500 Electrolyzer and BOSCO INDIA were based on technical specifications derived from ASPEN simulation for electrolysis and carbon capture. The total equipment purchase cost, amounting to 44.14 Million NPR (equivalent to 3.42 Million USD), was calculated using Eq. 3 and data from Table 3. This hydrogen production equipment, constituting 62% of the total cost whereas SNG reactor unit and CO_2 production account for 22% and 16% of the capital expenditure, respectively. The considerable variance in equipment costs is attributed to the notably lower technology readiness level (TRL) of the hydrogen production unit. (Pinsky et al., 2020). The Economic Assessment model was adapted from the economic analysis done by Ghimire et al., 2024.

The annual operating cost encompasses the electricity cost, determined by the average rate offered by the Nepal Electricity Authority (NEA). The computation of feed and cooling water expenses relied on rates provided by Kathmandu Upatyaka Khanepani Limited (KUKL) and data from R. Turton's book. Estimates for annual maintenance costs for the electrolyzer and other equipment were derived from a study conducted by Ali Khan et al., 2021. The service period for the PEM Electrolyzer was established at 40,000 h. In this analysis the stack exchange cost is not considered in the initial CAPEX and a 19% (Schmidt et al., 2017) of system is added after every 5 years. Insurance, property tax, and labour rates were sourced from the Nepal Government website. (Ministry Of Labour, 2023).

TABLE 3 The scale factor of the sized equipment.

Components	Scale factor	References
Hydrogen	0.75	(Green and Perry, 2008; Turton, 2012a; Alnouss et al., 2022)
• Electrolyzer Unit	0.84	
• Reciprocating Compressor		
Carbon Dioxide	0.6	
• Carbon Capture Unit	0.84	
• Compressor		
Synthetic Natural Gas	0.71	
• Heat Exchangers	0.6	
• Reactors	0.8	
• Compressor	0.43	
• Pumps	0.6	
• Cooling tower	0.65	
• Preheater		

TABLE 4 CAPEX of the SNG production plant.

System	Components/Description (number)	Size	Capital costs		Manufacturer/ Source
		(Material)	(130 NPR/USD)		
Electrolyser system	Electrolyser Unit (1)	2.5 MW	**In USD**	**In NPR**	NEL Hydrogen and Jianggsu Minnuo Group Co. Ltd
	(Compact System with the cooling unit, water pumps, Deionizer, Controllers))	(SS 316)	1,329,430	171,496,513	
Storage tank	Buffer Storage Tank 1 set (15 pcs)	1000 L at 45bars 5	377,691	48,722,241	Light Bridge Inc
		(SS 316)			
Compressor with Cooling Unit	High-pressure compressor with Heat Exchanger (1)	25 to 360 Bar	359,691	48,722,241	Jiangsu Minnuo Group Co. Ltd
Carbon Capture Unit	Reboilers (1), Drivers, Pumps (5), Heat Exchangers (1) etc.)	15%–17% CO_2 to 99.999% pure CO_2	476,000	61,404,000	BOSCO India
		(Mainly SS 304, Stripper Tower and reboiler CS,)			
SNG Production Unit	Heat Exchanger (6)	at 2.24 m² HE area	219,708	28,342,332	ASPEN PLUS Economic Analyzer and DSB Engineering
	Reactor (3)	(SS 304)	327,710	42,2742,590	ASPEN Economics and (Becker et al., 2019)
	Others (1)	Fixed Bed Reactor with 90% Cascaded efficiency of 3 reactors	314,332	40,548,828	
		(SS 316)			
		Reciprocating Compressor, Pumps, Cooling Tower, preheaters, etc			
Additional Costs		**Unit**		**Cost**	
Total Equipment Costs		154% of the total equipment cost	**USD**	**NPR**	
Fixed Capital Investment (FCI) (Purchase equipment installation, Piping, Electrical installation, Building, land, Location factors)		(Towler et al., 2008; Turton, 2012b)	3,422,036	441,442,708	
Working Capital Investment 10%		20% of FCI	5,269,936	685,091,707	
and Contingency Cost of 10% (Towler et al., 2008)			1,053,987	135,964,354	

With no revenue expected during the first operational year, given the construction, establishment, and testing phases, a preliminary liquidity reserve of 10% is included to ensure smooth operations. Furthermore, a contingency cost of 10% is incorporated into the project budget to address unforeseen fluctuations (Authors Estimation).

TABLE 5 OPEX of the SNG plant.

System	Unit	Unit cost (In NPR)	Total annual cost (In NPR)	Total annual cost (In USD)	Source
Electricity	3085 kW	8/kWh	190,649,030	1,466,531	Aspen Plus/ NEA
Maintenance	2.5% of CAPEX		13,701,740	105,398	(Ali Khan et al., 2021)
Deionized Water	500 kg/h	0.001USD/kg	569,400	4,380	(Turton, 2012b
Insurance		0.01 (FCI)	6,850,870	52,699	Devkota et al., 2021)
Catalyst		0.0075* (FCI)	5,138,120	39,524	(Becker et al., 2019)
					And Liaoning Haitai Sci-Tech Development Co Ltd
Labor	30 (Turton, 2012b)	750/day	9,931,350	76,395	(Ministry Of Labour, 2023)

FIGURE 3
Economy of the scale for SNG production plant in Nepal.
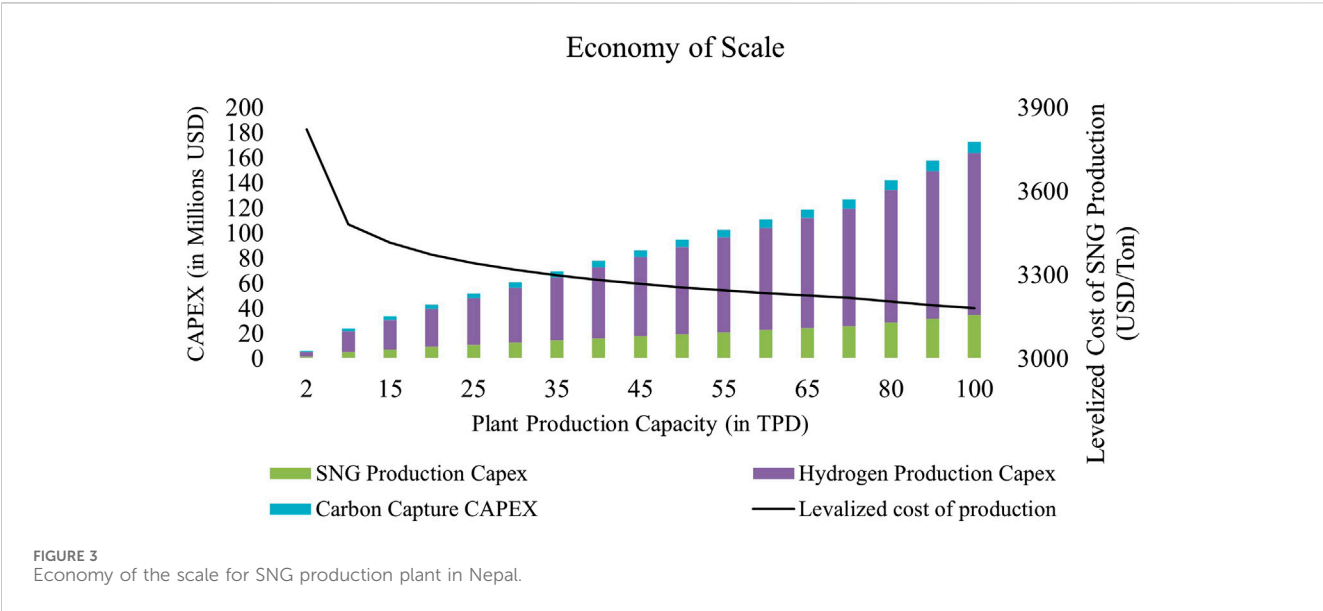
3.1 Economy of scale

An economy-of-scale analysis was conducted based on the CAPEX and OPEX data from Table 4 and Table 5 for the 2 TPD plant, along with the sizing factor of various plants and equipment as outlined in Table 3. The reference commercial scale of SNG plant is selected such that to replace the use of conventional fuel (72%) in the Industries of the Makwanpur District as mentioned in Section 2.1.

The decrease in the levelized cost of Synthetic Natural Gas (SNG) production is noted as the plant scale is increased as shown in Figure 3. The most suitable size for investment from the demand perspective (equivalent energy required) is determined to be a 40 TPD plant, with an approximate levelized cost of production of 3282.48 USD/ton (423,439 NPR/ton) at an electricity rate of 0.06 USD/kWh (8 NPR/kWh). Beyond this stage, the slope of the levelized cost decreases, but it surpasses the off-takers. However, the slope of the LCOE will not saturate and become more profitable at

100 TPD. In this study, the techno-economic assessment was conducted for both the base scale (2 TPD) and the commercial or reference (40 TPD) to evaluate the feasibility of such plants in Nepal.

3.2 Net Present Value

The total CAPEX and OPEX for the 2 TPD and 40 TPD SNG production units were calculated. In both scenarios, annual OPEX exceeds CAPEX. Assuming a selling cost of SNG at USD 3.5 per kg to ensure profit on the cost of production per kg and a positive IRR for both plant scales. The analysis includes cash flow, NPV, and discounted payback period determination. Project acceptability is assessed by comparing the present value of cash inflows to outflows, known as NPV (Turton, 2012b).

Figure 4 Cash Flow Diagram for 40 TPD SNG Plant and 2 TPD SNG Plant with Electrolyzer Stack Exchange

FIGURE 4
Cumulative distribution of NPV for 2 TPD and 40 TPD SNG Plant (left to right).
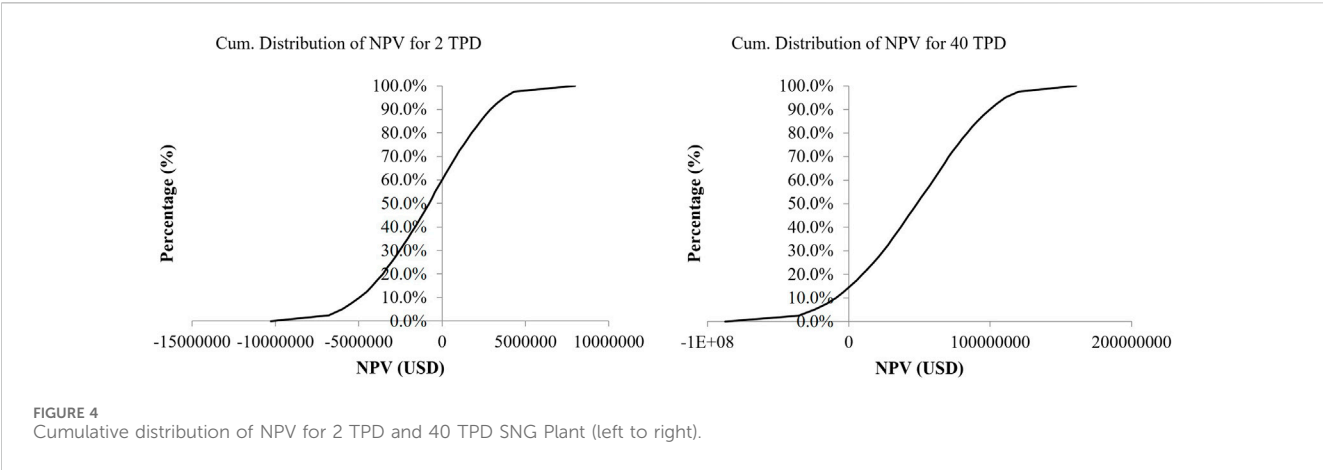
TABLE 6 Optimistic, pessimistic, and Most Likely Scenarios for various Cost Parameters of SNG Plant.

Cost parameters	Optimistic	Most likely	Pessimistic
CAPEX			
Electrolyzer System	0.6*TCI	TCI	1.6*TCI
Carbon Capture Unit	0.9* TCI	TCI	1.1*TCI
SNG Reactor Unit	0.9* TCI	TCI	1.2*TCI
Other Cost	0.8* (FCI-TEC)	FCI-TEC	1.2*(FCI-TEC)
OPEX			
Maintenance Cost	0.02*FCI	0.025*FCI	0.03*FCI
Electricity Cost	NPR 2/kWh	NPR 8/kWh	NPR 10/kWh
Labor Costs	4% of all other OPEX	5% of all other OPEX	6% of all other OPEX
Deionized Water cost	USD 0.0005/kg	USD 0.001/kg	USD 0.08/kg

$$PV\ (i)\ I\sum_{n=0}^{N}\frac{A_n}{(1+i)^n}$$

Where, A_n = net cash flow at the end of period n i = Discount rate or minimum attractive rate of return (MARR) N = Service life of the project

The IRR was calculated based on a 25-year service life for the SNG production plant system and an 8% discount rate, with corresponding revenues as per the production capabilities (assuming stack change after every 5 years).

For 2 TPD, the NPV comes out to be USD -2 Million (IRR 4% < 8%) suggesting the proposed scale is economically not feasible. For 40 TPD, the NPV comes out to be USD 29 Million suggesting the feasibility of the proposed scale of the plant. The IRR comes out to be 12% for the electricity tariff rate of 8 NPR/kWh (0.061 USD/kWh). The discounted payback time for the 40 TPD plant comes out to be at the end of the 13th year with stack exchange.

3.3 Uncertainty and sensitivity analysis

A Monte Carlo simulation was conducted to assess the uncertainty regarding statistical data and the key risk factors associated with investing in the proposed plant. This analysis involves the generation of a wide range of potential outcomes and their associated probabilities through 10,000 simulations. The Monte Carlo simulation was executed using Microsoft Excel software, with the assistance of an optimistic, pessimistic, and most likely values for various cost Parameters as represented in Table 6. Subsequently, the corresponding Net Present Value (NPV) is calculated and plotted to evaluate the range of NPVs and determine the probabilities associated with project-related risks.

In a Monte Carlo simulation for a 2 TPD pilot project, NPV ranged from USD 79.9 Million (IRR: 24.74%) to USD -9.9 Million, with positive NPV in 40% of cases, as depicted in Figure 4. For a 40 TPD commercial scale, NPV ranged from USD 160.7 Million (IRR: 38%) to −87.2 Million, showing positive NPV in over 85% of instances, as illustrated in Figure 4. The positive NPV does not ensure a project profitability but it can be taken as an indicator of the risk of failure. The variance in risk percentage is attributable to differences in profit margins per kilogram of SNG, particularly high for commercial-scale plants.

Sensitivity Diagram

FIGURE 5
Parameter Sensitivity of SNG Production Plant.
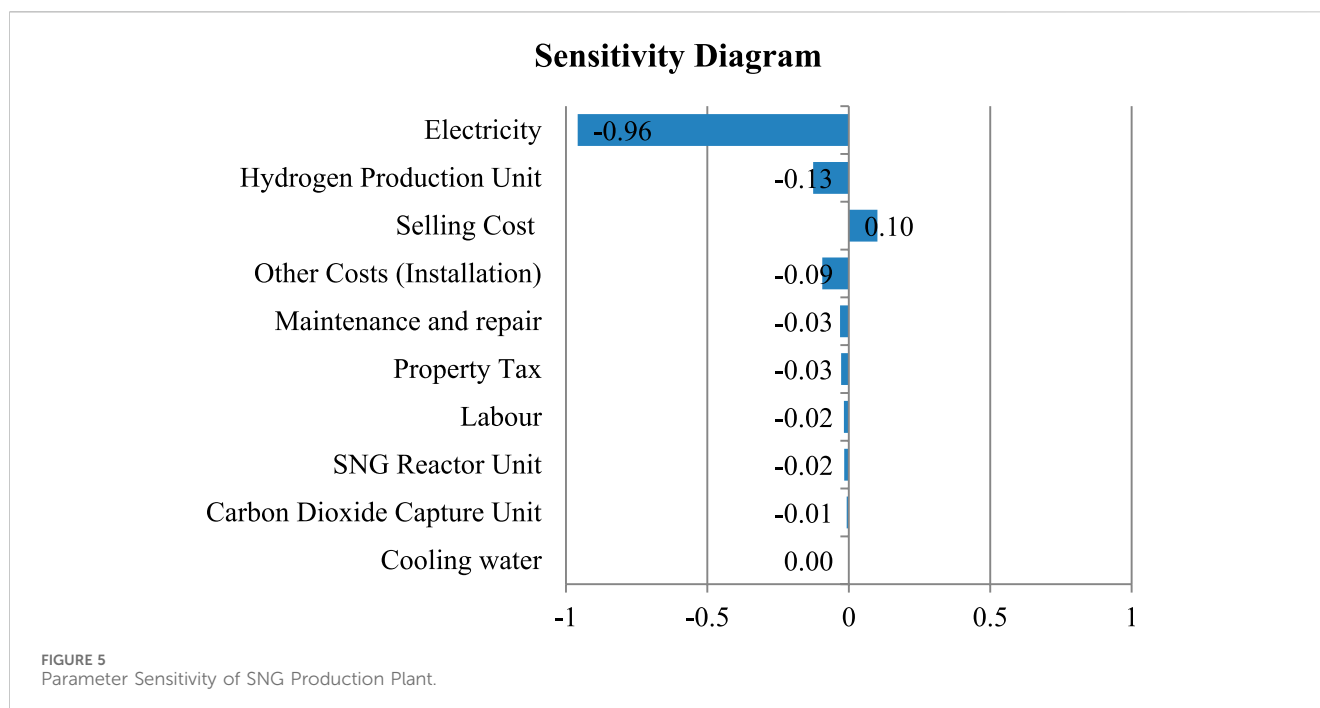
Sensitivity analysis was conducted to identify the most influential parameter affecting NPV. It was found that the most sensitive parameter is the electricity cost followed by electrolyser cost both having negative correlation with NPV as shown in Figure 5. Sensitivity in the Hydrogen production unit is linked to evolving technology and the current low Technology Readiness Level (TRL), leading to cost differences between suppliers and literature. However, the sensitivity of the CO_2 and SNG unit is low, given minimal discrepancies between literature and market costs for the associated equipment.

Considering the results from the uncertainty analysis, which highlights the pivotal role of the electricity tariff rate in the study, sensitivity analysis has been conducted to assess the impact of electricity cost on the Net Present Value and Internal Rate of Return (IRR) of SNG production. The analysis reveals that the levelized cost of SNG production decreases significantly with a reduction in electricity cost, the cost of electricity was taken feasible such that the IRR >8% and NPV is positive at the point. It was found that for the 40 TPD plant to satisfy the condition mentioned above, the electricity cost should be lower or equal to 0.066 USD/kWh (8.7 NPR/kWh). Similarly, for the 2 TPD plant to be profitable (Positive NPV and IRR >8%), the electricity cost must be below 0.053 USD/kWh (6.9 NPR/kWh) at the selling price of 3.5 USD/kg, as shown in Figure 6.

3.4 Assessing market competitiveness of Synthetic Natural Gas (SNG) production

Figure 5 illustrates the electricity to be most sensitive parameter for levelized cost of Production (LCOP) and in this analysis different plant scales were evaluated for the price of electricity at which the LCOP of SNG becomes cost competitive to the current Liquified Petroleum Gas (LPG) price. LPG was selected as the point of comparison due to the lack of price competitiveness of SNG production costs when compared to

other inexpensive fossil fuels such as coal. Additionally, LPG represents a substantial portion of imported fossil fuel, further justifying its selection for comparison purposes. The highest unsubsidized rate of Liquefied Petroleum Gas (LPG) in Nepal recorded at 227.04 NPR/kg (1.74 USD/kg) (adapted from Bhandari and Pandit, 2018) and this amount has been used for the comparison basis.

At a given plant scale if, $LCOP\ of\ SNG\ (energy\ equivalent\ to\ 1\ kg\ of\ LPG) \leq 227.04\ \frac{NPR}{kg}$ the scale is cost competitive to LPG. The outcomes derived from the graph above demonstrate that, given a subsidized electricity cost of 4.3 NPR/kWh, plant scales equal to or exceeding 100 TPD meet the criteria for comparison and are deemed economically competitive with LPG. Likewise, to ascertain the viability of 40 TPD and 2 TPD plants in terms of market competitiveness against LPG, the subsidized electricity rate must fall below 3.5 NPR/kWh and significantly below 2.5 NPR/kWh, respectively as shown in Figure 7.

4 Conclusion

This study involved an economy-of-scale analysis for an SNG production plant, drawing data from various literature and suppliers. The SNG as a fuel can act as a balance between the storage of spilled hydroelectricity from runoff rivers, excessive fossil fuel import, and the economical adaptability of clean fuel in the current heating infrastructure. A techno-economic analysis was conducted for a pilot-scale 2 TPD plant in the Hetauda Industrial district, using technical data from ASPEN Plus. The 40 TPD plant was found feasible to replace the use of CO_2 emitting fuel with SNG fuel in the Industries of Makwanpur district. The economy of scale analysis was done to find the effect on the levelized cost and CAPEX with increasing plant scale.

Economic analyses for both the 2 TPD and 40 TPD plants were carried out, with CAPEX and OPEX calculated using secondary data from suppliers and a literature review. The levelized cost of
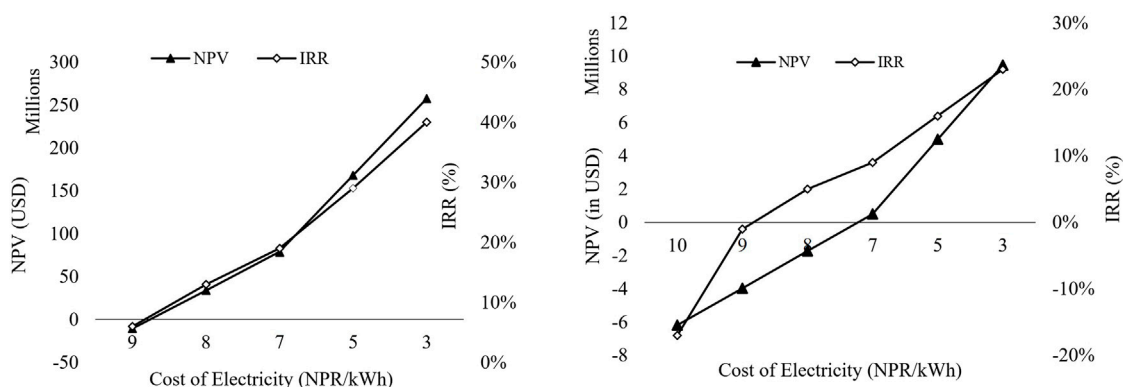
FIGURE 6
NPV v/s IRR v/s per unit Electricity tariff cost (in NPR) for 40 TPD and 2 TPD plant (left to right).
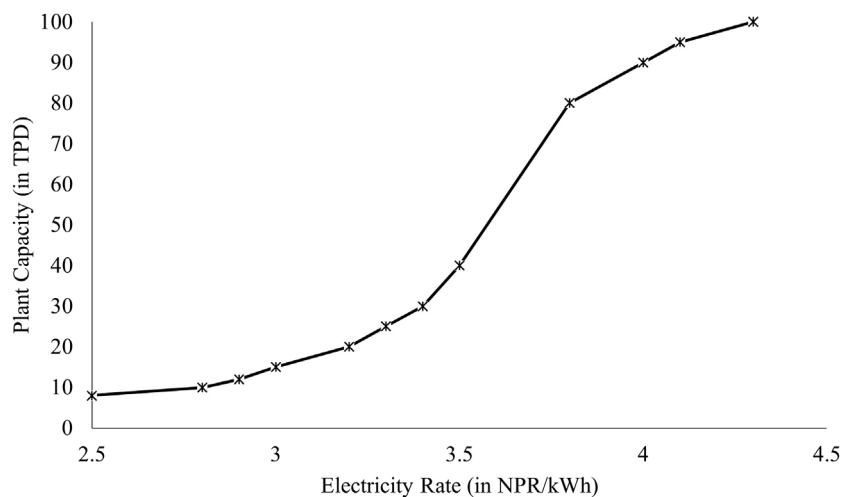
FIGURE 7
Electricity Rate vs. Feasible Scale of SNG Production Plant (in comparison to LPG prices in Nepal).

production for both the commercial and pilot-scale plants was determined, with a selling cost of 3.55 USD/kg of SNG set to ensure a positive NPV for the 2 TPD plant. Despite higher initial capital requirements for the 40 TPD plants, breakeven was achieved in the 13th year at a discounted rate of 8%. In contrast, the 2 TPD plant found it difficult to breakeven even at the 25th year. The NPV for the 2 and 40 TPD plants were calculated at USD -2 Million with a 4% (< discount rate, 8%) Internal Rate of Return (IRR) and USD 29.2 Millions a 12% (> discount rate, 8%) IRR, respectively.

Furthermore, the Monte Carlo analysis revealed that the 2 TPD plant is about two times riskier than the 40 TPD plant from the investment point of view. Notably, the Monte Carlo equation emphasized a substantial negative correlation between NPV and electricity cost, surpassing correlations with other factors. Consequently, the plants' sensitivity to electricity rates was simulated, concluding that both scales of plants can become profitable if the electricity cost could be reduced below 6.9 NPR/unit at 3.5 USD/kg selling price. However, for SNG to effectively compete with the LPG market in Nepal, electricity costs should be lowered to 3.5 NPR/kWh for the 40 TPD plant and well lower than 2 NPR/kWh for the 2 TPD plant.

Overall, the viability and scalability of the SNG plant in Nepal depend upon the support from government policies such as promoting affordable electricity for clean fuel application, categorisation of clean fuels as premium fuels, etc. Additionally, the integration of carbon financing mechanisms and use of flue gas heat in the carbon capture can reduce the utility cost and can further enhance the business's feasibility. It should be noted that this study is constrained by the precision and reliability of simulation software and data obtained from the literature. The study primarily concentrates on SNG production and does not delve into the specifics of auxiliary components. This study is positioned to serve as a stimulus for further research, contributing to policymakers' and investors' comprehensive understanding of prospects and enabling well-informed decision-making.

Data availability statement

The original contributions presented in the study are included in the article/Supplementary material, further inquiries can be directed to the corresponding author.

Author contributions

BT: Formal Analysis, Funding acquisition, Methodology, Resources, Supervision, Validation, Writing–original draft, Writing–review and editing. BP: Formal Analysis, Project administration, Software, Validation, Writing–original draft, Writing–review and editing. RG: Conceptualization, Investigation, Software, Writing–review and editing.

Funding

The author(s) declare that no financial support was received for the research, authorship, and/or publication of this article.

Conflict of interest

The authors declare that the research was conducted in the absence of any commercial or financial relationships that could be construed as a potential conflict of interest.

Publisher's note

All claims expressed in this article are solely those of the authors and do not necessarily represent those of their affiliated organizations, or those of the publisher, the editors and the reviewers. Any product that may be evaluated in this article, or claim that may be made by its manufacturer, is not guaranteed or endorsed by the publisher.

References

Ali Khan, M. H., Daiyan, R., Han, Z., Hablutzel, M., Haque, N., Amal, R., et al. (2021). Designing optimal integrated electricity supply configurations for renewable hydrogen generation in Australia. *iScience* 24 (6), 102539. doi:10.1016/j.isci.2021.102539

Alnouss, A., Mckay, G., and Al-Ansari, T. (2022). Evaluation of oxygen and steam fed biomass gasification within energy, water, and food nexus. *Sustain. Energy-Water-Environment Nexus Deserts*, 499–508. doi:10.1007/978-3-030-76081-6_63

Arita, K., and Iizuka, S. (2015). Production of CH&lt;sub&gt;4&lt;sub&gt; in a Low-Pressure CO&lt;sub&gt;2&lt;/sub&gt;/H&lt;sub&gt;2&lt;/sub&gt; Discharge with Magnetic Field. *J. Mater. Sci. Chem. Eng.* 03 (12), 69–77. doi:10.4236/msce.2015.312011

Becker, W. L., Penev, M., and Braun, R. J. (2019). Production of synthetic natural gas from carbon dioxide and renewably generated hydrogen: a techno-economic analysis of a power-to-gas strategy. *J. Energy Resour. Technol. Trans. ASME* 141 (2). doi:10.1115/1.4041381

Bhandari, R., and Pandit, S. (2018). Electricity as a cooking means in Nepal-A modelling tool approach. *Sustain. Switz.* 10 (8), 2841. doi:10.3390/su10082841

Bosoaga, A., Masek, O., and Oakey, J. E. (2009). CO2 capture technologies for cement industry. *Energy Procedia* 1, 133–140. doi:10.1016/j.egypro.2009.01.020

Buchholz, O. S., Van Der Ham, A. G. J., Veneman, R., Brilman, D. W. F., and Kersten, S. R. A. (2014). Power-to-Gas: storing surplus electrical energy a design study. *Energy Procedia* 63, 7993–8009. doi:10.1016/j.egypro.2014.11.836

Chein, R. Y., and Wang, C. C. (2020). Experimental study on co2 methanation over ni/al2o3, ru/al2o3, and ru-ni/al2o3 catalysts. *Catalysts* 10 (10), 1112–1117. doi:10.3390/catal10101112

Devkota, S., Pokhrel, R., Rayamajhi, B., and Uprety, B. (2021). Design and cost estimation of a CO2 capture plant from cement flue gas for urea production in Nepal. *Int. J. Greenh. Gas Control* 111, 103484. doi:10.1016/j.ijggc.2021.103484

Dutta, S. (2014). A review on production, storage of hydrogen and its utilization as an energy resource. *J. Industrial Eng. Chem.* 20 (4), 1148–1156. doi:10.1016/j.jiec.2013.07.037

Falbo, L., Martinelli, M., Visconti, C. G., Lietti, L., Bassano, C., and Deiana, P. (2018). Kinetics of CO2 methanation on a Ru-based catalyst at process conditions relevant for Power-to-Gas applications. *Appl. Catal. B Environ.* 225, 354–363. doi:10.1016/j.apcatb.2017.11.066

Francesco, DOLCI (2018). Green hydrogen opportunities in selected industrial processes Workshop summary report. Available at: https://ec.europa.eu/jrc.

Ghimire, R., Niroula, S., Pandey, B., Subedi, A., and Thapa, B. S. (2024). Techno-economic assessment of fuel cell-based power backup system as an alternative to diesel generators in Nepal: a case study for hospital applications. *Int. J. Hydrogen Energy* 56, 289–301. doi:10.1016/j.ijhydene.2023.12.174

Giglio, E., Lanzini, A., Santarelli, M., and Leone, P. (2015). Synthetic natural gas via integrated high-temperature electrolysis and methanation: Part II-Economic analysis. *J. Energy Storage* 2, 64–79. doi:10.1016/j.est.2015.06.004

Green, D. W., and Perry, R. H. (2008). "Chemical engineers' handbook," in *Perry's chemical engineers' handbook* (New York: McGraw-Hill Education). Available at: https://www.accessengineeringlibrary.com/content/book/9780071422949/toc-chapter/chapter2/section/section2.

Grubler, A., Wilson, C., Bento, N., Boza-Kiss, B., Krey, V., McCollum, D. L., et al. (2018). A low energy demand scenario for meeting the 1.5 °C target and sustainable development goals without negative emission technologies. *Nat. Energy* 3 (6), 515–527. doi:10.1038/s41560-018-0172-6

Hosseini, S. E., and Wahid, M. A. (2016). Hydrogen production from renewable and sustainable energy resources: promising green energy carrier for clean development. *Renew. Sustain. Energy Rev.* 57, 850–866. doi:10.1016/j.rser.2015.12.112

Intergovernmental Panel on Climate Change (2022). "Summary for policymakers," in *Global warming of 1.5°C* (Cambridge, United Kingdom: Cambridge University Press), 1–24. Available at: https://www.cambridge.org/core/product/identifier/9781009157940%23prf2/type/book_part.

International Energy Agency (2015). Energy technology perspectives 2015 mobilising innovation to accelerate climate action. Available at: http://www.iea.org/t&c/.

International Energy Agency (2023). Net zero roadmap A global pathway to keep the 1.5 °C goal in reach. Available at: https://www.iea.org/t&c/.

Leahy, S., Clark, H., and Reisinger, A. (2020). Challenges and prospects for agricultural greenhouse gas mitigation pathways consistent with the Paris agreement. *Front. Sustain. Food Syst.* 4. doi:10.3389/fsufs.2020.00069

Lei, Y., Zhang, Q., Nielsen, C., and He, K. (2011). An inventory of primary air pollutants and CO2 emissions from cement production in China, 1990-2020. *Atmos. Environ.* 45 (1), 147–154. doi:10.1016/j.atmosenv.2010.09.034

Li, R., Wang, W., and Xia, M. (2017). Cooperative planning of active distribution system with renewable energy sources and energy storage systems. *IEEE Access* 6, 5916–5926. doi:10.1109/ACCESS.2017.2785263

Makwanpur District District Development Committee Makwanpur Government of Nepal Ministry of Environment Alternative Energy Promotion Centre (2011). DISTRICT CLIMATE AND ENERGY PLAN. Available at: https://www.climatenepal.org.np/sites/default/files/doc_resources/DISTRICT%20CLIMATE%20AND%20ENERGY%20PLAN%20Makwanpur%20District.pdf (Accessed January 4, 2024).

Ministry Of Labour (2023). Employment and social security. Available at: https://moless.gov.np/np/post/show/291 (Accessed: October 10, 2023).

Nepal Electricity Authority (2023). A year in review fiscal year 2022/23. Available at: https://www.nea.org.np/annual_report (Accessed October 2, 2023).

Nepal Oil Corporation (2023). *Import Sales*. Available at: https://noc.org.np/import (Accessed October 3, 2023).

Pinsky, R., Sabharwall, P., Hartvigsen, J., and O'brien, J. (2020). Comparative review of hydrogen production technologies for nuclear hybrid energy systems. Available at: https://www.sciencedirect.com/science/article/pii/S014919702030069X.

Plaza, M. G., Martínez, S., and Rubiera, F. (2020). Co2 capture, use, and storage in the cement industry: state of the art and expectations. *Energies* 13 (21), 5692. doi:10.3390/en13215692

Schmidt, O., Gambhir, A., Staffell, I., Hawkes, A., Nelson, J., and Few, S. (2017). Future cost and performance of water electrolysis: an expert elicitation study. *Int. J. Hydrogen Energy* 42 (52), 30470–30492. doi:10.1016/j.ijhydene.2017.10.045

Shastri, Y., Therasme, O., Managi, S., Ryota Keeley, A., and Takeda, S. (2022). OPEN ACCESS EDITED BY A systematic review of the techno-economic assessment of various hydrogen production methods of power generation. *Front. Sustain.* 3.

Shiva Kumar, S., and Himabindu, V. (2019). Hydrogen production by PEM water electrolysis – a review. *Mater. Sci. Energy Technol.* 2 (3), 442–454. doi:10.1016/j.mset.2019.03.002

Szima, S., and Cormos, C. C. (2021). Co2 utilization technologies: a techno-economic analysis for synthetic natural gas production. *Energies* 14 (5), 1258. doi:10.3390/en14051258

Thapa, B. S., Neupane, B., Yang, H. S., and Lee, Y. H. (2021). Green hydrogen potentials from surplus hydro energy in Nepal. *Int. J. Hydrogen Energy* 46 (43), 22256–22267. doi:10.1016/j.ijhydene.2021.04.096

Towler, G., et al. (2008). CHEMICAL ENGINEERING DESIGN principles, practice and economics of plant and process design. Available at: http://elsevier.com.

Turton, R. (2012a). *Analysis, synthesis, and design of chemical processes*. Hoboken, New Jersey, USA: Prentice Hall.

Turton, R. (2012b). *Analysis, synthesis, and design of chemical processes*. Hoboken, New Jersey, USA: Prentice Hall.

Warsi, Y., Kabanov, V., Zhou, P., and Sinha, A. (2020). Novel carbon dioxide utilization technologies: a means to an end. *Front. Energy Res.* 8. doi:10.3389/fenrg.2020.574147

Water and Energy Commission Secretariat (2022). Government of Nepal water and energy commission Secretariat Nepal ENERGY SECTOR SYNOPSIS REPORT-2022.

https://wecs.gov.np/source/Energy%20Sector%20Synopsis%20Report%2C%202022.pdf.

Wirkert, F. J., Roth, J., Jagalski, S., Neuhaus, P., Rost, U., and Brodmann, M. (2020). A modular design approach for PEM electrolyser systems with homogeneous operation conditions and highly efficient heat management. *Int. J. Hydrogen Energy* 45 (2), 1226–1235. doi:10.1016/j.ijhydene.2019.03.185

Wulf, C., Linßen, J., and Zapp, P. (2018). Review of power-to-gas projects in Europe. *Energy Procedia* 155, 367–378. doi:10.1016/j.egypro.2018.11.041

Zimmermann, A. W., Wunderlich, J., Müller, L., Buchner, G. A., Marxen, A., Michailos, S., et al. (2020). Techno-economic assessment guidelines for CO2 utilization. *Front. Energy Res.* 8. doi:10.3389/fenrg.2020.00005

frontiers | Frontiers in Chemistry

Chitosan nanoparticle applications in dentistry: a sustainable biopolymer

Roma Mascarenhas [ID] [1], Shreya Hegde [ID] [1] and Nidhi Manaktala [ID] [2]*

[1]Department of Conservative Dentistry and Endodontics, Manipal College of Dental Sciences Mangalore, Manipal Academy of Higher Education, Manipal, India, [2]Department of Oral Pathology and Microbiology, Manipal College of Dental Sciences Mangalore, Manipal Academy of Higher Education, Manipal, India

The epoch of Nano-biomaterials and their application in the field of medicine and dentistry has been long-lived. The application of nanotechnology is extensively used in diagnosis and treatment aspects of oral diseases. The nanomaterials and its structures are being widely involved in the production of medicines and drugs used for the treatment of oral diseases like periodontitis, oral carcinoma, etc. and helps in maintaining the longevity of oral health. Chitosan is a naturally occurring biopolymer derived from chitin which is seen commonly in arthropods. Chitosan nanoparticles are the latest in the trend of nanoparticles used in dentistry and are becoming the most wanted biopolymer for use toward therapeutic interventions. Literature search has also shown that chitosan nanoparticles have anti-tumor effects. This review highlights the various aspects of chitosan nanoparticles and their implications in dentistry.

KEYWORDS

chitosan, sustainable nanomaterials, organic-inorganic hybrid nanomaterial, bio-medical applications, dentistry

1 Introduction

Over the years, scientific progress in the field of biomedicine has paved the way for the evolution of newer nano-biomaterials which have proved to be progressively efficient and biocompatible. The process of extraction of marine-based nano-biomaterials is at its peak with lot of relevant research being conducted on the same (Bonderer et al., 2008; Ghosh and Urban, 2009). Recent literature search has shown that marine based nano-biomaterials like chitosan is used extensively in medical and dental fields (Ladet et al., 2008; Jones, 2010). As stated in the "European Commission's Recommendation", nanomaterial can be elaborated as a natural or synthetic material incorporated with particles, in a bound or unbound state, where 50% or more of the particles are in the range of 1–100 nm (Raura et al., 2020). One of the most commonly used nanoparticle in dentistry is silver (Ag) which has been used in contrasting forms of carbon substrates and ion-oxide species. Nanoparticles are procured with unique physiological and chemical properties like nano-size, better chemical wettability and reactivity and larger surface to volume ratio for better bonding characteristics (Boverhof et al., 2015). These properties of the nanoparticles have been immensely used in treatment of oral—health related problems like treatment of dentinal hypersensitivity, eradication of oral biofilms, diagnosis and treatment of oral cancers.

The chemical nature and properties of chitosan like biodegradability, non-toxicity and bioacompatibility lends it to be sustainable. Chitosan is a natural nanopeptide obtained from the purification of chitin which is the main ingredient found in the exoskeletons of

FIGURE 1
Diagrammatic illustration of de-acetylation process of chitin to chitosan.
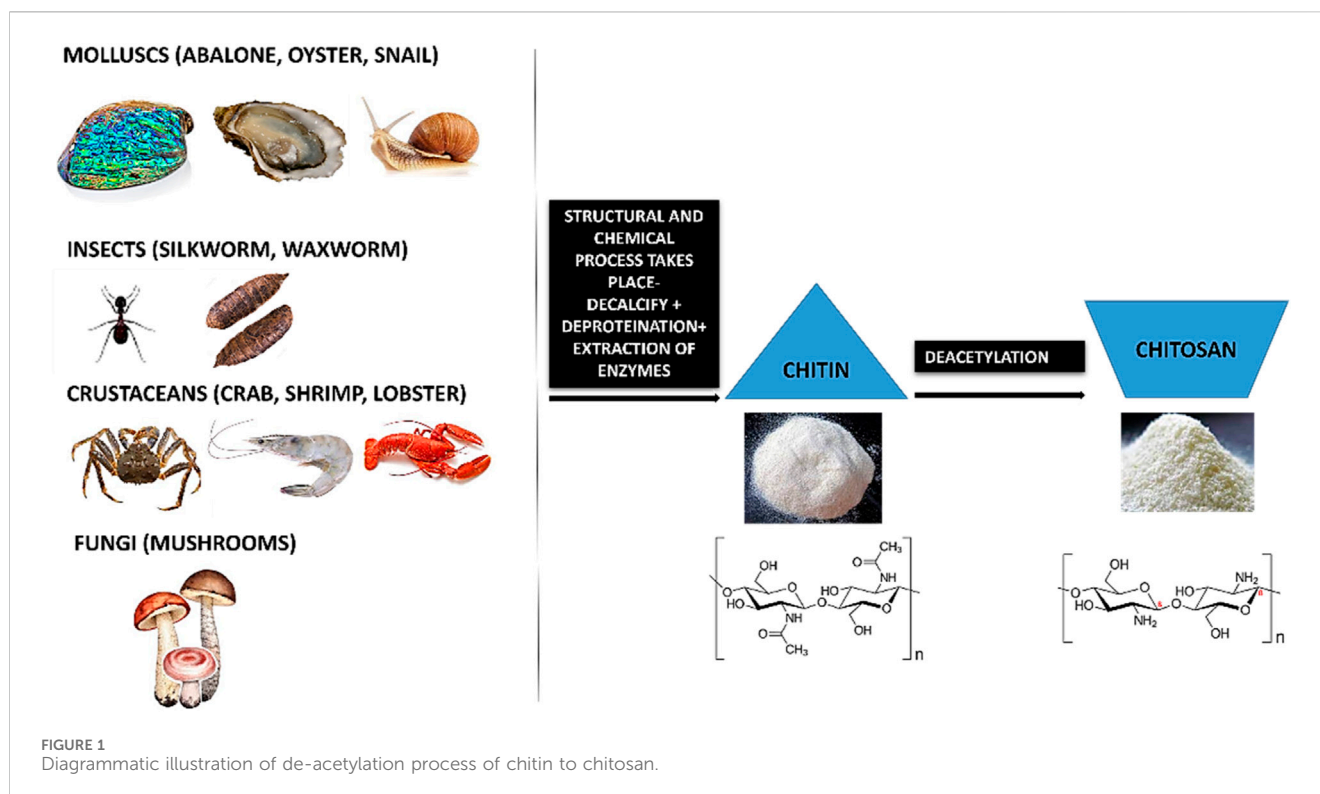
TABLE 1 Chemical analysis of Chitin (CH) and Chitosan (CS).

Characteristics	Chitin (CH)	Chitosan (CS)
Molecular weight	Mw > 1000 kDa	Mw > 100 kDa
Chemical name	β-(1–4)-poly-N-acetyl-D-glucosamine	(1,4)-2-Amino-2-deoxy- beta-D-glucan
Empirical formula	$(C_8H_{13}NO_5)_n$	$(C_6H_{11}NO_4)_n$
Water solubility	Water insoluble	Poorly soluble
Sources	Exoskeleton of marine crustaceans	Derivative of Chitin
Enzymes for synthesis	Chitin synthase	Chitinase

marine crustaceans like crabs and prawns (Paul and Sharma, 2004; Younes and Rinaudo, 2015). Other major sources of chitin include fungi (Blumenthal and Roseman, 1957; Merzendorfer, 2011), insects like silkworm, waxworm, etc (Finke, 2007; Mohan et al., 2020), certain spore-bearing plants like mushrooms, fungi (Wu et al., 2004; Vetter, 2007; Ifuku et al., 2011; Nitschke et al., 2011) and molluscs like snail, oysters, etc (Kurita, 2001; Manni et al., 2010; Rasti et al., 2017; Taser et al., 2021). This macromolecule is processed by the repeated formation of D-glucosamine, which is further extracted from de-acetylation of chitin which is a byproduct of marine shells. During the manufacturing process, the shells and the exoskeleton of these marine creatures undergo de-proteinization to form insoluble chitin (CH) which is then converted to CS (Chitosan soluble under acidic conditions) by the removal of acetyl groups (Figure 1).

Chitin (CH) is considered as the second most abundant polysaccharide after cellulose (Elieh-Ali-Komi and Hamblin, 2016). This natural amino-polysaccharide copolymer is the building block of the exoskeleton of the marine crustaceans

giving them durability and stability against the natural forces. Through enzymatic de-acetylation, chitosan (CS), derivative of chitin is formed. Chitosan is a natural fiber, analogous to cellulose and cannot be digested. This biomaterial is natural, biocompatible, hydrophilic and has a broad antimicrobial and antibacterial spectrum. These natural occurring biopolymers (Chitin and Chitosan) are profusely being used for biomedical applications. Table 1 summarizes the characteristic differences between chitin and chitosan (Imai et al., 2003; Eijsink et al., 2010; Azuma et al., 2015). Chitosan (CS) is composed of N-acetyl glucosamine and glucosamine polymer units (Figure 2) which is derived from Chitin (CH).

Chitosan (CS) has wide range of commendable properties that have been used as a marker for biomedical research. Chitosan has been shown to have positive response for osteo-conductivity when amalgamated with bioactive compounds like Poly-caprolactone (Hayashi et al., 2007; Ignatova et al., 2007; Sarasam et al., 2008; Fakhri et al., 2020). These distinctive characteristics have made a
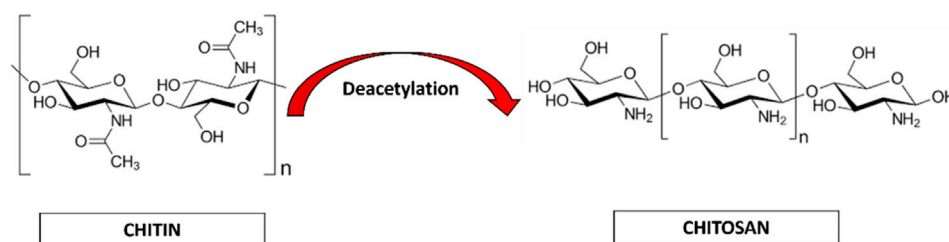
FIGURE 2
Chemical representation of Chitin to Chitosan.
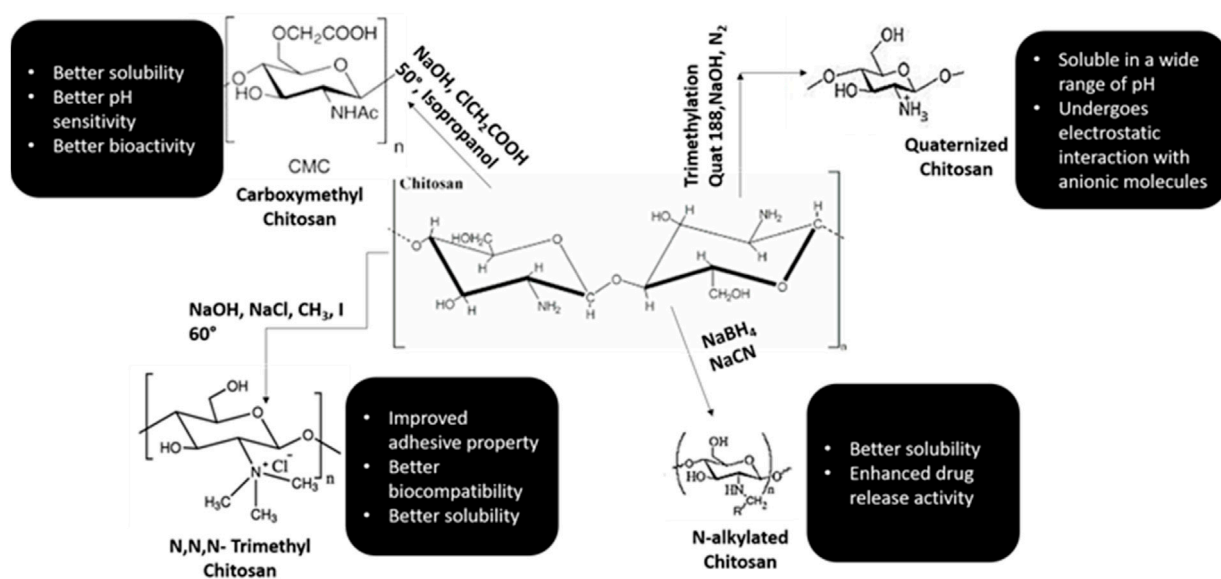
FIGURE 3
Synthetic monologues of Chitosan.

remarkable entry in the field of tissue engineering and biomedical research (Guo et al., 2006; Panahi et al., 2017; Farhadian et al., 2018; Shrestha, 2018). Additionally, Chitosan has also been used as a scaffold substrate for regenerative medicine (Shi et al., 2006; Vázquez et al., 2015) and substratum for growth factor delivery for wound healing (Caetano et al., 2015; Vijayan and Kumar, 2019).

Chitosan is considered to be the only cationic poly-aminosaccharide which can be chemically altered based on the property and function (Fakhri et al., 2020). The degree of deacetylation has a strong influence on its physio-chemical-biological nature. Chitosan and it is by products like chitosan oligosaccharides are similar in nature. These nano-biopolymers can be broken down into simpler compounds through enzymatic process which are biocomapatible and based on required application, they can be modified through chemical or enzymatic reactions to variegated smaller conjugates and various forms like gels, fibers, and sponges (Xia et al., 2011; Qin and Li, 2020). Chitosan and its analogues based on their multitudinous features like cross-linking can be a vital source for the conglomerates of various biomedical materials (Pichayakorn and Boonme, 2013; Li et al., 2014).

Chitosan is well known for its antimicrobial activities, but there are several theories based to this property of chitosan (Rabea et al., 2003; De Carvalho et al., 2011). One theory explains that when chitosan comes in contact with bacterial cell wall, it displaces the calcium ions of the cell membrane resulting in destruction of the membrane (Yadav and Bhise, 2004). Various literature has shown that chitosan is an effective anti-plaque agent and enhances the periodontal health by minimizing the colonies formed by *Porphyromonas gingivalis, Actinobacillus actinomycetemcomitans* and *Prevotella intermedia* (Ikinci et al., 2002; Hanes and Purvis, 2003; Akncbay et al., 2007). In animal studies, chitosan has manifested high potency of biocompatibility and shown to have positive response with implantation of nanomaterials (Levengood and Zhang, 2014; Oryan and Sahvieh, 2017; Li et al., 2021; Sivanesan et al., 2021). Various synthetic monologues of chitosan and their properties are categorized in Figure 3.

The framework of dental materials still holds a place for improvement and lot of research has been carried out for the scope of amelioration. The aim of this review is to highlight the applications of chitosan in dentistry and emphasize its importance in the treatment of various oral diseases. The bioactive properties of

FIGURE 4
Summarization of properties of Chitosan.
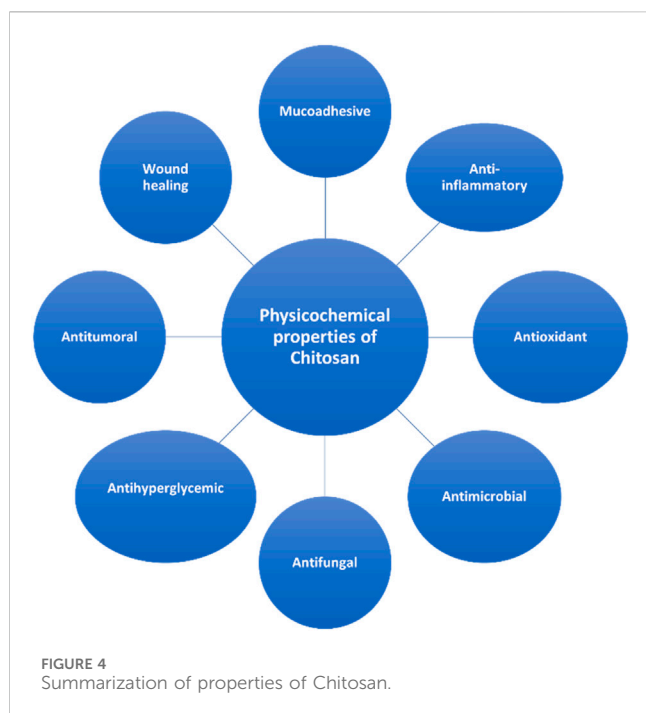
chitosan help in synthesis of various drugs and scaffolds for pulpo-dentinal regeneration. Chitosan has shown excellent oseteoconductivity, proliferation of osteoblasts, and mesenchymal cells thereby inducing *in vivo* neovascularization. (Kim et al., 2008; Costa-Pinto et al., 2011; Saravanan et al., 2013). Chitosan with the above-mentioned properties, makes it the most suitable component for tissue engineering. (Saranya et al., 2011; Sacco et al., 2018; Islam et al., 2020).

Chitosan is the only polycationic nanopolymer and its charge frequency hinges on the degree of acetylation and the pH condition of the media. The solubility of the chitosan depends on molecular weight and acetylation degree. High molecular weight chitosan molecules are easily soluble in acidic media. Hence enormous number of chitosan synthetic derivatives with increased solubility are produced. (Saranya et al., 2011).

The physiochemical properties of Chitosan are shortlisted in Figure 4.

2 Bio-dental applications of chitosan and its derivatives

Chitosan distinctive properties like biocompatibility (Zhang et al., 2002; Rodrigues et al., 2012; Norowski et al., 2015; Elieh-Ali-Komi and Hamblin, 2016), bioactive nature (Saranya et al., 2011; Prabaharan, 2014; Ainola et al., 2016; Sacco et al., 2018; Islam et al., 2020), antifungal and antimicrobial (Goy et al., 2009; Sahariah and Másson, 2017; Hassan et al., 2018; Kim, 2018; Yilmaz, 2020), anticancer activity (Wimardhani et al., 2014a; Adhikari and Yadav, 2018; Kim, 2018; Alamry et al., 2020) and ability to whisk with other materials.

Chitosan is a natural biopolymer which is easily available and extracted from natural sources. Its biomedical nature makes it one of the most efficient natural nanoparticle which can be used in

dentistry. The anti-inflammatory, antifungal, antibacterial, anodyne effect, mucoadhesiveness, osseintegrative property makes it most viable material to be integrated in dentistry. It was also observed that when chitosan was laser coated with chitosan, the osteoblastic activity was enhanced which helps in better remineralization effects. Chitosan, when modulated with apatite coating, enhanced the bioactivity of chitosan which improves the physiological response. (Zhang et al., 2002; Rodrigues et al., 2012; Norowski et al., 2015).

2.1 Classification of nanoparticles in dentistry

Nanoparticles are classified on the basis of origin, dimension, and structural configuration (Hassan et al., 2018; Raura et al., 2020). The classification is summarized in Figure 5.

2.2 Synthesis of nanoparticles in dentistry

There are two main approaches for the synthesis of nanoparticles (Figure 6):

1) **Top-down approach**: In this approach the bulk of the material is made to shrink to a nanoscale structure with specialized treatments like grinding, ablation, etching, and sputtering. These techniques are used for manufacturing micron sized particles. This is a simpler technique involving miniaturization of the bulk material to a small sized structure with desired properties. The basic drawback of this technique is the imperfection of the surface architecture. Nanowires made by lithography is an example of top-down approach (Yanat and Schroën, 2021; Abid et al., 2022; Indiarto et al., 2022).

2) **Bottom-up approach**: In this latter approach the material is made to undergo chemical reactions. This technique is economical, and boasts of reduced wastage of the material. This refers to building-up of the material; i.e., atom-by-atom, molecule-by-molecule, or cluster-by cluster. Some of the well-known bottom-up techniques are organo-metallic chemical route, revere-micelle route, sol-gel synthesis, colloidal precipitation, hydrothermal synthesis, template assisted sol-gel, electrodeposition etc. Luminescent nanoparticles are an example of bottom-up approach (Yanat and Schroën, 2021; Abid et al., 2022; Indiarto et al., 2022).

Besides these, there are some physical, chemical and biological methods for synthesis of nanoparticles which are enlisted in Table 2 (Yanat and Schroën, 2021; Abid et al., 2022; Indiarto et al., 2022).

Chitosan is cationic polymer and is efficacious against fungi and bacteria. This microbial action is attributed to the reactive hydroxyl groups at the C-3 and C-6 positions, the structure, physicochemical traits, and environmental factors of chitosan. Chitosan with it is High-MW, potential antimicrobial effects included serving as a chelator of critical metals, inhibiting nutrients from being taken up extracellularly from cells, and changing cell permeability because it is typically unable to permeate the cell wall and cell membrane. Nevertheless, low-MW chitosan affects RNA, protein synthesis, and
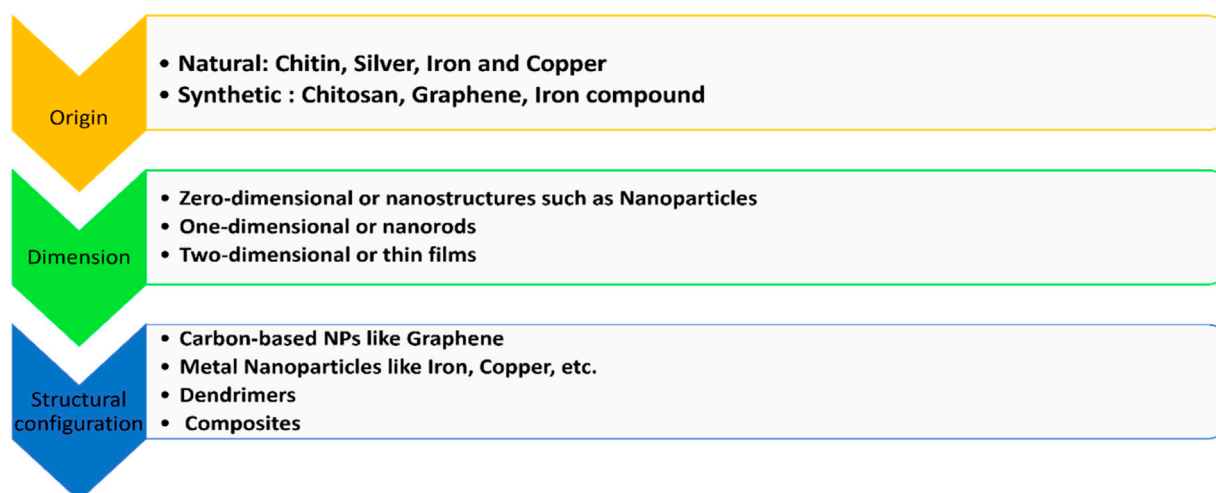
FIGURE 5
Classification of various nanoparticles used in dentistry.
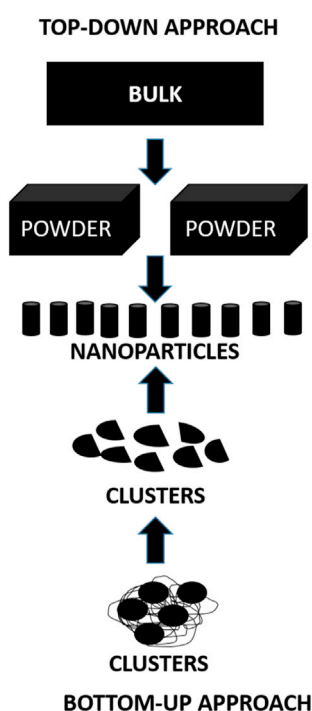
FIGURE 6
Diagrammatic representation of synthesis of nanoparticles.

mitochondrial function in addition to having extracellular and intracellular antibacterial activity. Moreover, the kind of bacteria that chitosan is targeting greatly influences its manner of antimicrobial action. (Ke et al., 2021).

1) Antimicrobial Activity against Bacteria

The cell wall structures of Gram-positive and Gram-negative bacteria differ significantly; Gram-positive bacteria have thicker peptidoglycans, whereas Gram-negative bacteria are more abundant in lipopolysaccharides (LPS). Because LPS is frequently linked to phosphorylated groups, Gram-negative bacteria have a greater negative charge than Gram-positive bacteria. When the pH of the surrounding environment is lower than 6.5, cationic chitosan can attach to phospholipids on more negatively charged cell surfaces. Gram-negative bacteria may be more sensitive to chitosan than Gram-positive bacteria, according to certain theories.

Gram-positive bacteria's teichoic acids are negatively charged as well because of the phosphate groups that are present in their structure. Nevertheless, *Staphylococcus aureus* developed a greater resistance to chitosan with loss of the teichoic acid production pathway, suggesting that chitosan's mechanism of action involves more than just electrostatic interactions. Interestingly, research have shown that DNA transcription can be inhibited by chitosan (≤ 50 kDa) that can penetrate the cell wall. Therefore, even though chitosan's molecular size (MW) is crucial for targeting, chitosan's structure—rather than its MW—determines whether it has extracellular, intracellular, or both extracellular and intracellular antibacterial action.

2) Antimicrobial Activity against Fungi

Chitosan has been demonstrated to have fungicidal effects on a variety of human and plant fungal diseases. The way chitosan interacts with the cell wall or membrane is mostly responsible for its antifungal qualities. However, the MW and level of deacetylation (DDA) of chitosan, the pH of the solvent, and the kind of fungus being targeted are all strongly correlated with the minimum inhibitory concentrations (MICs) of chitosan against fungi. Additionally, it has been suggested that there may be a positive correlation between the amount of unsaturated fatty acids on the cell membrane and chitosan susceptibility. This is because a higher amount of unsaturated fatty acids promotes improved membrane fluidity, which increases the negative charge on the membrane. The contrasting traits between chitosan-resistant and chitosan-sensitive The presence of unsaturated fatty acids in cell membranes is

TABLE 2 Physio-Chemico-Biological methods for synthesis of Nanoparticles.

Physical methods	Chemical methods	Biological methods
High energy Ball milling	Sol-Gel synthesis	Microorganisms assisted biogenesis
Inert Gas Condensation	Micro-emulsion Technique	Bio template assisted biogenesis
Pulse Vapor Deposition	Hydrothermal synthesis	Plant extracts assisted biogenesis
Laser Pyrolysis	Polyol synthesis	
Flash Spray Pyrolysis	Chemical Vapor synthesis	
Electro spraying	Plasma enhanced Chemical Vapor deposition	
Melt mixing		
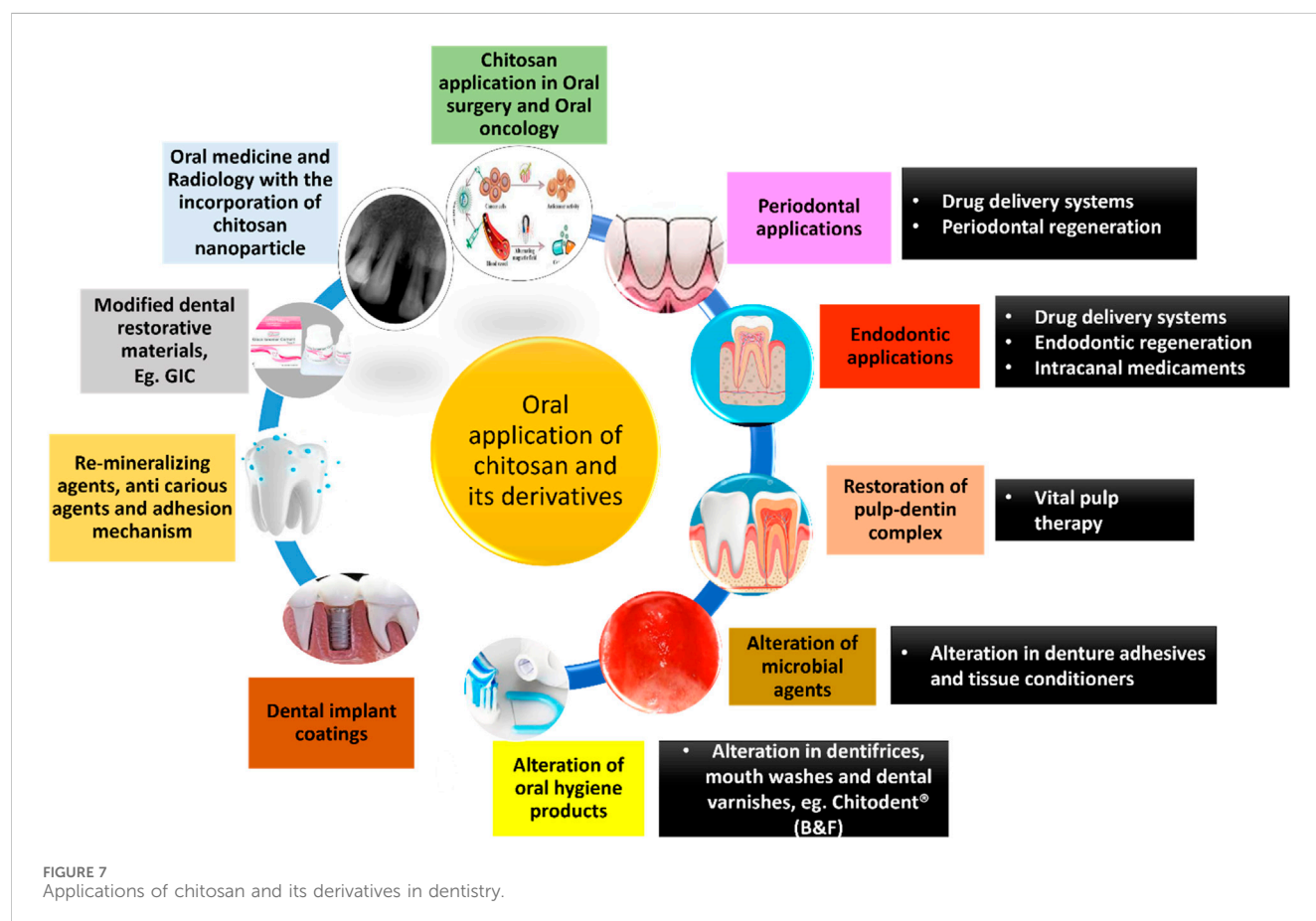
FIGURE 7
Applications of chitosan and its derivatives in dentistry.

associated with strains of Neurospora crassa. Low-MW chitosan has the ability to pierce both the cell surface and wall, which inhibits the creation of proteins and DNA/RNA.

2.3 Applications of chitosan in dentistry

Chitosan has a plethora of applications in the field of dentistry. A schematic diagram summarizing the same has been given below (Figure 7). (Agrawal et al., 2023; Arora et al., 2023; Nava Juárez, 2023; Paradowska-Stolarz et al., 2023; Qu et al., 2023; Minervini et al., 2024)

2.3.1 Oral drug delivery systems

A lot of research has been conducted to confirm the potentiality of chitosan as an oral drug carrier. The basic aim of drug delivery analogues is to produce controlled and sustained release of drugs with prolonged contact time for a specified target with reduced dosage. This results in improving the drug efficacy and reduced side effects of systemic administration (Zivanovic et al., 2007; Priyadarsini et al., 2018). Research has shown that Chitosan-based composites (CBCs) are used to make full-bodied drug delivery carrier systems that have high mechanical strength; maintain good contact time and sustain release of the drug when they are in close contact with the oral mucosa. Chitosan based

composites have been used in treatment of oral diseases (Dhand et al., 2015; Huang et al., 2016; Jeyaraj et al., 2019; Sanap et al., 2020).

The Food and Drug Administration (FDA) has approved Chitosan to be used as food supplement. Oral Chitosan nanospheres are non-toxic in nature and help in prolonged activity of drug at the site of pathology (Saboktakin et al., 2010; Stenhagen et al., 2019; Hu et al., 2020). Chitosan has been shown to have promising ingredients for drug delivery of various organic molecules like DNA, RNA, and various growth factors (Zhang et al., 2011; Soran et al., 2012; Abdel Mouez et al., 2014; Ding et al., 2017).

The proton-amino groups on D-glucosamine of the CS microstructure undergoes electrostatic linkage with negatively charged mucus layer and then invades the deepest layers of the epithelium (Kumari and Singh, 2013; Singh et al., 2013). Based on the mucoadhesive property, chitosan can be used as vehicle for drugs which are administered through various routes like nasal, buccal, ocular, and pulmonary (Keegan et al., 2012; Wang et al., 2013). The insoluble nature of chitosan can be modified through chemical alterations like carboxymethylation, acetylation, thiolation, quaternization, etc (Aguilar et al., 2019; Bakshia et al., 2019). Modified chitosan such as Quaternized chitosan with positive ions, thiolated chitosan obtained by chemical alteration of amino groups with thioglycolic acid, carboxymethyl chitosan and N-acylated chitosan are profusely used in pharmaceutical industry due to increased solubility, high pH, high mucoadhesive property and improved drug penetration (Khutoryanskiy, 2011; Bernkop-Schnürch and Dünnhaupt, 2012; Mansuri et al., 2016; Bakshia et al., 2019). CS based drug delivery systems are highly used in the treatment of dental caries, periodontitis, pulp space therapies and prolonged anesthesia.

The adverse effects of systemic administration of drugs have resulted in poor patient compliance; so, to overcome this, local drug deliveries for periodontal pockets has come to the forefront. Local drug delivery systems permit prolonged release of the drug in periodontal pockets with a long contact time resulting in better treatment outcome (Chen et al., 2017; Zhang et al., 2018a; Wang et al., 2020). These systems act as an adjunct to oral prophylaxis and decrease the systemic adverse effects.

Chitosan nanoparticles have been shown to have anti-inflammatory effects on human gingival fibroblasts by reducing the number of receptors on inflammatory cytokines and chemokines such as IL-1β, TNF-αand CXCL-8. Various studies have shown that human gingival fibroblasts tend to have increased metabolic ability and cellular viability in the presence of chitosan nanoparticles which help in reconstitution of gingival tissue (Goodson et al., 1985; Mahmood et al., 2017; Shen et al., 2017).

Chitosan microspheres are spherical patches ranging from few micrometers to 1000 μm and contain medicinal agents in a polymerized matrix. These patches protect against salivary digestive enzymes and can be applied in mucosal membranes and sub-gingival sites (Greenstein and Polson, 1998; Joshi et al., 2016). Recently, there are micro-formulations of chitosan with anionic bio-particles like alginate, xanthan gum, hyaluronic acid and pectins. These micro-formulations are termed as polyelectrolyte complexes (PEC) which provide sustained release of drugs and are less toxic when compared to cross-linked polymers (Agnihotri et al., 2004; Sinha et al., 2004; Arancibia et al., 2013; Silva et al., 2013; Babrawala et al., 2016). Yadav and co—workers in a study used chitosan, calcium and sodium alginate combination microspheres to contain antibiotics like ornidazole and doxycycline and proved the efficacy, muco-adhesive activity and biodegradability of these microspheres (Yadav et al., 2018). Many attempts to combine microspheres and hydrogel to provide two-layered barrier system has been tried (Zhao et al., 2014).

Chitosan nanoparticles have propitious results when treating oral pathologies. These group drug delivery devices benefit from the small particulate size and the innate characteristics of the polymer. Owing to sizing of the nanoparticles, these particles can penetrate through impervious barriers and also contact the tissues over a larger surface area (Fakhri et al., 2020). These chitosan nanoparticles protect the gastrointestinal tract from enzymatic degradation and acidic environment (Wang et al., 2011; Alcaraz et al., 2016). The beneficial aspects of chitosan nanoparticles encapsulated with antibiotics like doxycycline (Madi et al., 2018; Hu et al., 2019), silver nanocrystals (Xue et al., 2019), tetracycline (Parsa et al., 2019) and ciprofloxacin (Zhao et al., 2013) have been studied and confirmed. A lot of research is conducted on chitosan/PLGA (Polylactic co-glycolic acid) nanoparticles and has shown to have improved stability, enhanced drug release and non-toxic behavior (Lu et al., 2019). Chitosan laden PLGA, Lovastatin and Tetracycline nanoparticles have been explicated and have been revealed to induce osseous formation, alkaline phosphatase activity, biocompatibility, antibacterial activity and controlled and sustained release of these drugs to treat existing pathological condition (Lee et al., 2016).

Chitosan nanofilms are gaining popularity and are effectively used in the interproximal pockets (Salari et al., 2018). The advantages of films as drug delivery devices include biodegradability and ease of placement without intervening with daily activities. The films can be altered and adjusted according to the size of the defect site (Soskolne, 1997). The placement of films in the oral cavity gets disturbed due to saliva and its lubricating efficacy. Muco-adhesiveness is considered to be a pre-requisite property for the manufacturing of nanofilms. In a study by Ghafar et al., thiolated chitosan based nanofilms were introduced for the release of calcium fluoride for dental caries and for the release of lignocaine for diminishing pain. Based on this study, it was found that the thiol groups from the films get released and interact with the oral mucosa for long duration increasing the contact time of the drug, and also regulating the release of fluoride. Hence, thiolated chitosan based nanofilms can be suggested for oral problems (Ghafar et al., 2020). Chitosan–alginate complex films are durable, have improved physical and mucoadhesive properties. These films are said to have higher alginate content with increased concentration which aids in slow drug release (Kilicarslan et al., 2018). CS-alginate films have been used to incorporate natamycin and silver nanoparticles (da Silva et al., 2013). Chitosan laden with risedronate and zinc hydroxyapatite (CRZHF) films are introduced for treatment of periodontitis as anti-resorptive medicament. These CRZHF films are flexible and have good mucoadhesive strength resulting in hard detachment after the placement of the film into the periodontal pockets. Clinical trials with CRZHF have shown increased alkaline phosphatase activity, resulting in bone formation and improved successful treatment outcome (Khajuria et al., 2018). Chitosan-based films with local anesthetics have been implemented to relieve pain and discomfort in patients. Chitosan/collagen films incorporated with lidocaine, tetracaine and benzocaine for effective delivery of local anesthetics have also been tried. These films have good mucoadhesion, and improved flexibility (DiMartino et al., 2019).

Another form of drug delivery systems are chitosan gels. These gels include drug macromolecules incorporated into the polymeric structure and help in controlled and sustained release of the drug. These hydrogels are manufactured by chemical crosslinking to form permanent bonds and physical crosslinking to form provisional bonds. These cross-linked hydrogels have good viscosity, high mucoadhesive properties, better injectability and prolonged release of the drug at the site (Bhattarai et al., 2010). Chitosan gels combined with 15% metronidazole have been used as an adjunct to mechanical debridement for periodontitis to improve the treatment outcome (Akıncıbay et al., 2007). Recently, thermosensitive gels have been introduced into dentistry; these hydrogels reform their gelation nature according to alterations in temperature and display sol-to gel transformation when administered into the body. The first thermosensitive hydrogel composed of chitosan, quarternized chitosan and β-glycerophosphate was introduced against periodontal pathogens like *P. gingivalis* and *P. intermedia* (Akncbay et al., 2007; Ji et al., 2010). Chitosan, β-GP hydrogel in injectable form packed with ornidazole and BMP-7 was used for periodontal regeneration of furcation defects (Bansal et al., 2018). Bacterial plaque causes low pH environment in the oral cavity which can alter the release of the drugs from the hydrogel *in situ*. To overcome this, pH sensitive hydrogels like N-carboxymethyl chitosan-based hydrogel, injectable chitosan-grafted-dihydrocaffeic acid/oxidized pullulan hydrogel, etc. have been introduced. These hydrogels are pH- dependent and exhibit good swelling behavior, drug release and muco-adhesiveness. These hydrogels are well-known for cancer therapy and tumors which create an alteration in pH in the oral environment (Liang et al., 2019). Hydrogels which control the drug release have been found to be very efficient with characteristics like eletro-responsiveness and pH sensitivity and are manufactured by implanting polyaniline onto chitosan and crosslinking with oxidized dextran (CS-P/DO). These hydrogels are cyto-compatible and biodegradable (Alinejad et al., 2016).

Chitosan fibers also form one of the recently introduced drug delivery systems. Chitosan has known to have high fiber-forming property. Chitosan fibers are constructed through electrospinning process producing fibers ranging from nanometers to micrometers. CS fibers are extravagantly used for neural and osseous tissue engineering. These fibers tend to have low molecular weight; hence they are reticulated with epichlorohydrin, hydroxyapatite, PLGA, poly-caprolactone, cellulose, polyvinyl alcohol, etc. (Wei et al., 1992; Tanir et al., 2014). The Electrospun chitosan fibers with drug are potentially used in guided tissue engineering. Chitosan-Polycaprolactone cross-linked with metformin membrane stimulates bone formation, alkaline phospahatase activity and mineralization of bone mesenchymal stem cells (Zhu et al., 2020). Chitosan-Gelatin nano-carriers laden with calcium hydroxide are used for endodontic infections for sustained release of calcium hydroxide for longer duration. The combination of chitosan with calcium hydroxide has shown excellent antibacterial activity against endodontic pathogens like *Enterococcus faecalis* (Shaik et al., 2014; Malinowska et al., 2017). Table 3 mentions a list of a few of the many studies on nanoparticle drug delivery modes with antibiotics.

2.3.2 Alteration of antimicrobial agents

The positively charged amino groups of N-acetyl glucosamine combines with negatively charged ions of the bacterial cell wall containing lipids, phospholipids, carbohydrates and proteins (Kong et al., 2010). This basis remains the same for fungal and viral micro-organisms. The underlying mechanism for the antibacterial action of chitosan is still not clear, but the theories state that the amino groups interact with the negatively charged particles of bacterial cell wall leading to cell wall leakage, increasing the permeability and ultimately leading to cell destruction (Matica et al., 2019). Another theory for the mechanism of action of chitosan believed, is that the low molecular weight of chitosan can penetrate the bacterial cells and impede the bacterial activities like RNA and protein synthesis. High molecular weight molecules of chitosan particles >100 kDa, tend to deposit a polymer material around the cell membrane and cuts down the nutrient supply (Younes et al., 2014). However, the bio-properties of chitosan are magnified by decreasing the deacetylation process and modifying the pH of the environment (Lim and Hudson, 2004; Li et al., 2016).

On the whole, intensifying the positive charges of chitosan molecules increases the electrostatic reciprocity with the cellular contents and thereby increases the antimicrobial efficacy of chitosan. Certain cross-linking methods like carboxymethylation, sulfonation, quaternization, and phosphorylation enhance the solubility of chitosan and increase its antimicrobial efficiency (Lim and Hudson, 2004; Xu et al., 2011). Quaternized chitosan and its derivatives have been extensively studied on the aspects of their antimicrobial efficacy and shown to have the best results (Zhang et al., 2002; Ignatova et al., 2007; De Carvalho et al., 2011; Wang et al., 2016; Xu et al., 2018). Ammonium salts of Chitosan are shown to be highly effective against *E. coli* and *S. aureus* (Kim et al., 1997).

Chitosan and its compounds are effective on fungal and bacterial substrates. Congregation of literature has divulged the efficacy of chitosan film on medical instruments against contamination (Ghosh et al., 2011; Islam et al., 2019). Based on the efficacy, chitosan can be cross-linked to tissue conditioners or denture adhesives and help in the prevention of denture stomatitis (Lee et al., 2018; Namangkalakul et al., 2020). Tissue conditioners made of chitosan and chitosan oligosaccharide are excellent alternatives for treatment of denture stomatitis. High anti-microbial property and water solubility of Chitosan oligosaccharide makes it an ideal choice for reducing *Candida albicans* infections. Tissue conditioners made of quaternized chitosan can be used as provisional lining materials for treating denture stomatitis (Saeed et al., 2019).

Chitosan has played a vital role in the treatment of endodontic infections. Calcium hydroxide cross-linked with chitosan as intracanal medicament has been effective in reducing the periapical infections. Chitosan has anti-biofilm property which aids in controlling the microbial load and effective against *E. faecalis, Streptococcus mutans*, and various other microbes (Elshinawy et al., 2018; del Carpio-Perochena et al., 2017; Loyola-Rodríguez et al., 2019; Ganss et al., 2011; Young et al., 1997; Ganss et al., 2014). Antibacterial efficacy of endodontic sealers incorporated with chitosan has been seen to be effective for longer periods of time (Pini et al., 2020).

2.3.3 Alteration of oral health products

Use of oral hygiene products like toothpastes, brushes and mouth wash plays a very key role in oral hygiene maintenance. Dentifrices are

TABLE 3 Studies illustrating on the drug delivery modes with antibiotics.

Ref	Type of delivery system	Biomaterial/ Polymer	Drug inoculated	Conclusions
Goodson et al. (1985)	Hydrogel	Chitosan	5% Tetracycline	• Great antibacterial activity against Gram-negative and Gram-positive bacteria • Can be used as wound dressing
Greenstein and Polson (1998)	Nanospheres	Chitosan	Ciprofloxacin	• Excellent antibacterial activity against *E. coli*
Agnihotri et al. (2004)	Polyelectrolyte films	Chitosan + Alginate	Clindamycin	• Good drug delivery system for periodontal therapy
Ghafar et al. (2020)	Nanoparticle	Chitosan + Dextran	IL-17RB siRNA and doxorubicin (DOX)	• Co-delivery of IL17RB siRNA and DOX have shown excellent results in the treatment of breast cancer
Khattak et al. (2019)	Intracanal medicament	Chitosan	Calcium hydroxide + Triple antibiotic paste	• Highly effective against *E. faecalis* and C. albicans to treat endodontic infections

known to fend off the demineralization effects of tooth substrate due to acidic drinks. Numerous dentifrice formulations have been studied and enlisted in table 4. Various toothpaste preparations containing nanoparticles with hydroxyapatite, 5% KNO_3, etc., aim at providing fluoride (F) release towards tooth re-mineralization of enamel substrate. In a study by Ganss et al., a non-fluoride, chitosan-based dentifrice (Chitodent® (B&F)) was investigated and showed significant reduction in tooth tissue loss (Costa et al., 2014). This was attributed to the cationic character of chitosan combined with low pH, and affinity to bind to negatively charged structures like enamel and dental biofilm. The presence of nanoparticles like chitosan helps in formation of organic protective layer over the mineralized structures (Costa et al., 2014; Farias et al., 2019; Pini et al., 2020). Certain toothpastes containing Strontium (Sr) and potassium nitrate have shown to diminish the erosion of dentin (Covarrubias et al., 2018). F/Sr containing toothpastes combined with chitosan tend to have anti-erosive and anti-abrasive properties. Pini et al., in their study concluded that increasing the viscosity of chitosan to F/Sr toothpaste, helps in complete inhibition of enamel tissue loss thereby retaining the enamel surface (Costa et al., 2014).

Recently, a lot of research has been involved in the manufacture of chitosan-based oral hygiene maintenance products like mouthwash, varnishes, nanogels (Table 4). Costa and his co-workers, studied the efficacy of chitosan based mouthwashes on biofilm formation and microbial attachment of *E. faecalis, C. albicans, S. mutans* and *P. intermedia* and concluded that these mouth washes are effective in controlling dental caries, periodontal problems and fungal infections. Various formulations of mouthwashes like *Mentha piperita* essential oil (MPEO) with chitosan have shown to have prolonged anti-caries effects. Currently, a new lineage of anti-carious products containing combinations of metallic compounds like silver or copper with chitosan have been experimented and documented that chitosan undergoes electrostatic interaction with tooth structure and bacterial cell wall, thereby escalating anti-biofilm property (Arnaud et al., 2010; Costa et al., 2014; Zafar and Ahmed, 2014; Wassel and Khattab, 2017; Covarrubias et al., 2018; Farias et al., 2019).

2.3.4 Re-mineralization of enamel

Restoration of lost enamel is one of the most challenging tasks in dentistry since enamel is formed only once in the human body and is avascular (Zhang et al., 2018b). Various bioactive dental materials have

been developed for regeneration of enamel but till date majority of them are disbelieving. Chitosan structure gets protonated with free amino groups and creates a positive charge around it. This property helps chitosan to bind to negatively charged structures like tooth enamel. In addition, chitosan can invade into the deeper layers of enamel producing mineral content and thereby helping in re-mineralization of carious lesions. Hence, chitosan-based materials help in re-mineralization of lost enamel and prevent the progression of carious lesions (Ren et al., 2019; Zhang et al., 2019). In a study, it was demonstrated that Chitin-bioglass complex helps in deposition of mineral content and refines the eroded or carious enamel surface; improves the microhardness of surface and sub-surface areas. Chitosan nanoparticles coupled with amelogenin in the form of hydrogel help calcium and phosphate ions to reorganize and form enamel like structure. (Ren et al., 2019). The above-mentioned hydrogel has got excellent anti-bacterial and re-mineralization capacities.

2.3.5 Bonding to tooth structure and adhesion mechanism with chitosan

The resin-dentin bond and the longevity of the bond strength has received a lot of attention and is being researched upon. Dental materials like composites are used for bulk filling and dentin replacement which tend to cause polymerization shrinkage and involves technique sensitive steps like acid etching and bonding, and removal of smear layer (Murray et al., 2003). When there is incomplete removal of smear layer, the resin monomer does not flow in properly resulting in polymerization shrinkage and ultimately microleakage (Chen et al., 2003). To overcome this demerit, chitosan hydrogels and polymeric bio adhesives have come into demand. In a study, chitosan hydrogels incorporated with propolis, β carotene and nystatin were evaluated and shown to have increased shear bond strengths over a period of time. The shear bond strengths with respect to chitosan hydrogel have been deemed higher than conventional dentin-bonding systems (Perchyonok et al., 2013).

2.3.6 Chitosan coated dental implants

The extent of osseo-integration of dental implants with alveolar bone marks the clinical outcome of the dental implants (Javed et al., 2014; Alghamdi, 2018). To improve the osseo-integration effects, numerous methods such as chemical surface treatments, and surface coating for implants have been tried and shown favorable results

TABLE 4 Studies highlighting the effectiveness of chitosan modified oral hygiene aids.

Ref	Type of study	Type of oral hygiene aid	Chitosan-coupled groups	Comparative groups	Conclusions
Ganss et al. (2011)	In-vitro	Tooth paste	Fluoride-free CS-toothpaste (Chitodent)	NaF-toothpastes, NaF/KNO$_3$, NaF/HA, Zn/carbonate/HA, SnF$_2$/NaF, SnCl$_2$/NaF,SnF$_2$	SnF$_2$ most effective
					Chitodent reduced tissue loss by 30%
Ganss et al. (2014)	In-vitro	Tooth paste	AmF/NaF/SnCl$_2$/CS 0.5%	NaF, SnF$_2$ gel, toothpaste	AmF/NaF/SnCl$_2$/CS showed significant reduction in tissue loss with or without brushing
Pini et al. (2020)	In-vitro	Tooth paste	F/Sn/CS-toothpaste	F/Sn-toothpaste	Chitosan with higher viscosity of (1000 mPas) showed the best anti-erosion/abrasion effects
Costa et al. (2014)	In- vivo	Mouthwash	HMW CS 0.4 v/v	Chlorhexidine	Chitosan incorporated mouthwash was highly effective against Streptococci and Enterococci with the lowest cytotoxicity
			LMW CS 0.4 v/v		
Farias et al. (2019)	In-vitro	Mouthwash	MPEO/CS/biosurfactant	Biosurfactant/MPEO, fluoride-free mouthwash	Mouthwash containing chitosan showed high antimicrobial activity against cariogenic bacteria with least toxicity
			Biosurfactant/CS		
Covarrubias et al. (2018)	In-vitro	Varnish	CSnP/NaF, CSnP	Miswak, Miswak/F, Propolis, Propolis/F, NaF	NaF coupled with chitosan nanoparticles exhibited highest anti-bacterial and anti-demineralization activity

(Najeeb et al., 2016; Guglielmotti et al., 2019). Various bioactive layering on the surface of implants have resulted in improved bone health and osseo-integration in immunocompromised patients (Abtahi et al., 2012; Pang and Huang, 2012; Diz et al., 2013; Javed et al., 2014; Najeeb et al., 2017; Duarte et al., 2021). Multitude of studies have highlighted the beneficial aspects of chitosan coatings for dental implants (Redepenning et al., 2003; El Nady et al., 2017; Li B. et al., 2019; Alnufaiy et al., 2020; Yilmaz, 2020). The chitosan coating on dental implants tends to decrease the surface roughness, hydrophilicity which helps in apaptite formation, cell adhesion and proliferation thus increasing the bioactivity. Chitosan bio-coatings show excellent biocompatibility, no cytotoxicity and better antibacterial activity. It is also stated that increased thickness of chitosan coating on dental implants prolonged the antibacterial activity (Norowski et al., 2011). Literature has also reported that chitosan layering on dental implants reduce stress concentrations by changing the elastic modulus of the bone-implant interface (Levengood and Zhang, 2014). In addition, research has shown that antibiotics can be incorporated on the chitosan coatings for better healing around the implant area (D'Almeida et al., 2017; Cohenca et al., 2013). Antibacterial coatings on implants and medical devices have shown to have good clinical success, but still further investigation is required.

2.3.7 Chitosan modified dental restorative materials

Over the recent years, a lot of noteworthy research has been tried and tested to create opportunities for bioactive dental materials. The level of destruction to the pulpo-dentinal complex dictates the treatment prognosis with the use of biomimetic materials (Drummond, 2008). However, certain flaws have been delineated which include poor adhesion, less mechanical strength when compared to ceramic or resin-based materials (Wimardhani et al., 2014a). Owing to these disparities, poor interfacial bond is

created between the tooth and the material resulting in microleakage (Bentley and Drake, 1986; Ho et al., 1999).

Glass ionomers (GI) are tooth colored restorative materials comprising calcium fluor aluminosilicate glass powder and polyacrylic acid liquid. GIs bond chemically to the tooth structure and exhibits anticariogenic property with the release of fluoride (Forsten, 1994). There are numerous applications of Glass ionomers like luting/cementation of crowns and bridges, restorative materials for class V lesions and non-carious lesions like erosions, sandwich technique for class II restorations, core build-ups, atraumatic restorative treatment, lining material under composite restorations and pit and fissure sealants (Sidhu and Nicholson, 2016). Despite all the advantages, GIs have certain limitations like poor mechanical strength, low fracture toughness, low abrasion resistance and poor esthetics. Hence the application of conventional glass ionomers on high stress bearing areas is avoided (Khoroushi and Keshani, 2013). To overcome these discrepancies, experimentation has been done to integrate bioactive polymers into restorative materials and modify their properties.

Currently, nanoparticles like chitosan have been coupled with glass ionomers to modify their mechanical and antibacterial properties. The anionic groups of polyacrylic acid of Glass ionomers co-agglomerate with cationic amine groups of chitosan to form interpenetrating polymerized network. It can be predicted that inclusion of nano-chitosan particles to Glass ionomer materials would enhance the mechanical strength and anti-cariogenic property for high stress bearing area applications (El-Negoly et al., 2014; Senthil et al., 2017). It has also been proved that application of chitosan to liquid component of GIs improves the chemical adhesion and antibacterial activity (Soygun et al., 2021). Chitosan modified GIs have been clinically accepted as a root coverage material for gingival recession which promises minimal to no-genotoxicity and cytotoxicity effects and enhances the proliferation of human gingival fibroblasts (Zhou et al., 2019). It is also noted that chitosan modified GIs helps in sustained release of

proteins, growth factors and bioactive polymers which is apt for vital pulp and regenerative therapies. In a study, it was reported that ion release from Chitosan modified Glass ionomers was advantageous to the tooth substrate (Mulder and Anderson-Small, 2019), and also helps in sustained release of proteins without any cytotoxic effects to pulp cells (Limapornvanich et al., 2009). Various bio-molecules like Tumor Necrosis factor, growth factors, peptides, TGFβ-1 can be applied to chitosan modified GICs to stimulate pulp regeneration (Rakkiettiwong et al., 2011).

Enormous amount of research is being carried out to modify the physical properties of various dental materials. Recently, chitosan-based nanocomposites have been developed and are claimed to have superior features like strength, heat stability, electrical conductivity, photoluminescence, antimicrobial, and biomedical features which increase the longevity of dental restorations (Diolosà et al., 2014; Kausar, 2021). In addition, chitosan modified zinc oxide eugenol cements, root canal sealers have also been investigated (Dragland et al., 2019).

2.3.8 Chitosan and pulpal regeneration

Regeneration of dental pulp is one of the most unpredictable situation in dentistry. Tissue engineering approaches like stem-cell based transplantation have been experimented to simulate the dentin-pulp complex. Stem cells are harvested from various sources like dental pulp stem cells (DPSCs), stem cells from human exfoliated deciduous teeth (SHEDs) and stem cells from apical papilla (SCAP) (Huang et al., 2008). These cells have highest potential of differentiating into odontoblast like cells, high proliferation capability, and multi-cell differentiation capacity. DPSCs are easily extracted from human permanent or deciduous teeth. Transplanting human DPSCs onto the chitosan scaffold for pulpo-dentinal complex regeneration is still under research. However, cell homing via DPSCs seem to have promising results in regenerative endodontics. Some of the clinical trials have shown to form connective tissue similar to dental pulp with neovascularization and in some cases, dentin deposition was also noticed (Eramo et al., 2018).

The stimulation of mesenchymal stem cells to form odontoblastic cells forms the basis for endodontic regeneration. It has been reported that porous chitosan scaffolds when coupled with bioactive molecules like growth factors and peptides, help in release of odontoblastic markers like dentin sialo-phosphoprotein, alkaline phosphate, and dentin matrix acidic phosphoprotein which form an extracellular polymerized matrix which acts as niche for the multiplication and proliferation of DPSCs into odontoblastic cells resulting in mineralization process (Soares et al., 2018; Bakopoulou et al., 2019; Raddall et al., 2019; Moreira et al., 2021). In addition, Chitosan scaffolds enriched with signaling molecules like BMP 1and7, vascular endothelial growth factor (VEGF), brain-derived neurotrophic factor (BNF), fibroblast growth factor (FGF) and drugs like simvastatin and metformin help in inducing reparative dentin formation by promoting cell adhesion and proliferation of DPSCs (Guo et al., 2006; Jingwen et al., 2016; Schmalz et al., 2017; Retana-Lobo, 2018; Soares et al., 2018; Yang et al., 2020). Biomolecules like TGF β-1 when loaded with chitosan are proving to be excellent alternatives to calcium hydroxide as a pulp capping material since it regulates the differentiation of odontoblastic stem cells, alkaline phosphatase, OCN gene/protein expression and bio-mineralization (Farea et al., 2014; Abbass et al., 2020). SCAP/carboxymethyl chitosan/TGF-

β1 scaffold is also reported to be favorable for pulp regeneration as it releases CS nanoparticles, dentin matrix protein-1 and dentin sialo-phosphoprotein (Bellamy et al., 2016).

Zhu and his co-workers brought a breakthrough in the field of vital pulp therapy. They introduced injectable Ag-BG/chitosan thermosensitive chitosan hydrogels which promote odontogenic regeneration due to their viscosity, flexibility and thermosensitive nature (Zhu et al., 2019). These hydrogels possess high antibacterial and anti-inflammatory potential and the chitosan release odontogenic markers like PGE2, TNFα, IL-1β, −6 and −8 which are ideal for endodontic regeneration (Silva et al., 2013; Aguilar et al., 2019; Zhu et al., 2019). Another innovation reported with the development of pulp regeneration was chitosan-cellularized fibrin hydrogel which led to proliferation of collagen type I and dental pulp mesenchymal cells producing 3-D collagenous network analogous to innate pulpal tissue (Ducret et al., 2019). Qin et al. in their study inoculated chitosan–metformin with Calcium phosphate cements to enhance the strength, mineralization and osteogenic potential (high alkaline phosphatatse activity and increased proliferation of DPSCs) of biomembranes (Qin et al., 2018). Chitosan along with hDPSCs have shown to have promising results for endodontic regeneration.

2.3.9 Chitosan modified wound dressings

These dressings are highly effectual for controlling hemorrhage and infection after surgical operative procedures. As stated earlier, the positively charged amino groups of chitosan electrostatically interact with negatively charged elements of blood, i.e., RBCs to bring about the hemostatic property (Caetano et al., 2015; Minervini et al., 2024).

Quaternized chitosan-G-polyaniline and benzaldehyde group functionalized poly (ethylene glycol)-co-poly (glycerol sebacate) (PEGS-FA) hydrogels have high antibacterial, antioxidant, antimicrobial property, good self-healing capacity which makes it ideal for the manufacture of wound dressings. These self-healing hydrogels are bestowed with free radical scavenging capacity, adhesiveness, biocompatibility and excellent *in vivo* blood clotting capacity which stimulate the wound healing mechanism, granulation tissue formation and collagen deposition by upregulating the growth factors like Transforming Growth Factor-β (TGF- β), Epidermal growth factor (EGF) and Vascular endothelial growth factor (VEGF) (Zhao et al., 2017). It is also proved that Chitosan dressings when refined with polyphosphate and silver, escalates the hemostatic and antimicrobial activity. Chitosan-polyphosphate formulation (ChiPP) enhances blood clotting, platelet adhesion, faster thrombin generation and better absorption of blood (Dai et al., 2011).

pH-responsive hydrogel wound dressings containing quaternized chitosan/benzaldehyde-terminated pluronic F127 (PF127) coupled with curcumin have shown enhanced antimicrobial, anti-inflammatory, and improved wound healing activity. These hydrogels enhance the wound healing process by minimizing the inflammatory markers and upregulating the wound healing-related growth factors (Qu et al., 2018). Recently, a major breakthrough, i.e., in the treatment of infected wounds, a photothermal self-healing nanocomposite hydrogels with antibiotics have been introduced. These nanocomposite hydrogels are presented with N-carboxyethyl chitosan/PF127/carbon nanotube and exhibit stable hemostatic,

mechanical properties, remarkable photothermal antibacterial property and an increased pH-responsive moxifloxacin release capacity to enhance the healing process (He et al., 2020).

2.3.10 Chitosan based tissue engineering aspects

Periodontitis is a chronic inflammatory disease affecting the periodontium and the tooth supporting structures resulting in loss of alveolar bone and mobility of teeth. To overcome this situation, surgical approaches like guided tissue regeneration (GTR) and guided bone regeneration (GBR) can be considered. In these procedures, a scaffold barrier is placed to allow osteloblastic proliferation and osseous formation around the bone defect. The barrier obstructs the epithelial cell migration resulting in formation of long junctional epithelium *in lieu* of bone formation (Newman et al., 2011).

The basic aim of tissue engineering is to construct a 3-D scaffold which bears a close similitude to the structure of bone. Tissue engineering aims to create a regenerated tissue on polymerized decomposable scaffold as a layering for stem cell attachment, adhesion, and proliferation. The manufacture of bio-membrane should be biocompatible, non-toxic, biodegradable and should resemble the extracellular matrix (ECM) containing glycosaminoglycans, glycolipids and glycolipids for neo-regeneration of the tissue (Baranwal et al., 2018).

Natural and synthetic biopolymers are present to provide scaffolding. Chitosan and various subordinates meet the fundamental requirements of tissue engineering. It has been advocated that chitosan implantation does not provoke any immune response and the breakdown of chitosan by lysozyme upon the formation of new tissue does not produce any toxic effects. In dentistry, chitosan scaffolds are extensively used for pulpo-periodontal-bone regeneration (Li et al., 2014; Vázquez et al., 2015; Sultankulov et al., 2019). Chitosan is amenable to the characteristics of scaffold; however it lacks superior mechanical property and bioactivity which are the essential basis for osseous tissue engineering (Azevedo et al., 2014). To achieve this point, chitosan is coupled with synthetic biopolymers, growth factors and proteins to enhance the osseous regeneration with improved mechanical strength. Chitosan membrane laden with bioactive nanoparticles like hydroxyapaptite (HA), silica and tricalcium phosphate (TCP) stimulates bone formation and improves mechanical properties (Faqhiri et al., 2019). Additionally, nano-ceramic particles like Bioactive glass can be applied to chitosan to promote osteogenesis in load bearing areas (Denuziere et al., 1998). Chitosan/chondroitin sulfate/Bioactive glass nanoparticles facilitate osteogenesis *in-vivo* (Nie et al., 2019). Nanocomposite scaffolds containing chitosan-gelatin- nanobioactive glass are proven to create a sterile environment for cell attachment to promote protein adsorption and mineral deposition to promote osseous formation (Januariyasa et al., 2020). Combination of nanomaterials with bioactive growth factors on a 3-D scaffold directs the mesenchymal stem cells to differentiate to osseous formation (Guo et al., 2006; Oryan and Sahvieh, 2017).

Various studies have reported that chitosan-hydroxyapaptite combination coated scaffolds provide excellent environment for cell differentiation and proliferation promoting osseous formation similar to the original bone structure. The incorporation of nanohydroxyapatite in the scaffold increases the apatite content

in the defective area which provides the basis for bone tissue engineering which led to the development of chitosan double faced membranes (Gümüşderelioğlu et al., 2020). These membranes were used for periodontal regeneration. The porous side of the membrane (in contact with bone) was loaded with nanohydroxyapatite and BMP-6, and the opposite side was laden with poly-caprolactone nanofibers to mitigate the epithelial cell migration. The porous surface induced multiplication of MC3T3-E1 preosteoblasts, while the other side of the membrane acted as a guard against epithelial cell migration (Marrazzo et al., 2016; Suneetha et al., 2020).

Injectable hydrogels have always been reliable and used as a part of tissue engineering process. Chitosan membranes in the form of injectable hydrogels do not require surgical intervention. These hydrogels are highly used for the treatment of periodontal pockets. It has been observed that PEC hydrogels coupled with chitosan and sodium alginate in a polymerized network have improved mechanical properties and biocompatibility which are requisites for osseous tissue engineering. These hydrogels tend to form porous ladder like interconnected mesh with fibrous structure on which osteoblasts proliferation is enhanced (Tatullo et al., 2017). Drug–based chitosan scaffolds have gained lot of popularity and are extensively used for bone and periodontal healing. (Agrawal et al., 2023; Arora et al., 2023; Nava Juárez, 2023).

Cell-based approaches are becoming a trend in regenerative medicine to treat health related conditions. However, safety concerns with respect to the adverse effects of the cell-based approach is always controversial (Sukpaita et al., 2019). These cell-based approaches are gaining attention in the field of dentistry. The human pulp stem cells, Dental pulp Stem cells (PDSCs), Stem cells from Apical Papilla (SCAP), Stem cells from exfoliated deciduous teeth (SHED), and human periodontal ligament cells (HPLCs) have high multi-differential potential and are giving promising results in regenerative dentistry. Besides these, another cell fraction has been identified from periapical granulation tissues and are termed as "human periapical cyst-mesenchymal stem cells (hPCy-MSCs)" and suffice with high proliferation and multi-differentiation capacity (Tatullo et al., 2017; Liao et al., 2020). Periodontal regeneration with human periodontal ligament cells (HPLCs) has resulted in excellent clinical success. Clinical trials have reported that HPLCs when seeded on chitosan scaffolds enhance osteogenesis without any toxic effects. It is said that the above-mentioned cells along with chitosan tend to increase the gene expression of osteoblastic cells (RUNX2, ALP, OPN) resulting in enhanced osteogenic potential (Li Y. et al., 2019). Recently in a study by Liao et al., Mesoporous hydroxyapatite/chitosan scaffold recombined with human amelogenenin promoted the proliferation of HPLCs leading to formation of cementum and bone (Liao et al., 2020). Studies have revealed that Stem cells from human exfoliated teeth (SHED) with TGF-β1 when inoculated on chitosan scaffolds show osteogenic potential (Li Y. et al., 2019). Chitosan laden scaffolds and sponges are considered as good delivery vehicles for periodontal regeneration (Su et al., 2014; Vining and Mooney, 2017).

Understanding the mechano-biology of stem cells, a sterile artificial environment which fulfills all the requisites of tissue engineering including the biochemical and mechanical forces should be designed. Stem cells respond to intracellular and

extracellular forces. The physiological environment can be altered to regulate the stem cell behavior to achieve their beneficial effects. Mechanical cues like stiffness and viscoelasticity of the scaffold on which the cells are seeded, can regulate the organogenesis and the cell fate *ex-vivo* (Thomas et al., 2017). Modifying the viscoelasticity and stiffness of the chitosan-hyaluronic acid hydrogel as connective tissue tends to promote the proliferation of chondrocytes and the gene expression of ECM markers (Jagodzinski et al., 2004; Brindley et al., 2011).

Mechano-regulation of stem cells through gene expression, proliferation, differentiation forms the basis for osseous regeneration (Lovecchio et al., 2019). It is believed that shear and compressive forces enhance the proliferation of human mesenchymal cells into osteoblasts and produce extracellular matrix. Human bone marrow stromal cells (hBMSCs) due to cyclic loading tend to enhance collagen–I fiber, AL and OC levels leading to osteogenesis (Choi et al., 2018). Tissue engineering models are conducted on 3-D scaffolds to create a physiochemical environment for stem cells. It has been evaluated that cell proliferation, and differentiation and ECM matrix deposition occurs when hBMSCs cultured on chitosan-graphene 3-D scaffold undergo mechano-stimulation (Choi et al., 2018).

2.3.11 Chitosan in medical imaging

Targeted tumor therapy using chitosan nanoparticles permit exceptional prospects beyond standard cancer therapies. Combining such nanoparticles with diagnostic test such as computed tomography, magnetic resonance imaging, and ultrasound imaging, or multi-modal imaging compounds aids easy cancer detection (Sun et al., 2014). Chitosan nanoparticles with multiple contrast agents have been tested for multimodal imaging procedures to counteract disadvantages of single imaging modality. A multimodal approach provides both *in-vitro* and *in-vivo* results effectively. Sun et al. reported that solubility of glycol chitosan when treated with hydrophilic ethylene glycol or PEGylation made it suitable for tumor imaging (Zhang et al., 2013). Besides, chitosan nanoparticles show passive targeting due to higher permeability and retention in cancerous lesions for prolonged duration (Min et al., 2015). This property is also known as enhanced permeability and retention effect.

The traditional method for synthesizing gold nanoparticles lacks stability due to presence of sodium citrate salt. Hence, Sun et al., modified the surface of the gold nanoparticles by eliminating the salt and including a reducing agent, glycol chitosan, which acts as a stabilizer biologically. Also, glycol chitosan is already known as an effective tumor targeting agent in animal models. Coating success was established after observing the change in the refractive index around the coated nanoparticles, using a UV-visible spectrometer, transmission electron microscopy, and Fourier transform infrared spectroscopy. The targeted accumulation in the tumor and its bio-distribution was assessed *in-vivo* using computed tomography (CT) in mice induced with colon cancer. The study results showed enhanced stability of the nanoparticles biologically due to a stabilizing surface coat of chitosan. Moreover, high contrast images of tumor were acquired from the mice by using the coated nanoparticles as a CT contrast agent. The images matched the results of cellular uptake and were highly sensitive to metastatic zones. A selective uptake of the coated nanoparticles was observed in the colon cancer cells compared to macrophages. Thus, the

characteristics accumulation of the glycol chitosan coated nanoparticles in cancerous cells demonstrates its efficient tumor targeting capacity which promotes imaging. The authors observed that the ample amine groups of glycol chitosan coated gold nanoparticles serves as zones for chemical conjugation for chemotherapeutic agents and enhances stability to support cancer imaging (Sun et al., 2014).

Zhang et al., studied the efficacy of gadolinium loaded chitosan nanoparticles as magnetic resonance imaging (MRI) contrast agents to target cancerous tissues by enhanced permeability and retention effect. To counteract the shortcomings of gadolinium based chelates such as easy renal filtration and poor contrast, gadolinium was chemically conjugated using ionic gelation with chitosan to prevent its early release and achieve improved retention for extended imaging time. *In-vitro* MRI revealed comparatively high relaxation time of gadolinium loaded chitosan nanoparticles because of surface modification demonstrating its capability as an effective contrast agent. Compared to another commercial contrast agent Magnevist® (same amount of gadonilium without chitosan coating), gadolinium loaded chitosan nanoparticles presented advanced imaging capacity and a high sensitivity aiding early diagnosis. During *in-vivo* MRI, gadolinium loaded chitosan nanoparticles showed higher brightness and retention time compared to Magnevist®, prolonging the imaging time considerably. This improvement was attributed to chitosan conjugation with gadolinium. The authors concluded that chemically conjugated gadolinium loaded chitosan nanoparticles holds vast possibility as MRI contrast agent (Zhang et al., 2013).

Min et al., developed an echogenic glycol chitosan-based nanoparticles for ultrasound-based imaging of malignant lesions. The authors used a chemotherapeutic bio-inert agent named perfluoropentane (PFP) which served as an ultrasound gas precursor. The components were turned into glycol chitosan nanoparticles using an oil-water emulsion approach, bearing an anti-cancer drug (docetaxel or doxorubicin)/PFP inner core coated with hydrophilic glycol chitosan. The authors demonstrated that the hydrophobic inner core was essential to stabilize the glycol chitosan coating. The ultrasound imaging capacity of echogenic particles were confirmed by injecting them intravenously in cancer induced mice. Within a minute of injection strong bright images were detected via ultrasound imaging due to effective accumulation of the particles in the cancerous cells. PFP gas production within the nanoparticles helped in retaining the ultrasound signals for an hour. The accumulation was noticed until 2 days after the injection because of due to the enhanced permeability and retention effect produced by promising size of the coated nanoparticles. The ultrasound treated samples displayed 4–7 times increased accumulation and wider distribution of chitosan coated nanoparticles in excised growths. This represents the thorough penetration of chitosan coated nanoparticles into the major vessels and its effective spread to the cancerous tissues. Based on their experimental observations the authors concluded that the echogenic glycol chitosan coated nanoparticles may be tried as ultrasound contrast enhancers in cancer imaging (Min et al., 2015).

Choi et al., developed iodine based echogenic diatrizoic acid-conjugated glycol chitosan nanoparticles as multimodal contrast agents for computed tomography-ultrasound dual imaging. Glycol chitosan-diatrizoic acid compound was formulated chemical

conjugating with the amine groups on chitosan. Oil-water emulsion technique was used to introduced iodinated nanoparticles. The resultant contrast agents were directly inserted into cancerous tissues. Notably, the iodide-based echogenic glycol chitosan nanoparticles showed significant accumulation in cancerous tissues. Clear signals were obtained on injecting the contrast agents into tumor sites using both computed tomography and ultrasound imaging modalities. The authors considered the developed agent to perform effectively during a multi-modal imaging approach (Choi et al., 2018).

With all the clinical trial data challenge remains to replicate the same responses in human subjects with tumors and other cancer drug interactions. It is necessary to observe the immune responses and related toxicities. Genetic mutations and varied vascularity of cancerous tissues may generate dissimilar response compared to lab animals. If all such limitations are taken care of then chitosan would have a promising future in targeted cancer imaging and drug therapy.

2.3.12 Chitosan in oral pathology and oncology

Chitosan modified nanocarrier systems can be used as a potential vehicle to target anti-cancer drugs to the various tumors and cause tumor apoptosis as per the individual efficacy of loaded drugs (Figure 8). Surface modifications of chitosan nanoparticles have been postulated which aim to enhance the tumor targeting ability via different mechanisms like receptor or carrier mediated transcytosis. Chitosan presents significant biocompatibility and promotes wound healing at molecular and cell level. Chitosan also acts as a bio-adhesive or mucoadhesive and hydrates the underlying tissues to effectively heal ulcers and relieve pain. It repairs tissues, contracts wound by acting as hemostat,

secretes inflammatory mediators, and induces macrophage actions by providing a non-proteinaceous matrix for 3D-tissue growth. Chitosan serves as collagen depositor by releasing N-acetyl-D-glucosamine on depolymerization to promote fibroblast formation. Chitosan modifies bacterial surface morphology, improves cell permeability, causes intracellular constituents' seepage, and prevents nutrient transport. Hence prevents erythema and secondary infections related to cancer therapy. Chitosan also presents fungistatic property by improving permeability of yeast cells (Mahima et al., 2015).

Min et al., developed an echogenic glycol chitosan-based nanoparticles for ultrasound-based drug delivery to areas of induced squamous cell carcinoma (SCC7 cell lines). An echogenic approach is known to enhance the drug release because of external ultrasound and result in a targeted burst release of the therapeutic agents to tumor sites. In the study the inner core behaved as an efficient reservoir for both the anti-cancer agents and PFPs. The gas precursor successfully retarded gas expansion and maintained stability. The authors demonstrated that the chitosan coated nanosized echogenic particles persisted in the bloodstream for longer periods promoting targeted delivery. Moreover, the outer glycol chitosan coating improved the overall physiochemical characteristics and targeted delivery (Min et al., 2015).

Wimardhani et al., studied the influence of low-molecular-weight chitosan on Ca9-22 cells derived from gingival carcinoma. The study was based on the premise that the low-molecular-weight chitosan showed anticancer effects and were relatively less toxic to non-cancerous cells. Cytotoxic effects were observed with low-molecular-weight chitosan on Ca9-22 cells leading to cell cycle arrest, upsurge in apoptotic DNA fragmentation, and subtle elevation in caspase expressions. The author concluded that the

FIGURE 8
Nanoparticles as a drug-carriers in targeted therapy for treatment of cancers.
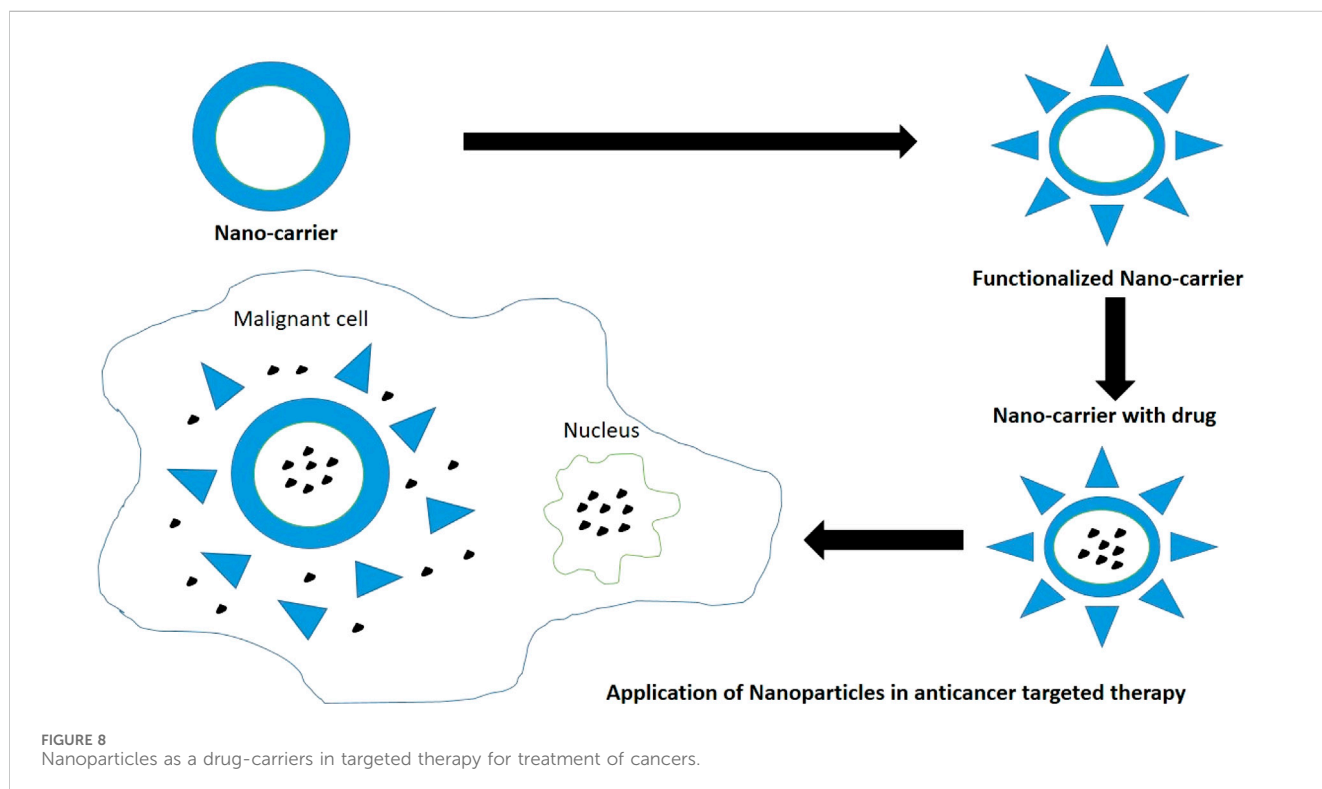
short-term exposure to low-molecular-weight chitosan has encouraging application as an anti-cancer agent (Wimardhani et al., 2014b).

Muthukrishnan et al., studied the effect of chitosan with zinc sulphate for treating and preventing oral mucositis as a side effect of radiotherapy. A WHO mucositis scale was used to grade oral mucositis three times a week. Although during early treatment days no significant changes were observed, around the sixth week a reduced severity was noticed. Pain levels and dysphagia were also reduced. The authors concluded that chitosan-zinc sulphate combination lowered the mucositis severity and aids healing (Muthukrishnan and Shanmughapriya, 2017).

Mahima V.G., examined the influence of 1% chitosan mouthwash on oral mucositis on 20 patients developed after radio-chemotherapy. The study showed significant results in lowering symptoms of oral mucositis such as pain, erythema, ulcerations, and other associated side effects. Chitosan not only demonstrated enhanced healing but also acted as a promising occlusive dressing to alleviate pain and ulcer discomfort due to bio-adhesive properties. No secondary infections and adverse biocompatibility issues were reported during the tests reinforcing chitosan's ability to work effectively as solution to side effects of radio-chemotherapy. The authors concluded that chitosan is far more efficient than chlorhexidine in alleviating symptoms of oral mucositis (Mahima et al., 2015).

Pornpitchanarong et al., investigated a muco-adhesive based on catechol-modified chitosan/hyaluronic acid nanoparticles as a carrier of doxorubicin for oral cancer. Chitosan and catechol functionalized drug delivery were already reported to boost muco-adhesion individually. Muco-adhesion provides prolonged retention with sustained release of the agents. The authors demonstrated that a significant portion of drug could be loaded into the nanoparticles and sustained release was attainable. A better muco-adhesive property was observed. The combination also induced effective apoptosis of HN22 human oral cancer cells. The authors concluded the said combination as a potential drug carrier for doxorubicin to prevent localized oral cancers (Pornpitchanarong et al., 2020). Figure 7 depicts the usage of nanoparticles as drug carriers in targeted therapy for treatment of various cancers (Sharifi-Rad et al., 2021).

Zhu et al. also reported that a fluorinated chitosan-chlorin e6 (FC-Ce6) nanocarrier for intracellular delivery catalase enhanced photodynamic therapy of oral cancer. They established that fluorine conjugated chitosan nanoparticles exhibited superior anti-cancer activity in contrast to free Ce6 and non-fluorinated CS-Ce6/catalase nanoparticles. Chen et al., tested chitosan nanoparticles encapsulated with 5-aminolevulinic acid (a photo-sensitizer), and IR780 (a near-infrared fluorescence dye used as a photo-thermal agent). However, a single approach using 5-aminolevulinic acid and IR780 had many drawbacks such as tumor recurrence, hydrophilicity of 5-aminolevulinic acid, and low specificity. Chitosan served as a nano-carrier with high biocompatibility and cell membrane permeability. Hence, a combination of photo-thermal and photodynamic agents for a non-invasive oral cancer treatment was developed in the study. The author demonstrated that the said combination displayed improved accumulation in cancerous tissues and showed fluorescence during imaging. Improved

photo-thermally augmented photodynamic result for tumor excision was reported with no apparent toxicity. The authors concluded that the combination was safe for use as non-invasive oral cancer therapy (Zhu et al., 2021). Chen et al. formulated a new photothermally enhanced photodynamic therapy platform based on orally administered Chitosan Nanoparticles. Improved photodynamic cytotoxicity to cancer cells was seen with a combination of PTT (photothermal therapy) and PDT (photodyanamic therapy) when compared with photodynamic therapy alone. Additionally, 5-ALA (5-aminolevulinic acid) &IR780 coated Chitosan Nanoparticles exhibited high tumor accumulation and greater ability to fluorescently image tumor tissue (Chen et al., 2020).

Takeuchi et al., designed a sustained release film loaded with rebamipide and chitosan for treating side effects of oral mucositis after chemotherapy. Rebamipide was enforced as a gargle to counter side effects of oral mucositis but its effects were short lived. Chitosan was reinforced into rebamipide for its muco-adhesive and antibacterial characteristics. Along with chitosan, pluronic was added as adhesion enhancer and hydroxyl-propyl methylcellulose served as film former. The release behavior was studied. The authors reported that chitosan caused suppression in the release of rebamipide for nearly half an hour. Whereas, hydroxyl-propyl methylcellulose helped in sustained release and maintained the films shape. The authors concluded that the combination can be effectively used as base for sustained drug delivery. However, additional clinical trials are warranted (Takeuchi et al., 2019).

3 Conclusion

Chitosan shows a notable range of properties which makes it valuable for sustainable development due to it being plentiful, decomposable, eco-friendly, and adaptable. Chitosan production has improved in terms of green chemistry due to the harmful chemicals being replaced by solvents with minimum melting points (Eutectic). This has also lead to an overall decrease in energy consumption. An important reason for using chitosan is the presence of a large number of organic groups (hydroxyl and amino groups) in its structure which makes it amenable to chemical modifications (Maliki et al., 2022). This versatility of chitosan makes it especially remarkable for the preparation of suspensions, composites, functionalized materials, or (nano)hybrids for diverse environment-friendly usage and in industrial and health related applications. Chitosan-based nanocomposites, hydrogels, and membranes are being used in regenerative medicine and dentistry. In field of dentistry, it has gained enormous popularity due to its natural existence and biocompatibility and decreased cytotoxicity. However, it still presents certain limitations with regard to its structure and molecular weight. Nonetheless, this natural nanomaterial is being extensively used and has an excellent potential to stretch out its biotic properties in the near future. There is hardly any clinical evidence of chitosan-based derivatives in the field of dentistry and more clinical data should be added on. Being the second abundant biopolymer in nature after cellulose, the potential of chitosan as sustainable future material in dentistry and medical needs further exploration. Continuous investigation into nanobiotechnology related to computer science ought to be carried out to enhance the present state of medicine and create pharmaceuticals with strong therapeutic efficacy

to reduce patients' discomfort while optimizing the effectiveness of therapeutic agents.

Author contributions

RM: Conceptualization, Project administration, Validation, Writing–original draft, Writing–review and editing. SH: Data curation, Supervision, Writing–original draft, Writing–review and editing. NM: Writing–original draft, Writing–review and editing.

Funding

Conflict of interest

The authors declare that the research was conducted in the absence of any commercial or financial relationships that could be construed as a potential conflict of interest.

Publisher's note

All claims expressed in this article are solely those of the authors and do not necessarily represent those of their affiliated organizations, or those of the publisher, the editors and the reviewers. Any product that may be evaluated in this article, or claim that may be made by its manufacturer, is not guaranteed or endorsed by the publisher.

References

Abbass, M. M. S., El-Rashidy, A. A., Sadek, K. M., El Moshy, S., Radwan, I. A., Rady, D., et al. (2020). Hydrogels and dentin–pulp complex regeneration: from the benchtop to clinical translation. *Polymers* 12, 2935. doi:10.3390/polym12122935

Abdel Mouez, M., Zaki, N. M., Mansour, S., and Geneidi, A. S. (2014). Bioavailability enhancement of verapamil HCl via intranasal chitosan microspheres. *Eur. J. Pharm. Sci.* 51, 59–66. doi:10.1016/j.ejps.2013.08.029

Abid, N., Khan, A. M., Shujait, S., Chaudhary, K., Ikram, M., Imran, M., et al. (2022). Synthesis of nanomaterials using various top-down and bottom-up approaches, influencing factors, advantages, and disadvantages: a review. *Adv. Colloid Interface Sci.* 300, 102597. doi:10.1016/j.cis.2021.102597

Abtahi, J., Tengvall, P., and Aspenberg, P. (2012). A bisphosphonate-coating improves the fixation of metal implants in human bone. A randomized trial of dental implants. *Bone* 50, 1148–1151. doi:10.1016/j.bone.2012.02.001

Adhikari, H. S., and Yadav, P. N. (2018). Anticancer activity of chitosan, chitosan derivatives, and their mechanism of action. *Int. J. Biomaterials* 2018, 1–29. doi:10.1155/2018/2952085

Agnihotri, A. S., Mallikarjuna, N. N., and Aminabhavi, T. M. (2004). Recent advances on chitosan based micro-and nanoparticles in drug delivery. *J. Control. Release* 100 (1), 5–28. doi:10.1016/j.jconrel.2004.08.010

Agrawal, A., Reche, A., Agrawal, S., and Paul, P. (2023). Applications of chitosan nanoparticles in dentistry: a review. *Cureus* 15 (12), e49934. doi:10.7759/cureus.49934

Aguilar, A., Zein, N., Harmouch, E., Hafdi, B., Bornert, F., Offner, D., et al. (2019). Application of chitosan in bone and dental engineering. *Molecules* 24 (16), 3009. doi:10.3390/molecules24163009

Ainola, M., Tomaszewski, W., Ostrowska, B., Wesolowska, E., Wagner, H. D., Swieszkowski, W., et al. (2016). A bioactive hybrid three-dimensional tissue-engineering construct for cartilage repair. *J. Biomater. Appl.* 30, 873–885. doi:10.1177/0885328215604069

Akıncıbay, H., Şenel, S., and Yetkin, Z. A. (2007). Application of chitosan gel in the treatment of chronic periodontitis. *J. Biomed.Mater. Res. B Appl. Biomater.* 80 (2), 290–296. doi:10.1002/jbm.b.30596

Akncbay, H., Senel, S., and Ay, Z. Y. (2007). Application of chitosan gel in the treatment of chronic periodontitis. *J. Biomed. Mater Res. B Appl. Biomater.* 80 (2), 290–296. doi:10.1002/jbm.b.30596

Alamry, K. A., Almehmadi, S. J., Elfaky, M. A., Al-Shareef, H. F., Samah, J. A., and Hussein, M. A. (2020). Enhanced antimicrobial activity of new arylidene-based polyketone nanocomposite materials. *Polymer-Plastics Technol. Mater.* 59 (18), 1973–1986. doi:10.1080/25740881.2020.1784213

Alcaraz, A. L., Mendoza, J. L., Goycoolea, F., Ciapara, L. H., and Monal, W. A. (2016). Preparation of chitosan nanoparticles by nanoprecipitation and their ability as a drug nanocarrier. *RSC Adv.* 6 (64), 59250–59256. doi:10.1039/c6ra06563e

Alghamdi, H. S. (2018). Methods to improve osseointegration of dental implants in low quality (Type-IV) bone: an overview. *J. Funct. Biomater.* 9 (1), 7. doi:10.3390/jfb9010007

Alinejad, V., Somi, M. H., Baradaran, B., Akbarzadeh, P., Atyabi, F., Kazerooni, H., et al. (2016). Co-delivery of IL17RB siRNA and doxorubicin by chitosan-based nanoparticles for enhanced anticancer efficacy in breast cancer cells. *Biomed. Pharmacother.* 83, 229–240. doi:10.1016/j.biopha.2016.06.037

Alnufaiy, B. M., Lambarte, R. N. A., and Al-Hamdan, K. S. (2020). The osteogenetic potential of chitosan coated implant: an *in vitro* study. *J. Stem Cells Regen. Med.* 16 (2), 44–49. doi:10.46582/jsrm.1602008

Arancibia, R., Maturana, C., Silva, D., Tobar, N., Tapia, C., Salazar, J., et al. (2013). Effects of chitosan particles in periodontal pathogens and gingival fibroblasts. *J.Dent. Res.* 92 (8), 740–745. doi:10.1177/0022034513494816

Arnaud, T. M. S., de Barros, B. N., and Diniz, F. B. (2010). Chitosan effect on dental enamel deremineralization: an *in vitro* evaluation. *J. Dent.* 38 (11), 848–852. doi:10.1016/j.jdent.2010.06.004

Arora, S., Das, G., Alqarni, M., Grover, V., Manzoor Baba, S., Saluja, P., et al. (2023). Role of chitosan hydrogels in clinical dentistry. *Gels* 9 (9), 698. doi:10.3390/gels9090698

Azevedo, A. S., Sá, M. J., Fook, M. V., Neto, P. I. N., Sousa, O. B., Azevedo, S. S., et al. (2014). Use of chitosan and β-tricalcium phosphate, alone and in combination, for bone healing in rabbits. *J. Mater Sci. Mater Med.* 25 (2), 481–486. doi:10.1007/s10856-013-5091-2

Azuma, K., Izumi, R., Osaki, T., Ifuku, S., Morimoto, M., Saimoto, H., et al. (2015). Chitin, chitosan, and its derivatives for wound healing: old and new materials. *J. Funct. biomaterials* 6 (1), 104–142. doi:10.3390/jfb6010104

Babrawala, I. S., Prabhuji, M. L. V., Karthikeyan, B. V., and Divya, K. (2016). A novel approach using natural 1% (W/W) chitosan as a local drug delivery system in the management of non-surgical periodontal treatment: a pilot study. *J. Int. Acad. Periodontology* 18 (4), 129–133.

Bakopoulou, A., Georgopoulou, A., Grivas, I., Bekiari, C., Prymak, O., Loza, K., et al. (2019). Dental pulp stem cells in chitosan/gelatin scaffolds for enhanced orofacial bone regeneration. *Dent. Mater.* 35 (2), 310–327. doi:10.1016/j.dental.2018.11.025

Bakshia, P. S., Selvakumara, D., Kadirvelub, K., and Kumara, N. (2019). Chitosan as an environment friendly biomaterial–a review on recent modifications and applications. *Int. J. Biol. Macromol.* 150, 1072–1083. doi:10.1016/j.ijbiomac.2019.10.113

Bansal, M., Mittal, N., Yadav, S. K., Khan, G., Gupta, P., Mishra, B., et al. (2018). Periodontal thermoresponsive, mucoadhesive dual antimicrobial loaded *in-situ* gel for the treatment of periodontal disease: preparation, *in-vitro* characterization and antimicrobial study. *J. Oral Biol. Craniofac. Res.* 8 (2), 126–133. doi:10.1016/j.jobcr.2017.12.005

Baranwal, A., Kumar, A., Priyadharshini, A., Oggu, G. S., Bhatnagar, I., Srivastava, A., et al. (2018). Chitosan: an undisputed bio-fabrication material for tissue engineering and bio-sensing applications. *Int. J. Biol. Macromol.* 110, 110–123. doi:10.1016/j.ijbiomac.2018.01.006

Bellamy, C., Shrestha, S., Torneck, C., and Kishen, A. (2016). Effects of a bioactive scaffold containing a Sustained transforming growth factor-β1–releasing nanoparticle system on the Migration and differentiation of stem cells from the apical papilla. *J. Endod.* 42 (9), 1385–1392. doi:10.1016/j.joen.2016.06.017

Bentley, C., and Drake, C. (1986). Longevity of restorations in a dental school clinic. *J. Dent. Educ.* 50, 594–600. doi:10.1002/j.0022-0337.1986.50.10.tb02046.x

Bernkop-Schnürch, A., and Dünnhaupt, S. (2012). Chitosan-based drug delivery systems. *Eur. J.Pharm. Biopharm.* 81 (3), 463–469. doi:10.1016/j.ejpb.2012.04.007

Bhattarai, N., Gunn, J., and Zhang, M. (2010). Chitosan-based hydrogels for controlled, localized drug delivery. *Adv. Drug Deliv. Rev.* 62 (1), 83–99. doi:10.1016/j.addr.2009.07.019

Blumenthal, H. J., and Roseman, S. (1957). Quantitative estimation of chitin in fungi. *J. Bacteriol.* 74, 222–224. doi:10.1128/jb.74.2.222-224.1957

Bonderer, L. J., Studart, A. R., and Gauckler, L. J. (2008). Bioinspired design and assembly of platelet reinforced polymer films. *Science* 319, 1069–1073. doi:10.1126/science.1148726

Boverhof, D. R., Bramante, C. M., Butala, J. H., Clancy, S. F., Lafranconi, M., West, J., et al. (2015). Comparative assessment of nanomaterial definitions and safety evaluation considerations. *Regul. Toxicol. Pharmacol.* 73 (1), 137–150. doi:10.1016/j.yrtph.2015.06.001

Brindley, D., Moorthy, K., Lee, J. H., Mason, C., Kim, H. W., and Wall, I. (2011). Bioprocess forces and their impact on cell behavior: implications for bone regeneration therapy. *J. Tissue Eng.* 2011, 620247. doi:10.4061/2011/620247

Caetano, G. F., Frade, M. A. C., Andrade, T. A. M., Leite, M. N., Bueno, C. Z., Moraes, A. M., et al. (2015). Chitosan-alginate membranes accelerate wound healing. *J. Biomed. Mater. Res. Part B. Appl. Biomaterials* 103 (5), 1013–1022. doi:10.1002/jbm.b.33277

Chen, G., Zhao, Y., Xu, Y., Zhu, C., Liu, T., and Wang, K. (2020). Chitosan nanoparticles for oral photothermally enhanced photodynamic therapy of colon cancer. *Int. J. Pharm.* 589, 119763. doi:10.1016/j.ijpharm.2020.119763

Chen, K., Guo, B., and Luo, J. (2017). Quaternized carboxymethyl chitosan/organic montmorillonite nanocomposite as a novel cosmetic ingredient against skin aging. *Carbohydr. Polym.* 173, 100–106. doi:10.1016/j.carbpol.2017.05.088

Chen, R., Liu, C., Tseng, W., Jeng, J., and Lin, C. (2003). Cytotoxicity of three dentin bonding agents on human dental pulp cells. *J. Dent.* 31, 223–229. doi:10.1016/s0300-5712(02)00088-x

Choi, D., Jeon, S., You, D. G., Um, W., Kim, J. Y., Yoon, H. Y., et al. (2018). Iodinated echogenic glycol chitosan nanoparticles for X-ray CT/US dual imaging of tumor. *Nanotheranostics* 2 (2), 117–127. doi:10.7150/ntno.18643

Cohenca, N., Paranjpe, A., and Berg, J. (2013). Vital pulp therapy. *Dent. Clin. N. Am.* 57, 59–73. doi:10.1016/j.cden.2012.09.004

Costa, E., Silva, S., Madureira, A., Cardelle-Cobas, A., Tavaria, F., and Pintado, M. (2014). A comprehensive study into the impact of a chitosan mouthwash upon oral microorganism's biofilm formation *in vitro*. *Carbohydr. Polym.* 101, 1081–1086. doi:10.1016/j.carbpol.2013.09.041

Costa-Pinto, A. R., Reis, R. L., and Neves, N. M. (2011). Scaffolds based bone tissue engineering: the role of chitosan. *Tissue Eng. Part B Rev.* 17 (5), 331–347. doi:10.1089/ten.teb.2010.0704

Covarrubias, C., Trepiana, D., and Corral, C. (2018). Synthesis of hybrid copper-chitosan nanoparticles with antibacterial activity against cariogenic Streptococcus mutans. *Dent. Mat. J.* 37 (3), 379–384. doi:10.4012/dmj.2017-195

Dai, T., Tanaka, M., Huang, Y. Y., and Hamblin, M. R. (2011). Chitosan preparations for wounds and burns: antimicrobial and wound-healing effects. *Expert Rev. Anti Infect. Ther.* 9 (7), 857–879. doi:10.1586/eri.11.59

D'Almeida, M., Attik, N., Amalric, J., Brunon, C., Renaud, F., Abouelleil, H., et al. (2017). Chitosan coating as an antibacterial surface for biomedical applications. *PLoS ONE* 12 (12), e0189537. doi:10.1371/journal.pone.0189537

da Silva, M. A., Iamanaka, B. T., Taniwaki, M. H., and Kieckbusch, T. G. (2013). Evaluation of the antimicrobial potential of alginate and alginate/chitosan films containing potassium sorbate and natamycin. *Packag. Technol. Sci.* 26 (8), 479–492. doi:10.1002/pts.2000

De Carvalho, M., Stamford, T., Pereira, E., Dos Santos, P., and Sampaio, F. (2011). Chitosan as an oral antimicrobial agent. *Formatex* 2012, 13.

del Carpio-Perochena, A., Kishen, A., Felitti, R., Bhagirath, A. Y., Medapati, M. R., Lai, C., et al. (2017). Antibacterial properties of chitosan nanoparticles and propolis associated with calcium hydroxide against single-and multispecies biofilms: an *in vitro* and *in situ* study. *J. Endod.* 43 (8), 1332–1336. doi:10.1016/j.joen.2017.03.017

Denuziere, A., Ferrier, D., Damour, O., and Domard, A. (1998). Chitosan-chondroitin sulfate and chitosan-hyaluronate polyelectrolyte complexes: biological properties. *Biomaterials* 19 (14), 1275–1285. doi:10.1016/s0142-9612(98)00036-2

Dhand, C., Dwivedi, N., Loh, X. J., Ying, A. N. J., Verma, N. K., Beuerman, R. W., et al. (2015). Methods and strategies for the synthesis of diverse nanoparticles and their applications: a comprehensive overview. *RSC Adv.* 5, 105003–105037. doi:10.1039/c5ra19388e

DiMartino, A., Drannikov, A., Surgutskaia, N. S., Ozaltin, K., Postnikov, P. S., Marina, T. E., et al. (2019). Chitosan-collagen based film for controlled delivery of a combination of short life anesthetics. *Int. J. Biol. Macromol.* 140, 1183–1193. doi:10.1016/j.ijbiomac.2019.08.228

Ding, C. M., Chen, Z. X., and Li, J. S. (2017). From molecules to macrostructures: recent development of bioinspired hard tissue repair. *Biomater. Sci.* 5, 1435–1449. doi:10.1039/c7bm00247e

Diolosà, M., Donati, I., Turco, G., Cadenaro, M., Di Lenarda, R., Breschi, L., et al. (2014). Use of methacrylate-modified chitosan to increase the durability of dentine bonding systems. *Biomacromolecules* 15 (12), 4606–4613. doi:10.1021/bm5014124

Diz, P., Scully, C., and Sanz, M. (2013). Dental implants in the medically compromised patient. *J. Dent.* 41 (3), 195–206. doi:10.1016/j.jdent.2012.12.008

Dragland, I. S., Wellendorf, H., Kopperud, H., Stenhagen, I., and Valen, H. (2019). Investigation on the antimicrobial activity of chitosan-modified zinc oxide-eugenol cement. *Biomaterial Investigations Dent.* 6 (1), 99–106. doi:10.1080/26415275.2019.1697621

Drummond, J. L. (2008). Degradation, fatigue, and failure of resin dental composite materials. *J. Dent. Res.* 87, 710–719. doi:10.1177/154405910808700802

Duarte, F., Pinheiro, L., Ramos, C., and Silva, J. N. (2021). Rehabilitation of down syndrome with zygomatic implants-case report. *SVOA Dent.*, 15–19.

Ducret, M., Montembault, A., Josse, J., Pasdeloup, M., Celle, A., Benchrih, R., et al. (2019). Design and characterization of a chitosan-enriched fibrin hydrogel for human dental pulp regeneration. *Dent. Mat.* 35 (4), 523–533. doi:10.1016/j.dental.2019.01.018

Eijsink, V., Hoell, I., and Vaaje-Kolstada, G. (2010). Structure and function of enzymes acting on chitin and chitosan. *Biotechnol. Genet. Eng. Rev.* 27, 331–366. doi:10.1080/02648725.2010.10648156

Elieh-Ali-Komi, D., and Hamblin, M. R. (2016). Chitin and chitosan: production and application of versatile biomedical nanomaterials. *Int. J. Adv. Res.* 4 (3), 411–427.

El Nady, D. G., Hashem, A. M., Shoeib, M. A., Shalaby, H. A., and Abdelraouf, R. M. (2017). Electro-deposition of biological active chitosan/composite coating on titanium dental implant. *Egypt. Dent. J.* 63 (4), 1417–1428.

El-Negoly, S. A., El-Fallal, A. A., and El-Sherbiny, I. M. (2014). A new modification for improving shear bond strength and other mechanical properties of conventional glass-ionomer restorative materials. *J. Adhes. Dent.* 16 (1), 41–47. doi:10.3290/j.jad.a30541

Elshinawy, M. I., Al-Madboly, L. A., Ghoneim, W. M., and El-Deeb, N. M. (2018). Synergistic effect of newly introduced root canal medicaments; ozonated olive oil and chitosan nanoparticles, against persistent endodontic pathogens. *Front. Microbiol.* 9, 1371. doi:10.3389/fmicb.2018.01371

Eramo, S., Natali, A., Pinna, R., and Milia, E. (2018). Dental pulp regeneration via cell homing. *Int. Endod.J* 51 (4), 405–419. doi:10.1111/iej.12868

Fakhri, E., Eslami, H., Maroufi, P., Pakdel, F., Taghizadeh, S., Ganbarov, K., et al. (2020). Chitosan biomaterials application in dentistry. *Int. J. Biol. Macromol.* 162, 956–974. doi:10.1016/j.ijbiomac.2020.06.211

Faqhiri, H., Hannula, M., Kellomäki, M., Calejo, M. T., and Massera, J. (2019). Effect of melt-derived bioactive glass particles on the properties of chitosan scaffolds. *J. Funct. Biomater.* 10 (3), 38. doi:10.3390/jfb10030038

Farea, M., Husein, A., Halim, A. S., Abdullah, N. A., Mokhtar, K. I., Lim, C. K., et al. (2014). Synergistic effects of chitosan scaffold and TGFβ1 on the proliferation and osteogenic differentiation of dental pulp stem cells derived from human exfoliated deciduous teeth. *Archives Oral Biol.* 59 (12), 1400–1411. doi:10.1016/j.archoralbio.2014.08.015

Farhadian, N., Godiny, M., Moradi, S., Azandaryani, A. H., and Shahlaei, M. (2018). Chitosan/gelatin as a new nano-carrier system for calcium hydroxide delivery in endodontic applications: development, characterization and process optimization. *Mater. Sci. Eng. C* 92, 540–546. doi:10.1016/j.msec.2018.07.002

Farias, J. M., Stamford, T. C. M., Resende, A. H. M., Aguiar, J. S., Rufino, R. D., Luna, J. M., et al. (2019). Mouthwash containing a biosurfactant and chitosan: an eco-sustainable option for the control of cariogenic microorganisms. *Int. J. Biol. Macromol.* 129, 853–860. doi:10.1016/j.ijbiomac.2019.02.090

Finke, M. D. (2007). Estimate of chitin in raw whole insects. *Zoo. Biol.* 26, 105–115. doi:10.1002/zoo.20123

Forsten, L. (1994). Flouride release of glass ionomers. *J. Esthet. Dent.* 6 (5), 216–222. doi:10.1111/j.1708-8240.1994.tb00862.x

Ganss, C., Klimek, J., and Schlueter, N. (2014). Erosion/abrasion-preventing potential of NaF and F/Sn/chitosan toothpastes in dentine and impact of the organic matrix. *Caries Res.* 4, 163–169. doi:10.1159/000354679

Ganss, C., Lussi, A., Grunau, O., Klimek, J., and Schlueter, N. (2011). Conventional and anti-erosion fluoride toothpastes: effect on enamel erosion and erosion-abrasion. *Caries Res.* 45, 581–589. doi:10.1159/000334318

Ghafar, H., Khan, M. I., Sarwar, H. S., Yaqoob, S., Hussain, S. Z., Tariq, I., et al. (2020). Development and characterization of bioadhesive film embedded with lignocaine and calcium fluoride nanoparticles. *AAPS PharmSciTech* 21 (2), 60–12. doi:10.1208/s12249-019-1615-5

Ghosh, B., and Urban, M. W. (2009). Self-repairing oxetane-substituted chitosan polyurethane networks. *Science* 323, 1458–1460. doi:10.1126/science.1167391

Ghosh, S., Ranebennur, T. S., and Vasan, H. N. (2011). Study of antibacterial efficacy of hybrid chitosan-silver nanoparticles for prevention of specific biofilm and water purification. *Int. J. Carbohydr. Chem.* 2011, 1–11. doi:10.1155/2011/693759

Goodson, J., Offenbacher, S., Farr, D., and Hogan, P. (1985). Periodontal disease treatment by local drug delivery. *J. Periodontol.* 56 (5), 265–272. doi:10.1902/jop.1985.56.5.265

Goy, R. C., de Britto, D., and Assis, O. B. G. (2009). A review of the antimicrobial activity of chitosan. *Polímeros Ciência Tecnol.* 19 (3), 241–247. doi:10.1590/s0104-14282009000300013

Greenstein, G., and Polson, A. (1998). The role of local drug delivery in the management of periodontal diseases: a comprehensive review. *J. Periodontol.* 69 (5), 507–520. doi:10.1902/jop.1998.69.5.507

Guglielmotti, M. B., Olmedo, D. G., and Cabrini, R. L. (2019). Research on implants and osseointegration. *Periodontol. 2000* 79 (1), 178–189. doi:10.1111/prd.12254

Gümüşderelioğlu, M., Sunal, E., Demirtaş, T. T., and Kiremitçi, A. S. (2020). Chitosan-based double faced barrier membrane coated with functional nanostructures and loaded with BMP-6. *J. Mat. Sci. Mat. Med.* 31 (1), 4. doi:10.1007/s10856-019-6331-x

Guo, T., Zhao, J. N., Chang, J. B., Ding, Z., Hong, H., Chen, J. N., et al. (2006). Porous chitosan-gelatin scaffold containing plasmid DNA encoding transforming growth factor-β1 for chondrocytes proliferation. *Biomaterials* 27, 1095–1103. doi:10.1016/j.biomaterials.2005.08.015

Hanes, P. J., and Purvis, J. P. (2003). Local anti-infective therapy: pharmacological agents. A systematic review. *Ann. Periodontol.* 8 (1), 79–98. doi:10.1902/annals.2003.8.1.79

Hassan, M. A., Omer, A. M., Abbas, E., Baset, W. M. A., and Tamer, T. M. (2018). Preparation, physicochemical characterization and antimicrobial activities of novel two phenolic chitosan Schiff base derivatives. *Sci. Rep.* 8, 11416. doi:10.1038/s41598-018-29650-w

Hayashi, Y., Ohara, N., Ganno, T., Yamaguchi, K., Ishizaki, T., Nakamura, T., et al. (2007). Chewing chitosan-containing gum effectively inhibits the growth of cariogenic bacteria. *Arch. Oral Biol.* 52, 290–294. doi:10.1016/j.archoralbio.2006.10.004

He, J., Shi, M., Liang, Y., and Guo, B. (2020). Conductive adhesive self-healing nanocomposite hydrogel wound dressing for photothermal therapy of infected full-thickness skin wounds. *Chem. Eng. J.* 394, 124888. doi:10.1016/j.cej.2020.124888

Ho, T. F. T., Smales, R. J., and Fang, D. T. S. (1999). A 2-year clinical study of two glass ionomer cements used in the atraumatic restorative treatment (ART) technique. *Community Dent. Oral Epidemiol.* 27, 195–201. doi:10.1111/j.1600-0528.1999.tb02010.x

Hu, D., Ren, Q., Li, Z., and Zhang, L. (2020). Chitosan-based biomimetically mineralized composite materials in human hard tissue repair. *Molecules* 25, 4785. doi:10.3390/molecules25204785

Hu, F., Zhou, Z., Xu, Q., Fan, C., Wang, L., Ren, H., et al. (2019). A novel pH responsive quaternary ammonium chitosan-liposome nanoparticles for periodontal treatment. *Int. J. Biol. Macromol.* 129, 1113–1119. doi:10.1016/j.ijbiomac.2018.09.057

Huang, G., Zhai, J., Cheng, S., Wang, Y., Yang, L., Liu, H., et al. (2016). The application of chitosan and its derivatives as nanosized carriers for the delivery of chemical drugs and genes or proteins. *Curr. Drug Targets* 17, 811–816. doi:10.2174/1389450116666151019100106

Huang, G. T., Sonoyama, W., Liu, Y., Liu, H., Wang, S., and Shi, S. (2008). The hidden treasure in apical papilla: the potential role in pulp/dentin regeneration and bioroot engineering. *J. Endod.* 34 (6), 645–651. doi:10.1016/j.joen.2008.03.001

Ifuku, S., Nomura, R., Morimoto, M., and Saimoto, H. (2011). Preparation of chitin nanofibers from mushrooms. *Materials* 4, 1417–1425. doi:10.3390/ma4081417

Ignatova, M., Manolova, N., and Rashkov, I. (2007). Novel antibacterial fibers of quaternized chitosan and poly(vinyl pyrrolidone) prepared by electrospinning. *Eur. Polym. J.* 43, 1112–1122. doi:10.1016/j.eurpolymj.2007.01.012

Ikinci, G., Senel, S., Akincibay, H., Kaş, S., Erciş, S., Wilson, C. G., et al. (2002). Effect of chitosan on a periodontal pathogen Porphyromonas gingivalis. *Int. J. Pharm.* 235 (1-2), 121–127. doi:10.1016/s0378-5173(01)00974-7

Imai, T., Watanabe, T., Yui, T., and Sugiyama, J. (2003). The directionality of chitin biosynthesis: a revisit. *Biochem. J.* 374 (Pt 3), 755–760. doi:10.1042/bj20030145

Indiarto, R., Indriana, L. P. A., Andoyo, R., Subroto, E., and Nurhadi, B. (2022). Bottom–up nanoparticle synthesis: a review of techniques, polyphenol-based core materials, and their properties. *Eur. Food Res. Technol.* 248, 1–24. doi:10.1007/s00217-021-03867-y

Islam, M. M., Shahruzzaman, M., Biswas, S., Nurus Sakib, M., and Rashid, T. U. (2020). Chitosan based bioactive materials in tissue engineering applications-A review. *Bioact. Mater* 5 (1), 164–183. doi:10.1016/j.bioactmat.2020.01.012

Islam, N., Dmour, I., and Taha, M. O. (2019). Degradability of chitosan micro/nanoparticles for pulmonary drug delivery. *Heliyon* 5 (5), e01684. doi:10.1016/j.heliyon.2019.e01684

Jagodzinski, M., Drescher, M., Zeichen, J., Hankemeier, S., Krettek, C., Bosch, U., et al. (2004). Effects of cyclic longitudinal mechanical strain and dexamethasone on osteogenic differentiation of human bone marrow stromal cells. *Eur. Cell Mater* 7, 35–41. doi:10.22203/ecm.v007a04

Januariyasa, I. K., Ana, I. D., and Yusuf, Y. (2020). Nanofibrous poly (vinyl alcohol)/chitosan contained carbonated hydroxyapatite nanoparticles scaffold for bone tissue engineering. *Mat. Sci. Eng. C* 107, 110347. doi:10.1016/j.msec.2019.110347

Javed, F., Vohra, F., Zafar, S., and Almas, K. (2014). Significance of osteogenic surface coatings on implants to enhance osseointegration under osteoporotic-like conditions. *Implant Dent.* 23, 679–686. doi:10.1097/id.0000000000000161

Jeyaraj, M., Gurunathan, S., Qasim, M., Kang, M. H., and Kim, J. H. (2019). A comprehensive review on the synthesis, characterization, and biomedical application of platinum nanoparticles. *Nanomaterials* 9 (12), 1719. doi:10.3390/nano9121719

Ji, Q. X., Zhao, Q. S., Deng, J., and Lü, R. (2010). A novel injectable chlorhexidine thermosensitive hydrogel for periodontal application: preparation, antibacterial activity and toxicity evaluation. *J. Mat. Sci. Mat. Med.* 21 (8), 2435–2442. doi:10.1007/s10856-010-4098-1

Jingwen, Y., Guohua, Y., and Zhi, C. (2016). Pulp regeneration: current approaches and future challenges. *Front. Physiology* 7, 58. doi:10.3389/fphys.2016.00058

Jones, N. (2010). Food: a taste of things to come? *Nature* 468, 752–753. doi:10.1038/468752a

Joshi, D., Garg, T., Goyal, A. K., and Rath, A. (2016). Advanced drug delivery approaches against periodontitis. *Drug Deliv.* 23 (2), 363–377. doi:10.3109/10717544.2014.935531

Kausar, A. (2021). Polymer and modified chitosan-based nanocomposite: impending material for technical application. *Polymer-Plastics Technol. Mater.* 58 (9), 934–947. doi:10.1080/25740881.2019.1587771

Ke, C.-L., Deng, F.-S., Chuang, C.-Y., and Lin, C.-H. (2021). Antimicrobial actions and applications of chitosan. *Polymers* 13, 904. doi:10.3390/polym13060904

Keegan, G. M., Smart, J. D., Ingram, M. J., Barnes, L., Burnett, G. R., and Rees, G. D. (2012). Chitosan microparticles for the controlled delivery of fluoride. *J. Dent.* 40, 229–240. doi:10.1016/j.jdent.2011.12.012

Khajuria, D. K., Zahra, S. F., and Razdan, R. (2018). Effect of locally administered novel biodegradable chitosan based risedronate/zinc-hydroxyapatite intra-pocket dental film on alveolar bone density in rat model of periodontitis. *J. Biomater. Sci. Polym. Ed.* 29 (1), 74–91. doi:10.1080/09205063.2017.1400145

Khattak, S., Wahid, F., Liu, L. P., Jia, S. R., Chu, L. Q., Xie, X. Y., et al. (2019). Applications of cellulose and chitin/chitosan derivatives and composites as antibacterial materials: current state and perspectives. *Appl. Microbiol. Biotechnol.* 103 (5), 1989–2006. doi:10.1007/s00253-018-09602-0

Khoroushi, M., and Keshani, F. (2013). A review of glass-ionomers: from conventional glass-ionomer to bioactive glass-ionomer. *Dent. Res. J. (Isfahan)* 10 (4), 411–420.

Khutoryanskiy, V. V. (2011). Advances in mucoadhesion and mucoadhesive polymers. *Macromol. Biosci.* 11 (6), 748–764. doi:10.1002/mabi.201000388

Kilicarslan, M., Ilhan, M., Inal, O., and Orhan, K. (2018). Preparation and evaluation of clindamycin phosphate loaded chitosan/alginate polyelectrolyte complex film as mucoadhesive drug delivery system for periodontal therapy. *Eur. J. Pharm. Sci.* 123, 441–451. doi:10.1016/j.ejps.2018.08.007

Kim, C. H., Choi, J. W., Chun, H. J., and Choi, K. S. (1997). Synthesis of chitosan derivatives with quaternary ammonium salt and their antibacterial activity. *Polym. Bull.* 38 (4), 387–393. doi:10.1007/s002890050064

Kim, I. Y., Seo, S. J., Moon, H. S., Yoo, M. K., Park, I. Y., Kim, B. C., et al. (2008). Chitosan and its derivatives for tissue engineering applications. *Biotechnol. Adv.* 26 (1), 1–21. doi:10.1016/j.biotechadv.2007.07.009

Kim, S. (2018). Competitive biological activities of chitosan and its derivatives: antimicrobial, antioxidant, anticancer, and anti-inflammatory activities. *Polysaccharides Biomed. Appl.* 2018, 1–13. doi:10.1155/2018/1708172

Kong, M., Chen, X. G., Xing, K., and Park, H. J. (2010). Antimicrobial properties of chitosan and mode of action: a state of the art review. *Int. J. Food Microbiol.* 144 (1), 51–63. doi:10.1016/j.ijfoodmicro.2010.09.012

Kumari, S., and Singh, R. P. (2013). Glycolic acid-functionalized chitosan-Co3O4-Fe3O4 hybrid magnetic nanoparticles-based nanohybrid scaffolds for drug-delivery and tissue engineering. *J. Mat. Sci.* 48, 1524–1532. doi:10.1007/s10853-012-6907-z

Kurita, K. (2001). Controlled functionalization of the polysaccharide chitin. *Prog. Polym. Sci.* 26, 1921–1971. doi:10.1016/s0079-6700(01)00007-7

Ladet, S., David, L., and Domard, A. (2008). Multi-membrane hydrogels. *Nature* 452, 76–79. doi:10.1038/nature06619

Lee, B. S., Lee, C. C., Wang, Y. P., Chen, H. J., Lai, C. H., Hsieh, W. L., et al. (2016). Controlled-release of tetracycline and lovastatin by poly (d, l-lactide-co-glycolide acid)-chitosan nanoparticles enhances periodontal regeneration in dogs. *Int. J. Nanomedicine* 11, 285–297. doi:10.2147/ijn.s94270

Lee, H. L., Wang, R. S., Hsu, Y. C., Chuang, C. C., Chan, H. R., Chiu, H. C., et al. (2018). Antifungal effect of tissue conditioners containing poly (acryloyloxyethyltrimethyl ammonium chloride)-grafted chitosan on Candida albicans growth *in vitro*. *J. Dent. Sci.* 13 (2), 160–166. doi:10.1016/j.jds.2017.06.004

Levengood, S. L., and Zhang, M. (2014). Chitosan-based scaffolds for bone tissue engineering. *J. Mater Chem. B* 2 (21), 3161–3184. doi:10.1039/c4tb00027g

Li, B., Xia, X., Guo, M., Jiang, Y., Zhang, Z., Liu, S., et al. (2019a). Biological and antibacterial properties of the micro-nanostructured hydroxyapatite/chitosan coating on titanium. *Sci. Rep.* 9, 14052. doi:10.1038/s41598-019-49941-0

Li, H., Li, P., Yang, Z., Gao, C., Fu, L., Liao, Z., et al. (2021). Meniscal regenerative scaffolds based on biopolymers and polymers: recent status and applications. *Front. Cell Dev. Biol.* 9, 661802. doi:10.3389/fcell.2021.661802

Li, J., Wu, Y., and Zhao, L. (2016). Antibacterial activity and mechanism of chitosan with ultra-high molecular weight. *Carbohydr. Polym.* 148, 200–205. doi:10.1016/j.carbpol.2016.04.025

Li, W., Long, Y., Liu, Y., Long, K., Liu, S., Wang, Z., et al. (2014). Fabrication and characterization of chitosan–collagen crosslinked membranes for corneal tissue engineering. *J. Biomater. Sci. Polym. Ed.* 25, 1962–1972. doi:10.1080/09205063.2014.965996

Li, Y., Qiao, Z., Yu, F., Hu, H., Huang, Y., Xiang, Q., et al. (2019b). Transforming growth factor-β3/chitosan sponge (TGF-β3/CS) facilitates osteogenic differentiation of

human periodontal ligament stem cells. *Int. J. Mol. Sci.* 20 (20), 4982. doi:10.3390/ijms20204982

Liang, Y., Zhao, X., Ma, P. X., Guo, B., Du, Y., and Han, X. (2019). pH-responsive injectable hydrogels with mucosal adhesiveness based on chitosan-grafted-dihydrocaffeic acid and oxidized pullulan for localized drug delivery. *J. Colloid Interface Sci.* 536, 224–234. doi:10.1016/j.jcis.2018.10.056

Liao, Y., Li, H., Shu, R., Chen, H., Zhao, L., Song, Z., et al. (2020). Mesoporous hydroxyapatite/chitosan loaded with recombinant-human amelogenin could enhance antibacterial effect and promote periodontal regeneration. *Front. Cell. Infect. Microbiol.* 10, 180. doi:10.3389/fcimb.2020.00180

Lim, S. H., and Hudson, S. M. (2004). Synthesis and antimicrobial activity of a water-soluble chitosan derivative with a fiber-reactive group. *Carbohydr. Res.* 339 (2), 313–319. doi:10.1016/j.carres.2003.10.024

Limapornvanich, A., Jitpukdeebodintra, S., Hengtrakool, C., and Kedjarune-Leggat, U. (2009). Bovine serum albumin release from novel chitosan-fluoro-aluminosilicate glass ionomer cement: stability and cytotoxicity studies. *J. Dent.* 37 (9), 686–690. doi:10.1016/j.jdent.2009.05.007

Lovecchio, J., Gargiulo, P., Vargas Luna, J. L., Giordano, E., and Sigurjónsson, Ó. E. (2019). A standalone bioreactor system to deliver compressive load under perfusion flow to hBMSCseeded 3D chitosan-graphene templates. *Sci. Rep.* 9 (1), 16854. doi:10.1038/s41598-019-53319-7

Loyola-Rodríguez, J. P., Torres-Méndez, F., Espinosa-Cristobal, L. F., García-Cortes, J. O., Loyola-Leyva, A., González, F. J., et al. (2019). Antimicrobial activity of endodontic sealers and medications containing chitosan and silver nanoparticles against *Enterococcus faecalis*. *J. Appl. Biomater. Func.* 17 (3), 228080001985177. doi:10.1177/2280800019851771

Lu, B., Lv, X., and Le, Y. (2019). Chitosan-modified PLGA nanoparticles for control-released drug delivery. *Polymers* 11 (2), 304. doi:10.3390/polym11020304

Madi, M., Pavlic, V., Samy, W., and Alagl, A. (2018). The anti-inflammatory effect of locally delivered nano-doxycycline gel in therapy of chronic periodontitis. *Acta Odontol. Scand.* 76 (1), 71–76. doi:10.1080/00016357.2017.1385096

Mahima, V. G., Patil, K., Kulkarni, P. K., Tayal, S., and Keshari, D. (2015). Use of chitosan mouth-wash in radio-chemotherapy induced oral mucositis: a case-control study. *J. Adv. Clin. Res. Insights* 2, 248–252. doi:10.15713/ins.jcri.88

Mahmood, A., Lanthaler, M., Laffleur, F., Huck, C. W., and Bernkop-Schnürch, A. (2017). Thiolated chitosan micelles: highly mucoadhesive drug carriers. *Carbohydr. Polym.* 167, 250–258. doi:10.1016/j.carbpol.2017.03.019

Maliki, S., Sharma, G., Kumar, A., Moral-Zamorano, M., Moradi, O., Baselga, J., et al. (2022). Chitosan as a tool for sustainable development: a mini review. *Polym. (Basel)* 14 (7), 1475. doi:10.3390/polym14071475

Malinowska, S. K., Kaczmarek, U., Malicka, B., Walczak, K., and Zietek, M. (2017). Application of chitosan and propolis in endodontic treatment: a review. *Mini Rev. Med. Chem.* 17 (5), 410–434. doi:10.2174/1389557516666160418122510

Manni, L., Ghorbel-Bellaaj, O., Jellouli, K., Younes, I., and Nasri, M. (2010). Extraction and characterization of chitin, chitosan, and protein hydrolysates prepared from shrimp waste by treatment with crude protease from Bacillus cereus SV1. *Appl. Biochem. Biotechnol.* 162 (2), 345–357. doi:10.1007/s12010-009-8846-y

Mansuri, S., Kesharwani, P., Jain, K., Tekade, R. K., and Jain, N. (2016). Mucoadhesion: a promising approach in drug delivery system. *React. Funct. Polym.* 100, 151–172. doi:10.1016/j.reactfunctpolym.2016.01.011

Marrazzo, P., Paduano, F., Palmieri, F., Marrelli, M., and Tatullo, M. (2016). Highly efficient *in vitro* reparative behaviour of dental pulp stem cells cultured with standardised platelet lysate supplementation. *Stem Cells Int.* 2016, 1–16. doi:10.1155/2016/7230987

Matica, M. A., Aachmann, F. L., Tøndervik, A., Sletta, H., and Ostafe, V. (2019). Chitosan as a wound dressing starting material: antimicrobial properties and mode of action. *Int. J. Mol. Sci.* 20 (23), 5889. doi:10.3390/ijms20235889

Merzendorfer, H. (2011). The cellular basis of chitin synthesis in fungi and insects: common principles and differences. *Eur. J. Cell Biol.* 90, 759–769. doi:10.1016/j.ejcb.2011.04.014

Min, H. S., You, D. G., Son, S., Jeon, S., Park, J. H., Lee, S., et al. (2015). Echogenic glycol chitosan nanoparticles for ultrasound-triggered cancer theranostics. *Theranostics* 5 (12), 1402–1418. doi:10.7150/thno.13099

Minervini, G., Franco, R., Marrapodi, M. M., Di Blasio, M., Cicciù, M., and Ronsivalle, V. (2024). The effectiveness of chitosan as a hemostatic in dentistry in patients with antiplatelet/anticoagulant therapy: systematic review with meta-analysis. *BMC Oral Health* 24 (1), 70. doi:10.1186/s12903-023-03568-w

Mohan, K., Ganesan, A. R., Muralisankar, T., Jayakumar, R., Sathishkumar, P., Uthayakumar, V., et al. (2020). Recent insights into the extraction, characterization, and bioactivities of chitin and chitosan from insects. *Trends Food Sci. Technol.* 105, 17–42. doi:10.1016/j.tifs.2020.08.016

Moreira, M. S., Sarra, G., Carvalho, G. L., Gonçalves, F., Caballero-Flores, H. V., Pedroni, A. C. F., et al. (2021). Physical and biological properties of a chitosan hydrogel scaffold associated to photobiomodulation therapy for dental pulp regeneration: an *in vitro* and *in vivo* study. *BioMed Res. Int.* 2021, 1–10. doi:10.1155/2021/6684667

Mulder, R., and Anderson-Small, C. (2019). Ion release of chitosan and nanodiamond modified glass ionomer restorative cements. *Clin. Cosmet. Investig. Dent.* 11, 313–320. doi:10.2147/ccide.s220089

Murray, P. E., Windsor, L. J., Hafez, A. A., Stevenson, R. G., and Cox, C. F. (2003). Comparison of pulp responses to resin composites. *Oper. Dent.* 28 (3), 242–250.

Muthukrishnan, A., and Shanmughapriya, G. (2017). Chitosan in the treatment of radiotherapy induced oral mucositis in head and neck cancer patients: a randomisd clinical trial. *Oral Surg. Oral Med. Oral Pathology Oral Radiology* 124, E198–E199. doi:10.1016/J.Oooo.2017.05.502

Najeeb, S., Khurshid, Z., Siddiqui, F., Zohaib, S., and Zafar, M. S. (2017). Outcomes of dental implant therapy in patients with down syndrome: a systematic review. *J. Evid. Based Dent. Pract.* 17 (4), 317–323. doi:10.1016/j.jebdp.2017.05.003

Najeeb, S., Khurshid, Z., Zohaib, S., and Zafar, M. S. (2016). Bioactivity and osseointegration of PEEK are inferior to those of titanium-A systematic review. *J. Oral Implantol.* 42, 512–516. doi:10.1563/aaid-joi-d-16-00072

Namangkalakul, W., Benjavongkulchai, S., Pochana, T., Promchai, A., Satitviboon, W., Howattanapanich, S., et al. (2020). Activity of chitosan antifungal denture adhesive against common Candida species and Candida albicans adherence on denture base acrylic resin. *J. Prosthet. Dent.* 123 (1), 181. e1–e181.e7. doi:10.1016/j.prosdent.2019.09.026

Nava Juárez, E. (2023). Biological effects of chitosan in Dentistry. *Mexican J. Med. Res. ICSA* 11 (22), 36–40. doi:10.29057/mjmr.v11i22.10635

Newman, M. G., Takei, H., Klokkevold, P. R., and Carranza, F. A. (2011). *Carranza's clinical periodontology*. Elsevier health sciences.

Nie, L., Wu, Q., Long, H., Hu, K., Li, P., Wang, C., et al. (2019). Development of chitosan/gelatin hydrogels incorporation of biphasic calcium phosphate nanoparticles for bone tissue engineering. *J. Biomater. Sci. Polym. Ed.* 30 (17), 1636–1657. doi:10.1080/09205063.2019.1654210

Nitschke, J., Altenbach, H., Malolepszy, T., and Mölleken, H. (2011). A new method for the quantification of chitin and chitosan in edible mushrooms. *Carbohydr. Res.* 346, 1307–1310. doi:10.1016/j.carres.2011.03.040

Norowski, P. A., Courtney, H. S., Babu, J., Haggard, W. O., and Bumgardner, J. D. (2011). Chitosan coatings deliver antimicrobials from titanium implants: a preliminary study. *Implant Dent.* 20 (1), 56–67. doi:10.1097/id.0b013e3182087ac4

Norowski, P. A., Fujiwara, T., Clem, W. C., Adatrow, P. C., Eckstein, E. C., Haggard, W. O., et al. (2015). Novel naturally crosslinked electrospun nanofibrous chitosan mats for guided bone regeneration membranes: material characterization and cytocompatibility. *J. Tissue Eng. Regen. Med.* 9, 577–583. doi:10.1002/term.1648

Oryan, A., and Sahvieh, S. (2017). Effectiveness of chitosan scaffold in skin, bone and cartilage healing. *Int. J. Biol. Macromol.* 104, 1003–1011. doi:10.1016/j.ijbiomac.2017.06.124

Panahi, F., Rabiee, S. M., and Shidpour, R. (2017). Synergic effect of chitosan and dicalcium phosphate on tricalcium silicate-based nanocomposite for root-end dental application. *Mater. Sci. Eng. C* 80, 631–641. doi:10.1016/j.msec.2017.07.012

Pang, X., and Huang, Y. (2012). Physical properties of nano-HAs/ZrO2 coating on surface of titanium materials used in dental-implants and its biological compatibility. *J. Nanosci. Nanotechnol.* 12, 902–910. doi:10.1166/jnn.2012.5666

Paradowska-Stolarz, A., Mikulewicz, M., Laskowska, J., Karolewicz, B., and Owczarek, A. (2023). The importance of chitosan coatings in dentistry. *Mar. Drugs* 21 (12), 613. doi:10.3390/md21120613

Parsa, P., Paydayesh, A., and Davachi, S. M. (2019). Investigating the effect of tetracycline addition on nanocomposite hydrogels based on polyvinyl alcohol and chitosan nanoparticles for specific medical applications. *Int. J. Biol. Macromol.* 121, 1061–1069. doi:10.1016/j.ijbiomac.2018.10.074

Paul, W., and Sharma, C. P. (2004). Chitosan and alginate wound dressings: a short review. *Trends Biomater. Artif. Organs* 18, 18–23.

Perchyonok, V. T., Zhang, S., Grobler, S. R., and Oberholzer, T. G. (2013). Insights into and relative effect of chitosan-H, chitosan-H-propolis, chitosan-H-propolis-nystatin and chitosan-H-nystatin on dentine bond strength. *Eur. J. Dent.* 7, 412–418. doi:10.4103/1305-7456.120666

Pichayakorn, W., and Boonme, P. (2013). Evaluation of cross-linked chitosan microparticles containing metronidazole for periodontitis treatment. *Mat. Sci. Eng. C* 33, 1197–1202. doi:10.1016/j.msec.2012.12.010

Pini, N. I. P., Lima, DANL, Luka, B., Ganss, C., and Schlueter, N. (2020). Viscosity of chitosan impacts the efficacy of F/Sn containing toothpastes against erosive/abrasive wear in enamel. *J. Dent.* 92, 103247. doi:10.1016/j.jdent.2019.103247

Pornpitchanarong, C., Rojanarata, T., Opanasopit, P., Ngawhirunpat, T., and Patrojanasophon, P. (2020). Catechol-modified chitosan/hyaluronic acid nanoparticles as a new avenue for local delivery of doxorubicin to oral cancer cells. *Colloids Surf. B Biointerfaces* 196, 111279. doi:10.1016/j.colsurfb.2020.111279

Prabaharan, M. (2014). Bioactivity of chitosan derivative. *Polysaccharides*, 1–14. doi:10.1007/978-3-319-03751-6_17-1

Priyadarsini, S., Mukherjee, S., and Mishra, M. (2018). Nanoparticles used in dentistry: a review. *J. oral Biol. craniofacial Res.* 8 (1), 58–67. doi:10.1016/j.jobcr.2017.12.004

Qin, W., Chen, J. Y., Guo, J., Ma, T., Weir, M. D., Guo, D., et al. (2018). Novel calcium phosphate cement with metformin-loaded chitosan for odontogenic differentiation of human dental pulp cells. *Stem Cells Int.* 2018, 1–10. doi:10.1155/2018/7173481

Qin, Y., and Li, P. (2020). Antimicrobial chitosan conjugates: current synthetic strategies and potential applications. *Int. J. Mol. Sci.* 21 (2), 499. doi:10.3390/ijms21020499

Qu, J., Zhao, X., Liang, Y., Zhang, T., Ma, P. X., and Guo, B. (2018). Antibacterial adhesive injectable hydrogels with rapid self-healing, extensibility and compressibility as wound dressing for joints skin wound healing. *Biomaterials* 183, 185–199. doi:10.1016/j.biomaterials.2018.08.044

Qu, S., Ma, X., Yu, S., and Wang, R. (2023). Chitosan as a biomaterial for the prevention and treatment of dental caries: antibacterial effect, biomimetic mineralization, and drug delivery. *Front. Bioeng. Biotechnol.* 11, 1234758. doi:10.3389/fbioe.2023.1234758

Rabea, E. I., Badawy, M. E., Stevens, C. V., Smagghe, G., and Steurbaut, W. (2003). Chitosan as antimicrobial agent: applications and mode of action. *Biomacromolecules* 4 (6), 1457–1465. doi:10.1021/bm034130m

Raddall, G., Mello, I., and Leung, B. M. (2019). Biomaterials and scaffold design strategies for regenerative endodontic therapy. *Front. Bioeng. Biotechnol.* 7, 317. doi:10.3389/fbioe.2019.00317

Rakkiettiwong, N., Hengtrakool, C., Thammasitboon, K., and Kedjarune-Leggat, U. (2011). Effect of novel chitosan-fluoroaluminosilicate glass ionomer cement with added transforming growth factor beta-1 on pulp cells. *J. Endod.* 37 (3), 367–371. doi:10.1016/j.joen.2010.11.031

Rasti, H., Parivar, K., Baharara, J., Iranshahi, M., and Namvar, F. (2017). Chitin from the mollusc Chiton: extraction, characterization and chitosan preparation. *Iran. J. Pharm. Res.* 16 (1), 366–379.

Raura, N., Garg, A., Arora, A., and Roma, M. (2020). Nanoparticle technology and its implications in endodontics: a review. *Biomater. Res.* 24 (21), 21–28. doi:10.1186/s40824-020-00198-z

Redepenning, J., Venkataraman, G., Chen, J., and Stafford, N. (2003). Electrochemical preparation of chitosan/hydroxyapatite composite coatings on titanium substrates. *J. Biomed. Mater Res. A* 66 (2), 411–416. doi:10.1002/jbm.a.10571

Ren, Q., Ding, L., Li, Z., Wang, X., Wang, K., Han, S., et al. (2019). Chitosan hydrogel containing amelogenin-derived peptide: inhibition of cariogenic bacteria and promotion of remineralization of initial caries lesions. *Arch. Oral Biol.* 100, 42–48. doi:10.1016/j.archoralbio.2019.02.004

Retana-Lobo, C. (2018). Dental pulp regeneration: insights from biological processes. *Odovtos* 20 (1), 10–16. doi:10.15517/ijds.v0i0.31269

Rodrigues, S., Dionísio, M., López, C. R., and Grenha, A. (2012). Biocompatibility of chitosan carriers with application in drug delivery. *J. Funct. Biomater.* 3 (3), 615–641. doi:10.3390/jfb3030615

Saboktakin, M. R., Tabatabaie, R., Maharramov, A., and Ramazanov, M. A. (2010). Synthesis and characterization of superparamagnetic chitosan—dextran sulfate hydrogels as nano carriers for colon-specific drug delivery. *Carbohydr. Polym.* 81, 372–376. doi:10.1016/j.carbpol.2010.02.034

Sacco, P., Furlani, F., De Marzo, G., Marsich, E., Paoletti, S., and Donati, I. (2018). Concepts for developing physical gels of chitosan and of chitosan derivatives. *Gels* 4 (3), 67. doi:10.3390/gels4030067

Saeed, A., Haider, A., Zahid, S., Khan, S. A., Faryal, R., and Kaleem, M. (2019). *In-vitro* antifungal efficacy of tissue conditioner-chitosan composites as potential treatment therapy for denture stomatitis. *Int. J. Biol. Macromol.* 125, 761–766. doi:10.1016/j.ijbiomac.2018.12.091

Sahariah, P., and Másson, M. (2017). Antimicrobial chitosan and chitosan derivatives: a review of the structure–activity relationship. *Biomacromolecules* 18 (11), 3846–3868. doi:10.1021/acs.biomac.7b01058

Salari, M., Khiabani, M. S., Mokarram, R. R., Ghanbarzadeh, B., and Kafil, H. S. (2018). Development and evaluation of chitosan based active nanocomposite films containing bacterial cellulose nanocrystals and silver nanoparticles. *Food Hydrocoll.* 84, 414–423. doi:10.1016/j.foodhyd.2018.05.037

Sanap, P., Hegde, V., Ghunawat, D., Patil, M., Nagaonkar, N., and Jagtap, V. (2020). Current applications of chitosan nanoparticles in dentistry: a review. *Int. J. Appl. Dent. Sci.* 6 (4), 81–84. doi:10.22271/oral.2020.v6.i4b.1050

Saranya, N., Saravanan, S., Moorthi, A., Ramyakrishna, B., and Selvamurugan, N. (2011). Enhanced osteoblast adhesion on polymeric nano-scaffolds for bone tissue engineering. *J. Biomed. Nanotechnol.* 7 (2), 238–244. doi:10.1166/jbn.2011.1283

Sarasam, A. R., Brown, P., Khajotia, S. S., Dmytryk, J. J., and Madihally, S. V. (2008). Antibacterial activity of chitosan-based matrices on oral pathogens. *J. Mat. Sci. Mat. Med.* 19, 1083–1090. doi:10.1007/s10856-007-3072-z

Saravanan, S., Sameera, D. K., Moorthi, A., and Selvamurugan, N. (2013). Chitosan scaffolds containing chicken feather keratin nanoparticles for bone tissue engineering. *Int. J. Biol. Macromol.* 62, 481–486. doi:10.1016/j.ijbiomac.2013.09.034

Schmalz, G., Widbiller, M., and Galler, K. M. (2017). Signaling molecules and pulp regeneration. *J. Endod.* 43 (9S), S7–S11. doi:10.1016/j.joen.2017.06.003

Senthil, K. R., Ravikumar, N., Kavitha, S., Mahalaxmi, S., Jayasree, R., Sampath, K. T. S., et al. (2017). Nanochitosan modified glass ionomer cement with enhanced mechanical properties and fluoride release. *Int. J. Biol. Macromol.* 104, 1860–1865. doi:10.1016/j.ijbiomac.2017.05.120

Shaik, J., Garlapati, R., Nagesh, B., Sujana, V., Jayaprakash, T., and Naidu, S. (2014). Comparative evaluation of antimicrobial efficacy of triple antibiotic paste and calcium hydroxide using chitosan as carrier against Candida albicans and *Enterococcus faecalis*: an *in vitro* study. *J. Conserv. Dent.* 17 (4), 335–339. doi:10.4103/0972-0707.136444

Sharifi-Rad, J., Quispe, C., Butnariu, M., Rotariu, L. S., Sytar, O., Sestito, S., et al. (2021). Chitosan nanoparticles as a promising tool in nanomedicine with particular emphasis on oncological treatment. *Cancer Cell Int.* 21 (1), 318. doi:10.1186/s12935-021-02025-4

Shen, J., Jin, B., Qi, Y. C., Jiang, Q. Y., and Gao, X. F. (2017). Carboxylated chitosan/silverhydroxyapatite hybrid microspheres with improved antibacterial activity and cytocompatibility. *Mat. Sci. Eng. C* 78, 589–597. doi:10.1016/j.msec.2017.03.100

Shi, C., Zhu, Y., Ran, X., Wang, M., Su, Y., and Cheng, T. (2006). Therapeutic potential of chitosan and its derivatives in regenerativeMedicine. *J. Surg. Res.* 133 (2), 185–192. doi:10.1016/j.jss.2005.12.013

Shrestha, A., and Kishen, A. (2016). Antibacterial nanoparticles in endodontics: a review. *J. Endod.* 42 (10), 1417–1426. doi:10.1016/j.joen.2016.05.021

Sidhu, S. K., and Nicholson, J. W. (2016). A review of glass-ionomer cements for clinical dentistry. *J. Funct. Biomater.* 7 (3), 16. doi:10.3390/jfb7030016

Silva, D., Arancibia, R., Tapia, C., Acuña-Rougier, C., Diaz-Dosque, M., Cáceres, M., et al. (2013). Chitosan and platelet-derived growth factor synergistically stimulate cell proliferation in gingival fibroblasts. *J. Periodontal Res.* 48 (6), 677–686. doi:10.1111/jre.12053

Singh, K., Tiwary, A. K., and Rana, V. (2013). Spray dried chitosan-EDTA superior microparticles as solid substrate for the oral delivery of amphotericin B. *Int. J. Biol. Macromol.* 58, 310–319. doi:10.1016/j.ijbiomac.2013.04.053

Sinha, V., Singla, A. K., Wadhawan, S., Kaushik, R., Kumria, R., Bansal, K., et al. (2004). Chitosan microspheres as a potential carrier for drugs. *Int. J. Pharm.* 274 (1–2), 1–33. doi:10.1016/j.ijpharm.2003.12.026

Sivanesan, I., Gopal, J., Muthu, M., Shin, J., and Oh, J. W. (2021). Reviewing chitin/chitosan nanofibers and associated nanocomposites and their attained medical milestones. *Polymers* 13 (14), 2330. doi:10.3390/polym13142330

Soares, D. G., Anovazzi, G., Bordini, E. A. F., Zuta, U. O., Silva Leite, M. L. A., Basso, F. G., et al. (2018). Biological analysis of simvastatin-releasing chitosan scaffold as a cell-free system for pulp-dentin regeneration. *J. Endod.* 44 (6), 971–976.e1. doi:10.1016/j.joen.2018.02.014

Soran, Z., Aydin, R. S., and Gumusderelioglu, M. (2012). Chitosan scaffolds with BMP-6 loaded alginate microspheres for periodontal tissue engineering. *J. Microencapsul.* 29, 770–780. doi:10.3109/02652048.2012.686531

Soskolne, W. A. (1997). Subgingival delivery of therapeutic agents in the treatment of periodontal diseases. *Crit. Rev. Oral Biol. Med.* 8 (2), 164–174. doi:10.1177/10454411970080020501

Soygun, K., Soygun, A., and Dogan, M. C. (2021). The effects of chitosan addition to glass ionomer cement on microhardness and surface roughness. *J. Appl. Biomater. Funct. Mater* 19, 228080002198970. doi:10.1177/2280800021989706

Stenhagen, I. S. R., Rukke, H. V., Dragland, I. S., and Kopperud, H. M. (2019). Effect of methacrylated chitosan incorporated in experimental composite and adhesive on mechanical properties and biofilm formation. *Eur. J. Oral Sci.* 127 (1), 81–88. doi:10.1111/eos.12584

Su, W. T., Wu, P. S., Ko, C. S., and Huang, T. Y. (2014). Osteogenic differentiation and mineralization of human exfoliated deciduous teeth stem cells on modified chitosan scaffold. *Mat. Sci. Eng. C* 41, 152–160. doi:10.1016/j.msec.2014.04.048

Sukpaita, T., Chirachanchai, S., Suwattanachai, P., Everts, V., Pimkhaokham, A., and Ampornaramveth, R. S. (2019). *In vivo* bone regeneration induced by a scaffold of chitosan/dicarboxylic acid seeded with human periodontal ligament cells. *Int. J. Mol. Sci.* 19, 4883. doi:10.3390/ijms20194883

Sultankulov, B., Berillo, D., Sultankulova, K., Tokay, T., and Saparov, A. (2019). Progress in the development of chitosan-based biomaterials for tissue engineering and regenerative medicine. *Biomolecules* 9 (9), 470. doi:10.3390/biom9090470

Sun, I. C., Na, J. H., Jeong, S. Y., Kim, D. E., Kwon, I. C., Choi, K., et al. (2014). Biocompatible glycol chitosan-coated gold nanoparticles for tumor-targeting CT imaging. *Pharm. Res.* 31 (6), 1418–1425. doi:10.1007/s11095-013-1142-0

Suneetha, M., Rao, K. M., and Han, S. S. (2020). Mechanically improved porous hydrogels with polysaccharides via polyelectrolyte complexation for bone tissue engineering. *Int.J. Biol. Macromol.* 144, 160–169. doi:10.1016/j.ijbiomac.2019.12.096

Takeuchi, I., Togo, C., and Makino, K. (2019). Rebamipide-containing film using chitosan and HPMC for oral mucositis induced by cancer chemotherapy. *Anticancer Res.* 39 (12), 6531–6536. doi:10.21873/anticanres.13868

Tanir, T. E., Hasirci, V., and Hasirci, N. (2014). Electrospinning of chitosan/poly (lactic acid-coglycolic acid)/hydroxyapatite composite nanofibrous mats for tissue engineering applications. *Polym. Bull.* 71 (11), 2999–3016. doi:10.1007/s00289-014-1234-y

Taser, B., Ozkan, H., Adiguzel, A., Orak, T., Baltaci, M. O., and Taskin, M. (2021). Preparation of chitosan from waste shrimp shells fermented with Paenibacillus jamilae BAT1. *Int. J. Biol. Macromol.* 183, 1191–1199. doi:10.1016/j.ijbiomac.2021.05.062

Tatullo, M., Codispoti, B., Pacifici, A., Palmieri, F., Marrelli, M., Pacifici, L., et al. (2017). Potential use of human periapical cyst-mesenchymal stem cells (hPCy-MSCs) as a novel stem cell source for regenerative medicine applications. *Front. Cell Dev. Biol.* 5, 103. doi:10.3389/fcell.2017.00103

Thomas, L. V., Rahul, V., and Nair, P. D. (2017). Effect of stiffness of chitosan-hyaluronic acid dialdehyde hydrogels on the viability and growth of encapsulated chondrocytes. *Int. J. Biol. Macromol.* 104, 1925–1935. doi:10.1016/j.ijbiomac.2017.05.116

Vázquez, M. R., Vega-Ruiz, B., Zúñiga, R. R., Koppel, D. A. S., and Olvera, L. F. Q. (2015). Chitosan and its potential use as a scaffold for tissue engineering in regenerative medicine. *BioMed Res. Int.* 2015, 1–15. doi:10.1155/2015/821279

Vetter, J. (2007). Chitin content of cultivated mushrooms Agaricus bisporus, Pleurotus ostreatus and Lentinula edodes. *Food Chem.* 102, 6–9. doi:10.1016/j.foodchem.2006.01.037

Vijayan, A. A. S., and Kumar, G. S. V. (2019). PEG grafted chitosan scaffold for dual growth factor delivery for enhanced wound healing. *Sci. Rep.* 9, 19165. doi:10.1038/s41598-019-55214-7

Vining, K., and Mooney, D. (2017). Mechanical forces direct stem cell behaviour in development and regeneration. *Nat. Rev. Mol. Cell Biol.* 18, 728–742. doi:10.1038/nrm.2017.108

Wang, C. H., Liu, W. S., Sun, J. F., Hou, G. G., Chen, Q., Cong, W., et al. (2016). Non-toxic Oquaternized chitosan materials with better water solubility and antimicrobial function. *Int. J. Biol. Macromol.* 84, 418–427. doi:10.1016/j.ijbiomac.2015.12.047

Wang, J. J., Zeng, Z. W., Xiao, R. Z., Xie, T., Zhou, G. L., Zhan, X. R., et al. (2011). Recent advances of chitosan nanoparticles as drug carriers. *Int. J. Nanomedicine* 6, 765–774. doi:10.2147/ijn.s17296

Wang, W., Meng, Q., Li, Q., Liu, J., Zhou, M., Jin, Z., et al. (2020). Chitosan derivatives and their application in biomedicine. *Int. J. Mol. Sci.* 21 (2), 487. doi:10.3390/ijms21020487

Wang, Y., Liu, P., Du, J., Sun, Y., Li, F., and Duan, Y. (2013). Targeted siRNA delivery by anti-HER2 antibody-modified nanoparticles of mPEG-chitosan diblock copolymer. *J. Biomater. Sci. Polym. Ed.* 24, 1219–1232. doi:10.1080/09205063.2012.745716

Wassel, M. O., and Khattab, M. A. (2017). Antibacterial activity against Streptococcus mutans and inhibition of bacterial induced enamel demineralization of propolis, miswak, and chitosan nanoparticles based dental varnishes. *J. Adv. Res.* 8 (4), 387–392. doi:10.1016/j.jare.2017.05.006

Wei, Y., Hudson, S., Mayer, J., and Kaplan, D. (1992). The crosslinking of chitosan fibers. *J. Polym. Sci. A Polym. Chem.* 30 (10), 2187–2193. doi:10.1002/pola.1992.080301013

Wimardhani, Y. S., Suniarti, D. F., Freisleben, H. J., Wanandi, S. I., Siregar, N. C., and Ikeda, M. A. (2014a). Chitosan exerts anticancer activity through induction of apoptosis and cell cycle arrest in oral cancer cells. *J. Oral Sci.* 56 (2), 119–126. doi:10.2334/josnusd.56.119

Wimardhani, Y. S., Suniarti, D. F., Freisleben, H. J., Wanandi, S. I., Siregar, N. C., and Ikeda, M. A. (2014b). Chitosan exerts anticancer activity through induction of apoptosis and cell cycle arrest in oral cancer cells. *J. Oral Sci.* 56 (2), 119–126. doi:10.2334/josnusd.56.119

Wu, T., Zivanovic, S., Draughon, F. A., and Sams, C. E. (2004). Chitin and chitosan--value-added products from mushroom waste. *J. Agric. Food Chem.* 52 (26), 7905–7910. doi:10.1021/jf0492565

Xia, W., Liu, P., Zhang, J., and Chen, J. (2011). Biological activities of chitosan and chitooligosaccharides. *Food Hydrocoll.* 25 (2), 170–179. doi:10.1016/j.foodhyd.2010.03.003

Xu, H., Fang, Z., Tian, W., Wang, Y., Ye, Q., Zhang, L., et al. (2018). Green fabrication of amphiphilic quaternized β-chitin derivatives with excellent biocompatibility and antibacterial activities for wound healing. *Adv. Mat.* 30 (29), 1801100. doi:10.1002/adma.201801100

Xu, T., Xin, M., Li, M., Huang, H., Zhou, S., and Liu, J. (2011). Synthesis, characterization, and antibacterial activity of N, O-quaternary ammonium chitosan. *Carbohydr. Res.* 346 (15), 2445–2450. doi:10.1016/j.carres.2011.08.002

Xue, Y., Hong, X., Gao, J., Shen, R., and Ye, Z. (2019). Preparation and biological characterization of the mixture of poly (lactic-co-glycolic acid)/chitosan/Ag nanoparticles for periodontal tissue engineering. *Int. J. Nanomedicine* 14, 483–498. doi:10.2147/ijn.s184396

Yadav, A., and Bhise, S. (2004). Chitosan: a potential biomaterial effective against typhoid. *Curr. Sci.* 87, 1176–1178.

Yadav, S. K., Khan, G., Bonde, G. V., Bansal, M., and Mishra, B. (2018). Design, optimization and characterizations of chitosan fortified calcium alginate microspheres for the controlled delivery of dual drugs. *Artif. Cells Nanomed. Biotechnol.* 46 (6), 1180–1193. doi:10.1080/21691401.2017.1366331

Yanat, M., and Schroën, K. (2021). Preparation methods and applications of chitosan nanoparticles; with an outlook toward reinforcement of biodegradable packaging. *React. Funct. Polym.* 161, 104849. doi:10.1016/j.reactfunctpolym.2021.104849

Yang, X., Han, G., Pang, X., and Fan, M. (2020). Chitosan/collagen scaffold containing bone morphogenetic protein-7 DNA supports dental pulp stem cell differentiation *in vitro* and *in vivo*. *J. Biomed. Mater Res. A* 108 (12), 2519–2526. doi:10.1002/jbm.a.34064

Yilmaz, A. H. (2020). Antibacterial activity of chitosan-based systems. *Funct. Chitosan*, 457–489. doi:10.1007/978-981-15-0263-7_15

Younes, I., and Rinaudo, M. (2015). Chitin and chitosan preparation from marine sources. Structure, properties and applications. *Mar. Drugs* 13, 1133–1174. doi:10.3390/md13031133

Younes, L., Sellimi, S., Rinaudo, M., Jellouli, K., and Nasri, M. (2014). Influence of acetylation degree and molecular weight of homogeneous chitosans on antibacterial and antifungal activities. *Int. J. Food Microbiol.* 185, 57–63. doi:10.1016/j.ijfoodmicro.2014.04.029

Young, A., Smistad, G., Karlsen, J., Rolla, G., and Rykke, M. (1997). Zeta potentials of human enamel and hydroxyapatite as measured by the Coulter® DELSA 440. *Adv. Dent. Res.* 11, 560–565. doi:10.1177/08959374970110042501

Zafar, M. S., and Ahmed, N. (2014). Nanomechanical characterization of exfoliated and retained deciduous incisors. *Technol. Health Care* 22, 785–793. doi:10.3233/thc-140852

Zhang, J., Boyes, V., Festy, F., Lynch, R. J., Watson, T. F., and Banerjee, A. (2018b). *In-vitro* subsurface remineralisation of artificial enamel white spot lesions pre-treated with chitosan. *Dent. Mat.* 34 (8), 1154–1167. doi:10.1016/j.dental.2018.04.010

Zhang, J., Lynch, R. J., Watson, T. F., and Banerjee, A. (2019). Chitosan-bioglass complexes promote subsurface remineralisation of incipient human carious enamel lesions. *J. Dent.* 84, 67–75. doi:10.1016/j.jdent.2019.03.006

Zhang, J., Tan, W., Wang, G., Yin, X., Li, Q., Dong, F., et al. (2018a). Synthesis, characterization, and the antioxidant activity of N, N, N-trimethyl chitosan salts. *Int. J. Biol. Macromol.* 118, 9–14. doi:10.1016/j.ijbiomac.2018.06.018

Zhang, L., Liu, Y., Yu, D., and Zhangl, N. (2013). Gadolinium-loaded chitosan nanoparticles as magnetic resonance imaging contrast agents for the diagnosis of tumor. *J. Biomed. Nanotechnol.* 9 (5), 863–869. doi:10.1166/jbn.2013.1584

Zhang, M., Li, X. H., Gong, Y. D., Zhao, N. M., and Zhang, X. F. (2002). Properties and biocompatibility of chitosan films modified by blending with PEG. *Biomaterials* 23 (13), 2641–2648. doi:10.1016/s0142-9612(01)00403-3

Zhang, Y., Wei, W., Lv, P., Wang, L., and Ma, G. (2011). Preparation and evaluation of alginate—chitosan microspheres for oral delivery of insulin. *Eur. J. Pharm. Biopharm.* 77, 11–19. doi:10.1016/j.ejpb.2010.09.016

Zhao, J., Guo, B., and Ma, P. X. (2014). Injectable alginate microsphere/PLGA–PEG–PLGA composite hydrogels for sustained drug release. *RSC Adv.* 4 (34), 17736–17742. doi:10.1039/c4ra00788c

Zhao, L., Zhu, B., Jia, Y., Hou, W., and Su, C. (2013). Preparation of biocompatible carboxymethyl chitosan nanoparticles for delivery of antibiotic drug. *Biomed. Res. Int.* 2013, 1–7. doi:10.1155/2013/236469

Zhao, X., Wu, H., Guo, B., Dong, R., Qiu, Y., and Ma, P. X. (2017). Antibacterial anti-oxidant electroactive injectable hydrogel as self-healing wound dressing with hemostasis and adhesiveness for cutaneous wound healing. *Biomaterials* 122, 34–47. doi:10.1016/j.biomaterials.2017.01.011

Zhou, J., Xu, Q., Fan, C., Ren, H., Xu, S., Hu, F., et al. (2019). Characteristics of chitosan-modified glass ionomer cement and their effects on the adhesion and proliferation of human gingival fibroblasts: an *in vitro* study. *J. Mat. Sci. Mat. Med.* 30 (3), 39. doi:10.1007/s10856-019-6240-z

Zhu, J., Ye, H., Deng, D., Li, J., and Wu, Y. (2020). Electrospun metformin-loaded polycaprolactone/chitosan nanofibrous membranes as promoting guided bone regeneration membranes: preparation and characterization of fibers, drug release, and osteogenic activity *in vitro*. *J. Biomater. Appl.* 34 (9), 1282–1293. doi:10.1177/0885328220901807

Zhu, N., Chatzistavrou, X., Ge, L., Qin, M., Papagerakis, P., and Wang, Y. (2019). Biological properties of modified bioactive glass on dental pulp cells. *J. Dent.* 83, 18–26. doi:10.1016/j.jdent.2019.01.017

Zhu, T., Shi, L., Ma, C., Xu, L., Yang, J., Zhou, G., et al. (2021). Fluorinated chitosan-mediated intracellular catalase delivery for enhanced photodynamic therapy of oral cancer. *Biomater. Sci.* 9 (3), 658–662. doi:10.1039/d0bm01898h

Zivanovic, S., Li, J. J., Davidson, P. M., and Kit, K. (2007). Physical, mechanical, and antibacterial properties of chitosan/PEO blend films. *Biomacromolecules* 8, 1505–1510. doi:10.1021/bm061140p

Efficient In/SSZ-39 catalysts for the selective catalytic reduction of NO with CH₄

Sufeng An[1]*, Peng Wang[1], Kuanling Wang[1], Xuehai Wang[1], Baozhong Li[1] and Xinwen Guo[2]*

[1]SINOPEC (Dalian) Research Institute of Petroleum and Petrochemicals, Dalian, China, [2]Dalian University of Technology, Chemical Engineering Institute, Dalian, China

The M/SSZ-39 catalysts (M = In, Co, Cu, Fe) with different metal species and metal loadings were synthesized using the wet impregnation method on a small-pore SSZ-39 molecular sieve. X-ray diffraction (XRD), transmission electron microscopy (TEM), nitrogen adsorption-dehydrogenation and hydrogen temperature program reduction (H_2-TPR) were employed to characterize the effects of various metal components and metal loadings on the performance of CH_4 selective catalytic reduction of NO reaction (CH_4-SCR). The characterization results showed that the In/SSZ-39 catalyst exhibited significantly higher catalytic activity compared to the Cu-, Co-, and Fe/SSZ-39 catalysts, suggesting that indium (In) is a more suitable active ingredient for the CH_4-SCR reaction. The xIn/SSZ-39 (x = 1, 2, 3, x represents the In loadings of 1.0 wt%, 2.0 wt% and 3.0 wt%) catalysts, with different In loadings, all present excellent CH_4-SCR performance. By varying the In loadings, the type of In species present in the catalyst can be regulated, thus enhancing DeNOx activity and CH_4 selectivity in the CH_4-SCR reaction. At a low temperature of 400 °C and a low CH_4/NO feed ratio (CH_4/NO = 1), the 3In/SSZ-39 catalyst, featuring highly active InOx clusters, achieves the best low-temperature CH_4-SCR performance, with a high NO conversion rate of up to 90% and a CH_4 selectivity of up to 74.2%.

KEYWORDS

CH_4-SCR, In/SSZ-39, highly dispersed InOx species, low temperature activation of CH_4, high CH_4 selectivity

1 Introduction

Nitrogen oxides (NOx) are major pollutants that not only directly jeopardize human health but also trigger a series of environmental issues such as acid rain, photochemical smog, ozone hole, etc (Wang et al., 2017). Thus, addressing the pressing requirements for NOx emission reduction (DeNO$_x$) is crucial for the sustainable development of human society. One of the primary sources of NOx emissions is industrial flue gas from thermal power plants, cement plants, and petrochemical facilities. The main method for reducing NO emissions is ammonia selective catalytic reduction (NH$_3$-SCR), which uses V_2O_5-WO_3 (MoO$_3$)/TiO$_2$ as the catalyst (Han et al., 2019; Wang et al., 2021). However, vanadium catalysts are biological toxicity, and using NH$_3$ as a reducing agent can lead to pipeline corrosion, obstructions, ammonia leaks and other secondary pollution issues (Martin et al., 2006; Mrad et al., 2015). Selective catalytic reduction of NO with methane (CH$_4$-SCR) is a promising new DeNO$_x$ technique. This method uses CH$_4$ as a reductant instead of NH$_3$,

enabling the synergistic purification of NOx and greenhouse gas CH_4, thus avoiding many issues associated with NH_3 (Campa et al., 2021; Wen et al., 2021).

As the primary component of natural gas, CH_4 is abundant and readily available. However, CH_4 is the most stable hydrocarbon molecule, which makes it less effective for selective reduction of NOx at low temperatures and more prone to undergo a non-selective catalytic combustion at high temperatures. Therefore, the CH_4-SCR technology is still meeting many challenges. Among them, developing effective CH_4-SCR catalysts is critically important. Currently, the two most developed catalytic systems are metal oxides and molecular sieves. Compared to metal oxide catalysts, molecular sieve catalysts have gained more attention due to their rich pore structure, adjustable acidity, and metal-ion exchange ability (Jin et al., 2009).

Catalysts containing Pd, Ag, Ni, In and Co supported by molecular sieve have been investigated in CH_4-SCR reaction (Lee et al., 2003; Shi et al., 2004; Chupin et al., 2006; Kubacka et al., 2006; Campa et al., 2015; Sazama et al., 2016). Noble metal-based molecular sieve catalysts can activate CH_4 at lower temperatures and display a broad reaction temperature window (350°C–500° C), but they are expensive and the CH_4 selectivity decreases rapidly as the temperature rises. Thus, high CH_4/NO feed ratios are generally required to achieve high NO conversion in CH_4-SCR reaction catalyzed by the noble metal-based molecular sieve catalysts (Chen et al., 2011; Costilla et al., 2011). Non-precious metal-based molecular sieve catalysts typically require higher reaction temperatures (>500 °C) for good CH_4-SCR performance. However, they also face issues of CH_4 susceptibility to non-selective catalytic combustion at high temperatures (Chen et al., 2011; Huang et al., 2018). Therefore, the key challenge is to design metal-based molecular sieve catalysts that can moderately activate CH_4 at low temperatures, promoting CH_4-SCR reactions and achieving high NOx conversion rates.

To develop effective CH_4-SCR catalysts with good low-temperature activity and high CH_4 selectivity. In this study, a series of M/SSZ-39 catalysts with different metal loadings (M = In, Co, Cu, Fe) were prepared using a simple wet impregnation method on a SSZ-39 molecular sieves. The physicochemical properties of the catalysts were systematically investigated, and their CH_4-SCR performance was evaluated to assess the impact of various metal and metal loadings. The catalytic evaluation results showed that In/SSZ-39 catalysts performed significantly better performance than Co-, Cu-, and Fe/SSZ-39 catalysts, with enhanced low-temperature DeNOx activity as In loading increased. Characterization results demonstrated that In species were highly dispersed without nanoparticle formation on the xIn/SSZ-39 catalysts prepared with different loadings (x = 1, 2, 3, x represents the In loadings of 1.0 wt%, 2.0 wt% and 3.0 wt%).

2 Experimental section

2.1 Materials and instruments

SSZ-39 molecular sieve with a Si/Al ratio of 11 was purchased from Dalian Zhongcaptor Molecular Sieve Factory; Indium nitrate tetrahydrate ($In(NO_3)_3$ $4H_2O$), analytically pure, was obtained from Aladdin Reagent; Analytically pure Cobalt nitrate hexahydrate ($Co(NO_3)_2$ $6H_2O$), Copper nitrate trihydrate ($Cu(NO_3)_2$ $3H_2O$) and Iron nitrate hydrate nine ($Fe(NO_3)_3$ $9H_2O$) were purchased from Tianjin Damao Reagent Factory.

Powder X-ray diffraction (XRD) patterns were recorded on a X′Pert PRO-type diffractometer (Panacor) with a nickel-filtered Cu Kα X-ray source at a scanning rate of 5°/min over the range of 5°–50°. N_2 adsorption-desorption isotherms were recorded at -196° C on a ASAP-2020-type physical adsorptive instrument. The sample (0.05–0.1 g) was degassed in a vacuum at 150 °C for 4 h prior to measurement. The Brunauer-Emmauer-Teller (BET) method was used to calculate the specific surface area of catalyst. The scanning electron microscopy (SEM) images were taken on a FEI-Verios 460L. Transmission electron microscopic (TEM) images were taken on a Tecnai G220 S-twin instrument (FEI Company) with an acceleration voltage of 200 kV. High-angle annular dark field-scanning transmission electron microscopy (HAADF-STEM) was carried out using a JEM-ARM200F instrument. Energy-dispersive X-ray spectroscopic (EDS) images were collected using a JED-2300T instrument. The H_2 temperature-programmed reduction (H_2-TPR) test was conducted on a AutoChem 2920-type chemisorptive instrument. The feeding gas of 10% H_2 + 90% Ar was fed into the reactor with 60 mL/min, and the H_2 intensity profiles were record from 50°C to 800° C at a heating rate of 10° C/min.

2.2 Preparation of catalysts

The In/SSZ-39 catalysts were prepared using the wet impregnation method with SSZ-39 molecular sieves as the carrier and $In(NO_3)_3$ $4H_2O$ as the indium source. Firstly, a suitable amount of $In(NO_3)_3$· $4H_2O$ was fully dissolved in deionized water. Then the SSZ-39 molecular sieve was added, and the mixture was agitated for 4 h at room temperature until the mixture slowly evaporated at 80° C. The obtained viscous sample was put into a blast drying oven at 120° C for 12 h. Subsequently, the sample was calcined at 550° C for 4 h with an increase rate of 5° C/min in a muffle furnace. The obtained catalysts were labeled as xIn/SSZ-39, where x represents the theoretical In loadings of 1.0 wt%, 2.0 wt%, and 3.0 wt%, respectively.

The xCo/SSZ-39, xCu/SSZ-39 and xFe/SSZ-39 catalysts were prepared using the same method as that of the xIn/SSZ-39 catalysts, except that $In(NO_3)_3$ $4H_2O$ was replaced by $Co(NO_3)_2$ $6H_2O$, $Cu(NO_3)_2$ $3H_2O$, and $Fe(NO_3)_3$ $9H_2O$, respectively, and x represents the theoretical metal loading 3.0 wt%.

2.3 Evaluation of the catalyst activities

Catalytic activity tests were conducted in a fixed-bed reactor at atmosphere pressure. A total of 0.75 mL catalyst with a particle size of 40–60 mesh was filled in a fixed-bed reactor with an inner diameter of 8 mm. The feed gas consisted of 0.1 vol% NO, 0.1 vol% CH_4, 6 vol% O_2 and balance N_2, with a GHSV of 8,000 h^{-1}. Before the measurement, the catalyst was pretreated at 400° C for 30 min under N_2 atmosphere to remove any adsorbed
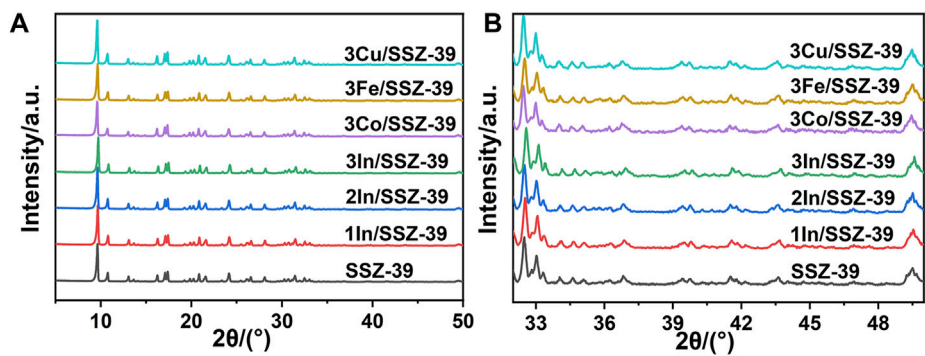
FIGURE 1
XRD patterns **(A)** and corresponding partial enlarged patterns **(B)** of different catalysts.

impurity gases and moisture on the catalyst. During tests, the steady-state outlet compositions (NO, NO$_2$, N$_2$O and CH$_4$ concentrations) at different reaction temperature (400, 450, 500°C and 550°C) were measured by an on-line infrared flue gas analyzer (MKS Instruments, Inc., 6030). The NO conversion rate, CH$_4$ conversion rate and CH$_4$ selectivity were calculated using Eqs 1–3, respectively, as shown below:

$$C_{NO} = \frac{\varnothing(NO)_{in} - \varnothing(NO)_{out} - \varnothing(NO_2)_{out}}{\varnothing(NO)_{in}} \times 100\% \quad (1)$$

$$C_{CH_4} = \frac{\varnothing(CH_4)_{in} - \varnothing(CH_4)_{out}}{\varnothing(CH_4)_{in}} \times 100\% \quad (2)$$

$$S_{CH_4} = \frac{\varnothing(NO)_{in} - \varnothing(NO)_{out} - \varnothing(NO_2)_{out}}{2[\varnothing(CH_4)_{in} - \varnothing(CH_4)_{out}]} \times 100\% \quad (3)$$

where C_{NO} and C_{CH_4} are the NO and CH$_4$ conversion rates, respectively. $\varnothing(NO)_{in}$, $\varnothing(NO)_{out}$, $\varnothing(CH_4)_{in}$ and $\varnothing(CH_4)_{out}$ are the concentrations of NO and CH$_4$ at the reactor inlet and outlet, respectively. $\varnothing(NO_2)_{out}$ is the NO$_2$ concentration at the reactor outlet. S_{CH_4} is the CH$_4$ selectivity.

3 Results and discussion

3.1 Characterization results of catalysts

Figure 1 presents the XRD spectra of M/SSZ-39 catalysts. A series of distinctive diffraction peaks at 2θ = 9°–11° and 2θ = 15°–18° are present in all samples, which are attributed to the typical AEI topology of SSZ-39 molecular sieves (Li et al., 2019; Du et al., 2023). The XRD spectra of M/SSZ-39 catalysts with different metals and different metal loadings do not change significantly, indicating that the loading of metals through the wet impregnation procedure does not affect the AEI topology of SSZ-39 molecular sieve. Figure 1B shows a localized enlarged XRD spectrum of Figure 1A, where no diffraction peaks of metal oxides are observed in all catalysts. This indicates that metal species exist as highly dispersed metal oxide clusters or ionic metal sites on SSZ-39 molecular sieve at higher metal loading. This phenomenon is attributed to the large specific surface area and regular cage structure of the small-pore SSZ-39 molecular sieve, which provides a lot of space and specific surface for dispersing metal species (Ren et al., 2011; Lim et al., 2020; Xu et al., 2022).
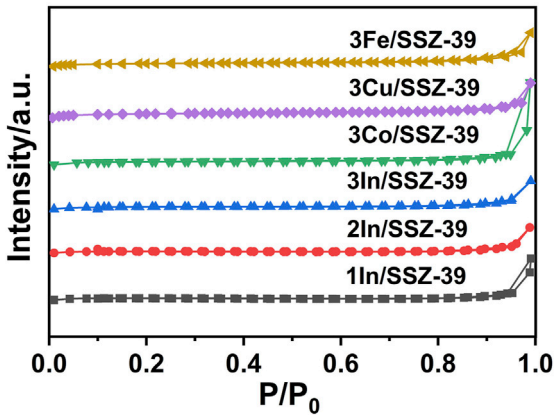

FIGURE 2
N$_2$ adsorption-desorption isotherms of different catalysts.

TABLE 1 Textual properties of differen catalysts.

Samples	S$_{BET}$ (m²/g)			Pore volume (cm³/g)	
	S$_{total}$[a]	S$_{micro}$[b]	S$_{ext}$[c]	V$_{total}$[d]	V$_{micro}$[d]
1In/SSZ-39	519.76	518.92	0.84	0.27	0.26
2In/SSZ-39	518.99	517.76	1.23	0.27	0.26
3In/SSZ-39	507.49	500.85	6.64	0.27	0.25
3Co/SSZ-39	523.15	518.16	4.99	0.27	0.26
3Cu/SSZ-39	502.72	495.54	7.18	0.27	0.25
3Fe/SSZ-39	506.35	500.18	6.17	0.27	0.25

[a]BET, surface area.
[b]t-plot micropore surface area.
[c]t-plot external surface area.
[d]t-plot micropore volume.

The textual properties of xIn/SSZ-39 catalysts were characterized by N$_2$ adsorption-desorption isotherms, as shown in Figure 2. All samples display type I adsorption isotherm
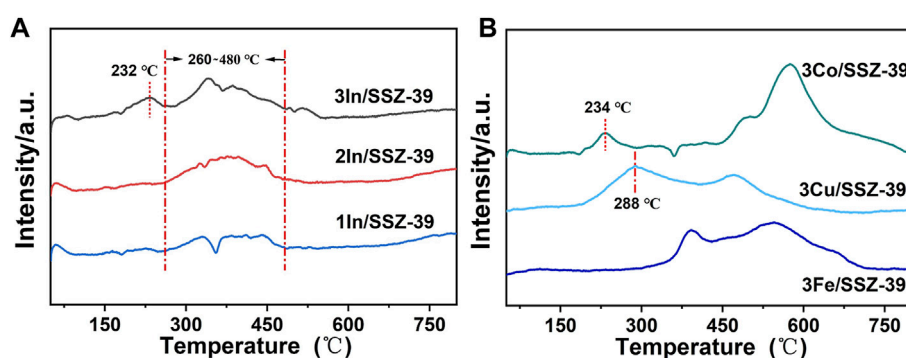
FIGURE 3
H2-TPR profiles of **(A)** xIn/SSZ-39 catalysts and **(B)** 3Co/SSZ-39, 3Cu/SSZ-39 and 3Fe/SSZ-39 catalysts.
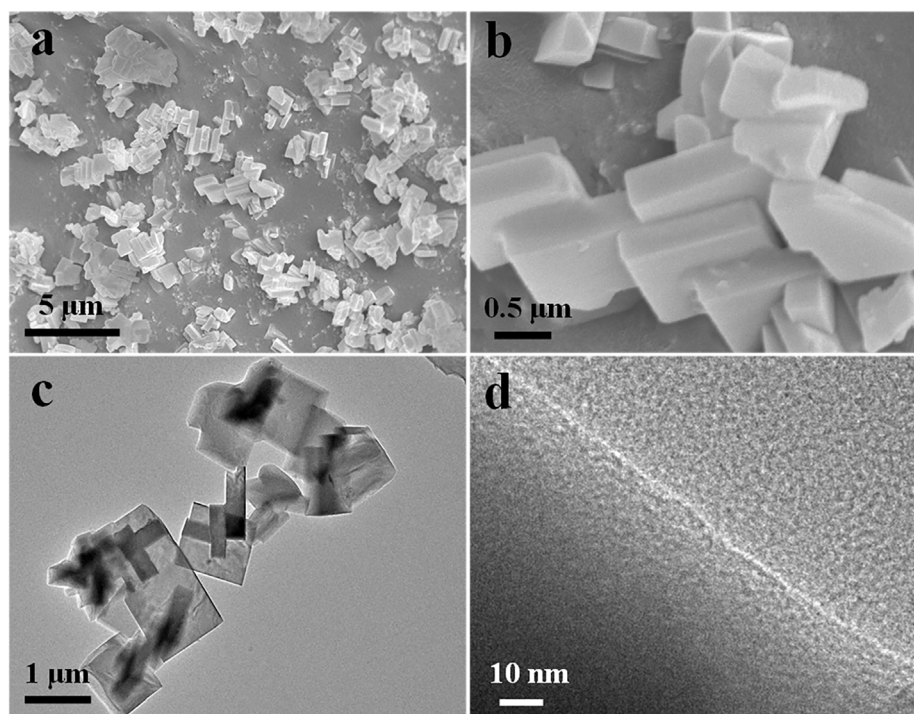

FIGURE 4
SEM **(A, B)**, TEM **(C)** and HRTEM **(D)** images of 3In/SSZ-39.

features, typical adsorption isotherm characteristics of microporous materials (Kruk et al., 2001). This is consistent with the uniform microporous nature of small-pore SSZ-39 molecular sieve. Table 1 shows the calculated textual properties of xIn/SSZ-39. With increasing In loading, all catalysts' specific surface areas only slightly decreased. Notably, the 1In/SSZ-39 and 2In/SSZ-39 catalysts exhibit nearly identical microporous specific surface area, exterior specific surface area, and microporous pore volume. This demonstrates that the In species are able to maintain a high degree of dispersion and do not obstruct the microporous pores of SSZ-39 when the loading of In is controlled to be no more than 2 wt%. When the In loading is increased to 3 wt%, the microporous specific surface area of 3In/SSZ-39 catalyst begins to decrease slightly, while its external specific surface area

became significantly larger. This may be attributed to the formation of highly dispersed InOx clusters on the external surface of SSZ-39, which increases the external specific surface area of 3In/SSZ-39 catalyst (no InOx nanoparticles were observed in the TEM images). The specific surface area of 3Co/SSZ-39, 3Cu/SSZ-39, and 3Fe/SSZ-39 catalysts are similar to that of In/SSZ-39 catalyst. It indicates that these metal species (Co, Cu and Fe) are also highly dispersed on SSZ-39.

The redox properties of catalyst are crucial for CH_4-SCR activity, therefore, H_2-TPR characterization was carried out to investigate the reducibility of metal oxide species in catalysts, as shown in Figure 3. In Figure 3A, it can be observed that the H_2-TPR spectra of all In/SSZ-39 catalysts display broad reduction signals between 260°C and

FIGURE 5
HAADF-STEM image and corresponding element mappings of 3In/SSZ-39.
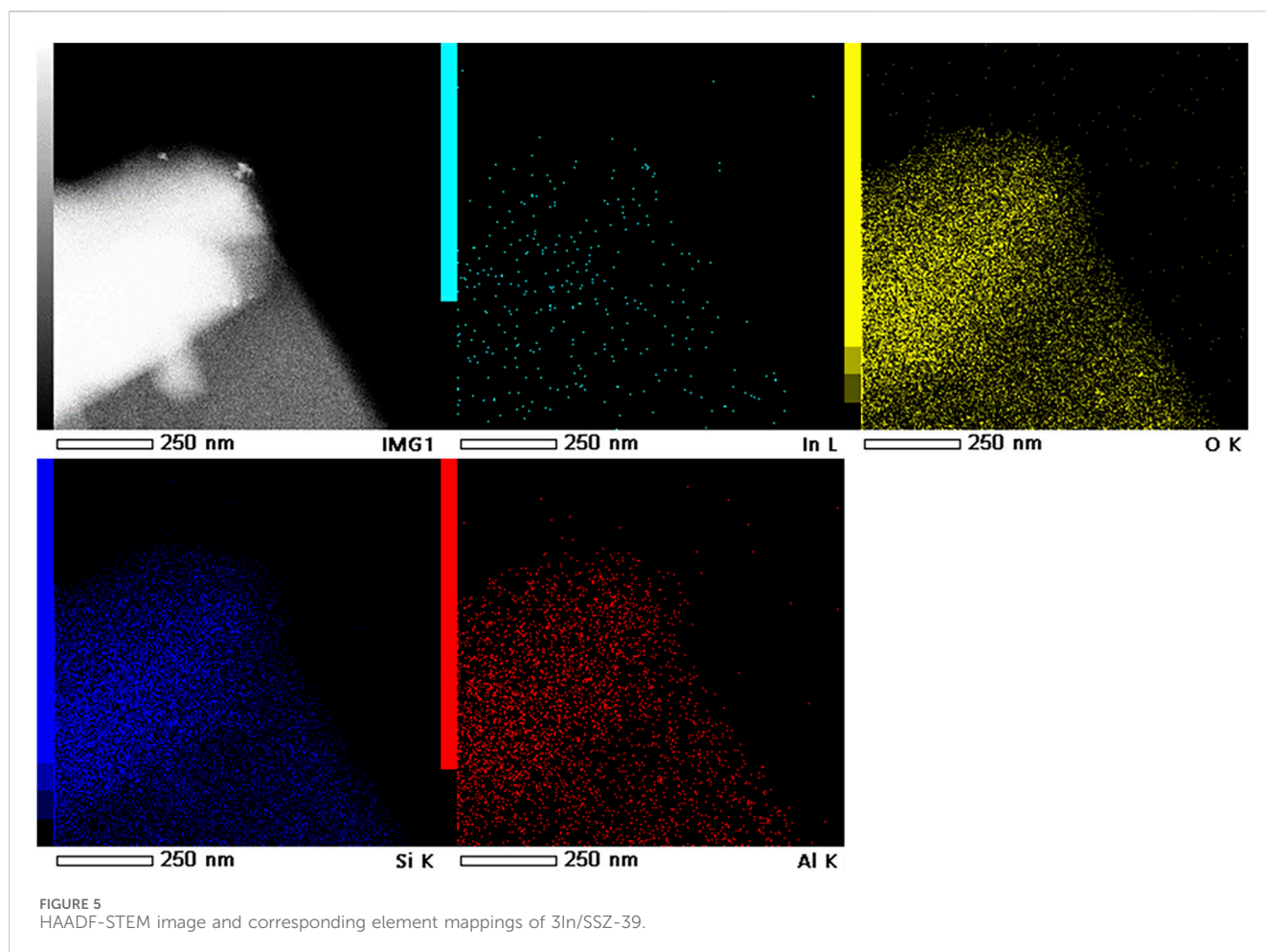
480° C, which are attributed to the reduction of InOx species to In⁺ sites (Yoo et al., 2015; Zhao et al., 2023). Moreover, the primary reduction peaks of three catalysts are almost located in the same positions, centered at 260°C–480° C, without shifting to lower or higher temperature regions. This demonstrates that the forms of the major InOx species in catalysts are essentially the same. The H_2 consumption gradually increased as In loading increased, corresponding to the increased area of the major reduction peaks in xIn/SSZ-39 catalysts. Remarkably, a notable reduction peak centered at a lower temperature of only ~232 °C appeared in the H_2-TPR profile of 3In/SSZ-39 catalyst, suggesting the better reducibility of highly dispersed InOx species. This phenomenon can be attributed to the formation of highly dispersed InOx clusters on the external surface of SSZ-39 resulting from the increased In loading, as corroborated by the N_2 physical adsorption-desorption test. This fraction of the InOx species exhibits better reducibility as it is not constrained by the pores or cavities of SSZ-39, which is essential for the moderate activation of CH_4 and contributes significantly to the enhancement of low-temperature CH_4-SCR performance (Yoo et al., 2015; Zhao et al., 2023).

In Figure 3B, the 3Co/SSZ-39, 3Cu/SSZ-39 and 3Fe/SSZ-39 catalysts display a significantly different H_2-TPR spectrum compared to the 3In/SSZ-39 catalyst. A primary reduction peak is located at a lower temperature of 288° C in 3Cu/SSZ-39 catalyst which is much lower than that of 3Co/SSZ-39, 3Fe/SSZ-39 and 3In/SSZ-39 catalysts, suggesting the good reducibility of major CuOx

species. This is conducive to activating CH_4 at low-temperatures. However, the major CuOx species, with good reducibility, also facilitates the non-selective catalytic combustion reaction, may leading to very low N_2 selectivity of 3Cu/SSZ-39 catalyst. In the H_2-TPR spectrum of 3Fe/SSZ-39 catalyst, there are not any reduction peaks located at lower temperatures can be observed, and the major reduction peaks are almost located at higher temperatures between 375°C and 700° C. The results suggest that FeOx species are not conducive to the activation of CH_4 at low temperatures. For 3Co/SSZ-39 catalysts, a small reduction peak centered at 234 °C appeared in the H_2-TPR profile similar to that of 3In/SSZ-39. But, the major reduction peak located at higher temperatures between 450°C and 700° C which are much higher than that (260°C–480° C) of 3In/SSZ-39 catalysts. In the H_2-TPR spectrum of 3In/SSZ-39 catalyst, a small reduction peak located at lower temperature of 232° C and a major reduction peak located at medium temperature of 342° C are observed, indicating the moderate reducibility of highly dispersed InOx species. Compared to the 3Co/SSZ-39, 3Cu/SSZ-39 and 3Fe/SSZ-39 catalysts, the InOx species in 3In/SSZ-39 catalyst, with moderate reducibility, may promote the moderate activation of CH_4 and enhance the CH_4-SCR activity at low temperatures.

Figures 4A,B depict the SEM images of 3In/SSZ-39 catalyst, revealing typical zeolite particles with a regular and smooth hexahedral structure, and no nanoparticles are observed on the
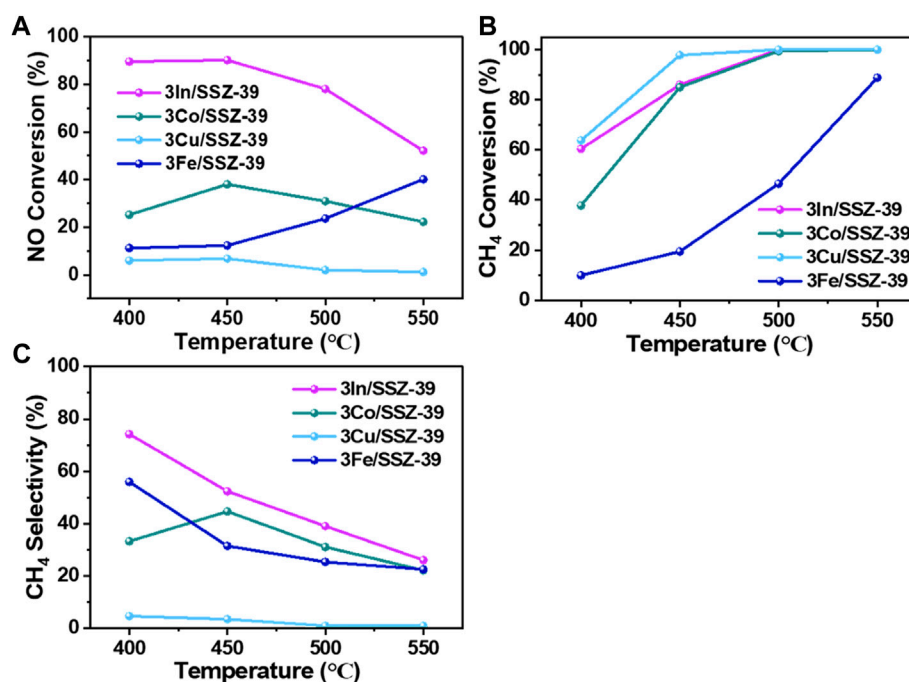
FIGURE 6
NO conversion rates **(A)**, CH_4 conversion rates **(B)** and CH_4 selectivities **(C)** as a function of temperatures in CH_4-SCR over 3In/SSZ-39, 3Co/SSZ-39, 3Cu/SSZ-39 and 3Fe/SSZ-39 catalysts (NO/CH_4 = 1).

surface of the smooth hexahedral structure. Further, TEM and EDS characterizations were conducted to examine the dispersion form of InOx species on SSZ-39 molecular sieve, as shown in Figure 4C, 4days and Figure 5. The basic hexahedral structure of SSZ-39 remains intact, consistent with the SEM results. Figure 4D presents the high-resolution TEM image of 3In/SSZ-39 catalyst, where no distinct InOx nanoparticles were observed, aligning with the XRD results. The combination of N_2 physical adsorption-desorption tests and H_2-TPR characterizations strongly indicates that the InOx species are highly dispersed on the SSZ-39 molecular sieve, possibly existing in the form of InOx clusters or In^+ sites, and do not aggregate to form nanoparticles. This hypothesis is further supported by the EDS characterization, which shows that no InOx nanoparticles are generated since the In elements are extremely uniformly dispersed in SSZ-39 molecular sieves (Figure 5).

3.2 CH_4-SCR performance of catalysts

The CH_4-SCR performance of M/SSZ-39 catalysts (40–60 mesh) was tested in a fixed-bed reactor at 400°C–550° C, using a feed gas composed of 0.1 vol% NO, 0.1 vol% CH_4, 6 vol% O_2 and the balance N_2 with a GHSV of 8,000 h^{-1}. Initially, the effects of different metal components on the performance of catalysts for CH_4-SCR were investigated. Figure 6A displays the temperature-dependent NO conversion curves of 3In/SSZ-39, 3Co/SSZ-39, 3Cu/SSZ-39, and 3Fe/SSZ-39 catalysts. It is evident that the activities of catalysts follow the order: In > Co > Fe > Cu when the reaction temperature is below 530° C. Notably, the 3In/SSZ-39 catalyst exhibits significant performance compared to the 3Co, 3Cu, and 3Fe/SSZ-39 catalysts,

underscoring the significance of In as an active component in catalyzing the selective catalytic reduction of NOx by CH_4 (Zhao et al., 2023). As indicated by the H_2-TPR results, compared to the 3Co/SSZ-39, 3Cu/SSZ-39 and 3Fe/SSZ-39 catalysts, the highly dispersed InOx species in 3In/SSZ-39 catalyst, with moderate reducibility, can promote the moderate activation of CH_4 and enhance the SCR process at low temperatures. Therefore, the 3In/SSZ-39 catalyst exhibits excellent CH_4-SCR activity and good CH_4 selectivity, achieving a high NO conversion rate over 90% at lower temperatures (400°C–450° C) and a lower CH_4/NO feed ratios (CH_4/NO = 1/1).

The NO conversion rate of 3In/SSZ-39 catalyst remains almost unchanged at 90% (Figure 6A) as the reaction temperature is increased from 400°C to 450 °C. However, as shown in Figure 6B, the CH_4 conversion rate increased from 60% to 86%. This suggests that 26% of the converted CH_4 undergoes non-selective catalytic combustion rather than a selective reduction of NOx, demonstrating that the 3In/SSZ-39 catalyst achieves the highest CH_4 selectivity and NO conversion rate at 400 °C, as depicted in Figure 6C. In contrast, compared to NO conversion rates, the CH_4 conversion rates of the 3Co/SSZ-39 and 3Cu/SSZ-39 catalysts are significantly higher, suggesting that the Co and Cu components are more prone to catalyzing the CH_4 combustion reaction, leading to lower CH_4 selectivity, as illustrated in Figure 6C. As for the 3Fe/SSZ-39 catalyst, both lower NO and CH_4 conversion rates are achieved, indicating that the Fe component is less effective in catalyzing CH_4 catalytic combustion and CH_4-SCR reaction. In conclusion, the types of metal components can be tuned to control the competition between CH_4 non-selective catalytic combustion and CH_4-SCR reactions.
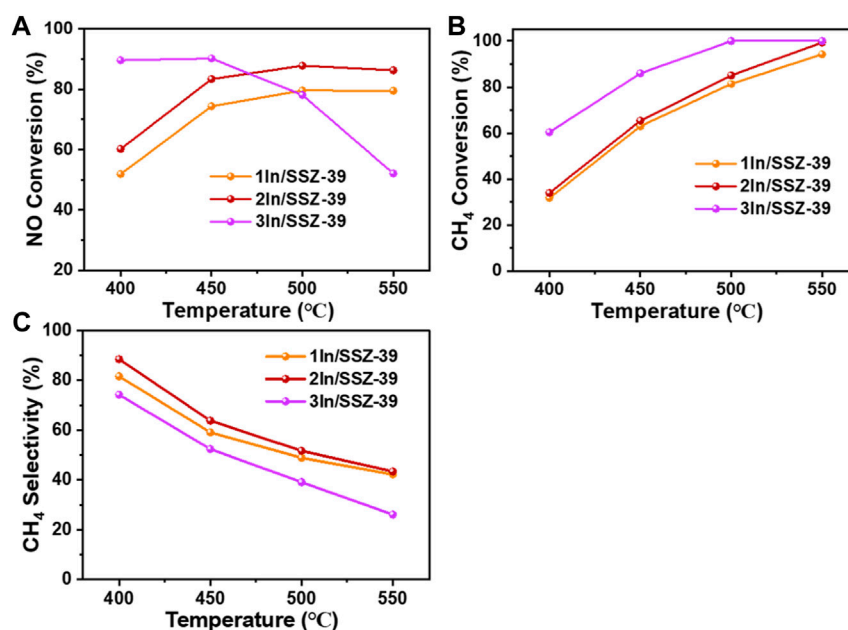
FIGURE 7
NO conversion rates **(A)** CH_4 conversion rates **(B)** and CH_4 selectivities **(C)** as a function of temperatures in CH_4-SCR over 1In/SSZ-39, 2In/SSZ-39 and 3In/SSZ-39 catalysts (NO/CH_4 = 1).

For the xIn/SSZ-39 catalysts with superior CH_4-SCR performance, the impact of various In loadings on the catalytic performance was further investigated, as shown in Figure 7. It is evident that both the NO and CH_4 conversion rates of catalysts increase with temperature when the in loading is less than 2 wt%, corresponding to their high CH_4 selectivity, as illustrated in Figure 7C. Among these, the 2In/SSZ-39 catalyst exhibits a 60% NO conversion rate and a 34% CH_4 conversion rate at 400° C, indicating that the ratio of converted NO to CH_4 molecules is close to 2, which is the theoretical NO/CH_4 ratio when a reaction proceeds in accordance with the stoichiometric ratio. This demonstrates that the 2In/SSZ-39 catalyst can achieve a very high CH_4 selectivity (up to 88.5%) at 400°C, as shown in Figure 7C. For the 3In/SSZ-39 catalyst, it is NO conversion rate decreases rapidly as the temperature raised from 450°C to 550° C, indicating a rapid decrease in CH_4 selectivity as well. This can be attributed to the presence of highly dispersed InOx clusters on the external surface of SSZ-39 (as indicated by H_2-TPR results). These clusters exhibit the best reducibility (low-temperature reduction peak of only ~232° C), which promote the moderate activation of CH_4 and enhance the CH_4-SCR activity at low temperatures. However, at higher temperatures, these highly active InOx clusters can lead to over-activation of CH_4, which increases the likelihood of converted CH_4 undergoing a non-selective catalytic combustion reaction and thus reducing the CH_4 selectivity.

4 Conclusion

In this paper, a series of M/SSZ-39 catalysts (M = In, Co, Cu, Fe) were prepared using the wet impregnation method on a small-pore SSZ-39 molecular sieve. The effects of different metal loadings and metal loadings on the performance of CH_4-SCR were investigated. The characterization results revealed that the performance of In/SSZ-39 catalysts are significantly higher than that of the Cu-, Co-, and Fe/SSZ-39 catalysts, indicating that indium (In) is a more suitable active ingredient for the CH_4-SCR reaction. The low-temperature CH_4-SCR activity of catalysts is notably enhanced with increasing In loadings. Among them, the 3In/SSZ-39 catalyst exhibits a high NO conversion rate of up to 90% and a CH_4 selectivity of up to 74.2% at a reaction temperature of 400 °C and a low CH_4/NO feed ratio (CH_4/NO = 1). TEM and EDS characterization results showed that the In species were highly dispersed on the SSZ-39 molecular sieves, greatly promoting the moderate activation of CH_4 and enhancing the CH_4-SCR activity at low temperatures. These findings demonstrate a potentially generalizable approach toward the design and synthesis of high-efficiency CH_4-SCR catalyst.

Data availability statement

The original contributions presented in the study are included in the article/Supplementary Material, further inquiries can be directed to the corresponding authors.

Author contributions

SA: Data curation, Investigation, Writing–original draft, Writing–review and editing. PW: Formal Analysis,

Writing–review and editing. KW: Formal Analysis, Writing–review and editing. XW: Writing–review and editing. BL: Writing–review and editing. XG: Funding acquisition, Project administration, Writing–review and editing.

Conflict of interest

The authors declare that the research was conducted in the absence of any commercial or financial relationships that could be construed as a potential conflict of interest.

Publisher's note

All claims expressed in this article are solely those of the authors and do not necessarily represent those of their affiliated organizations, or those of the publisher, the editors and the reviewers. Any product that may be evaluated in this article, or claim that may be made by its manufacturer, is not guaranteed or endorsed by the publisher.

References

Campa, M. C., Doyle, A. M., and Fierro, G. (2021). Pietrogiacomi D., Simultaneous abatement of NO and N_2O with CH_4 over modified Al_2O_3 supported Pt, Pd, Rh. *Catal. Today.* 384-386, 76–87. doi:10.1016/j.cattod.2021.06.020

Campa, M. C., Pietrogiacomi, D., and Occhiuzzi, M. (2015). The simultaneous selective catalytic reduction of N_2O and NOx with CH_4 on Co- and Ni-exchanged mordenite. *Appl. Catal. B Environ.* 168–169, 293–302. doi:10.1016/j.apcatb.2014.12.040

Chen, S. W., Yan, X. L., Wang, Y., Chen, J. Q., Pan, D. H., Ma, J. H., et al. (2011). Effect of SO_2 on Co sites for NO-SCR by CH_4 over Co-Beta. *Catal. Today.* 175 (1), 12–17. doi:10.1016/j.cattod.2011.05.024

Chen, X. M., Zhu, A. M., Au, C., and Shi, C. (2011). Enhanced low-temperature activity of Ag-promoted Co-ZSM-5 for the CH_4-SCR of NO. *Catal. Lett.* 14, 207–212. doi:10.1007/s10562-010-0435-8

Chupin, C., van Veen, A. C., Konduru, M., Després, J., and Mirodatos, C. (2006). Identity and location of active species for NO reduction by CH_4 over Co-ZSM-5. *J. Catal.* 241 (1), 103–114. doi:10.1016/j.jcat.2006.04.025

Costilla, I. O., Sanchez, M. D., Volpe, M. A., and Gigola, C. E. (2011). Ce effect on the selective catalytic reduction of NO with CH_4 on Pd-mordenite in the presence of O_2 and H_2O. *Catal. Today.* 172 (1), 84–89. doi:10.1016/j.cattod.2011.03.025

Du, J., Han, S., Huang, C., Shan, Y., Zhang, Y., Shan, W., et al. (2023). Comparison of precursors for the synthesis of Cu-SSZ-39 zeolite catalysts for NH_3-SCR reaction. *Appl. Catal. B Environ.* 338, 123072. doi:10.1016/j.apcatb.2023.123072

Han, L. P., Cai, S. X., Gao, M., Hasegawa, J., Wang, P., Zhang, J., et al. (2019). Selective catalytic reduction of NOx with NH_3 by using novel catalysts: state of the art and future prospects. *Chem. Rev.* 119 (19), 10916–10976.

Huang, F. J., Hu, W., Chen, J. J., Wu, Y., Qu, P. F., Yuan, S., et al. (2018). Insight into enhancement of NO reduction with methane by multifunctional catalysis over a mixture of Ce/HZSM-5 and $CoO_{<i>x</i>}$ in excess of oxygen. *Ind. Eng. Chem. Res.* 57 (40), 13312–13317. doi:10.1021/acs.iecr.8b00773

Jin, G. H., Li, J. H., Yang, D., and Hao, J. M. (2009). Progress of selective catalytic reduction of NOx with methane over zeolite-based catalysts. *Chem. Ind. Eng. Prog.* 28 (3), 504–510.

Kruk, M., and Jaroniec, M. (2001). Gas adsorption characterization of ordered organic-inorganic nanocomposite materials. *Chem. Mater.* 13 (10), 3169–3183. doi:10.1021/cm0101069

Kubacka, A., Janas, J., and Sulikowski, B. (2006). In/Co-Ferrierite: a highly active catalyst for the CH_4-SCR no process under presence of steam. *Appl. Catal. B Environ.* 69 (1), 43–48. doi:10.1016/j.apcatb.2006.05.014

Lee, T. J., Nam, I. S., Ham, S. W., Baek, Y. S., and Shin, K. H. (2003). Effect of Pd on the water tolerance of Co-ferrierite catalyst for NO reduction by CH_4. *Appl. Catal. B Environ.* 41 (1), 115–127. doi:10.1016/s0926-3373(02)00197-2

Li, G., Jiao, F., Miao, D., Wang, Y., Pan, X., Yokoi, T., et al. (2019). Selective conversion of syngas to propane over ZnCrO -SSZ-39 OX-ZEO catalysts. *J. Energy Chem.* 36, 141–147. doi:10.1016/j.jechem.2019.07.006

Lim, J. B., Shin, J., Ahn, N. H., Heo, I., and Hong, S. B. (2020). Selective catalytic reduction of NO with CH_4 over cobalt-exchanged cage based, small-pore zeolites with different framework structures. *Appl. Catal. B Environ.* 267, 118710. doi:10.1016/j.apcatb.2020.118710

Martin, J., Avila, P., Suarez, S., Yates, M., Martinrojo, A., Barthelemy, C., et al. (2006). Influence of support acid pretreatment on the behaviour of $CoOx/\gamma$-alumina monolithic catalysts in the CH_4-SCR reaction. *Appl. Catal. B Environ.* 67 (3-4), 270–278. doi:10.1016/j.apcatb.2006.05.010

Mrad, R., Aissat, A., Cousin, R., Courcot, D., and Siffert, S. (2015). Catalysts for NOx selective catalytic reduction by hydrocarbons (HC-SCR). *Appl. Catal. A Gen.* 504, 542–548. doi:10.1016/j.apcata.2014.10.021

Ren, L., Zhu, L., Yang, C., Chen, Y., Sun, Q., Zhang, H., et al. (2011). Designed copper-amine complex as an efficient template for one-pot synthesis of Cu-SSZ-13 zeolite with excellent activity for selective catalytic reduction of NOx by NH_3. *Chem. Commun.* 47 (35), 9789–9791. doi:10.1039/c1cc12469b

Sazama, P., Pilar, R., Mokrzycki, L., Vondrova, A., Kaucky, D., Plsek, J., et al. (2016). Remarkably enhanced density and specific activity of active sites in Al-rich Cu-Fe-and Co-beta zeolites for selective catalytic reduction of NOx. *Appl. Catal. B Environ.* 189, 65–74. doi:10.1016/j.apcatb.2016.02.020

Shi, C., Cheng, M. J., Qu, Z. P., and Bao, X. H. (2004). Investigation on the catalytic roles of silver species in the selective catalytic reduction of NO with methane. *Appl. Catal. B-Environ.* 51, 171–181. doi:10.1016/j.apcatb.2003.12.003

Wang, C., Wang, J., Wang, J., Yu, T., Shen, M., Wang, W., et al. (2017). The effect of sulfate species on the activity of NH_3-SCR over Cu/SAPO-34. *Appl. Catal. B Environ.* 204, 239–249. doi:10.1016/j.apcatb.2016.11.033

Wang, X. F., Zhao, Z., Xu, Y., and Li, Q. B. (2021). Promoting effect of Ti addition on three-dimensionally ordered macroporous Mn-Ce catalysts for NH_3-SCR reaction: enhanced N_2 selectivity and remarkable water resistance. *Appl. Surf. Sci.* 569, 151047. doi:10.1016/j.apsusc.2021.151047

Wen, N. N., Lin, R., Su, Y. X., Deng, W. Y., Zhou, H., and Zhao, B. T. (2021). SCR of NO with CH_4 over Fe/Ga_2O_3-Al_2O_3 and the mechanism. *J. Environ. Chem. Eng.* 9 (1), 105014. doi:10.1016/j.jece.2020.105014

Xu, Y., Wang, X. F., Qin, M. Y., and Li, Q. B. (2022). Selective catalytic reduction of NOx with CH_4 over zeolite catalysts: research progress, challenges and perspectives. *J. Environ. Chem. Eng.* 10 (2), 107270. doi:10.1016/j.jece.2022.107270

Yoo, J. S., Khan, T. S., Abild-Pedersen, F., Nørskov, J. K., and Studt, F. (2015). On the role of the surface oxygen species during A-H (A =C, N, O) bond activation: a density functional theory study. *Chem. Commun.* 51, 2621–2624. doi:10.1039/c4cc08658a

Zhao, J. H., Li, H. Y., Wang, Y. G., Zhu, R. S., Sun, S. L., Zhang, J. G., et al. (2023). Desilication tuning of In/Hβ catalysts for sulfur- and steam-resistant CH_4-SCR of NO. *Catal. Commun.* 175, 106619. doi:10.1016/j.catcom.2023.106619

Frontiers in
Chemistry

Explores all fields of chemical science across the periodic table

Advances our understanding of how atoms, ions, and molecules come together and come apart. It explores the role of chemistry in our everyday lives - from electronic devices to health and wellbeing.

Discover the latest Research Topics

See more →

frontiers | Research Topics